Aix-Marseille Université

THÈSE

presentée pour obtenir le titre de
DOCTEUR
d'Aix-Marseille Université

Ecole doctorale : Sciences pour l'ingénieur
Laboratoire : Mécanique, Modélisation et Procédés Propres (M2P2)
Unité de recherche : CERFACS
Spécialité : Mécanique des Fluides

par

Florian Renard

Hybrid Lattice Boltzmann Method for Compressible Flows

---

soutenue le 19/03/2021 devant le jury composé de :

Pierre Sagaut	Aix-Marseille Université	Directeur
Jean-François Boussuge	CERFACS	Co-directeur
Jonas Latt	Université de Genève	Rapporteur
Paola Cinnella	Sorbonne Université	Rapporteur
Rémi Abgrall	Université de Zurich	Examinateur
Alois Sengissen	Airbus	Invité
Romain Pain	Safran Tech	Invité

Remerciements

Pour commencer, je tiens à remercier les rapporteurs qui ont pris le temps de lire et d'évaluer ce manuscrit. Merci à l'examinateur et aux invités d'avoir participé et animé (à distance) la soutenance de thèse et d'avoir soulevé des questions pertinentes et constructives. Je regrette seulement que la discussion ne se soit pas prolongée de manière moins formelle autour d'un pot de thèse, la faute aux circonstances de l'époque [1].

J'aimerais ensuite remercier mes encadrants Jean-François et Pierre pour leurs suivis et conseils avisés pendant la thèse. Merci d'avoir misé sur moi, pour la confiance et la liberté que vous m'avez accordé, ce qui m'a permis de travailler et d'évoluer avec autonomie. J'exprime aussi ma profonde reconnaissance à Airbus et Safran-Tech d'avoir financé cette thèse au sein du CERFACS. Je remercie tout particulièrement Alois, pour son intérêt pour mes travaux, pour les formations dont j'ai pu profiter, les ressources qu'il a mises à disposition et pour son accueil à chaque fois chaleureux sur le site d'Airbus. Merci à toutes les personnes côté CS, Renault et M2P2 pour leurs échanges constructifs lors des points "gaz parfait" et "haut Mach" et en particulier merci à Yongliang qui, au travers de nos échanges, m'a aidé de façon significative à mieux comprendre le socle des méthodes compressibles hybrides.

Du côté CERFACS, je remercie chaleureusement l'équipe admin : Michelle, Marie, Lydia et Chantal pour leur super travail, leur bienveillance et leur bonne humeur, ainsi que l'équipe CSG : Fred, Isabelle, Gérard, Fabrice, Patrick pour leur redoutable efficacité à régler les problèmes informatiques, mais aussi pour les nombreuses choses que j'ai pu apprendre lors de diverses discussions et formations. Je remercie également les stagiaires, doctorants, post-doctorants et seniors de l'équipe CFD (dont je faisais partie), pour les nombreuses discussions et moments passés en pause-café. Je pense particulièrement à Maxime et ses gâteaux du mercredi matin, Laurent pour ses discussions du midi à s'en fendre les tympans, Minh pour ses inestimables relectures d'anglais, JF pour ses blagues graveleuses, Thomas M. pour ses goûts musicaux, mais aussi à tous les autres Thomas (×7), Paul, Johan, PAM, Quentin, Pamphile, Dominik, Guillaume, Robin, Alexia, Rémi, Matthieu, Valentin, Lucien,...

Toujours du côté du CERFACS, comment ne pas rendre grâce à notre team "LBM" (L3B5M6, comprenne qui pourra) initialement composée de : Totof, Wiscot, Tastoulette, Bastibilly et Danish [2]. Au-delà de simples collègues, ce sont de réels amis que j'ai rencontré pendant cette thèse car comme dirait Shurik'n du groupe IAM : "Devant l'adversité, les coudes se soudent". Vous m'avez donné support et réconfort pendant les moments difficiles, que ce soit par le biais d'explications papier crayons ou avec un verre au bar, ou bien avec les deux en même temps. Merci Totof pour avoir ouvert la voix

[1] Je ne remercie donc pas la pandémie de Sars-Cov2 qui nous aura bien brisé les alibofi...

[2] Christophe Coreixas, Gauthier Wissocq, Thomas Astoul, Bastien Rochette et Danny Lewis

du compressible au CERFACS et pour tes précieuses explications en début de thèse [3]. Merci Wiscott pour les nombreuses discussions autour de la LBM, ton aide inestimable et tes supers frites maison post soirée sous fond d'installation de Civ V à 4h du mat. Merci Tastoul (le démon) de m'avoir tiré un nombre incalculable de fois de la grosse déprime qui me guettait en me proposant une "p'tite session kite" (et merci de m'y avoir initié), merci pour les soirées et les cointreau flambés qui resteront gravés à jamais dans ma main. Merci Bastibilly d'avoir partagé le bureau avec moi pendant ces trois années, merci pour les délires, les fous rires et d'avoir partagé, parfois bien malgré toi, les "snif snif". Et bien sûr, je "n'oublierai pas" de remercier Danish pour ses talents de trompettiste proufechioneil (je n'ai jamais vu quelqu'un tenir une note aussi longtemps). Bref, merci à vous les copains, et merci à vos formidables moitiés : Mai et ses talents d'entremetteuse lors de ses soirées endiablées, Laura pour ses tartes pomme-camembert et Adélie pour ses gougères, sa gentillesse et sa joie de vivre.

Je tiens maintenant à remercier tous les membres du groupe KSC "étendu" composé en outre de Tastoulette, Bastibilly et Mai, mais aussi de : Lucky-Luc (je suis ton père), Adélita de la pampa *alias* la marmotte (non)matinale, le gros Romain et ses pétoles chroniques, Cricri le cranteur précoce, Dave l'écrevisse pédestre, la ptite Gigi connue aussi sous le nom de Hilda, Yann et ses éternel Slingshot Rally, Eloi le DJ fou (j'espère que tu trouveras enfin ton support gopro pour trou de nez) et enfin Louise pour ses master class de "yoga gueule de bois". Entre weekends-kite, RTTs-kite et voyages-kite (Maroc, Espagne, Portugal, Colombie), la liste des 'king of the air', crashs, cuites, délires et moments inoubliables en tout genre est longue...

Je remercie maintenant tous mes amis de Marseille de longue date : Victor, Mathias, Titou, Sandro, Léa, Timothé, Camille et Loïs ainsi que les potos de la licence et master, Seb, Renat, Laeticia, Mat, Aurore, Keshav, Boris, et tous les autres. J'espère revenir bientôt dans la région pour passer un peu plus de temps avec vous.

Enfin, je remercie ma famille pour leur soutien indéfectible et pour m'avoir permis d'arriver où j'en suis aujourd'hui. Merci à mon père, ma mère sans qui je ne serais pas là (au sens littéral), et grâce à qui je n'ai jamais manqué de rien. Un cadre idéal avec le bateau, les calanques, la planche à voile, la mer et pour couronner le tout un grand frère un peu relou mais sympa quand même. Merci à ma grand-mère, pour son accueil dans les Alpes pour la dernière ligne droite de rédaction et j'adresse aussi une énorme pensée à mon grand-père. Ces derniers remerciements sont adressés à mon Octavie, merci pour ta présence, ta confiance et ton support quotidien même pendant les moments difficiles de cette aventure, et dieu sait qu'ils ont été nombreux.

[3] Par contre, je ne te remercie pas pour le shooter épicé "****** blaster" servi en début de thèse.

Résumé

Ces dernières années, les méthodes de simulations numériques appliquées à la mécanique des fluides sont devenues des outils indispensables pour l'industrie aéronautique. Ces méthodes sont utilisées de concert avec les approches expérimentales. Elles permettent, par exemple, d'avoir une compréhension précise d'un écoulement pour développer et dimensionner un composant d'avion. Ainsi, ces méthodes sont sans cesse améliorées pour restituer plus fidèlement la physique des écoulements simulés. Grâce à son coup de calcul réduit, sa facilité d'implémentation et d'utilisation, la méthode de Boltzmann sur réseau (LBM) s'est peu à peu imposée comme une solution alternative aux méthodes numériques traditionnelles. De plus, cette méthode possède les avantages d'être intrinsèquement instationnaire et est parfaitement adaptée aux géométries complexes. Malheureusement, sous sa forme standard, elle reste limitée à la simulation d'écoulements isothermes et faiblement compressibles, ce qui écarte de nombreuses applications aéronautiques. Néanmoins, des variantes compressibles existent. Parmi les plus prometteuses, on peut trouver la méthode hybride (HLBM) qui utilise la LBM pour calculer les équations de la masse et de la quantité de mouvement et un schéma aux différences finies pour calculer l'équation d'énergie. Cette thèse se consacre au développement et à l'étude de méthodes hybrides pour la simulation d'écoulements compressibles.

Tout d'abord, la LBM standard et ses limitations sont présentées ainsi qu'une étude bibliographique exhaustive sur ses variantes compressibles. Ensuite, les composants et le fonctionnement général de la méthode hybride sont montrés. Un modèle simple utilisant l'approximation de Boussinesq est développé et testé avec succès. Cependant, son extension naïve aux équations compressibles est trouvée numériquement instable à cause du couplage gaz parfait, et de la nature instable de la LBM à hauts nombres de Mach.

Ces deux problèmes sont par la suite résolus en adoptant un opérateur de collision plus robuste pour la LBM et une équation d'entropie pour la partie énergie. Un modèle hybride compressible stable, basé sur un réseau de vitesse discrète standard D2Q9, est ainsi obtenu et validé sur des cas tests subsoniques et supersoniques comprenant des ondes de choc. Néanmoins, pour la simulation d'ondes de choc fortes, le modèle montre des problèmes de conservativité. Ces derniers sont essentiellement attribués à l'utilisation de l'équation d'entropie qui est non-conservative. Des solutions sont par la suite proposées.

Ensuite, la stabilité et les propriétés spectrales des schémas HLBM sont étudiées grâce à l'approche de von Neumann. Cette étude met en exergue l'effet de nombreux paramètres sur la stabilité numérique tels que le modèle de collision, le choix de l'équation d'énergie ou encore l'influence de paramètres numériques comme le nombre CFL. Les mécanismes d'instabilités et les méthodes de stabilisation sont montrés, confirmant par la même occasion le gain en stabilité des modèles basés sur une équation d'entropie. Par ailleurs, grâce à une analyse plus approfondie, cette étude permet d'expliquer les comportements non-physiques observés de certains modèles en les attribuant à des transferts de mode.

Finalement, la méthode hybride est implémentée dans le code LBM industriel ProLB. Elle est ensuite testée sur des cas tests compressibles subsoniques et supersoniques tridimensionnels contenant des conditions limites et des raffinements de maillages.

Abstract

In recent years, computational fluid dynamic (CFD) methods have become essential for the aeronautics industry. These methods are used in conjunction with experimental approaches. They allow, for example, to have a precise understanding of a flow in order to help the design of aircraft components. Thus, these methods are constantly being improved to accurately reproduce the physics of simulated flows. Thanks to its reduced computational cost, its ease of implementation and use, the lattice Boltzmann method (LBM) has gradually emerged as an alternative approach to traditional numerical methods. In addition to its efficiency, this method has the advantages of being inherently unsteady and is perfectly adapted to complex geometries. Unfortunately, in its standard form, it remains limited to the simulation of isothermal and weakly compressible flows, which excludes many aeronautical applications. Nevertheless, compressible versions of this method do exist. Among the most promising ones, one can find the Hybrid method (HLBM) which uses the LBM to compute the mass and momentum equations and a finite difference scheme to computed the energy equation. This thesis focuses on the development and study of hybrid methods for the simulation of compressible flows.

First, the standard LBM and its limitations are presented as well as an exhaustive bibliographical study of its compressible versions. Then, the components and general functioning of the hybrid method are shown. A simple model is developed under the Boussinesq approximation and successfully tested. However, its naive extension to the compressible equations is found to be numerically unstable due to: (1) the perfect gas coupling, and (2) the unstable nature of the LBM at high Mach numbers.

These two problems are then solved by adopting a more robust collision operator for the LBM part and an entropy equation for the energy part. A stable compressible hybrid model, based on a standard D2Q9 discrete velocity lattice, is thus obtained and validated on subsonic and supersonic test cases including shock waves. Nevertheless, for the simulation of strong shock waves, the model shows conservativity problems. These are mainly attributed to the use of the entropy equation which is non-conservative. Solutions are then proposed.

Then, the stability and spectral properties of HLBM schemes are studied using the von Neumann approach. This study highlights the effect of numerous parameters on numerical stability such as the collision model, the choice of the energy equation or the influence of numerical parameters like the CFL number. Instability mechanisms and stabilization methods are shown, confirming at the same time the gain in terms of stability of models based on an entropy equation. Moreover, thanks to a more in-depth analysis, this study allows to explain the observed non-physical behavior of certain models and attributes them to mode transfers.

Finally, the hybrid method is implemented in the ProLB industrial LBM solver. It is then tested on subsonic and supersonic three-dimensional compressible test cases containing boundary conditions and mesh refinements.

Nomenclature

Miscellaneous variables and constants

β	Thermal expansion coefficient ($= 1/T$ for an ideal gas)
$\boldsymbol{u}$	Fluid velocity
$\boldsymbol{x}$	Space variable
Δx, Δt	Discrete mesh size and time step
κ	$\lambda/(\rho c_p)$, Thermal diffusivity
λ	Thermal conductivity
i	Complex number ($\mathrm{i}^2 = -1$)
μ	Dynamic viscosity
μ_b	Bulk viscosity
ν	Kinematic viscosities ($\nu = \mu/\rho$)
ρ	Fluid density
c	Speed of sound
c_p	Heat capacity at constant pressure ($= \gamma_g r_g/(\gamma_g - 1)$
c_v	Heat capacity at constant volume ($= r_g/(\gamma_g - 1)$)
D	Number of spatial dimensions
E	Total energy ($= \boldsymbol{u}^2/2 + e$)
e	Internal energy ($= c_v T$)
p	Static pressure
r_g	Specific gas constant
s	Entropy ($= c_v \ln\left(T/\rho^{\gamma_g - 1}\right)$)

T	Static temperature
t	Time variable

Dimensionless numbers

γ_g	Heat capacity ratio ($= c_p/c_v$)
CFL	Courant-Friedrichs-Lewy number
Ma	Mach number ($= \sqrt{u_\alpha^2}/c$)
Pr	Prandtl number
Ra	Rayleigh number
Re	Reynolds number

Variables related to lattice Boltzmann

$\mathcal{H}^{(n)}$	n^{th}-order Hermite polynomial
$\mathbf{\Pi}$	Stress tensor
$\mathbf{\Pi}^{(1)}$, $\boldsymbol{a}^{(1)}$	Viscous stress tensor
$\boldsymbol{\xi}$	Velocity space variable
$\boldsymbol{\xi}_i$	Discrete lattice velocity
$\boldsymbol{a}^{(n)}$, $\boldsymbol{a}_{eq}^{(n)}$	n^{th}-order Hermite moments of f and f^{eq}
$\boldsymbol{c}_i$	Dimensionless discrete lattice velocity
$\boldsymbol{m}^{(n)}$, $\boldsymbol{m}_{eq}^{(n)}$	n^{th}-order raw moments of f and f^{eq}
$\boldsymbol{Q}$	Heat flux tensor
$\boldsymbol{Q}^{(1)}$	Conductive heat flux
$\check{\tau}$	Relaxation time after the change of variable ($= \tau + \Delta t/2$)
$\check{F}_i$	Discretized body-force term
ρ_r	Reference density (only used to get dimensionless LBM variables)
τ	Relaxation time of the collision model
τ^*	Dimensionless relaxation time ($= \tau/\Delta t$)
θ	Dimensionless fluid temperature ($= T/T_r$)

θ_0	Dimensionless fictitious constant fluid temperature ($= T_0/T_r$)
c_s	Lattice constant ($= \sqrt{r_g T_r}$)
c_s^*	Dimensionless lattice constant ($= c_s/r$)
$E_{1,\alpha\beta}$	Correction term of the lattice closure error
$E_{2,\alpha\beta}$	Correction term of the polyatomic inconsistency
f	Mass distribution function
$f^{(1)}$	First-order off-equilibrium distribution function
$f^{eq,N}$	Truncated equilibrium distribution function at order N in Hermite polynomials
f^{eq}	Maxwell-Boltzmann equilibrium distribution function
f_i	Discrete distribution function
g_i	Discrete distribution function after explicit change of variable
$g_i^{(1)}$	Discrete off-equilibrium distribution function after explicit change of variable
p_0	Barotropic pressure ($= \rho r_g T_0$)
Q	Quadrature order of the lattice of velocities
r	Discrete velocity norm
T_0	Fictitious constant fluid temperature
T_r	Reference temperature
$w(\boldsymbol{\xi})$	Weight function
w_i	Lattice weights

Variables related to the linear stability analysis

ω	Complex temporal pulsation
$\overline{\rho}, \overline{u_\alpha}, \overline{T}$	Mean flow density, velocity and temperature
$\overline{\tau}$	Mean relaxation time ($= \mu/\overline{p}$)
$\overline{f_i}$	Mean flow distribution function ($= \overline{f_i^{eq}}\left(\overline{\rho}, \overline{u_\alpha}, \overline{T}\right)$)
$\widehat{f_i}$	Complex amplitude of f_i'
f_i'	Fluctuating distribution function

k_α	Wave number
v^Φ	Phase velocity
v^g	Group velocity

Contents

Remerciements i

Résumé iii

Abstract v

1 Introduction 1

2 The lattice Boltzmann method 9
2.1 Introductory phase . . . 11
2.1.1 Origin of the LBM . . . 11
2.1.2 Stabilization strategies . . . 12
2.1.3 Presentation of the major problems and organization of the chapter 13
2.2 Introduction to the kinetic theory of gas . . . 14
2.2.1 The particle distribution function . . . 15
2.2.2 The Boltzmann equation . . . 16
2.2.3 The collision operator . . . 17
2.2.4 The Maxwell-Boltzmann equilibrium . . . 18
2.2.5 Hydrodynamic limits of the Boltzmann equation . . . 19
2.3 Velocity space discretization . . . 27
2.3.1 Gauss-Hermite quadrature . . . 28
2.3.2 1D, 2D and 3D on-grid standard and multispeed velocity lattices . 32
2.3.3 Impact of the velocity discretization on the macroscopic equations . 37
2.4 Space and time discretization . . . 40
2.4.1 The collide and stream algorithm . . . 40
2.4.2 The change of variable on the macroscopic quantities . . . 42
2.5 Collision operators . . . 44
2.5.1 Multiple-relaxation-time collision . . . 44
2.5.2 Regularized collision . . . 45
2.5.3 Entropic collision . . . 46
2.6 Initial and boundary conditions . . . 47
2.6.1 Initial conditions . . . 48
2.6.2 Boundary conditions . . . 48
2.7 Literature review: Compressible Lattice Boltzmann methods . . . 50

2.7.1 Compressible lattice Boltzmann models . . . 51
2.7.2 Single distribution function multi speed method . . . 53
2.7.3 Double distribution function method . . . 55
2.7.4 Hybrid method . . . 59
2.7.5 Synthesis and choice of a compressible LBM . . . 61
2.8 Summary of this chapter . . . 63

3 The Hybrid Lattice Boltzmann Method 65
3.1 HLBM's framework . . . 67
3.1.1 Numerical method . . . 67
3.1.2 Mesh element . . . 67
3.1.3 Temporal communication . . . 68
3.2 Energy equations for HLBM . . . 69
3.2.1 Variables and formulations of the energy equations . . . 69
3.2.2 Interest in the total energy equation . . . 70
3.2.3 Interest in the entropy equation . . . 71
3.3 Introduction to finite volume schemes . . . 71
3.4 Introduction to finite difference schemes . . . 74
3.4.1 Principle . . . 74
3.4.2 Some finite difference schemes . . . 76
3.4.3 Equivalent wave number . . . 77
3.5 Time integration . . . 79
3.5.1 Runge-Kutta schemes . . . 79
3.5.2 Stability domain of times integrators . . . 81
3.6 Some spatio temporal schemes . . . 83
3.6.1 Scheme terminology . . . 83
3.6.2 Numerical stability . . . 85
3.7 Hybrid lattice Boltzmann scheme under the Boussinesq approximation . . . 88
3.7.1 The macroscopic equations . . . 89
3.7.2 LBM with buoyancy force term . . . 90
3.7.3 Diffusion and transport of a temperature profile . . . 90
3.7.4 Natural convection in square cavity . . . 93
3.7.5 Discussion . . . 96
3.8 Hybrid lattice Boltzmann method under perfect gas coupling . . . 98
3.8.1 The macroscopic equations . . . 99
3.8.2 Coupling strategies . . . 99
3.8.3 Perfect gas coupling induced instabilities . . . 101
3.8.4 Discussion . . . 106
3.9 High Mach number instabilities . . . 107
3.10 Conclusion and perspective . . . 110

4 Compressible Hybrid Lattice Boltzmann Method 113
4.1 Introduction . . . 115
4.2 Hybrid Discrete Velocity Boltzmann Equation on standard lattice . . . 116
4.2.1 Governing equations . . . 116
4.2.2 The equilibrium distribution function . . . 117
4.2.3 Lattice closure relation and correction term . . . 118
4.2.4 Thermo-hydrodynamic limits of the model . . . 119
4.2.5 Speed of sound . . . 123
4.3 Extended HLBM for high Mach number compressible flows . . . 123
4.3.1 Space/time discretization of the DVBE . . . 123
4.3.2 Correction term enhancement and discretization . . . 125
4.3.3 Hybrid Recursive Regularised collision operator . . . 125
4.3.4 Entropy equation discretization . . . 128
4.3.5 CFL number and HLBM algorithm . . . 130
4.4 Numerical validations of the improved HLBM . . . 131
4.4.1 Viscosity computation . . . 132
4.4.2 Supersonic isentropic vortex . . . 132
4.4.3 Acoustic damping . . . 135
4.4.4 Thermal Couette flow . . . 139
4.5 Numerical validation and model capabilities . . . 141
4.5.1 Acoustic cases . . . 141
4.5.2 Shock tube problem . . . 142
4.5.3 Shock vortex interaction . . . 144
4.6 The model's Achille's heel: case involving entropic mode . . . 146
4.7 Conclusions . . . 152

5 Shock capturing techniques for HLBM 155
5.1 Limitation of the primitive variable formulation of the entropy equation . . . 156
5.1.1 Two-dimensional Riemann problems . . . 156
5.1.2 Shock tube with high pressure ratio . . . 159
5.1.3 One-dimensional stationary shock . . . 160
5.1.4 Outcomes of the test-cases . . . 163
5.1.5 Problem identification and proposals for solutions . . . 164
5.2 HLBM on total energy equation . . . 165
5.2.1 HLLC Riemann solver for energy discretization . . . 165
5.2.2 One-dimensional stationary shock . . . 168
5.2.3 Shock tube with high pressure ratio . . . 169
5.2.4 Two-dimensional Riemann problems . . . 170
5.2.5 Convected and stationary isentropic vortex . . . 172
5.2.6 Conclusion . . . 174
5.3 HLBM with artificial viscosity . . . 177
5.3.1 Definition of the problem . . . 178
5.3.2 Correcting the physics using the viscous terms . . . 178
5.3.3 Guided artificial viscosity through Jameson-like shock sensor . . . 181

5.3.4 Discussion . . . 183
5.4 Conclusion . . . 185

6 Linear Stability Analysis of the HLBM 187
6.1 Introduction . . . 188
6.2 Hybrid Lattice Boltzmann Method . . . 189
6.2.1 Corrected Discrete Velocity Boltzmann Equation . . . 190
6.2.2 Energy equation . . . 191
6.2.3 LBM with corrective terms . . . 192
6.2.4 Discrete energy equation . . . 193
6.3 The linear stability analysis . . . 194
6.3.1 Method and concept . . . 194
6.3.2 Comments on the corrected athermal DVBE LSA . . . 196
6.3.3 Von Neumann analysis of the athermal LBM schemes . . . 198
6.3.4 Two-dimensional LBM instabilities . . . 203
6.4 Extended linear analyses of the hybrid systems . . . 206
6.4.1 Method and concepts . . . 206
6.4.2 Linear analysis of the HDVBE . . . 209
6.4.3 Von Neumann analysis of the HLBM scheme . . . 211
6.5 Linear investigations of the HLBM scheme . . . 215
6.5.1 Stability results of various HLBM classes . . . 215
6.5.2 Stability range of HLBM entropic classes . . . 217
6.6 LBM coupled with an entropy equation . . . 219
6.6.1 Conservative form: shear-to-entropy production . . . 219
6.6.2 Primitive form: entropy-to-shear production . . . 224
6.7 Conclusion . . . 228

7 Hybrid Lattice Boltzmann Method on D3Q19 lattice 231
7.1 The ProLB solver . . . 232
7.2 Three-dimensional HLBM . . . 232
7.2.1 Developed D3Q19 lattice closure correction terms . . . 232
7.3 Boundary condition . . . 234
7.4 Mesh refinement algorithm . . . 236
7.5 Numerical validation . . . 238
7.5.1 Shock vortex interaction . . . 238
7.5.2 Blasius boundary layer . . . 240
7.5.3 Supersonic viscous flow past a NACA0012 aerofoil . . . 244
7.5.4 Supersonic flow around a sphere . . . 247
7.5.5 Performance . . . 250
7.6 Conclusion . . . 252

8 Conclusion and perspectives 253

A Moment matching equilibrium 257
A.1 D1Q3 Equilibrium construction . . . 257

B The entropy equation **261**
B.1 The entropy expression from the Gibbs relation . . . 261
B.2 The speed of sound . . . 262
B.3 The entropy equation . . . 262
B.4 Intrinsic pressure work in the entropy equation . . . 263

C Linear investigation of the supersonic limit of LBM schemes **265**
C.1 Supersonic limit of the athermal LBM . . . 265
C.2 Supersonic limit of the hybrid LBM . . . 266

D Calculation details of the linear stability analysis **269**
D.1 Athermal Matrix . . . 269
D.1.1 Corrected DVBE . . . 269
D.1.2 Corrected LBM . . . 270
D.2 Thermal Matrix . . . 271
D.2.1 HDVBE . . . 272
D.2.2 HLBM . . . 273
D.3 Dispersion relation of the Navier Stokes systems . . . 276
D.3.1 Athermal equations . . . 276
D.3.2 Compressible equations . . . 277
D.4 Modified wave number of finite difference schemes . . . 278

Bibliography **281**

Chapter 1

Introduction

Funding

This thesis has been funded by two aeronautical companies: Airbus and Safran-Tech, and took place at CERFACS (Centre Européen de Recherche et de Formation Avancée en Calcul Scientifique) within the CFD team. This Ph.D work concerns the development of numerical methods for compressible fluid mechanics in the context of aeronautical flows.

The role of numerical methods

In the field of aeronautics, fluid mechanics plays an important role in the design and creation phases of a new aircraft. In most of the aeronautical applications, the continuous equations related to fluid flows are known and are the so called Navier-Stokes equations. This set of non-linear equations allows the prediction, comprehension, and explanation of multiple phenomena such as the acoustic noise or the unsteady aerodynamic loads produced by the interaction of an aircraft component and a given fluid flow. For simple systems, these equations can be directly solved, allowing for analytical solutions; but for more complex configurations, hypothesis must be done leading either to analytical models or simply to no solutions at all. In general, most applications targeted in the aeronautical industry are too sophisticated for a full resolution of the problem using the analytical approach. In such cases, the experimental approach can be employed. Through the use of instruments such as wind tunnels or in-flight sensors, the impact of aerodynamic phenomena can be directly measured. However, experiments can often be very expensive and time-consuming to carry out, and a large amount of important information is often not accessible with current measurement methods. Another alternative is Computational Fluid Dynamics (CFD), which allows to simulate fluid flow by numerically approximating discrete solutions of the Navier-Stokes equations. CFD allows the simulation of very complex configurations using supercomputers. For the aeronautics industry, CFD is thus of particular interest since multiple prototypes can be developed and studied during the day, while ideally the numerical simulations can be performed at night, allowing for more rapid, less expensive optimization.

Limitations and modelling of current CFD approaches

Although theoretically CFD can solve any fluid flow problem, it is nonetheless limited by the available computational power of supercomputers. Roughly speaking, the calculation cost of a run increases according to the number of points chosen for the discretization of space and time. From a general point of view, most of the fluid flows encountered in industrial applications are turbulent and can be seen as a sum of eddies of varying sizes, with the smallest size varying in inverse proportion to the so called Reynolds number, characterizing the laminar/turbulent nature of the flow. Thus, the higher the Reynolds number, the smaller the size of the vortices and the larger the number of points will be, resulting in a high computational cost. In most cases, the applications targeted aircraft manufacturers are at high Reynolds number and thus correspond to highly turbulent flows. The characteristic size of the smallest eddies is therefore small and the calculation cost is high.

There are three main approaches that can be adopted in CFD to treat turbulent flows. These methods can be differentiated by the form of the equations that are discretized, and can be found ordered below from most to least expensive:

1. Direct Numerical Simulation (DNS): The Navier-Stokes equations are directly discretized in time and space. This very expensive method completely solves the unsteady flow dynamic from the largest to the smallest scales. It requires a very fine discretization of space and time which limits its application to canonical academic cases only.

2. Large Eddy Simulation (LES): A spatial filter is applied to the Navier-Stokes equations before the space and time discretization. This method solves the time and space evolution of the largest scales (large structures of the turbulence) of the flow up to a certain length-scale. The smallest scales are assumed to have a more general behavior and are modeled using subgrid-scale models. This method is much more affordable than DNS while still allowing the simulation of unsteady turbulent flows. However, LES is still today in its early stages for industrial applications due to its relatively high CPU (Central Processing Unit) cost.

3. Reynolds Averaged Navier-Stokes (RANS) simulation: A time averaged version of the Navier-Stokes equation is discretized. This method solves only the mean flow field and the unsteady dynamics of the flow is modeled by means of turbulence closure models. Thanks to its low CPU cost, this method is the most widely used in industry. However, due to its averaged construction it can not model transient (unsteady) fluid flows limiting its application range.

Therefore, the current two most affordable approaches for the calculation of industrial configurations are the LES and the RANS approaches. Unfortunately, limitations in current computational power mean that for many industrial cases, only RANS simulations can be achieved overnight and thus be fully integrated into an industrial design cycle.

The need for high fidelity methods

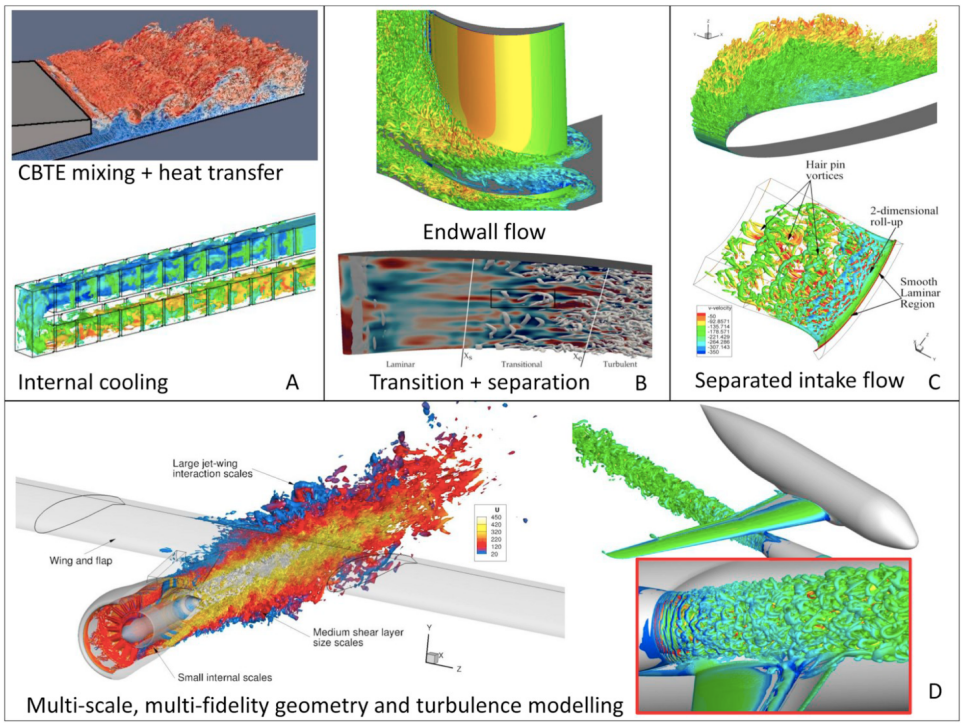

Figure 1.1 – Example unsteady flow physics, encountered in the aeronautical field, computed by way of the numerical resolution of the LES equations. This figure is from the work of Tyacke et al. [1]

At the same time, the understanding of unsteady phenomena is becoming more and more essential to face new industrial aeronautical challenges, making the use of high fidelity methods such as LES compulsory. Fig. 1.1, from the work of Tyacke et al. [1], illustrates common unsteady flow physics, encountered in the aeronautical field, and computed using LES solvers. These highly unsteady physical phenomena, involving a wide range of turbulent structures, would be impossible to model using low-fidelity approaches such as RANS. However, the fact remains that solving numerically the LES equations is computationally expensive, and it is therefore difficult to integrate it into an industrial design cycle. The development of less expensive numerical schemes that can effectively produce LES level resolution is therefore an important field of research in CFD.

CFD is a broad science and thus a multitude of numerical methods exist to discretize fluid mechanics equations. The best known of these are the finite volume method, the finite difference method, the finite element method and the spectral method, and of course within these techniques many variants exist. These methods can be compared according to several criteria, such as their computational cost, their numerical properties (accuracy and stability), or their ease of implementation and use. Although there is no real consensus on the question: "which is the best numerical method for CFD", in the industrial world, the finite volume method has become established over the years thanks

to the good balance that it offers among all the points mentioned above. Recently, due to its low computational cost, a new method has become increasingly popular within an industrial context: the Lattice Boltzmann Method.

The Lattice Boltzmann Method

While conventional CFD methods are based on governing equations defined at the macroscopic level (the Navier-Stokes Equations), the Lattice Boltzmann Method (LBM) is based on the kinetic equation that defines fluid flows at the mesoscopic level. This method, which was first developed in the early 90's, produces an efficient time and phase-space (geometric and velocity spaces) discretization of the Boltzmann equation. A Cartesian numerical method relying on a simple "collide and stream" algorithm is thus obtained and allows for the numerical resolution of fluid flows, just as with traditional Navier-Stokes methods.

The LBM offers many advantages reviewed over the years by several researchers. Its simple algorithm is mainly local and requires solely a single communication step involving only the nearest neighbours. It makes it an easy to implement and highly efficient method for parallel computing on manycore processors, especially on GPU (Graphics Processing Unit) or more generally on multi CPU massively parallel supercomputers. It can use ad hoc boundary conditions, easy to implement and which can account for flows in complex geometries. It is based on Cartesian grids and uses octree type mesh refinement techniques, allowing for the use of automatic mesh generation methods. This circumvents the process of mesh generation, which often requires a great deal of time even from someone trained in mesh generation. Also, this mesh refinement technique is time adaptive, and thus further reduces the computational cost. Moreover, its octree type always conserves the Cartesian nature of the grid maintaining the isotropy of the scheme. Significant losses of accuracy on non-uniform grids due to discontinuous variations of cell size are thus avoided maintaining the low dissipation properties of the LBM.

All these advantages have made the LBM an appealing CFD method for industrial aeronautical applications. However, although the LBM has many benefits, it also has many drawbacks, as it is the case for any CFD method. Among these deficiencies, one is particularly problematic for many aeronautical industrial applications: the LBM in its standard formulation is limited to the computation of weakly compressible and isothermal flows. Despite the fact that the LBM has developed very rapidly over the last two decades, the fact remains that its extension to compressible flows remains an active topic of research.

Ph.D. objective

The overview

This thesis work deals with the study and development of an LBM approach for the simulation of aeronautical compressible flows. This approach must therefore be designed

to model numerically the following compressible Navier-Stokes equations for perfect gas:

$$\frac{\partial \rho}{\partial t} + \frac{\partial \rho u_\alpha}{\partial x_\alpha} = 0, \tag{1.0.1}$$

$$\frac{\partial \rho u_\alpha}{\partial t} + \frac{\partial}{\partial x_\beta}\left[\rho u_\alpha u_\beta + p\delta_{\alpha\beta} - \mu\left(\frac{\partial u_\alpha}{\partial x_\beta} + \frac{\partial u_\beta}{\partial x_\alpha} - \frac{2}{D}\frac{\partial u_\gamma}{\partial x_\gamma}\delta_{\alpha\beta}\right)\right] = 0, \tag{1.0.2}$$

$$\frac{\partial (\rho E)}{\partial t} + \frac{\partial}{\partial x_\alpha}\left[\rho u_\alpha E + u_\alpha p - \lambda\frac{\partial T}{\partial x_\alpha} - \mu\left(\frac{\partial u_\beta}{\partial x_\alpha} + \frac{\partial u_\alpha}{\partial x_\beta} - \frac{2}{D}\frac{\partial u_\gamma}{\partial x_\gamma}\delta_{\alpha\beta}\right)u_\beta\right] = 0, \tag{1.0.3}$$

$$p = \rho r_g T, \tag{1.0.4}$$

where one can recognize the equations of conservation of mass ρ, momentum ρu_α and total energy ρE. Details about notations and variables will be given later. This method will eventually have to be implemented in the industrial LBM solver ProLB, currently restricted to the simulations of weakly compressible flows.

The ProLB software

The ProLB software, originally LaBS (Lattice Boltzmann Solver), was developed within a consortium of industrial companies (Renault, Airbus, CS), academic laboratories (Aix-Marseille University, École Centrale de Lyon) and strong long-term partnerships with others entities (ONERA, CERFACS, Safran). This parallel C++ based solver relies on a D3Q19 velocity lattice, leading to a compact stencil i.e., only the first neighbor points are involved, and uses an advanced regularized collision model that combines robustness and precision. For turbulence modeling, it employs LES approaches based either on the Shear-Improved Smagorinsky Model (SISM) or on the Approximate Deconvolution Model (ADM), and a pressure-gradient-sensitive wall-law can be employed when the turbulent boundary layer is too expensive to solve. The boundary conditions can handle curved geometries using an immersed boundary model based on an inverse distance weighting method. The numerical domain is discretized using an on-board parallel octree mesher taking into consideration the user-defined grid refinement regions specified during the pre-processing step. All of these features allows ProLB to treat in an accurate way complex aerodynamic and aeroacoustic problems with a competitive turnaround time which, it should be remembered, is particularly desirable in the industrial world.

In view of all of the advantages offered by this solver, the prospect of it being extended to compressible regimes is particularly interesting to Safran and Airbus. The aim is therefore to find an LBM compressible approach that is the most promising from an industrial point of view and the easiest to implement in the current architecture of the ProLB software. To respect this last point, the "collide and stream" type methods will be preferred and if possible on compact stencils. These two criteria are essential in order to benefit as much as possible from the functions already present in ProLB, e.g. boundary conditions, mesh transitions, etc.

Strategy

To extend the LBM to compressible flows, different variants exist in the literature. Among them, the hybrid Lattice Boltzmann method (HLBM) seems to be the one that best corresponds to the above-mentioned specifications. Indeed, this method has proven its effectiveness in the industrial sector and seems at first glance to be the most suitable for the architecture of the ProLB solver. Nevertheless, the state of the art of this method in the topic of compressible flows seems to be very limited from an academic point of view and rather held by software. This thesis therefore concerns the development of stable HLBM models for compressible applications, the study of their numerical properties and their validation on simple but representative cases of industrial problems.

Outline of this manuscript

The present manuscript is organized as follows:

- **Chapter 1** corresponds to the present introduction.

- **Chapter 2** is dedicated to the standard construction of the lattice Boltzmann method. An exhaustive bibliographic review on the compressible LBMs is presented, and leads to the choice of the HLBM for this PhD work.

- **Chapter 3** presents in details the construction of the HLBM model. First of all, a basic HLBM scheme is derived and successfully tested in the incompressible limit. The naive extension of this method within the compressible framework proves to be more complicated. Instabilities, at high Mach number and induced by the thermodynamic coupling, makes the use of more advanced numerical models and more appropriate forms of the energy equation mandatory.

- **Chapter 4** presents a stable compressible HLBM model for subsonic flows addressing the instabilities highlighted in chapter 3. Its extension to the supersonic regime is performed and validated on canonical test cases of smooth flows and flows including discontinuities. However, in the presence of strong flow discontinuities the model suffers from conservativeness issues. Moreover, its numerical stability remains unknown, and for entropic cases discrepancies are observed.

- **Chapter 5** explores the conservativeness issues of the HLBM detected in the Chapter 4. The cause of the error is identified and two solutions are proposed and tested.

- **Chapter 6** aims to better understand the stability of the HLBM scheme by the way of a von Neumann spectral analysis. This analysis is also performed on various compressible HLBM models, and permits a better understanding of the choices made in the construction of the model of Chapter 4. The entropic discrepancies observed in Chapter 4 are finally identified as a mode transfer phenomenon.

- **Chapter 7** treats the extension of the compressible HLBM in three dimensions and its implementation in the industrial solver ProLB. Boundary conditions and mesh refinement algorithms are detailed and the method is validated on compressible test cases.

- **Chapter 8** draws the conclusions and perspectives of this PhD work.

Finally, one can find on Fig.1.2 the layout of the present manuscript. This figure aims to provide to the reader a first overview on how the manuscript has been constructed. It depicts how subsequent chapters are linked to previous ones based on issues raised by the latter.

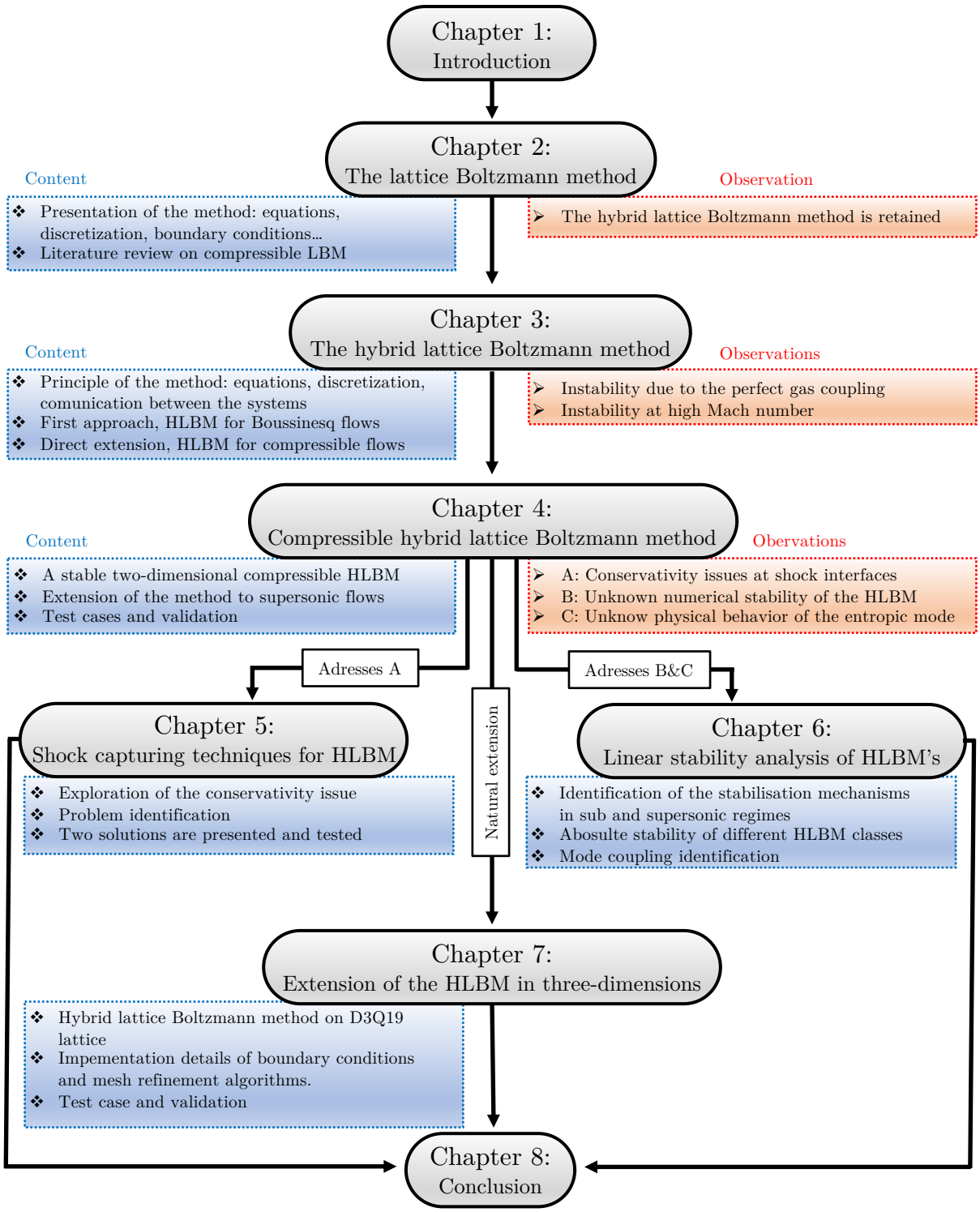

Figure 1.2 – Visual summary of the manuscript. This figures contains the layout of the manuscript, a synthesis of the chapters and how they are tied together.

Chapter 2

The lattice Boltzmann method

Contents

2.1 Introductory phase 11

2.1.1 Origin of the LBM 11

2.1.2 Stabilization strategies 12

2.1.3 Presentation of the major problems and organization of the chapter 13

2.2 Introduction to the kinetic theory of gas 14

2.2.1 The particle distribution function 15

2.2.2 The Boltzmann equation 16

2.2.3 The collision operator 17

2.2.4 The Maxwell-Boltzmann equilibrium 18

2.2.5 Hydrodynamic limits of the Boltzmann equation 19

2.2.5.a Initial approach 19

2.2.5.b The Chapmann-Enskog expansion 21

2.2.5.c Discussion on the macroscopic equations 25

2.3 Velocity space discretization 27

2.3.1 Gauss-Hermite quadrature 28

2.3.1.a Decomposition of the Maxwell-Boltzmann function on the Hermite basis 28

2.3.1.b A lattice construction from the Gauss-Hermite quadrature 30

2.3.2 1D, 2D and 3D on-grid standard and multispeed velocity lattices 32

2.3.3 Impact of the velocity discretization on the macroscopic equations 37

2.4 Space and time discretization 40

2.4.1 The collide and stream algorithm 40

2.4.2 The change of variable on the macroscopic quantities 42

2.5 Collision operators 44
2.5.1 Multiple-relaxation-time collision 44
2.5.2 Regularized collision 45
2.5.3 Entropic collision 46
2.6 Initial and boundary conditions 47
2.6.1 Initial conditions 48
2.6.2 Boundary conditions 48
2.7 Literature review: Compressible Lattice Boltzmann methods 50
2.7.1 Compressible lattice Boltzmann models 51
2.7.2 Single distribution function multi speed method 53
2.7.2.a Principle and history 53
2.7.2.b Compressible models 55
2.7.3 Double distribution function method 55
2.7.3.a Principle and history 55
2.7.3.b Compressible models 57
2.7.4 Hybrid method 59
2.7.4.a Principle and history 59
2.7.4.b Compressible models 60
2.7.5 Synthesis and choice of a compressible LBM 61
2.8 Summary of this chapter 63

This chapter is dedicated to the a priori construction of the lattice Boltzmann scheme. Starting from the statistical definition of the fluid, the links to the macroscopic quantities and macroscopic equation are presented. The phase space discretization of the Boltzmann equation is derived which leads to the lattice Boltzmann numerical method. Finally an exhaustive bibliographic review on the compressible lattice Boltzmann methods is presented, and leads to the choice of the method used in this PhD work.

2.1 Introductory phase

2.1.1 Origin of the LBM

Historically, the lattice Boltzmann Method originated from the lattice gas automata (LGA, or lattice gas cellular automata (LGCA) or lattice gas models [2]) introduced in 1973 by Hardy, Pomeau and de Pazzis (HPP) [3]. The LGA aims to model microscopic fluid particle interactions where each particle of the gas is represented by a boolean state coded by a binary digit [4]. In other words, at a given site the particle is present or not, and propagates in certain discrete directions (called, in a contemporary way, velocity lattice). The original HPP model was in two dimensions and used a square velocity lattice with four discrete velocities aligned along the main axes. In the LGA, each time step is characterised by two operations: the propagation of the particle (along the lattice direction, from a site to a neighbouring site), and the collision of the particle with another particle or its surrounding. The boolean operations of the latter are designed to conserve mass and momentum. Later, Fricsh, Hasslacher and Pomeau [5] in 1986 extended this method on an hexagonal lattice (six velocities) and found a quantitative way to simulate fluid flows, giving rise to the FHP model. This model proved that complex macroscopic dynamics (fluid flow) can emerge from simple elementary microscopic rules, opening new possibilities in the field of computational fluid dynamics. However, due to its boolean construction the model suffered from many drawbacks such as statistical noise, exponential complexity, velocity-dependent pressure, low Reynolds restriction, spurious invariants that correspond to unphysical hydrodynamical quantities and Galilean invariance [4, 6]. In the effort to obtain a noiseless LGCA, in 1988 McNamara and Zanetti [7] rewrote the same Boolean method but used a mean population of particles which could be any number between 0 and 1 in contrary to Boolean variables. This solved the noise issue and gave rise to the earliest Lattice Boltzmann scheme dealing with distribution function [4]. However, due to the new distribution function formalism, the collision rules turned out to be significantly more complex, rendering the method unpractical [6]. In an attempt to reduce the complexity of the collision Higuera, Succi and Benzi [8] linearized the collision term and designed a relaxation matrix tailored to recover the Navier-Stokes behavior. This matrix in the collision operation was later replaced and drastically simplified in 1992 by Qian, D'humiere and Lallemand [6] who introduced the so-called BGK collision operator [9] to model the collision step. The lattice Boltzmann method (LBM) was born. This single-relaxation time operator (SRT) made it possible to link this method to the

kinetic theory of gases. In 1997, He and Luo [10] added the last stone and derived from the kinetic Boltzmann-BGK equation the LBM by the discretization in both time and phase space. Using a multiscale technique (also known as the Chapmann-Enskog expansion [11]), the Navier-Stokes equations were formaly obtained to second order accuracy by computing the statistical moments of the discrete distribution functions. On a chosen square velocity lattice with a properly selected polynomial equilibrium distribution, a local and efficient numerical scheme for the simulation of fluid dynamics is thus obtained. The simple numerical coding, relative robustness, ease implementation of boundary conditions along with the efficient parallel implementation of the method, have made the LBM a serious competitor to older, more traditional methods in the field of computational fluid dynamics. Inheriting from the propagation and collision steps of the LGA [3] (nowadays called the collide and stream algorithm), the BGK formulation began a new era of conquest for this Cartesian method and eventually led to the LBM as it is known today.

2.1.2 Stabilization strategies

Over the years, the LBM has become more diversified, allowing the resolution of multiscale problems ranging from magneto-hydrodynamics [12, 13], meteorological flows [14], multiphase flows [15, 16], turbulent flows [17, 18], relativistic flows [19], porous media [20] or even hemodynamics and biomedical applications [21, 22]. However, in the field of fluid mechanics, and for cases of increasing complexity, the traditional LBM is proving to be less and less robust, especially for flows involving low viscosity fluids or moderate to high speeds. Indeed, severe stability issues were encountered in these configurations with LBMs based on the BGK collision operator [23–25]. This marked the beginning of new research efforts intended to increase the stability of the LBM. In 1998, one of the most important developments was brought by Shan and He [26], who introduced the Hermite expansion of the distribution function. This expansion made it possible to derive the lattice Boltzmann scheme with the use of Gauss-Hermite quadrature. At this point, a systematic link between the distribution functions and continuum theory could thus be made via macroscopic moments. This link highlighted an important new possibility: the system could be rewritten using a matrix of macroscopic moments, and thus multiple relaxation parameters corresponding to each moment could be used and tuned independently. It is this principle that gave birth, a few years earlier, to the so called multiple-relaxation time operator (MRT) which was firstly introduced in 1992 by D'Humieres [27] and further linearly investigated in 2000 by Lallemand and Luo [23]. The MRT is more general than the SRT collision and can be used to enhance the accuracy and numerical stability of the scheme compared to the LBM-BGK. At that time, the numerical stability was essentially questioned by the type of collision operator and therefore problems of instability in low viscosity regime were mainly attributed to the SRT operator. Nevertheless in 1998, Karlin and Succi [28] noticed that the collision model could be modified so that a numerical equivalent of Boltzmann's H-theorem could be ensured. This gave rise to the first entropic lattice Boltzmann method. Instead of targeting the SRT operator, they rather focussed their work on the equilibrium distribution

function, which they proposed to construct based on a suitable entropy maximum principle. This new construction allowed for the retention of the original SRT operator while maintaining stability for high Reynolds number cases, effectively making entropic LBMs a competitor to the MRT method. Finally, in 2006 Latt and Chopard [29] introduced a new stabilization technique based on the shape of the distribution function itself. Using the Hermite formalism, they assumed that the pre-collision distribution functions can be regularised in terms of equilibrium and non-equilibrium contributions, based on the same physical considerations as the Chapmann-Enskog analysis. This strategy enhanced the LBM-BGK numerical scheme in terms of stability in the hydrodynamic regime. The MRT, entropic LB, and regularized LB are the three main stabilisations strategies present in the literature in response to low viscosity instabilities. Over time, many variants of this method have been developed, and they still remain active fields of research today.

2.1.3 Presentation of the major problems and organization of the chapter

Although many efforts have been made to enhance the numerical stability of LBM schemes, the LBM also presents significant physical limitations. The LBM in its original form only allows for the simulation of weakly compressible (low Mach number), isothermal flows. These two limitations are thus physical rather than numerical, and are mostly due to: (1) the discretization of the velocity space using so-called standard lattices, and (2) the shape of the equilibrium distribution function. Difficulties therefore remain for the simulation of compressible flows which is the main subject of this thesis. To circumvent this issue and make the simulation of thermal compressible flows possible, three methods emerged:

- The first is the single distribution function (SDF) multispeed (MS) method. The SDF-MS method was introduced in 1993 by Alexander, Chen, and Sterling [30]. While standard-lattices fail to recover compressible and thermal behavior, this problem can be solved by adding a sufficient number of discrete velocities (hence the terms "higher-order lattices" and MS). In their work, Alexander et al. added four discrete velocities and used the "moment-matching" technique to derive the proper form fo the equilibrium distribution function. The four additional degrees of freedom of this new D2Q13 lattice allowed for the simulation of thermal weakly compressible test cases such as adiabatic sound propagation and Couette flow with heat transfer. In its original form, this method was restricted to a fixed Prandtl number (mostly due to the use of the SRT operator). However, in its standard form, this method suffered from instabilities related to the algebraic coupling among different aero and thermal modes as pointed out by Lallemand et al. [31].

- The second is the double distribution function (DDF) method. The DDF was introduced in 1998 by He, Chen, and Doolen [32] and includes a separate set of populations, which are used to account for temperature fluctuations. These populations are computed alongside those of the standard density distribution function

from which the macroscopic density and velocity fields are still simulated. Thanks to its formalism, this method naturally resolves the fixed Prandtl issue of the MS method while keeping the SRT operator for both of the distribution functions. Their work allowed for the simulation of Rayleigh–Bénard natural convection for different Prandtl and Rayleigh number.

- The third is the hybrid lattice Boltzmann method (HLBM). The HLBM was introduced in 2003 by Lallemand and Luo [31] in large part to deal with the instability problems of SDF-MS methods. The principle of the HLBM is similar to that of the DDF method, but uses a different method to solve the energy equation. It involves the use of an extra energy equation discretized using finite difference (FD) or finite volume (FV) schemes, which is solved alongside the LBM system which resolves mass and momentum. The versatility of the HLBM allows for the choose of types of energy equations and as the DDF is not restricted to fixed Prandl number in a SRT framework.

Many variants of these methods allowing the simulation of thermal flow have been developed over the years in varying the type of lattice, collision operator equilibrium function etc. However, in most cases, temperature is kept either independent or only weakly coupled (through the Boussinesq hypothesis) to density, and thus the weakly-compressible limitation is retained. Indeed, only very few variants are available for real compressible flow under the perfect gas equation of state. In this configuration, the numerical stability of the SDF, DDF and hybrid methods strongly differs from the standard LBM, making the development of a stable method difficult. The stability of these compressible methods remains poorly understood, and is still an active field of research today.

For this thesis work, we have chosen to work with the hybrid method to extend the classical LBM to compressible flow. This chapter therefore aims to discuss the advantages and the flaws of each method and explains what motivated the choice of the HLBM. To do so, the basic features of the LBM must be introduced first. As described previously, historically the lattice Boltzmann method evolved from the LGA. In hindsight, an alternative interpretation of LBM can be obtained by considering the Boltzmann equation directly. The present chapter follows this path. Starting from the Boltzmann equation and some basic notions on the kinetic theory, the velocity discretization step leading to the lattice Boltzmann equation (LBE) is introduced. Next, the discretization in space and time, which yields the LBM and the collide and stream algorithm, is presented. Finally the leading popular collision operators are introduced followed by an exhaustive literature review on the state of the art of LBM for compressible flows.

2.2 Introduction to the kinetic theory of gas

A gas is a large set of atoms or molecules, also referred to as particles, subject to some interactions forces and collisions between particles and their surrounding [4, 33]. In standard molecular dynamics, the particles are governed by Newton's classical equations.

This corresponds to a microscopic description of the gas where for a particle i the position $x_{i,\alpha}$ and the microscopic velocity $\xi_{i,\alpha}$ are systematically computed. Considering the appropriate statistical averaging over the particles quantities, one can get access to the macroscopic variables such as the density, pressure and temperature. However, to simulate the behavior of even a small amount of gas, one would have to solve a number of equations of the order of magnitude of the number of particles i composing the gas, i.e. the Avogadro number $\mathcal{N}_A \sim 10^{23}$, far too big for any computer [4].

The work of James Clerk Maxwell and Ludwig Boltzmann at the end of the 19th century gave birth to the kinetic theory of gases [34, 35]. Considering a sufficiently large number of particles with the same mass, and under other appropriate assumptions, a statistical approach can be held to model the dynamics of the gas. This corresponds to a mesoscopic description of the gas that bridges the gap between the microscopic and macroscopic scales. In the following, the basic notions of the kinetic theory of gases are presented to better understand the origins of the LBM.

2.2.1 The particle distribution function

The probability density function (PDF) $n(\boldsymbol{x}, \boldsymbol{\xi}, t)$, represents the number of particles of mass m varying in space $\boldsymbol{x}$, microscopic velocity $\boldsymbol{\xi}$ and time t. The function n is positive or null by definition and is called in the following the particle distribution function. Considering an infinitesimal phase space finite volume $\mathrm{d}V = \mathrm{d}\boldsymbol{\xi}\mathrm{d}\boldsymbol{x}$, the number of particles $\mathrm{d}N$ at time t, positioned between $\boldsymbol{x}$ and $\boldsymbol{x} + \mathrm{d}\boldsymbol{x}$ owning a microscopic velocity between $\boldsymbol{\xi}$ and $\boldsymbol{\xi} + \mathrm{d}\boldsymbol{\xi}$ reads:

$$\mathrm{d}N(t) = n(\boldsymbol{x}, \boldsymbol{\xi}, t)\mathrm{d}\boldsymbol{V}. \tag{2.2.1}$$

Here the phase-space volume reads $\mathrm{d}\boldsymbol{V} = \mathrm{d}x\mathrm{d}\xi_x$ in one dimension, $\mathrm{d}\boldsymbol{V} = \mathrm{d}x\mathrm{d}y\mathrm{d}\xi_x\mathrm{d}\xi_y$ in two dimensions and $\mathrm{d}\boldsymbol{V} = \mathrm{d}x\mathrm{d}y\mathrm{d}z\mathrm{d}\xi_x\mathrm{d}\xi_y\mathrm{d}\xi_z$ in three dimensions. Defining a particle's mass distribution function $f(\boldsymbol{x}, \boldsymbol{\xi}, t) = m \cdot n(\boldsymbol{x}, \boldsymbol{\xi}, t)$, one can access the total mass of particle in $\mathrm{d}\boldsymbol{V}$ *i.e.* $\mathrm{d}M = f\mathrm{d}\boldsymbol{\xi}\mathrm{d}\boldsymbol{x}$ and subsequently the density $\mathrm{d}\rho = \mathrm{d}M/\mathrm{d}\boldsymbol{x} = f\mathrm{d}\boldsymbol{\xi}$. In fact, the moments of f (also called the kinetic moments) are the link between the mesoscopic scale and the macroscopic scales [33]. Considering D as the spatial dimension and taking the limit $\mathrm{d}\boldsymbol{V} \to 0$, the zeroth moment gives access to the density:

$$\rho(\boldsymbol{x}, t) = \int_{\mathbb{R}^D} f(\boldsymbol{x}, \boldsymbol{\xi}, t)\mathrm{d}\boldsymbol{\xi}, \tag{2.2.2}$$

the first moment gives the momentum:

$$\rho(\boldsymbol{x}, t)u_\alpha(\boldsymbol{x}, t) = \int_{\mathbb{R}^D} \xi_\alpha f(\boldsymbol{x}, \boldsymbol{\xi}, t)\mathrm{d}\boldsymbol{\xi} \tag{2.2.3}$$

and half of the trace of the second order moment yields the total energy :

$$\rho(\boldsymbol{x}, t)E(\boldsymbol{x}, t) = \frac{1}{2}\int_{\mathbb{R}^D} \xi_\alpha^2 f(\boldsymbol{x}, \boldsymbol{\xi}, t)\mathrm{d}\boldsymbol{\xi}, \tag{2.2.4}$$

with $E = e + u_\alpha^2/2$ defined as the sum of the kinetic and internal energy per unit mass. The Greek subscript α denotes the spatial direction in Cartesian coordinate. Combining Eq. (2.2.3) and Eq. (2.2.4), one can also access to the expression of the internal energy:

$$\rho(\boldsymbol{x},t)e(\boldsymbol{x},t) = \frac{1}{2}\int_{\mathbb{R}^D} v_\alpha^2 f(\boldsymbol{x},\boldsymbol{\xi},t)\mathrm{d}\boldsymbol{\xi}, \tag{2.2.5}$$

with $v_\alpha = \xi_\alpha - u_\alpha$ being the relative velocity *i.e.* the deviation of the particle velocity from the local mean velocity u_α. Thus, in order to derive hydrodynamic moments from kinetic theory, one has to "project out" the information contained in the velocity space onto real-space macroscopic fields [4]. The distribution function f is the central variable of the kinetic theory and is expressed in the SI unit as $[f] = kg.s^3.m^{-6}$ in three dimensions. The space, time and velocity evolution of this function is detailed in the next subsection.

2.2.2 The Boltzmann equation

The phase space and time evolution of the distribution function f is given by the so-called Boltzmann equation. Inspired of [2], a basic derivation of this equation is presented. Similarly to molecular gas dynamics, the particles are subject to: (1) interaction forces and (2) collisions between particles. Starting from (1), one can consider packets of particles only affected by an external forces $\boldsymbol{F}$. The force will change the particles velocity from $\boldsymbol{\xi}$ to $\boldsymbol{\xi} + \boldsymbol{F}\mathrm{d}t$ and their position from $\boldsymbol{x}$ to $\boldsymbol{x} + \boldsymbol{\xi}\mathrm{d}t$, resulting in a simple advection along a characteristic line:

$$f(\boldsymbol{x} + \boldsymbol{\xi}\mathrm{d}t, \boldsymbol{\xi} + \boldsymbol{F}\mathrm{d}t, t + \mathrm{d}t)\mathrm{d}\boldsymbol{x}\,\mathrm{d}\boldsymbol{\xi} - f(\boldsymbol{x},\boldsymbol{\xi},t)\mathrm{d}\boldsymbol{x}\,\mathrm{d}\boldsymbol{\xi} = 0. \tag{2.2.6}$$

Now if (2) is considered *i.e.* the gas particles collide, a gain or loss of particles must be taken into account. Instead of being uniformly altered as with $\boldsymbol{F}$, when the particles collide with each other they exchange momentum, which alters their microscopic velocity. Thus, due to this collision in the interval $\mathrm{d}t$, a gain or loss of particles belonging to the volume $\mathrm{d}\boldsymbol{x}\,\mathrm{d}\boldsymbol{\xi}$ must be taken into account. This is modeled by Ω_f the collision operator, and transforms Eq. (2.2.6) into :

$$f(\boldsymbol{x} + \boldsymbol{\xi}\mathrm{d}t, \boldsymbol{\xi} + \boldsymbol{F}\mathrm{d}t, t + \mathrm{d}t)\mathrm{d}\boldsymbol{x}\,\mathrm{d}\boldsymbol{\xi} - f(\boldsymbol{x},\boldsymbol{\xi},t)\mathrm{d}\boldsymbol{x}\,\mathrm{d}\boldsymbol{\xi} = \Omega_f \mathrm{d}\boldsymbol{x}\,\mathrm{d}\boldsymbol{\xi}\,\mathrm{d}t. \tag{2.2.7}$$

Considering now $\mathrm{d}t \to 0$ and keeping in mind that the variables $\boldsymbol{x}$, $\boldsymbol{\xi}$ and t are independent, one gets:

$$\frac{\partial f}{\partial t} + \xi_\alpha \frac{\partial f}{\partial x_\alpha} + F_\alpha \frac{\partial f}{\partial \xi_\alpha} = \Omega_f. \tag{2.2.8}$$

corresponding to the so-called Boltzmann equation (BE). In addition to the H-function and the attendant H-theorem providing quantitative measure of irreversibility, the Boltzmann equation is one of the greatest accomplishments in theoretical physics of the 19th century. The evolution of f is thus governed by an advection-collision equation, the left-hand side terms corresponds to the advective part in terms of geometrical and velocity space, and the right-hand side refers to as the degree of variation of f due to the collision. The collision operator thus models the inter-particles long-range and short-range

interactions altering the microscopic velocity of the particles. Details about this term are given in the following subsection.

2.2.3 The collision operator

In standard kinetic theory, the particles are considered as hard spheres of same mass, interacting together only through elastic shock. The particles can thus be imagined as billiard balls which change their respective velocity solely by colliding one by one (only binary collisions are considered). Due to these assumptions, the collision operator must satisfy the conservation of mass, momentum and total energy. This condition expressed in terms of velocity integral reads:

$$\int_{\mathbb{R}^D} \left(1, \xi_\alpha, \xi_\alpha^2/2\right) \Omega_f \mathrm{d}\boldsymbol{\xi} = 0, \tag{2.2.9}$$

and $(\rho, \rho u_\alpha, \rho E)$ are called collision invariants. The hypothesis made about the particles refers to as the ideal monatomic gas framework which remains sufficient for the notions introduced in this section. Even though based on these relatively simple hypotheses, the original collision operator is a rather complicated integral which is not worth mentioning here. Indeed, a much simpler model is employed for the numerical Lattice Boltzmann Method, and whose design proves to be at the origin of many other variants as shown later. Under the assumption that the collisions drive the gas towards a local equilibrium state, Prabhu Lal Bhatnagar, Eugene P. Gross and Max Krook in 1954 proposed the BGK [9] operator. This most common and simple collision operator reads:

$$\Omega_f^{BGK} = -\frac{1}{\tau}(f - f^{eq}), \tag{2.2.10}$$

and represent the relaxation of f toward a reference equilibrium state f^{eq} during a characteristic time τ. This characteristic time is in the order of magnitude of the mean time between two collisions. When the system is at local thermodynamic equilibrium (i.e., $f = f^{eq}$) the value of the BGK collision operator is zero, a necessary condition for any collision operators. Moreover, it is straightforward to see that the invariant condition Eq.(2.2.9) is satisfied as long as the zeroth, first and half of the trace of the second order moment of f^{eq} corresponds to ρ, ρu_α and ρE respectively; and gives clues on the form of the equilibrium function. In practice, the Maxwell-Boltzmann equilibrium distribution function naturally satisfies this condition. The latter is commonly employed in the LBM framework, and will be defined in the next section. Finally, once plugged in Eq. (2.2.8), the so-called Boltzmann-BGK equation is obtained and reads:

$$\boxed{\frac{\partial f}{\partial t} + \xi_\alpha \frac{\partial f}{\partial x_\alpha} + F_\alpha \frac{\partial f}{\partial \xi_\alpha} = -\frac{1}{\tau}(f - f^{eq})}. \tag{2.2.11}$$

This equation can be seen as the starting point of the derivation of the lattice Boltzmann method.

2.2.4 The Maxwell-Boltzmann equilibrium

The works of James Clerk Maxwell and Ludwig Boltzmann on the kinetic theory of gas in the end of the 19th century gave rise to a distribution function describing the particle speed of an idealized gas at local thermodynamic equilibrium. This function is the so-called Maxwell-Boltzmann distribution function and often called the local Maxwellian distribution function:

$$\boxed{f^{eq} = \rho\left(\frac{1}{2\pi r_g T}\right)^{\frac{D}{2}} \exp\left(-\frac{(\boldsymbol{\xi}-\boldsymbol{u})^2}{2r_g T}\right)} \tag{2.2.12}$$

It is composed of three local parameters: $T(\boldsymbol{x},t)$ the temperature, $\rho(\boldsymbol{x},t)$ the density and $u_\alpha(\boldsymbol{x},t)$ the macroscopic velocity. D stands for the spatial dimension and r_g is the specific gas constant. In fact, r_g refers to the thermodynamic properties of particles considered, which can be illustrated through the formulas:

$$\begin{cases} r_g = R/M \\ r_g = k_B/m \\ r_g = c_p - c_v \end{cases} \tag{2.2.13}$$

Above, $R = k_B \mathcal{N}_A$ is the universal gas constant, $M = m\mathcal{N}_A$ is the molar mass, $k_B = 1.380649 \cdot 10^{-23}\,\mathrm{J\,K^{-1}}$ is the Boltzmann constant and c_p, c_v are respectively the specific heat for constant pressure and volume. This equilibrium function has been constructed considering particles as hard spheres of equal mass [2] therefore it models monatomic particles with only translational degree of freedom. Using this function, no vibrational nor rotational contributions are taken into account in the internal energy. The moments of this Maxwell-Boltzmann function can be computed explicitly and are equal to the mass, momentum and total energy:

$$\int_{\mathbb{R}^D} \left(1, \xi_\alpha, \xi_\alpha^2/2\right) f^{eq}(\boldsymbol{x},\boldsymbol{\xi},t)\mathrm{d}\boldsymbol{\xi} = \left(\rho, \rho u_\alpha, \rho E\right), \tag{2.2.14}$$

where $E = \left(D r_g T + u_\alpha^2\right)/2 = e + u_\alpha^2/2$. As a consequence, it is worth noting that once inserted in the BGK operator Eq. (2.2.10), the present equilibrium respects the collision invariant relation Eq.(2.2.9). Moreover, for an ideal gas the internal energy is defined as $e = c_v T$. The heat capacity ratio of the gas being obtained *via* $\gamma_g = c_p/c_v$, using Eq. (2.2.13) the monatomic expression of γ_g and reads:

$$\gamma_g = \left(D+2\right)/D. \tag{2.2.15}$$

For more elaborated functions which take into account the rotational or vibrational energy one can refer to [36].

Finally, it is now useful to calculate the following tensors corresponding to the local equilibrium distribution. Using a standard Gaussian integral, which can be found in

mathematical handbooks, one get:
Second-order equilibrium tensor:

$$\begin{aligned}\Pi^{eq}_{\alpha\beta} &= \int_{\mathbb{R}^D} \xi_\alpha \xi_\beta f^{eq} \mathrm{d}\boldsymbol{\xi} \\ &= \rho u_\alpha u_\beta + \rho r_g T \delta_{\alpha\beta},\end{aligned} \tag{2.2.16}$$

Third-order equilibrium tensor:

$$\begin{aligned}Q^{eq}_{\alpha\beta\gamma} &= \int_{\mathbb{R}^D} \xi_\alpha \xi_\beta \ \xi_\gamma f^{eq} \mathrm{d}\boldsymbol{\xi} \\ &= \rho u_\alpha u_\beta u_\gamma + \rho r_g T \left[u_\alpha \delta_{\beta\gamma} + u_\beta \delta_{\alpha\gamma} + u_\gamma \delta_{\alpha\beta} \right],\end{aligned} \tag{2.2.17}$$

Fourth-order equilibrium tensor:

$$\begin{aligned}R^{eq}_{\alpha\beta\gamma\delta} &= \int_{\mathbb{R}^D} \xi_\alpha \xi_\beta \xi_\gamma \xi_\delta f^{eq} \mathrm{d}\boldsymbol{\xi} \\ &= \rho u_\alpha u_\beta u_\gamma u_\delta + \rho r_g T \left(u_\alpha u_\beta \delta_{\gamma\delta} + u_\alpha u_\gamma \delta_{\beta\delta} + u_\alpha u_\delta \delta_{\beta\gamma} + u_\beta u_\gamma \delta_{\alpha\delta} + u_\beta u_\delta \delta_{\alpha\gamma} + u_\gamma u_\delta \delta_{\alpha\beta} \right) \\ &\quad + \rho \left(r_g T \right)^2 \left(\delta_{\alpha\beta}\delta_{\gamma\delta} + \delta_{\alpha\gamma}\delta_{\beta\delta} + \delta_{\alpha\delta}\delta_{\beta\gamma} \right),\end{aligned} \tag{2.2.18}$$

where $\delta_{\alpha\beta}$ refers to the Kronecker symbol. These computations can be found in detail in [37]. Theses expressions will be used in the next section to establish the link between the Boltzmann and the macroscopic equations.

2.2.5 Hydrodynamic limits of the Boltzmann equation

2.2.5.a Initial approach

The purpose here is to derive macroscopic equations in the hydrodynamic limits so as to make the link between the mesocopic and macroscopic world. It was previously established that the macroscopic variables can be accessed via the velocity moments of the distribution function f. Thus, a naive approach would be to apply the same reasoning on the overall Boltzmann-BGK equation to make the link between the mesoscopic and macroscopic equations. For the sake of simplicity, and with no loss of generality, let us considers the force-free Boltzmann-BGK equation integrated over the three-first moments:

$$\int_{\mathbb{R}^D} \left(1, \xi_\alpha, \xi_\alpha^2/2\right) \left[\frac{\partial f}{\partial t} + \xi_\beta \frac{\partial f}{\partial x_\beta} \right] \mathrm{d}\boldsymbol{\xi} = -\int_{\mathbb{R}^D} \left(1, \xi_\alpha, \xi_\alpha^2/2\right) \frac{1}{\tau} (f - f^{eq}) \mathrm{d}\boldsymbol{\xi}. \tag{2.2.19}$$

When considering the collisional invariant condition Eq.(2.2.9), it is to be noted that the right-hand side of the equation vanish. In addition, since $\boldsymbol{x}$, t and $\boldsymbol{\xi}$ are independent

variables, they can be permuted so as to compute the moments of f. Using the definition of the mass Eq. (2.2.2), momentum Eq. (2.2.3) and total energy Eq. (2.2.4), the resulting system of equations reads:

$$\frac{\partial \rho}{\partial t} + \frac{\partial (\rho u_\alpha)}{\partial x_\alpha} = 0 \tag{2.2.20a}$$

$$\frac{\partial (\rho u_\alpha)}{\partial t} + \frac{\partial \Pi_{\alpha\beta}}{\partial x_\beta} = 0, \quad \text{with} \quad \Pi_{\alpha\beta} = \int_{\mathbb{R}^D} \xi_\alpha \xi_\beta f \mathrm{d}\boldsymbol{\xi}, \tag{2.2.20b}$$

$$\frac{\partial (\rho E)}{\partial t} + \frac{1}{2}\frac{\partial Q_{\alpha\alpha\beta}}{\partial x_\beta} = 0, \quad \text{with} \quad Q_{\alpha\alpha\beta} = \int_{\mathbb{R}^D} \xi_\alpha^2 \xi_\beta f \mathrm{d}\boldsymbol{\xi}. \tag{2.2.20c}$$

From this system, the first equation is equivalent to the conservation of mass and is directly obtained owing to the definition of f. However, only an *ersatz* of momentum and total energy equations are obtained. Indeed, the tensor $\Pi_{\alpha\beta}$, referring to as the momentum-flux tensor, and $Q_{\alpha\alpha\beta}$ being some part of the heat flux tensor, remain unknown to fully determine the system. As a first attempt, one can try to explicitly compute these tensors using simple manipulations on the relative velocity $v_\alpha = \xi_\alpha - u_\alpha$. Knowing the following relations:

$$\xi_\alpha \xi_\beta = v_\alpha v_\beta + u_\beta \xi_\alpha + \left(u_\alpha \xi_\beta - u_\alpha u_\beta\right), \tag{2.2.21a}$$

$$\xi_\alpha^2 \xi_\beta = v_\alpha^2 v_\beta + u_\beta \xi_\alpha^2 + 2\xi_\alpha \xi_\beta u_\alpha - 2\xi_\alpha u_\alpha u_\beta + \left(u_\alpha^2 u_\beta - u_\alpha^2 \xi_\beta\right), \tag{2.2.21b}$$

one can re-express these tensors such as:

$$\Pi_{\alpha\beta} = \rho u_\alpha u_\beta + \Pi^*_{\alpha\beta} \quad \text{with} \quad \Pi^*_{\alpha\beta} = \int_{\mathbb{R}^D} v_\alpha v_\beta f \mathrm{d}\boldsymbol{\xi}, \tag{2.2.22a}$$

$$\frac{1}{2} Q_{\alpha\alpha\beta} = \rho E u_\beta + \underbrace{u_\alpha \Pi_{\alpha\beta} - \rho u_\alpha^2 u_\beta}_{=\Pi^*_{\alpha\beta} u_\alpha} + \frac{1}{2} Q^*_\beta, \quad \text{with} \quad Q^*_\beta = \int_{\mathbb{R}^D} v_\alpha^2 v_\beta f \mathrm{d}\boldsymbol{\xi}, \tag{2.2.22b}$$

and obtain a more familiar form of the momentum and energy equations:

$$\frac{\partial (\rho u_\alpha)}{\partial t} + \frac{\partial \left(\rho u_\alpha u_\beta\right)}{\partial x_\beta} + \frac{\partial \Pi^*_{\alpha\beta}}{\partial x_\beta} = 0, \tag{2.2.23a}$$

$$\frac{\partial (\rho E)}{\partial t} + \frac{\partial \left(\rho E u_\beta\right)}{\partial x_\beta} + \frac{\partial \left(\Pi^*_{\alpha\beta} u_\alpha\right)}{\partial x_\beta} + \frac{1}{2}\frac{\partial Q^*_\beta}{\partial x_\beta} = 0. \tag{2.2.23b}$$

Thanks to this manipulation, the convective fluxes on each equations can be identified. The terms $\Pi^*_{\alpha\beta}$ and Q^*_β that emerged correspond respectively to the stress tensor and the

heat flux. If one were to compare these results to the Navier-Stokes equations, one could guess that $\Pi^*_{\alpha\beta}$ gathers the pressure and viscous stresses while Q^*_β corresponds to the heat diffusion term. However, at this point their expression can not be explicitly computed since they depend on the form of f. Thus, in order to close the system of equations the expression of f must be somehow known, and the hypotheses on f are actually the crux of the matter when calculating macroscopic equations.

As a first attempt, the distribution function can be assumed to be near the equilibrium i.e. $f \simeq f^{eq}$. Using this approximation, the stress tensor can be explicitly computed using Eq. (2.2.21b) and Eq. (2.2.16) giving $\Pi^*_{\alpha\beta} = \rho r_g T \delta_{\alpha\beta}$ which can be identified as a normal stress. Similarly, the heat flux can be obtained using Eq. (2.2.21b), Eq. (2.2.16) and Eq. (2.2.18) and is found to be $Q^*_\beta = 0$. Thus using this assumption, one recovers the Euler equations:

$$\frac{\partial \rho}{\partial t} + \frac{\partial(\rho u_\alpha)}{\partial x_\alpha} = 0, \tag{2.2.24a}$$

$$\frac{\partial(\rho u_\alpha)}{\partial t} + \frac{\partial\left(\rho u_\alpha u_\beta\right)}{\partial x_\beta} + \frac{\partial p}{\partial x_\beta}\delta_{\alpha\beta} = 0, \tag{2.2.24b}$$

$$\frac{\partial(\rho E)}{\partial t} + \frac{\partial\left(\rho E u_\beta\right)}{\partial x_\beta} + \frac{\partial\left(p u_\beta\right)}{\partial x_\beta} = 0, \tag{2.2.24c}$$

where the pressure is found to be $p = \rho r_g T$ by identification with the Euler equations and correspond to the ideal gas equation of state. Moreover, using the mass and momentum equations one can manipulate the total energy equation to obtain the internal energy equation:

$$\frac{\partial(\rho e)}{\partial t} + \frac{\partial\left(\rho e u_\beta\right)}{\partial x_\beta} + p\frac{\partial u_\beta}{\partial x_\beta} = 0. \tag{2.2.25}$$

The important thing to remember here is that replacing f by its equilibrium expression leads to the equations of fluid in the inviscid limit. In order to recover the viscous contributions, one must use a more elaborated expression of f. For doing so, the Chapmann-Enskog expansion provides a more refined approximation of f and is the most common way to recovers the equivalent set of equations in the LBM.

2.2.5.b The Chapmann-Enskog expansion

The principle is based on a multi-scale development of the Boltzmann equation where f is no longer considered at equilibrium but close to it. Considering that L is a characteristic length-scale of the flow, $\sqrt{r_g T_0}$ is the characteristic speed of the particles, one can recast the Boltzmann-BGK equation in dimensionless form:

$$\varepsilon\left(\frac{\partial f}{\partial t} + \xi_\alpha \frac{\partial f}{\partial x_\alpha}\right) = -\left(f - f^{eq}\right). \tag{2.2.26}$$

Here $\varepsilon = \tau\sqrt{r_g T_0}/L$ and represents the ratio of the mean free path of the particle $l_0 = \tau\sqrt{r_g T_0}$ over the characteristic length of the system L. This can be identified as the Knudsen number Kn and controls the convergence of kinetic theory to hydrodynamics

as sketched by Fig. 2.1. For the continuum approach (which is the case in classical fluid mechanics), the Knudsen number is a small parameter so that Kn << 1 [38].

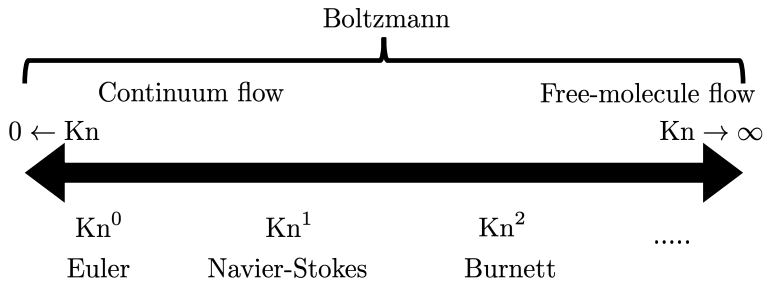

Figure 2.1 – Illustration of Knudsen number regimes and hydrodynamic levels generated by the Chapman–Enskog expansions adapted from [4].

Following the approach proposed by David Hilbert [4], Sydney Chapman (1888-1970) and David Enskog (1884-1947) [2,11], the distribution function can be expanded in powers of smallness parameter ε such that:

$$f = \sum_{n=0}^{\infty} \varepsilon^n f^n = f^{(0)} + \varepsilon f^{(1)} + \varepsilon^2 f^{(2)} + \dots \tag{2.2.27}$$

Once plugged into Eq. (2.2.26), the different orders of ε can be gathered and one obtains:

$$\varepsilon^0 : \quad f^{(0)} = f^{eq} \tag{2.2.28a}$$

$$\varepsilon^1 : \quad f^{(1)} = -\left(\frac{\partial f^{eq}}{\partial t} + \xi_\alpha \frac{\partial f^{eq}}{\partial x_\alpha}\right) \tag{2.2.28b}$$

$$\varepsilon^2 : \quad f^{(2)} = -\left(\frac{\partial f^{(1)}}{\partial t} + \xi_\alpha \frac{\partial f^{(1)}}{\partial x_\alpha}\right) \tag{2.2.28c}$$

$$\dots$$

$$\varepsilon^n : \quad f^{(n)} = -\left(\frac{\partial f^{(n-1)}}{\partial t} + \xi_\alpha \frac{\partial f^{(n-1)}}{\partial x_\alpha}\right), \quad \forall n \geq 1. \tag{2.2.28d}$$

From the system above, it can be noticed that each order of ε forms a semi-independent equation by itself where low order equations directly interact with the higher order ones. It is the key issue of this development where, in order to know the dynamics at higher order, the lower order dynamic must be known. Moreover, for the zeroth-order one obtains $f^{(0)} = f^{eq}$ which indicates that:

- The function f is well expanded around an equilibrium state.
- The off-equilibrium contributions $f^{(n\geq 1)}$ are expressed in power of Knudsen number.

Finally, since $f^{(0)} = f^{eq}$ and in the light of Eq.(2.2.9) and Eq.(2.2.10), one imposes the three solvability conditions:

$$\int_{\mathbb{R}^D} \left(1, \xi_\alpha, \xi_\alpha^2/2\right) f^{(n\geq 1)} \mathrm{d}\boldsymbol{\xi} = 0, \tag{2.2.29}$$

and means that the off-equilibrium contributions are not involved in the computation of mass, momentum and energy variables.

As shown previously when $f = f^{eq}$ the Euler equations Eq. (2.2.24) are recovered and correspond in the present case to an expansion up to ε^0. Therefore one can hint that refining the approximation on the form of f in terms of the Knudsen number may lead to the recovery of the viscous contributions. In practice, a first-order expansion $f = f^{(0)} + \varepsilon f^{(1)}$ is needed to recover the full set of Navier-Stokes equations. Thus, such development provides a refined form of f which reads at the first order:

$$f = f^{eq} + \varepsilon f^{(1)} = f^{eq} + \varepsilon \left(\frac{\partial f^{eq}}{\partial t} + \xi_\alpha \frac{\partial f^{eq}}{\partial x_\alpha} \right), \tag{2.2.30}$$

and can be used to compute the moments $\Pi^*_{\alpha\beta}$ and Q^*_β of Eq. (2.2.23). Considering the development Eq. (2.2.27) up to the first order, these moments read:

$$\Pi^*_{\alpha\beta} = \int_{\mathbb{R}^D} v_\alpha v_\beta \left(f^{eq} + \tau f^{(1)} \right) \mathrm{d}\boldsymbol{\xi} = p\delta_{\alpha\beta} + \tau \int_{\mathbb{R}^D} v_\alpha v_\beta f^{(1)} \mathrm{d}\boldsymbol{\xi} = p\delta_{\alpha\beta} + \Pi^{(1)}_{\alpha\beta}, \tag{2.2.31a}$$

$$Q^*_\beta = \int_{\mathbb{R}^D} v_\alpha^2 v_\beta \left(f^{eq} + \tau f^{(1)} \right) \mathrm{d}\boldsymbol{\xi} = 0 + \tau \int_{\mathbb{R}^D} v_\alpha^2 v_\beta f^{(1)} \mathrm{d}\boldsymbol{\xi} = Q^{(1)}_\beta, \tag{2.2.31b}$$

where ε has been replaced by τ to consider the dimensional form of the equation. Here, the newly defined tensors $\Pi^{(1)}_{\alpha\beta}$ and $Q^{(1)}_\beta$ constitute the off-equilibrium contributions of $\Pi_{\alpha\beta}$ and Q_β Eq. (2.2.20b) and Eq. (2.2.20c) respectively. Using Eq. (2.2.29), one can note that:

$$\Pi^{(1)}_{\alpha\beta} = -\tau \int_{\mathbb{R}^D} v_\alpha v_\beta f^{(1)} \mathrm{d}\boldsymbol{\xi} = -\tau \int_{\mathbb{R}^D} \xi_\alpha \xi_\beta f^{(1)} \mathrm{d}\boldsymbol{\xi} \tag{2.2.32a}$$

$$\begin{aligned} Q^{(1)}_\beta = -\tau \int_{\mathbb{R}^D} v_\alpha^2 v_\beta f^{(1)} \mathrm{d}\boldsymbol{\xi} &= -\tau \int_{\mathbb{R}^D} \left(\xi_\alpha^2 \xi_\beta - 2u_\alpha \xi_\alpha \xi_\beta \right) f^{(1)} \mathrm{d}\boldsymbol{\xi} \\ &= -\tau \int_{\mathbb{R}^D} \xi_\alpha^2 \xi_\beta f^{(1)} \mathrm{d}\boldsymbol{\xi} - 2u_\alpha \Pi^{(1)}_{\alpha\beta}, \end{aligned} \tag{2.2.32b}$$

which indicates that due to the conservation laws Eq. (2.2.29), the non-equilibrium momentum flux $\Pi^{(1)}_{\alpha\beta}$ from the absolute and the relative reference frames is identical. In order words, the non-equilibrium momentum flux is invariant regardless of whether it is

in the absolute or relative frame [39]. Once Eq. (2.2.28b) is inserted into the expressions above, one finally obtains:

$$\Pi^{(1)}_{\alpha\beta} = -\tau \int_{\mathbb{R}^D} \xi_\alpha \xi_\beta \left(\frac{\partial f^{eq}}{\partial t} + \xi_\gamma \frac{\partial f^{eq}}{\partial x_\gamma} \right) \mathrm{d}\boldsymbol{\xi} = -\tau \left(\frac{\partial \Pi^{eq}_{\alpha\beta}}{\partial t} + \frac{\partial Q^{eq}_{\alpha\beta\gamma}}{\partial x_\gamma} \right), \tag{2.2.33a}$$

$$Q^{(1)}_{\beta} = -\tau \int_{\mathbb{R}^D} \xi^2_\alpha \xi_\beta \left(\frac{\partial f^{eq}}{\partial t} + \xi_\gamma \frac{\partial f^{eq}}{\partial x_\gamma} \right) \mathrm{d}\boldsymbol{\xi} - 2u_\alpha \Pi^{(1)}_{\alpha\beta} = -\tau \left(\frac{\partial Q^{eq}_{\alpha\alpha\beta}}{\partial t} + \frac{\partial R^{eq}_{\alpha\alpha\beta\gamma}}{\partial x_\gamma} \right) - 2u_\alpha \Pi^{(1)}_{\alpha\beta}. \tag{2.2.33b}$$

Above, the independent variables have been permuted so as to compute the integrals, and the expression of equilibrium tensors $\boldsymbol{\Pi}^{eq}$, $\boldsymbol{Q}^{eq}$ and $\boldsymbol{R}^{eq}$ which can be found in Eq. (2.2.16), Eq. (2.2.17) and Eq. (2.2.18) respectively. To go forward, the point here is to obtain an equivalent expression of the temporal derivatives in terms of spatial derivatives. Here it is recalled that the key principle of the Chapmann-Enskog expansion lies in the fact that the higher order dynamics in ε rely on the lower order one[1]. Thus the temporal derivatives present in the ε^1 order terms can be obtained using the equations found at ε^0 i.e. the Euler equations (2.2.24). Starting by $\partial \Pi^{eq}_{\alpha\beta}/\partial t$ in Eq. (2.2.33a), knowing the fact that $p = (\gamma_g - 1)\,\rho e$ and using the chain rule one obtains:

$$\begin{aligned} \frac{\partial \Pi^{eq}_{\alpha\beta}}{\partial t} &= \frac{\partial}{\partial t} \left(\rho u_\alpha u_\beta + p \delta_{\alpha\beta} \right) \\ &= u_\beta \frac{\partial \left(\rho u_\alpha \right)}{\partial t} + \rho u_\alpha \frac{\partial u_\beta}{\partial t} + \left(\gamma_g - 1 \right) \frac{\partial e}{\partial t} \delta_{\alpha\beta}. \end{aligned} \tag{2.2.34}$$

Above, the expression of the first and third right-hand side term can be found in Eq. (2.2.24b) and Eq. (2.2.25) respectively. The second term can be obtained using the momentum and the mass equation and reads:

$$\rho u_\alpha \frac{\partial u_\beta}{\partial t} = -\rho u_\alpha u_\gamma \frac{\partial u_\beta}{\partial x_\gamma} + u_\alpha \frac{\partial p}{\partial x_\gamma} \delta_{\beta\gamma}. \tag{2.2.35}$$

Once the expression of $\partial \Pi^{eq}_{\alpha\beta}/\partial t$ is computed, it can be plugged back into Eq. (2.2.33a) and after some mathematical manipulations the expression ultimately reduces to:

$$\Pi^{(1)}_{\alpha\beta} = -\tau p \left(\frac{\partial u_\alpha}{\partial x_\beta} + \frac{\partial u_\beta}{\partial x_\alpha} - \frac{2}{D} \frac{\partial u_\gamma}{\partial x_\gamma} \delta_{\alpha\beta} \right). \tag{2.2.36}$$

Using the very same reasoning to compute $\partial Q^{eq}_{\alpha\alpha\beta}/\partial t$ in Eq. (2.2.33b), after some math one obtains:

$$Q^{(1)}_{\beta} = -\tau c_p p \frac{\partial T}{\partial x_\beta}, \tag{2.2.37}$$

[1]Strictly speaking, it would have been necessary to also expand $\partial/\partial t$ in powers of smallness parameter ε to show it as Chapman and Enskog did. For the sake of simplicity, this has been omitted and replaced by this explication.

with $c_p = r_g\gamma_g$ and $\gamma_g = (D+2)/D$ the heat capacity ratio in the monatomic limit. Full details of the mathematical operations can be found well documented in [37, 40, 41]. Finally, once these two off-equilibrium tensors are plugged back into $\Pi^*_{\alpha\beta}$ and Q^*_β Eq. (2.2.31) and which in turn are themselves injected into Eq. (2.2.23) the following system is obtained:

$$\frac{\partial \rho}{\partial t} + \frac{\partial(\rho u_\alpha)}{\partial x_\alpha} = 0, \tag{2.2.38a}$$

$$\frac{\partial(\rho u_\alpha)}{\partial t} + \frac{\partial\left(\rho u_\alpha u_\beta\right)}{\partial x_\beta} + \frac{\partial}{\partial x_\beta}\left(p\delta_{\alpha\beta} + \Pi^{(1)}_{\alpha\beta}\right) = 0, \tag{2.2.38b}$$

$$\frac{\partial(\rho E)}{\partial t} + \frac{\partial\left(\rho E u_\beta\right)}{\partial x_\beta} + \frac{\partial}{\partial x_\beta}\left(p u_\beta + u_\beta \Pi^{(1)}_{\alpha\beta}\right) + \frac{\partial Q^{(1)}_\beta}{\partial x_\beta} = 0. \tag{2.2.38c}$$

and corresponds to the Navier-Stokes equations with:

$$\mu = \tau p \quad \text{and} \quad \lambda = \tau c_p p, \tag{2.2.39}$$

being respectively the dynamic viscosity and the heat conductivity.

To summarize, in order to recover the equations at macroscopic level, one must at some point make an assumption on the form of the distribution function f. Based on a multi-scale expansion of f in power of Knudsen number $\sim \varepsilon$, the Champann-Enskog development is a way to recover :

- The Euler equation for ε^0,
- The Navier-Stokes equation for ε^1.

Using a higher order development of f, other equations describing the higher order kinetic dynamic can be found. For instance, the Burnett equations are retrieved when $f = f^{eq} + \varepsilon f^1 + \varepsilon^2 f^2$ [2] as illustrated on Fig. 2.1.

2.2.5.c Discussion on the macroscopic equations

Finally, some remarks must be made on these macroscopic equations which have been found from the Boltzmann-BGK kinetic equation and using the Maxwell-Boltzmann equilibrium function.

- The equations model monatomic gas with a heat capacity ratio linked to the number of space dimensions D such as:

  $$\gamma_g = \frac{D+2}{D}. \tag{2.2.40}$$

  Thus, only translations in the D directions of the physical space are allowed for gas molecules and is a consequence of the use of the Maxwell-Boltzmann equilibrium. To properly recover the behavior of polyatomic gases, rotational and vibrational degrees of freedom should also be included in the definition of the internal energy. To circumvent this issue, several approaches used in the LBM community are based on a modified form of equilibrium and can be found in [42–44].

- A perfect gas equation of state is recovered:

$$p = \rho r_g T, \tag{2.2.41}$$

and makes the link between the three state variables p, ρ and T. This thermodynamic closure is sufficient for most of the applications presented in this manuscript. Therefore, for more elaborated equations of state, the equilibrium can also be modified along with the use of forcing terms, and is a common procedure to address multi-phase flow in the LBM community [2].

- Both viscous and thermal diffusion coefficients depend on the same relaxation parameter τ. Therefore, only flows with Prandtl number of unity can be modeled:

$$\mathrm{Pr} = \frac{\mu c_p}{\lambda} = \frac{\tau p c_p}{\tau c_p p} = 1. \tag{2.2.42}$$

It is a direct consequence of using a Maxwell-Boltzmann equilibrium along with a classical BGK collision operator. To address the problem while keeping the same equilibrium, more sophisticated collision models such as the multiple-relaxation-time (MRT) [23, 27] can be employed. This enables the use of two independent relaxation times defining the viscous and thermal diffusion coefficients therefore eliminating the Pr = 1 constraint. Detailed about this operator will be given later in Sec. 2.5. Finally, using an advanced form of the equilibrium distribution function such as the Shakhov model [45, 46] or the statistical ellipsoidal model [36, 47], making it possible to get a variable Prandtl number while keeping the BGK collision operator.

- The macroscopic equations have been found to rely directly on the moments of f^{eq}. This dependency can be shown by recasting Eq. (2.2.38) such as:

$$\underbrace{\frac{\partial \rho}{\partial t}}_{m^{eq,(0)}} + \underbrace{\frac{\partial (\rho u_\alpha)}{\partial x_\alpha}}_{\boldsymbol{m}^{eq,(1)}} = 0, \tag{2.2.43a}$$

$$\underbrace{\frac{\partial (\rho u_\alpha)}{\partial t}}_{\boldsymbol{m}^{eq,(1)}} + \frac{\partial}{\partial x_\beta} \underbrace{(\rho u_\alpha u_\beta + p\delta_{\alpha\beta})}_{\boldsymbol{m}^{eq,(2)}} + \frac{\partial}{\partial x_\beta} \underbrace{\left(\Pi^{(1)}_{\alpha\beta}\right)}_{\boldsymbol{m}^{eq,(2)},\boldsymbol{m}^{eq,(3)}} = 0, \tag{2.2.43b}$$

$$\underbrace{\frac{\partial (\rho E)}{\partial t}}_{\boldsymbol{m}^{eq,(2),*}} + \frac{\partial}{\partial x_\beta} \underbrace{(\rho E u_\beta + p u_\beta +)}_{\boldsymbol{m}^{eq,(3),*}} + \frac{\partial}{\partial x_\beta} \underbrace{\left(u_\beta \Pi^{(1)}_{\alpha\beta} + Q^{(1)}_\beta\right)}_{\boldsymbol{m}^{eq,(3),*},\boldsymbol{m}^{eq,(4),*}} = 0, \tag{2.2.43c}$$

where $\boldsymbol{m}^{eq,(n)}$ refers to the nth order moment of f^{eq} i.e.:

$$\left(m^{eq,(0)}, \boldsymbol{m}^{eq,(1)}, \boldsymbol{m}^{eq,(2)}, \boldsymbol{m}^{eq,(3)}, \boldsymbol{m}^{eq,(4)}\right) = \left(\rho, \rho\boldsymbol{u}, \boldsymbol{\Pi}^{eq}, \boldsymbol{Q}^{eq}, \boldsymbol{R}^{eq}\right). \tag{2.2.44}$$

Finally, the superscript $*$ means that only part of the tensor is involved to compute the underlined term. Thus, it appears clearly that the zeroth to fourth order equilibrium moments are required to recover the full set of Navier-Stokes Fourier equations. This information is crucial and is proving to be the corner stone of the velocity space discretization presented in the next section.

2.3 Velocity space discretization

It is worth recalling one of the the goals of this chapter which is to build a numerical method based on the Boltzmann equation to model fluid dynamics. This equation describes the evolution of the distribution function f defined on the continuous geometrical space $\boldsymbol{x}$, velocity space $\boldsymbol{\xi}$ and time t. While standard CFD methods are directly based on the resolution of the Navier-Stokes equations where only $\boldsymbol{x}$ and t are discretized, in the present case the velocity space $\boldsymbol{\xi}$ has to be also discretized such that:

$$f(\boldsymbol{x}, \boldsymbol{\xi}, t) \to f_i(\boldsymbol{x}, t), \quad \forall i \in [\![0, m-1]\!]. \tag{2.3.1}$$

This transformation produces m discrete distribution functions f_i associated with the discrete velocity $\boldsymbol{\xi_i}$, and the space and time evolution of f_i is now given by the so-called discrete velocity Boltzmann equation (DVBE):

$$\frac{\partial f_i}{\partial t} + \xi_{i,\alpha} \frac{\partial f_i}{\partial x_\alpha} = -\frac{1}{\tau}\left(f_i - f_i^{eq}\right), \quad \forall i \in [\![0, m-1]\!]. \tag{2.3.2}$$

It is worth noting that the same procedure as seen in Sec.2.2.5 can be employed to compute the macroscopic equation associated to the DVBE system (6.2.1).

This discretization turns out to be a critical step in deriving the LBM from the continuous Boltzmann equation since it has a direct impact on the numerical cost of method (m equations (6.2.1) must be solved for each space and time steps) and on the macroscopic equations found by the discrete Boltzmann system. As a matter of fact, Sec. 2.2.5 showed that the equilibrium moments are directly responsible for the recovered macroscopic equations. These moments are computed from the integrals of the distribution function over the velocity space, and so once this space has been discretized the integrals will turn into sums. Thus, to obtain the correct macroscopic equations the moments must be conserved during the discretization process such that:

$$\int_{\mathbb{R}^D} P_n(\boldsymbol{\xi})\, f^{eq}(\boldsymbol{x}, \boldsymbol{\xi}, t)\, \mathrm{d}\boldsymbol{\xi} = \sum_{i=0}^{m-1} P_n(\boldsymbol{\xi}_i)\, f_i^{eq}(\boldsymbol{x}, t), \tag{2.3.3}$$

with P_n being a polynomial of order $n \in [\![0, N]\!]$. As seen in Sec. 2.2.5, the moments up to the fourth order (thus $N = 4$) are needed to recover the Navier-Stokes equations. Therefore the goal is to determine the minimal discrete velocity sets to get the least expensive numerical method while modeling the correct physics. Thus, the velocity discretization has a direct impact on the type of macroscopic equation solved, and this is one of the main features of this numerical method.

Several ways exist to jump from the continuous to the discrete velocity space and the most common methodologies are based on the moment matching construction and the Hermite projection. The former aims at discretizing the velocity space in a top-down fashion, i.e. the discrete velocities and the equilibrium distribution function are determined by enforcing the corresponding macroscopic equations to match the thermohydrodynamic equations with certain accuracy [33]. According to Guo et al. [33], the initial moment

matching construction can be attributed by McNamara et al. [48] in 1995. Regarding the Hermite construction, it performs the velocity discretization from the continuous Boltzmann equation following certain systematic discretization techniques [49,50]. For reasons of brevity, and as the majority of this work takes place in the Hermite formalism, the description of the former can be found in Appendix A.

2.3.1 Gauss-Hermite quadrature

The Gauss-Hermite quadrature together with a Hermite polynomial expansion of the equilibrium distribution function [26, 49–51] allows for the first N equilibrium moments to be exactly recovered by the discrete equilibrium distribution function. The velocity discretization resulting from this technique is widely used in the LBM community.

2.3.1.a Decomposition of the Maxwell-Boltzmann function on the Hermite basis

In 1949 H.Grad [51] first introduced the decomposition of the Boltzmann distribution function in terms of Hermite polynomials. Lets consider the Maxwell-Boltzmann equilibrium distribution function Eq. (2.2.12) on the following form [24, 49]:

$$f^{eq} = \underbrace{\frac{1}{(2\pi r_g T_r)^{\frac{D}{2}}} \exp\left(-\frac{\boldsymbol{\xi}^2}{2 r_g T_r}\right)}_{w(\boldsymbol{\xi})} \underbrace{\rho \exp\left(\frac{2\boldsymbol{\xi}.\boldsymbol{u} - \boldsymbol{u}^2}{2 r_g T}\right)}_{f_H(\boldsymbol{\xi})}. \tag{2.3.4}$$

where w is a Gaussian weight function and T_r a constant reference temperature which will be discussed later in Sec. 2.3.1.b. H. Grad [51] showed that f_H can be identified as a generating function of the power series:

$$f_H(\boldsymbol{\xi}) = \sum_{n=0}^{+\infty} \frac{\boldsymbol{a}^{eq,(n)}}{n!(r_g T_r)^n} : \mathcal{H}^{(n)}(\boldsymbol{\xi}), \tag{2.3.5}$$

where $n! = n \times (n-1) \times ... \times 2 \times 1$, : corresponds to the Frobenius inner product, $\mathcal{H}^{(n)}(\boldsymbol{\xi})$ is the nth order Hermite polynomial given by the Rodrigues' formula:

$$\mathcal{H}^{(n)}(\boldsymbol{\xi}) = \frac{(-r_g T_r)^n}{w(\boldsymbol{\xi})} \frac{\partial^n w}{\partial \boldsymbol{\xi}^n}, \tag{2.3.6}$$

and $\boldsymbol{a}^{eq,(n)}$ is the projection of f_H onto the nth-order Hermite polynomial:

$$\boldsymbol{a}^{eq,(n)} = \langle f_H | \mathcal{H}^{(n)} \rangle = \int_{\mathbb{R}^D} f^{eq}(\boldsymbol{\xi}) \mathcal{H}^{(n)}(\boldsymbol{\xi}) \mathrm{d}\boldsymbol{\xi}, \tag{2.3.7}$$

according to the scalar product [50]:

$$\langle h(\boldsymbol{\xi}) | g(\boldsymbol{\xi}) \rangle = \int_{\mathbb{R}^D} w(\boldsymbol{\xi}) h(\boldsymbol{\xi}) g(\boldsymbol{\xi}) \mathrm{d}\boldsymbol{\xi}. \tag{2.3.8}$$

Above, the functions h and g belong to the Hermite basis. The moments $\boldsymbol{a}^{eq,(n)}$ are called Hermite moments of the equilibrium distribution function. The final expression of the Maxwell-Boltzmann equilibrium distribution function developed in terms of Hermite polynomials reads:

$$f^{eq}(\boldsymbol{\xi}) = w(\boldsymbol{\xi}) \sum_{n=0}^{+\infty} \frac{\boldsymbol{a}^{eq,(n)}}{n!(r_g T_r)^n} : \mathcal{H}^{(n)}(\boldsymbol{\xi}), \tag{2.3.9}$$

where $1/\left(n!(r_g T_r)^n\right)$ is a normalization factor. An interesting property of the Hermite polynomials is that they form an orthogonal basis of the Hilbert space [26, 50, 51] with respect to the scalar product Eq.(2.3.8), i.e.:

$$\langle \mathcal{H}^{(n)}_{\alpha_1..\alpha_n} | \mathcal{H}^{(m)}_{\beta_1..\beta_m} \rangle = \begin{cases} n!(r_g T_r)^n & \text{if } n = m \text{ and } \alpha_1..\alpha_n \hat{=} \beta_1..\beta_m \\ 0 & \text{otherwise} \end{cases}, \tag{2.3.10}$$

where the operator $\hat{=}$ is defined as the equal sign taking into account any indice permutations e.g. $xxy \hat{=} xyx$. This property allows the series Eq.(2.3.9) to be truncated up to an order N without affecting the value of the Hermite equilibrium moments up to the Nth-order [50] and thus allows the equilibrium distribution to be written as:

$$f^{eq,(N)}(\boldsymbol{\xi}) = w(\boldsymbol{\xi}) \sum_{n=0}^{N} \frac{\boldsymbol{a}^{eq,(n)}}{n! c_s^{2n}} : \mathcal{H}^{(n)}(\boldsymbol{\xi}), \tag{2.3.11}$$

where the notation $c_s = \sqrt{r_g T_r}$ has been adopted. The nth-order Hermite polynomials read, up to the fourth order, as:

$$\mathcal{H}^{(0)} = 1, \tag{2.3.12a}$$

$$\mathcal{H}^{(1)}_{\alpha} = \xi_\alpha, \tag{2.3.12b}$$

$$\mathcal{H}^{(2)}_{\alpha\beta} = \xi_\alpha \xi_\beta - c_s^2 \delta_{\alpha\beta}, \tag{2.3.12c}$$

$$\begin{aligned} \mathcal{H}^{(3)}_{\alpha\beta\gamma} &= \xi_\alpha \xi_\beta \xi_\gamma - c_s^2 \left(\xi_\alpha \delta_{\beta\gamma} + \xi_\beta \delta_{\alpha\gamma} + \xi_\gamma \delta_{\alpha\beta}\right), \\ \mathcal{H}^{(4)}_{\alpha\beta\gamma\delta} &= \xi_\alpha \xi_\beta \xi_\gamma \xi_\delta - c_s^2 \left(\xi_\alpha \xi_\beta \delta_{\gamma\delta} + \xi_\alpha \xi_\gamma \delta_{\beta\delta} + \xi_\alpha \xi_\delta \delta_{\beta\gamma} + \xi_\beta \xi_\gamma \delta_{\alpha\delta} + \xi_\beta \xi_\delta \delta_{\alpha\gamma} + \xi_\gamma \xi_\delta \delta_{\alpha\beta}\right) \\ &\quad + c_s^4 \left(\delta_{\alpha\beta}\delta_{\gamma\delta} + \delta_{\alpha\gamma}\delta_{\beta\delta} + \delta_{\alpha\delta}\delta_{\beta\gamma}\right). \end{aligned} \tag{2.3.12d}$$

along with the Hermite equilibrium moments:

$$a^{eq,(0)} = \rho, \tag{2.3.13a}$$

$$a^{eq,(1)}_{\alpha} = \rho u_\alpha, \tag{2.3.13b}$$

$$a^{eq,(2)}_{\alpha\beta} = \rho u_\alpha u_\beta + \rho c_s^2 (\theta - 1) \delta_{\alpha\beta}, \tag{2.3.13c}$$

$$\begin{aligned} a^{eq,(3)}_{\alpha\beta\gamma} &= \rho u_\alpha u_\beta u_\gamma + \rho c_s^2 (\theta - 1) \left(u_\alpha \delta_{\beta\gamma} + u_\beta \delta_{\alpha\gamma} + u_\gamma \delta_{\alpha\beta}\right), \\ a^{eq,(4)}_{\alpha\beta\gamma\delta} &= \rho u_\alpha u_\beta u_\gamma u_\delta + \rho c_s^4 (\theta - 1)^2 \left(\delta_{\alpha\beta}\delta_{\gamma\delta} + \delta_{\alpha\gamma}\delta_{\beta\delta} + \delta_{\alpha\delta}\delta_{\beta\gamma}\right) \\ &\quad + \rho c_s^2 (\theta - 1) \left(u_\alpha u_\beta \delta_{\gamma\delta} + u_\alpha u_\gamma \delta_{\beta\delta} + u_\alpha u_\delta \delta_{\beta\gamma} + u_\beta u_\gamma \delta_{\alpha\delta} + u_\beta u_\delta \delta_{\alpha\gamma} + u_\gamma u_\delta \delta_{\alpha\beta}\right), \end{aligned} \tag{2.3.13d}$$

with $\theta = r_g T/c_s^2 = T/T_r$ being commonly defined as the dimensionless temperature. The function $f^{eq,(N)}$ shares by construction the same Hermite moments (see Eq. (2.3.7)) and raw-moments as the Maxwellian function f^{eq}. To convince us of the last statment, we can compute briefly the first four raw-moments of $f^{eq,(3)}$ in function of the Hermite moments whose relations can be easily obtained inverting Eq. (2.3.12). This gives:

$$\int_{\mathbb{R}^D} 1 f^{eq,(3)} \mathrm{d}\boldsymbol{\xi} = \langle \mathcal{H}^{(0)} | f^{eq,(3)}/w \rangle = \rho = m_{eq}^{(0)}, \tag{2.3.14a}$$

$$\int_{\mathbb{R}^D} \xi_\alpha f^{eq,(3)} \mathrm{d}\boldsymbol{\xi} = \langle \mathcal{H}_\alpha^{(1)} | f^{eq,(3)}/w \rangle = \rho u_\alpha = \boldsymbol{m}_{eq}^{(1)}, \tag{2.3.14b}$$

$$\int_{\mathbb{R}^D} \xi_\alpha \xi_\beta f^{eq,(3)} \mathrm{d}\boldsymbol{\xi} = \langle \mathcal{H}_{\alpha\beta}^{(2)} + \mathcal{H}^{(0)} c_s^2 \delta_{\alpha\beta} | f^{eq,(3)}/w \rangle = \rho u_\alpha u_\beta + \rho c_s^2 \theta = \boldsymbol{m}_{eq}^{(2)}, \tag{2.3.14c}$$

$$\begin{aligned} \int_{\mathbb{R}^D} \xi_\alpha \xi_\beta \xi_\gamma f^{eq,(3)} \mathrm{d}\boldsymbol{\xi} &= \langle \mathcal{H}_{\alpha\beta\gamma}^{(3)} + c_s^2 \left(\mathcal{H}_\alpha^{(1)} \delta_{\beta\gamma} + \mathcal{H}_\beta^{(1)} \delta_{\alpha\gamma} + \mathcal{H}_\gamma^{(1)} \delta_{\alpha\beta} \right) | f^{eq,(3)}/w \rangle \\ &= \rho u_\alpha u_\beta u_\gamma + \rho c_s^2 \theta \left(u_\alpha \delta_{\beta\gamma} + u_\beta \delta_{\alpha\gamma} + u_\gamma \delta_{\alpha\beta} \right) = \boldsymbol{m}_{eq}^{(3)}. \end{aligned} \tag{2.3.14d}$$

where the orthogonality property Eq. (2.3.10) has been employed to compute the scalar products. It can be seen that this property (also valid for $N > 3$) is the key point to recover the correct equilibrium moments using a polynomial type expansion. Therefore considering $N = 4$, the present polynomial equilibrium allows the recovery of the Navier-Stokes equations.

2.3.1.b A lattice construction from the Gauss-Hermite quadrature

The idea is to discretize the velocity space while maintaining the maximum of macroscopic informations contained in the moments of the Maxwell-Boltzmann function. It has been shown previously that projecting this function in the Hermite basis produces a finite series of polynomials preserving the Maxwell-Boltzmann moments up to a desired order. The previous Hermite expansion is particularly acknowledged when discretizing the velocity space since it allows the use of the so-called Gauss-Hermite quadrature [26, 50]. Considering m discrete velocity points, this exact quadrature reads:

$$\int_{\mathbb{R}^D} \mathcal{H}^{(M)} f^{eq,(N)} \mathrm{d}\boldsymbol{\xi} = \sum_{i=0}^{m-1} \mathcal{H}_i^{(M)} f_i^{eq,(N)}, \quad \text{if} \quad M + N \leq Q, \tag{2.3.15}$$

equivalently:

$$\int_{\mathbb{R}^D} w \mathcal{H}^{(M)} \sum_{n=0}^{N} \frac{\boldsymbol{a}^{eq,(n)}}{n! c_s^{2n}} : \mathcal{H}^{(n)} \mathrm{d}\boldsymbol{\xi} = \sum_{i=0}^{m-1} w_i \mathcal{H}_i^{(M)} \sum_{n=0}^{N} \frac{\boldsymbol{a}^{eq,(n)}}{n! c_s^{2n}} : \mathcal{H}_i^{(n)}, \tag{2.3.16}$$

where w_i corresponds to the Gaussian weight of the quadrature, Q the order of accuracy of the quadrature, $\mathcal{H}_i^{(n)} = \mathcal{H}^{(n)}(\boldsymbol{\xi}_i)$ with $\boldsymbol{\xi}_i$ the ith discrete velocity. This quadrature

preserves the orthogonality properties Eq. (2.3.10) of the Hermite polynomials up to a requested order M. Then, the Mth-order equilibrium moment of the Nth-order equilibrium function can be exactly recovered if $N \geq M$, and if the quadrature order is greater than $2N-1$.

Thus, finding $\boldsymbol{\xi}_i$ and w_i using the present quadrature allows to build velocity lattices. To provide an example, let us consider the D1Q3 lattice [6], a one-dimensional discretization of the velocity space composed of three velocities i.e. $m = 3$. According to the Gauss-Hermite quadrature, the discrete velocities ξ_i are found by computing the roots of the mth order Hermite polynomial [50, 52]. In the present case, the three roots of $\mathcal{H}^{(3)}$ are found to be:

$$\mathcal{H}^{(3)}(\xi) = 0 \iff \xi^3 - 3\xi c_s^2 = 0 \quad \rightarrow \quad \xi_i = \begin{cases} 0 & \text{for } i = 0 \\ +\sqrt{3c_s^2} & \text{for } i = 1 \\ -\sqrt{3c_s^2} & \text{for } i = 2 \end{cases}, \tag{2.3.17}$$

The Gaussian weight of the quadrature can be found according to the following formula [50, 52, 53]:

$$w_i = \frac{d_m}{d_{m-1}} \frac{\langle \mathcal{H}^{(m-1)} | \mathcal{H}^{(m-1)} \rangle}{\mathcal{H}^{(m-1)}(\xi_i)\mathcal{H}^{(m)\prime}(\xi_i)}, \tag{2.3.18}$$

where the prime denotes the derivative of the polynomial with respect to the variable ξ and d_m the coefficient of the highest monomial of the polynomial $\mathcal{H}^{(m)}$. Knowing that $\mathcal{H}^{(3)\prime} = 3\xi^2 - 3c_s^2$ and using Eq.2.3.10 the weights are found to be:

$$w_0 = \frac{d_3}{d_2} \frac{\langle \mathcal{H}^{(2)} | \mathcal{H}^{(2)} \rangle}{\mathcal{H}^{(2)}(\xi_0)\mathcal{H}^{(3)\prime}(\xi_0)} = \frac{1}{1} \frac{2!c_s^4}{(-c_s^2)(-3c_s^2)} = \frac{2}{3} \tag{2.3.19a}$$

$$w_1 = \frac{d_3}{d_2} \frac{\langle \mathcal{H}^{(2)} | \mathcal{H}^{(2)} \rangle}{\mathcal{H}^{(2)}(\xi_1)\mathcal{H}^{(3)\prime}(\xi_1)} = \frac{1}{1} \frac{2!c_s^4}{(3c_s^2 - c_s^2)(9c_s^2 - 3c_s^2)} = \frac{1}{6} \tag{2.3.19b}$$

$$w_2 = \frac{d_3}{d_2} \frac{\langle \mathcal{H}^{(2)} | \mathcal{H}^{(2)} \rangle}{\mathcal{H}^{(2)}(\xi_2)\mathcal{H}^{(3)\prime}(\xi_2)} = \frac{1}{1} \frac{2!c_s^4}{(3c_s^2 - c_s^2)(9c_s^2 - 3c_s^2)} = \frac{1}{6}. \tag{2.3.19c}$$

In the LBM framework, the discrete velocity norm $r = \sqrt{3c_s^2}$ (from Eq. 2.3.17) is commonly used to obtain the dimensionless system, and reads:

$$c_0 = \frac{\xi_0}{r} = 0, \tag{2.3.20a}$$

$$c_{1,2} = \frac{\xi_{1,2}}{r} = \pm 1, \tag{2.3.20b}$$

$$c_s^* = \frac{c_s}{r} = \frac{1}{\sqrt{3}}, \tag{2.3.20c}$$

where c_i corresponds to the dimensionless discrete velocity, and c_s^* refers to as the so-called lattice speed of sound also sometimes called the lattice constant. This choice of normalization is advantageous because it allows to work with dimensionless velocities

whose norms are unity. The resulting dimensionless D1Q3 velocity lattice is sketched on Fig.2.2. Finally, the values of the velocity norm and weights ensure the validity of Eq. (2.3.15) up to $Q = 5$.

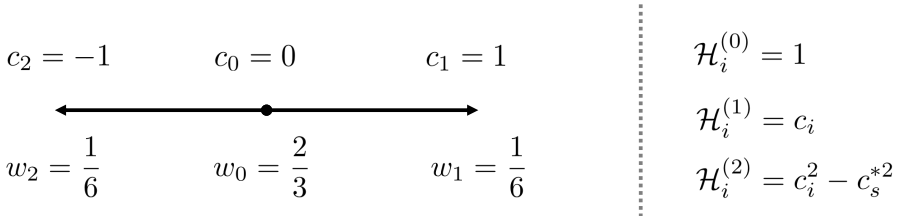

Figure 2.2 – Dimensionless D1Q3 lattice with its associated discrete weights, velocities and Hermite polynomial basis.

From this derivation, one can seen that the quadrature rule used to build this D1Q3 lattice is only able to conserve moments up to the second-order ($\mathcal{H}^{(0)}$, $\mathcal{H}^{(1)}$ and $\mathcal{H}^{(2)}$), the quadrature order being $Q = 5$. Thus, according to Eq. (2.2.43) it can be hinted that the full set of the Navier-Stokes equation cannot be retrieved. With the aim of getting the macroscopic behavior related to higher order moments, more degrees of freedom are needed. In other words, velocities with higher norm values need to be incorporated in the velocity space discretization. For instance, using a zero-one-three (ZOT) version of the D1Q5 (composed of $\xi_i \in \{0, \pm 1, \pm 3\}$) where $Q = 7$ or a D1Q7 lattice where $Q = 9$, the third and four order moments can be recovered [53–55].

Finally a discussion should be held on the constant reference temperature T_r appearing in the Gaussian weight function $w(\boldsymbol{\xi})$ in Eq. (2.3.4). Through the Rodrigues' formulae Eq. (2.3.6), one can see that the function $w(\boldsymbol{\xi})$ is used to generate the orthogonal Hermite polynomials, which in turn are used to determine the discrete velocity lattice via their roots. The latter are found to be dependent on T_r through $c_s = \sqrt{r_g T_r}$. Thus, if the temperature T was chosen instead of the constant T_r, a temperature-dependent velocity lattice would have been obtained, and whose discrete velocity norm would locally adapt in space and time. Although some LB numerical methods rely on the principle of non-constant discrete velocities such as the adaptative model of Sun et al. [56–58], the LBM algorithm (shown later in Sec. 2.4) lies on the streaming principle. The latter imposes a constant norm of the discrete velocities to ensure a node-to-node propagation on grid, and therefore imposing a constant velocity norm using the constant reference temperature T_r.

2.3.2 1D, 2D and 3D on-grid standard and multispeed velocity lattices

According to Shan et al. [50], no known general Gauss quadrature theory can be used to extend the velocity space discretization to $D > 1$ formulae. Nevertheless, a class of Gauss–Hermite formulae known as 'production' formulae can be derived from one-dimensional formulae The extension in higher dimension can be also achieved by solving an optimization problem based on the the norm and the orthogonality of the Hermite

polynomial tensors. For more details on their mathematical derivations, the interested reader may refer to [50, 53].

While hexagonal lattices have the advantage of a unique velocity magnitude, the most commonly chosen lattices topology in two and three dimension are nowadays square lattices. In this subsection, an overview of the most common velocity lattices in one, two and three dimension is provided. The lattices presented are only obtained using an on-grid quadrature. It means that the abscissas of the quadrature coincide with the grid points of a Cartesian grid. In other words, considering for instance $\boldsymbol{c_0}$ on a node of a Cartesian mesh, each discrete velocity is exactly pointing on a neighbor node. These on-grid models are also termed as space-filling models [33]. Other lattices with the very same number of velocities can be obtained solving an optimization problem without this on-grid constraint as described in [53]. A small discussion on these models (off-grid lattice or off-lattice) will be conducted later in Sec.2.7. However, these off-grid lattices are out of the scope of this PhD work which, it should be recalled, concerns the extension of LBM methods to compressible flow on Cartesian meshes using the collide and stream algorithm.

The velocity lattices in one and two dimension are provided in table 2.1, while lattices in three dimension can be found in table 2.2. The same convention as [50] is adopted to describe the lattice structure: $E^m_{D,Q}$, where D is the number of physical dimensions, Q is the order of the quadrature and m is the number of discrete velocities. In the tables, the discrete velocities are written in their dimensionless form with $\boldsymbol{c_i} = \xi_i/r$. Finally, these lattices can be found illustrated for $D = 1$ on Fig. 2.3a, for $D = 2$ Fig. 2.3b and for $D = 3$ on Fig. 2.3c from which their on-grid nature is clearly highlighted. Finally, in the LBM community the lattices involving only the first neighbor nodes are called "standard lattices" and those that take into account more distant neighbours nodes are designated as "multi-speed lattices". The lattices presented in this section can therefore be classified according to these two categories:

- **Multi-speed**: D1Q5, D1Q7, D2Q17, D2Q37, D3Q39, D3Q103.
- **Standard**: D1Q3, D2Q9, D3Q19, D3Q27.

It will be shown later that using the LBM algorithm, the standard lattices offer a compact stencil because only immediate neighbors nodes play a role in updating the solutions at the current node. This is not the case with Multi-speed lattices. The standard lattices therefore offer better performance in the context of parallel calculation, and have contributed, among other things, to the renown of the LBM. However, in the following section it will be shown that they have a non-negligible impact on macroscopic physics.

Lattice	$E^m_{D,Q}$	$\boldsymbol{c}_i$	Group	p	w_i	$1/c_s^*$
D1Q3	$E^3_{1,5}$	(0)	1	1	$2/3$	$\sqrt{3}$
		(± 1)	2	2	$1/6$	
D1Q5	$E^5_{1,7}$	$(0,0)$	1	1	$4(4 \pm \sqrt{10})/45$	$\sqrt{(5 \pm +\sqrt{10})/3}$
		(± 1)	2	2	$3(8 \pm \sqrt{10})/80$	
		(± 3)	3	2	$(16 \pm 5\sqrt{10})/720$	
D1Q7	$E^5_{1,9}$	$(0,0)$	1	1	0.47667	1.19698
		(± 1)	2	2	0.233915	
		(± 2)	3	2	0.0269381	
		(± 3)	4	2	0.00812129	
D2Q9	$E^9_{2,5}$	$(0,0)$	1	1	$4/9$	$\sqrt{3}$
		$(1,0)$	2	4	$1/9$	
		$(1,1)$	3	4	$1/36$	
D2V17	$E^{17}_{2,7}$	$(0,0)$	1	1	$(575 + 193\sqrt{193})/8100$	$\sqrt{5(25 + \sqrt{193})/72}$
		$(1,0)$	2	4	$(3355 - 91\sqrt{193})/18000$	
		$(1,1)$	3	4	$(655 + 17\sqrt{193}/27000$	
		$(2,2)$	6	4	$(685 - 49\sqrt{193})/54000$	
		$(3,0)$	7	4	$(1445 - 101\sqrt{193})/162000$	
D2V37	$E^{37}_{2,9}$	$(0,0)$	1	1	0.23315066913235250228650	1.19697977039307435897239
		$(1,0)$	2	4	0.10730609154221900241246	
		$(1,1)$	3	4	0.05766785988879488203006	
		$(2,0)$	4	4	0.01420821615845075026469	
		$(2,1)$	5	8	0.00535304900051377523273	
		$(2,2)$	6	4	0.00101193759267357547541	
		$(3,0)$	7	4	0.00024530102775771734547	
		$(3,1)$	8	8	0.00028341425299419821740	

Table 2.1 – One and two dimensional velocity lattices [49, 50, 53] presented in the same format as [50].

Lattice	$E^m_{D,Q}$	$\boldsymbol{c}_i$	Group	p	w_i	$1/c_s^*$
D3Q19	$E^{19}_{3,5}$	$(0,0,0)$	1	1	1/3	$\sqrt{3}$
		$(1,0,0)$	2	6	1/18	
		$(1,1,0)$	3	12	1/36	
D3Q27	$E^{27}_{3,5}$	$(0,0,0)$	1	1	8/27	$\sqrt{3}$
		$(1,0,0)$	2	6	2/27	
		$(1,1,0)$	3	12	1/54	
		$(1,1,1)$	4	8	1/216	
D3Q39	$E^{39}_{3,7}$	$(0,0,0)$	1	1	1/12	$\sqrt{3/2}$
		$(1,0,0)$	2	6	1/12	
		$(1,1,1)$	4	8	1/27	
		$(2,0,0)$	5	6	2/135	
		$(2,2,0)$	7	12	1/432	
		$(3,0,0)$	9	6	1/1620	
D3Q103	$E^{103}_{3,9}$	$(0,0,0)$	1	1	0.032633351764471159466	1.19697977039307435897239
		$(1,0,0)$	2	6	0.097656833590334574221	
		$(1,1,1)$	4	8	0.028097750290257335627	
		$(2,0,0)$	5	6	0.001045259560430061466	
		$(2,1,0)$	6	24	0.005705329016894815990	
		$(2,2,0)$	7	12	0.000611939269829747839	
		$(2,2,2)$	8	8	0.000155964159374283722	
		$(3,0,0)$	9	6	0.000284443251800055207	
		$(3,1,1)$	10	24	0.000130698375985191585	
		$(3,3,3)$	11	8	0.000001223194501323058	

Table 2.2 – Three dimensional velocity lattices [50, 53] presented in the same format as [50].

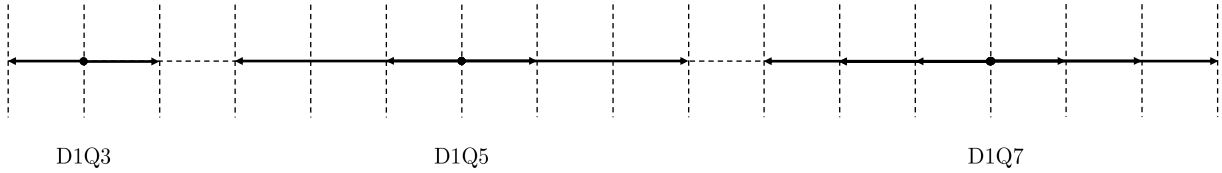

(a) One-dimensional on-grid velocity lattices.

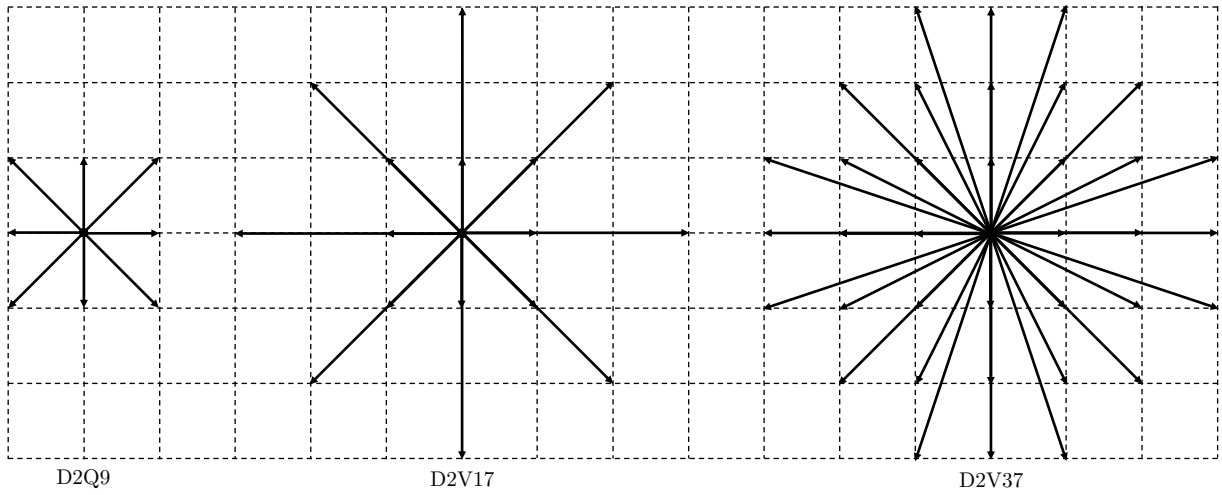

(b) Two-dimensional on-grid velocity lattices.

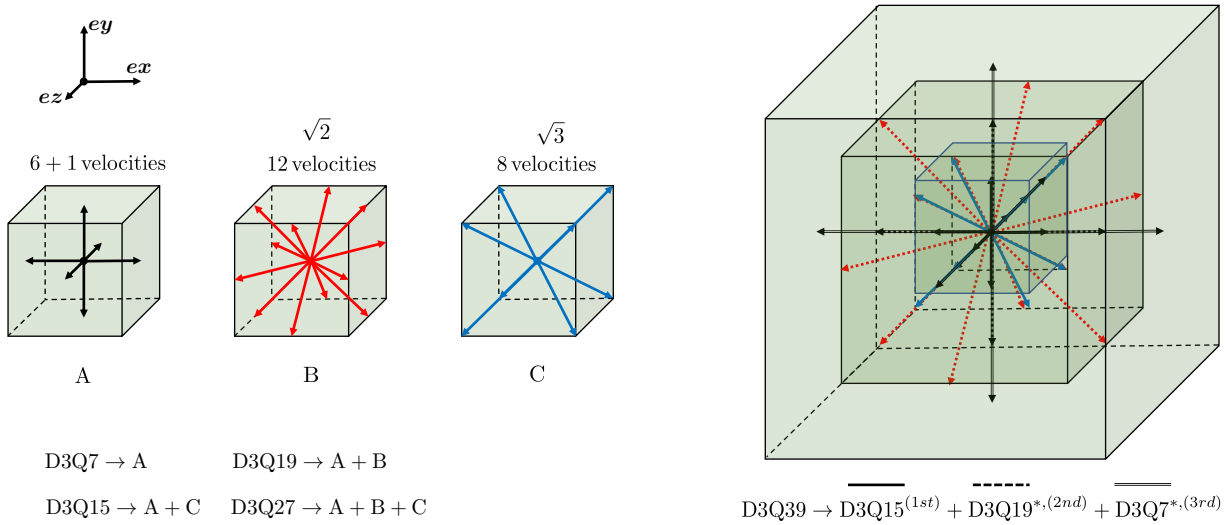

(c) Three-dimensional on-grid velocity lattices. The superscript $*$ indicates that the zeroth velocity has been removed and $1st$, $2nd$, $3rd$ refer to as the first, second or third layer of points. Here $\sqrt{2}$ makes reference to bi-diagonal directions and $\sqrt{3}$ to tri-diagonal directions.

Figure 2.3 – Sketches of some on-grid Cartesian velocity lattices [49, 50, 53]. Their structure can be found in Table 2.1 for $D = 1$ and $D = 2$ and in Table 2.2 for $D = 3$.

2.3.3 Impact of the velocity discretization on the macroscopic equations

In this section it is proposed to discuss the impact of the velocity space discretization on the macroscopic equations. For convenience, the macroscopic equations at the Navier-Stokes level derived in Sec. 2.2.5.c with their equilibrium raw-moments dependency are recalled bellow:

$$\underbrace{\frac{\partial \rho}{\partial t}}_{m^{eq,(0)}} + \underbrace{\frac{\partial (\rho u_\alpha)}{\partial x_\alpha}}_{\boldsymbol{m}^{eq,(1)}} = 0, \tag{2.3.21a}$$

$$\underbrace{\frac{\partial (\rho u_\alpha)}{\partial t}}_{\boldsymbol{m}^{eq,(1)}} + \frac{\partial}{\partial x_\beta} \underbrace{(\rho u_\alpha u_\beta + p\delta_{\alpha\beta})}_{\boldsymbol{m}^{eq,(2)}} + \frac{\partial}{\partial x_\beta} \underbrace{\left(\Pi^{(1)}_{\alpha\beta}\right)}_{\boldsymbol{m}^{eq,(2)},\boldsymbol{m}^{eq,(3)}} = 0, \tag{2.3.21b}$$

$$\underbrace{\frac{\partial (\rho E)}{\partial t}}_{\boldsymbol{m}^{eq,(2),*}} + \frac{\partial}{\partial x_\beta} \underbrace{(\rho E u_\beta + p u_\beta +)}_{\boldsymbol{m}^{eq,(3),*}} + \frac{\partial}{\partial x_\beta} \underbrace{\left(u_\beta \Pi^{(1)}_{\alpha\beta} + Q^{(1)}_\beta\right)}_{\boldsymbol{m}^{eq,(3),*},\boldsymbol{m}^{eq,(4),*}} = 0. \tag{2.3.21c}$$

It is also useful to write the relationship between the raw and the Hermite equilibrium moments along with the required quadrature order Q to compute them from a velocity lattice:

$$\underline{Q \geq 0:} \quad m^{(0)}_{eq} = a^{eq,(0)} \tag{2.3.22a}$$

$$\underline{Q \geq 2:} \quad m^{eq,(1)}_{\alpha} = a^{eq,(1)}_{\alpha} \tag{2.3.22b}$$

$$\underline{Q \geq 4:} \quad m^{eq,(2)}_{\alpha\beta} = a^{eq,(2)}_{\alpha\beta} + c_s^2 a^{eq,(0)} \delta_{\alpha\beta}, \tag{2.3.22c}$$

$$\underline{Q \geq 6:} \quad m^{eq,(3)}_{\alpha\beta\gamma} = a^{eq,(3)}_{\alpha\beta\gamma} + c_s^2 \left(a^{eq,(1)}_{\alpha} \delta_{\beta\gamma} + a^{eq,(1)}_{\beta} \delta_{\alpha\gamma} + a^{eq,(1)}_{\gamma} \delta_{\alpha\beta}\right), \tag{2.3.22d}$$

$$\begin{aligned} \underline{Q \geq 8:} \quad m^{eq,(4)}_{\alpha\beta\gamma\delta} &= a^{eq,(4)}_{\alpha\beta\gamma\delta} + c_s^4 a^{eq,(0)} (\delta_{\alpha\beta}\delta_{\gamma\delta} + \delta_{\alpha\gamma}\delta_{\beta\delta} + \delta_{\alpha\delta}\delta_{\beta\gamma}) \\ &+ c_s^2 (a^{(2)}_{\alpha\beta}\delta_{\delta\gamma} + a^{(2)}_{\alpha\gamma}\delta_{\beta\delta} + a^{(2)}_{\alpha\delta}\delta_{\beta\gamma} + a^{(2)}_{\beta\gamma}\delta_{\alpha\delta} + a^{(2)}_{\beta\delta}\delta_{\alpha\gamma} + a^{(2)}_{\gamma\delta}\delta_{\alpha\beta}). \end{aligned} \tag{2.3.22e}$$

From Eq. (2.3.21) and Eq. 2.3.22 it can be seen that the quadrature order Q of the velocity lattice has a direct impact on the macroscopic equation. Thus, depending on lattice used, one can recovers a totally different macroscopic behavior:

- **D1Q7/D2Q37/D3Q103, multi-speed lattices with $Q = 9 \rightarrow \boldsymbol{f}_i^{\boldsymbol{eq},(4)}$.**
  With these lattices the equilibrium distribution function can be expanded to $N = 4$ allowing a correct value for any equilibrium moment up to the fourth-order. The full set of Navier-Stokes equations is recovered without error.

- **D1Q5/D2Q17/D3Q39, multi-speed lattices with $Q = 7 \rightarrow \boldsymbol{f}_i^{\boldsymbol{eq},(3)}$.**
  With these lattices the equilibrium distribution function can be expanded to $N = 3$ allowing a correct value for any equilibrium moment up to the third-order only.

The mass and momentum equations are recovered without errors. However, due to the lack of discrete velocities, an error is introduced in the energy equation through $\boldsymbol{m}^{eq,(4)}$ since $\boldsymbol{a}^{eq,(4)} = 0$. This leads to an incorrect evaluation of the thermal diffusive terms, and thus the energy equation is found to be incorrect. The temperature of the system is therefore constant i.e. $\theta = \theta_0 = T_0/T_r$ leading to a barotropic equation of state [59]:

$$p_0 = \rho c_s^2 \theta = \rho r_g T_0. \tag{2.3.23}$$

Above, T_0 is constant and can be considered as a fictitious temperature due to the absence of an energy equation. Using such lattices, only an athermal version of the Navier-Stokes equation can be recovered.

- **D1Q3/D2Q9/D3Q19/D3Q27, standard lattices with $Q = 5 \rightarrow \boldsymbol{f}_i^{eq,(2)}$.** With these lattices the equilibrium distribution function can be expanded to $N = 2$ which allows only for equilibrium moments up to second order to be evaluated correctly. Only the mass equation is recovered without errors and the energy equation can not be used for obvious reasons due to $\boldsymbol{a}^{eq,(4)} = \boldsymbol{a}^{eq,(3)} = 0$, biasing both the convective and diffusive parts. Because of $\boldsymbol{a}^{eq,(3)} = 0$, the momentum equation is found with a defect in the viscous stress tensor. Starting from the Chapmann-Enskog expression of this tensor Eq. (2.2.33a), and using Eq. (2.3.22d), the error can be derived following:

$$\begin{aligned}
\Pi_{\alpha\beta}^{(1),Q=5} &= -\tau \left(\frac{\partial m_{\alpha\beta}^{eq,(2)}}{\partial t} + \frac{\partial m_{\alpha\beta\gamma}^{eq,(3)}}{\partial x_\gamma} \right) \\
&= -\tau \left(\frac{\partial m_{\alpha\beta}^{eq,(2)}}{\partial t} + \frac{\partial}{\partial x_\gamma} \left(\cancelto{=0}{a_{\alpha\beta\gamma}^{eq,(3)}} + c_s^2 \left(a_\alpha^{eq,(1)} \delta_{\beta\gamma} + a_\beta^{eq,(1)} \delta_{\alpha\gamma} + a_\gamma^{eq,(1)} \delta_{\alpha\beta} \right) \right) \right) \\
&= \Pi_{\alpha\beta}^{(1),exact} + \underbrace{\tau \frac{\partial a_{\alpha\beta\gamma}^{eq,(3)}}{\partial x_\gamma}}_{error}.
\end{aligned} \tag{2.3.24}$$

Here, $\Pi_{\alpha\beta}^{(1),Q=5}$ is the viscous stress tensor recovered using lattices of quadrature $Q = 5$ with $N = 2$ and $\Pi_{\alpha\beta}^{(1),exact}$ is the correct tensor which can be found in Eq. (2.2.36). The error in the momentum equation is thus linked to the second-order spatial derivative of the third-order Hermite moment:

$$a_{\alpha\beta\gamma}^{eq,(3)} = \rho u_\alpha u_\beta u_\gamma + \rho c_s^2 (\theta - 1) \left(u_\alpha \delta_{\beta\gamma} + u_\beta \delta_{\alpha\gamma} + u_\gamma \delta_{\alpha\beta} \right).$$

As well as the case of $Q = 7$, these kind of lattices cannot compute the energy equation. The temperature is thus considered constant $\theta = \theta_0$ leading to a barotropic equation of state Eq. (2.3.23). Finally, by considering $\theta_0 = 1$ ($T_0 = T_r$), the momentum equation is recovered with the famous $O\left(\mathrm{Ma}^3\right)$ error [60, 61] also known as Galilean invariance defect of the LBM model. The latter can produces an antidissipative behavior when the Mach number becomes too large [62, 63]. Because of this

error, the system is only able to recover the so-called athermal weakly compressible Navier-Stokes equations. Nevertheless, for standard lattices, as pointed out by Prasianakis and Karlin [64], this error can be removed by introducing a correction term into the Boltzmann-BGK equation. This point will be further discussed in the following the manuscript. Finally, it is worth noting that taking $\theta_0 \neq 1$ would leads to a $O\left(\mathrm{Ma}^1\right)$ error in the tensor.

To put it in a nutshell, the quadrature order Q determines the maximum order of truncation N of $f_i^{eq,(N)}$ in terms of Hermite polynomials. Thus, with the knowledge of Q, a systematic link between the order of truncation N and the macroscopic behavior can be done through a Chapman-Enskog expansion [49, 50]:

- Q = 9 with $f_i^{eq,(4)}$: Navier-Stokes equation
- Q = 7 with $f_i^{eq,(3)}$: Athermal Navier-Stokes equation
- Q = 5 with $f_i^{eq,(2)}$: Athermal weakly compressible Navier-Stokes equations.

The assumptions above are strictly valid for one-dimensional lattices. However, in higher dimensions some of the errors can be mitigated. Taking for example the case of the D2Q9 lattice, which can be seen as a tensor product of the D1Q3 lattice [50], the Hermite polynomials that are quadradic per direction form an orthogonal basis [49]. Thus, instead of being restricted to the second order, the complete Hermite basis of the D2Q9 lattice reads [65]:

$$\mathcal{B}^{D2Q9} = (\mathcal{H}_i^{(0)}, \mathcal{H}_{i,x}^{(1)}, \mathcal{H}_{i,y}^{(1)}, \mathcal{H}_{i,xx}^{(2)}, \mathcal{H}_{i,xy}^{(2)}, \mathcal{H}_{i,yy}^{(2)}, \mathcal{H}_{i,xxy}^{(3)}, \mathcal{H}_{i,xyy}^{(3)}, \mathcal{H}_{i,xxyy}^{(4)}), \tag{2.3.25}$$

and allows to recover these few more Hermite moments $(a_{xxy}^{eq,(3)}, a_{xyy}^{eq,(3)}, a_{xxyy}^{eq,(4)})$. This feature provide an opportunity to reduce the error in the viscous tensor Eq. (2.3.24) by enhancing the $N = 2$ equilibrium with the these third-order terms:

$$f_i^{eq,D2Q9} = f_i^{eq,2} + w_i \left[\frac{1}{2c_s^6} \left(\mathcal{H}_{i,xxy} a_{xxy}^{eq,(3)} + \mathcal{H}_{i,xyy} a_{xyy}^{eq,(3)} \right) \right]. \tag{2.3.26}$$

With this equilibrium, the only source of error that remains in the momentum equation is the one related to $\mathcal{H}_{i,\alpha\alpha\alpha} = 0$ which still restricts the model to athermal and weakly compressible simulations. This characteristic is also valid for the D3Q27 lattice which also derives from the D1Q3 using tensor products. However this is not valid for the D3Q19 which allows only to recovers moments up to $N = 2$ [65]. Finally, a more striking example can be seen in the case of the D3Q39 lattice. Although $Q = 7$ on this lattice, equipped with an adequate discrete equilibrium, the latter allows to recovers the full set of compressible Navier-Stokes equations as shown by Latt et al [66], instead of the athermal version.

Lastly, the athermal hypothesis must be discussed in more details. In fact, contrary to what has been discussed above, the momentum equation does not remain completely unchanged because of the barotropic equation of state Eq. (2.3.23). Unlike the perfect

gas relation, the barotropic relation makes pressure directly proportional to density. As a consequence, the temporal derivatives of the pressure in the term $\partial \boldsymbol{m}^{eq,(2)}/\partial t$ in the Chapmann-Enskog expression of $\Pi^{(1)}_{\alpha\beta}$ is transformed into a temporal derivative of density. This affects the trace of the tensor that becomes:

$$\Pi^{(1),athermal}_{\alpha\beta} = -\mu\left(\frac{\partial u_\alpha}{\partial x_\beta} + \frac{\partial u_\beta}{\partial x_\alpha} - \frac{2}{D}\frac{\partial u_\gamma}{\partial x_\gamma}\delta_{\alpha\beta}\right) - \mu_b \frac{\partial u_\gamma}{\partial x_\gamma}\delta_{\alpha\beta}. \tag{2.3.27}$$

Here, $\mu_b = 2\mu/D$ is a non-zero bulk viscosity appearing because of the athermal restriction and is also called the compressibility error [67]. Thus a divergence-free viscous stress tensor (similar to that obtained for an incompressible system) is recovered. A final point needs to be raised regarding this athermal approximation and concerns the speed of sound. In contrast to the thermal case where the sound waves relate to adiabatic process leading to the common isentropic speed of sound:

$$c = \sqrt{\left.\frac{\partial p}{\partial \rho}\right|_s} = \sqrt{\gamma_g c_s^2 \theta} = \sqrt{\gamma_g r_g T}, \tag{2.3.28}$$

due to the the constant temperature, the acoustic process is thus considered isothermic leading to a Newtonian sound speed:

$$c = \sqrt{\frac{\partial p}{\partial \rho}} = \sqrt{c_s^2 \theta_0} = \sqrt{r_g T_0}. \tag{2.3.29}$$

Even if an isothermal and weakly compressible flow is considered, the sound propagation will be biased by a factor $\sqrt{\gamma_g}$ which can be problematic for acoustic simulations. However, in the LBM context it is still possible to override this limitation. By setting the fictitious temperature as $T_0 = \gamma_g T_f$, the desired sound speed can be recovered where T_f refers to as the constant simulated fluid temperature.

2.4 Space and time discretization

In this section, the particular discretization of the discrete velocity Boltzmann equation leading to the lattice Boltzmann method is presented. The resulting numerical scheme is the so-called collide and stream algorithm. By nature of the streaming process, the lattice dictates the spatial mesh and time step. Using on-grid Cartesian lattices will thus produce a regular Cartesian discretization of the geometrical space.

2.4.1 The collide and stream algorithm

The last step is now the space and time discretization of the discrete velocity Boltzmann equation. Classical finite Volumes, elements or differences schemes can be used, as discussed latter in Sec. 2.7, but the LBM is a standalone method. Lets consider the discrete velocity Boltzmann-BGK equation (6.2.1) rewritten in the following form [68]:

$$\frac{D}{Ds} f_i\left(x_\alpha + \xi_{i,\alpha} s, t + s\right) = -\frac{1}{\tau}\left[f_i\left(x_\alpha + \xi_{i,\alpha} s, t + s\right) - f_i^{eq}\left(x_\alpha + \xi_{i,\alpha} s, t + s\right)\right]. \tag{2.4.1}$$

where D/Ds denotes the total derivative along the characteristic line $(x'_\alpha(s), t'(s)) = (x_\alpha + \xi_{i,\alpha} s, t + s)$ parametrized by s [69]. Integrating the equation from $s = 0$ to $s = \Delta t$ along the characteristic gives:

$$f_i\left(x_\alpha + \xi_{i,\alpha}\Delta t, t + \Delta t\right) - f_i\left(x_\alpha, t\right) = -\frac{1}{\tau}\int_0^{\Delta t}\left[f_i(x_\alpha + \xi_{i,\alpha} s, t + s) - f_i^{eq}(x_\alpha + \xi_{i,\alpha} s, t + s)\right] \mathrm{d}s \tag{2.4.2}$$

where the left-hand side corresponds to the exact integral of the convective term between t and $t + \Delta t$. The time integral of the collision term on the r.h.s of the equation is thereafter evaluated using the second-order trapezium rule and gives:

$$\begin{aligned} f_i\left(x_\alpha + \xi_{i,\alpha}\Delta t, t + \Delta t\right) - f_i\left(x_\alpha, t\right) = -\frac{\Delta t}{2\tau}\big[\, & f_i(x_\alpha + \xi_{i,\alpha}\Delta t, t + \Delta t) - f_i^{eq}(x_\alpha + \xi_{i,\alpha}\Delta t, t + \Delta t) \\ & + f_i\left(x_\alpha, t\right) - f_i^{eq}\left(x_\alpha, t\right) \big] + \mathcal{O}\left(\Delta t^3\right). \end{aligned} \tag{2.4.3}$$

At this point, the resulting scheme is implicit. Following the work of He et al. [32, 68], the implicitness of the equation can be removed by further introduce a new variable g_i which reads:

$$g_i = f_i + \frac{\Delta t}{2\tau}\left(f_i - f_i^{eq}\right). \tag{2.4.4}$$

Substituting Eq. (2.4.4) into Eq. (2.4.3), one finally obtain the LBM scheme:

$$g_i\left(x_\alpha + \xi_{i,\alpha}\Delta t, t + \Delta t\right) = g_i\left(x_\alpha, t\right) - \frac{\Delta t}{\check{\tau}}\left[g_i\left(x_\alpha, t\right) - f_i^{eq}\left(x_\alpha, t\right)\right] + \mathcal{O}\left(\Delta t^3\right), \tag{2.4.5}$$

with:

$$\check{\tau} = \tau + \Delta t/2, \tag{2.4.6}$$

a novel expression of the relaxation time induced by the change of variable. It is useful to recall the discrete velocity norm $r = \sqrt{r_g T_r}/c_s^*$ which is commonly used to obtain the dimensionless discrete velocities $c_{i,\alpha}$. Due to the construction of the method, the characteristic integration imposes:

$$r = \frac{\Delta x}{\Delta t}, \tag{2.4.7}$$

and leads to the nodes-to-nodes propagation of the distribution functions. This characteristic propagation is the so-called streaming process (illustrated on Fig. 2.4), imposing a cubic meshing (i.e. $\Delta x = \Delta y = \Delta z$) when Cartesian lattices are used. This streaming-step definitely settle the link between the time-step and the space-step, where the former is computed as:

$$\Delta t = \frac{\Delta x}{r} = \frac{\Delta x}{\sqrt{r_g T_r}} c_s^*. \tag{2.4.8}$$

The relation above is the so-called acoustic scaling [2].

In summary, the LBM discretization consists to integrate exactly the advection part of the DVBE using the method of characteristics while the collision part is evaluated using second-order trapezium rule. The LBM can be decomposed into four-steps:

$$\begin{aligned}
&\underline{\text{Equilibrium :}} && f_i^{eq} = f_i^{eq}(\rho, u_\alpha, T) \\
&\underline{\text{Collide :}} && g_i^{coll} = g_i - \frac{\Delta t}{\breve{\tau}}\left(g_i - f_i^{eq}\right) \\
&\underline{\text{Stream :}} && g_i(x_\alpha, t+\Delta t) = g_i^{coll}(x_\alpha - \xi_{i,\alpha}\Delta t, t) \\
&\underline{\text{Macroscopic :}} && (\rho, \rho u_\alpha, \rho E) = \textstyle\sum_{i=0}^{m-1}\left(1, \xi_{i,\alpha}, \xi_{i,\alpha}^2\right) g_i\left(x_\alpha, t+\Delta t\right).
\end{aligned} \tag{2.4.9}$$

and corresponds to the so-called collide and stream algorithm [2]. Here g_i^{coll} is the post-collision distribution function and $g_i(x_\alpha, t+\Delta t)$ is the streamed distribution function. This numerical scheme is second-order accurate in time and space [70]. In general, Δt, Δx and a reference density ρ_r are commonly employed to get a dimensionless system. Finally, by looking at the collide and stream algorithm Eq. (2.4.9), one can notice that Equilibrium, Collide and Macroscopic routines are local while only the Stream routine is not. This special feature is responsible for the popularity of LBM, where the communication between the nodes is only needed in one routine (the Stream), and made the LBM particularly attractive in the field of high performance massively parallel computing.

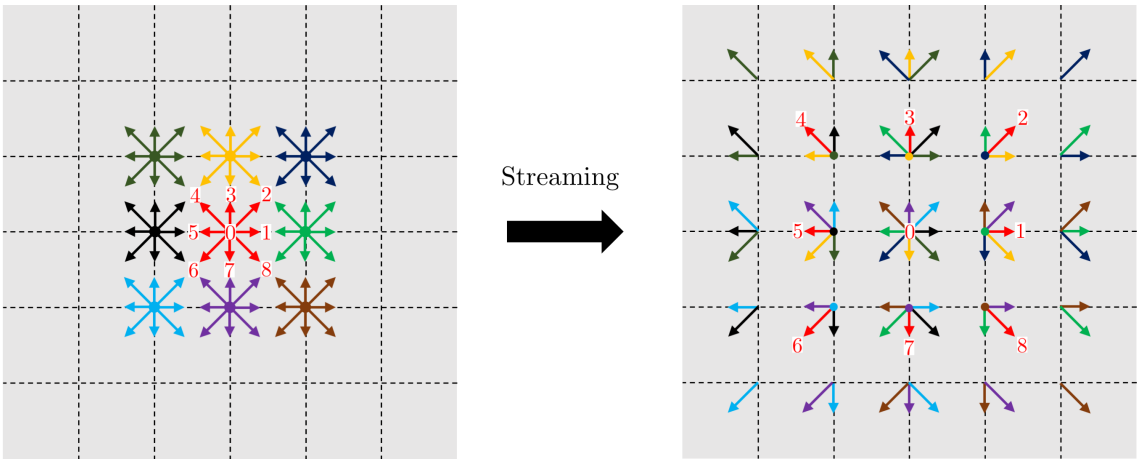

Figure 2.4 – Illustration of the streaming step on a D2Q9 lattice. The g_0 populations are represented in plain circles except for the red population

2.4.2 The change of variable on the macroscopic quantities

At this point, a discussion must be held regarding the macroscopic quantities recovered by g_i. It was seen earlier that the kinetic moments of f_i leads to the Navier-Stokes equations. So what about the moments of g_i? This answer lies in the remarkable property of the change of variable Eq. (2.4.4) since it verifies the collisional invariant Eq. (2.2.9).

Computing the three-first macroscopic moments of interest of g_i leads to:

$$\sum_{i=0}^{m-1}\left(1,\xi_{i,\alpha},\xi_{i,\alpha}^2/2\right)g_i=\sum_{i=0}^{m-1}\left(1,\xi_{i,\alpha},\xi_{i,\alpha}^2/2\right)f_i+\underbrace{\sum_{i=0}^{m-1}\left(1,\xi_{i,\alpha},\xi_{i,\alpha}^2/2\right)\frac{\Delta t}{2\tau}\left(f_i-f_i^{eq}\right)}_{=0}, \tag{2.4.10}$$

and gives the following equalities:

$$\rho=\sum_{i=0}^{m-1}g_i=\sum_{i=0}^{m-1}f_i \tag{2.4.11}$$

$$\rho u_\alpha=\sum_{i=0}^{m-1}\xi_{i,\alpha}g_i=\sum_{i=0}^{m-1}\xi_{i,\alpha}f_i \tag{2.4.12}$$

$$2\rho E=\sum_{i=0}^{m-1}\xi_{i,\alpha}\xi_{i,\alpha}g_i=\sum_{i=0}^{m-1}\xi_{i,\alpha}\xi_{i,\alpha}f_i \tag{2.4.13}$$

Thus the mass, momentum and total energy are well recovered by the moments of g_i. Nevertheless the above equalities are not necessarily true for all the kinetic moments of g_i. Indeed others non-conserved moments are affected by this change of variable [67,70]. The latter are related to the off-equilibrium part of the distribution function. It is therefore necessary to find the relation between $g_i^{(1)}$ and $f_i^{(1)}$. Inverting Eq. (2.4.4), one obtains:

$$f_i=g_i\frac{2\tau}{2\tau+\Delta t}+f_i^{eq}\frac{\Delta t}{2\tau+\Delta t}. \tag{2.4.14}$$

With this expression one can compute $f_i^{(1)}$ as a function of g_i, it follows:

$$\begin{aligned}f_i-f_i^{(eq)}&=g_i\frac{2\tau}{2\tau+\Delta t}+f_i^{eq}\frac{\Delta t}{2\tau+\Delta t}-f_i^{eq}\\&=\underbrace{\frac{2\tau}{2\tau+\Delta t}}_{\tau/\check{\tau}}\left(g_i-f_i^{eq}\right)\end{aligned} \tag{2.4.15}$$

Considering for example the viscous stress tensor $\Pi_{\alpha\beta}^{(1)}$, one can access to this moment computing:

$$\Pi_{\alpha\beta}^{(1)}=\frac{\tau}{\check{\tau}}\check{\Pi}_{\alpha\beta}^{(1)} \tag{2.4.16}$$

with:

$$\check{\Pi}_{\alpha\beta}^{(1)}=\sum_{i=0}^{m-1}\xi_{i,\alpha}\xi_{i,\beta}\left(g_i-f_i^{eq}\right). \tag{2.4.17}$$

More generally, if one consider $\boldsymbol{m}^{(1),n}$ and $\check{\boldsymbol{m}}^{(1),n}$ being respectively the off-equilibrium raw-moments of order $n\geq 2$ of f_i and g_i, this change of variables implies the following rules [67,70]:

$$\check{\boldsymbol{m}}^{(1),n}=\underbrace{\left(1+\frac{\Delta t}{2\tau}\right)}_{=\check{\tau}/\tau}\boldsymbol{m}^{(1),n} \tag{2.4.18}$$

The relation between discrete version and continuous version of the off-equilibrium moments boil down to a simple multiplication with $\check{\tau}/\tau$. In the following of the manuscript, the superscript $\check{}$ will always refers to the moments of g_i in agreement with the discrete version of the relaxation time $\check{\tau} = \tau + \Delta t/2$.

2.5 Collision operators

Stability is of key importance for an effective lattice Boltzmann algorithm. Over the years, several authors made considerable efforts in improving the stability and physical properties of the LBM-BGK schemes while maintaining the efficient collide and stream algorithm. If the algorithm is unchanged, one of the few factors affecting the stability of the method is the collision operator. Indeed, despite its simplicity, the BGK operator suffers from several drawbacks in the LBM frameworks such as numerical instabilities for high Reynolds number and a Prandtl number limitation. The basic LBM-BGK scheme is also subject to severe numerical instabilities when the Mach number and the temperature fluctuations increase [23, 24]. Some authors attribute these instabilities to non-hydrodynamic modes [59, 71] (i.e., unphysical waves inherited by the DVBE and unexpected by the Navier-Stokes equations [63]). The modal interactions occurring between these modes and hydrodynamic ones can produce numerical errors, and a so-called eigenvalue collision phenomenon leading to severe linear instabilities even for well-resolved cases [63]. In order to improve stability, other operators have been derived such as MRT (Multiple-Relaxation-Times) operators [27] which are based on the use of different relaxation times per macroscopic moments. This makes it possible to isolate the higher order non-hydrodynamic contributions responsible for instabilities and to apply to them specific relaxation times that stabilize the computation. The family of the regularized collision operators [29] is also well known in LBM community and allows to enhance the numerical stability by removing (filtering out) the non-hydrodynamic contributions [72]. More recently, the novel operator KBC [73] based on the H-theorem and the concept of MRT collision operator, has been developed and proved its stability for under resolved turbulent flow similation [74, 75] thank to its build-in sub-grid scale model. Although these collision operators are built on different assumptions, most of them remain based on the same principle of the BGK operator [9] i.e. the relaxation of the distribution function f_i toward a reference state over a characteristic time. The aim of this section is to briefly introduce the principle of the most used collision operators in LBM i.e. multi-relaxation time, regularized and entropic collision . For the sake of compactness in the following, the post streamed population will be noted $g_i^+ = g_i\left(\boldsymbol{x} + \boldsymbol{c}_i\Delta t, t + \Delta t\right)$.

2.5.1 Multiple-relaxation-time collision

The first MRT (Multiple-Relaxation-Time) collision model can be attributed to D'Humiere in 1992 [27] and has been further developed an investigated later in the early 2000s' [23, 76]. The idea behind this operator is to apply the collision step in momentum space.

The general form of the LBM-MRT equation reads:

$$g_i^+ = g_i - \boldsymbol{M}^{-1}\boldsymbol{S}\boldsymbol{M}\left(g_i - f_i^{eq}\right), \tag{2.5.1}$$

where $\boldsymbol{M^{-1}M} = \boldsymbol{I}$ with $\boldsymbol{M}$ being the transformation matrix allowing to compute the moments of the discrete distribution functions, for instance $M_{ij}f_i = (\rho, \rho u_x, \rho u_y, ...)$. $\boldsymbol{S}$ is a diagonal matrix composed of relaxation times. The aim of the MRT is to relax each moments in an independent manner allowing to modify the physical properties of the flow or to increase the stability of the scheme [23]. Originally, $\boldsymbol{M}$ has been based on the raw-moments of g_i and constructed using the Gram-Schmidt orthogonalization procedure to ensure the orthogonality of the moment basis [76]. However, many other variants have been developed over the years depending on the choice of this matrix with for instance the MRT in Hermite moment space [77], in central-moments space (also called cascaded model) [78], or in cumulant space [79]. The two-relaxation-times (TRT) [80, 81] models can also be considered as a minimalist MRT model. In the TRT, the matrix $\boldsymbol{M}$ is divided into a symmetric part (even macroscopic moments) and an antisymmetric one (odd macroscopic moments), each of them equipped with a relaxation time. While the former relaxation time is set by the physics, the latter is a free parameter. An exhaustive comparison of these collision models can be found in [82]. Regarding the matrix $\boldsymbol{S}$, here again many variants can be found depending on the choice of each relaxation times. These parameters are usually sought to increase the robustness of the LB scheme using linear stability analysis, and allow to filter out non-hydrodynamic modes responsible for instabilities [23, 80, 83, 84]. It is worth noting that for the canonical choice of $\boldsymbol{S} = \Delta t/(\tau + \Delta t/2)\boldsymbol{I}$ the LBM-BGK is recovered. Finally, in addition to improve the numerical stability, this type of operator also allows to influence the physical parameters of the flow. Taking for example the LBM-MRT equation written in the Hermite framework [77]:

$$g_i^+ = g_i - \sum_{n=2}^{N} \frac{\Delta t}{\tau_n + \Delta t/2} \frac{1}{n!\,(c_s^2)^n} \left[\check{\boldsymbol{a}}^{(n)} - \boldsymbol{a}^{eq}\right] \mathcal{H}^{(n)}, \tag{2.5.2}$$

this permits to assign a τ_n to each hydrodynamic moments via the Hermite modes [77]. For instance choosing $\tau_2 = \mu/p$ and $\tau_3 = \lambda/pc_p$ allows to get an adjustable Prandtl number $\mathrm{Pr} = \tau_2/\tau_3$.

2.5.2 Regularized collision

The regularized collision models aim at filtering out non-hydrodynamic contributions that appear during the streaming step. The concept has been originally proposed by Skordos [85] in 1993, and further investigated in 2006 by Latt and Chopard [29] for its stability properties for standard athermal LBM. These models increase, in some respect, the numerical stability of the LB scheme [72] and are based on a common principle: filtering the distribution functions, before the collision step, by reconstructing them as:

$$g_i = f_i^{eq} + g_i^{(1)} \qquad \text{with} \qquad g_i^{(1)} = w_i \sum_{n=2}^{N_r} \frac{1}{n!\,(c_s^2)^n} \check{\boldsymbol{a}}^{1,(n)} : \mathcal{H}_i^{(n)}. \tag{2.5.3}$$

Here, $\check{\boldsymbol{a}}^{1,(n)}$ is the nth-order off-equilibrium Hermite moment and N_r refers to the reconstruction order. The regularization procedure transforms the LBM-BGK equation into:

$$g_i^+ = f_i^{eq} + \left(1 - \frac{\Delta t}{\check{\tau}}\right) g_i^{(1)}, \tag{2.5.4}$$

referred to as the collide-and-stream regularized scheme. This collision is based on the orthogonality properties of the Hermite polynomials [26, 50, 51], and can be viewed as a projection before each collision step of the off-equilibrium distribution functions onto the Hermite basis up to a desired order N_r. Using this operator, the higher-order contributions (greater than N_r) related to non-hydrodynamic modes are then canceled, improving the stability of the scheme. Three main variants of regularized schemes can be found in the litterature: the projected regularized (PR) [86], the recursive regularized (RR) [65, 87] and the hybrid recursive regularized (HRR) [88] collision operators. Their major difference lies in the way off-equilibrium moments $\check{\boldsymbol{a}}^{1,(n)}$ are reconstructed. The original regularized collision model [86] was developed in such way that only the second-order moment ($N_r = 2$) is computed by projecting the off-equilibrium part onto the second-order Hermite polynomials, in the present context as:

$$\check{a}_{\alpha\beta}^{1,(2)\ \mathrm{PR}} = \sum_{i=0}^{m-1} \mathcal{H}_{i,\alpha\beta} \left(g_i - f_i^{eq}\right). \tag{2.5.5}$$

This off-equilibrium moment is indeed sufficient to recover the viscous stress tensor for athermal standard LBM. This technique can also be applied for thermal problems using higher order regularization ($N_r > 2$). The recursive regularization [65, 87] is similar to the PR as it maintains $N_r = 2$. The difference lies in the calculation of the higher-order moments which are obtained using recursive formulae derived from the Chapmann-Enskog expansion. Finally the HRR collision operator [88] shares common features with the aforementioned RR operator where the difference lies in the way $\check{a}_{\alpha\beta}^{1,(2)}$ is computed. In this instance, it is partially reconstructed using PR and finite differences schemes discretizing the viscous stress tensor. Finally, it is worth noting that some of this regularized operators can be reinterpreted in terms of MRT collision model based on the Hermit basis, the interested reader may refer to the work of Coreixas et al. [82].

2.5.3 Entropic collision

The entropic LBMs were first introduced by Karlin and Succi [28] in 1998. They noticed that the LBM could be equipped with a discrete form of the H-theorem used to (1) build a discrete equilibrium function and (2) control the relaxation toward the equilibrium in the collision process. In this context, the entropic equilibrium distribution function [28, 89, 90] is usually found as the minimizer of a convex discrete entropy functional under macroscopic conservation constraints using Lagrange multipliers [91, 92]. This entropy functional usually reads [93–96]:

$$H = \sum_i g_i \ln\left(\frac{g_i}{w_i}\right), \tag{2.5.6}$$

along with the minimization condition:

$$\frac{\partial H}{\partial g_i} = 0, \tag{2.5.7}$$

and where H is actually a Lyapunov functional, analogous to Boltzmann's H function [90]. The entropic collision operator relies directly on this entropy functional, and the modified LBM-BGK equation equipped by this operator reads [95, 97]:

$$g_i^+ = g_i + \alpha \frac{\Delta t}{2\tau + \Delta t} \left(f_i^{eq} + g_i \right). \tag{2.5.8}$$

This equation deviates from the standard LBM-BGK by a parameter α multiplying the discrete relaxation time, the latter being directly related to the fluid viscosity. This parameter is computed as the root of the entropy estimate:

$$H\left(g_i + \alpha \left(f_i^{eq} - g_i\right)\right) = H\left(g_i\right), \tag{2.5.9}$$

which defines the maximum possible change of populations in the relaxation step [95]. The root of Eq. (2.5.9) is usually found using a Newton-Raphson iterative solver. Through the entropy estimate Eq. (2.5.9), the dynamic parameter α guarantees nonlinear stability of the scheme with Eq. (2.5.6) being a non increasing Lyapunov function of Eq. (2.5.8) [95]. When $\alpha = 2$ in Eq. (2.5.8), the well known LBM-BGK equation is recovered. However, for different values of α the hydrodynamic moment related to the fluid viscosity will be changed aiming at stabilizing the simulation. Changing locally the viscosity can obviously bias the desired physics, and for that reason more elaborated version of this operator have been developed. The KBC model [73] (Karlin-Bösch-Chikatamarla) relies on moments decomposition of the distribution function. Using the KBC operator, only the higher-order moments (non-hydrodynamic) are affected by the entropy-enforcing parameter α, allowing to maintain the correct fluid viscosity. This collision can be seen as a kind of dynamic multi-relaxation operator and proved its robustness for under resolved simulations of turbulent flows in athermal [74] and thermal [75] configurations.

2.6 Initial and boundary conditions

The lattice Boltzmann method consists of successive advection and collision of discrete distribution functions and allows for the numerical simulation of a fluid behaving according to the Navier-Stokes equations. In order to simulate a flow, the boundary and initial conditions must be specified aiming at obtaining the targeted fluid flow behavior. These conditions are generally acquired from the Navier-Stokes equations and therefore apply directly to the macroscopic quantity of the discretized system. Thus, unlike a standard Navier-Stokes solver these conditions can not be directly used in LBM which deals with distribution functions instead of macroscopic variables. Therefore, an appropriate mapping from the macroscopic fluid variables to the discrete distribution functions has to be done. To this end, a brief overview of the initial and boundary conditions used in LBM are presented. These conditions are equally important than the numerical scheme itself and can have a great impact on the quality of the results.

2.6.1 Initial conditions

The most basic solution to initialize the distribution functions is to impose the latter at equilibrium [2, 33]:

$$g_i = f_i^{eq}(\rho, u_\alpha, T), \tag{2.6.1}$$

where ρ, u_α and T are the density, velocity and temperature fields at $t = 0$. This technique give reasonably good results for the initialization of steady or quasi-steady flows. However, for unsteady flows containing large gradients this scheme may lead to large errors. To take into account these gradients and improve the accuracy of the initialization, the non-equilibrium part of distribution function $g_i^{(1)}$ can be considered so that [2, 33, 85]:

$$g_i = g_i^{eq}(\rho, u_\alpha, T) + g_i^{(1)}(\rho, T, \partial u_\alpha/\partial x_\beta). \tag{2.6.2}$$

In this context, the expression of $g_i^{(1)}$ is obtained using the Chapmann-Enskog expansion, and its shape depends on the velocity lattice used for the simulation and the collision operator. The gradients in the off-equilibrium part can be computed using finite differences schemes as proposed by Skordos [85] in 1993.

2.6.2 Boundary conditions

Here, the most common boundary conditions (BCs) used in LBM are briefly presented. Compared to the standard Navier-Stokes solvers where the BCs directly apply on the macroscopic variables, in the LBM framework the BCs must be directly imposed on the distribution functions. After the streaming step, some of the distributions at the edges of the computational domain or coming from solid walls are missing. Therefore, the boundary condition is responsible for determining these unknown distributions. Fig. 2.5 illustrates the problem for distributions functions located on a boundary node.

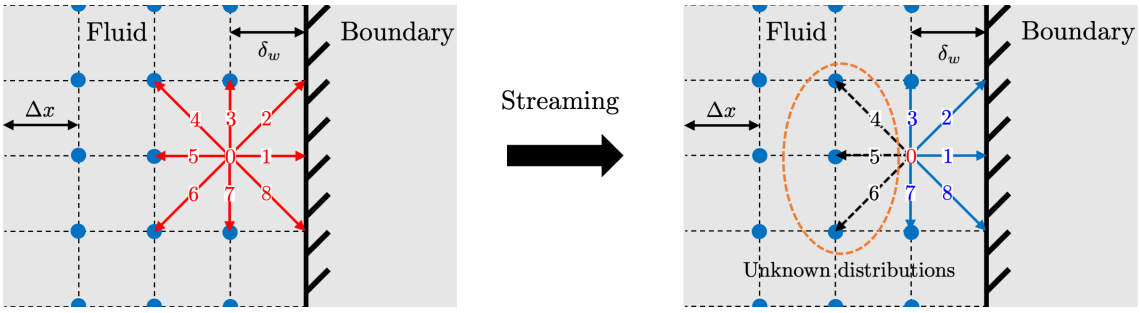

Figure 2.5 – Sketch of the boundary problem for D2Q9 lattice. The pre-streamed red distribution functions g_i are located on a boundary node at a distance δ_w from the boundary surface. After the streaming step, the distribution functions coming from the boundary (g_4, g_5, g_6) are unknown unlike the ones coming from the fluid (g_1,g_2,g_3,g_7,g_8) or staying at the boundary node g_0.

Depending on the type of boundary targeted (wall, inflow, outflow, etc), several approaches are available. The best known of solid-wall BCs schemes are without any doubts

the bounce-back schemes, and can be found below with, when it is possible, an explanation in connection with Fig. 2.5.

- Standard bounce-back(SBB), $\delta_w = 0$: The SBB rule is the most widely used scheme to model stationary no-slip walls. It assumes that a particle just reverses its velocity after colliding. On Fig. 2.5 this gives:

$$\begin{aligned} g_4 &= g_8, \\ g_5 &= g_1, \\ g_6 &= g_2. \end{aligned} \tag{2.6.3}$$

  This scheme is first-order accurate [98] and the wall is located on the boundary node i.e. $\delta_w = 0$. In the standard bounce-back scheme, the distribution functions are not collided on the boundary nodes. The macroscopic values remain therefore unknown at wall. A modified bounce-back scheme, including a collision-step at the wall can overcome the issue [33]. Moreover, additional terms to take into account non-zero velocity at wall can be included. This type of BCs gives a staircase approximation when a curved or slanted geometry is considered.

- Halfway bounce-back (HBB), $\delta_w = \Delta x/2$: This scheme allows to model stationary no-slip wall. It is based on the same principle as the SBB except that the wall is located at a halfway distance of the boundary node i.e., $\delta_w = \Delta x/2$. On Fig. 2.5 this gives:

$$\begin{aligned} g_4 &= g_8, \\ g_5 &= g_1, \\ g_6 &= g_2. \end{aligned} \tag{2.6.4}$$

  This scheme is second-order accurate [98] and the distribution functions are collided on the boundary nodes giving access to the macroscopic variables. Similarly to SBB, additional terms to take into account non-zero velocity at wall can be included [33]. This type of BCs also gives a staircase approximation if curved or slanted geometries are considered.

- Linear Bounce Back (LBB), $0 \leq \delta_w \leq \Delta x$: This scheme is based on interpolated no-slip bounce-back rules at first and second order [99, 100]. It allows to capture the curvature of geometry more accurately contrarily to SBB and HBB where the coarseness of the stair stepping determines the accuracy of the results.

The schemes above consist to relate the incoming distributions to the outgoing distribution when lattice links are crossed by a boundary surface. By using the most standard form of this kind of schemes, the macroscopic informations at the boundary are not needed and the distributions functions are self sustained. However, although such schemes are sufficient to model solid-wall conditions, for certain other conditions the macroscopic informations are required (e.g. in the case of a prescribed inflow velocity). In the aim at solving the BCs in a unified manner, Zou and He in 1997 [101], among others, developed a scheme based on the bounce-back rule on the off-equilibrium part of the distribution function [102]. Wall, inflow and outflow BCs can be achieved by such a scheme. However,

these schemes required special treatments for corner nodes and most of the applications are focused on flows with simple flat boundaries [103].

Another way to impose BCs in a unified manner and taking into account of the geometry curvature, is based on the partial or total reconstruction of the distribution functions at the boundary nodes. Knowing the fact that $g_i = f_i^{eq} + g_i^{(1)}$ (similarly to Sec. 2.6.1), the boundary macroscopic variables are used to compute the equilibrium f_i^{eq} and off-equilibrium part $g_i^{(1)}$ of the distribution function. This type of boundary scheme permits to adapt the Navier-Stokes BCs to the LBM formalism in a straightforward way. For instance, using this type of scheme Wissocq et al. [104] adapted the so-called characteristic boundary conditions [105] to LBM. The principle relies on a spatial interpolation of the macroscopic variables from the boundary surface to the boundary nodes in order to obtain f_i^{eq}. To obtain $g_i^{(1)}$ which contains the macroscopic gradients, many variants exist. For instance Latt et al. [102] in 2008 exploited the symmetry of non-equilibrium tensors to obtain $g_i^{(1)}$, and Skordos [85] in 1993 and Filippova [106] in 1998 reconstructed $f^{(1)}$ using its Chapmann-Enskog expression discretized with finite difference schemes. The latter technique will be discussed in detail for wall, inflow and outflow BCs on curved geometries in Sec. 7.3.

2.7 Literature review: Compressible Lattice Boltzmann methods

The accuracy, efficiency and scalability of the standard Lattice Boltzmann Method have been widely demonstrated over the past decades. Nevertheless, the LBM has only achieved great successes for athermal low speed flows where temperature variations are ignored, and which strictly restrains its application range. To circumvent this issue and make the simulation of compressible flows possible, three methods emerged:

1. The single distribution function (SDF) on multispeed (MS) lattices introduced by alexander et al. in 1993 [30], where higher-order lattices are considered to recover a thermal equation.

2. The double distribution function (DDF) method introduced by Shan et al. in 1997 [107], where an additional thermal LB population is introduced to compute the energy. In the state of the art, this method can be used on standard as well as MS lattices to compute compressible flows.

3. The hybrid lattice Boltzmann method (HLBM) [31], where an extra energy equation, discretized using finite differences (FD) schemes, is coupled to the LBM. As well as the DDF method, standard or MS lattices can be employed to simulate compressible flows.

The purpose of this section is therefore to review these different methods allowing to remove these limitations.

Among all the models resulting from these methods, we will see that the majority of them are able to model the weakly compressible thermal equations (under Bousinesq hypothesis), but that only a small part of them is able to simulate in a stable way the compressible Navier-Stokes equations. This lack of stability for truly thermal compressible simulations can be partly attributed to the use of the collide and stream scheme. This is why over the years several models based on another discretization of the Boltzmann equation have been developed. Although the latter do not use the collide and stream algorithm (thus they are out of the scope of this thesis), it is important to recall their existence in this literature review.

2.7.1 Compressible lattice Boltzmann models

It should be noted that other numerical solvers of the Boltzmann equation exist and could also be used for the computation of compressible flows. Some of these methods, called sometimes in the literature "Lattice Boltzmann Model", can be mistakenly confused with the Lattice Boltzmann Method of interest for the author. According to the author's PhD context, the compressible LBM method must be based on the standard collide and stream algorithm described in Sec. 2.4.1 so that the functionalities already present in the ProLB industrial solver can be directly used.

However, for compressible applications the standard algorithm turned out to be at first sight limited in terms of stability. The streaming step from nodes to nodes of g_i strongly constrains the space-step and the time-step together. For the simplest choice of equilibria and collision models, this limitation results in high numerical instability making any simulations impossible. To cope with these instability problems, many authors have deviated from the standard algorithm. In that vein, various numerical methods based on other type of space and time discretization of the Boltzmann equation have been developed. Part of these methods are listed below along with a brief description, for more details the reader may refer to the associated references:

1. Gas Kinetic Scheme (GKS) [108–111]: This method is based on a finite volume discretization of the Boltzmann-BGK equations integrated over the conserved moments. The fluxes at cell interfaces are computed using the moments of the distribution function f where the time evolution of the latter is modeled starting from a formal solution of the Boltzmann-BGK equation. The hydrodynamic variables are then updated in time and space using the fluxes as a classical finite volume solver. This scheme can simulate flows from low to high Knudsen number. Although this model does not use a lattice to discretize the velocity space, we still felt it was important to mention its existence.

2. Unified Gas Kinetic Scheme (UGKS) [110, 112, 113]: The unified scheme is an extension of the GKS from low to high Knudsen number regime with the discretization of particle velocity space. The distribution function f is thus discretized on a set of discrete microscopic velocity points supposed to recover the whole microscopic velocity space. The size of the microscopic velocity domain depends on the flow velocity and temperature. The kinetic moments are computed using quadrature

rules giving access to the fluxes at cell interfaces. The hydrodynamic variables are updated in the same way of the GKS method. Due to the high number of velocity points, this method is particularly expensive in terms of computer memory and computational efficiency.

3. Discrete Unified Gas Kinetic Scheme (DUGKS) [114, 115]: This method share traits with the LBM. It relies on a particular finite volume discretization of the DVBE where the lattice is obtained using Gauss-Hermite quadrature. A mid point rule is employed for the integration of the convective term while the collision terms is integrated using the trapezoidal rule inside each cell. The same change of variable employed by standard LBMs is employed to remove the implicitness of the method.

4. Lattice Boltzmann Flux Solver (LBFS) [116, 117]: This method directly solves the Euler or Navier-Stokes equations using finite volume method along with conventional Runge-Kutta scheme for the time evolution. However, instead of using standard flux functions such as MUSCL schemes, the fluxes at cell interface are computed using a local application of an LBM solution (using 1D or 2D lattices) for one streaming step and using spatial interpolations.

5. Off-lattice approach [56–58]: This approach relies on the collide and stream algorithm for the discretization of the DVBE. The norm of the velocities composing the lattice can be constant or can be adapted according to the the mean flow velocity or temperature. For this model, the exact node-to-node streaming step is not respected since the discrete velocities of the lattice do not exactly link the neighbor nodes. After the streaming step, spatial interpolations are thus needed to compute the distributions at nodes [33, 118], which ultimately results in a loss of accuracy compared to the direct propagation. Paradoxically, the numerical dissipation induced by this interpolations can enhance the stability compared to the standard collide and stream scheme, and allows the simulation of high Mach number flows. However, these interpolations can also lead to a loss of conservativity of the macroscopic variables. Compared to classic LBM, the implementation of such model is rather difficult and may bring many difficulties in practical applications in the case of flow dependent discrete velocity [33].

6. Miscellaneous: Other compressible methods relying on the concept of velocity lattices and a FV/FD discretization of the DVBE exist. Here are some examples of numerical scheme applied to the DVBE that can be found in the literature: McNamara et al. [48, 119] (1995) used a Lax-Wendroff scheme to stabilize the original thermal MS-LBM [30] and used two relaxation times operator to get variable Prandtl number values, Mai and Shyy [120] (1998) employed FD in curvilinear coordinates, Xi et al. [121] (1999) used FV method using bilinear interpolation to determine fluxes, Watari and Tsutara [122] (2003) discretized spatial derivatives upwind schemes giving rise to the WT model, Kataoka, Takeshi and Tsutahara [123] (2004) used a Crank-Nicolson scheme giving rise to the KT scheme, Li et al. [42] used an IMEX Runge-Kutta scheme in time and a WENO scheme in space, Dellar [124] (2008)

used the Strang splitting method [125] and combined the Beam–Warming scheme for advection with an exact solution of the collision equation, Chen et al. [126, 127] (2010/2011) proposed to extend the KT model on a 16 velocities lattices using MRT collision operator, He et al. [128] (2013) used a second order TVD IMEX FD scheme, Li et al. [129, 130] (2015) used a FV third order MUSCL scheme, and many others... However, it is to be noted that in the author point of view the DVBE discretized with classical FD/FV methods do not seem to present any advantage compared to standard Navier-Stokes solvers. Indeed, most of the methods mentioned above make the use of multipseed lattices on single (SDF) or double distribution function (DDF) to model compressible fluid flows. Thus, the resulting system of PDEs relies on a larger number of variables (scaling as the number of discrete velocities) than classical hydrodynamic variables, making them more costly than classical compressible solvers.

As mentioned in the beginning of the section, parts of these methods have been developed to eliminate the coupling issue between the mesh spacing and the time step present in standard LBM. Moreover, most of these methods can be effectively applied on non-uniform grids thanks to the finite volume formalism which is a benefit to accurately model curved solid boundaries. However, it loses the primary advantages of LBM such as simple implementation and algebraic operation. Thus, from this brief review it has been observed that none of these methods rely on the standard collide & stream algorithm or, for some of them, on the use of velocity lattices. Although it was still important to remember that these methods exist, they are out of the scope of the present work.

The compressible methods of interest, thus based only on the LBM numerical scheme will be presented in the next sections.

2.7.2 Single distribution function multi speed method

2.7.2.a Principle and history

The first category is the single distribution function (SDF) multi-speed (MS) method which is a direct extension of the LBM standard approach to compressible flows. By increasing the number of discrete velocities, this method allows to compute the third and the fourth order moments of the equilibrium distribution function allowing to recover the fully compressible thermal Navier-Stokes equations. To do so, the development equilibrium function f_i^{eq} has to include necessarily the notion of temperature without which the thermal moments won't be recovered. The mass ρ, the momentum $\rho\boldsymbol{u}$ and the energy ρE are then conserved statistical moments and are computed on a single velocity lattice with a single distribution function g_i.

The first attempt in LBM to compute the compressible Navier–Stokes equations was proposed by Alexander et al. [131] in 1992. Through the modification of certain parameters included in the equilibrium distribution, they obtain a selectable sound speed. Keeping this sound speed as low as possible allowed them to recover the compressible Navier-Stokes equation in the isothermal limit by confining the cubic Mach error term. However, their numerical validation was only on the simulation of a 1D Burgers equation

where they were able to track a shock formation. Although this model used a D2Q7 lattice (at that time known as FHP7-bit model), and thus were not based on a MS lattice, it can be nevertheless (in the author point of view) considered as the precursor of the compressible SDF models. Following their own path, one year later (1993) Alexander, Chen and Sterling [30] overcome the isothermal restriction by including to the standard D2Q9 of Qian et al. [6] four discrete velocities (hence the terms of 'higher-order lattices' and MS), and used the 'moment-matching' technique to derive the proper form of their discrete equilibrium. The four additional degrees of freedom of the D2Q13 lattice, allowed them to perform thermal weakly compressible test cases such as adiabatic sound propagation and Couette flow with heat transfer. In its original form, this method was restricted to a fixed Prandtl number (mostly due to the use of the SRT operator). In the effort to obtain lattice BGK simulations of flow with a freely controllable Prandtl number, Chen et al. [132] in 1997 developed a two-relaxation-time model on a 17 velocity lattice. One dimensional low speed shear viscosity and heat conductivity measurements shown the effectiveness of the approach. However, the model was still restricted in terms of fluid flows modelling due to the monatomic values of the heat capacity ratio $\gamma_g = (D+2)/D$. Yan et al. [133] in 1999 went further in the race for compressibility, by proposing a compressible LBM model based on multispeed [30, 134] 17 discrete velocities lattice with a specific heat γ_g ratio appearing as a chosen parameter of the model. This model includes energy in the statistical description of the equilibrium function which allowed them to compute 1D Sod's shock tube [135] and Lax's [136] problems for $\gamma_g = 1.4$. However, this model was developed to simulate the Euler equations and not the Navier-Stokes system. In addition, according to the author, this model unfortunately suffered from too many tunable parameters in the definition of the equilibrium function making it not sufficiently generic. Later, Yu et al. [137] in 2000 used the same idea than [131] but decrease the sound speed via the implementation of a force term instead of tunable parameters in the equilibrium function. The simulation of a Mach cones up to Ma = 5 demonstrate qualitatively the effectiveness of the model although the latter was still restricted to the simulation of isothermal flows. Moreover the simulations were only conducted for $\check{\tau} = 1$ which is a ridiculously high value and does not corresponds to real applications.

At that very moment, there was a big question about the stability of the SDF-MS methods allowing for the calculation of thermal compressible flows. Although the correct thermohydrodynamic equations are recovered by the models, most of the test cases were performed in 1D only and for low speed flows and fixed specific heat ratio. The majority of them being subject to numerical instabilities, a lots a authors migrated toward different discretizations of the DVBE as discussed in the previous subsection 2.7.1. Lallemand and Luo in 2000 performed the linear stability analysis and shown that the momentum and energy modes in thermal MS-LBE models have an unphysical coupling, which seriously affects the numerical stability [23]. As a solution, they proposed the Hybrid approach to solves the instability problem, this point will be discussed in detail in Sec. 2.7.4. Later, Siebert et al. [24] in 2008 also performed a linear stability analysis of thermal SDF-MS models and highlighted the strong instability issues when the temperature deviate from the reference temperature T_r in an Hermite framework.

2.7.2.b Compressible models

At that time, numerical instabilities has put a big stop to the development of thermal SDF-MS methods equipped with the collide and stream algorithm. A stable SDF-MS model will not be published until 2014. Instead of changing the numerical scheme but rather the collision operator, Frapolli et al. [96] performed thermal computations on a D2Q25 lattice equipped with the entropic collision controlling the relaxation process using the entropy estimate Eq. (2.5.9). Their equilibrium function was also found under minimization of the entropy function Eq. (2.5.6), and two relaxation parameters related to viscosity and thermal conductivity allowed them to computed thermal fluid flows with variable Prandtl number. Although being stable under the perfect gas coupling which allowed them to get good results on Rayleigh-Bénard natural convection test case, their model was restricted to low Mach number flows due to the presence in the energy equation of fourth-order error terms in velocity. This error can be attributed to the equilibrium construction on the D2Q25 lattice not containing enough discrete velocities, and certainly due to this defect they restricted their shock tube test case to low pressure ratio with high viscosity value. Additionally, the model was restricted to the monatomic value of γ_g. Nevertheless, this first entropic SDF-MS model has opened the way to others promising approaches for compressible flows. It will be seen in the next section that Frapolli and coworkers removed the compressibility flaw and the monatomic restriction in: (1) using a higher order lattice to remove compressibility errors, and (2) using a second population (DDF method) to remove the monatomic restriction. Finally, and still in the same spirit of stabilizing the LBM with collision operators, a recursive regularized collision model for thermal MS method on raw and central Hermit moments have been proposed respectively by Coreixas et al. [87] and Mattila et al. [138] in 2017. Using a D2V37 lattice, they performed a single compressible test case (1D sod shock tube) to validate their thermal models; both were restricted to a fixed Prandtl and monatomic value of γ_g. Although the restrictions on Prandtl and γ_g can eventually be addressed, the validation of a 2D model on a 1D test case is clearly not sufficient to prove the viability and robustness of a model for other compressible thermal applications.

2.7.3 Double distribution function method

2.7.3.a Principle and history

The second category is the double distribution function (DDF) which uses two populations: the first one g_i to compute the mass and the momentum equations, and the second h_i to compute the temperature of the system, and reads:

$$\begin{cases} g_i\left(x_\alpha + \xi_{i,\alpha}\Delta t, t + \Delta t\right) = g_i\left(x_\alpha, t\right) - \dfrac{\Delta t}{\check{\tau}_g}\left[g_i\left(x_\alpha, t\right) - f_i^{eq}\left(x_\alpha, t\right)\right] \\ h_i\left(x_\alpha + \xi_{i,\alpha}\Delta t, t + \Delta t\right) = h_i\left(x_\alpha, t\right) - \dfrac{\Delta t}{\check{\tau}_h}\left[h_i\left(x_\alpha, t\right) - h_i^{eq}\left(x_\alpha, t\right)\right] \end{cases} \tag{2.7.1}$$

Compared to thermal SDF-MS methods, the advantages of this method lies in the fact that both aerodynamic $\check{\tau}_g$ and thermodynamic $\check{\tau}_h$ relaxation times are naturally decou-

pled, which eventually allows to independently choose both dynamic and thermal diffusivity coefficient. Thus, contrarily to thermal SDF-MS schemes, a variable Prandtl number $\mathrm{Pr} = \tau_g/\tau_h$ is directly built in the method.

This methods has been originally introduced by Shan [107] in 1997 based on multi-component LBE model dealing with binary mixtures. Using the assumption that both components share common velocity, he had the idea of considering the density of the second component as the temperature of the system. Considering that only the zeroth-order moment is conserved by h_i, the resulting macroscopic equation is an advection-diffusion equation on the temperature. By including a buoyancy force terms, he was able to compute 2D and 3D Rayleigh Bénard natural convection cases on D2Q9 (for 2D case) and D3Q15 (for 3D case) lattice for both g_i and h_i populations.

Since then, a variety of DDF have been developed depending on the type of lattice used or the energy distribution function considered. As Shan's model were only able to model an advection-diffusion equation over temperature, He, Chen and Doolen [32] proposed in 1998 a DDF method built on the internal energy equation (known as the HCD model). Using the definition of the internal energy equation Eq. (2.2.5), they derived the evolution equation for the internal energy distribution function. Once derived in velocity space using Gauss-Hermite quadrature and in time and space using the basic discretization of LBM, the latter model was able to recover viscous heat production and compression works terms, both being missing when considering only a passive scalar equation of temperature. Using a D2Q9 lattice for both g_i and h_i, simulations of heated Couette flows for different values of Pr along with Rayleigh–Bénard convection proved the effectiveness of the model in low Mach regime.

However, when heating by viscous effect are negligible, one could ask the question of the importance of the pressure work for low-Mach fluid flows and under Boussinesq approximation. It is perhaps following this way that Guo et al. [103] developped in 2002 a model for thermal incompressible flows. Based on his previous work [139] they imposed $\nabla \cdot \boldsymbol{u} = 0$ using a modified pressure-based equilibrium of the aerodynamic population. The thermal population was built to model a simple advection-diffusion equation on temperature, and the authors stressed that a D2Q4 lattice would be sufficient for doing so instead of the D2Q9 lattice used in the work of Shan et al. [107]. The peculiarity of this model therefore lies in the fact of using two different lattices in the aerodynamic (D2Q9) and thermal (D2Q4) parts. The model was validated on two-dimensional natural convection flow in a square cavity. Later, Guo et al. in 2007 [43] developed a thermal model for low Mach number flow in the same spirit as the HCD scheme [32]. However, instead of the internal energy distribution function, this DDF method was built on the total energy distribution function which makes, according to the authors, the inclusion of compression work and viscous dissipation to be easier compared to the HCD model. They validated the model on heated Couette flows and two-dimensional natural convection flow in a square cavity using a buoyancy force term.

It is worth noting that all the previous presented DDF schemes are limited to Boussinesq flows even if they imply internal or total energy equations. Indeed, these models recover only decoupled hydrodynamic and energy equations. The aerodynamic distributions do not received any energy feedback from the thermal distribution except via the

linear buoyancy force term induced by the Boussinesq assumption. Thus the pressure gradient in the momentum equation remains isothermal excluding the computation of real compressible flows using such barotropic $p_0 = \rho c_s^2$ equation of state.

Some of the authors claimed that DDF has better stability compare to thermal SDF-MS methods [32]. However, this point needs to be clarified since the DDF methods presented above are not valid under perfect gas assumption, unlike the thermal SDF-MS methods. It will be shown in this manuscript that the perfect gas coupling between two systems could be a strong source of instability. As an example, in 2012 Li et al. [44] proposed a perfect gas coupled DDF model for low Mach flows on standard D2Q9 lattice. This model is based on the total energy model of Guo et al. [43], and is able to simulate flows with large temperature difference and thus beyond the Boussinesq assumption. For this purpose, they imposed $p = \rho c_s^2 \theta$ in keeping the temperature dependency in the Hermite expansion of the aerodynamic distribution function. To enhance the stability, they used corrective terms [64] to remove the $\mathcal{H}_{\alpha\alpha\alpha} = 0$ error induced by the standard D2Q9 lattice along with MRT collision operator. The model was tested on thermal Couette flows, attenuation-driven acoustic streaming and natural convection with large and small temperature difference. Despite their good results, in the author point of view, due to the use of the MRT collision operator, this model suffers of too much free parameters. Indeed, in function of the test cases, rather different relaxation parameters where employed, and may emphasize the fact that these parameters have to be tuned according to the test cases in order to stabilize the method.

2.7.3.b Compressible models

At this time, no DDF model that has been presented is usable for the calculation of real compressible flow. This can be attributed to fact that either:

- only incompressible equations are recovered by the model,
- the lack of robustness of the collide and stream algorithm,
- the models has a lack of stability under perfect gas coupling.

It tooks a while before real compressible DDF-LBM emerged and whose principle is very different from that presented above. In order to improve their thermal SDF-MS model on a D2Q25 lattice [96], Frapolli et al. [92] in 2015 used a lattice issued from a tensorisation of the D1Q7 lattice (so D2Q49 for $D = 2$ and D3Q343 for $D = 3$) to remove the fourth-order error terms in velocity in the energy equation. Although the compressibility error has been removed using this higher order lattice, the model was still restricted to a fixed value of adiabatic exponent. Indeed, f_i^{eq} was constructed under the minimization of the entropy function Eq. (2.5.6) with the constraints of the conservation mass, momentum, and translational energy only. Thus, f_i^{eq} was matched to the Maxwell-Boltzmann distribution where nor vibrational or rotational degrees of freedom is taken into account. To overcome this limitation, they used a concept introduced in 1975 by Rykov [140], and introduced a new population h_i aiming at carrying the energy related to

these degrees of freedom and thus enabling a variable γ_g. Setting $h_i^{eq} = (c_v - D/2)\,T f_i^{eq}$, the first moments reads:

$$\rho e = \sum_{i=0}^{m-1} h_i^{eq} = \left(c_v - \frac{D}{2}\right)\rho T, \tag{2.7.2}$$

where the specific heat c_v can be freely chosen by the user depending on wether polyatomic or monatomic fluid is modeled. Thus, the trick here is to replace in the total energy computation, the monatomic internal energy component of f_i^{eq} (namely $\rho D/2T$), by the polyatomic one (namely $\rho c_v T$) modeled by the second population h_i^{eq}. This gives:

$$\begin{aligned}\rho E &= \sum_{i=0}^{m-1} c_{i,\alpha}^2 f_i^{eq} + \sum_{i}^{m-1} h_i^{eq} \\ &= \rho\frac{D}{2}T + \frac{1}{2}\rho u_\alpha^2 + \left(c_v - \frac{D}{2}\right)\rho T \\ &= \rho\left(\frac{1}{2}u_\alpha^2 + c_v T\right),\end{aligned} \tag{2.7.3}$$

where the heat capacity ratio becomes $\gamma_g = (c_v + r_g)/c_v$ and can takes from now on any values. Thus instead of computing the whole energy of the system as the initial DDF approaches, the present DDF-MS method uses the second population solely to tune the heat capacity ratio. Using this method, the fully compressible Navier-Stokes equations for arbitrary Pr and γ_g values are recovered. Equipped with the same entropic collision operator that their precedent model [96], the authors successfully validated this entropic DDF-MS methods using a D3Q343 lattice on each populations, on cases of bow shock in front of an airfoil and the simulation of decaying compressible turbulence with shocklets. Although this entropic DDF-MS used the collide and stream algorithm and has proved good stability properties, the fact of using 686 discrete velocities makes it not affordable from the industry point of view.

It is worth noting that during the present thesis, Sadaat et al. [141] developed a compressible entropic DDF on the standard D2Q9 lattice. Using an entropic construction of equilibria along with appropriate correction terms to remove the Galilean invariance defect, their model is able to recover the Navier-Stokes compressible equation. However, they applied the concept of shifted lattices [142] to extend the model to supersonic applications. Due to this notion, the lattice cannot be considered as a space-filling lattice anymore, and interpolation is required during the advection step to reconstruct populations at the grid points. Thus, this model can be considered as an off-lattice approach as discussed in Sec. 2.7.1, and therefore does not meet the pre-requisites of this PhD work.

Finally, in the same vein of the model of Frapolli et al. [92], Latt et al. [66] also developed during this thesis (in 2019) an entropic DDF-MS methods on a reduced set of discrete velocities. Using a D3Q39 lattice the model recover the full set of Navier-Stocked equation for variable γ_g and Pr. One-dimensional Riemann problem and 2D and 3D supersonic flow past a NACA0012 aerofoil and a sphere showed the good behavior and robustness of the model. Thanks to its more moderate number of discrete velocities (78), this model seems to be the most promising DDF-MS model for compressible flows.

2.7.4 Hybrid method

2.7.4.a Principle and history

Finally the third category is the hybrid lattice Boltzmann method (HLBM). Similarly to the basic DDF method, it uses two different systems to solve separately the aerodynamic and the energy variables. However, unlike the DDF method, the computation of the energy part is done by the use of finite difference schemes applied on the desired energy equation. The recovered system is then composed of LBM and finite difference schemes hence his name: Hybrid method. Considering for instance the conservative formulation of the internal energy equation, the HLBM system can be sketched as:

$$\text{LBM}\begin{cases}\dfrac{\partial \rho}{\partial t}+\dfrac{\partial(\rho u_\alpha)}{\partial x_\alpha}=0\\[2ex] \dfrac{\partial(\rho u_\alpha)}{\partial t}+\dfrac{\partial}{\partial x_\beta}\left(\rho u_\alpha u_\beta+p\delta_{\alpha\beta}\right)=-\dfrac{\partial \Pi^{(1)}_{\alpha\beta}}{\partial x_\beta}\end{cases} \tag{2.7.4a}$$

$$\text{FD}\left\{\frac{\partial \rho e}{\partial t}+\frac{\partial}{\partial x_\alpha}\left(\rho u_\alpha e\right)=-p\frac{\partial u_\alpha}{\partial x_\alpha}+\frac{\partial}{\partial x_\alpha}\left(\lambda\frac{\partial T}{\partial x_\alpha}\right)-\Pi^{(1)}_{\alpha\beta}\frac{\partial u_\alpha}{\partial x_\beta}\right. \tag{2.7.4b}$$

with $e = c_v T = r_g T/(\gamma_g - 1)$ the internal energy. The system above highlights the advantages of this method which are twofold:

- Similarly to the DDF method it naturally allows for variable Prandtl number $\text{Pr} = \mu c_p/\lambda$). Indeed, μ is still specified by relaxation time of the LBM system while λ can be chosen in an independent manner in the energy system.
- This methods permits to get a variable heat capacity ratio γ_g without any efforts. Indeed, the latter can be directly specified in the energy system.

This versatility therefore makes this method very attractive compared to SDF-MS or DDF-MS compressible methods. Finally, the FD schemes discretizing the energy equation are perfectly adapted with the LBM of interest since the latter is built on Cartesian mesh making them easier to implement.

To the best of the author knowledge, the first HLBM has been introduced by Fillipova and Hanël in 1998 [143, 144] aiming to extend the LBM-BGK to reactive flows. Using a pressure-based formulation of the equilibrium, they used finite-difference scheme for solving the transport equations of energy and species. The model recovered the weakly compressible flow equations and allowed for the computation of reactive flows with significant density changes (depending on the local temperature). According to the authors, using such pressure-based LBM the acoustic fluctuations dissipate relatively fast [144] and allowed them to compare the results with an incompressible NS solver. Good agreements were found between the HLBM and the NS solver, with an efficiency advantage for HLBM which does not needs to solve the rather costly Poisson equation. Later, Lallemand and Luo in 2003 [31], published a HLBM with the aim of proposing a more stable scheme than SDF-MS for thermal flows computations. Using D2Q9 and D3Q13

lattices equipped with MRT collision operator, they discretized an advection-diffusion of temperature using finite differences, and coupled the momentum and the energy using appropriated terms in the MRT moment formulation. This model recovered a thermal Navier-Stokes like system with a tunable γ_g but an athermal speed or sound. Due to this flaw, this method cannot be considered as a compressible HLBM as evidenced by their validation test cases: 3D Rayleigh-Bénard convective flow [71] (2003), 2D natural convection [145] (2004) and radiation–natural convection [146] (2007) using buoyancy force term. So most of these calculations were done under the Boussinesq hypothesis keeping a barotropic equation of state, and as stressed by the authors this model is restricted to low/moderate Mach number flows [71].

Finally, it is important to note that in general, most of the HLBM models have been developed using a Boussinesq coupling and not perfect gas coupling [13, 145–149]. As pointed out by Lallemand [71] using a simple linear force terms to link the energy to the momentum allows to find almost the same numerical stability properties as the athermal LBM models. This therefore suggests that getting a numerically stable perfect gas coupled HLBM can be somehow tricky, and thus the HLBMs could share the same stability trend as for the basic DDF models as discussed in the previous section. In addition, we recall that we are looking for an LBM method for the simulation of compressible flow. Therefore, in addition to having a stable perfect gas coupling, the system must also be robust and valid for Mach numbers above 0.3.

2.7.4.b Compressible models

Nie, Shan and Chen [150] in 2009 were among the firsts to develop a real compressible HLBM. This model is based on a MS D3Q39 LBM-BGK model [50] coupled with a non-conservative entropy energy equation discretized by a Lax-Wendroff scheme. Thanks to the seventh-order of quadrature of the lattice, the mass and momentum were recovered without error. In the same spirit of Yu et al. [137], a forcing term was added in the equations to artificially decrease the numerical speed of sound to reach higher Mach numbers while preserving the stability. To further stabilize the model, they employed a fractional model [151] to improve the CFL condition while maintaining the efficiency of the collide and stream algorithm. The perfect gas coupling was achieved in keeping the temperature dependency in the Hermite expansion of f_i^{eq}. Based on positivity arguments of the equilibrium function, they developed the latter partially up to the fift-order in terms of Hermite polynomials. Finally to handle flows with discontinuities they used a shock sensor to add locally an artificial bulk viscosity. Simulation of flow around a 2D transonic RAE 2822 aerofoil proved the accuracy and the robustness of the method. The same year, Li et al. [152] applied this model on a three-dimensional case and compute subsonic flow around the DLR-F4 aircraft for a Mach number of 0.5. Later, Fares et al. [153] (2014) performed supersonic and transonic turbulent computations around complex geometries and accurately captured unsteady flow phenomena. The same year, Lew et al. [154] used a reduced version of the model of Nie et al. [150] using the standard D3Q19 lattice. With an extended collision operator [155] (US patent) and an improved temperature coupling algorithm between the LBM and the entropy equation [156, 157] (US patent, EU patent),

they accurately computed high subsonic jets flows up to Mach 0.9.

The relevance of this method (on D3Q19 for subsonic and D3Q39 for supersonic flows) has been successfully evaluated in the aeronautical context for turbofan broadband noise prediction [158], aeroacoustics of subsonic and supersonic cavities [159, 160] or high subsonic single flow hot jet computation [161]. Most of these works are based on the industrial PowerFLOW solver [162], which has been the only one, so far, showing mature results for compressible cases. Although it can be the strength of the HLBM, it also remains its weakness as most of the papers mentioned above are either AIAA conference papers or registered patents. The deep details of the method allowing it to be stable and accurate are therefore very little available from an academic point of view. Up to this day, all the LBM solvers used in the industry are based on the HLBM.

2.7.5 Synthesis and choice of a compressible LBM

During this literature review, different compressible LBM method have been presented. The publications reflecting the most advanced state of the art of each methods in 2017 (the beginning of this thesis) can be found in Table 2.3.

	Representative refs	Year	Velocity lattice	Collision model	Most advanced test case
SDF	Frapolli et al. [96]	2014	D2Q25	ELB	Shock tube, RB instability
	Coreixas et al [87]	2017	D2V37	RR	1D shock tube
	Mattila et.al [138]	2017	D2V37	CHR	1D shock tube
DDF	Frapolli et al. [163]	2015	D3Q343	ELB	sup. airfoil
	Frapolli et al. [164]	2016	D3Q343	ELB	sup. airfoil, 3D sup. double cone
HLBM	Nie et al. [150]	2009	D3Q39	FBGK	transonic airfoil
	Fares et al. [153]	2014	D3Q39	BGK	3D nozzle, transonic airfoil.
	Lew et al. [154]	2014	D3Q19	CHR	3D high subsonic jet noise prediction.

Table 2.3 – Chronological classification of the three families of compressible models with their representative state of the art references. CHR : Central Hermite regularization; FBGK: Fractional BGK

From this table it can be seen that only the HLBM and the DDF methods show a sufficient level of maturity for real compressible applications. This can be seen, in the first instance, by looking at the most advanced test cases of the SDF-MS [87, 96, 138] which are confined to very simple academic cases. Moreover, according to what has been shown, the present SDF-MS methods are limited to monatomic values of γ_g which is

prejudicial for the simulation of real flows, and it is precisely to overcome this flaw that the DDF-MS methods have been developed. We therefore eliminate the SDF-MS method from potential candidates.

Regarding the DDF-MS method [163, 164], it can be seen that the latter has the physical criteria sought, namely a variable Prandtl number and heat capacity ratio. In addition, it seems to be a fairly robust numerical method that can simulate subsonic to supersonic flows around geometries that can be assimilated to real configurations. However, the present DDF-MS model involves a large discrete velocity set which requires high storage and computational costs. Compared to a standard LBM solver that uses 19 or 27 populations, using a naive calculation, the fact of using 686 discrete velocities makes the model 25 times more expensive than a standard LBM solver. The efficient aspect of the LBM could therefore be lost which could eventually make it less competitive against the classic Navier-Stokes solver. We therefore eliminate the DDF-MS method from potential candidates.

Finally, the HLBM [150,153,154] is much less demanding in terms of discrete velocities thanks to its hybridization with finite difference solving the energy equation. It naturally recovers the compressible Navier-Stokes equation without any constraints on the either the Prandtl number or heat capacity ratio. The model based on the D3Q39 MS lattice shows to handle compressible flows from subsonic to supersonic regime, and that's for realist configurations that can be found in the industrial world [165]. In addition, the HLBM proved its robustness for the computation of high subsonic compressible flows using the standard D3Q19 lattice [154]. A compressible LBM method involving only the first neighboring nodes is highly desirable in terms of ease of implementation, e.g., for mesh refinement and boundary condition implementation. Moreover, it can therefore be considered that this method can have similar numerical efficiency than the basic athermal LBM on D3Q19 lattice, by means of the additional numerical cost induced by finite difference schemes solving the energy equation. With regard to the latter, one could indeed eventually ask the question of its numerical cost. Nevertheless, finite difference schemes are olds and well documented methods, and works perfectly on structured mesh such as the Cartesian grid. They are therefore easy to implement and well-documented schemes, so one can assume to find a scheme combining a reasonable numerical cost for an acceptable accuracy.

The characteristics of the HLBM perfectly fit the requirements of the present PhD work in terms of validity domain, ability to handle complex geometries, 'Collide and Stream' algorithm and octree based refinement technique. In addition, the fact that this model has a version based on standard lattice makes it a very attractive candidate. Indeed, beside to its reduced numerical cost compared to MS lattices, most of the existing routines of the ProLB solver e.g., boundary condition and mesh refinement, can be directly adapted to the present methods with minimal efforts. Due to its versatility in terms of energy equation, heat capacity ratio and arbitrary Prandtl number, the hybrid method is thus retained. Although the state of the art of the HLBM method is held by a company [162], and therefore its academic content is reduced, it seems to be the most efficient and promising of the LBM approaches for the simulation of compressible flow.

2.8 Summary of this chapter

In this chapter, the construction of the lattice Boltzmann method has been presented. Starting from the kinetic theory of gas, the several discretization steps leading to the so called collide and stream algorithm have been derived. The impact of the velocity discretization on the macroscopic equations has also been demonstrated, and which, highlighted the restriction of the standard LBM to the computation of athermal weakly compressible flows. Through a literature review, the different methods allowing to overcome this limitation have been presented while discarding those which do not fit the requirements of the present PhD work such as:

- On-grid lattices ensuring direct node-to-node propagation.
- Space and time discretization of the DVBE using the collide and stream algorithm.

The remaining methods were SDF-MS, DDF-MS and Hybrid LBM. The HLBM method stands out from the others since it has been found to be compliant with all the requirements of the industry:

- It recovers the compressible Navier-Stokes equations.
- It has been proved to be a robust method.
- It is apriori the least expensive method and can uses standard velocity lattices.
- It can be adapted to the ProLB solver with minimal changes.

Based on the foregoing, the present work will focus on the hybrid lattice Boltzmann method for the simulation of thermal and compressible flows. Due to its versatility, the HLBM offers numerous variants depending on collision models, velocity sets, energy equations, finite difference schemes, and coupling between the two systems. It can be assumed that the stability, efficiency and precision of the method is highly dependent on these parameters. Part of this PhD work aims at answering these questions.

Chapter 3

The Hybrid Lattice Boltzmann Method

Contents

3.1 HLBM's framework 67
3.1.1 Numerical method 67
3.1.2 Mesh element 67
3.1.3 Temporal communication 68
3.2 Energy equations for HLBM 69
3.2.1 Variables and formulations of the energy equations 69
3.2.2 Interest in the total energy equation 70
3.2.3 Interest in the entropy equation 71
3.3 Introduction to finite volume schemes 71
3.4 Introduction to finite difference schemes 74
3.4.1 Principle 74
3.4.2 Some finite difference schemes 76
3.4.3 Equivalent wave number 77
3.5 Time integration 79
3.5.1 Runge-Kutta schemes 79
3.5.2 Stability domain of times integrators 81
3.6 Some spatio temporal schemes 83
3.6.1 Scheme terminology 83
3.6.2 Numerical stability 85
3.6.2.a Spectral properties 85
3.6.2.b Stability condition 87
3.7 Hybrid lattice Boltzmann scheme under the Boussinesq approximation 88

3.7.1 The macroscopic equations 89
3.7.2 LBM with buoyancy force term 90
3.7.3 Diffusion and transport of a temperature profile 90
3.7.4 Natural convection in square cavity 93
3.7.5 Discussion 96
3.8 Hybrid lattice Boltzmann method under perfect gas coupling 98
3.8.1 The macroscopic equations 99
3.8.2 Coupling strategies 99
3.8.2.a Explicit coupling strategy via a force term 99
3.8.2.b Implicit coupling strategy via the equilibrium 100
3.8.3 Perfect gas coupling induced instabilities 101
3.8.4 Discussion 106
3.9 High Mach number instabilities 107
3.10 Conclusion and perspective 110

In this chapter, the main principles of the hybrid lattice Boltzmann method as well as the multiple possibilities to build it are presented. At first, the different choices of energy equations and numerical schemes are highlighted as well as some of their numerical properties. Then, using a basic LBM scheme, a first HLBM solving the Navier-Stokes equations under the Boussinesq approximation is presented and successfully tested on canonical test cases. Modifying slightly the LBM and energy systems in an ad hoc way, an HLBM solving the compressible Navier-Stokes equations is obtained. By means of simulations and on the basis of the existing literature, two types of instabilities are identified, thus demonstrating that the development of compressible HLBMs is challenging. Finally, conclusions and perspectives are drawn.

3.1 HLBM's framework

The HLBM combines two systems, an LBM system and an energy system solved by conventional numerical schemes. This combination therefore makes the world of HLBMs immense, as one can select any combination of LBM systems and energy systems separately. The aim of this section is not to list all the possible combinations that could give rise to a hybrid system, but simply to present the context in which one will subsequently develop. Most of the previous chapter focussed on the LBM part, therefore in the following sections, more emphasis will be placed on the energy part of the method.

3.1.1 Numerical method

In order to compute the energy equation, numerous numerical methods can be employed such as finite element, finite difference or finite volume methods, spectral method, spectral difference method etc. This method we are looking for must be easy to implement and relatively efficient so as not to degrade the performance of the LBM part. In addition, it would be preferable for the latter to offer, if necessary, sufficient degrees of freedom in terms of numerical properties to be able to adapt as well as possible to the LBM.

Most of the HLBM found in the literature are based on finite difference or finite volume methods. The latter combine simplicity of implementation and a wide choice of schemes with different numerical properties. In addition, these methods are particularly easy to implement on octree based mesh used in LBM. Therefore, the focus will be on these types of methods for the development of HLBM schemes.

3.1.2 Mesh element

Several mesh elements can be adopted within the finite difference and volume frameworks and originate from structured or unstructured grid generation. For instance, triangles or quadrilaterals of arbitrary shapes can be used in two-dimension as well as tetrahedra or hexahedron in three-dimension. The choice of these elements is generally associated with the properties of the solver and the level of geometrical complexity of the problem considered. For details one can refer to [166].

In spite of the advantages that certain methods could gain from the use of these mesh elements, a different choice than the mesh used by the LBM part would be tedious. For instance, spatial interpolations, between the LBM and FD/FV elements, would be needed to makes the systems communicate at each time step. For that reason, one therefore restricts the type of element to those used by LBM i.e., quadrilaterals (hexahedron in 3D) of equidistant sides, respectively squares in two-dimension and cubes in three-dimension, thus giving rise to Cartesian grid. In addition, FD and FV methods are particularly easy to implement on this type of mesh.

3.1.3 Temporal communication

In the previous chapter, one has seen that the LBM is an explicit single-step temporal method. To update the density and velocity fields from t to $t + \Delta t$, the LBM system will therefore require all the informations at time t including the energy variable ϕ computed by the energy system (ϕ will be defined in the next section 3.2). The same statement applies for the energy system to compute ϕ at time $t+\Delta t$ e.g., the density and the velocity fields at time t will be needed. Thus, in order to progress in time, the two systems: LBM and energy, must exchange informations at some points.

For the FV or FD methods, the optimal time step is not necessarily the same as the one used by the LBM. However, choosing a different time step would lead to a temporal desynchronisation of the two systems, and interpolations will be required to move forward in time. In fact, following this idea, there are an endless number of possibilities to make the two systems communicate with each other.

At first attempt, a simple choice without interpolation is therefore preferable. Moreover, and unless otherwise specified, if a multiple step temporal integrator is employed on the energy system (e.g., Runge-Kutta schemes [167]), the density and velocity variables will be considered constant during sub-iterations, and consequently no time interpolations will be used. In the following, the two systems LBM and energy have the same time step Δt defined by Eq. (2.4.8), and the communication will take place at each iterations as illustrated on Fig. 3.1. It turns out that the time step defined the LBM verifies, in most cases, the stability conditions of the FD/FV schemes used on energy.

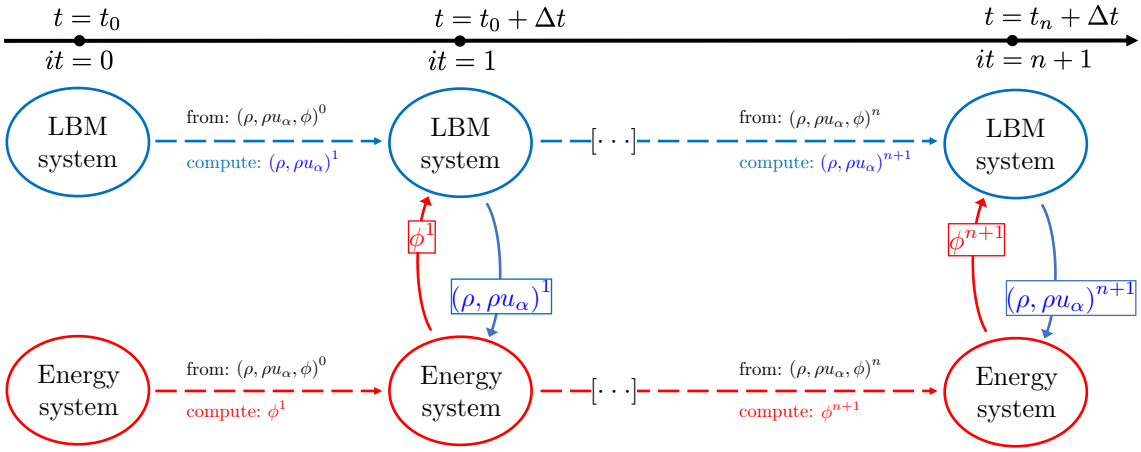

Figure 3.1 – Temporal communication between the LBM and the energy system. Both systems have the same time step and communicate at each iteration. Here, ϕ is the energy variable (see Sec. 3.2).

3.2 Energy equations for HLBM

Several energy equations can be considered in the hybrid method. In this section, some of these equations will presented along with their advantages and disadvantages.

3.2.1 Variables and formulations of the energy equations

The energy equation can be written in a general conservative form as:

$$\frac{\partial(\rho\phi)}{\partial t} + \frac{\partial(\rho u_\alpha \phi)}{\partial x_\alpha} = \mathcal{P}_\phi + \mathcal{F}_\phi + \mathcal{V}_\phi, \tag{3.2.1}$$

or, after expanding the left-hand side term of Eq. (3.2.1) and using the mass equation (2.2.38a), in a non-conservative form as:

$$\frac{\partial \phi}{\partial t} + u_\alpha \frac{\partial \phi}{\partial x_\alpha} = \frac{1}{\rho}\left(\mathcal{P}_\phi + \mathcal{F}_\phi + \mathcal{V}_\phi\right). \tag{3.2.2}$$

The quantity $\phi \in \{e, s, E\}$ corresponds to the energy variable, where $e = c_v T$ refers to the internal energy, $E = e + u_\alpha^2/2$ to the total energy and $s = c_v \ln\left(T/\rho^{\gamma_g - 1}\right)$ to the entropy, with $c_v = r_g/(\gamma_g - 1)$ the heat capacity at constant volume. $\mathcal{P}_\phi$ is the pressure work term modeling heat production induced by compressibility effects, $\mathcal{F}_\phi$ is the Fourier term referring to the heat losses by diffusion and $\mathcal{V}_\phi$ is the viscous production term modeling the heat source by friction. The expression of the temperature, as well as the source terms associated to each energy variable, are detailed in Table 3.1. It is worth noting the non-linear nature of the viscous heat production terms $\mathcal{V}_e$ and $\mathcal{V}_s$ which only involve product of partial derivatives, contrary to $\mathcal{V}_E$. The Fourier term $\mathcal{F}$, for its part, is similar for the three energy variables. Finally, the pressure work term $\mathcal{P}_\phi$ is different for the three equations, and even does not appear at all for the entropy equation.

terms \ variables	E	e	s
T	$\frac{1}{c_v}\left(E-\frac{1}{2}u_\alpha^2\right)$	$\frac{e}{c_v}$	$\rho^{\gamma_g-1}\exp\left(\frac{s}{c_v}\right)$
$\mathcal{P}_\phi$	$-\frac{\partial(u_\alpha p)}{\partial x_\alpha}$	$-p\frac{\partial u_\alpha}{\partial x_\alpha}$	$\varnothing$
$\mathcal{F}_\phi$	$\frac{\partial}{\partial x_\alpha}\left(\lambda\frac{\partial T}{\partial x_\alpha}\right)$	$\frac{\partial}{\partial x_\alpha}\left(\lambda\frac{\partial T}{\partial x_\alpha}\right)$	$\frac{1}{T}\frac{\partial}{\partial x_\alpha}\left(\lambda\frac{\partial T}{\partial x_\alpha}\right)$
$\mathcal{V}_\phi$	$-\frac{\partial}{\partial x_\beta}\left(a^{(1)}_{\alpha\beta}u_\alpha\right)$	$-a^{(1)}_{\alpha\beta}\frac{\partial u_\alpha}{\partial x_\beta}$	$-\frac{a^{(1)}_{\alpha\beta}}{T}\frac{\partial u_\alpha}{\partial x_\beta}$

Table 3.1 – Energy variables and source terms associated to each form of the energy equation. $\lambda = \mu/\mathrm{Pr}$ is the heat conductivity of the fluid.

3.2.2 Interest in the total energy equation

A remark on the conservative formulation Eq. (3.2.1) of these energy equations must be done. Even though energy equations based on the internal and entropy variables gather the mass in the temporal derivative and in the advection term, they can not be considered strictly speaking as a conservative form of equation [166]. Indeed, a conservative form derives from expressing a conservation equation in a divergence form i.e., the equation has the form of local time derivative plus a divergence of the flux. From Eq. (3.2.1) combined with Table (3.1) one can see that the only energy variable fitting with such definition is the total energy, and its conservative expression yields:

$$\frac{\partial(\rho E)}{\partial t}+\frac{\partial}{\partial x_\alpha}\left(\rho u_\alpha E+u_\alpha p-\lambda\frac{\partial T}{\partial x_\alpha}+a^{(1)}_{\beta\alpha}u_\beta\right)=0. \tag{3.2.3}$$

The notion of conservative form takes its full meaning when one integrates the above equation on a control volume V. Using the divergence theorem, it follows:

$$\int_V\frac{\partial(\rho E)}{\partial t}\mathrm{d}v+\oint_{\delta v}\left(\rho u_\alpha E+u_\alpha p-\lambda\frac{\partial T}{\partial x_\alpha}+a^{(1)}_{\beta\alpha}u_\beta\right)n_\alpha\mathrm{d}S=0, \tag{3.2.4}$$

where δv is a closed surface of V and n_α is the unit outward normal vector of δV. From this equation, one can observe that the temporal evolution of ρE inside V is solely related to incoming and out-coming advective and diffusive fluxes. Thus, there is no source or sink terms inside V meaning that ρE is a conserved quantity. For internal energy, the terms $\mathcal{P}_e$ and $\mathcal{V}_e$ cannot be casted into a divergence form as well as $\mathcal{V}_s$ and $\mathcal{F}_s$ in the case of the entropy variable. These terms will act as source or sink terms in the control volume altering the conservation of these variables. Thus, from these equations, ρE is the unique conserved quantity contrarily to ρe or ρs.

This property is the basis of the construction of the finite volume method described later.

3.2.3 Interest in the entropy equation

One can observes that the pressure work term $\mathscr{P}_\phi$ is different for the three equations, and even does not appear at all for the entropy equation. An interesting feature of the entropy equation precisely relies on this fact. The pressure work is indeed implicitly present in the definition of the entropy itself so that it is taken into account in the advection part of the entropy equation. This can be shown by using a chain rule over the advection part of s with respect to ρ and e and using the mass equation Eq. (2.2.38a):

$$\frac{\partial s}{\partial t} + u_\alpha \frac{\partial s}{\partial x_\alpha} = \frac{1}{T}\left[\frac{\partial e}{\partial t} + u_\alpha \frac{\partial e}{\partial x_\alpha} - \frac{\mathscr{P}_e}{\rho}\right], \tag{3.2.5}$$

so that the non-conservative equation on e can be recovered, including the pressure work. Details on this derivation can be found in App. B. The second advantage of this formulation yields in the fact that, for isentropic phenomena such as vortex convection or acoustics, and in low viscosity limit, the primitive variable formulation of the entropy equation is naturally reduced to $s = constant$. In such thermal cases, the value of the (non constant) temperature can be directly computed from the knowledge of a constant entropy, so that the LBM is not actually coupled with a m+1 partial differential equation[1], but with a closure relation on the entropy.

3.3 Introduction to finite volume schemes

The finite volume (FV) method is the most widely applied numerical method in CFD. It is based on cell-averaged values and can be easily implemented for arbitrary grids. The FV method was originally derived to solve the so-called conservative formulation (see the discussion in Sec. 3.2.2) of an equation or a system of equations. One considers the following one-dimensional conservative system:

$$\frac{\partial \boldsymbol{U}}{\partial t} + \frac{\partial \boldsymbol{F}(\boldsymbol{U})}{\partial x} = \boldsymbol{0}. \tag{3.3.1}$$

In this equation, $\boldsymbol{U}$ is the vector of unknowns e.g., mass, momentum and total energy (or it can be a simple scalar when one considers solely one equation) and $\boldsymbol{F}$ corresponds to the associated flux vector. With this conservative form, this type of equation can be transformed into an integral equation over a control volume V using the divergence theorem, which leads to:

$$\int_V \frac{\partial \boldsymbol{U}}{\partial t} \mathrm{d}v + \oint_{\delta V} \boldsymbol{F}(\boldsymbol{U}) \cdot n \mathrm{d}S = \boldsymbol{0}. \tag{3.3.2}$$

Here, δV is the closed surface of V and n represent the unit outward normal vector of δV. From the resulting formulae, it clearly appears that the time evolution of $\boldsymbol{U}$ inside V, is now essentially controlled by the surface values of the fluxes.

[1] One recalls that m is the number of discrete velocities of a lattice. In the HLBM context, the LBM part solves m PDEs to obtain mass and momentum.

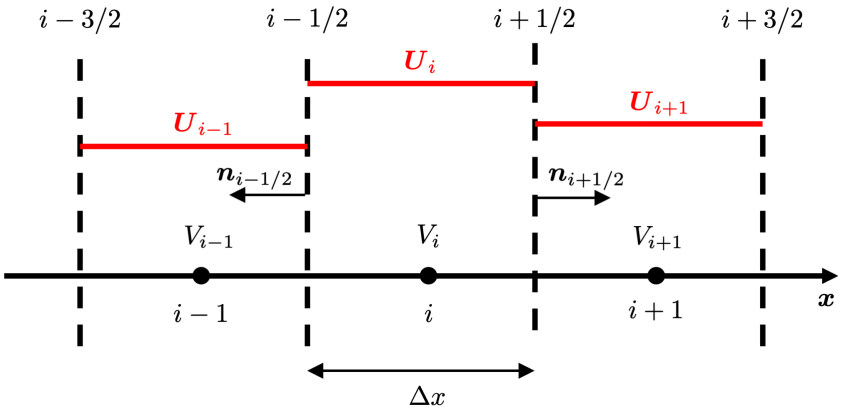

Figure 3.2 – Representation of a one-dimensional uniform numerical Cartesian domain discretized by cells. $\boldsymbol{U}_i$ is the cell averaged value of $\boldsymbol{U}$.

Now, Eq. (3.3.2) must be somehow discretized on a one-dimensional uniform Cartesian grid, to obtain a numerical scheme solving this equation at a discrete mesh point i positioned at $x = x_i = (i+1/2)\Delta x$. In this respect, the volume integral V is now called V_i and corresponds to the local finite volume of the ith cell surrounding the point i. Fig. 3.2 illustrates the x-axis, where such space discretization has been performed. Expressing now the volume integral of Eq. (3.3.2) as the averaged values over the cell, one obtains:

$$\boldsymbol{U}_i = \frac{1}{V_i}\int_{V_i} \boldsymbol{U}\,(x,t)\,\mathrm{d}v, \tag{3.3.3}$$

and leads to a piecewise constant approximation of $\boldsymbol{U}$ inside the cells. Moreover, the surface integral of Eq. (3.3.2) is expressed as the sum over all the j faces of surface ΔS_j of V_i yielding:

$$\frac{\partial \boldsymbol{U}_i}{\partial t} V_i + \sum_j \boldsymbol{F}\cdot n_j \Delta S_j = \boldsymbol{0}. \tag{3.3.4}$$

It is worth noting that for a Cartesian grid, $V_i = \Delta x^D$ and all surfaces of the cell are equal and correspond to $\Delta S_j = \Delta x^{D-1}$. Thus, for the one dimensional problem considered on Fig. 3.2, it yields:

$$\frac{\partial \boldsymbol{U}_i}{\partial t} + \frac{1}{\Delta x}\left(\boldsymbol{F}_{i+1/2} - \boldsymbol{F}_{i-1/2}\right) = \boldsymbol{0}, \tag{3.3.5}$$

where $\boldsymbol{F}_{i\pm1/2} = \boldsymbol{F}(x \pm \Delta x/2, t)$ corresponds to the value of the fluxes at the cell interface. To evaluate the time derivative, one can consider the following integration of Eq. (3.3.5):

$$\int_t^{t+\Delta t}\left[\frac{\partial \boldsymbol{U}_i}{\partial t} + \frac{1}{\Delta x}\left(\boldsymbol{F}_{i+1/2} - \boldsymbol{F}_{i-1/2}\right)\right]\mathrm{d}t = \boldsymbol{0}, \tag{3.3.6}$$

and define the following time average of the flux:

$$\boldsymbol{F}^n_{i\pm1/2} = \frac{1}{\Delta t}\int_{t^n}^{t^{n+1}} \boldsymbol{F}\left(x_{i\pm1/2}, t\right)\mathrm{d}t. \tag{3.3.7}$$

Once time integrated, Eq. (3.3.8) gives the basic formulation of the explicit finite volume method:

$$\boldsymbol{U}_i^{n+1} = \boldsymbol{U}_i^n - \frac{\Delta t}{\Delta x}\left(\boldsymbol{F}_{i+1/2} - \boldsymbol{F}_{i-1/2}\right), \tag{3.3.8}$$

where $\boldsymbol{U}_i^{n+1} = \boldsymbol{U}_i\left(t + \Delta t\right)$ and $\boldsymbol{U}_i^n = \boldsymbol{U}_i\left(t\right)$. Different FV schemes can be derived depending on the evaluation of the intercell flux $\boldsymbol{F}_{i\pm1/2}^n$. Moreover, starting from the semi-discrete form of Eq. (3.3.5), is worth noting that enhanced time integrations leading to higher accuracy schemes can be adopted. These time integrators will be presented thereafter in Sec. 3.5. Finally, it is worth noting that finite volume schemes can also be derived using a primitive variable formulation of equations. For more details, one can refers to the works of Toro et al. [168] with for instance the PRICE schemes [169].

Above, one has seen the standard derivation of the FV method for the discretization of a system of equations. However, in the present hybrid context, the focus would rather be only on the scalar case to discretize an energy equation seen previously in Sec. 3.2. The very same principle can be applied. For instance, if one considers solely the transport of a scalar ϕ at constant velocity u:

$$\frac{\partial \phi}{\partial t} + \frac{\partial u\phi}{\partial x} = 0, \tag{3.3.9}$$

it yields the following FV discretization:

$$\phi_i^{n+1} = \phi_i^n - \frac{\Delta t}{\Delta x}\left(u\phi_{i+1/2} - u\phi_{i-1/2}\right). \tag{3.3.10}$$

Since u is considered constant, the fluxes (i.e., $u\phi$) at the cell interfaces are simply reduced to the evaluation of the scalar ϕ. To estimate these values, one can use for instance the average value between two cells e.g.:

$$\phi_{i+1/2} = \frac{\phi_i + \phi_{i+1}}{2} \quad \text{and} \quad \phi_{i-1/2} = \frac{\phi_i + \phi_{i-1}}{2}. \tag{3.3.11}$$

Once these expressions inserted into Eq. (3.3.10), it yields:

$$\phi_i^{n+1} = \phi_i^n - u\frac{\Delta t}{2\Delta x}\left(\phi_{i+1} - \phi_{i-1}\right), \tag{3.3.12}$$

which corresponds to a first-order accurate in time and second-order accurate in space FV scheme. This scheme is however unconditionally unstable for $u \neq 0$, the numerical properties of the schemes will be discussed later. One will also see later on, that this scheme can be also derived using the finite difference method. Indeed, on Cartesian grid and for a certain type of equation, the two methods share some similarities [166], and differ only by the way that they are constructed.

Finally, in this chapter FV schemes will be used only very rarely, as here the finite difference method will be preferred. It was nevertheless found to be important to introduce these basic notions since later, in Chap. 4 and Chap. 5 schemes based on the FV method will be employed.

3.4 Introduction to finite difference schemes

3.4.1 Principle

In a different way than the FV method which deals with cell-averaged quantities, the main numerical quantities in the framework of the finite difference method are the local function values at the mesh points. The technique is mainly based on a Taylor expansion of the considered variable, let's say randomly $\phi(x+\Delta x)$ (considered sufficiently smooth), around x:

$$\phi(x+\Delta x) = \phi(x) + \Delta x\frac{\partial\phi}{\partial x} + \frac{\Delta x^2}{2!}\frac{\partial^2\phi}{\partial x^2} + \frac{\Delta x^3}{3!}\frac{\partial^3\phi}{\partial x^3} + ... \tag{3.4.1}$$

Once this expansion is carried out, once can rearrange it as:

$$\underbrace{\frac{\phi(x+\Delta x)-\phi(x)}{\Delta x}}_{\text{FD approximation}} = \underbrace{\frac{\partial\phi}{\partial x}}_{\text{Approximated derivative}} + \underbrace{\frac{\Delta x}{2!}\frac{\partial^2\phi}{\partial x^2} + \frac{\Delta x^2}{3!}\frac{\partial^3\phi}{\partial x^3} + ...}_{\text{Truncation error}} \tag{3.4.2}$$

Thus, knowing the values of ϕ at positions x and $x+\Delta x$ gives access to an approximation of the first-order derivative of ϕ. In view of the leading order term appearing in the truncation error, one can see that this FD approximation is first-order accurate. The aim is now to evaluate the derivative at point i, on a one-dimensional uniform Cartesian grid. Thus, the position $x = x_i = i\Delta x$ is considered and one define $\phi(x_i) = \phi_i$ and $\phi(x_i+\Delta x) = \phi_{i+1}$. Once inserted in Eq. 3.4.2, it yields:

$$\text{Forward}: \quad \left.\frac{\partial\phi}{\partial x}\right|_i = \frac{\phi_{i+1}-\phi_i}{\Delta x} + \underbrace{\mathcal{O}(\Delta x)}_{=-\Delta x/2\,(\partial^2\phi/\partial x^2)+...}, \tag{3.4.3}$$

and corresponds to a the first-order forward FD formula. The term "forward" derives from the fact that this formula takes into account the current point and the point after. A first-order backward FD formula can also be derived using the expansion of $\phi(x-\Delta x)$ around x. It yields:

$$\text{Backward}: \quad \left.\frac{\partial\phi}{\partial x}\right|_i = \frac{\phi_i-\phi_{i-1}}{\Delta x} + \underbrace{\mathcal{O}(\Delta x)}_{=+\Delta x/2\,(\partial^2\phi/\partial x^2)+...}, \tag{3.4.4}$$

These forward and backward approximations have the same order of accuracy but, they remain different in terms of truncation error. The error terms are identical with the exception of the plus/minus sign appearing in front of the even derivatives. Depending on the problem being solved, the truncation errors of these FD formulas are of crucial importance for the overall numerical stability of a scheme. Indeed, looking for instance to the leading order of Eq. (3.4.3), one may see that depending on the sign of a possible coefficient placed as a factor of the derivative, let's say randomly u, a dissipative (for $u<0$) or anti-dissipative (for $u>0$) phenomena can be introduced by the leading order error term $\partial^2\phi/\partial x^2$. The notion of numerical stability of a scheme will be discussed later.

Finally, On can obtain a centered FD approximation by simply taking the average of the forward Eq. (3.4.3) and backward Eq. (3.4.4) FD formulas, it yields:

$$\text{Centered}: \quad \left.\frac{\partial \phi}{\partial x}\right|_i = \frac{\phi_{i+1} - \phi_{i-1}}{2\Delta x} + \underbrace{\mathcal{O}\left(\Delta x^2\right)}_{=\Delta x^2/6\,(\partial^3\phi/\partial x^3)+\ldots} . \tag{3.4.5}$$

Since the even derivatives appearing in the truncation error of the forward and backward are of opposite sign, they cancel out, and a second-order accurate centered FD formula is obtained. It is worth noting that the truncation error of this formula contains only odd derivatives, and therefore no diffusive phenomena are introduced using this type of formula. The implications of this will be discussed at a later stage.

Finally, the finite difference formula described above can be now used to discretize the same equation as seen previously in the FV Sec. 3.3. A transport equation of ϕ at constant velocity u is then considered:

$$\frac{\partial \phi}{\partial t} + \frac{\partial u\phi}{\partial x} = 0. \tag{3.4.6}$$

All the partial derivatives of this equation can be approximated using the finite difference formula described above. For instance, considering the first-order forward scheme to approximate the time derivative, and the second-order centered scheme for the spatial derivative, it eventually yields:

$$\frac{\phi_i^{n+1} - \phi_i^n}{\Delta t} + \frac{u\phi_{i+1}^n - u\phi_{i-1}^n}{2\Delta x} = 0 + \mathcal{O}\left(\Delta t, \Delta x^2\right), \tag{3.4.7}$$

with $\phi_i^{n+1} = \phi\left(x, t + \Delta t\right)$. This expression can be rearranged into:

$$\phi_i^{n+1} = \phi_i^n - u\frac{\Delta t}{2\Delta x}\left(\phi_{i+1} - \phi_{i-1}\right), \tag{3.4.8}$$

and corresponds to an explicit first- and second-order accurate in time and space FD scheme modeling the transport equation (3.4.6). It is worth noting that the present scheme is the very same than the one obtained previously by the FV method Eq. (3.3.12), and one recalls that it is unconditionally unstable for $u \neq 0$. Combining differently the FD formula to discretize Eq. (3.4.8) would lead to other stable schemes of same or different nature (e.g., implicit scheme), which illustrates the richness and numerous possibilities offered by this method.

Many types of FD formulas (forward, backward, centred, mixed) can be derived. They differ in their order of accuracy and in the type of truncation error. The latter drive the spectral properties of a scheme in terms of stability and accuracy, which is of utmost importance in the domain of the numerical simulation. For more details on this method applied to CFD, one can refer for instance to [166].

3.4.2 Some finite difference schemes

Different centered, backward and forward finite difference approximations will be used in this work to model a first-order derivative. Most of them can be found in most CFD books. On a uniform grid and for different orders of accuracy, one can express them as:

$$\left.\frac{\partial \phi}{\partial x}\right|_i \simeq \begin{cases} \text{Centered}: & \frac{1}{\Delta x}\sum_{k=0} a_k \left(\phi_{i+k} - \phi_{i-k}\right), \\ \text{Backward}: & \frac{1}{\Delta x}\sum_{k=0} a_k \phi_{i-k}, \\ \text{Forward}: & \frac{1}{\Delta x}\sum_{k=0} a_k \phi_{i+k}. \end{cases} \tag{3.4.9}$$

The coefficients for generating the FD formulas can be found in Table 3.2, together with their associated order of accuracy. For practical reasons, a name has been assigned to each of these formulas. For instance, D1CO2 stands for a scheme modeling a first-order derivative (D1), using a centered second-order scheme (CO2). In the same spirit, D1UPO1 stands for a first-order accurate upwind scheme (UPO1). The terminology "upwind" will take on its full meaning later on. Finally, it is worth noting that for the first-order derivative, considering the opposite sign of the coefficients of the backward approximation gives the forward approximation. These two types of numerical schemes therefore have the same numerical properties up to the plus/minus sign, which explains why they share the same name.

To give an example, following Eq. (3.4.9) and Table 3.2, the second-order centered scheme gives:

$$\text{D1CO2}: \quad \left.\frac{\partial \phi}{\partial x}\right|_i = \frac{\phi_{i+1} - \phi_{i-1}}{2\Delta x} + \mathcal{O}\left(\Delta x^2\right), \tag{3.4.10}$$

and for the backward first-order scheme it follows:

$$\text{D1UPO1}: \quad \left.\frac{\partial \phi}{\partial x}\right|_i = \frac{\phi_i - \phi_{i-1}}{\Delta x} + \mathcal{O}\left(\Delta x\right). \tag{3.4.11}$$

Finally, to model all the terms of the energy equations seen in Sec 3.2, FD schemes able to approximate a second-order derivative are needed. Although several different schemes exist, only one type will be used in the following:

$$\text{D2CO2}: \quad \left.\frac{\partial^2 \phi}{\partial x^2}\right|_i = \frac{\phi_{i+1} - 2\phi_i + \phi_{i-1}}{\Delta x^2} + \mathcal{O}\left(\Delta x^2\right), \tag{3.4.12}$$

and corresponds to a scheme modeling a second-order derivative (D2), using a centered second-order scheme (CO2). In the work that follows, it was not considered useful to consider higher-order scheme to model this derivative.

	Name	Coefficients / Accuracy	a_0	a_1	a_2	a_3	a_4
Centered	D1CO2	2	0	1/2			
	D1CO4	4	0	2/3	−1/12		
	D1CO6	6	0	3/4	−3/20	1/60	
	D1CO8	8	0	4/5	−1/5	4/105	−1/280
Backward	D1UPO1	1	1	−1			
	D1UPO2	2	3/2	−2	1/2		
	D1UPO3	3	11/6	−3	3/2	−1/3	
Forward	D1UPO1	1	−1	1			
	D1UPO2	2	−3/2	2	−1/2		
	D1UPO3	3	−11/6	3	−3/2	1/3	

Table 3.2 – Coefficients and order of accuracy for the centered, backward and forward finite difference approximations of a first-order derivative. The formulas can be generated using Eq. (3.4.9).

3.4.3 Equivalent wave number

To see the effect of the truncation error of FD schemes, it can be interesting to derive the equivalent wave number of the FD formula. Note that this practice is well known in literature, and allows to see how well an FD formula models a continuous differential operator. The point here is to evaluate the form of the spatial FD operator in the Fourier space denoted $\mathcal{K}_{scheme}$. Let's consider the following second-order accurate FD formula:

$$\text{D1CO2}: \quad \frac{\phi_{i+1}^n - \phi_{i-1}^n}{2\Delta x} = \frac{\partial \phi}{\partial x} + \mathcal{O}\left(\Delta x^2\right). \tag{3.4.13}$$

Classically, one can linearize the scheme by considering a small perturbation ϕ' around a mean flow $\bar{\phi}$:

$$\phi_i^n = \bar{\phi} + \underbrace{\hat{\phi} e^{\mathrm{i}(\omega t^n - k x_i)}}_{\phi_i'^n}, \tag{3.4.14}$$

where the perturbation $\phi_i'^n$ corresponds to a complex monochromatic plane wave. Here, $t^n = n\Delta t$, $x_i = i\Delta x$, $\mathrm{i}^2 = -1$, k is the wave number, ω the complex pulsation and $\hat{\phi}$ is the complex amplitude of the perturbation. Once plugged in Eq. 3.4.13, and assuming that the mean flow $\bar{\phi}$ is constant, it results in:

$$\text{D1CO2}: \quad \underbrace{\frac{e^{\mathrm{i}(-k\Delta x)} - e^{\mathrm{i}(k\Delta x)}}{2\Delta x}}_{\mathcal{K}_{\text{D1CO2}}} \hat{\phi} e^{\mathrm{i}(\omega t^n - k x_i)} = \left[\underbrace{-\mathrm{i}k}_{\mathcal{K}_{\text{exact}}} + \underbrace{\mathcal{O}\left(\Delta x^2\right)}_{\mathcal{K}_{\text{error}}} \right] \hat{\phi} e^{\mathrm{i}(\omega t^n - k x_i)}. \tag{3.4.15}$$

and thus:

$$\mathcal{K}_{\text{D1CO2}} = -\mathrm{i}\frac{\sin\left(k\Delta x\right)}{\Delta x}. \tag{3.4.16}$$

$\mathcal{K}_{\mathrm{D1CO2}}$ is the so-called equivalent wave number of the D1CO2 FD formula. By looking at Eq. (3.4.15), one can see that it contains $\mathcal{K}_{exact} = -\mathrm{i}k$ and $\mathcal{K}_{error}$. The former corresponds to the exact wave number obtain by the exact first-order derivative operator $\partial/\partial x$ applied to Eq. (3.4.14). The latter contains the error of the FD formula. Thus, by looking at the real part $\mathrm{Re}\left(\mathcal{K}_{\mathrm{D1CO2}}\right)$ and imaginary part $\mathrm{Im}\left(\mathcal{K}_{\mathrm{D1CO2}}\right)$, one can access to respectively the dissipation and dispersion errors occasioned by the truncation error of the FD formula. This error is function of $k\Delta x$ which corresponds to one over the number of point per wavelength N_{ppw}[2]. The imaginary part relates to the odd derivatives and the real part to the even derivatives contained in the error. The very same manipulation can be done to other spatial schemes, and results for instance in:

$$\mathcal{K}_{\mathrm{D1UO1}} = \frac{2\sin^2\left(k\Delta x/2\right) - \mathrm{i}\sin\left(k\Delta x\right)}{\Delta x}, \tag{3.4.17a}$$

$$\mathcal{K}_{\mathrm{D2CO2}} = 2\frac{\cos\left(k\Delta x\right) - 1}{\Delta x^2}. \tag{3.4.17b}$$

Finally, $\mathrm{Re}\left(\mathcal{K}_{\mathrm{scheme}}\right)$ and $\mathrm{Im}\left(\mathcal{K}_{\mathrm{scheme}}\right)$ of different FD formulas presented previously in Sec. 3.4.2 (only the first-order derivative) can be found plotted on Fig. 3.3, and are compared to the theoretical wave number $\mathcal{K}_{exact} = -\mathrm{i}k$. From this figure, it is clear that the centered formulas have no even derivative in their truncation error ($\mathrm{Re}\left(\mathcal{K}_{\mathrm{centered}}\right) = 0$), as corroborated, for instance for the D1CO2, by Eq. (3.4.5) and Eq. (3.4.16). The backward (forward) FD operators have both real and imaginary contributions (thus odd and even derivatives in the error). Finally, one can see that for $k\Delta x \to 0$ (i.e., when $N_{ppw} \to \infty$), all the schemes converge towards the exact solution.

[2] $k\Delta x = 2\pi\Delta x/L_w = 1/N_{ppw}$ with $L_w = N_{ppw}\Delta x$ the wavelength.

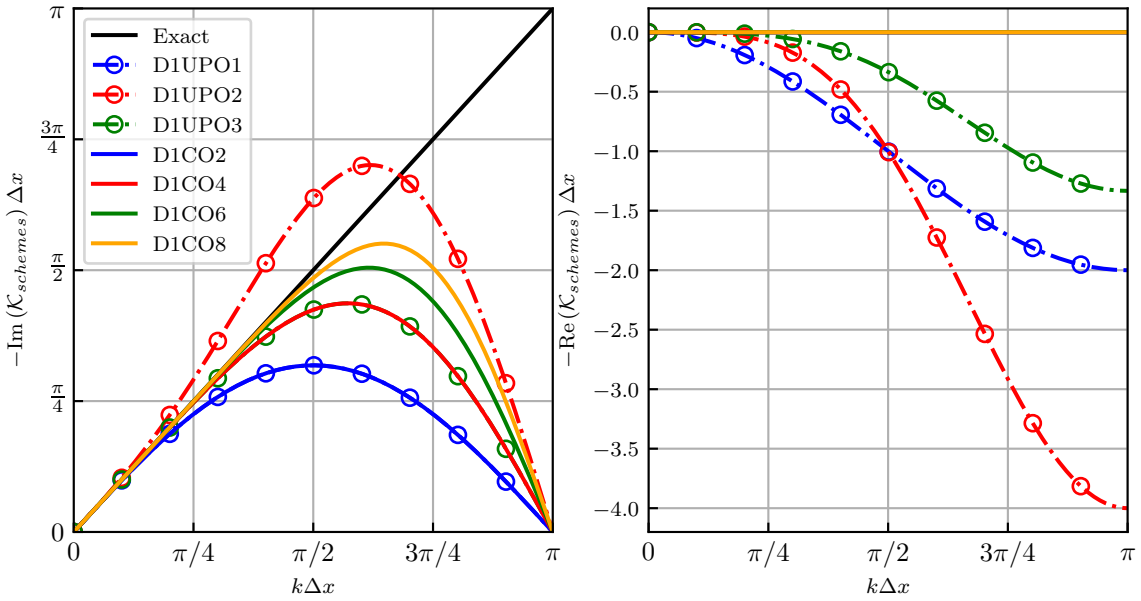

Figure 3.3 – Real and imaginary part of the modified wave number for different first-order derivative finite difference formulas. It can be observe that the centered schemes introduce zero dissipation contrarily to upwind schemes.

3.5 Time integration

Several time integrators can be employed to discretize the time derivative of PDEs. They can lead to implicit methods, which are in general unconditionally stable and allow the use of a large time step, or explicit methods which are conditionally stable and are restricted to relatively low time steps (specially for convection dominated problems). While the former seems to offers much more advantages than the latter, it remains nevertheless more complicated in terms of development and implementation and costly in terms of CPU cost compared to explicit method [166]. Moreover, one has to keep in mind that the purpose is to couple FD/FV schemes with the LBM i.e., with an explicit method. As discussed in Sec. 3.1.3, it is therefore natural at first attempt to consider explicit schemes based on the LBM time step to ensure the communication. Among the most famous, one can find the Runge–Kutta schemes which can achieve high orders of accuracy by introducing multiple stages. These schemes will be presented in the following along with a brief stability analysis.

3.5.1 Runge-Kutta schemes

Different time integrator schemes are collected in Table 3.3 and correspond to the most common techniques that can be found in the literature [166, 167]. One considers to apply these schemes on the following equation:

$$\frac{\partial \phi}{\partial t} = \mathcal{S}^H(\phi)\,, \tag{3.5.1}$$

where $\mathcal{S}^H$ gather sources or spatial convective or diffusive discrete FD operators applied to ϕ.

	K_1	K_2	K_3	K_4	$\phi^{n+1} =$	Order
RK1 (Euler)	$\mathcal{T}$	$\varnothing$	$\varnothing$	$\varnothing$	$\phi^n + \Delta t K_1$	1
RK2	$\mathcal{T}$	$\mathcal{J}$	$\varnothing$	$\varnothing$	$\phi^n + \Delta t K_2$	2
RK2 (Heun)	$\mathcal{T}$	$\mathcal{J}$	$\varnothing$	$\varnothing$	$\phi^n + \Delta t/2\,(K_1 + K_2)$	2
RK3	$\mathcal{T}$	$\mathcal{J}$	$\mathcal{K}$	$\varnothing$	$\phi^n + \Delta t/6\,(K_1 + 4K_2 + K_3)$	3
RK4	$\mathcal{T}$	$\mathcal{J}$	$\mathcal{K}^*$	$\mathcal{L}$	$\phi^n + \Delta t/6\,(K_1 + 2K_2 + 2K_3 + K_4)$	4

$$\begin{array}{c|c|c} \mathcal{T} = \mathcal{S}^H\left(\phi^n\right) & \mathcal{J} = \mathcal{S}^H\left(\phi^n + \dfrac{\Delta t}{2} K_1\right) & \mathcal{K} = \mathcal{S}^H\left(\phi^n + \Delta t\left(2K_2 - K_1\right)\right) \\ & \mathcal{K}^* = \mathcal{S}^H\left(\phi^n + \dfrac{\Delta t}{2} K_2\right) & \mathcal{L} = \mathcal{S}^H\left(\phi^n + \Delta t K_3\right) \end{array} \tag{3.5.2}$$

Table 3.3 – Standard Runge-Kutta time integrators that can be found in the literature [166, 167].

For example, from Table 3.3 the second-order two-stage Runge-Kutta (RK2 (Heun)) applied to Eq. (3.5.1) yields:

$$\begin{aligned} K_1 &= \mathcal{S}^H\left(\phi^n\right), \\ K_2 &= \mathcal{S}^H\left(\phi^n + \frac{\Delta t}{2} K_1\right), \\ \phi^{n+1} &= \phi^n + \frac{\Delta t}{2}\left(K_1 + K_2\right). \end{aligned} \tag{3.5.3}$$

In the present manuscript, only the most popular Runge-Kutta integrators that are presented in Table 3.3 will be considered. They are sufficient for the purpose of the work. The RK1 scheme (also called Euler scheme) is the most common explicit time integrator that can be found in the literature. It was employed for instance, to derive the FD scheme Eq. (3.4.8). This techniques is among the least expensive methods and is first-order accurate. The RK2 scheme is more expensive and can be seen as an explicit pedictor-corrector scheme. It first performs a predictor step to evaluate the signal at $\Delta t/2$, then perform a full time step using the approximated signal. Due to its construction, this method is also called the mid-point rule method [167]. Similarly, the RK2 Heun scheme is also a two-step method and can be seen as an explicit trapezoidal rule. Both of these RK2 schemes are second-order accurate. Finally, higher order methods can be also derived such as the multi-stages RK3 and RK4 schemes, which are respectively third- and fourth-order accurate.

As hinted by the reader, an infinite number of Runge-Kutta schemes can be defined depending on the arrangement of the stages and the coefficient that weight them. Interest-

ing properties can be obtained by playing on these parameters leading to schemes which minimize dispersion or dissipation of the scheme. These optimized schemes are of particular interest in the aeroacoustic field for instance which needs to accurately capture unsteady waves by minimizing numerical errors. For more details about Runge-Kutta schemes, one can refer to [167].

3.5.2 Stability domain of times integrators

The stability analysis for numerical methods for PDEs usually deals with a linear advection prototype equation. Let's then consider our well known convection equation on ϕ at constant velocity u:

$$\frac{\partial \phi}{\partial t} = -u\frac{\partial \phi}{\partial x}. \tag{3.5.4}$$

Classically, one can linearize the scheme using $\phi = \bar{\phi} + \phi'$. Once a spatial Fourier transform is applied $\phi'(x,t) \rightarrow \tilde{\phi}(k,t)$ one obtains:

$$\frac{\partial \tilde{\phi}}{\partial t} = \underbrace{-\bar{u}\underbrace{(-\mathrm{i}k)}_{\mathcal{K}_{exact}}}_{\lambda}\tilde{\phi}, \tag{3.5.5}$$

where λ corresponds to the eigenvalue of the equation.

At this point, some observations and remarks can be done for a better understanding of the following. First, if the equation is analytically solved in time, the imaginary part $\mathrm{Im}(\lambda)$ will give the propagation of the wave, while the real part $\mathrm{Re}(\lambda)$ will rules the dissipation of the wave. If $\mathrm{Re}(\lambda) > 0$ the wave has an exponential growth rate while if $\mathrm{Re}(\lambda) < 0$ the signal will decay exponentially. Secondly, it worth noting that when looking at Eq. 3.5.5, $\mathrm{Im}(\lambda) = 0$ means that the physics are essentially propagative. Finally, in the present case the spatial derivative in the Fourier space is exactly solved and gives $\mathcal{K}_{exact} = -\mathrm{i}k$. However, it is important to note that the stability analysis that will follow can also be applied to the discrete case by considering $\mathcal{K}_{scheme}$ instead.

Applying now a semi-discrete scheme in time to solve the equation, for instance the RK1 method (first order Euler), gives:

$$\tilde{\phi}^{n+1} = \tilde{\phi}^n + \Delta t \underbrace{\lambda\tilde{\phi}^n}_{\mathrm{K}_1} \tag{3.5.6}$$

where $\tilde{\phi}^n$ corresponds to the solution at the nth time step. It can be observed that in the Fourier space, the space evolution of the signal, noted K_1, results in a simple linear product with the eigenvalue i.e. $\mathrm{K}_1 = \lambda\tilde{\phi}$. Computing the amplification factor $\tilde{G} = \tilde{\phi}^{n+1}/\tilde{\phi}^n$ gives the temporal evolution of the signal between two time steps. The equation (3.5.6) is then transformed as:

$$\tilde{G} = 1 + \underbrace{\Delta t \mathrm{K}_1}_{z}. \tag{3.5.7}$$

The amplification factor can be interpreted as how the signal behaves from an iteration to another i.e, $|\tilde{G}| < 1$ if it is attenuated, $|\tilde{G}| = 1$ if it does not grow, $|\tilde{G}| > 1$ if it is amplified. Thus, a stability condition $|\tilde{G}| \leq 1$ can be naturally imposed, and once inserted in Eq. (3.5.7) gives:

$$|1 + z| \leq 1. \tag{3.5.8}$$

For a higher order scheme, the same process can be applied which results for instance for the second order Runge-Kutta:

$$\begin{aligned} \tilde{\phi}^{n+1} &= \tilde{\phi}^n + \Delta t \mathrm{K}_2 \\ &= \tilde{\phi}^n + \Delta t \lambda \left(\tilde{\phi}^n + \frac{\Delta t}{2} \mathrm{K}_1 \right) \\ &= \tilde{\phi}^n + \Delta t \lambda \left(\tilde{\phi}^n + \frac{\Delta t}{2} \lambda \tilde{\phi}^n \right) \end{aligned} \tag{3.5.9}$$

giving the stability condition: $|1 + z + z^2/2| \leq 1$. Using the same methodology applied to all the other temporal schemes considered in Table 3.3, it yields:

$$\mathrm{RK1}: \quad |1 + z| \leq 1 \tag{3.5.10a}$$

$$\mathrm{RK2}: \quad |1 + z + \frac{z^2}{2}| \leq 1 \tag{3.5.10b}$$

$$\mathrm{RK3}: \quad |1 + z + \frac{z^2}{2} + \frac{z^3}{6}| \leq 1 \tag{3.5.10c}$$

$$\mathrm{RK4}: \quad |1 + z + \frac{z^2}{2} + \frac{z^3}{6} + \frac{z^4}{24}| \leq 1 \tag{3.5.10d}$$

It is worth noting that the formulae obtained for the Heun scheme is similar to the standard RK2 scheme. In fact, methods of order K with K stages have the same stability domain [166].

The stability conditions Eq. (3.5.10) are illustrated on Fig. 3.4 in the complex plane for each time integrator. On this figure, the real axis relates to the diffusion phenomenon while the imaginary axis corresponds to the convection phenomenon. A purely advective physical behavior moves at $\mathrm{Re}(\lambda \Delta t) = 0$ along the positive and negative part of the imaginary axis, while a purely diffusive physics moves at $\mathrm{Im}(\lambda \Delta t) = 0$ along the negative real axis. If $\mathrm{Re}(\lambda \Delta t) > 0$ then there is an anti-diffusion phenomenon leading to an exponential growth of the solution i.e., the solution is unstable. The time integrators are stable inside the contour and unstable outside the contour.

For the simulation of purely convective physics, and when replacing K1 in Eq. (3.5.6) by a centered FD formula, one can see that the RK1 method coupled with a centered difference in space (which corresponds to Eq. (3.4.8)) is found linearly unconditionally unstable. Indeed, one can observe in the zoomed region of Fig. 3.4 that the stability region of the Euler scheme at $\mathrm{Re}(\lambda \Delta t) = 0$ does not include the imaginary axis. Since centered schemes do not contain any dissipation terms in $\mathcal{K}_{scheme}$, the scheme irremediably fall into the unstable domain for non-zero advection velocity. For the sake of stability, this time integrator must be then coupled to spatial schemes introducing non-zero numerical dissipation such as upwind schemes. The same conclusion can be drawn for the RK2

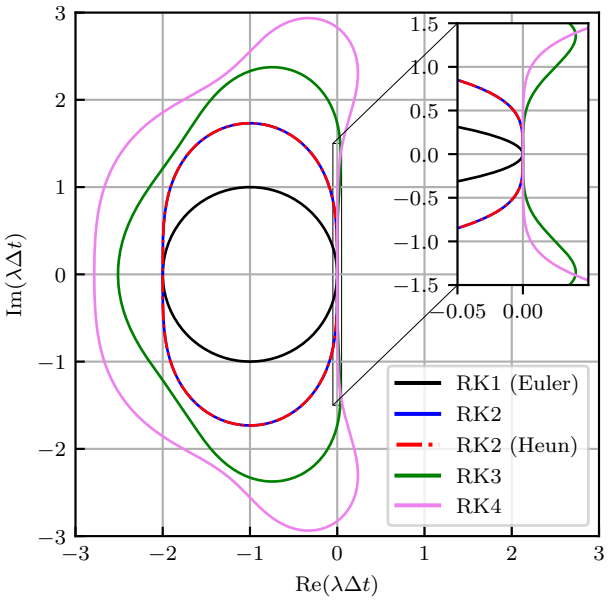

Figure 3.4 – Stability domain of different Runge-Kutta time integrators. The time integrator is stable inside the contour and unstable outside. The diffusion phenomenon moves along the real axis while the convection moves along the imaginary axis.

schemes. Looking now at the third and higher order RK methods, one can notice that they contain a segment of the imaginary axis in their stability region. These kind of schemes are then of particular interest when solving convective physics using centered schemes.

3.6 Some spatio temporal schemes

3.6.1 Scheme terminology

To obtain spatio temporal schemes solving an advection equation on ϕ, various combinations of time integrators seen in Sec. 3.5.1 and FD schemes seen in Sec. 3.4.2 can be used. In the present work, these schemes will only differ in the way in which the temporal and advection terms are modeled, since unless otherwise specified, all the other source terms will be discretized using second-order centered schemes. For practical reasons, a name has been assigned to each of these schemes. For instance, the name RK1CO2 stands for a scheme using a first-order RK1 for the time marching procedure and a second-order D1CO2 scheme on the advection term. This scheme corresponds to the one derived previously with the FV and FD methods Eq. (3.4.8).

Regarding the schemes using backward or forward FD formulas for the convection term, for reasons of stability, an additional condition needs to be imposed. As already mentioned in Sec. 3.4.1, although being very similar, these formulas differ from the sign of the even derivatives present in their truncation error. Thus, depending on the sign of

the velocity, backward or forward formulas must be employed to ensure the positivity of the diffusivity coefficient of these derivatives, it yields:

$$u\frac{\partial \phi}{\partial x_\alpha} : \begin{cases} \text{Forward if } u < 0 \\ \text{Backward if } u > 0 \end{cases} . \tag{3.6.1}$$

For a multivariate space problem, one can eventually give an example on the discretization of the following advection-diffusion equation:

$$\frac{\partial \phi}{\partial t} + u_x \frac{\partial \phi}{\partial x_\alpha} = \kappa \frac{\partial^2 \phi}{\partial x_\alpha^2}. \tag{3.6.2}$$

Considering a two-dimensional problem, the scheme RK1CO2 discretizing this equation reads:

$$\begin{aligned} \phi_{i,j}^{n+1} = \phi_{i,j}^n &+ u_x \frac{\Delta t}{2\Delta x}\left(\phi_{i+1,j}^n - \phi_{i-1,j}^n\right) + u_y \frac{\Delta t}{2\Delta x}\left(\phi_{i,j+1}^n - \phi_{i,j-1}^n\right) \\ &+ \kappa \frac{\Delta t}{\Delta x^2}\left(\phi_{i+1,j}^n - 2\phi_{i,j}^n + \phi_{i-1,j}^n\right) + \kappa \frac{\Delta t}{\Delta x^2}\left(\phi_{i,j+1}^n - 2\phi_{i,j}^n + \phi_{i,j-1}^n\right), \end{aligned} \tag{3.6.3}$$

where one can recognize the D2CO2 FD formula for the discretization of the diffusive terms. The indices i and j simply refer to a node positioned at $x = x_i = i\Delta x$ and $y = y_j = j\Delta x$. Moreover, for the discrete advection-diffusion equation, it can be useful to define two dimensionless numbers:

$$\mathrm{CFL}_{adv,\alpha} = u_\alpha \frac{\Delta t}{\Delta x} \quad \text{and} \quad \mathrm{CFL}_{diff} = \kappa \frac{\Delta t}{\Delta x^2}. \tag{3.6.4}$$

They correspond respectively to the advective and diffusive[3] Courant-Friedrich-Levy (CFL) number [170]. For a D dimensional problem, D advective CFL numbers emerge which can be eventually re-expressed into polar coordinates. Thus, for $D = 2$ one can define CFL_{adv} and $\mathrm{CFL}_{adv,\theta}$ respectively as the norm and the angle formed by the two CFL numbers. These numbers will be useful to characterize the numerical stability of the schemes, presented in the next section.

Finally, a last numerical scheme will be considered in this chapter. It is the Lax-Wendroff scheme [171] (later named LW) and reads in two-dimension[4]:

$$\begin{aligned} \phi_{i,j}^{n+1} = \phi_{i,j}^n &+ u_x \frac{\Delta t}{2\Delta x}\left(\phi_{i+1,j}^n - \phi_{i-1,j}^n\right) + u_y \frac{\Delta t}{2\Delta x}\left(\phi_{i,j+1}^n - \phi_{i,j-1}^n\right) \\ &+ \frac{1}{2}\left[\left(u_x \frac{\Delta t}{\Delta x}\right)^2\left(\phi_{i+1,j}^n - 2\phi_{i,j}^n + \phi_{i-1,j}^n\right) + \left(u_y \frac{\Delta t}{\Delta x}\right)^2\left(\phi_{i,j+1}^n - 2\phi_{i,j}^n + \phi_{i,j-1}^n\right)\right] \\ &+ \frac{u_x u_y}{4}\left(\frac{\Delta t}{\Delta x}\right)^2\left(\phi_{i+1,j+1}^n - \phi_{i-1,j+1}^n - \phi_{i+1,j-1}^n + \phi_{i-1,j-1}^n\right). \end{aligned} \tag{3.6.5}$$

Its derivation is based on a Taylor expansion of ϕ in time up to the second-order. All the time derivatives are subsequently replaced by equivalent spatial derivatives (e.g., for the linear advection problem $\phi_t = -u\phi_x$ and $\phi_{tt} = u^2\phi_{xx}$). The final form of the scheme is obtained by discretizing these derivatives using common D1CO2 and D2CO2 FD formulas. This scheme is second-order accurate in space and time.

[3] CFL_{diff} is also known as the von Neumann number [166].

[4] The one-dimensional formula can be easily obtained imposing $u_y = 0$ in Eq. (3.6.5)

3.6.2 Numerical stability

Several techniques exist to study the stability of numerical schemes. In the first place, one can think for instance to the "heuristic" stability approach [172,173]. In the same way as the construction of the FD formulas seen in Sec. 3.4.1, it is possible to develop each term of the numerical scheme into Taylor series. This gives access to the so-called equivalent equation of the scheme i.e., the continuous equation plus the truncation errors associated to the space-time discretization. The study of this equivalent equation gives insight into the nature of both dissipative and dispersive errors, thus also giving information on stability. Moreover, the equivalent equation also permits to verify the consistency of the scheme i.e., it should tend to the differential equation to which it is related, when $\Delta t \to 0$ and $\Delta x \to 0$. This notion is important since from the Lax equivalence theorem, for a well-posed linear problem, if a scheme is stable and consistant, the simulation will satisfy convergence [166].

To study the stability of numerical schemes, another approach is the von Neumann stability analysis [174]. This analysis can evidence the numerical effects of the discretization on both stability and accuracy. This analysis will be presented into more details in Chap. 6, this is why it will be only introduced very briefly here. The results of this analysis on the numerical stability of the considered schemes will be very important for the rest of the chapter.

3.6.2.a Spectral properties

The von Neumann analysis consists in studying the behavior of a numerical scheme, from one step to another, when a monochromatic plane wave is injected into it i.e., how it is propagated and dissipated. Replacing ϕ_i^n in a given numerical scheme by Eq. (3.4.14), one can obtain the following equation:

$$\underbrace{\frac{\phi_i'^{n+1}}{\phi_i'^{n}}}_{e^{\mathrm{i}\omega\Delta t}} = \lambda, \tag{3.6.6}$$

with λ the eigenvalue of the problem. The real and imaginary parts of ω, respectively $\mathrm{Re}(\omega)$ and $\mathrm{Im}(\omega)$, provide information on the propagation and the dissipation of the wave from one time step to another. If $-\mathrm{Im}(\omega) > 0$, the wave is exponentially amplified in time, and thus the scheme is unstable. On the other hand, if $-\mathrm{Im}(\omega) < 0$ the wave is damped with time, the scheme is then linearly stable.

The great interests of performing such analysis lies in the fact that it strips off the scheme and exposes it numerical properties. For $\mathrm{CFL}_{adv} = 0.1$, $\mathrm{CFL}_{adv,\theta} = 0$ and $\mathrm{CFL}_{diff} = 0.05$, Fig. 3.5a compares the spectral properties of different schemes to the exact solution in terms of dispersion and dissipation. The deviation from the exact solution gives access to the error made by each scheme from one step of time to another. All the schemes that are displayed on this figure are stable. Depending on the scheme, different spectral behaviors can be observed, and where one can recognize the well known dissipative nature

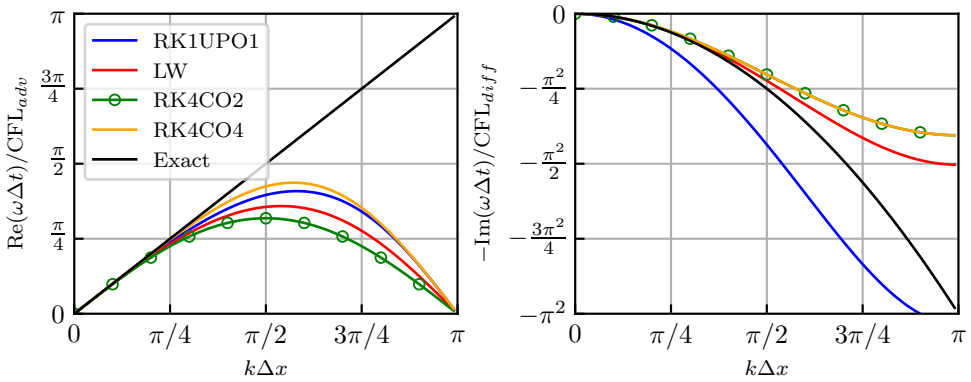

(a) Spectral properties of different schemes for $\mathrm{CFL}_{adv} = 0.1$.

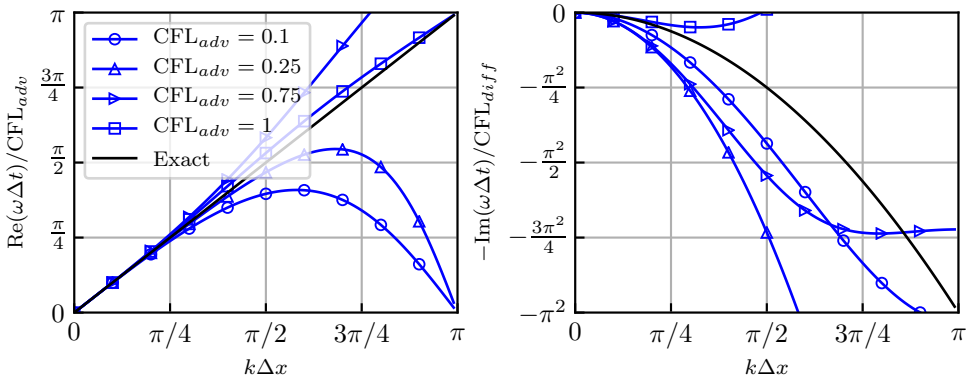

(b) Spectral properties of the RK1UPO1 scheme for different CFL_{adv}.

Figure 3.5 – Dispersion and dissipation properties provided by the von Neumann spectral analysis for and $\mathrm{CFL}_{diff} = 0.05$ and $\mathrm{CFL}_{adv,\theta} = 0$. The graphs are plotted along the advection direction.

of upwind schemes (such as the RK1UPO1), as well as the dispersive nature of centered schemes. The calculated solution will therefore be sensitive to the scheme used.

Also, it turns out that for the same numerical scheme, the dispersion and dissipation properties are not fixed. Indeed, they depend on the two numerical parameters CFL_{adv} and CFL_{diff}. For a fixed $\mathrm{CFL}_{diff} = 0.05$, Fig. 3.5b illustrates the effect of the CFL_{adv} parameter on the RK1UOP1 scheme. On the dispersion graph, one can see that for a judicious choice of this parameter, the dispersion error can be greatly reduced. In the special case of $\mathrm{CFL}_{adv} = 1$, the RK1UOP1 scheme results in an integration along the characteristic, and thus the equation is exactly solved [5]. This interesting configuration shares trait with the characteristic integration giving rise to the LBM. Nevertheless, this exact integration property cannot be respected all over the simulation since CFL_{adv} will vary locally. Finally, it can also be seen on the dispersion graph that for $\mathrm{CFL}_{adv} = 1$, the RK1UOP1 scheme is found to be unstable. This illustrates the fact that, due to their explicit nature, all the numerical schemes presented are conditionally stable. The stability of these schemes is therefore ensured only for a certain choice of CFL_{adv} and CFL_{diff} parameters.

3.6.2.b Stability condition

Although the stability condition of these schemes can be found analytically, it can also be found numerically, by using the same script that was used to plot the spectral properties on Fig. 3.5. A stability study on the parametric space formed by $[\mathrm{CFL}_{adv,\theta}, \mathrm{CFL}_{diff}, k_x\Delta x, k_y\Delta x]$ is carried out for one-dimensional and two-dimensional schemes. This space is scanned to find the maximum CFL_{adv} number allowed by the schemes. The maximum CFL_{adv} number is found using a bisection method with a convergence criterion taken as $\Delta\mathrm{CFL}_{adv} < 0.01$, where the delta represents the difference of the values found between two iterations. For both one- and two-dimensional studies, one hundred values equally spaced are considered for $\mathrm{CFL}_{diff} \in [0, 1]$. For the two-dimensional case, the angle $\mathrm{CFL}_{adv,\theta}$ is scanned for 13 values evenly distributed between 0 and 45 degrees. The wavenumber space is defined such as $k_x\Delta x \in [-\pi, \pi]$ and $k_y\Delta y \in [0, \pi]$, and discretized by 200 and 100 points respectively. For the one-dimensional case, $k\Delta x \in [0, \pi]$ and is discretized by 100 points.

Fig. 3.6 displays the results of this study for both one- and two-dimensional cases. One can see that for the same numerical scheme, the stability condition is changed according to the dimension of the problem. For example and for $\mathrm{CFL}_{diff} = 0$, this figure shows the classic stability condition of the Lax-Wendroff scheme i.e., $\mathrm{CFL}_{adv} \leq 1$ in one-dimension and $\mathrm{CFL}_{adv} \leq 0.5$ in two-dimension. Moreover, for $\mathrm{CFL}_{adv} = 0$, one can also find the well-known stability condition of an RK1 scheme in time and D2CO2 in space solving a pure diffusion equation i.e., $\mathrm{CFL}_{diff} \leq 0.5$ in one-dimension and $\mathrm{CFL}_{diff} \leq 0.25$ in two-dimension. Finally, one can also note that the multi-stage of the RK4 method allows for stability even for CFL numbers greater than one..

[5] The slight deviation observed on Fig. 3.5b is due to dispersion error brought by the fact that $\mathrm{CFL}_{diff} = 0.05$. For $\mathrm{CFL}_{diff} = 0$ and $\mathrm{CFL}_{adv} = 1$, the dispersion property of the RK1UPO1 scheme perfectly matches the exact solution.

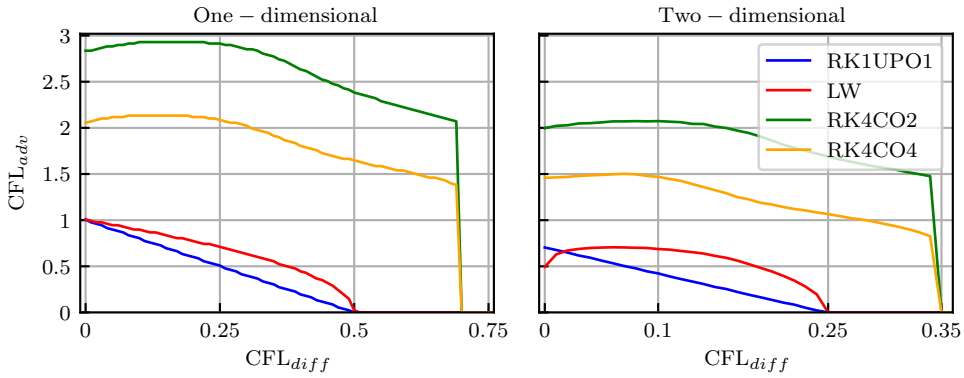

Figure 3.6 – Stability domain of different spatio-temporal FD schemes discretizing the advection diffusion equation. The schemes are stable under the graph and unstable above.

As a matter of fact, knowledge of the stability of these numerical schemes is important for the future development of a hybrid method. In the rest of the chapter, the numerical schemes used to discretize the energy equation will always be used within their range of stability.

3.7 Hybrid lattice Boltzmann scheme under the Boussinesq approximation

For a first attempt, and following the idea of Lallemand et Luo [71], an HLBM based on the Boussinesq approximation is derived on the D2Q9 lattice. This first approach will make it possible to validate the very basic concept of the HLBM i.e, link the LBM system with a FD/FV system computing a thermal equation, in a simpler context than the compressible equations.

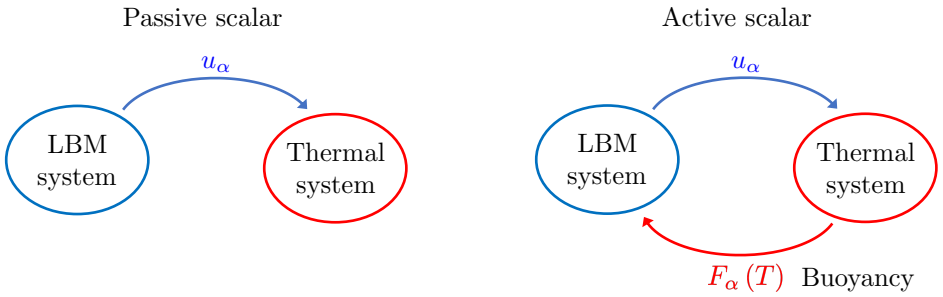

Figure 3.7 – Communication between the LBM and thermal system under the Boussinesq approximation. Depending on the presence of external body force terms F_α, the thermal system is either considered as an active or passive scalar.

In this framework, the link between the aero and thermal system is depicted on Fig. 3.7. Two cases are envisaged: 1) the passive scalar case where the LBM system is

standalone and communicates the velocity to the thermal system and 2) the active scalar case where the thermal system also communicates back a coupling term F_α which will alter the LBM system. Thus in case 1), the velocity field is given and not modified by the transported thermal field, while in case 2) it is altered by F_α which will be referred to as a buoyancy force term as a function of a local temperature. These passive/active scalar notions will take their full meaning when the fluid equation of motion under the Boussinesq hypothesis will be presented in the following section.

Finally, one has to note that in the present context, three different temperatures with different meanings are used. Therefore, it can be useful to briefly recall them:

- $\underline{T}$: This is the physical temperature of the flow used by the thermal system.
- $\underline{T_r}$: This is the constant reference temperature used by the LBM system to compute the time step $\Delta t = c_s^* \Delta x / \sqrt{r_g T_r}$.
- $\underline{T_0}$: This is the constant fictitious temperature used by the LBM system. It is linked with T_r through the parameter $\theta_0 = T_0/T_r$ and appears in the barotropic equation of state $p_0 = \rho c_s^2 \theta_0$. Its value rules the speed of sound and it is usually imposed as $T_0 = T_r$ for standard LBM's.

3.7.1 The macroscopic equations

Here the incompressible Navier-Stokes equations with the Boussinesq approximation are considered. This approximation allows the modelization of an incompressible dilatable fluid flow under weak density and temperature variations and negligible viscous heat production.

The considered equations can be written as follows:

$$\frac{\partial u_\alpha}{\partial x_\alpha} = 0, \tag{3.7.1}$$

$$\frac{\partial u_\alpha}{\partial t} + u_\beta \frac{\partial u_\alpha}{\partial x_\beta} = -\frac{1}{\rho_0}\frac{\partial p}{\partial x_\alpha}\delta_{\alpha\beta} + \nu \frac{\partial^2 u_\alpha}{\partial x_\alpha^2} + \frac{F_\alpha}{\rho_0} \tag{3.7.2}$$

$$\frac{\partial T}{\partial t} + u_\alpha \frac{\partial T}{\partial x_\alpha} = \kappa \frac{\partial^2 T}{\partial x_\alpha^2}, \tag{3.7.3}$$

where ρ_0 is a reference density and ν and κ are respectively the kinematic viscosity and the heat diffusivity evaluated at ρ_0. F_α/ρ_0 is a body-force term related to the buoyancy effect induced by the gravity field a_α or inertial forces for rotating flows. For the former it follows:

$$F_\alpha = \left(1 - \beta\left(T - T_0\right)\right) \rho a_\alpha, \tag{3.7.4}$$

with T_0 taken as the mean flow temperature and β the thermal expansion coefficient (usually set to $\beta = 1/T$ for a perfect gas). Since gravity is a conservative force, the temperature independent term in Eq. (3.7.4) is usually absorbed into the pressure gradient [43]. This leads to:

$$F_\alpha = -\beta\left(T - T_0\right) \rho a_\alpha, \tag{3.7.5}$$

which now accounts for the buoyancy force.

The mass and momentum equations Eq. (3.7.1) and Eq. (3.7.2) can be modeled by the standard athermal LBM. Indeed, it recovers a weakly compressible version of the Navier-stokes equation fitting with these equations, and although $\boldsymbol{\nabla}\cdot\boldsymbol{u} = 0$ is not strictly respected one can perform computations when low Mach number flows are considered. The inclusion of the buoyancy force term as well as the standard LBM equation for low mach numbers will be presented in the following. Regarding the temperature equation (3.7.3), standard discretization FD schemes for the advection diffusion equation presented in Sec. 3.6 can be used.

3.7.2 LBM with buoyancy force term

External body force terms can be included in the momentum equation in several manners. A comparison of these force terms in the context of natural convection problems can be found in the work of Mohamad et al. [175]. In the present context, one can consider the Guo et al. [176]'s force scheme which gives for the LBM-BGK system:

$$g_i^+ = g_i - \frac{\Delta t}{\check{\tau}}\left(g_i - f_i^{eq}\right) + \Delta t \check{F}_i, \tag{3.7.6}$$

with,

$$\check{F}_i = w_i\left(1 - \frac{1}{2\check{\tau}}\right)\left[\frac{c_{i,\alpha} - u_\alpha}{c_s^2} + \frac{c_{i,\alpha}\left(c_{i,\beta}u_\beta\right)}{c_s^4}\right]F_\alpha, \tag{3.7.7}$$

the discrete forcing term. Using this technique, the velocity needs to be shifted when computing the equilibrium and the macroscopic quantities according to:

$$u_\alpha = \frac{1}{\rho}\sum_i c_{i,\alpha} g_i + \frac{\Delta t F_\alpha}{2\rho}. \tag{3.7.8}$$

This shift appears because of the change of variable which contains the force terms and alters the first order moment of the distribution g_i. This technique has already been successfully tested in the context of natural convection computation in the DDF framework [43], which can be used latter as a comparison for the present Boussinesq HLBM. Finally, the very standard second-order equilibrium distribution function is adopted and reads:

$$f_i^{eq,2} = w_i\rho\left(1 + \frac{c_{i,\alpha}u_\alpha}{c_s^2} + \frac{\left(c_{i,\alpha}c_{i,\beta} - c_s^2\delta_{\alpha\beta}\right)\left(u_\alpha u_\beta + c_s^2\left(\theta_0 - 1\right)\delta_{\alpha\beta}\right)}{2c_s^4}\right). \tag{3.7.9}$$

It is worth recalling that the present equilibrium allows to recover the mass and momentum equations in the low Mach number limit. This equilibrium will be used in the following on the D2Q9 lattice.

3.7.3 Diffusion and transport of a temperature profile

To assess the correct behavior of the numerical scheme of the energy system, an advection-diffusion of a Gaussian shaped temperature spot is performed. No external

forces are considered and hence the temperature can be considered to be a passive scalar. A uniform Cartesian grid of $N_x \times N_y = 200 \times 200$ points is considered and discretizes a periodic square domain of length $L = 1\,\mathrm{m}$. The reference temperature is set to $T_r = 300\,\mathrm{K}$, $\theta_0 = 1$ and a constant pressure $p = 101325\,\mathrm{Pa}$ is imposed in the domain. The initial temperature profile is defined as:

$$T(r) = T_\infty + \Delta T \exp\left(-r^2/2\right) \quad \text{with} \quad r = \sqrt{(x-x_c)^2 + (y-y_c)^2}/R, \tag{3.7.10}$$

where $(x_c = L/2, y_c = L/2)$ is the initial position of the spot center, $\Delta T = 0.1T_\infty$ and $T_\infty = 300$. Finally, the radius of the temperature spot is set to $R = 10\Delta x$. Two cases will be considered: 1) a purely advective case along $\boldsymbol{e}_x$ at $\mathrm{CFL}_{adv} = 0.1$ and 2) a purely diffusive case at $\mathrm{CFL}_{diff} = 0.1$. Case 1) will compare four different discretization schemes namely LW, RK1UPO1, RK4CO2 and RK4CO4 for the advection part while case 2) aims to simply ensure the correct behavior of the diffusive D2CO2 scheme using a RK1 temporal scheme. For case 1), the exact solution consists in the simple advection of the initial condition Eq. (3.7.10) over the time. For case 2), the exact solution reads:

$$T(x,y,t) = T_\infty + \Delta T \frac{R^2}{R^2 + R_\kappa^2} \exp\left(-r_\kappa^2/2\right) \quad \text{with} \quad r_\kappa^2 = \frac{(x-x_c)^2 + (y-y_c)^2}{R^2 + R_\kappa^2}, \tag{3.7.11}$$

and $R_\kappa = \sqrt{2\kappa t}$. Finally, it is worth noting that the relevant dimensionless number characterizing the physics of the present test case is the Péclet number. It can be defined as $\mathrm{Pe} = Ru_x/\kappa$ and thus its values are set to $\mathrm{Pe} = \infty$ case 1) and $\mathrm{Pe} = 0$ for case 2).

For the advection only problem, Fig. 3.8 compares the reduced temperature field and iso-contours obtained with the different schemes for different flow-through-times t_c. One can observes different behaviors as a function of the numerical schemes. It can be easily observed that the RK1UOP1 is the least accurate scheme leading to a consequent dissipation of the solution in the direction of the flow. The behavior of the LW and RK4CO2 schemes are found to be rather similar to each other. At $t = 10t_c$, oscillations at the rear of the Gaussian profile can be observed on both of these schemes, and are related to dispersion effects. Indeed, such behavior is due to the fact that the phase and group velocities of the waves contained in the Gaussian profile are altered (slowed down) by the scheme which generates this kind of oscillating trail. It can be shown using the von Neumann spectral analysis that for the present CFL parameters, the dispersion graphs of these schemes are quite the same, and which explains why similar results are obtained. Regarding the fourth-order RK4CO4 scheme, one can see that the initial profile is remarkably well transported until $t = 10t_c$ without apparent dispersion or dissipation numerical errors.

The left graph of Fig. 3.9 compares the reduced temperature profiles obtained by the schemes at the three characteristic times with respect to the analytical solution. These profiles confirm the dissipative nature of the RK1UPO1 scheme along with the dispersive effect of the LW and RK4CO2 schemes. Finally, the RK4CO4 scheme is the only scheme fitting almost perfectly with the exact solution at final time $t = 10t_c$. To obtain more accurate results using the lower order schemes, a finer mesh grid could have been used, however this would engender an increase of numerical cost. Nonetheless, the

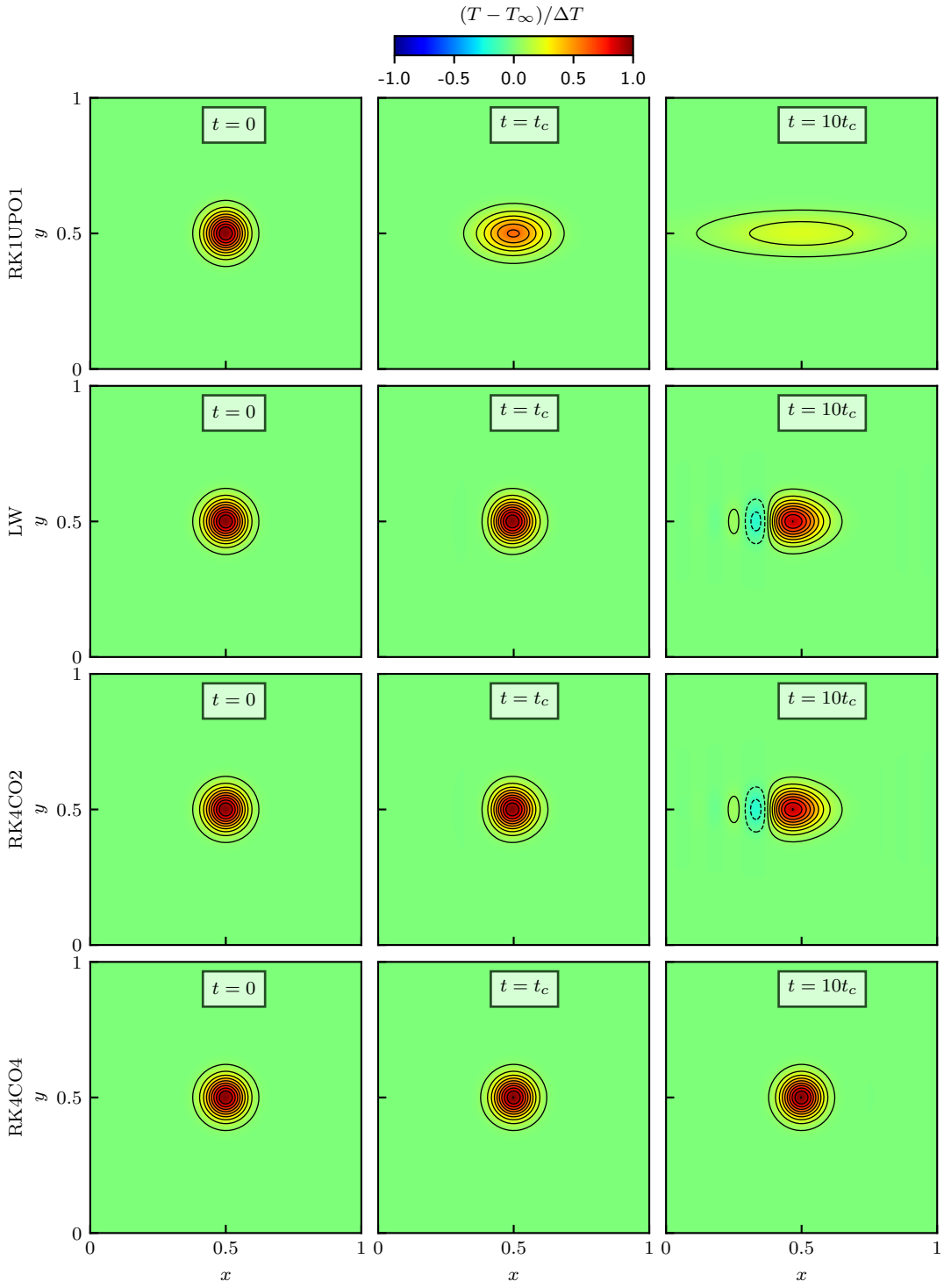

Figure 3.8 – Case 1): reduced temperature field and iso-contours at different characteristic times and for different numerical schemes. Twenty iso-contours equally distributed from −1 to 1 are displayed; solid and dashed lines corresponds respectively to positive and negative values. From left to right columns: $t = 0$, $t = t_c$ and $t = 10t_c$; from top to bottom rows RK1UPO1, LW, RK4CO2 and RK4CO4.

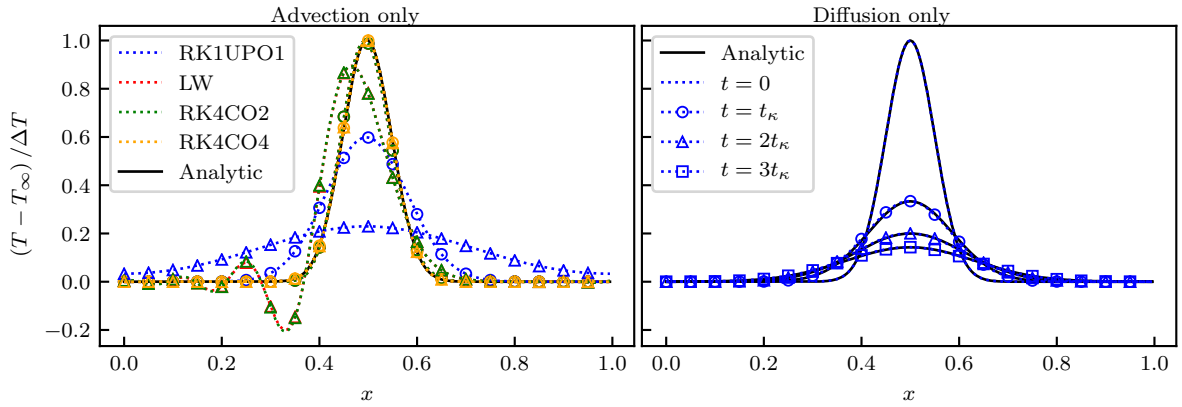

Figure 3.9 – Reduced temperature profiles for case 1) (left) and case 2) (right) at $y = L/2$. The left plot compares the different schemes for different convective times: $t = 0$ (no symbols), $t = t_c$ (circles) and $t = 10t_c$ (triangles). The right plot displays the solution at different diffusive characteristic times.

RK4CO4 scheme is expected to be more costly and less practical to be implemented in practice (e.g. at boundaries) due to its non-local stencil. In fact, all these remarks highlight a major problematic in CFD: what scheme offers the best trade-off between ease of implementation, numerical cost and accuracy? This is still a subject of active research, and although very interesting, in order not to deviate from the main subject of this manuscript we will not enter into the details.

Regarding the purely diffusive case, the right graph of Fig. 3.9 displays the analytical and computed solutions at different diffusive characteristic times $t_\kappa = R^2/\kappa$. A good agreement with the analytical solution is found and confirms that the diffusive part of the equation is well modeled using the simple D2CO2 scheme.

Finally, it is worth noting that a computation with both advection and diffusion phenomenon could have been performed. However, the purpose here was to point out the existence of dispersion and dissipation defects related to the different parts of the advection diffusion equation. The present study showed a well known fact in the CFD word, that it is much more challenging to solve numerically hyperbolic problems than parabolic ones. Since most of the compressible applications in aeronautics are convection dominated problems, it is therefore useful to keep in mind this kind of numerical phenomenon for the following.

3.7.4 Natural convection in square cavity

Here, the HLBM is assessed on natural convection flows in a two-dimensional square cavity of length $L = 1\,\mathrm{m}$. The two side-walls, left and right, are maintained at two different temperatures, respectively $T_c = 270\,\mathrm{K}$ and $T_h = 330\,\mathrm{K}$ while the bottom and top walls are adiabatic. For the sake of simplicity, the no-slip condition on walls is imposed using the simple full way bounce-back. The fluid domain is initialized at rest with a temperature $T = 300\,\mathrm{K}$ and a pressure $p = 101325\,\mathrm{Pa}$. A uniform Cartesian grid of $N_x \times N_y = 129 \times 129$

points is employed, $\theta_0 = 1$ with $T_r = 300\,\mathrm{K}$ and the LW scheme is used to solve the energy part. Five million iterations are considered, ensuring that a steady state is reached for all the cases[6] . Finally, the problem can be found sketched on Fig. 3.10.

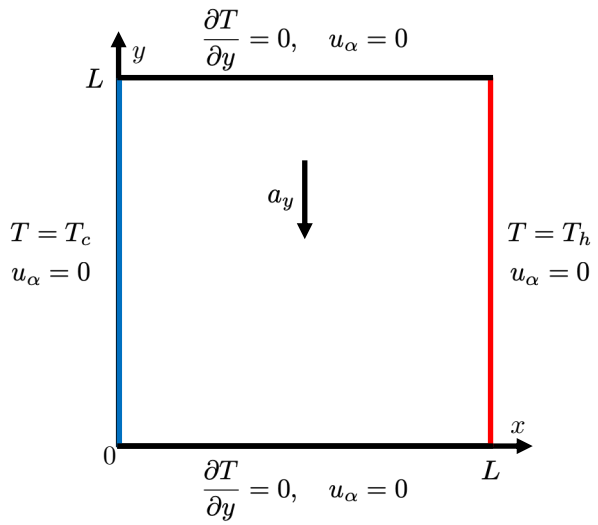

Figure 3.10 – Configuration of the natural convection flow in square cavity.

The two dimensionless numbers describing the physics are the Prandtl number, and the Rayleigh number which reads:

$$\mathrm{Ra} = \frac{a_y \beta (T_h - T_c) L^3}{\nu \kappa}, \tag{3.7.12}$$

and represents the buoyancy effect versus the thermal and viscous dissipations. In the present study, the Prandtl number is fixed to $\mathrm{Pr} = 0.71$ and four different Rayleigh numbers will be considered ranging from $\mathrm{Ra} = 10^3$ to $\mathrm{Ra} = 10^6$. The present HLBM will be compared with the finite volume method of Hortmann et al. [177] who used mesh refinement along the walls and two types of DDF methods of Guo and co-workers based on the temperature equation [103] and the total energy equation [43]. It is worth noting that all of these references use the Boussinesq approximation to model the buoyancy effect (and not the perfect gas coupling) and both DDF methods use the same uniform Cartesian grid as the present calculations.

Fig. 3.11 shows the reduced temperature field with iso-contours and velocity streamlines for different Rayleigh numbers. At first, it is worth noting that when the temperature iso-contours are vertical, the heat transfer regime is predominantly conductive, otherwise the regime is convective. Thus, it appears clearly from Fig. 3.11a to Fig. 3.11d that when the Rayleigh number increases, the heat transfer regime become predominantly convective. The flow being heated at the right wall of the cavity, one can observe that a positive vertical velocity is produced. The flow continue alongside the top adiabatic

[6] It is worth recalling that $\Delta t = \Delta x / \sqrt{(3 r_g T_r)}$. So regardless of the acoustic physic, the number of iterations can be drastically reduced if one considers a lower value of T_r.

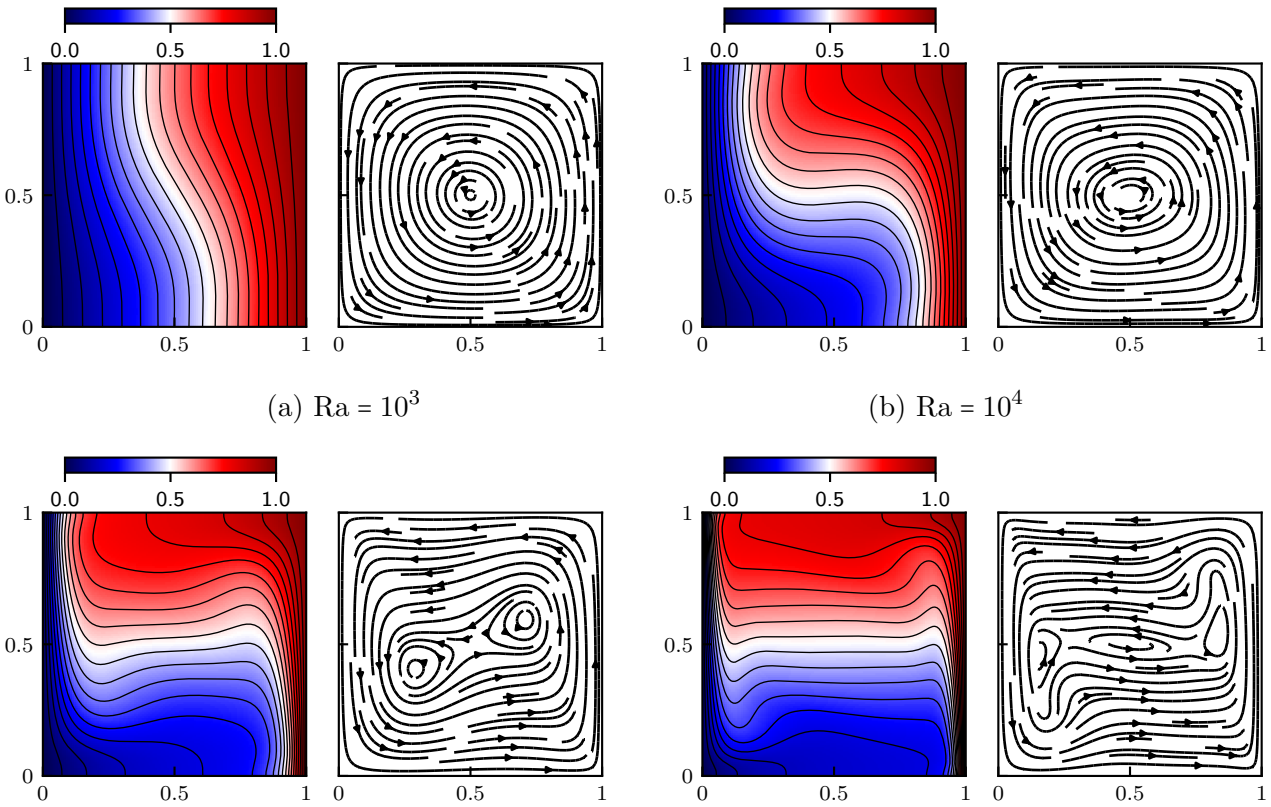

(a) Ra = 10^3 (b) Ra = 10^4

(c) Ra = 10^5 (d) Ra = 10^6

Figure 3.11 – Reduced temperature field $((T - T_c) / (T_h - T_c))$ and iso-contours (left) and velocity streamlines (right) for different Rayleigh numbers at Pr = 0.71. Twenty iso-contours equally distributed from T_c to T_h are displayed.

wall and reach the left cooled wall which induces a negative vertical velocity. Thus a counter-clockwise convective circulation of the fluid appears in the cavity inducing a convective heat transfer. On Fig. 3.11a, one can observe a vortex appearing at the center of the cavity for Ra = 10^3. According to the literature [43, 103, 177], when the Rayleigh increase (10^4), this vortex tends to become elliptic as illustrated on Fig. 3.11b. This last one breaks up into two vortices for a Rayleigh number of 10^5 (as shown on Fig. 3.11c) and moves toward the wall to give way to a third vortex in the center of the cavity for Ra = 10^6 (Fig. 3.11d). This feature of the flow is then qualitatively in good agreements with the one observed in the literature [43, 103, 177] for Rayleigh numbers ranging from 10^3 to 10^6.

More quantitatively, one can characterize the heat transfer with the help of the Nusselt number Nu representing the total heat flux over the diffusive heat flux. In the present context, the quantity of interest will be its averaged value along the heated wall, and

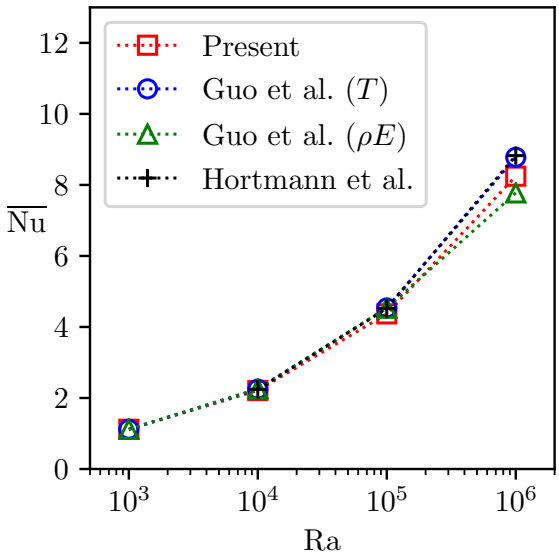

Figure 3.12 – Mean Nusselt number along the hot wall obtained by the current model and compared to the DDFs of Guo et al (T) [43], Guo et al (ρE) [43] and the finite volume of Hotmann et al [177]

which can be computed using the following first-order approximation:

$$\overline{\mathrm{Nu}} = \sum_{j=0}^{N_y-1} \frac{(T_{wall} - T_{fluid})_j}{T_h - T_c}. \tag{3.7.13}$$

Above, $T_{wall} = T_h$ and T_{fluid} is the temperature at the first fluid node. On Fig. 3.12, the mean Nusselt number is displayed in function of the Rayleigh number. As expected, $\overline{\mathrm{Nu}}$ grows as Ra increases, and confirms that the heat transfer regime becomes predominantly convective for high Rayleigh number values. Excellent matching can be found for the first three values while a little deviation can be seen for the highest Rayleigh number value. Finally, Table 3.4 displays the maximum horizontal and vertical velocity components at the mid-width and height of the cavity as well as the locations of their maxima. One can observe the overall agreement of the present results with the multiple references. Possibly, the results could be further improved by implementing more precise boundary conditions such as the half-way bounce-back or nonequilibrium extrapolation method as used by Guo et al. [43].

3.7.5 Discussion

In this section, a rather simple HLBM under the Boussinesq approximation has been derived and tested in passive and active scalar configurations. The former highlighted the eventual numerical discrepancies arising from the discretization of the energy part, while the latter validated the present segregated approach using a buoyancy coupling force term. Even through the use of the very basic BGK collision operator, no blatant

Ra		$\overline{\mathrm{Nu}}$	$u_x^{max}(y)$	$u_y^{max}(x)$
10^3	Present	1.1196	3.5735 (0.8125)	3.6178 (0.1797)
	Guo et al. [103]	1.1168	3.6554 (0.8125)	3.6985 (0.1797)
	Guo et al. [43]	1.1195	3.6430 (0.8047)	3.6919 (0.1719)
	Hortmann et al. [177]	∅	∅	∅
10^4	Present	2.2113	15.9470 (0.8203)	19.2330 (0.1250)
	Guo et al. [103]	2.2477	16.0761 (0.8203)	19.6368 (0.1172)
	Guo et al. [43]	2.2545	16.1254 (0.8203)	19.5577 (0.1172)
	Hortmann et al. [177]	2.2448	16.1802 (0.8265)	19.6295 (0.1193)
10^5	Present	4.3690	33.9455 (0.8516)	66.4895 (0.0703)
	Guo et al. [103]	4.5345	34.8343 (0.8594)	68.2671 (0.0625)
	Guo et al. [43]	4.5278	34.6033 (0.8516)	68.0820 (0.0703)
	Hortmann et al. [177]	4.5216	34.7399 (0.8558)	68.6396 (0.0657)
10^6	Present	8.2456	61.7830 (0.8516)	206.4261 (0.0391)
	Guo et al. [103]	8.7775	65.3606 (0.8516)	216.415 (0.0391))
	Guo et al. [43]	7.7746	64.9059 (0.8516)	218.900 (0.0391)
	Hortmann et al. [177]	8.8251	64.8367 (0.8505)	220.461 (0.0390)

Table 3.4 – Comparisons of the average Nusselt number (plotted on Fig. 3.12) and the maximum horizontal and vertical velocity components at the mid-width and height of the cavity. The data in parentheses are the locations of the maxima and the velocities are dimensionless and are obtained using the characteristic diffusive velocity κ/L.

instabilities induced by such a coupling have been noticed, and the simulations were stable under the present incompressible approximation. Under this approximation, the thermal coupling methodology between the momentum and the energy equation boils down to a single buoyancy force term, which seems to help recover similar stability properties as in the athermal case.

However, the main topic of this manuscript is the extension of the LBM to compressible flows. In order to do so, a more elaborated energy equation accounting for the pressure work and viscous heat dissipation terms has to be used. Moreover, the barotropic equation of state must be replaced by the perfect gas law, redefining the type of coupling between the LBM and the energy system. This extension is presented in the next section.

3.8 Hybrid lattice Boltzmann method under perfect gas coupling

Here, a compressible extension of the HLBM based on the Boussinesq approximation seen in Sec 3.7 is derived. The modifications of the LBM and thermal system to account for compressibility effects will be presented.

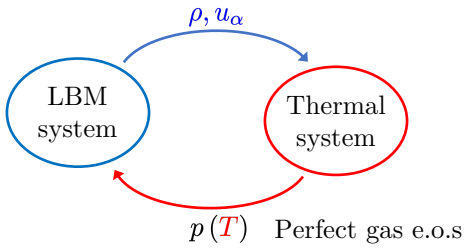

Figure 3.13 – Communication between the LBM and thermal system under the perfect gas coupling.

In this compressible framework, the LBM and thermal systems are now linked through the perfect gas relation defining the pressure. As depicted on Fig. 3.13, the LBM system communicates the density and the velocity to the thermal system while the latter communicates back the temperature through the equation of state.

In this context, it must be noted that two different temperatures with different meanings are used. Therefore, it can be useful to briefly recall them:

- $\underline{T}$: This is the physical temperature of the flow used by both thermal and LBM systems. It appears in the perfect gas equation of state present in the momentum equation through $p = \rho c_s^2 \theta$ with $\theta = T/T_r$. Its value rules the speed of sound which can therefore vary locally depending on the temperature field.

- $\underline{T_r}$: This is the constant reference temperature used by the LBM system to compute the time step $\Delta t = c_s^* \Delta x / \sqrt{r_g T_r}$.

3.8.1 The macroscopic equations

Using the HLBM, the aim is to numerically model the following compressible Navier-Stokes equations:

$$\frac{\partial \rho}{\partial t} + \frac{\partial \rho u_\alpha}{\partial x_\alpha} = 0, \tag{3.8.1}$$

$$\frac{\partial \rho u_\alpha}{\partial t} + \frac{\partial \rho u_\alpha u_\beta}{\partial x_\beta} = -\frac{\partial p}{\partial x_\alpha}\delta_{\alpha\beta} + \frac{\partial}{\partial x_\beta}\left[\mu\left(\frac{\partial u_\alpha}{\partial x_\beta} + \frac{\partial u_\beta}{\partial x_\alpha} - \frac{2}{D}\frac{\partial u_\gamma}{\partial x_\gamma}\delta_{\alpha\beta}\right)\right], \tag{3.8.2}$$

$$\begin{aligned}\frac{\partial T}{\partial t} + u_\alpha \frac{\partial T}{\partial x_\alpha} &= \frac{\lambda}{\rho c_v}\frac{\partial^2 T}{\partial x_\alpha^2} \\ &\quad - (\gamma_g - 1)\, T \frac{\partial u_\alpha}{\partial x_\alpha} + \frac{\mu}{\rho c_v}\left[\left(\frac{\partial u_\alpha}{\partial x_\beta} + \frac{\partial u_\beta}{\partial x_\alpha} - \frac{2}{D}\frac{\partial u_\gamma}{\partial x_\gamma}\delta_{\alpha\beta}\right)\right]\frac{\partial u_\alpha}{\partial x_\beta}.\end{aligned} \tag{3.8.3}$$

Contrarily to the Boussinesq approximation, the energy and the momentum equations are now linked through a perfect gas equation of state $p = \rho r_g T$. As seen in Sec.3.2, various energy equations exist depending on the variable chosen to express the conservation of energy. In the present case, the energy equation corresponds to the internal energy equation in primitive variable formulation for constant heat capacities, heat conductivity and dynamic viscosity. As a first approach, this equation has been adopted since it is a direct extension of the advection-diffusion equation of T seen previously in Sec 3.7.1. The form of the equation therefore remains almost the same, except that two additional terms related to compressibility and viscous effects have been added: the pressure work and the viscous heat production terms. These two terms are discretized using second-order centered finite difference.

3.8.2 Coupling strategies

To obtained a perfect gas coupled HLBM, two strategy can be envisaged.

3.8.2.a Explicit coupling strategy via a force term

The thermodynamic coupling of the two systems can be taken into account through a forcing term in the momentum equation [2]. For instance, one can consider the same LBM system as seen in Sec. 3.7.2 for Boussinesq flows, with $f_i^{eq,(2)}$ and a constant fictitious temperature $\theta_0 = T_0/T_r$. This system yields the following momentum equation:

$$\frac{\partial(\rho u_\alpha)}{\partial t} + \frac{\partial}{\partial x_\beta}\left(\rho u_\alpha u_\beta + p_0 \delta_{\alpha\beta}\right) + \frac{\partial}{\partial x_\beta}\left(\Pi_{\alpha\beta}^{(1)}\right) = F_\alpha, \tag{3.8.4}$$

with $p_0 = \rho r_g T_0$ the barotropic equation of state. This thermodynamic closure can be modified by choosing the following force term:

$$F_\alpha = \frac{\partial}{\partial x_\alpha}\left[\rho r_g \left(T_0 - T\right)\right]\delta_{\alpha\beta}, \tag{3.8.5}$$

leading to the perfect gas equation of state. Thus, this technique simply removes the barotropic e.o.s in Eq. (3.8.4) and replaces it with the desired thermodynamic closure. In practice, F_α can be injected in the LBM system using the Guo et al. [176]'s force scheme as in Sec. 3.7.2 or any other force term techniques. It is worth noting that this type of modification of the pressure is commonly found in the multiphase side of LBM [2,178,179] to obtain for instance non-ideal gas equation of state.

However, this coupling strategy requires the evaluation of the gradient of Eq. (3.8.5) using finite difference schemes. For simulations with walls, the computation of the gradients can be challenging and, as noted by Gopalakrishnan et al. [156], this finite difference calculations can also affects the isotropic nature of the LBM. Finally, these coupling strategies will not be further investigated since an ad hoc solution can be employed without the use of FD and it will be presented in the following.

3.8.2.b Implicit coupling strategy via the equilibrium

The implicit coupling strategy is in fact the one naturally present when considering the thermal LBM i.e., when $f_i^{eq,N}$ is directly developed in terms of $\theta = T/T_r$ as shown in Sec. 2.3.3. It is worth recalling the link between the terms of the momentum equation and the equilibrium moments $\boldsymbol{m}^{eq,(n)}$:

$$\underbrace{\frac{\partial(\rho u_\alpha)}{\partial t}}_{\boldsymbol{m}^{eq,(1)}} + \frac{\partial}{\partial x_\beta}\underbrace{\left(\rho u_\alpha u_\beta + p\delta_{\alpha\beta}\right)}_{\boldsymbol{m}^{eq,(2)}} + \frac{\partial}{\partial x_\beta}\underbrace{\left(\Pi^{(1)}_{\alpha\beta}\right)}_{\boldsymbol{m}^{eq,(2)},\boldsymbol{m}^{eq,(3)}} = 0, \tag{3.8.6}$$

which clearly brings the light on where the pressure derived from the moments of $f_i^{eq,N}$. The latter is directly related to the second-order raw-moment $\boldsymbol{m}^{eq,(2)}$ of the equilibrium distribution function. Knowing the relation between the raw and the Hermite moments (see Eq. (2.3.22)), it yields:

$$\begin{aligned} m^{eq,(2)}_{\alpha\beta} &= a^{eq,(2)}_{\alpha\beta} + c_s^2 a^{eq,(0)}\delta_{\alpha\beta}, \quad \text{with} \quad \begin{cases} a^{eq,(0)} = \rho \\ a^{eq,(2)}_{\alpha\beta} = \rho u_\alpha u_\beta + \rho c_s^2\left(\theta - 1\right)\delta_{\alpha\beta} \end{cases}, \\ &= \rho u_\alpha u_\beta + \rho c_s^2 \theta \delta_{\alpha\beta}. \end{aligned} \tag{3.8.7}$$

From this relation, it clearly appears that a second-order expansion of $f_i^{eq,N}$ in terms of Hermite polynomials is mandatory to recovers the moment of interest yielding:

$$p = \rho c_s^2 \theta, \tag{3.8.8}$$

and which corresponds to the perfect gas equation of state. Therefore, simply injecting the temperature calculated by the FD scheme in the second-order Hermite moments of $f_i^{eq,N}$ through θ, allows to obtain the appropriate thermodynamic relation between the momentum and energy equations. At first glance, choosing $N = 2$ seems to be sufficient to recover the momentum equation of interest.

However, and as already mentioned in Sec. 2.3.3, considering only a second-order expansion of $f_i^{eq,N}$ with a variable θ will introduce an error of order $\mathcal{O}\left(\mathrm{Ma}^1\right)$ in the

definition of the viscous stress tensor $\Pi^{(1)}_{\alpha\beta}$ of Eq. (3.8.6). Therefore, this error cannot be neglected even for low Mach number flows, contrarily to the athermal case where the latter is of order $\mathcal{O}\left(\mathrm{Ma}^3\right)$ when $\theta_0 = 1$. To find the correct momentum equation, a third-order development of the equilibrium function is required. However, for a proper evaluation of $\boldsymbol{a}^{eq,(3)}$, a seventh-order quadrature lattice is required such as the D2V17. Eventually, in order to use a standard lattice such as the D2Q9, the error introduced by the incorrect evaluation of $\boldsymbol{a}^{eq,(3)}$ can be corrected by means of a corrective term ψ_i. For the D2Q9 this term reads [180]:

$$\psi_i = w_i \frac{\mathcal{H}_{i,\alpha\beta}}{2c_s^4} \frac{\partial}{\partial x_\alpha} \left(-a^{eq,(3)}_{\alpha\alpha\alpha}\right) \delta_{\alpha\beta}, \tag{3.8.9}$$

and where the derivative can be evaluated by means of a standard second-order centered FD scheme. This term is introduced in the LBM-BGK equation following [180]:

$$g_i^+ = g_i - \frac{\Delta t}{\check{\tau}} \left(g_i - f_i^{eq}\right) + \frac{2\check{\tau} - \Delta t}{2\check{\tau}} \Delta t \psi_i. \tag{3.8.10}$$

Details about the derivation of this new LBM equation and the correction term will be given later in chapter 4.

To put it in the nutshell, the implicit perfect gas coupling in the HLBM framework is achieved by:

1. Injecting the temperature computed by the energy part in the equilibrium distribution function.

2. Considering at least a third-order development of the equilibrium function $f_i^{eq,N\geq 3}$.

3. Accounting for a corrective term when standard lattices are considered.

These are the only three requirements to obtain the correct equation of state Eq. (3.8.8) while keeping a correct momentum equation. Thereafter and unless otherwise specified, only this implicit coupling will be considered.

3.8.3 Perfect gas coupling induced instabilities

Here, one proposes to briefly investigate the numerical behavior of HLBM schemes under perfect gas coupling. A primitive variable formulation of the internal energy equation (Eq. (3.8.3)) is considered for the energy part. The Lax-Wendroff scheme is employed to discretize the advective part of this equation while second-order centered schemes discretize the source terms. Two different HLBM-BGK schemes based on respectively standard and multispeed lattice will be considered:

- A D2Q9 HLBM using a third-order equilibrium distribution $f_i^{eq,(3)}$ and the correction term ψ_i Eq. (3.8.9). The spatio-temporal evolution of g_i is carried out by Eq. (3.8.10).

- A D2V17 HLBM (see Table 2.1) using a third-order equilibrium distribution $f_i^{eq,(3)}$. The spatio-temporal evolution of g_i is carried out by Eq. (2.4.5)

It is important to recall that the momentum equation resulting from these two HLBMs is error-free. Indeed, the compressibility error is removed using either a correction term or a higher-order lattice.

Both models will be tested on almost the same test case seen previously in Sec. 3.7.3 i.e., a simple transport of a Gaussian temperature profile. However, in contrary to the HLBM model under Boussinesq assumption, the density can not be considered constant anymore due to the perfect gas coupling of the model. Therefore, it must be initialized thanks to the equation of state, and the initial density profile now reads:

$$\rho(r) = \frac{p}{r_g T(r)}. \tag{3.8.11}$$

The present initialization aims to assess the scheme for a test case involving the entropy mode. The same advection velocity value as Sec 3.8.2.b is imposed $u_x \simeq 50.83\,\mathrm{m.s^{-1}}$ (which corresponded to $\mathrm{CFL}_{adv} = 0.1$). The reference temperature is set to $T_r = 300\,\mathrm{K}$ i.e., $\theta = 1$ and the heat capacity ratio is imposed at $\gamma_g = 1.4$. The dynamic viscosity is set to zero as well as the heat conductivity, so that zero dissipation is introduced. In this compressible context, the Mach number is an interesting dimensionless number which helps to characterize the flow. Given the advection velocity and the fluid temperature, the Mach number corresponding to the flow is $\mathrm{Ma} \simeq 0.15$, which corresponds to an incompressible regime. During this test case, the Gaussian entropy profile is expected to be simply advected along $\boldsymbol{e}_x$ in the domain without being deformed or dissipated.

Fig. 3.14 displays the density and vorticity field obtained for both D2Q9 (two top rows) and D2V17 (two bottom rows) based HLBMs. The results are displayed at the initial state and after 30 and 60 iterations which corresponds respectively to $t \simeq 0.01 t_c$ and $t \simeq 0.03 t_c$. At the iteration 60, one can observe for both models on the vorticity fields, a high frequency instability emerging which results in a crash of both computations after a few subsequent iterations.

This instability is directly related to the perfect gas coupling. In fact, although the two parts of the model (LBM and energy) are numerically stable when considered separately [7], it turns out that once coupled, the resulting segregated system is unfortunately found to be unstable. The causes of this instability can be very numerous eg., choice of the collision operator, FD schemes, energy equation etc. For example, by removing the pressure work from the energy equation Eq. (3.8.3), it is possible to delay this instability as shown in Fig. 3.15. On this figure, it can be seen that both models can perform up to 1500 iterations before the calculations diverge. This instability, linked to the perfect gas coupling, will be further discussed in the next section 3.8.4.

Finally, it is worth noting that for such entropic test cases, no fluid flow should appear. The vorticity field must therefore remains constant along the computation. Just before the calculation diverges, one can nevertheless understand that a variation of this field

[7] or even weakly coupled as demonstrated by the HLBM under the Boussinesq approximation in Sec. 3.7.3

may appears due to the high frequency instability caused by the perfect gas coupling. Nevertheless, looking at the vorticity field at the intermediate time on both Fig. 3.14 and Fig. 3.15, one can observe for both models all around the spot, the emergence of several pairs of azimuthally-distributed counter rotating vortices. In fact, this phenomenon does not result of the unstable numerical behavior of the model. One will see later in chapter 6 (Sec. 6.6.2 precisely) that it can be attributed to a mode transfer between the entropy mode and the shear mode.

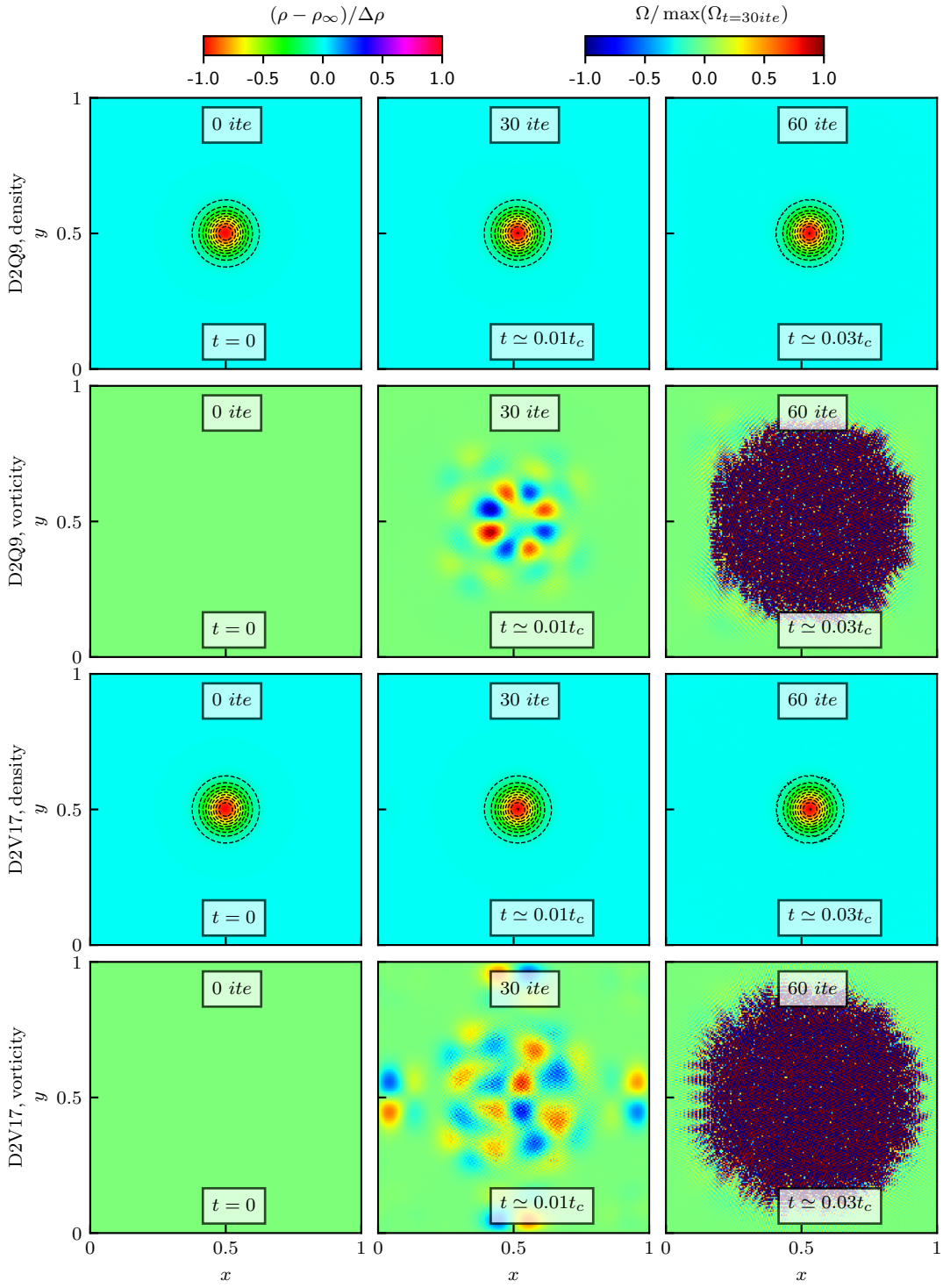

Figure 3.14 – Convected entropic spot computed with HLBMs using D2Q9-BGK and D2V17-BGK and based on a primitive variable formulation of the internal energy equation (3.8.3). Reduced density field and normalized vorticity at initialization (left), after 30 iterations (middle) and after 60 iterations (right). Both computations crashed shortly after 60 iterations. Twenty density iso-contours equally distributed from −1 to 1 are displayed.

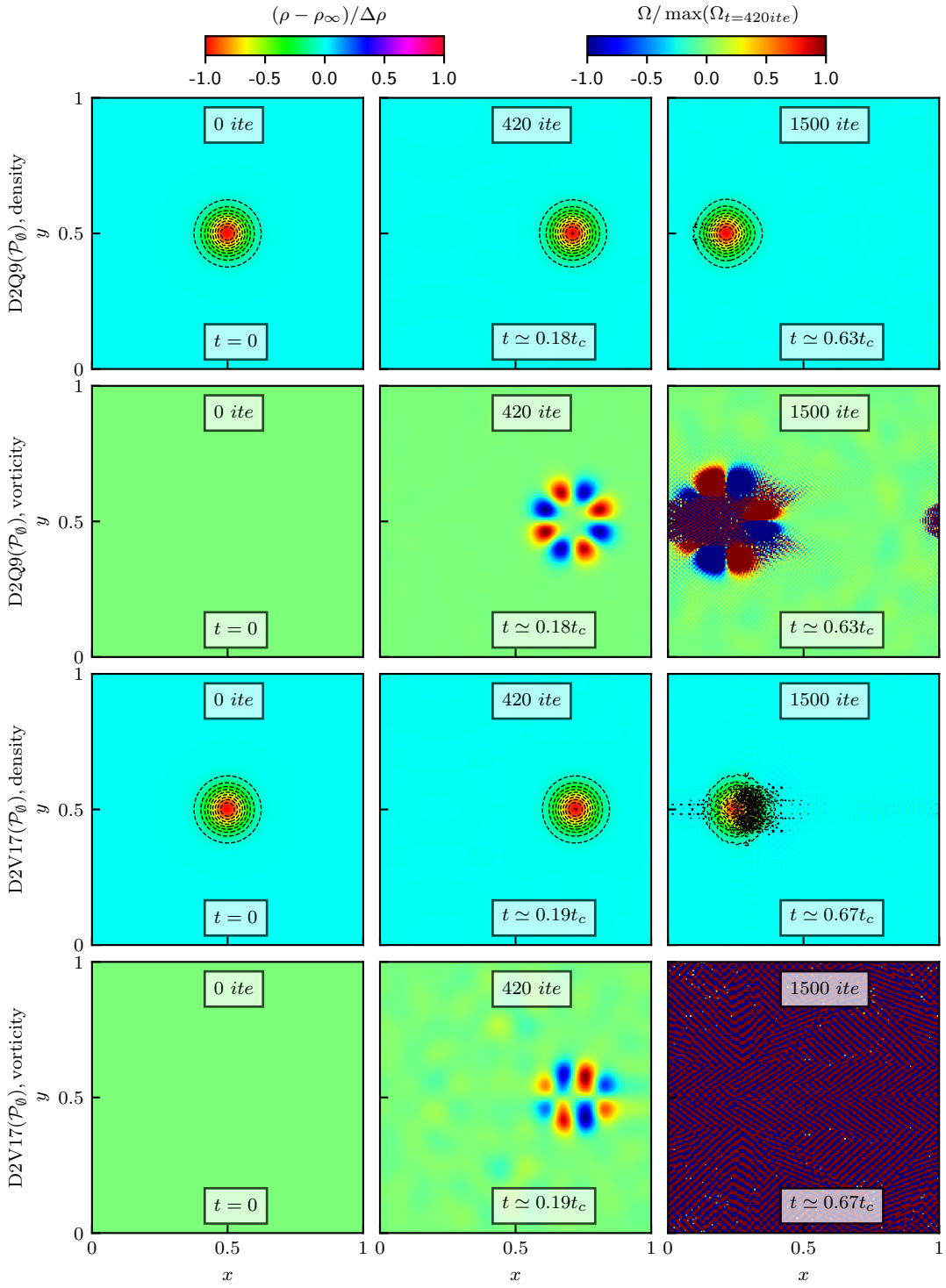

Figure 3.15 – Convected entropic spot computed with HLBMs excluding the pressure work ($\mathscr{P}_\emptyset$) in the primitive variable formulation of the internal energy equation (3.8.3) and based on D2Q9-BGK and D2V17-BGK. Reduced density field and normalized vorticity at initialization (left), after 420 iterations (middle) and after 1500 iterations (right). Both computations crashed shortly after. It must be noted that, with the same number of iterations, the simulation times of D2Q9 and D2V17 sightly differ, because they have different values of Δt ($c^*_{s,\mathrm{D2Q9}} \neq c^*_{s,\mathrm{D2V17}}$). Finally, twenty density iso-contours equally distributed from −1 to 1 are displayed.

3.8.4 Discussion

The previous numerical test has shown that the development of a stable perfect gas coupled model is not straightforward. When coupled together, the resulting system becomes highly unstable even for an incompressible advective velocity regime. Both standard and multispeed lattices are subjected to this numerical instability. Several additional tests have been carried out by either increasing the fluid viscosity, reducing the advective velocity (e.g., setting Ma = 0), changing the reference temperature T_r or even using more dissipative FD schemes on the energy part such as the RK1UOP1. Although very slight improvements have been noted for some cases, none of these tests have been effective in dealing with this instability issue. Finally, it should also be noted that this problem of instability occurs for other test cases involving shear or acoustic modes (e.g, isentropic vortex or acoustic pulse).

In order to stabilise the system, other strategies involving the change of the LBM scheme have been explored. Tests have been carried out for HLBMs based on enhanced collision operators, such as projected [29] or recursive [87] regularized operators. The collide and stream algorithm has also been slightly altered by using a fractional propagation scheme originally proposed by Qian in 1997 [181] and later explored by several authors [151,182,183]. By altering the streaming step, this scheme introduces a numerical dissipation which helps to reduce instabilities and has already been used in the compressible HLBM framework [150,152,153]. Finally, the explicit coupling strategy described in Sec. 3.8.2.a has also been tested. Again, although very slight improvements have been noted in some cases, none of these test have been effective in dealing with this problem of instability.

Finally, this type of instability might explain why other HLBM models introduced in the literature are mostly restricted to academic configurations within the framework of the Boussinesq approximation [13, 14, 147, 149], which is in line with the discourse held in the end of Sec. 2.7.4.a. For ideal gas coupled LBM, Lallemand et Luo in 2003 [31, 71] detected and identified modal interactions as potentially responsible for the severe numerical instabilities, making the coupling between the LBM and an extra energy equation much more delicate. The fact that the adopted equation of state is responsible for a lack of robustness of the model can be supplied by observations of DDF approaches, where most of the Boussinesq-based models show correct stability properties [43,103,184], while an ideal gas one was more unstable [44]. Finding a stable compressible LBM scheme for ideal gases is still an important matter of academic research.

Later in this thesis work, it will be shown that a collision operator allowing to suppress instable modal interactions is mandatory to obtain a stable perfect gas coupled HLBM. In addition, this choice of operator will have to be supplemented by a judicious choice of the energy equation. Regarding the latter, the observations made from the test case of Sec. 3.8.3 gives us some clues. Indeed, removing the pressure work term from the energy equation has greatly reduced the growth of instabilities. Nevertheless, removing this term on the basis of stability arguments would be catastrophic from a physical point of

view, especially in a compressible context [8]. However, and as discussed in Sec. 3.2.3, the energy equation based on the entropy variable has the particularity to implicitly contain the pressure work term. A linear stability analysis will show later in Chap. 6 (specially in Sec.6.5.1) that HLBMs based on this equation tend to be more robust, which possibly explains why the state of the art in compressible HBLMs uses an entropy equation [150].

3.9 High Mach number instabilities

As shown in the previous section, even for a low Mach number case, the presented HLBM experienced severe numerical instabilities caused by the perfect gas coupling. Unfortunately, even under the assumption that these instabilities would be resolved, another major problem remains to be addressed to get a stable HLBM method for compressible applications. This issue, which also affects the athermal LBM, is related to the unstable numerical behavior of the LBM when the Mach number becomes too large. This problem is still an active field of research in the LBM community and it will be briefly presented in the following.

At first sight, one can relate this high Mach number instability to two distinct phenomena:

1. The first one concerns the continuous equations (i.e., the DVBE). The instability can be attributed to the use of standard lattices and/or the use of a simple second-order expansion $f_i^{eq,(2)}$ (as discussed in Sec. 2.3.3), which both introduce a cubic error in term of Mach number in the viscous stress tensor. When the Mach number is too large, this error leads to an anti-dissipative behavior of the momentum equation, and the DVBE system becomes linearly unstable. In the literature, it has been observed [63] and demonstrated [185] that for the specific value of $\mathrm{Ma} > \sqrt{3} - 1 (\simeq 0.73)$, the stability is altered due to this error.

2. The second phenomena concerns numerical errors introduced by the time and space discretization of the DVBE. Even though the impact of these errors can be mitigated using an advanced collision operator as discussed in Sec. 2.5, they remain nevertheless in the zero-viscosity limit, responsible for instabilities occurring much sooner than the continuous limit of $\mathrm{Ma} \simeq 0.73$.

[8] One recalls that this term is responsible for the heating or cooling of the gas according to the local dilatation $\nabla \cdot \boldsymbol{u}$.

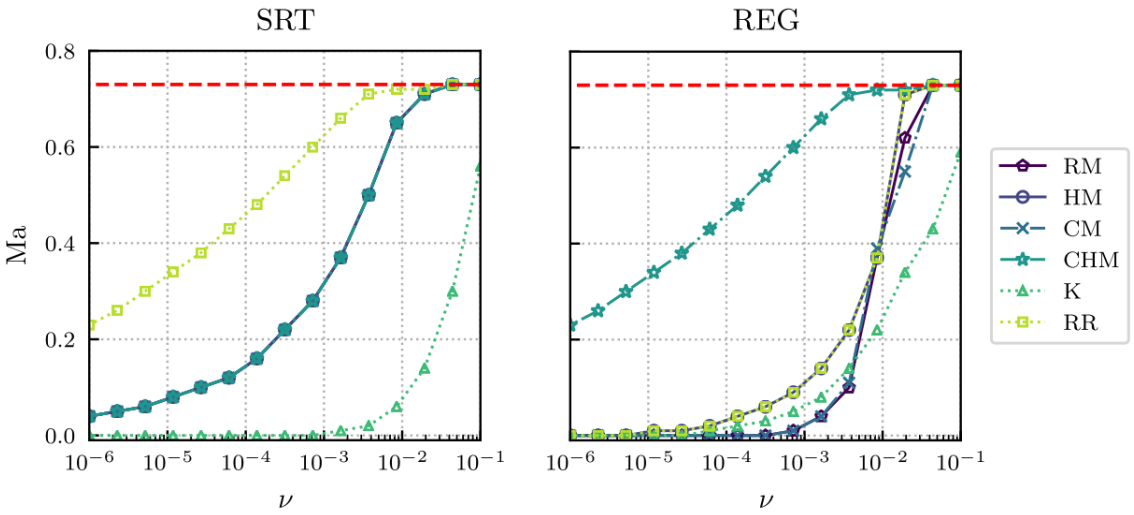

Figure 3.16 – Maximum achievable Mach number as function of the kinematic viscosity for D2Q9-LBM models. Results can be found for different models (Raw, Hermite, Central and Central Hermite Moments, cumulent (K) and Recursive Regularized) and for two standard configurations: single relaxation time (SRT) and equilibration of high-order moments (REG) (i.e., equilibrium moments are imposed in the collision process for moments higher than two). The red dotted line corresponds to Ma $\simeq 0.73$. This graph has been obtained from a von Neumann stability analysis and was taken from the work of Coreixas et al. [186].

While the former phenomenon can be solved by using a third-order expansion $f_i^{eq,(3)}$ on higher-order lattices or correction terms such as the one briefly presented in Sec. 3.8.2.b, the second phenomenon remains the main cause of instability. The results obtained by von Neumann stability analysis on Fig. 3.16 are very representative of this unstable phenomena. For athermal LBM schemes based on the D2Q9 lattice (without correction) and on different collision models and polynomial basis, it compares the maximum reachable Mach number as function of the viscosity. From this figure, it can be observed that for low values of kinematic viscosity, most of the LBMs are restricted to Mach number well below the theoretical continuous limit of Ma $\simeq 0.73$ (represented by the red dotted line). From these figures, the only models reaching a decent maximum Mach number for low viscosity values are the SRT-RR [9] and the REG-CHM which can achieve Ma ~ 0.2. This value is therefore far from being satisfactory for making compressible simulations.

[9] It corresponds to a fourth-order Recursive Regularized operator on the complete D2Q9 basis $\mathcal{B}^{D2Q9}$ Eq. (2.3.25)

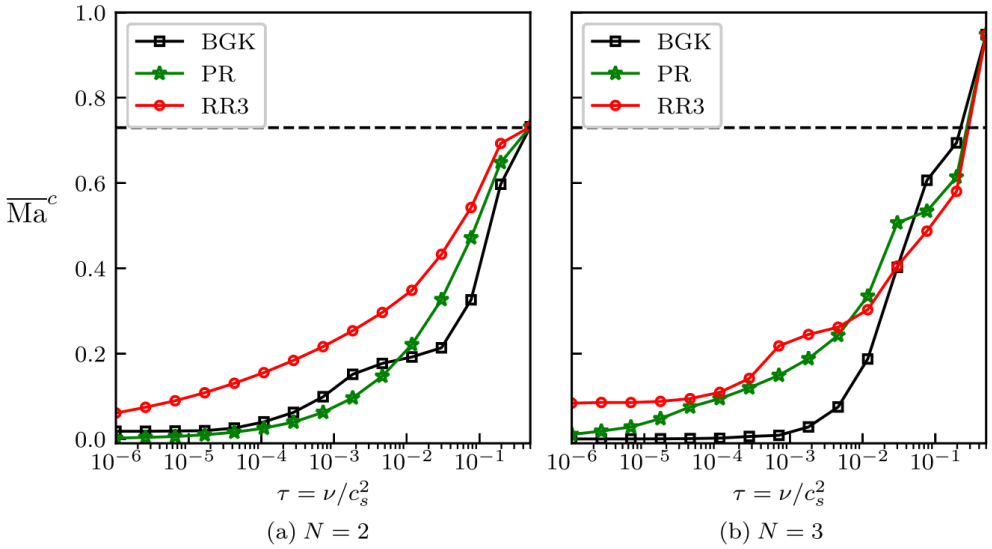

Figure 3.17 – Maximum achievable Mach number as a function of the kinematic viscosity for BGK- and regularized-D2V17-LBM models in the Hermit basis. Results are displayed for equilibrium distribution $f_i^{eq,(N)}$ at order $N = 2$ (left) and $N = 3$ (right). The red dotted line corresponds to Ma $\simeq 0.73$. This graph was taken from the work of Wissocq et al. [72] and have been obtained using a von Neumann stability analysis.

There is numerical evidence that one of the instability mechanisms is related to the presence of non-hydrodynamic modes [59, 71] present in the LBM system. Their interaction with hydrodynamic ones can lead, in certain configurations, to severe linear instabilities such as the so-called eigenvalue collision phenomenon highlighted by the works of Wissocq et al. [40, 63]. It is worth noting that the standard BGK operator is particularly subject to this collision phenomenon compared to advanced collision operators which suppress some of these destructive modal interactions [72].

In an attempt to gain stability, higher-order lattices with more velocities than the D2Q9 lattice can be considered. Generally speaking, the number of non-hydrodynamic modes relates on the number of discrete velocities m of the lattice minus the number of hydrodynamic modes N_h of the considered LBM system[10]. Thus, considering higher-order lattices increases the number of non-hydrodynamic modes. The stability of the models is therefore even more questionable due to the increasing number of potentially destructive modal interactions [63]. Fig 3.17 from Ref [72], illustrates this phenomenon by showing the maximum achievable Mach number for BGK- and regularized-D2V17-LBMs. In their work, Wissocq et al. [72] observed no improvement in terms of stability at low viscosity values compared to D2Q9-LBMs as evidenced by the figure and with regard to Fig. 3.16. Finally, it can be noted from the figure that for $f_i^{eq,(3)}$, the limit of Ma $\simeq 0.73$ can be overcome by the D2V17-RR3, the model being no longer subjected to the cubic Mach error. However it only happens for very high viscosity values, which always brings us

[10]For an athermal LBM system: $N_h = 2$ for $D = 1$, (two acoustic modes); $N_h = 3$ for $D = 2$ (two acoustics and one shear modes); and $N_h = 4$ for $D = 3$ two acoustics and two shear modes).

back to the same problem of numerical stability for low viscosity values.

Finally, because of this instability, making compressible applications using the LBM remains challenging. Even in the absence of the additional complexity brought by the hybrid method, this issue is already present for athermal-LBM schemes. The use of higher-order lattices does not necessary help for increasing the maximum reachable Mach number [37, 63]. Using collision operators more advanced than the BGK, however, can help to increase stability. Nevertheless, the maximum Mach number allowed for low viscosity values is well below those required for compressible applications.

3.10 Conclusion and perspective

In this chapter one has seen the main principles of the HLBM. This segregated method relies on two systems, the LBM system that solves the mass and momentum equations and a FD system that solves an extra energy equation. Once the LBM system is given, multiple choices are possible to build this method such as: the type of energy equation, the type of formulation, its discretization, the communication between the LBM and the energy system etc.

Two HLBMs solving respectively the weakly compressible and compressible Navier-Stokes equations were presented. The first one was derived within the framework of the Boussinesq approximation. Under this assumption, the thermal coupling methodology between the momentum and the energy equation boils down to a single buoyancy force term, which seems to help recovering similar stability properties as in the athermal case. The second HLBM was derived for a more realistic equation of state i.e., the ideal gas one. However, severe numerical instabilities were observed, making the coupling between the LBM and an extra energy equation a much more delicate task.

Finally, it was also shown that even for athermal LBM, an unstable numerical behavior emerges when the Mach number becomes too large. Even though the latter can be mitigated when very high values of viscosities are considered, for realistic values such as the one encountered in industrial configurations, the numerical instabilities restrict the LBMs to Mach number well below the compressible regime.

It is worth recalling that to compute compressible cases, a numerical method must be able to solve the compressible Navier-Stokes equations (under perfect gas coupling) and to handle flows with Mach number higher than $\mathrm{Ma} > 0.3$. Thus, to put it in a nutshell, in order to develop a stable compressible HLBM one has to face these two issues:

- The instabilities introduced by the perfect gas coupling,
- The instabilities restricting the LBM to relatively low Mach number computations,

which, according to the literature, both originate from destructive modal interactions. Finally, the use of higher-order lattices does not necessarily solve the problem.

Because of these instabilities, finding a stable compressible HLBM scheme remains thus very challenging. Fortunately, the richness in the world of HLBMs is immense,

as one can select any combination of LBM system and energy system separately. One year after the beginning of this thesis, an interesting model was published by Feng et al. [187]. The authors proposed a stable perfect gas coupled compressible HLBM based on the standard D2Q9 lattice. The stability of the model was achieved by the use of an hybrid recursive regularized (HRR) collision operator [88], removing both coupling and high Mach number instabilities. The consequent gain in terms of stability of this operator allowed the authors to hybridize the LBM system with an entropy equation, thus recovering the full set of compressible Navier-Stokes equation. This model was successfully assessed on compressible one- and two-dimesional high-subsonic test cases.

The characteristics of this HLBM perfectly fit the requirements of the present PhD work. The fact that this model is based on standard lattices makes it very attractive, since it can be directly adapted to the ProLB solver with minimal effort. The following chapter is dedicated to the description of this method and its improvement.

Chapter 4

Compressible Hybrid Lattice Boltzmann Method

Contents

4.1 Introduction 115

4.2 Hybrid Discrete Velocity Boltzmann Equation on standard lattice 116

4.2.1 Governing equations 116

4.2.2 The equilibrium distribution function 117

4.2.3 Lattice closure relation and correction term 118

4.2.4 Thermo-hydrodynamic limits of the model 119

4.2.5 Speed of sound 123

4.3 Extended HLBM for high Mach number compressible flows 123

4.3.1 Space/time discretization of the DVBE 123

4.3.2 Correction term enhancement and discretization 125

4.3.3 Hybrid Recursive Regularised collision operator 125

4.3.3.a The off-equilibrium definition with corrective terms . . 126

4.3.3.b From the corrected LBM-BGK to the corrected regularized LBM equation 127

4.3.3.c Partial finite difference off-equilibrium reconstruction . 127

4.3.4 Entropy equation discretization 128

4.3.5 CFL number and HLBM algorithm 130

4.4 Numerical validations of the improved HLBM 131

4.4.1 Viscosity computation 132

4.4.2 Supersonic isentropic vortex 132

4.4.3 Acoustic damping 135

4.4.4 Thermal Couette flow 139

4.5 Numerical validation and model capabilities 141
4.5.1 Acoustic cases 141
4.5.2 Shock tube problem 142
4.5.3 Shock vortex interaction 144
4.6 The model's Achille's heel: case involving entropic mode . . 146
4.7 Conclusions 152

In this chapter, a stable perfect gas coupled D2Q9 HLBM is proposed for the simulation of both compressible subsonic and supersonic flows. This HLBM is an extension of the model of Feng et al. [187], which has been found, via different test cases, to be unstable for supersonic regimes. The improvements consist of: (1) a new discretization of the lattice closure correction term making possible to properly simulate supersonic flows, (2) a corrected viscous stress tensor that takes into account polyatomic gases, and (3) a novel discretization of the viscous heat production term fitting with the regularized formalism. This method is successfully assessed with both smooth flows and flows involving shocks. Finally, the strengths and weaknesses of the model will be shown and suggestions for improvements will be made.

4.1 Introduction

The accuracy, the efficiency and scalability of the Lattice Boltzmann Method (LBM) on standard lattices (D1Q3, D2Q9 and D3Q19/Q27) has been widely demonstrated over the past decades, e.g. [2, 4, 33], for aeronautics applications involving turbulence and acoustics [188, 189]. Nevertheless, most existing standard LBM schemes relying on these lattices are restricted to isothermal and weakly compressible simulations, leading to a limitation of their range of application, particularly in the field of aeronautics. In order to perform fully compressible computations while retaining the advantages of the standard LBM, two key issues must be resolved: the compressibility defect (Galilean invariance) of standard lattices [190, 191], and the inability to correctly resolve the energy equation [30, 33].

To address these issues, it has been chosen to employ the HLBM in this Ph.D. work. Although the development under the Boussinesq hypothesis (incompressible) of an HLBM is relatively straightforward, it has been shown in the previous chapter that HLBM under perfect gas coupling remains challenging in terms of stability. Nevertheless, to model fully compressible flows, such coupling is mandatory and therefore stabilization strategies must be employed, such as the use of a more advanced collision operator than the BGK. Indeed, as mentioned by Lallemand et al. [31] the standard BGK operator is largely responsible for numerical instabilities when using a thermal LBM model. They proposed to use a Multiple Relaxation Times (MRT) operator to overcome this issue. Nonetheless, the manifolds relaxation times present in this operator make the LBM model case-dependent as illustrated in the work of Li et al. [41]. Very recently, Feng et al. [187] in early 2018 developed a compressible HLBM based on the standard D2Q9 lattice and succeeded in performing stable high-subsonic computations. They used a new Hybrid Regularized Recursive (HRR) collision operator [88] based on a single degree of freedom, which increased the stability of the original recursive regularized approach [65, 87]. In their model, the Galilean invariance defect of the D2Q9 was corrected using a Hermite-based force term ψ_i computed with finite differences (already briefly mentioned in Sec 3.8.2.b). Finally, they employed a primitive variable formulation of the entropy equation for the energy part. The present work follows the path paved by this new approach, and further extends it to the simulation of transonic and supersonic flows involving discontinuities.

The Chapter is articulated in five parts. In Sec. 4.2 the general construction and associated macroscopic equations of the hybrid scheme of Feng et al. [187] is introduced. In Sec. 4.3, the space and time discretization of the scheme is derived with its three-fold improvements: (1) a new corrective term that correctly retrieves the viscous stress tensor, (2) a novel discretization technique of the viscous heat production term in the energy equation and (3) a tailored numerical scheme for the compressibility correction terms that increases stability for high Mach number flows. In Sec. 4.4, the improvements of the model are validated through several canonical test cases assessing: (1) the viscous dissipation/production and thermal dissipation, (2) the capacity of the scheme to capture vortical flows and acoustics in subsonic and supersonic regimes. Throughout this validation stage, the improved scheme is compared to the original one, which is shown to be restricted to the computation of subsonic flows due to stability problems. In Sec. 4.5, the acoustic validation of the improved model is completed. This is followed by two test cases aimed at assessing: (1) the ability to handle flow with discontinuities (2) the ability to capture non-linear acoustics in a transonic case. Finally, conclusions are drawn in Sec.4.7.

4.2 Hybrid Discrete Velocity Boltzmann Equation on standard lattice

In this section, the continuous equations in space and time resolved by the hybrid model [187] are presented. First, the governing equations are given in their general form. Next, the choice of the equilibrium distribution function is detailed. The thermal and compressible restrictions of the standard lattices are then presented, and the correction term allowing to solve the compressibility issue is introduced. Afterwards, the Chapmann-Enskog expansion is used to retrieve the equivalent macroscopic equations solved by the hybrid model. Finally, the speed of sound relation generated by the thermodynamic closure of the hybrid model will be discussed.

4.2.1 Governing equations

In this HLBM, the mass and momentum are computed by the following DVBE-BGK equation $\mathcal{B}_i$:

$$\mathcal{B}_i : \frac{\partial f_i}{\partial t} + c_{i,\alpha}\frac{\partial f_i}{\partial x_\alpha} = -\frac{1}{\tau}\left(f_i - f_i^{eq}\right) + \psi_i, \quad \forall i \in [0, m-1]\,. \tag{4.2.1}$$

based on the standard D2Q9 lattice (defined in Table 2.1). The local thermodynamic equilibrium distribution function f_i^{eq} and the correction term ψ_i will be detailed in Sec. 4.2.2 and Sec. 4.2.3 respectively. In the following, all variables are considered dimensionless using T_r, ρ_r as a reference density, and Δx and $\Delta t = \Delta x/r$ (r being the discrete velocity norm) being respectively an arbitrary length and time. Computing the moments of the

distribution functions yields the mass at the zeroth order:

$$\rho \equiv \sum_{i=0}^{m-1} f_i = \sum_{i=0}^{m-1} f_i^{eq}, \tag{4.2.2}$$

and the momentum at first-order:

$$\rho u_\alpha \equiv \sum_{i=0}^{m-1} c_{i,\alpha} f_i = \sum_{i=0}^{m-1} c_{i,\alpha} f_i^{eq}, \tag{4.2.3}$$

which are collision invariant by construction.

The Hybrid approach uses an entropy equation to compute the dimensionless temperature $\theta = T/T_r$ of the system. The usual equation for entropy is given by:

$$\frac{\partial s}{\partial t} + u_\alpha \frac{\partial s}{\partial x_\alpha} = -\frac{1}{\rho\theta}\frac{\partial}{\partial x_\alpha}\left(-\lambda \frac{\partial \theta}{\partial x_\alpha}\right) + \frac{\Phi}{\rho\theta}, \tag{4.2.4}$$

where Φ the viscous heat production term defined as:

$$\Phi = \mu\left(\frac{\partial u_\alpha}{\partial x_\beta} + \frac{\partial u_\beta}{\partial x_\alpha} - \frac{2}{D}\frac{\partial u_\gamma}{\partial x_\gamma}\delta_{\alpha\beta}\right)\frac{\partial u_\alpha}{\partial x_\beta}. \tag{4.2.5}$$

The entropy s is directly derived from the Gibbs equation and reads:

$$s = c_v \ln\left(\frac{\theta}{\rho^{(\gamma_g - 1)}}\right), \tag{4.2.6}$$

Finally, the Hybrid DVBE system on the standard D2Q9 lattice consists of a set of ten partial differential equations (PDE). Eq. (4.2.1) resolves the mass and the momentum while a single PDE Eq. (4.2.4), is used to solve the entropy from which the temperature is obtained. The dependency of the entropy equation on the DVBE can be explicitly seen through ρ and u_α, while the thermal coupling of the entropy equation to the DVBE is described in Sec. 4.2.2.

4.2.2 The equilibrium distribution function

The usual expansion of the equilibrium distribution function f^{eq} on Hermite polynomials seen in Sec 2.3.1 is adopted and reads for the discrete velocity case:

$$f_i^{eq} = w_i \sum_{n=0}^{N} \frac{1}{n! c_s^{2n}} \boldsymbol{a}^{eq,(n)} : \boldsymbol{\mathcal{H}}_i^{(n)}, \tag{4.2.7}$$

where it is worth to recall that : stands for the full contraction of indexes, also known as Frobenius inner product. The coefficients $\boldsymbol{a}^{eq,(n)}$ are the nth-order Hermite moments of the Maxwell-Boltzmann equilibrium distribution function and can be found up to the fourth order in Sec. 2.3.1.a Eq. (2.3.13). $\boldsymbol{\mathcal{H}}_i$ refers to the discrete Hermite polynomial in terms of velocity, and can also be found in Sec. 2.3.1.a Eq. (2.3.12).

Unlike the standard isothermal LBM, the present equilibrium distribution function is developed in term of temperature θ ensuring an implicit coupling between the LBM and the thermal system as already discussed in Sec. 3.8.2.b. A perfect gas thermodynamic closure $p = \rho c_s^{\star 2}\theta$ is thus recovered. This relation, will be shown later in detail in Sec. 4.2.4, and appears naturally once the macroscopic equation are recovered using the Chapman-Enskog development. In the following, only the moments computable with the D2Q9 basis described in the next section 4.2.3 are kept to build the equilibrium distribution function.

4.2.3 Lattice closure relation and correction term

For the D2Q9 lattice, the discrete equilibrium distribution functions f_i^{eq} truncated at the second-order in terms of Hermite series expansion, allows for recovering the zeroth, first, and second-order equilibrium moments without error. However, higher order moments are not properly recovered due to the closure relation [55]. This relation, also referred to the low symmetry of the lattice [41], is the root cause limitation of the lattice to recover the correct moments of the equilibrium distribution function. This gives rise to a linear dependency of higher order moments on lower order ones. For the D2Q9 lattice this relation reads:

$$c_{i,\alpha}^3 = c_{i,\alpha}, \tag{4.2.8}$$

which can be rewritten in terms of Hermite polynomial as:

$$\mathcal{H}_{i,\alpha\alpha\alpha}^{Q9} = \left(1 - 3c_s^2\right)\mathcal{H}_{i,\alpha} = 0. \tag{4.2.9}$$

This limitation leads to a biased evaluation of the third and higher order moments which reduces the ability of the lattice to recover the desired set of macroscopic equations. The third-order equilibrium moment is therefore null:

$$a_{\alpha\alpha\alpha}^{eq,Q9} = \sum_{i=0}^{m-1} \mathcal{H}_{i,\alpha\alpha\alpha}^{Q9} f_i^{eq} = 0. \tag{4.2.10}$$

Once a Chapman-Enskog expansion is carried out (performed latter in Sec. 4.2.4), it is clear that this closure relation is directly responsible for the well-known Galilean invariance issue observed on standard lattices (D1Q3, D2Q9, D3Q27). Moreover, higher order moments associated to the temporal evolution of the energy are also biased leading to the isothermal restriction. The Hermite polynomials supported by the D2Q9 basis read [65, 87]:

$$\mathcal{B}_{D2Q9}^{\mathcal{H}} = \left(\mathcal{H}_{i,0}, \mathcal{H}_{i,x}, \mathcal{H}_{i,y}, \mathcal{H}_{i,xx}, \mathcal{H}_{i,xy}, \mathcal{H}_{i,yy}, \mathcal{H}_{i,xxy}, \mathcal{H}_{i,yyx}, \mathcal{H}_{i,xxyy}\right), \tag{4.2.11}$$

with their associated Hermite equilibrium moments:

$$\left(a_0^{eq}, a_x^{eq}, a_y^{eq}, a_{xx}^{eq}, a_{xy}^{eq}, a_{yy}^{eq}, a_{xxy}^{eq}, a_{yyx}^{eq}, a_{xxyy}^{eq}\right), \tag{4.2.12}$$

which are used to build the equilibrium distribution function Eq. (4.2.7). Developing f_i^{eq} up to the fourth order for the present lattice increases the numerical stability [37,40,63,72],

which presents a further improvement over the original model, which goes only to third order [187].

Thus, this closure relation results in a null third-order Hermite equilibrium moment $a^{eq}_{\alpha\alpha\alpha}$, whose spatial derivative is of paramount importance to recover the correct viscous part of the momentum equation as shown later in Sec. 4.2.4. However, this defect can be corrected by injecting a corrective term into the DVBE under the following form:

$$E_{1,\alpha\beta} = \frac{\partial}{\partial x_\alpha} \underbrace{\left(\rho u_\alpha \left(1 - \theta - u_\alpha^2\right)\right)}_{=-a^{eq}_{\alpha\alpha\alpha}} \delta_{\alpha\beta}, \tag{4.2.13}$$

which must appears in the viscous stress tensor of the momentum equation. This is done through the force term ψ_i in Eq. (4.2.1) which reads:

$$\psi_i = w_i \frac{\mathcal{H}_{i,\alpha\beta}}{2c_s^4} E_{1,\alpha\beta}, \tag{4.2.14}$$

where $E_{1,\alpha\beta}$ corresponds to the second-order Hermite moment of ψ_i. In the standard athermal case ($\theta = 1$), this error only reduces to a cubic error term which can be neglected for low Mach number cases. However, for thermal cases where $\theta \neq 1$, a first-order error term in velocity arises, which is of utmost importance and cannot be neglected anymore. The corrective term includes a factor of the second-order Hermite polynomial, therefore it does not affect the computation of the macroscopic variables ρ in Eq. (4.2.2) and ρu_α in Eq. (4.2.3), thanks to the orthogonality properties of the Hermite polynomials [50]. Thus, due to its second order nature, this term acts only on the viscous part of the momentum equation as shown in the next section.

4.2.4 Thermo-hydrodynamic limits of the model

The equivalent macroscopic equations associated to the DVBE (Eq. (4.2.1)) are found by computing its velocity moments in the canonical basis after expanding the distribution functions in terms of the small parameter τ, which is related to the Knudsen number as discussed in Sec 2.2.5.b. This expansion is the so-called Chapman-Enskog development [11] and reads at the first order:

$$f_i \simeq f_i^{eq} - \tau \left(-\psi_i + \frac{\partial f_i^{eq}}{\partial t} + c_{i,\alpha} \frac{\partial f_i^{eq}}{\partial x_\alpha} \right), \tag{4.2.15}$$

or more commonly:

$$f_i \simeq f_i^{eq} + f_i^1, \tag{4.2.16}$$

where f_i^1 corresponds to the first-order approximation in τ of the off-equilibrium part of f_i. Before computing the moments of Eq. (4.2.1), it is worth noting that its first two Hermite moments are strictly equivalent to the raw moments as shown by Eq. (2.3.22). For higher order moments, the recursive relation on the second-order Hermite polynomial gives:

$$\mathcal{H}_{i,\alpha} c_{i,\beta} = \mathcal{H}_{i,\alpha\beta} + c_s^2 \delta_{\alpha\beta} \mathcal{H}_{i,0}, \tag{4.2.17}$$

and similarly for the third-order polynomial:

$$\mathcal{H}_{i,\alpha\beta}c_{i,\gamma} = \mathcal{H}_{i,\alpha\beta\gamma} + c_s^2\left(\mathcal{H}_{i,\alpha}\delta_{\beta\gamma} + \mathcal{H}_{i,\beta}\delta_{\alpha\gamma}\right), \tag{4.2.18}$$

will be useful for the following. Computing now the zeroth and first-order moment of Eq. (4.2.1), with the use of Eq. (4.2.2) and Eq. (4.2.3), leads respectively to the mass equation:

$$\sum_{i=0}^{m-1}\mathcal{H}_{i,0}\mathcal{B}_i \rightarrow \frac{\partial\rho}{\partial t} + \frac{\partial\rho u_\alpha}{\partial x_\alpha} = 0, \tag{4.2.19}$$

and the momentum equation:

$$\sum_{i=0}^{m-1}\mathcal{H}_{i,\alpha}\mathcal{B}_i \rightarrow \frac{\partial\rho u_\alpha}{\partial t} + \frac{\partial\Pi_{\alpha\beta}}{\partial x_\beta} = 0. \tag{4.2.20}$$

The second-order moment, thank to the use of Eq. (4.2.17) is expressed as follows:

$$\Pi_{\alpha\beta} = \sum_{i=0}^{m-1}\mathcal{H}_{i,\alpha\beta}f_i + \sum_{i=0}^{m-1}c_s^2\delta_{\alpha\beta}\mathcal{H}_{i,0}f_i. \tag{4.2.21}$$

Substituting Eq. (4.2.15) in Eq. (4.2.21) , using Eq. (4.2.18) and noting that the zeroth order off-equilibrium Hermite moment cancels out due to Eq. (4.2.19), this gives:

$$\begin{aligned}\Pi_{\alpha\beta} =& \rho u_\alpha u_\beta + \rho c_s^2\theta\delta_{\alpha\beta} - \tau\left(-E_{1,\alpha\beta} + \frac{\partial a^{eq}_{\alpha\beta}}{\partial t} + \frac{\partial a^{eq}_{\alpha\beta\gamma}}{\partial x_\gamma} + \frac{\partial}{\partial x_\gamma}\left[\rho c_s^2\left(u_\alpha\delta_{\beta\gamma} + u_\beta\delta_{\alpha\gamma}\right)\right]\right)\\ =& \Pi^{eq}_{\alpha\beta} + a^1_{\alpha\beta}.\end{aligned} \tag{4.2.22}$$

Here, $a^1_{\alpha\beta}$ is the second-order off-equilibrium Hermite moment and $E_{1,\alpha\beta}$ is the integrated correction term over the second-order Hermite polynomial. Classically, Eq. (4.2.19) and Eq. (4.2.20) yield the Euler equations when approximating each term by its equilibrium part. This is equivalent to keep only the terms in τ^0 and results in:

$$\frac{\partial\rho}{\partial t} + \frac{\partial\rho u_\alpha}{\partial x_\alpha} = 0 \tag{4.2.23a}$$

$$\frac{\partial\rho u_\alpha}{\partial t} + \frac{\partial}{\partial x_\beta}\left(\rho u_\alpha u_\beta + p\delta_{\alpha\beta}\right) = 0, \tag{4.2.23b}$$

with p the pressure found to be :

$$p = \rho c_s^{*2}\theta. \tag{4.2.24}$$

Up to this point, one can clearly guess that the viscous contribution in the momentum equation will be given by $a^1_{\alpha\beta}$. Moreover, it is important to recall that the Chapman-Enskog expansion has been done up to the first-order in τ (or Knudsen). Thus no higher power contributions are retained to compute:

$$\frac{\partial a^{eq}_{\alpha\beta}}{\partial t} = \frac{\partial\rho u_\alpha u_\beta}{\partial t} + \frac{\partial p}{\partial t}\delta_{\alpha\beta} - \frac{\partial\rho c_s^2}{\partial t}\delta_{\alpha\beta}, \tag{4.2.25}$$

reducing the choice to Eq. (4.2.23b) for the computation of the quadratic term in the temporal derivative:

$$\frac{\partial \rho u_\alpha u_\beta}{\partial t} = -u_\alpha \frac{\partial p}{\partial x_\gamma}\delta_{\beta\gamma} - u_\beta \frac{\partial p}{\partial x_\gamma}\delta_{\alpha\gamma} - \frac{\partial}{\partial x_\gamma}\left(\rho u_\alpha u_\beta u_\gamma\right), \tag{4.2.26}$$

and Eq. (4.2.23a) for the temporal derivative of the density:

$$-\frac{\partial \rho c_s^2}{\partial t}\delta_{\alpha\beta} = \rho c_s^2 \frac{\partial u_\gamma}{\partial x_\gamma}\delta_{\alpha\beta} + u_\gamma \frac{\partial \rho c_s^2}{\partial x_\gamma}\delta_{\alpha\beta}. \tag{4.2.27}$$

In Eq. (4.2.25), the time derivative of the pressure is found from the hybrid energy part. Indeed, if one compute the partial derivative of the entropy Eq. (4.2.6) with respect to the pressure and density, and replaces their expression in Eq. (4.2.4), the pressure equation is retrieved and reads:

$$\frac{\partial p}{\partial t}\delta_{\alpha\beta} = -u_\gamma \frac{\partial p}{\partial x_\gamma}\delta_{\alpha\beta} - \gamma_g p \frac{\partial u_\gamma}{\partial x_\gamma}\delta_{\alpha\beta}. \tag{4.2.28}$$

This equation does not includes the viscous and diffusive terms since the dynamic viscosity is assumed to be $\mu \simeq \mathcal{O}(\tau)$ and thus $\lambda = \mu/(c_p \mathrm{Pr}) \simeq \mathcal{O}(\tau)$ for the heat conductivity. Inserting now Eq. (4.2.25) in the expression of $a^1_{\alpha\beta}$ in Eq. (4.2.22) gives:

$$\begin{aligned} a^1_{\alpha\beta} = -\tau \Bigg(& -E_{1,\alpha\beta} + \frac{\partial a^{eq}_{\alpha\beta\gamma}}{\partial x_\gamma} - \gamma_g p \frac{\partial u_\gamma}{\partial x_\gamma}\delta_{\alpha\beta} \\ & + \rho c_s^2 \left(\frac{\partial u_\alpha}{\partial x_\beta} + \frac{\partial u_\beta}{\partial x_\alpha} + \frac{\partial u_\gamma}{\partial x_\gamma}\delta_{\alpha\beta} \right) \\ & + u_\alpha \frac{\partial}{\partial x_\beta}\left(\rho c_s^2 - p\right) + u_\beta \frac{\partial}{\partial x_\alpha}\left(\rho c_s^2 - p\right) \\ & + u_\gamma \frac{\partial}{\partial x_\gamma}\left(\rho c_s^2 - p\right)\delta_{\alpha\beta} - \frac{\partial}{\partial x_\gamma}\left(\rho u_\alpha u_\beta u_\gamma\right) \Bigg). \end{aligned} \tag{4.2.29}$$

On the other side, supposing that the third-order equilibrium Hermite moment is perfectly recovered by the lattice (which is not true for standard lattices), it yields the following relation on the derivatives of $a^{eq}_{\alpha\beta\gamma}$:

$$\begin{aligned} \frac{\partial a^{eq}_{\alpha\beta\gamma}}{\partial x_\gamma} = & p\left(\frac{\partial u_\alpha}{\partial x_\gamma}\delta_{\beta\gamma} + \frac{\partial u_\beta}{\partial x_\gamma}\delta_{\alpha\gamma} + \frac{\partial u_\gamma}{\partial x_\gamma}\delta_{\alpha\beta} \right) \\ & - \rho c_s^2 \left(\frac{\partial u_\alpha}{\partial x_\gamma}\delta_{\beta\gamma} + \frac{\partial u_\beta}{\partial x_\gamma}\delta_{\alpha\gamma} + \frac{\partial u_\gamma}{\partial x_\gamma}\delta_{\alpha\beta} \right) \\ & + u_\alpha \frac{\partial}{\partial x_\gamma}\left(p - \rho c_s^2\right)\delta_{\beta\gamma} + u_\beta \frac{\partial}{\partial x_\gamma}\left(p - \rho c_s^2\right)\delta_{\alpha\gamma} \\ & + u_\gamma \frac{\partial}{\partial x_\gamma}\left(p - \rho c_s^2\right)\delta_{\alpha\beta} + \frac{\partial}{\partial x_\gamma}\left(\rho u_\alpha u_\beta u_\gamma\right), \end{aligned} \tag{4.2.30}$$

and once inserted in Eq. (4.2.29) eventually yields:

$$a^{1,\mathrm{hypo}}_{\alpha\beta} = -\tau\left(-E_{1,\alpha\beta} + p\left(\frac{\partial u_\alpha}{\partial x_\beta} + \frac{\partial u_\beta}{\partial x_\alpha} - (\gamma_g - 1)\frac{\partial u_\gamma}{\partial x_\gamma}\delta_{\alpha\beta} \right) \right), \tag{4.2.31}$$

which corresponds to the viscous stress tensor. Thus, under the hypothesis that $a^{eq}_{\alpha\beta\gamma}$ is entirely recovered by the lattice, it can be seen that the correction term proves to be superfluous, and thus imposing $E_{1,\alpha\beta} = 0$ in Eq. (4.2.31) allows to recover a viscous stress tensor $a^{1,\text{hypo}}_{\alpha\beta}$ free of the lattice closure error.

However, one recalls the defect of the standard lattice Eq. (4.2.10) *i.e.*, $a^{eq,Q9}_{\alpha\alpha\alpha} = 0$ which also apply to the derivatives of this term:

$$\frac{\partial a^{eq,Q9}_{\alpha\alpha\alpha}}{\partial x_\alpha} = 0. \tag{4.2.32}$$

Therefore, Eq. (4.2.30) becomes in this context only partially recovered and thus making Eq. (4.2.31) wrong. Instead, one obtain a viscous stress tensor containing the so-called compressibility defect which reads:

$$a^1_{\alpha\beta} = -\tau\left(-E_{1,\alpha\beta} - \frac{\partial a^{eq}_{\alpha\alpha\alpha}}{\partial x_\alpha}\delta_{\alpha\beta} + p\left(\frac{\partial u_\alpha}{\partial x_\beta} + \frac{\partial u_\beta}{\partial x_\alpha} - (\gamma_g - 1)\frac{\partial u_\gamma}{\partial x_\gamma}\delta_{\alpha\beta}\right)\right). \tag{4.2.33}$$

In this situation, the correction $E_{1,\alpha\beta}$ takes on its full meaning, and looking at Eq.(4.2.33) one can ultimately settles its expression at a macroscopic level as:

$$E_{1,\alpha\beta} = -\frac{\partial}{\partial x_\alpha}\left(a^{eq}_{\alpha\alpha\alpha}\right)\delta_{\alpha\beta}. \tag{4.2.34}$$

At last, once Eq. (4.2.34) inserted in Eq. (eq:Pi neq inter3), it yields:

$$a^1_{\alpha\beta} = -\tau p\left(\frac{\partial u_\alpha}{\partial x_\beta} + \frac{\partial u_\beta}{\partial x_\alpha} - (\gamma_g - 1)\frac{\partial u_\gamma}{\partial x_\gamma}\delta_{\alpha\beta}\right), \tag{4.2.35}$$

which corresponds to the stress tensor computed by standard lattices and now free of the lattice closure error. By identification to the Navier-Stokes equations, the dynamic viscosity is found to be $\mu = \tau p$. It should be noted here that if the heat capacity ratio γ_g differs from the monatomic value $((D+2)/D)$, the viscous stress tensor is not traceless and therefore does not completely correspond to the expected macroscopic equation. The correction of this error will be presented later. The macroscopic set of equations recovered by the HLBM model is then:

$$\frac{\partial \rho}{\partial t} + \frac{\partial \rho u_\alpha}{\partial x_\alpha} = 0 \tag{4.2.36a}$$

$$\frac{\partial \rho u_\alpha}{\partial t} + \frac{\partial}{\partial x_\beta}\left(\rho u_\alpha u_\beta + p\delta_{\alpha\beta}\right) = -\frac{\partial a^1_{\alpha\beta}}{\partial x_\beta} \tag{4.2.36b}$$

$$\frac{\partial s}{\partial t} + u_\alpha\frac{\partial s}{\partial x_\alpha} = -\frac{1}{\rho\theta}\frac{\partial}{\partial x_\alpha}\left(-\lambda\frac{\partial \theta}{\partial x_\alpha}\right) + \frac{\Phi}{\rho\theta}, \tag{4.2.36c}$$

with

$$p = \rho c_s^{*2}\theta \qquad \text{and} \qquad s = c_v \ln\left(\frac{\theta}{\rho^{(\gamma_g - 1)}}\right), \tag{4.2.37}$$

and the Mayer's relation $c_p - c_v = c_s^{*2}$ giving the expression of the dimensionless heat capacities:

$$c_v = \frac{c_s^{*2}}{(\gamma_g - 1)} \qquad \text{and} \qquad c_p = \frac{\gamma_g c_s^{*2}}{(\gamma_g - 1)}. \tag{4.2.38}$$

4.2.5 Speed of sound

In the standard isothermal case, the athermal speed of sound is fixed and imposed by the lattice constant $c = c_s$. This fixes the choice of $r_g T_r$ to recover the desired acoustic speed. In the present case, and in the light of the previous section (Sec. 4.2.4), the Hybrid DVBE is able to solve the Navier-Stokes-Fourier equations with the perfect gas equation of state (e.o.s) $p = \rho c_s^{*2} \theta$. Inserting this e.o.s in the entropy expression (Eq. (4.2.6)), one can write the pressure as:

$$p = \rho^{\gamma_g} c_s^{*2} \exp\left(\frac{s\,(\gamma_g - 1)}{c_s^{*2}}\right). \tag{4.2.39}$$

The dimensionless isentropic speed of sound can be now expressed as:

$$c^{*2} = \frac{\partial p}{\partial \rho}\Big|_s = \gamma_g \frac{p}{\rho} = \gamma_g c_s^{*2} \theta, \tag{4.2.40}$$

which once redimensionalized by the arbitrary length Δx and time Δt reads:

$$c = \sqrt{\gamma_g r T}. \tag{4.2.41}$$

This Hybrid DVBE model therefore recovers the authentic isentropic acoustic speed, which depends locally on the temperature and heat capacity ratio.

4.3 Extended HLBM for high Mach number compressible flows

In this section, the improvements made to the original model [187], which allow it to be extended to supersonic regimes, are presented. First, the generic spatio-temporal discretization of the hybrid DVBE is presented, leading to the well known collide and stream algorithm. Secondly, an enhanced correction term is derived, engendering a traceless viscous stress tensor. The discretization scheme for the correction term is described, as well as the standard lattice closure term, where a new tailored scheme is proposed. Third, the hybrid recursive regularized collision operator [88] is presented, and slightly adapted according to the modification brought by the new correction term. Fourth, the discretization of the hybrid energy part is detailed, and a new numerical scheme for the heat production term, combining finite difference and LBM, is proposed. Finally, the algorithm of the present HLBM is detailed with a brief discussion on the Courant–Friedrichs–Lewy number.

4.3.1 Space/time discretization of the DVBE

Here the DVBE (4.2.1) is discretized in time and space which leads to the LBM scheme. This demonstration slighlty differs from the one previously seen in Sec. 2.4 since it includes the correction term ψ_i. Starting from the corrected DVBE-BGK equation:

$$\frac{\partial f_i}{\partial t} + c_{i,\alpha} \frac{\partial f_i}{\partial x_\alpha} = -\frac{1}{\tau}\left(f_i - f_i^{eq}\right) + \psi_i, \tag{4.3.1}$$

one can integrates between t and $t+\Delta t$ the LHS linear convection term along the characteristic $c_{i,\alpha}$, whereas the trapezoidal rule ensures a second-order accurate integration in time for the RHS collision and force terms. This strategy leads to:

$$\begin{aligned} f_i^+ - f_i = &- \frac{\Delta t}{2\tau}\left(f_i^+ - f_i^{eq,+} + f_i - f_i^{eq}\right) \\ &+ \frac{\Delta t}{2}\left(\psi_i^+ - \psi_i\right) + \mathcal{O}\left(\Delta t^2, \Delta x^2\right), \end{aligned} \tag{4.3.2}$$

where one recall that the superscript + denotes the solution at $(x + c_{i,\alpha}\Delta t, t + \Delta t)$ and Δt and $\Delta x = c_{i,\alpha}\Delta t$ refer respectively to the time and space step. To remove the implicit character of the formulation, a change of variable compliant with the conservation of mass and momentum is adopted [192] and reads:

$$g_i = f_i + \frac{\Delta t}{2\tau}\left(f_i - f_i^{eq}\right) - \frac{\Delta t}{2}\psi_i, \tag{4.3.3}$$

which once plugged back in Eq. (4.3.2) gives:

$$g_i^+ = f_i - \frac{\Delta t}{2\tau}\left(f_i - f_i^{eq}\right) + \frac{\Delta t}{2}\psi_i. \tag{4.3.4}$$

Inverting now Eq. (4.3.3), one obtains:

$$f_i = \frac{2\tau}{2\tau + \Delta t}\left(g_i + \frac{\Delta t}{2\tau} f_i^{eq} + \frac{\Delta t}{2}\psi_i\right), \tag{4.3.5}$$

and once inserted in Eq. (4.3.4), after some algebra, finally gives:

$$g_i^+ = g_i - \frac{\Delta t}{\check{\tau}}\left(g_i - f_i^{eq}\right) + \frac{2\check{\tau} - \Delta t}{2\check{\tau}}\Delta t\psi_i. \tag{4.3.6}$$

This is the collide-and-stream corrected LBM-BGK equation [192] with $\check{\tau} = \tau + \Delta t/2$ the new relaxation time induced by the change of variable. The function g_i is then computed in time and space following a collision step and a streaming step (i.e. a direct propagation from node to node along $c_{i,\alpha}$). Computing the moments of the distribution function yields the mass at the zeroth order:

$$\rho \equiv \sum_{i=0}^{m-1} g_i = \sum_{i=0}^{m-1} f_i^{eq}, \tag{4.3.7}$$

and the momentum at first-order:

$$\rho u_\alpha \equiv \sum_{i=0}^{m-1} c_{i,\alpha} g_i = \sum_{i=0}^{m-1} c_{i,\alpha} f_i^{eq}, \tag{4.3.8}$$

which are still left invariant by collision by construction thanks to the feature of Eq. (4.3.3). Indeed, although ψ_i is now included in the definition of g_i Eq. (4.3.3), it is essentially composed of second-order contribution in term of Hermit polynomial (see Eq. (4.2.14)) and therefore does not influence the two first moments thanks to the orthogonality property Eq. (2.3.10).

4.3.2 Correction term enhancement and discretization

Lets recall the expression of the viscous stress tensor found after the Chapmann-Enskog development in Sec. 4.2.4:

$$a^1_{\alpha\beta} = -\tau p\left(\frac{\partial u_\alpha}{\partial x_\beta} + \frac{\partial u_\beta}{\partial x_\alpha} - (\gamma_g - 1)\frac{\partial u_\gamma}{\partial x_\gamma}\delta_{\alpha\beta}\right). \tag{4.3.9}$$

Although this present term is free of the D2Q9 lattice closure error, it is still not correct if the heat capacity ratio γ_g differs from the monatomic value. This relates to a second error, the latter being inherent to the hybrid method. This error is a direct consequence of the monatomic modelling of LBM where, $\gamma_{lb} = (D+2)/D$ with D referring simply to the dimension, while the heat capacity ratio γ_g in the hybrid energy part can be chosen freely. This defect modifies the trace of the viscous stress tensor and introduces additional bulk viscosity impacting the dissipation rate of the acoustic waves. Following the same procedure as in Sec. 4.2.4 to find $E_{1,\alpha\beta}$, the second correction term $E_{2,\alpha\beta}$ is settled at the macroscopic level as:

$$E_{2,\alpha\beta} = p\left(\frac{D+2}{D} - \gamma_g\right)\frac{\partial u_\gamma}{\partial x_\gamma}\delta_{\alpha\beta}. \tag{4.3.10}$$

Thus, the enhanced correction term at the Boltzmann level is given by:

$$\psi_i = w_i \frac{\mathcal{H}_{i,\alpha\beta}}{2c_s^4}\left(E_{1,\alpha\beta} + E_{2,\alpha\beta}\right), \tag{4.3.11}$$

leading to the error-free viscous stress tensor:

$$a^1_{\alpha\beta} = -\tau p\left(\frac{\partial u_\alpha}{\partial x_\beta} + \frac{\partial u_\beta}{\partial x_\alpha} - \frac{2}{D}\frac{\partial u_\gamma}{\partial x_\gamma}\delta_{\alpha\beta}\right). \tag{4.3.12}$$

In the present work, the standard second-order centered finite difference is used for the discretization of $E_{2,\alpha\beta}$. However, for the $E_{1,\alpha\beta}$ correction term, an upwind biased finite difference scheme is adopted and reads for the x direction:

$$E_{1,xx} = \frac{[1+\mathrm{sgn}(u_x)]}{2}\frac{\Gamma_i - \Gamma_{i-1}}{\Delta x} + \frac{[1-\mathrm{sgn}(u_x)]}{2}\frac{\Gamma_{i+1} - \Gamma_i}{\Delta x}. \tag{4.3.13}$$

Here, $\Gamma = \rho u_x\left(1 - \theta - u_x^2\right)$ and i represents the spatial position on the grid. $\mathrm{sgn}(u_x)$ simply denotes the sign of u_x. This upwind discretization differs from the centered scheme used by the original model [187], and has been found much more stable and mandatory for high Mach number cases as demonstrated in the next section 4.4.

4.3.3 Hybrid Recursive Regularised collision operator

A Hybrid Recursive Regularised (HRR) [88] collision operator has been chosen. It offers fewer degrees of freedom compared to the Multiple Relaxation Time (MRT) operators and its efficiency and robustness in the HLBM case has already been demonstrated [187]. This HRR collision operator is based on a partial reconstruction of the off-equilibrium

part of the pre-collision distribution function $g_i^{(1)}$ using finite differences. This permits a significant gain in terms of numerical stability, partially filtering out non-hydrodynamics modes, and suppressing their interactions with the other physical modes [193]. However, before moving on to the description of the HRR, a few manipulations are necessary in order to obtain the regularized formulation of the LBM. The following derivation details can not necessarily be found in the literature but nevertheless remains, from the author's point of view, interesting and primordial to show.

4.3.3.a The off-equilibrium definition with corrective terms

As discussed in Sec. 2.5.2, the regularization procedure is based on the fact that the pre-collision distribution function g_i can be divided into an equilibrium part and an off-equilibrium part following:

$$g_i = g_i^{eq} + g_i^{(1)}. \tag{4.3.14}$$

In the absence of force terms, the expression of $g_i^{(1)}$ have been obtained by subtracting f_i^{eq} on both side of the standard change of variable Eq. (2.4.4) yielding to:

$$\underbrace{g_i - f_i^{eq}}_{g_i^{(1)} = g_i - g_i^{eq}} = \frac{\check{\tau}}{\tau} \underbrace{(f_i - f_i^{eq})}_{f_i^{(1)}}, \tag{4.3.15}$$

and making the link between continuous and discrete off-equilibrium raw-moments as discussed in Sec. 2.4.2. Thus, it can be seen that $g_i^{(1)} = g_i - f_i^{eq}$ and by definition of Eq. (4.3.14) it follows $g_i^{eq} = f_i^{eq}$, which correspond to the standard relations encountered in the regularized framework [29, 37].

Now the point is to find the expression of $g_i^{(1)}$ in the corrected framework i.e. when ψ_i is considered in the LBM equation. In that perspective, the very same reasoning as before can be employed. By subtracting f_i^{eq} on both side of the change of variable Eq. (4.3.3) one get:

$$g_i - f_i^{eq} = f_i - f_i^{eq} + \frac{\Delta t}{2\tau}(f_i - f_i^{eq}) - \frac{\Delta t}{2}\psi_i. \tag{4.3.16}$$

Re-arranging this expression, it yields:

$$\underbrace{g_i - f_i^{eq} + \frac{\Delta t}{2}\psi_i}_{g_i^{(1)} = g_i - g_i^{eq}} = \underbrace{\left(1 + \frac{\Delta t}{2\tau}\right)}_{\check{\tau}/\tau} \underbrace{(f_i - f_i^{eq})}_{f_i^{(1)}}, \tag{4.3.17}$$

and makes the link between continuous and discrete off-equilibrium raw-moments in the present corrected framework. From this equation and in the light of Eq. (4.3.14), it finally follows [180]:

$$g_i^{(1)} = g_i - f_i^{eq} + \frac{\Delta t}{2}\psi_i, \tag{4.3.18a}$$

$$g_i^{eq} = f_i^{eq} - \frac{\Delta t}{2}\psi_i. \tag{4.3.18b}$$

These two expressions will be used in the following to obtains the corrected regularized LBM equation.

4.3.3.b From the corrected LBM-BGK to the corrected regularized LBM equation

Here, the corrected LBM-BGK Eq. (4.3.6) must be transformed to take advantage of the regularized formalism defined by Eq. (4.3.14). Starting with the corrected LBM-BGK Eq. (4.3.6):

$$g_i^+ = g_i - \frac{\Delta t}{\check{\tau}}\left(g_i - f_i^{eq}\right) + \frac{2\check{\tau} - \Delta t}{2\check{\tau}}\Delta t\psi_i, \tag{4.3.19}$$

it can be re-arranged as:

$$g_i^+ = g_i + \frac{\Delta t}{2}\psi_i - \frac{\Delta t}{\check{\tau}}\left(g_i - \left(f_i^{eq} - \frac{\Delta t}{2}\psi_i\right)\right) + \frac{\Delta t}{2}\psi_i, \tag{4.3.20}$$

and using Eq.(4.3.18b) (i.e. $g_i^{eq} = f_i^{eq} - \frac{\Delta t}{2}\psi_i$), it follows:

$$g_i^+ = g_i + \frac{\Delta t}{2}\psi_i - \frac{\Delta t}{\check{\tau}}\left(g_i - g_i^{eq}\right) + \frac{\Delta t}{2}\psi_i. \tag{4.3.21}$$

Using now Eq. (4.3.14) (i.e. $g_i = g_i^{eq} + g_i^{(1)}$) one gets:

$$g_i^+ = g_i^{eq} + \frac{\Delta t}{2}\psi_i + \left(1 - \frac{\Delta t}{\check{\tau}}\right)g_i^{(1)} + \frac{\Delta t}{2}\psi_i, \tag{4.3.22}$$

and knowing from Eq. (4.3.18b) that $g_i^{eq} + \frac{\Delta t}{2}\psi_i = f_i^{eq}$ one finally obtains the corrected regularized LBM equation [180, 187]:

$$g_i^+ = f_i^{eq} + \left(1 - \frac{\Delta t}{\check{\tau}}\right)g_i^{(1)} + \frac{\Delta t}{2}\psi_i. \tag{4.3.23}$$

4.3.3.c Partial finite difference off-equilibrium reconstruction

Here the very essence of the HRR-operator is presented. Just before the collision step, the off-equilibrium part of the distribution functions is regularized according to:

$$g_i^{(1)} = w_i \sum_{n=2}^{N} \frac{1}{n!\left(c_s^{\star 2}\right)^n} \check{\boldsymbol{a}}^{1,(n)} : \boldsymbol{\mathcal{H}}_i^{(n)}, \tag{4.3.24}$$

and reconstructed following $g_i = g_i^{eq} + g_i^{(1)}$. It is reminded that the check notation stands for the moment of the LBM system after the change of variable. Moreover, one recalls that mass and momentum are collision invariants, so that the off-equilibrium reconstruction starts from the second-order moment, i.e. the viscous stress tensor.

As discussed in Sec. 2.5.2, the regularized operators differ in the way off-equilibrium moments $\check{\boldsymbol{a}}^{1,(n)}$ are reconstructed. In the HRR framework, this tensor is reconstructed as:

$$\check{a}^1_{\alpha,\beta} = \sigma \check{a}^{1,\mathrm{PR}}_{\alpha,\beta} + (1-\sigma)\,\check{a}^{1,\mathrm{FD}}_{\alpha,\beta}, \tag{4.3.25}$$

where $\sigma \in [0,1]$. Above, $\check{a}^{1,\mathrm{PR}}_{\alpha,\beta}$ is the standard second-order off-equilibrium moment obtained by projection [86]:

$$\check{a}^{1,\mathrm{PR}}_{\alpha,\beta} = \sum_{i=0}^{m-1} \mathcal{H}_{i,\alpha\beta}\left(g_i - f_i^{eq} + \frac{\Delta t}{2}\psi_i\right), \tag{4.3.26}$$

and $a^{1,\mathrm{FD}}_{\alpha,\beta}$ is reconstructed using second-order centered finite differences, discretizing the viscous stress tensor Eq. (4.3.12):

$$\check{a}^{1,\mathrm{FD}}_{\alpha\beta} = -\frac{\check{\tau}}{\tau}\mu\left(\frac{\partial^{\mathrm{FD}}u_\alpha}{\partial x_\beta} + \frac{\partial^{\mathrm{FD}}u_\beta}{\partial x_\alpha} - \frac{2}{D}\frac{\partial^{\mathrm{FD}}u_\gamma}{\partial x_\gamma}\delta_{\alpha\beta}\right), \tag{4.3.27}$$

with,

$$\frac{\partial^{\mathrm{FD}}\Gamma}{\partial x_\alpha} = \frac{\Gamma_{\boldsymbol{x}+\boldsymbol{e}_\alpha\Delta x} - \Gamma_{\boldsymbol{x}-\boldsymbol{e}_\alpha\Delta x}}{2\Delta x}, \tag{4.3.28}$$

being a second-order centered scheme applied on Γ at $\boldsymbol{x}$ along the unit vector $\boldsymbol{e}_\alpha$. The coefficient $\check{\tau}/\tau$ appears naturally due to the change of variable impacting the non-conserved moments as discussed in Sec. 2.4.2. Once the second-order off-equilibrium moment is determined using the previous procedure, one can retrieved the higher off-equilibrium moment using the recurrence formula of [87]. This is done up to the fourth order, and only for the moments supported by the lattice which read for the D2Q9:

$$\check{a}^1_{xxy} \simeq u_y\check{a}^1_{xx} + 2u_x\check{a}^1_{xy}, \tag{4.3.29}$$

$$\check{a}^1_{yyx} \simeq u_x\check{a}^1_{yy} + 2u_y\check{a}^1_{xy}, \tag{4.3.30}$$

$$\begin{aligned}\check{a}^1_{xxyy} \simeq{}& 2\left(u_x\check{a}^1_{yyx} + u_y\check{a}^1_{xxy}\right) + \left[c_s^{*2}(\theta-1) - u_x^2\right]\check{a}^1_{yy}\\ &+ \left[c_s^{*2}(\theta-1) - u_y^2\right]\check{a}^1_{xx} - 4u_xu_y\check{a}^1_{xy}.\end{aligned} \tag{4.3.31}$$

It will be shown that this collision operator is the key element to obtain a stable perfect gas coupling. Indeed, the finite difference reconstruction of $\check{a}^1_{\alpha,\beta}$, and controlled via the parameter σ, has a stabilizing effect on the model. When $\sigma = 0$, the tensor $\check{a}^1_{\alpha,\beta}$ is entirely reconstructed by finite difference, whereas $\sigma = 1$ corresponds to the classical third-order recursive regularized collision operator [37, 87].

4.3.4 Entropy equation discretization

Here, the discretization in time and space of the hybrid energy part is presented. The entropy equation:

$$\frac{\partial s}{\partial t} + u_\alpha\frac{\partial s}{\partial x_\alpha} = -\frac{1}{\rho\theta}\frac{\partial}{\partial x_\alpha}\left(-\lambda\frac{\partial\theta}{\partial x_\alpha}\right) + \frac{\Phi}{\rho\theta}, \tag{4.3.32}$$

is composed of an advection part on the LHS, and a diffusion and production terms on the RHS. These RHS terms correspond respectively to the Fourier diffusion and to the viscous heat production. A first-order backward Euler scheme (RK1) is used for the time discretization, while similarly to [187], the convective flux is computed using a MUSCL scheme with a van Albada flux limiter. For the present non-conservative formulation, it reads along the x direction:

$$u_x\frac{\partial s}{\partial x} = u_{x,i}\frac{s_{i+1/2} - s_{i-1/2}}{\Delta x}, \tag{4.3.33}$$

where i represents the index of grid rather than lattice discrete velocity indice. Here, $s_{i\pm1/2}$ are the intercell values and where $s_{i+1/2}$, for instance, reads:

$$s_{i+1/2} = \begin{cases} s^L_{i+1/2}, & \text{if} \quad u_{x,i} > 0 \\ s^R_{i+1/2}, & \text{if} \quad u_{x,i} < 0 \end{cases} . \tag{4.3.34}$$

The left and right values at the cell interface are given as:

$$s^L_{i+1/2} = s_i + \frac{\varphi(r_i)}{4}\left[(1-\chi)\,\delta s_{i-1/2} + (1+\chi)\,\delta s_{i+1/2}\right], \tag{4.3.35a}$$

$$s^R_{i+1/2} = s_{i+1} - \frac{\varphi(r_{i+1})}{4}\left[(1-\chi)\,\delta s_{i+3/2} + (1+\chi)\,\delta s_{i+1/2}\right], \tag{4.3.35b}$$

with $\chi = 1/3$, $\varphi(r_i) = 2r_i/(1-r_i^2)$ the van Albada limiter function and,

$$\delta s_{i+1/2} = (s_{i+1} - s_i) \quad \text{and} \quad \delta s_{i-1/2} = (s_i - s_{i-1}), \tag{4.3.36a}$$

$$\delta s_{i+3/2} = (s_{i+2} - s_{i+1}) \quad \text{and} \quad \delta s_{i-3/2} = (s_{i-1} - s_{i-2}), \tag{4.3.36b}$$

$$r_i = \frac{s_i - s_{i-1}}{s_{i+1} - s_i}. \tag{4.3.36c}$$

To discretize the Fourier term, a standard second-order centered finite difference scheme is employed. However in the present model, the viscous heat production term Φ, is partially computed using second-order centered finite differences and using $\check{a}^1_{\alpha\beta}$ computed by the LBM part Eq. (4.3.25). This term reads:

$$\begin{aligned} \Phi &= \mu\left(\frac{\partial u_\alpha}{\partial x_\beta} + \frac{\partial u_\beta}{\partial x_\alpha} - \frac{2}{D}\frac{\partial u_\gamma}{\partial x_\gamma}\delta_{\alpha\beta}\right)\frac{\partial u_\alpha}{\partial x_\beta} \\ &= -\frac{\tau}{\check{\tau}}\underbrace{\check{a}^1_{\alpha\beta}}_{\text{LBM}}\underbrace{\frac{\partial u_\alpha}{\partial x_\beta}}_{\text{FD}}. \end{aligned} \tag{4.3.37}$$

In addition to improving the consistency between the LBM and the energy system, this strategy allows for the reduction of the number of operations to compute this tedious term. Indeed, in the regularised framework, only the $\check{a}^1_{\alpha\beta}$ tensor needs to be stored in memory since the distribution functions g_i are entirely reconstructed before the collision step. Thus, since this tensor is available, it can be used without any additional cost to model Φ by a multiplication with the velocity gradient, modeled with a standard second order finite difference scheme. Moreover, if the $\check{a}^1_{\alpha\beta}$ tensor was not traceless thanks to the $E_{2,\alpha\beta}$ term in Eq. (4.3.10), it is worth noting that a spurious heat production would bias any thermal solutions. Finally, this discretization has been successfully tested on smooth flow (see Sec. 4.4.4), however due to the centered nature of the velocity gradient, in case of discontinuities it is preferable to model it using only finite difference scheme. Finally, the standard explicit Euler scheme is used for the time marching procedure.

4.3.5 CFL number and HLBM algorithm

In most of the cases, the operating point of an explicit numerical scheme is characterized by the Courant-Friedrichs-Lewy (CFL) number. Once the CFL restriction is known, this permits the choice of the appropriate time step value in function of the local mesh size and the maximum expected fluid velocity. The CFL number in the compressible Navier-Stokes framework is expressed as the ratio of the maximal physical information speed, i.e. $c\,(\mathrm{Ma}+1)$, over the numerical speed $\Delta x/\Delta t$. In the standard case, the athermal LBM speed of sound is imposed by the acoustic scaling $c_s\Delta x/\Delta t = \sqrt{r_g T_r}$, fixing the choice of the time step to recover the desired acoustic speed at $c = \sqrt{r_g T_r}$ (which reads $c^* = c_s^*$ for its dimensionless counterpart). However in the present case, this HLBM model is now function of the fluid temperature and independent of the reference temperature T_r. Then the time step can be freely chosen depending on the value of T_r, without any impact on the desired acoustic speed. Replacing the time step by its expression, this results in:

$$\mathrm{CFL} = (\mathrm{Ma}+1)\sqrt{\gamma_g c_s^{*2}\theta}. \tag{4.3.38}$$

As the Mach number and the heat capacity ratio belong to the physics of the problem, the CFL number is adjusted only using the numerical parameter T_r enabling to reduce or increase the time step, to tailor stability and/or convergence. However, one has to keep in mind that the present HLBM scheme is explicit, with a RK1 temporal integration for the energy part, and thus must obey the upper bound restriction of $\mathrm{CFL} < 1$. Thus, at first attempt, the speed convergence through T_r is constrained by the relation:

$$\theta_{max} < \frac{1}{\gamma_g\,(\mathrm{Ma}+1)^2\,c_s^{*2}}. \tag{4.3.39}$$

The question of the stability of the present HLBM according to parameters such as the CFL number will be addressed later in Chap. 6.

Finally, the present HLBM algorithm reads chronologically:

Algorithm 1 HLBM

Input:

1 : $\left[\,\rho,\, u_\alpha,\, \theta\,\right]^{(0)}$

Initialization:

2 : Compute $f_i^{eq,(0)}$ from $\left[\,\rho,\, u_\alpha,\, \theta\,\right]^{(0)}$; Eq. (4.2.7)

3 : Compute $\check{a}_{\alpha\beta}^{1,(0)} = \check{a}_{\alpha\beta}^{1,FD}$ from $\left[\,\rho,\, u_\alpha,\, \theta\,\right]^{(0)}$; Eq. (4.3.27)

4 : Compute $\psi_i^{(0)}$ from $\left[\,\rho,\, u_\alpha,\, \theta\,\right]^{(0)}$; Eq. (4.3.11)

for $n = 1 \rightarrow N$ **do:**

5 : Compute g_i^+ from $\left[\, f_i^{eq},\, \check{a}_{\alpha\beta}^{1},\, \psi_i \,\right]^{(n)}$; Eq. (4.3.23)

6 : Compute $\left[\,\rho,\, u_\alpha\,\right]^{(n+1)}$ from g_i^+ ; Eq. (4.3.7) and Eq. (4.3.8)

7 : Compute $s^{(n+1)}$ from $\left[\,\rho,\, u_\alpha,\, \theta,\, \check{a}_{\alpha\beta}^{1}\,\right]^{(n)}$; Eq. (4.3.32)

8 : Compute $\theta^{(n+1)}$ from $\left[\,s,\, \rho\,\right]^{(n+1)}$; Eq. (4.2.6)

9 : Compute $\psi_i^{(n+1)}$ from $\left[\,\rho,\, u_\alpha,\, \theta\,\right]^{(n+1)}$; Eq. (4.3.11)

10 : Compute $f_i^{eq,(n+1)}$ from $\left[\,\rho,\, u_\alpha,\, \theta\,\right]^{(n+1)}$; Eq. (4.2.7)

11 : Compute $\check{a}_{\alpha\beta}^{1,(n+1)}$ from g_i^+ and $\left[\, f_i^{eq},\, \psi_i,\, \rho,\, u_\alpha,\, \theta\,\right]^{(n+1)}$; Eq. (4.3.25)

where n and N stand respectively for the nth and final time step. It is worth noting that, the present scheme permits the natural initialization of the off-equilibrium part of g_i as discussed in Sec. 2.6.1, which might be of importance for initialisation-sensitive flows [2, 33] adversely affected by an equilibrium state initialization. Moreover, this algorithm slightly differs from the one of [187], in a sense that it does not take into account the two-step temporal integration for the energy equation. Tests have been done with and without this integration, and no substantial improvements in terms of stability or accuracy have been noticed with this two steps procedure.

Finally, from algorithm 1 one can note the blatant advantage in terms of memory of the regularized formalism. Indeed, the distribution functions g_i do not need to be stored from a time step to an other since they are reconstructed with their equilibrium and off-equilibrium moments. The equilibrium moments being essentially constructed from the macroscopic variables, only the off-equilibrium moments have to be stored in memory.

4.4 Numerical validations of the improved HLBM

In this section, the proposed improvements brought to the HLBM scheme are assessed in different configurations and compared to the original model of Feng et al. [187]. The improvements consist of: (1) a new discretization of the lattice closure correction term,

(2) a corrected viscous stress tensor that takes into account polyatomic gases, and (3) a novel discretization of the viscous heat production term fitting with the regularized formalism. The aim is to verify that, thanks to the improvements, all the physical phenomena related to the Navier-Stokes Fourier equations are correctly retrieved, both in the subsonic regime (and without regression compared to the original model), as well as in the supersonic regime. The simulations show the restriction of the original model to subsonic cases, while the new enhancements of the present model make it possible to overcome this limitation and extend the range of application of the HLBM to supersonic cases.

4.4.1 Viscosity computation

Here the kinematic viscosity ν will be computed from the response of the numerical system to a shear wave initialization. The domain is periodic and the initialization reads:

$$p = p_\infty,\ u_x = a_0 \sin\left(2\pi y / L_y\right),\ u_y = u_\infty,\ T = T_\infty,$$

where $T_\infty = 300\,\mathrm{K}$, $p_\infty = 101325\,\mathrm{Pa}$ and the amplitude of the perturbation has been arbitrary taken to $a_0 = 20\,\mathrm{m.s^{-1}}$. The domain length is $L_y = 1\,\mathrm{m}$ and the velocity propagation of the perturbation is $u_\infty = \mathrm{Ma}\, c_\infty$, with $c_\infty = \sqrt{\gamma_g r T_\infty}$ the speed of sound and $\gamma_g = 1.4$ in the present case. Similarly to [194] the setup is quasi one dimensional, 200 points per wavelength were considered, and the wave has one period along the y direction. The temporal decay of this wave is directly linked to the kinematic viscosity and the analytical solution for the velocity reads [77, 195]:

$$max\left(u_x\right) = a_0 \exp\left(-\nu \left(\frac{2\pi}{L_y}\right)^2 t\right). \tag{4.4.1}$$

Thus tracking the maximum of u_x along time and fitting the curve using a least square method yields the experimental value of the viscosity ν.

Fig. 4.1 shows a good match of the present model (symbols) with the theory Eq. (4.4.1) (solid lines), for different viscosities at a supersonic advection regime of Ma = 1.5. More results in terms of Mach number and viscosity can be found in Table 4.1, where the present model is compared to the original model [187] in terms of relative error. From this table, it worth noting that the present HLBM model ensures the retrieval of the correct kinematic viscosity from low to high Mach numbers. For the low Mach number case, similar results have been found compared to the original model. However, this last turns out to be unstable for Mach numbers greater or equal to unity restricting its application range to subsonic cases only. The results clearly show the enhancement of this scheme in terms of robustness without regressions in terms of accuracy, extending the validity of the model for this case, to supersonic regime.

4.4.2 Supersonic isentropic vortex

The convected isentropic vortex is an Euler benchmark that can be used to assess numerical schemes in term of dispersion, dissipation and robustness. Although the ini-

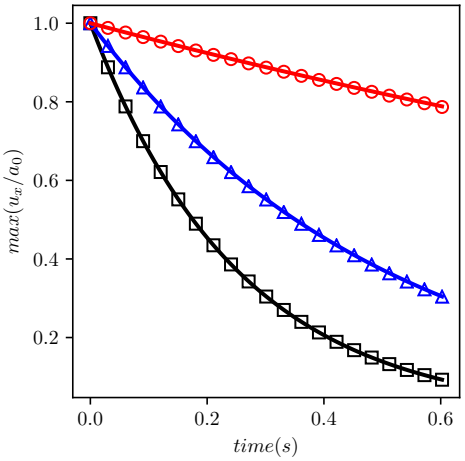

Figure 4.1 – Velocity decay of a shear wave along the time for different viscosities at Ma = 1.5. The analytical solution is plotted in solid line and the symbols correspond to the present HLBM model for $\nu = 0.01\,\mathrm{m^2.s^{-1}}$ ○ ; $\nu = 0.05\,\mathrm{m^2.s^{-1}}$ △ ; and $\nu = 0.1\,\mathrm{m^2.s^{-1}}$ □ . The numerical parameters were $\sigma = 0$ and $T_r = 800\,\mathrm{K}$.

	$\nu = 0.1\,\mathrm{m^2.s^{-1}}$		$\nu = 0.05\,\mathrm{m^2.s^{-1}}$	
Ma	$\epsilon\,(\mathrm{P})$ %	$\epsilon\,(\mathrm{O})$ %	$\epsilon\,(\mathrm{P})$ %	$\epsilon\,(\mathrm{O})$ %
0.5	$4.72.10^{-4}$	$4.72.10^{-4}$	$1.24.10^{-3}$	$1.24.10^{-3}$
1.0	$6.84.10^{-4}$	∅	$1.67.10^{-3}$	∅
1.5	$7.12.10^{-4}$	∅	$1.63.10^{-3}$	∅

Table 4.1 – Relative error on the viscosity associated to the original model [187] noted O, and the present model noted P. The symbol ∅ means that the computation diverged. For the shear wave the numerical parameters were $\sigma = 0$ and $T_r = 800\,\mathrm{K}$.

tialization of this vortex is based on the Euler equations, it has been intensively used to bench different LBM schemes solving the Navier-Stokes equation [194, 196]. Despite the lack of thermal and viscous diffusive effects in the solution, this case can still provide useful informations on the dispersion and stability properties thanks to its analytical solution. This exact solution is simply the advection of the initial condition over the time. The initialization can be seen as a small perturbation of the mean flow $\rho_\infty, T_\infty, u_\infty$ which reads:

$$u_r(r) = 0 \text{ and } u_\theta(r) = c_\infty \mathrm{Ma_v} r \exp\left[(1 - r^2)/2\right], \tag{4.4.2}$$

where u_r and u_θ are respectively the radial and tangential velocity in polar coordinates. Ma_v is the vortex Mach number and $r = \sqrt{(x - x_c)^2 + (y - y_c)^2}/R$ with R the vortex radius. This vortex is considered isentropic, i.e. $p/\rho^{\gamma_g} = cst$, leading naturally to the

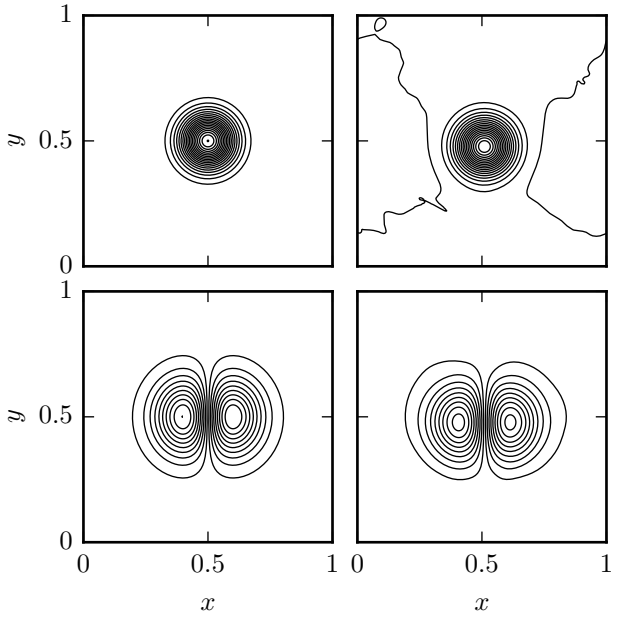

Figure 4.2 – Convected isentropic vortex at $\mathrm{Ma}_\infty = 1.3$ before (left) and after (right) 50 convective times. Iso-contour of density (top) and y component of the velocity (bottom) show excellent results in terms of isotropy.

following density field:

$$\rho(r) = \rho_\infty \left[1 - \frac{\gamma_g - 1}{2}\mathrm{Ma}_v^2 r \exp\left(1 - r^2\right)\right]^{\frac{1}{\gamma_g - 1}}, \tag{4.4.3}$$

and pressure fields:

$$p(r) = p_\infty \left(\frac{\rho(r)}{\rho_\infty}\right)^{\gamma_g}. \tag{4.4.4}$$

In this case, the value of the vortex velocity was chosen as $\mathrm{Ma}_v = \beta * \mathrm{Ma}_\infty$, with $\beta = 0.1$ representing the vortex intensity. Ma_∞ denotes the freestream Mach number. A $[200 \times 200]$ mesh was considered in a one-meter periodic box, and twenty points were taken in the vortex radius. The dynamic viscosity is taken as the same order as the air value $\mu = 1.10^{-5}\,\mathrm{kg.m^{-1}.s^{-1}}$, and the reference pressure and temperature are taken to $p_\infty = 101325\,\mathrm{Pa}$ and $T_\infty = 300\,\mathrm{K}$ respectively. The advection velocity range is taken from $\mathrm{Ma}_\infty = 0.3$ to $\mathrm{Ma}_\infty = 1.3$ which corresponds to typical Mach number regimes encountered in aeronautical flows i.e. approach (Ma = 0.3), cruise (Ma = 0.8) and local max velocity nozzle (Ma = 1.3). A unique $T_r = 1478.75\,\mathrm{K}$ (defining the time step) was chosen over all Mach numbers. This T_r value was calibrated on the stability of the higher Mach case, namely $\mathrm{Ma}_\infty = 1.3$, and corresponds in the present case to CFL $\simeq 0.7$.

The velocity and density contours in Fig. 4.2, show the respect of the isotropy of the fields by the present scheme. These results have been obtained for the highest Mach number case $\mathrm{Ma}_\infty = 1.3$ with $\sigma = 0$. More quantitatively, from Fig. 4.3, one can see on different profiles, the overall agreement of the solution (symbols) with the analytic (solid

lines), for three different Mach numbers, ranging from subsonic to supersonic regime. On these graphs, one can remark that the vortex is more dissipated for $\mathrm{Ma}_\infty = 1.3$ than the two lower Mach number cases. This is due to the similar time step employed for all the cases, which results in a variable CFL number, greater for the $\mathrm{Ma}_\infty = 1.3$ case. This behavior is common to several numerical methods, where an optimal trade off between accuracy, stability and speed convergence has to be found in terms of CFL number. Fig.4.4 shows a sensitivity analysis on the L^2 relative error depending on the σ parameter. For different Mach number regimes, one can observe that the accuracy and stability of the solution depends on the parameter σ similarly to the original model [187]. The higher the Mach number is, the smaller the σ parameter has to be, decreasing the accuracy of the solution for the benefit of stability. Thus, the more robust choice of parameters is $\sigma = 0$ independent of the Mach number, allowing for the model to be valid from subsonic to supersonic regime. This value will be chosen in the following to compare the present enhanced model against the original model [187].

Fig. 4.5 shows the L^2 relative error of the two models after 50 convective times of vortex. Different Mach numbers are considered from subsonic to supersonic regime. For all the advection cases, the present model shows to be more accurate than the original one which, turns out to be unstable for Mach numbers higher or equal to one. For the specific case of $\mathrm{Ma} = 1$, Fig. 4.6 shows the iso contours of density and velocity for the two models, just before the computation diverge for the original model. In contrary to the present model, it can be observe that, the original one, produces instabilities located in the supersonic region and not in the subsonic one. This clearly confirms observations made from Fig 4.5, where no stable computations using the original model has been found for supersonic cases, restricting its application range to subsonic regimes.

Throughout the study of this test case, it has been shown that the present HLBM model permits to increase the stability domain of the original one in terms of Mach number, allowing now the computation of supersonic flows.

4.4.3 Acoustic damping

The effect of the correction term $E_{2,\alpha\beta}$ in Eq. (4.3.10) of the present model, is assessed studying the decay of a well resolved sinusoidal acoustic wave. A quasi one dimensional periodic domain of $L_x = 1.10^{-1}\,\mathrm{m}$, discretized on $[200 \times 2]$ points is considered. The acoustic pressure profile reads:

$$\widetilde{p}(x) = \Delta p \sin\left(\frac{2\pi}{L_x} x\right), \tag{4.4.5}$$

with $\Delta p = 5\,\mathrm{Pa}$ being the amplitude of the perturbation. The present acoustic is considered isentropic, thus from the Laplace laws, the temperature field is found to be:

$$\widetilde{T}(r) = \left(\frac{\widetilde{p}(r)}{p_\infty}\right)^{\frac{\gamma_g - 1}{\gamma_g}} T_\infty, \tag{4.4.6}$$

and the velocity field is given by:

$$\widetilde{u_x} = \frac{\widetilde{p}}{\rho c_\infty}. \tag{4.4.7}$$

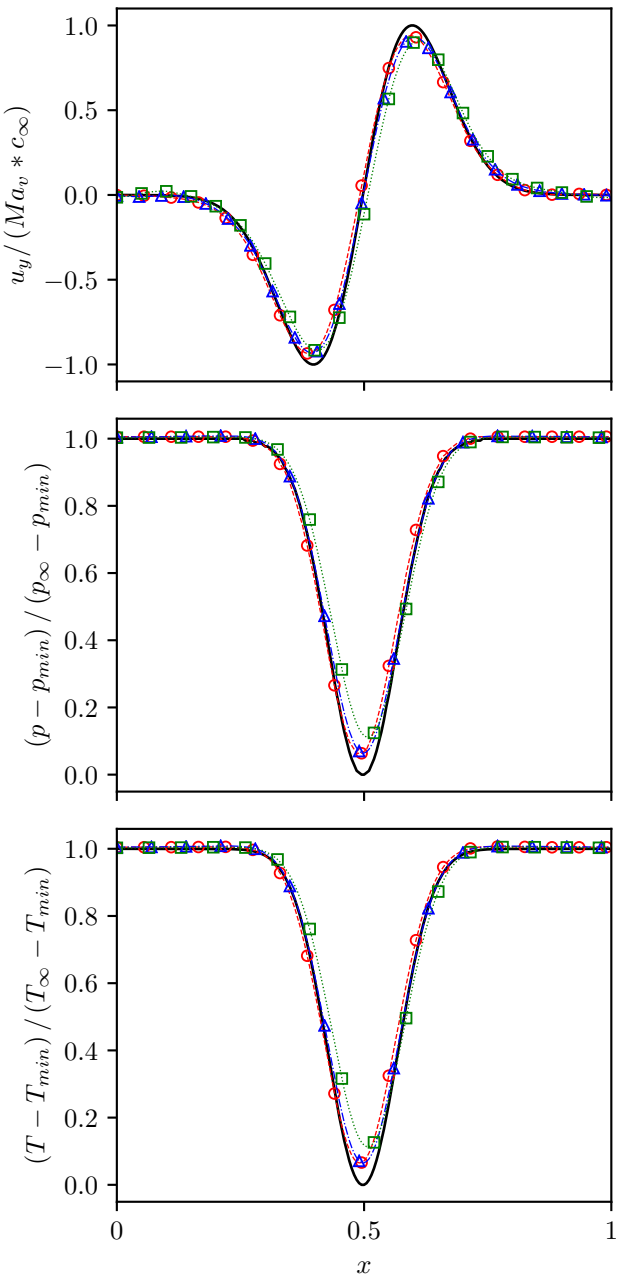

Figure 4.3 – Convected isentropic vortex for different Mach numbers after 50 convective times at $\sigma = 0$. The *min* subscript corresponds to the minimal value at the initialization. —corresponds to analytic; ·○· corresponds to $\mathrm{Ma}_\infty = 0.3$; ·△· to $\mathrm{Ma}_\infty = 0.8$ and ·□· to $\mathrm{Ma}_\infty = 1.3$.

Finally the initial field reads:

$$p = p_\infty + \widetilde{p}\ ;\ T = T_\infty + \widetilde{T}\ ;\ u_x = \widetilde{u_x}, \tag{4.4.8}$$

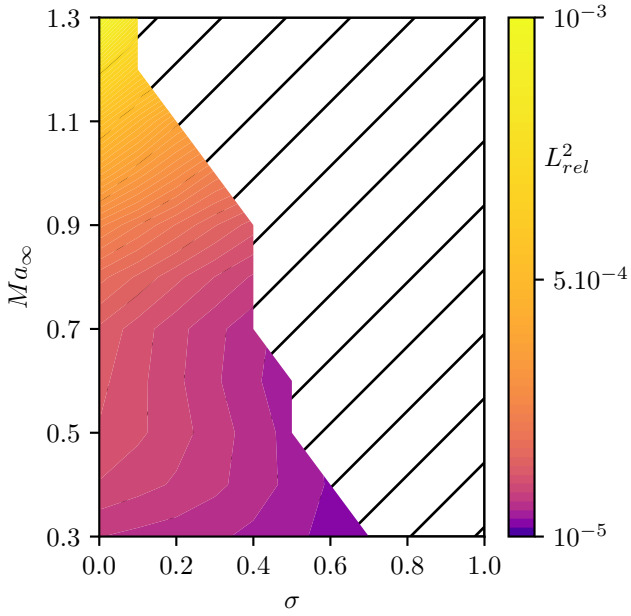

Figure 4.4 – Color map of the L^2 relative error on pressure after 50 convective times as a function of the Mach number and σ parameter. Simulations have been performed in intervals of 0.1 for both σ and Ma, representing in total hundred simulations. The dashed region refers to where the computation diverged or the total energy maximum was greater at the end of the computation.

where $p_\infty = 101325\,\text{Pa}$, $T_\infty = 300\,\text{K}$. In this case, $T_r = 1478.75\,\text{K}$, $\sigma = 0.95$, a Prandtl number of $\text{Pr} = 0.71$ is considered and the dynamic viscosity is taken as $\mu = 0.01\,\text{kg.m}^{-1}.\text{s}^{-1}$. The expected pressure decay rate reads [40]:

$$\max(p) = p_\infty + \Delta p \exp\left(-\alpha\left(\frac{2\pi}{L_x}\right)^2 t\right), \tag{4.4.9}$$

with

$$\alpha = \frac{D-1}{D}\nu + \frac{\gamma_g - 1}{2}\frac{\nu}{\text{Pr}}, \tag{4.4.10}$$

the acoustic decay rate for a fluid with zero bulk viscosity. This decay rate is computed from the simulation using the similar process described in Sec. 4.4.1. If the error is not corrected for a freely chosen value of γ_g, i.e. $\gamma_g = 1.4$ in the present case, a spurious bulk viscosity appears, increasing the acoustic decay rate. The results presented on Fig.4.7, clearly show that the correct acoustic decay rate is retrieved by the present model (square symbols), compared to the analytic (solid lines), and this for monatomic and polyatomic values of the heat capacity ratio. However, the original model [187] (circles symbols) over dissipate the acoustic wave in the polyatomic case, due to a spurious bulk viscosity. For a monatomic value $\gamma_g = \gamma_{lb}$, no error is found for both original and present models, which confirms the statement in Sec.4.3.2.

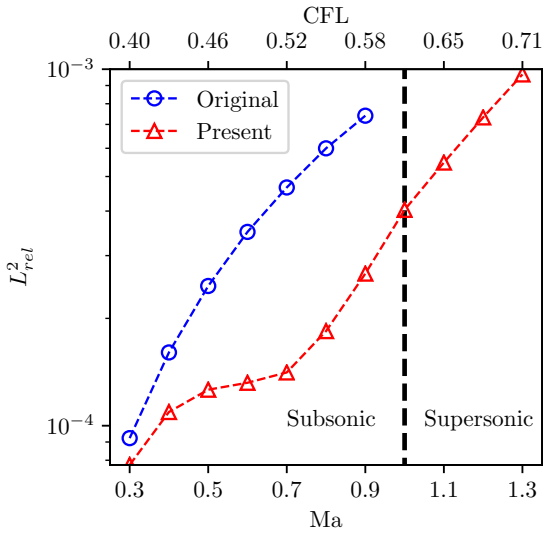

Figure 4.5 – L^2 relative error on pressure after 50 convective times in function of the Mach number (and equivalent CFL number). Each symbol correspond to a simulation. The lack of points means that the computation diverged or the total energy maximum was greater at the end of the computation. The original model [187] appears to be restricted to subsonic flows whereas the present one allows supersonic regimes.

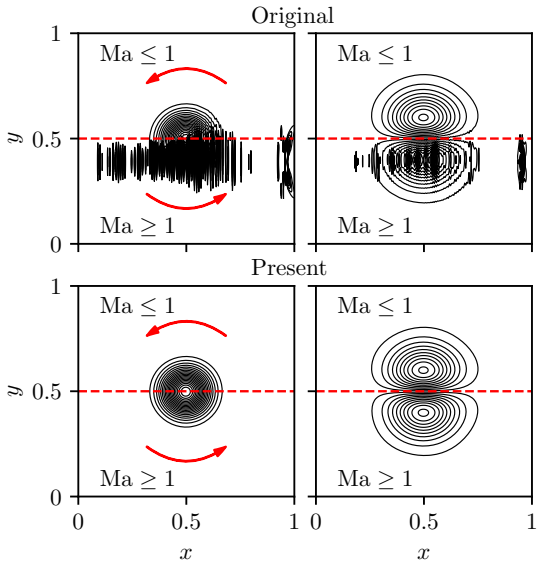

Figure 4.6 – Convected isentropic vortex after 3 convective times at $\mathrm{Ma}_\infty = 1$ and where the two, subsonic and supersonic, regions are distinguished by the dashed line. Iso-contour of density (left) and x component of the velocity (right) are displayed. Arrows indicate the sens of rotation of the vortex. The original model [187] model (top), shows instabilities in the supersonic region while the present model (bottom), is stable and present excellent results in terms of isotropy

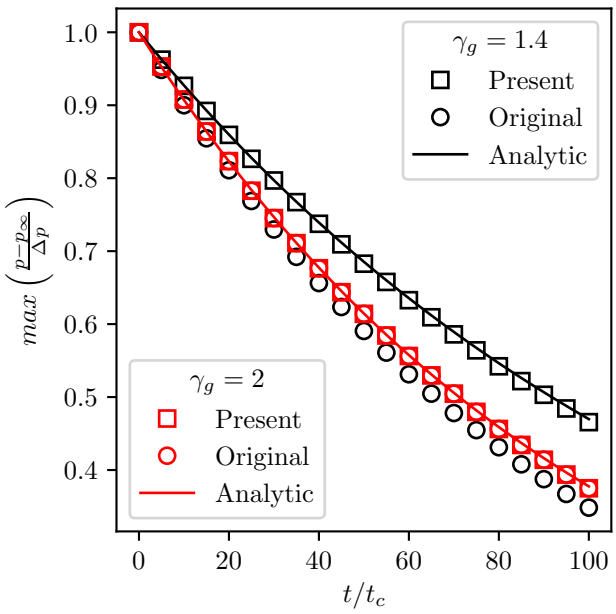

Figure 4.7 – Acoustic wave decay over dimensionless time t/t_c with $t_c = L_x/\sqrt{\gamma_g r T_\infty}$. As expected, a correct acoustic dissipation for monatomic value of the heat capacity ratio is retrieved for both models. For the polyatomic case, the original model [187] deviates from the analytic while the correct dissipation is retrieved by the present one.

4.4.4 Thermal Couette flow

Here the viscous heat production and dissipation of the scheme is assessed using the thermal Couette flow test case. It consists of two parallel plates, one stationary, and one translating along the x direction at constant velocity $U = Ma * c_\infty$. This motion generates a shear flow with a linear velocity profile, which produces a temperature increase by viscous friction. The steady state is reached once the heat dissipation balance the heat production. The analytical solution for the temperature profile between the plates exists in two variants consisting by, either keeping the plates at different temperature $\Delta T \neq 0$, or at the same temperature $\Delta T = 0$. In the first case, the analytical solution only depends on the Eckert and the Prandtl numbers while in the second case it depends on the heat capacity ratio, the Mach and Prandtl numbers. This last analytical solution reads:

$$\frac{T - T_w}{T_w} = \frac{y}{H}\mathrm{PrMa}^2\frac{\gamma_g - 1}{2}\left(1 - \frac{y}{H}\right), \tag{4.4.11}$$

with T_w the temperature of the plate and H the distance between the two plates. A simulation domain of $[2 \times 100]$ points was considered and regularized boundary conditions described in [187] were adopted. $T_r = 1500\,\mathrm{K}$ and $\sigma = 0.9$ so that 90% of the viscous stress tensor is modeled by projection of the f_i and 10% by finite difference. The temperature of the plates is taken at $T_w = T_\infty = 300\,\mathrm{K}$ and the initial pressure of the fluid is $p_\infty = 101325\,\mathrm{Pa}$. Fig. 4.8 shows the temperature profiles obtained by the present model (symbols), for different Mach numbers, heat capacity ratios and Prandtl numbers, and

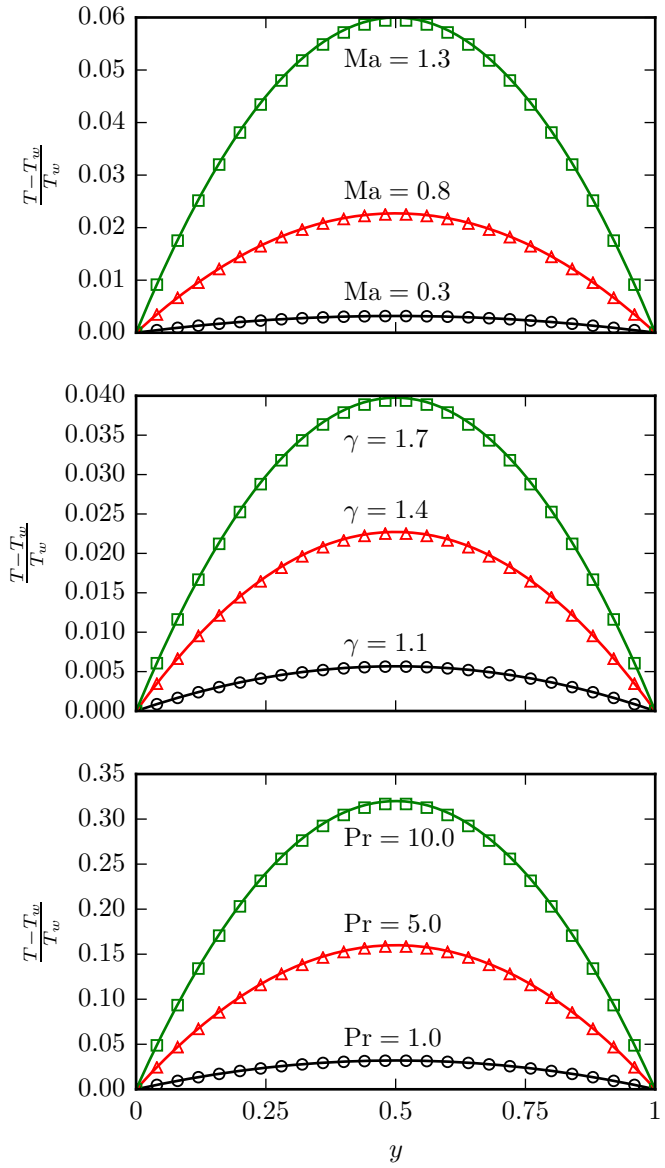

Figure 4.8 – Steady state temperature profile along the y direction of the thermal Couette flow, for different Mach numbers, Prandtl numbers and heat capacity ratios. Symbols correspond to HLBM and solid lines to the analytic. For all the plots, the missing variables are taken to Ma = 0.8, Pr = 0.71 and γ_g = 1.4.

are compared to the analytical solution (solid lines). For all the cases, the results are in good agreement with the analytical solution. Thus, the new discretization of viscous heat production terms Eq. (4.3.37), partially computed with the LBM part through $a^1_{\alpha\beta}$ and finite differences, shows to be a potential substitute to a full finite difference discretization. Finally, it is worth noting that for this test case, the major source of error is induced by the boundary conditions, and the correction term has no role to play in this configuration due to the nature of the flow (unidirectional and uniform).

4.5 Numerical validation and model capabilities

In the previous section, the limitation to subsonic flows of the original model [187] has been demonstrated throughout different test cases. The improvements of the present model permits to remove this limitation, and have been successfully validated on shear diffusion, vortical convection, acoustic decay, and viscous heat production and dissipation cases. These test cases have been done from subsonic to supersonic regimes, and comparisons with the original model [187], ensured no regressions for subsonic flows. Now the aim is to perform computations at high Mach number cases with discontinuities using the present HLBM scheme. However in a first time, and for the sake of completeness with regard to the previous test cases, the acoustic will be assessed in terms of propagation. Indeed, an isentropic speed of sound must be retrieved, which will finish to validate all the physical phenomena of interest related to the Navier-Stokes Fourier equations. In a second time, a shock tube test will be computed for a relatively low viscosity value, showing the robustness of the method to treat flows discontinuities. Eventually, a shock-vortex interaction case is performed, permitting the assessment of the present model in a configuration where all the physical phenomena previously validated are combined.

4.5.1 Acoustic cases

In order to assess the acoustic propagation, two test cases are considered. The first one is a Gaussian shaped acoustic pulse in a mean flow at two different Mach numbers, respectively $\mathrm{Ma} = 0$ and $\mathrm{Ma} = 1$. The small acoustic perturbation reads:

$$\widetilde{p}(r) = \Delta p \exp\left(-\frac{r^2}{2}\right), \tag{4.5.1}$$

with $\Delta p = 10\,\mathrm{Pa}$ of amplitude. The acoustic is considered isentropic, thus the temperature field can be found by the Laplace laws from Eq. (4.4.6). Finally the initial field reads:

$$p = p_\infty + \widetilde{p}\ ;\ T = T_\infty + \widetilde{T}\ ;\ u_x = \mathrm{Ma}\, c_\infty\ ;\ u_y = 0. \tag{4.5.2}$$

Six points have been taken in the pulse radius R, $T_\infty = 300\,\mathrm{K}$ and $p_\infty = 101323\,\mathrm{Pa}$. The numerical domain is a one meter square box discretized on $[201 \times 201]$ points. In the null Mach case, $\sigma = 0.95$ is considered and $\sigma = 0$ is employed in the sonic case. The reference temperature is taken to $T_r = 1478.75\,\mathrm{K}$ for both cases. The dynamic viscosity is set to $\mu = 1.10^{-5}\,\mathrm{kg.m^{-1}s^{-1}}$, the heat capacity ratio to $\gamma_g = 1.4$ and the Prandtl number to $\mathrm{Pr} = 0.71$. The $\mathrm{Ma} = 0$ pulse is initialized in the center of the numerical domain $[0.5; 0.5]$ while the $\mathrm{Ma} = 1$ pulse is placed at $[0.1; 0.5]$. For both cases, the simulation lasts $t = 0.4t_c$ with $t_c = L/c_\infty$ with L the domain length. For this particular choice of time and initial position, both solutions are expected to be equal. Fig. 4.9 shows good agreement with the analytical solution [197] for the subsonic and sonic cases. However, small dispersion and dissipation defects appear on the downstream acoustic part for $\mathrm{Ma} = 1$, meaning that the numerical error grows with respect to the CFL number. Nonetheless, this trend is in agreement with the observations in Sec. 4.4.2. The isocontours show correct isotropy of

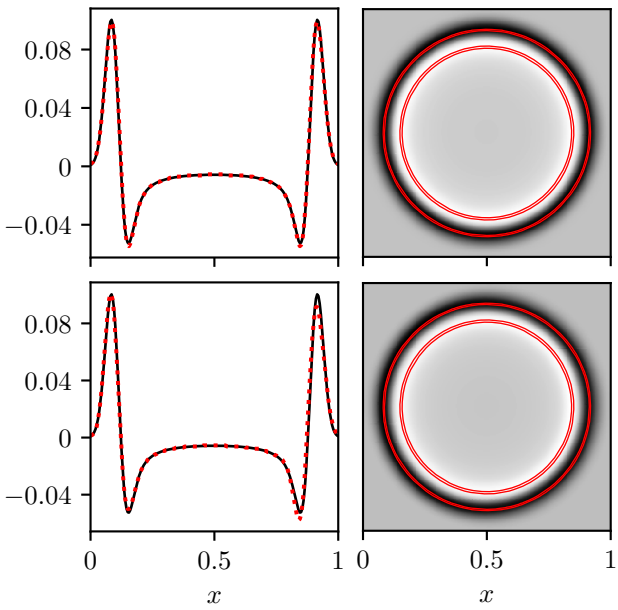

Figure 4.9 – Pressure profile for $y = 0.5$ (left) and pressure color map (right) of an acoustic pulse simulation for Ma = 0 (top) and Ma = 1 (bottom). On the left graphs, the analytical solution corresponds to the solid black line and the dotted red curve represents the observed response. On the right graphs, the two red contours correspond to the min and max value of the analytical solution.

the solution in both cases, meaning there is no flagrant directional bias in the acoustic propagation.

Next, the isentropic speed of sound is validated for different heat capacity ratios and fluid temperatures. To that end, the velocity of a well resolved Gaussian shaped acoustic wave, with 20 points in the radius R, is measured. The fluid is considered at rest and the pressure, temperature and velocity profiles are defined according to Eq. (4.5.1), Eq. (4.4.6) and Eq. (4.4.7) respectively. The speed measurement is done after 10 rounds of a one meter periodic domain discretized by $[200 \times 2]$ points. The time step remains the same as before and $\sigma = 0.95$ has been used. Fig. 4.10 shows good agreements between the computed velocity (symbols) and the theoretical value (solid lines). Thus it validates the perfect gas coupling Eq. (4.2.24) and the isentropic speed of sound Eq. (4.2.40) of this HLBM scheme.

4.5.2 Shock tube problem

Here the present model is assessed on a one-dimensional flow including discontinuity. The flow of the shock tube problem includes a shock wave, a slip line (contact surface) and an expansion wave permitting to assess a numerical scheme for these three physical phenomena. This test case is performed with $\gamma_g = 1.4$, $\mu = 1.10^{-5}\,\mathrm{kg.m^{-1}.s^{-1}}$, $\sigma = 0.4$ and

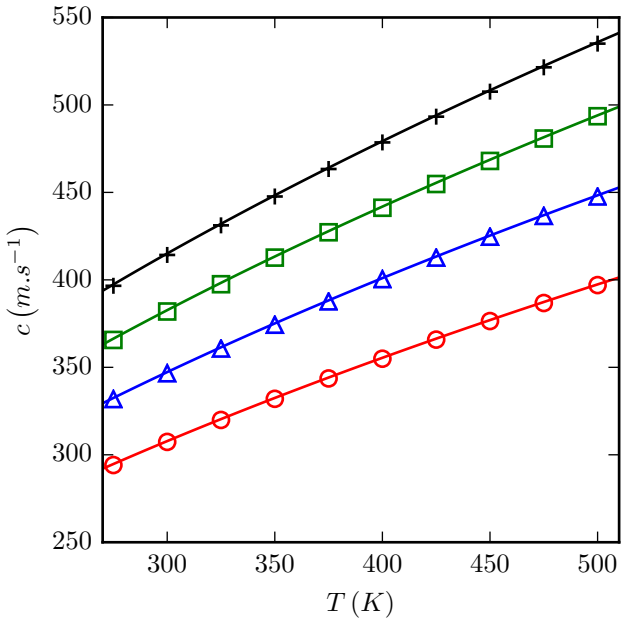

Figure 4.10 – Sound speed measurement for different fluid temperature and heat capacity ratio. Each symbols correspond to a simulation. Here ○ corresponds to $\gamma_g = 1.1$; △ to $\gamma_g = 1.4$; □ to $\gamma_g = 1.7$ and + to $\gamma_g = 2.0$. Solid lines corresponds to the theoretical values.

$T_r = 1460\,\mathrm{K}$. The initial conditions read:

$$(\rho, u, p) = \begin{cases} (3\rho_\infty, 0, 3p_\infty), & 0 \le x < 0.5 \\ (\rho_\infty, 0, p_\infty), & 0.5 \le x \le 1 \end{cases}, \tag{4.5.3}$$

where $T_\infty = 300\,\mathrm{K}$, $p_\infty = 101325\,\mathrm{Pa}$ and $\rho_\infty = p_\infty / (rT_\infty)$. We chose a quasi one dimensional domain of one meter with 401×2 points.

Fig. 4.11 shows on different profiles the overall agreement of the computed solutions (circle symbols) compared to the analytic (solid lines) and to a first order HLLC (Harten, Lax and van Leer plus Contact) Riemann solver [198] (triangle symbols) (described latter in Sec. 5.2.1). Nonetheless, a spurious oscillation at the bottom of the rarefaction wave is present which bias the solution. However, this defect can be easily handled since it disappears for a larger choice of viscosity. This viscosity can be added locally on the discontinuity with the help of a shock sensor in the manner of [37]. Moreover, the temperature profile is slightly underestimated between the shock and the contact discontinuity. Indeed, this is due to the non conservative nature of the energy equation, and it is well known that this form does not permit to capture efficiently the flow discontinuities within a numerical framework [198, 199]. To overcome this loss, Nie et al. in [150], used an artificial production term in the energy equation, benched on several shock tube cases, to balance this defect. But this leads to an additional free parameter dependencies of the model which is not the purpose in this work. Although this defect increases for higher

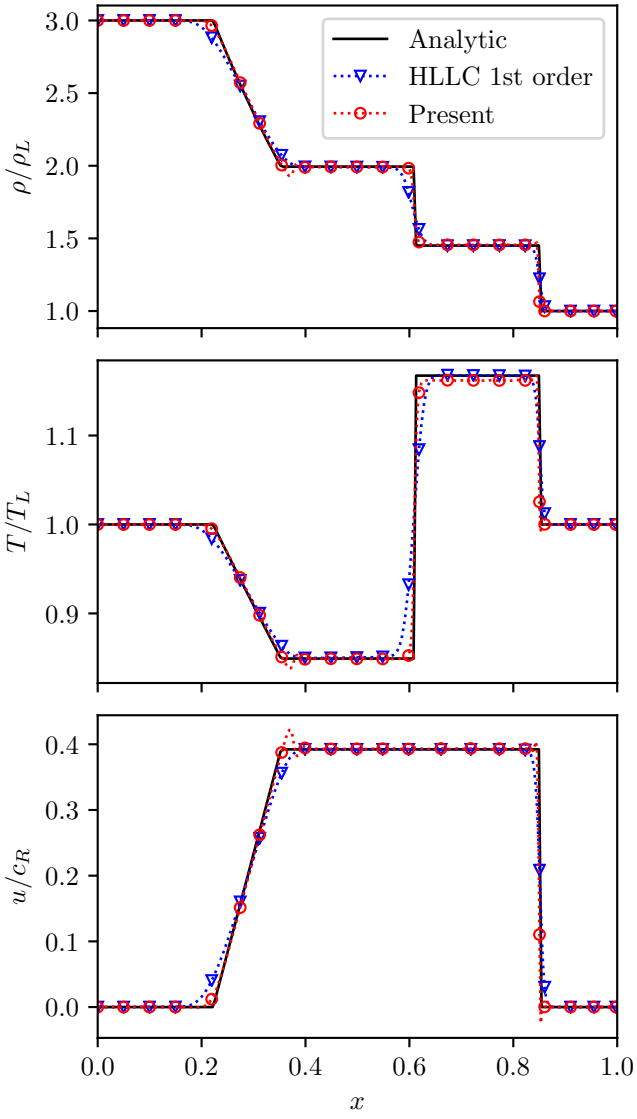

Figure 4.11 – Sod shock tube problem. The present model is compared to a first order HLLC Riemann solver [198] and to the analytical solutions.

ratios between the left and the right states, in the present case the model gives satisfying results, representative of a typical shock encountered in transonic aeronautical flows [150]. This conservativeness problem will be discussed in more details later in Chap. 5.

4.5.3 Shock vortex interaction

Here the present model is finally assessed for a two dimensional unsteady compressible viscous test case. It consists in the interaction between a vortex and a planar stationary shock wave, at advection Mach number of $\mathrm{Ma}_s = 1.2$. The results are compared with the direct numerical simulation (DNS) of [200]. A computational domain of $[-20R, +8R] \times$

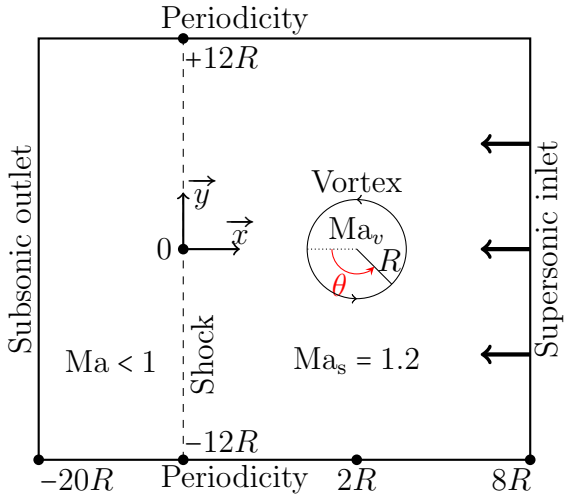

Figure 4.12 – Numerical setting for the shock vortex cases. For all the cases, the Mach number of the shock wave is taken at $\mathrm{Ma}_s = 1.2$. The vortex has an anticlockwise circulation and propagates from the right to the left of the domain.

$[-12R, +12R]$ on a 1681×1441 mesh is adopted, with R the vortex radius taken at $R = 1\,\mathrm{m}$. The planar shock wave is specified at $x = 0$ by imposing the density, velocity and pressure corresponding to the left and right states of the steady shock, using the Rankine-Hugoniot relations (detailed later in Sec. 5.1.3). The freestream (pre shock $x > 0$) quantities are taken to be $p_\infty = 101325\,\mathrm{Pa}$ and $T_\infty = 300\,\mathrm{K}$ while the time step is defined with $T_r = 1404\,\mathrm{K}$. The vortex is initialized at $x = 2R$ from the shock accordingly to the reference DNS [200] and travels from the right to the left of the shock. Although in their work Inoue and coworkers [200] specify that the vortex has no more influence $4R$ away from its center, for a reason unknown to the authors, they chose to initialize the vortex at $x = 2R$ from the discontinuity. Using such initialization, it is important to specify that the vortex is partially situated on the discontinuity at the beginning of the computation, and makes any calculation not comparable with an experimental reference. This calculation therefore belongs purely in the field of numerical simulation from the author point of view.

The velocity, density and pressure profiles of the vortex are defined according to Eq. (4.4.2), Eq. (4.4.3) and Eq. (4.4.4) respectively. The characteristic time is defined as $t_c = R/c_\infty$ where c_∞ is the speed of sound before the shock. The boundary conditions are imposed similarly to [187] and their type and the layout of the test case can be found in Fig. 4.12. Case A with $\mathrm{Ma}_v = 0.5$ and $\mathrm{Re} = 400$ and case C with $\mathrm{Ma}_v = 0.25$ and $\mathrm{Re} = 800$ from ref. [200] have been performed.

For case A, the isocontours of density displayed on Fig. 4.13 for $t = 8t_c$, clearly show the deformation of the shock wave, from which, a pair of reflected shock waves emanate due to the interaction with the vortex. The result is qualitatively in good agreements with the DNS isocontours, meaning that the overall feature of the flow is well modeled by the present scheme.

For quantitative results, the acoustic sound generation of case C is compared to the

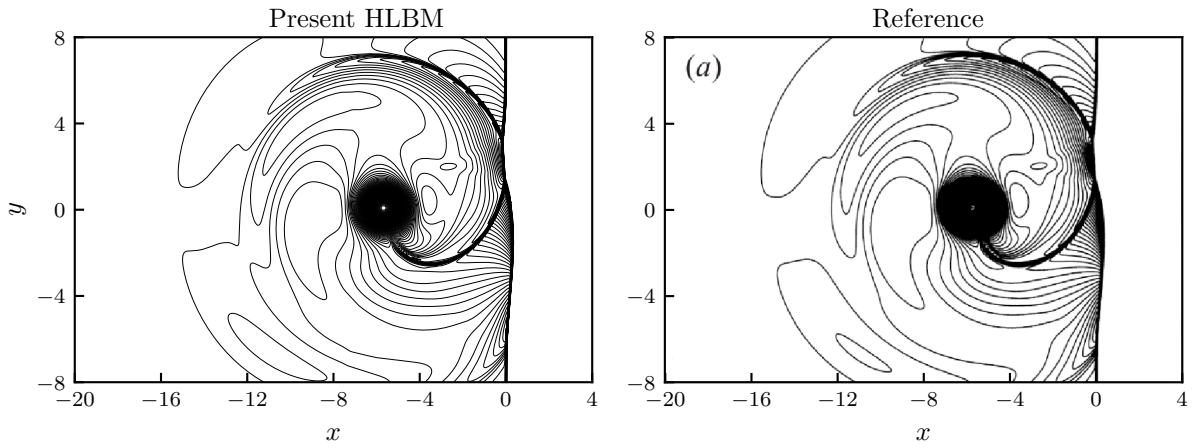

Figure 4.13 – Case A with $\sigma = 0$. Density isocontour at $t = 8t_c$, present HLBM (left) and ref. [200] (right) and. Contour ranges from $\rho_{min} = 0.92$ to $\rho_{max} = 1.55$ with an increment of 0.0053.

DNS [200]. This sound is defined as:

$$\Delta p = \frac{p - p_s}{p_s}, \tag{4.5.4}$$

with p_s the pressure behind the shock wave. Fig. 4.14 and Fig. 4.15, compare the circumferential and radial distributions of the sound pressure Δp computed by the present model (symbols) to the DNS results (solid lines). This is done for two different values of σ, $\sigma = 0$ and $\sigma = 0.9$. As shown in the previous section 4.4.2, in low viscosity cases a small value of σ is mandatory to obtain stable results which decreases the accuracy of the solution. However, the present case is viscous enough to get a stable simulation even with high value of σ permitting the study of its impact on the solution. When the vortex interacts with the shock, a precursor wave appears first, followed by a second acoustic wave (the second sound) [200], which are both of quadrupolar nature. Fig. 4.14 shows that the quadrupolar feature of these two waves is well captured on the circumferential profiles, and the results are found to be in agreement with the DNS data for both values of σ. As a general rule, the radial cuts of different instants on Fig. 4.15, show that better results are obtained for $\sigma = 0.9$. This is in accordance with the remarks in Sec. 4.4.2 where the error grow as the σ parameter decreases. Nevertheless, both calculations give satisfactory results for all the characteristic times for both the precursor and the second sound, which is generated once the vortex passes through the shock.

4.6 The model's Achille's heel: case involving entropic mode

In the previous sections, the model has been successfully validated on several compressible test cases. Nevertheless, on particular test cases related to entropic mode, one

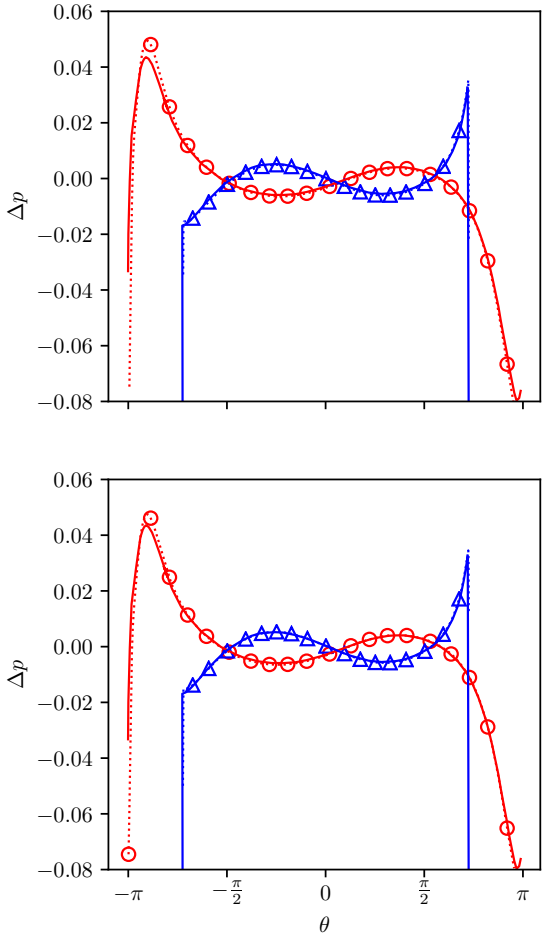

Figure 4.14 – Case C with $\sigma = 0$ (top) and $\sigma = 0.9$ (bottom). Circumferential cut of the pressure variation Δp at $t = 6t_c$. Here symbols correspond to the present HLBM model while solid line to the DNS [200]. The symbols ··△·· correspond to the precursor at $r = 6$ while ··○·· refer to the second sound at $r = 3.7$.

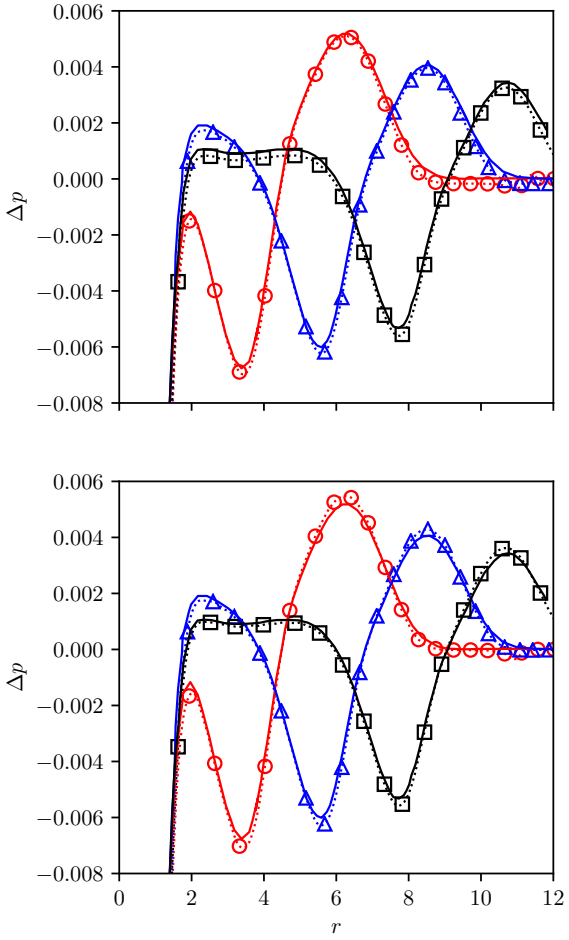

Figure 4.15 – Case C with $\sigma = 0$ (top) and $\sigma = 0.9$ (bottom). Radial cut at $\theta = -\pi/4$ of the pressure variation Δp. Solid lines correspond to the DNS [200] and symbols refers to the present HLBM for $t = 6t_c$ ··○·· , $t = 8t_c$ ··△·· and $t = 10t_c$ ··□··

noticed a curious behavior of the HLBM scheme. It is proposed here to highlight this behaviour.

One proposes to assess the model on almost the same test case that seen previously in Sec. 3.8.3: the transport of a Gaussian shaped entropic spot in a uniform field of constant velocity u_x in a periodic domain. This domain is considered the same as in Sec. 3.7.3. The pressure is considered constant $p = 101325\,\text{Pa}$ and the same initial Gaussian temperature profile $T(r)$ Eq. (3.7.10) is adopted with a different radius set to $R = 20\Delta x$. The density is simply initialized using the e.o.s.:

$$\rho(r) = \frac{p}{r_g T(r)}. \tag{4.6.1}$$

The reference temperature is set to $T_r = 600\,\text{K}$ i.e. $\theta = 0.5$ and $\sigma = 0$. The advective velocity is chosen as $u_x = \text{Ma}_\infty c_\infty$ with $\text{Ma}_\infty = 0.1$ and $\gamma_g = 1.4$. The dynamic viscosity is set to $\mu = 1.10^{-5}\,\text{kg.m}^{-1}.\text{s}^{-1}$ and finally the Prandtl number is imposed as $\text{Pr} = \infty$ so as zero dissipation is introduced by the Fourier term. The present initialization aims to assess the scheme for a test case involving the entropy mode. During this test case, the Gaussian entropy profile is expected to be simply advected along $\boldsymbol{e}_x$ in the domain without getting deformed or dissipated.

Fig. 4.16 compares the reduced temperature field and iso-contours obtained for different flow-through-time t_c. The first line (RK1MUSCL), corresponds to the entropic spot advected using the numerical scheme described in Sec. 4.3.4 and used all along this chapter. For $t = t_c$, a very small deformation can be observed along $\boldsymbol{e}_x$ which can be assimilated to dispersive effects of the advective numerical scheme. However, after ten flow-through-time ($t = 10t_c$), it can be observed that the Gaussian has become largely deformed and now presents a x-shaped profile. This kind of behaviour does not seems to correspond to numerical dispersion, since the latter should essentially be observed along the axis aligned with the advection velocity. To set aside the numerical dispersion effects of the convective scheme, the same simulation was carried out but with $u_x = 0$. The results are shown on the second line of the figure (RK1MUSCL, $u_x = 0$). For $t = 10t_c$, a very similar x-shaped profile can be observed and thus setting aside the dispersive effects of the convective scheme. By using a more dissipative numerical scheme on convection cases, this phenomenon can be observed only slightly, as one can see on the third (RK1UPO1) and fourth (RK1UPO1, $u_x = 0$) lines of the figure showing results for a first-order upwind scheme.

Finally, the very same test case has been performed however using centered schemes of different order applied to the convective part of the entropy equation. Fig. 4.17 displays results for a RK4 time integrator and a second-, fourth- and eight-order centered scheme. For $t = 10t_c$, and for all the cases, all results present an x-shaped profile instead of the initial Gaussian one. At first sight, this phenomena is therefore not related to the way of discretizing the energy part of the HLBM [1].

[1] Moreover, generally speaking and for flows without shock waves, as long as the convective scheme of the energy equation is stable, it does not really have a significant impact on the stability, as already noted by Nie et al. [150].

This entropic spot is thus somehow deformed over the time and the latter is not related to the numerical artifacts of the schemes applied on the energetic part. Actually, by looking at the vorticity field (not shown here), one can observes all around the spot the emergence of several pairs of azimuthally-distributed counter rotating vortices. The intensity of these vortices increases over time and eventually distort the temperature profile giving it its x-shaped profile. This phenomenon has been identified in this work as mode transfer between the entropy mode and the shear mode. It will be investigated in much more detail later in chapter 6 (Sec. 6.6.2 precisely) thanks to an enhanced von Neumann analysis of the present compressible HLBM.

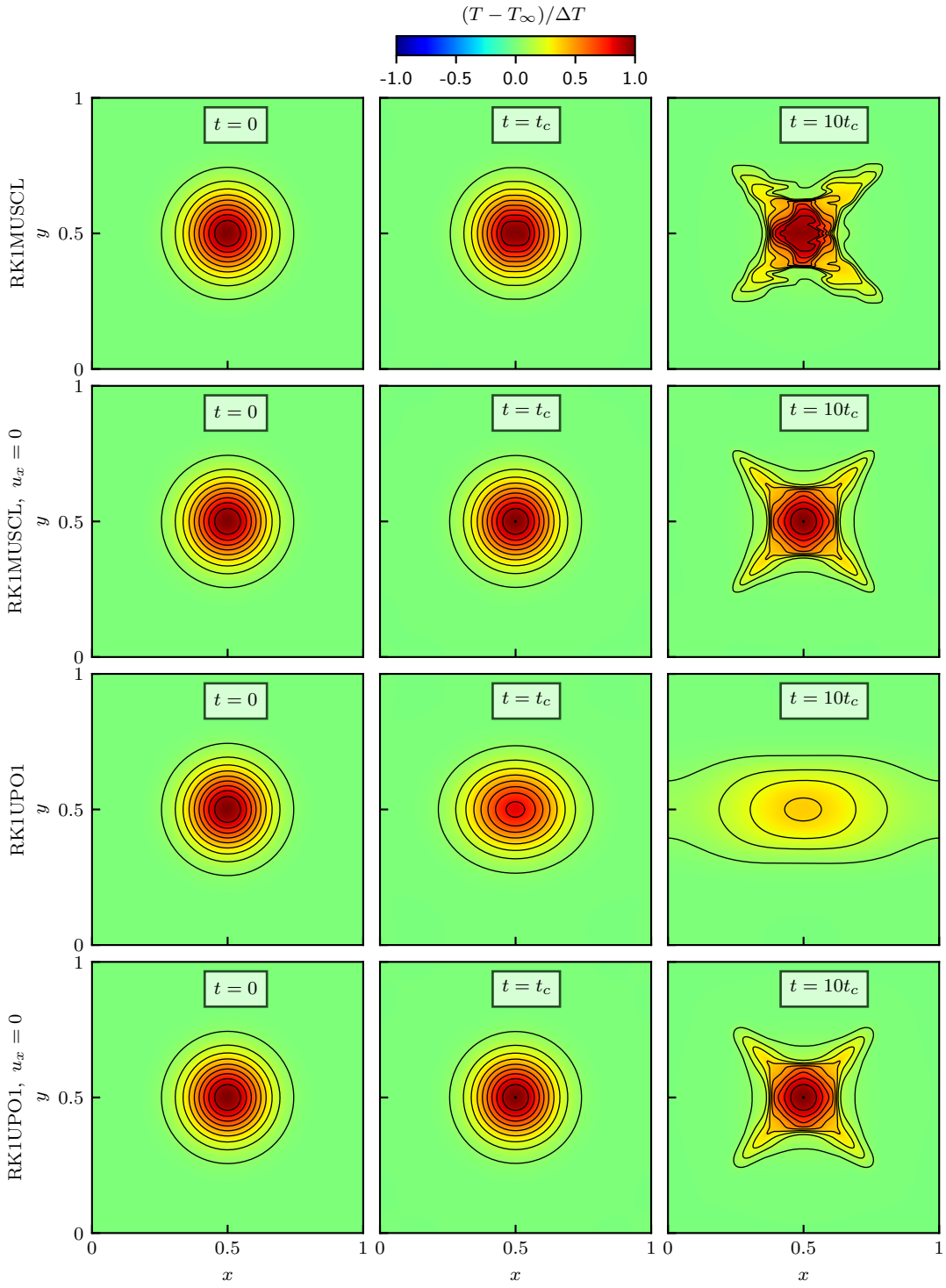

Figure 4.16 – Reduced temperature field and iso-contours at different characteristic times and for different numerical schemes. Twenty iso-contours equally distributed from −1 to 1 are displayed. From left to right columns: $t = 0$, $t = t_c$ and $t = 10t_c$; from top to bottom rows RK1MUSCL (the one used throughout this chapter), RK1MUSCL for $u_x = 0$, RK1UPO1 and RK1UPO1 for $u_x = 0$.

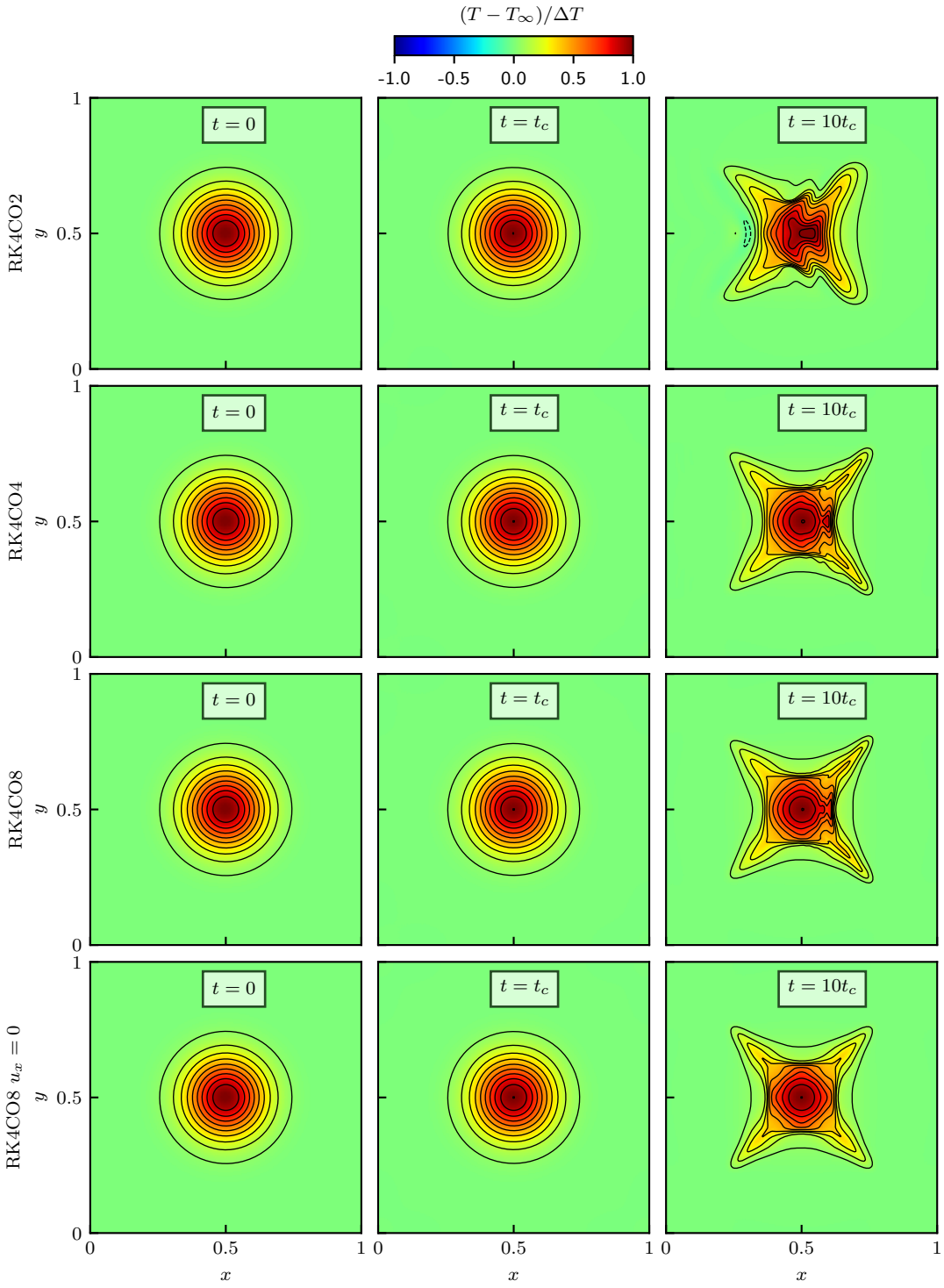

Figure 4.17 – Reduced temperature field and iso-contours at different characteristic times and for different numerical schemes. Twenty iso-contours equally distributed from −1 to 1 are displayed; solid and dashed lines corresponds respectively to positive and negative values. From left to right columns: $t = 0$, $t = t_c$ and $t = 10t_c$; from top to bottom rows RK4CO2 , RK4CO4, RK4CO8 and RK4CO8 for $u_x = 0$.

4.7 Conclusions

In this chapter, the compressible HLBM of Feng et al. [187] has been presented. Based on the standard D2Q9 lattice, it allows a stable perfect gas coupling between the LBM and the FD energy part. The cornerstone of the stability of this model lies in the use of the HRR collision operator [88] stabilizing the scheme by means of the σ parameter. However, it has been shown to be restricted to subsonic regimes thus reducing its application range in the aeronautical field.

In this present work an enhanced version of the original model has been proposed. Several new elements have been introduced compared to the original model, some of which have allowed the extension to supersonic flows. First, the correction of the trace of the viscous stress tensor, which removes the spurious bulk viscosity. Second, the viscous heat production term in the energy equation has been successfully modeled using LBM combined with finite difference, permitting to enforce the consistency between the two systems and has been validated on smooth flows. Finally, an upwinded discretization scheme for the correction term induced by the closure relation of the lattice was proposed. Through different test cases, these improvements of the original model [187] are observed to be not regressive. Most importantly, the upwinded discretization permits to dramatically extend the application range of the HLBM model to supersonic flows. This feature demonstrates the importance of the discretization of this term.

The present enhanced HLBM on standard lattice has been proven to retrieve the physics of the fully compressible Navier-Stokes-Fourier equations for arbitrary heat capacity ratio and Prandtl number. The use of such a lattice is a highly desirable feature for the implementation of boundary conditions, grid refinement and immersed boundary techniques. It has been shown that it is coherent for low and high Mach number flows with discontinuities, at relatively low viscosity, and only requires to specify the reference temperature T_r (controlling the CFL number) and a unique numerical parameter σ. Excellent results were obtained on smooth flow regions. Finally, to put it in a nutshell, the three most important ingredients to obtain this robust compressible HLBM are:

- The HRR collision operator allowing a stable perfect gas coupling.
- Upwinding the corrective term $E_{1,\alpha\beta}$ permitting to achieve supersonic computations.
- Use an entropy equation for the energy part granting a better numerical stability.

However, the stability of model has been shown to be very dependent on the free parameter σ (e.g. on Fig 4.4), and its value was most of the time chosen empirically depending on the test case to obtain satisfying results. Moreover, the reference temperature T_r controlling the CFL number was also chosen arbitrarily, nevertheless under the constraint CFL < 1, and its influence on the accuracy and stability of the scheme remains unknown. These questions, as well as the strange behaviour of the model on entropic mode observed in Sec. 4.6, will be answered later in Chap 6 thanks to a von Neumann stability analysis applied to this compressible HLBM scheme.

Finally, it has been shown that the model experienced some problem of conservativeness on discontinuities such as shock waves (see Sec. 4.5.2). One therefore proposes to study this issue in the next Chapter 5.

Chapter 5

Shock capturing techniques for HLBM

Contents

5.1 Limitation of the primitive variable formulation of the entropy equation . . . 156

5.1.1 Two-dimensional Riemann problems . . . 156

5.1.2 Shock tube with high pressure ratio . . . 159

5.1.3 One-dimensional stationary shock . . . 160

5.1.4 Outcomes of the test-cases . . . 163

5.1.5 Problem identification and proposals for solutions . . . 164

5.2 HLBM on total energy equation . . . 165

5.2.1 HLLC Riemann solver for energy discretization . . . 165

5.2.2 One-dimensional stationary shock . . . 168

5.2.3 Shock tube with high pressure ratio . . . 169

5.2.4 Two-dimensional Riemann problems . . . 170

5.2.5 Convected and stationary isentropic vortex . . . 172

5.2.6 Conclusion . . . 174

5.3 HLBM with artificial viscosity . . . 177

5.3.1 Definition of the problem . . . 178

5.3.2 Correcting the physics using the viscous terms . . . 178

5.3.3 Guided artificial viscosity through Jameson-like shock sensor . . . 181

5.3.4 Discussion . . . 183

5.4 Conclusion . . . 185

This chapter points out one of the weaknesses of the model for flows containing shock waves. The use of a non-conservative energy equation in the HLBM scheme results in an incorrect shock strength and thus an incorrect propagation speed. To address this issue, two different strategies are proposed: one aiming at enhancing the present model using a local heat production term, and another consisting in the change of the energy variable, equation formulation and numerical scheme. Finally, a discussion on their strengths, weaknesses and practical applications is conducted.

5.1 Limitation of the primitive variable formulation of the entropy equation

In this section, the HLBM derived in Chap.4 and based on the primitive variable formulation of the entropy equation, denoted in the following by HLBM-s, will be assessed on different test-cases containing flow discontinuities in realistic conditions, i.e, with low dynamic viscosity. These test-cases will highlight a defect in the numerical scheme which emerges when treating flows with shock waves. The most probable cause of this defect will be identified and solutions will be proposed.

5.1.1 Two-dimensional Riemann problems

It is proposed here to test the HLBM scheme for two-dimensional gas dynamics test-cases involving discontinuities. The two-dimensional Riemann problems consists of a square fluid domain separated into four distinct quadrants, each of them initialized by constant values of pressure, density and velocity. At each interface, the variables are chosen in such a way that one elementary wave is initialized, and can be either: a one-dimensional shock, a one-dimensional rarefaction, or a two-dimensional contact discontinuity. The various wave combinations lead to 19 genuinely different physical test-cases [201], where the exact solutions resulting from the four quadrant interaction are not analytically known. CFD is therefore one of the most effective means of studying these test cases, which have been examined by various authors [201–204] in the early 2000's.

In the present work, one considers: case 12 and case 15 from [201], which together contain the three different waves types. The initial conditions in terms of pressure, density and velocity can be found on Fig. 5.1 together with the type of wave initialized between each quadrants. The same convention as [201] is adopted to describe the structure of the two-dimensional Riemann problem between the quadrant i and the quadrant j: $\overrightarrow{S_{ij}}$ corresponds to a shock wave propagating from i to j (respectively from j to i for $\overleftarrow{S_{ij}}$), J^{+}_{ij} refers to a contact discontinuity with a positive tangential velocity (or negative tangential velocity for J^{-}_{ij}) and finally $\overrightarrow{R_{ij}}$ corresponds to a rarefaction wave propagating from i to j (respectively from j to i for $\overleftarrow{R_{ij}}$). The domain $(x, y) \in [0, L]$ with $L = 1\,\mathrm{m}$, is discretized into $N = 400{\times}400$ cells. The dimensionless variables have been obtained using $T_\infty = 300\,\mathrm{K}$, $p_\infty = 101325\,\mathrm{Pa}$ and a characteristic velocity $c_n = \sqrt{r_g T_\infty}\,\mathrm{m.s^{-1}}$ from which a characteristic time can be defined as $t_c = L/c_n$. In the simulation, $\gamma_g = 1.4$, $\mu = 1.10^{-5}\,\mathrm{kg.m^{-1}.s^{-1}}$, $\sigma = 0$

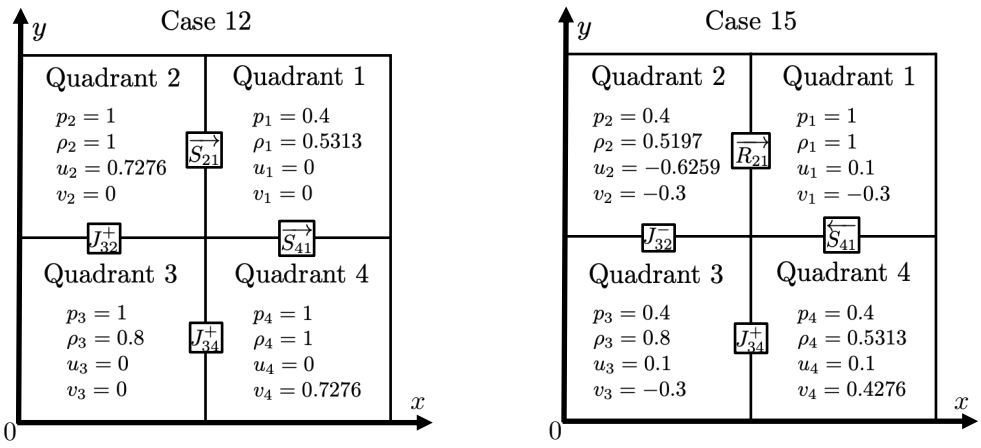

Figure 5.1 – Structure and initial conditions of the two-dimensional Riemann problems. Same convention as [201] is adopted to describe initial 1D waves.

and the reference temperature is chosen as $T_r \simeq 1500\,\mathrm{K}$. In theory, in order to have no edge effects on the simulation, the boundary conditions must be applied dynamically at each time step and must be analytical solutions to the 1D Riemann problem at each quadrant interfaces. In practice, to avoid unnecessary implementation work and to prevent the simulation from being disturbed by boundary interactions, similarly to [205] we choose to simulate twice the size of the domain and to impose periodicity conditions at the boundaries. The domain is thereafter clipped during post-processing.

Fig. 5.2 compares the present HLBM with the RK3 fifth-order WENO scheme from the work of Liska and Wendroff [204] (with same resolution i.e. $N = 400 \times 400$) in terms of pressure, density and velocity. The same density isocontours as the reference have been adopted, and the pressure color map was adjusted to match the reference work as closely as possible.

For the case 12 on Fig. 5.2a, the feature of the flow is in agreement with the analysis of Schulz-Rinne et al. [202]: the two contact discontinuities bend and end in spirals in the third quadrant, and the two shocks interact like the pair of shocks so that the reflected shocks in the first quadrant have an oval shape. The present simulation is in agreement with the WENO reference although some spurious density iso contours appear behind the shock wave. These are also visible on the pressure colormap and can be attributed to Gibbs phenomenon. The spirals present in the third quadrant are well captured by the HLBM in contrary to other NS schemes such as the third-order WENO present in [204], which demonstrates the relative accuracy of the scheme.

Regarding the case 15 on Fig. 5.2b, the flow dynamics are also in accordance with the reference analysis [202]: the two contact discontinuities bend and end in a spiral in the second quadrant; the rarefaction wave turns backward in front of the shock that ends at the contact discontinuity. The present HLBM is in agreement with the WENO reference even though some spurious density iso contours appear in the first region perpendicular to the rarefaction wave. However, the same feature can be observed on the pressure color map of the reference, and can be attributed, from the authors [204], to erroneous

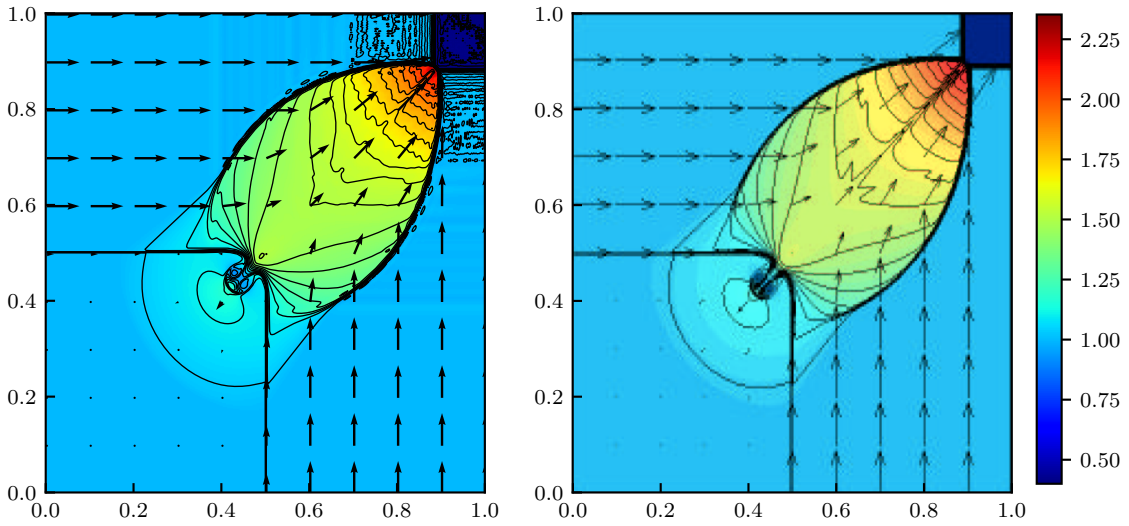

(a) Case 12 at $t = 0.25t_c$ with 30 density contours (0.54 to 1.7 step 0.04).

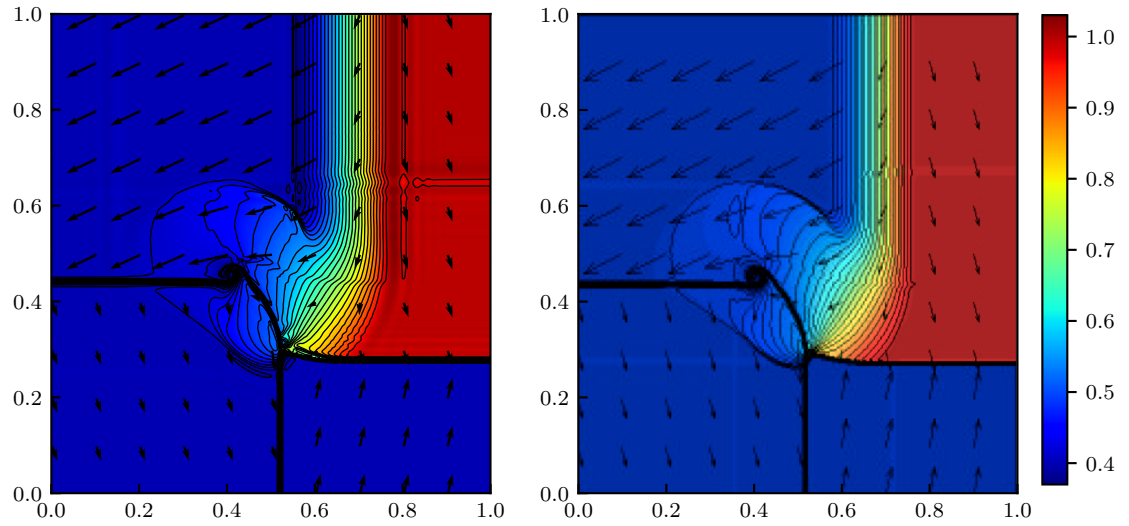

(b) Case 15 at $t = 0.2t_c$ with 29 density contours (0.43 to 0.99 step 0.02) .

Figure 5.2 – Two-dimensional Riemann problems computed by the HLBM-s model. Present model (left) and RK3 fifth-order WENO (right) from [204]. Pressure is displayed by color, density by contours and velocity by arrows.

waves emanated from the initial jumps. This error is also visible on the density field of the reference but for other values of iso contours [204]. Similarly to case 12, oscillations are visible behind the shock wave on the pressure colormap. Looking at the density isocontours, the rarefaction wave seems to be more spread out by the present HLBM compared to the reference as well as the spiral formed in the first quadrant. However, the latter remains rather well modeled compared to other NS schemes presented in [204] such as the third-order WENO.

Finally, it can be concluded that the HLBM scheme captures, in a qualitative point of view, the correct flow physics for two-dimensional test-cases involving discontinuities.

5.1.2 Shock tube with high pressure ratio

This time the HLBM model is assessed on a one-dimensional shock tube problem with an initial pressure ratio of ten. The initial conditions read:

$$(\rho, u, p) = \begin{cases} (10\rho_\infty, 0, 10p_\infty), & 0 \leq x < L/2 \\ (\rho_\infty, 0, p_\infty), & L/2 \leq x \leq L \end{cases}, \tag{5.1.1}$$

where $L = 1\,\mathrm{m}$, $T_\infty = 300\,\mathrm{K}$, $p_\infty = 101325\,\mathrm{Pa}$ and $\rho_\infty = p_\infty / (r_g T_\infty)$. Similarly to the standard Sod's shock tube, this initialization produces a shock wave, a contact discontinuity and an expansion wave. This test-case is performed with $\gamma_g = 1.4$, $\mu = 1.10^{-5}\,\mathrm{kg.m^{-1}.s^{-1}}$, $\sigma = 0.0$ and $T_r \simeq 1460\,\mathrm{K}$.

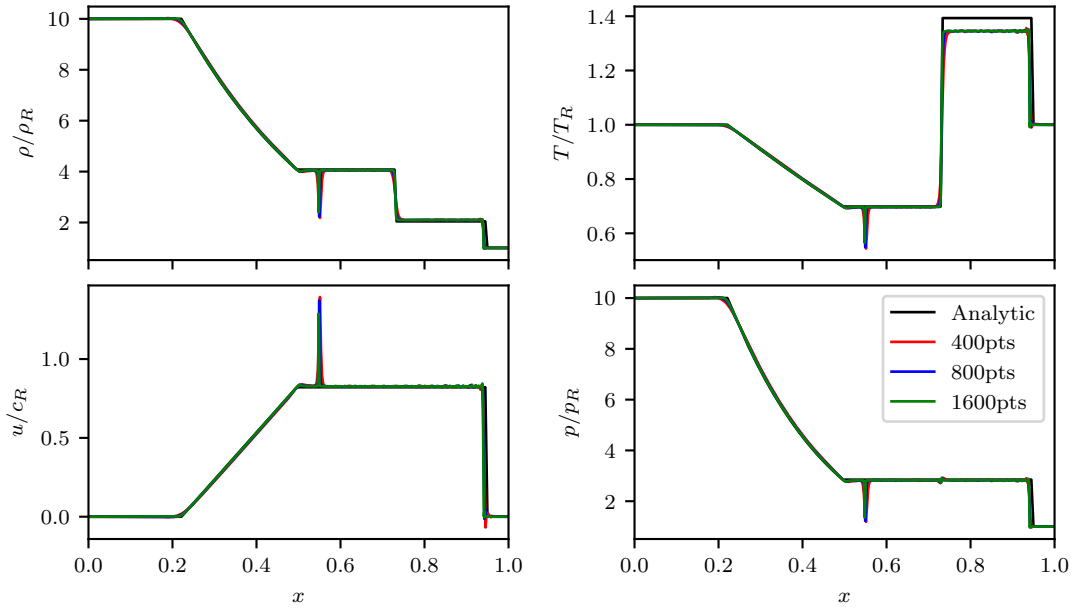

Figure 5.3 – Shock tube problem computed by the HLBM-s model. The present model is compared with the exact solution for different mesh resolutions.

Fig. 5.3 compares different profiles obtained by the model with the analytical solution for different mesh resolutions. From the density, velocity and pressure profiles, it can be observed that the three type of waves are well captured by the HLBM. However, on the temperature profile, and independently of the mesh resolution, one can observe a temperature loss between the contact discontinuity and the shock wave. Although it is less obvious, this defect can also be seen on the density profile (which is slightly above the theoretical value) since the system is coupled with a perfect gas e.o.s.. Moreover, it can be observed that regardless of the mesh resolution, the shock wave is slightly delayed

compared to the analytical solution. This is a direct consequence of the wrong evaluation of the temperature which alters its propagation speed. This test-case reveals an obvious error in the scheme on the modeling of a shock wave. It is therefore proposed to study this phenomenon in the next sub-section using a case containing only a shock wave.

Finally a small velocity overshoot can be seen at the shock interface, which can be attributed to insufficient dissipation of the scheme, and a pressure perturbation near the contact discontinuity can also be observed. Moreover it is worth noting that the overshoot appearing at $x \simeq 0.55$ appears only a few iterations after the computation starts. This overshoot is similar to the one observed on Fig. 4.11, but is more pronounced in the present case because of the higher pressure ratio. The use of a tangent hyperbolic profile to smooth the initial condition on more than two points, or a higher value of viscosity (as shown later in Sec.5.3.2), allows this overshoot to completely disappear.

5.1.3 One-dimensional stationary shock

To further investigates the artifact observed on the shock tube, it is proposed to focus the study of the HLBM scheme on the simulation of a one-dimensional pure shock wave propagating from the left to the right. Considering the Euler equations integrated over an appropriated control volume that includes a discontinuity such as a shock, one can obtains the Rankine–Hugoniot relations:

$$\begin{aligned} u_s\left(\rho_R - \rho_L\right) &= \rho_R u_R - \rho_L u_L, \\ u_s\left(\rho_R u_R - \rho_L u_L\right) &= \left(\rho_R u_R^2 + p_R\right) - \left(\rho_L u_L^2 + p_L\right), \\ u_s\left(\rho_R E_R - \rho_L E_L\right) &= u_R\left(\rho_R E_R + p_R\right) - u_L\left(\rho_L E_L + p_L\right), \end{aligned} \tag{5.1.2}$$

respectively from the equation of mass, momentum and energy. Here u_s refers to the speed of the shock wave, and the subscript R and L refer respectively to the pre and post-shocked variables. The shock propagates form the right to the left in the laboratory frame i.e. $u_s > u_L > 0$, and one considers a pre-shocked region with zero velocity $u_R = 0$. In order to study the scheme for a long time range, and to spare ourselves the modeling of an infinitely large domain, it is interesting to consider a simulation in the shock reference frame. For that purpose one subtracts u_s from u_s, u_R and u_L so that the shock is stationary with respect to the new reference frame. It follows:

$$\begin{aligned} \rho_R u_R^* &= \rho_L u_L^*, \\ \left(\rho_R u_R^{*2} + p_R\right) &= \left(\rho_L u_L^{*2} + p_L\right), \\ u_R^*\left(\rho_R E_R + p_R\right) &= u_L^*\left(\rho_L E_L + p_L\right), \end{aligned} \tag{5.1.3}$$

with $u_{R,L}^* = \left(u_{R,L} - u_s\right) < 0$ the new velocities in the shock reference frame. It clearly appears that in this reference frame, the mass, momentum and energy fluxes are conserved. Moreover, the third relation can be rewritten using the first one to yield the conservation of the total enthalpy through the shock $h_{t,R} = h_{t,L}$ with $h_{t,(R,L)} = h_{R,L} + u_{R,L}/2$. Finally, using the ideal gas relation and after some algebraic manipulations, one can obtains the

equations of interest i.e., the Rankine–Hugoniot relations for a polytropic gas [206]:

$$\begin{aligned}
\frac{u_L^*}{u_R^*} &= \frac{\rho_R}{\rho_L} = \frac{(\gamma-1)\mathrm{Ma}_s^2+2}{(\gamma+1)\mathrm{Ma}_s^2},\\
\frac{p_L}{p_R} &= \frac{2\gamma\mathrm{Ma}_s^2-(\gamma-1)}{(\gamma+1)},\\
\frac{T_L}{T_R} &= \frac{\left[2\gamma\mathrm{Ma}_s^2-(\gamma-1)\right]\left[(\gamma-1)\mathrm{Ma}_s^2+2\right]}{(\gamma+1)^2\mathrm{Ma}_s^2},\\
\mathrm{Ma}_L^2 &= \frac{(\gamma-1)\mathrm{Ma}_s^2+2}{2\gamma\mathrm{Ma}_s^2-(\gamma-1)},
\end{aligned} \tag{5.1.4}$$

with $\mathrm{Ma}_L = u_L^*/\sqrt{\gamma_g r_g T_L}$ the Mach number of the shocked state. These relations determine the left state (shocked state) as a function of the Mach number of the shock wave $\mathrm{Ma}_s = u_R^*/\sqrt{\gamma_g r_g T_R}$, and thus provides the initial condition for the computation.

Let us now consider a stationary shock wave initialized in the middle of a one-dimensional domain of length $L = 1\,\mathrm{m}$ discretized into $N = 400$ cells. The shocked region corresponds to $x \in [0, L/2]$ and the pre-shocked region to $x \in [L/2, L]$. Three different shock speeds are considered: $\mathrm{Ma}_s = 1.2$, $\mathrm{Ma}_s = 1.5$ and $\mathrm{Ma}_s = 2$ leading to three shocks of increasing strength. The pre-shocked variables are chosen such that $T_R = 300\,\mathrm{K}$, $p_R = 101325\,\mathrm{Pa}$ and $\rho_R = p_R/(r_g T_R)$. This test-case is performed with $\gamma_g = 1.4$, $\mu = 1.10^{-5}\,\mathrm{kg.m^{-1}.s^{-1}}$, $\sigma = 0.0$ and $T_r \simeq 1500\,\mathrm{K}$. It is recalled that the shocked variables are obtained using Eq. (5.1.4), and the analytical solution corresponds to the initial conditions. Finally, the variables of each cases are normalized using their respective right (pre-shocked) state, and a characteristic time can be defined for each cases as $t_c = L/u_R^*$.

Fig. 5.4 shows the density, temperature, velocity and pressure profiles for two different times. In Fig. 5.4a, for time $t = t_c$ and for $\mathrm{Ma}_s = 2$, one can observe a temperature loss behind the shock wave as well as a density increase. In addition, these two fields include a discontinuity around $x \simeq 0.15$ while the pressure and velocity fields remains constant in this region. In fact, this discontinuity corresponds to a spurious contact discontinuity generated by the initial shock condition. A rarefaction wave has also been generated at this interface, but is not visible on this graph since it was propagated outside the domain for $t = t_c$. Thus, the Riemann problem computed by the present HLBM scheme gives as solution a rarefaction, a contact discontinuity and a "novel" shock wave instead of the initial pure shock. Exactly the same observations can be made for $\mathrm{Ma}_s = 1.2$ and $\mathrm{Ma}_s = 1.5$ cases. For the latter, the contact discontinuity is not visible since it was already propagated outside the domain for $t = t_c$. Indeed, the initial left velocity value of both of these cases is higher than the $\mathrm{Ma}_s = 2$ case. Finally, it can be observed that the lower the Mach number is, the smaller the errors are, and they become almost imperceptible when using the present graph scale for the $\mathrm{Ma}_s = 1.2$ case.

On Fig.5.4b, one can find the profiles plotted later in time for $t = 4t_c$. In the same way as the rarefaction wave, the contact discontinuity for $\mathrm{Ma}_s = 2$ has moved out of the domain and only the "novel" shock wave modeled by the scheme remains. The left state

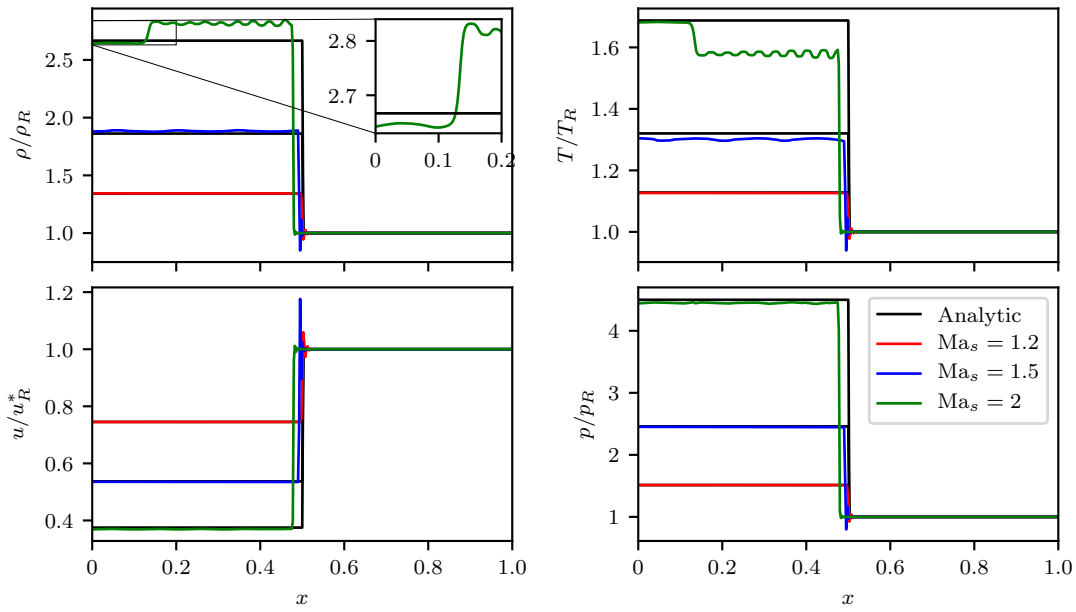

(a) Solution at $t = t_c$.

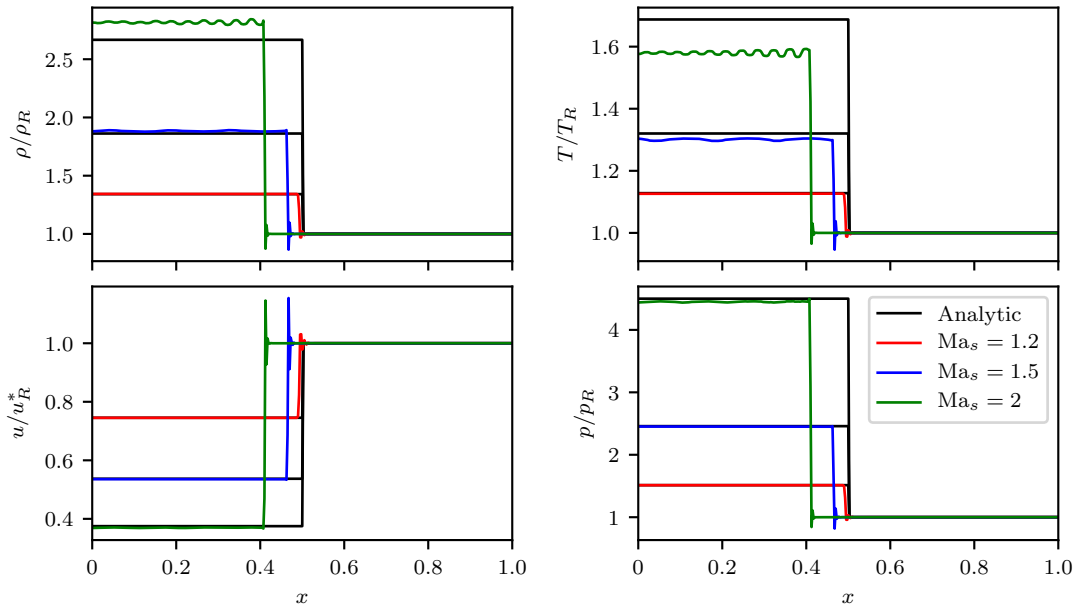

(b) Solution at $t = 4t_c$.

Figure 5.4 – Stationary shock problem at two different times computed by the HLBM-s model. The latter is compared with the exact solution for three different shock Mach numbers.

of this "novel" shock is found to be rather different from the initialization especially on the density and temperature profile. Moreover, it clearly appears that this shock drifts

as a function of time with respect to the analytical solution. Indeed, the new left state of this "novel" shock does not allow it to propagate at the same speed as the original shock which leads to $u_s \neq 0$. When comparing these three cases, one can see that the error grows with the strength of the shock. For $\mathrm{Ma}_s = 1.2$, one can only notice a minor deviation from the analytic solution in terms of position and left state values. However, if one waits long enough ($t >> 4t_c$), the shock will ultimately drift from its original position.

It is worth noting that very similar computations using a refined mesh with $N = 1600$ cells have been performed. Except for a small attenuation of the oscillations generated by the shock interface, the fluid behavior remained the same. This behavior is identical to the shock tube described in Sec. 5.1.2, where the defect is found to be independent of the mesh resolution.

Finally, if one summarizes the symptoms encountered during this simulation:

- an incorrect post chocked states,
- a position of the shock which drifts in time: $u_s \neq 0$, leading to unsteady flow,
- the issue is found to be mesh independent.

Based on these problems, one can conclude that the Rankine–Hugoniot relations Eq. (5.1.3) are not respected by the numerical scheme on the shock interface and thus the mass, momentum and energy fluxes are not conserved. It indicates that the numerical scheme is not conservative on this interface.

5.1.4 Outcomes of the test-cases

Finally, some conclusions must be drawn from the three test-cases presented in the above subsections. For the two-dimensional Riemann problems, the HLBM scheme adequately recovered the physics of the flow. Indeed, putting aside the oscillations behind the shocks, the complex two-dimensional structures created by the interaction of the different initial waves have been found to be qualitatively in agreement with the reference. One can therefore suggest, at least qualitatively, that the model is able to capture each wave and the result of their interactions without any apparent problem.

Then, a one-dimensional shock tube with pressure ratio of ten was computed for the purposes of quantitative comparisons. For this case, a few concerns have begun to emerge. While the rarefaction and contact discontinuity waves are still correctly captured by the model, some issue falling within the remit of conservativeness appears on the shock wave. Indeed, the HLBM does not properly model the temperature and density variation on the shock. This issue has been found to be mesh-independent and can therefore be totally attributed to the numerical system's inability to retrieve the correct equations in a non-linear configuration such as a shock wave.

Due to the unsteady nature of the previous test-case (which renders it limited in terms of physical time simulated), all the problems related to the lack of conservativeness of the model could not be studied. To further investigate this issue, the 1D stationary shock wave case has been performed. It has been shown that the HLBM solved an

erroneous Riemann problem leading to a different shock wave solution. The conservativity issue has been found to be dependent on the "strength" of the shock (determined by the the upstream Mach number). The stronger the shock is, the larger is the error on the post shocked variables, which ultimately impact the shock wave velocity. It means that for transonic or supersonic computations involving shock waves, there will be an error on the position of these discontinuities, and will ultimately bias the prediction of aerodynamic forces or noise generated by a profile. Although the latter is moderate for Mach numbers close to unity, which allows for the computation of cases such as the shock-vortex interaction in Sec. 4.5.3, computing supersonic flows with the current model is not desirable for aeronautical compressible applications.

Finally, for the three test-cases, spurious (Gibbs) oscillations on the shock could be observed. This feature is common for numerical schemes that do not add sufficient numerical dissipation on flow discontinuities to prevents the onset of Gibbs oscillations [207]. It will be seen later that this problem can be solved by using an artificial viscosity introduced locally on the shock with the help of a sensor.

5.1.5 Problem identification and proposals for solutions

Some clues on the explanation of this defect can be found in the literature. Theoretical results for scalar conservation laws [208] and computational experience on Euler systems [168, 209] have shown that in the presence of shock waves, primitive schemes[1] will compute a solution propagating at the wrong speed [168]. This can be attributed to the discretization of the non-conservative form of the equation which gives rise to internal sources of the same order as the truncation error of the scheme [166]. For smooth flows, these numerical source terms can therefore be neglected. However, in the presence of strong gradients (e.g., on shock waves), these sources can grow significantly across the discontinuity and give rise to large errors. In some cases, the error may be small for short times, making it difficult to detect numerically (e.g., the $\mathrm{Ma}_s = 1.2$ stationary shock in Sec. 5.1.3). But as a general rule, such errors increases over time, leading to significant problems for long term calculations.

In the light of this informations a question arises: does the conservativity problem come from:

1. The lattice Boltzmann part of the HLBM scheme?

2. The energy part of the HLBM scheme?

The present scheme uses a primitive variable formulation of the entropy equation. So following the aforementioned reasoning, it can be concluded that the energy part must be primarily responsible for the conservativity problem. Regarding the lattice Boltzmann part, and up to the authors knowledge, the topic of the conservativity at a shock interface is not directly addressed in the literature. Nevertheless, some publications of compressible SDF and DDF models [66, 87] were able to recover the correct results on a shock tube

[1] numerical schemes discretizing the primitive variable formulation of differential equations

test case similar to the one described in Sec. 5.1.2. This makes it possible, a priori, to exclude the LBM as the cause of the non-conservation error.

The energy part of the HLBM scheme is thus considered to be responsible for the conservativity problem. In the next sections, two different methods are proposed to address this issue.

5.2 HLBM on total energy equation

Here, one suggests to directly address HLBM's conservativeness problem on the shock by discretizing the total energy equation into the conservative form (i.e. $\partial(\rho E)/\partial t = ...$). Constructing a scheme from this equation (instead of the pressure or the entropy) turns out to be, according to Toro et al. [199], one way to have a conservative scheme on the shock. However, the stability of the HLBM system based on this equation proved to be very dependent on the numerical scheme used. After numerous tests (upwind or centered schemes at different orders of accuracy combined with various types of Runge-Kutta time advancing schemes), the only stable scheme found was a first-order HLLC approximate Riemann Solver. In this section, the concept of this scheme will be briefly presented as well as its applicability in the HLBM framework. The resulting hybrid method will be assessed on difference test-cases and its advantages and disadvantages will be finally discussed. In the following, this model will be denoted by HLBM-ρE.

5.2.1 HLLC Riemann solver for energy discretization

The HLLC approximate Riemann solver, introduced by Toro et al. [210] in 1994, is the enhanced version of the HLL solver [211] (named after its authors Harten, Lax and van Leer) where the contact discontinuity is restored. One considers the following explicit conservative scheme:

$$\boldsymbol{U}_x^{t+\Delta t} = \boldsymbol{U}_x^t - \frac{\Delta t}{\Delta x}\left[\boldsymbol{F}_{x+\Delta x/2} - \boldsymbol{F}_{x-\Delta x/2}\right], \tag{5.2.1}$$

derived from the control volume $[-\Delta x/2, \Delta x/2] \times [0, \Delta t]$ and where the variables are assumed to be piecewise constant in the cells. This scheme aims at solving the x-interface of the three-dimensional Euler equations with the vector variable $\boldsymbol{U}$ and the flux vector $\boldsymbol{F}$ which follow:

$$\boldsymbol{U} = \begin{bmatrix} \rho \\ \rho u_x \\ \rho u_y \\ \rho u_z \\ \rho E \end{bmatrix}, \quad \boldsymbol{F} = \begin{bmatrix} \rho u_x \\ \rho u^2 + p \\ \rho uv \\ \rho uw \\ u(E+p) \end{bmatrix}. \tag{5.2.2}$$

To update the solution in time in Eq. (5.2.1), the fluxes $\boldsymbol{F}_{x\pm\Delta x/2}$ must be calculated at the cell interfaces. The HLLC method allows to find these fluxes by giving an approximate

solution of the Riemann problem at the cell interfaces which reads:

$$\begin{aligned} &\frac{\partial \boldsymbol{U}}{\partial t} + \frac{\partial \boldsymbol{F}(\mathbf{U})}{\partial x} = \mathbf{0} \\ &\boldsymbol{U}(x,0) = \begin{cases} \boldsymbol{U}_L & \text{if} \quad x < 0 \\ \boldsymbol{U}_R & \text{if} \quad x > 0 \end{cases} \end{aligned}, \tag{5.2.3}$$

where the subscripts R and L denote respectively the right and left states of a cell interface. The HLLC scheme uses Godunov-type fluxes (or upwind, where the wave propagation is used explicitly), and reads for the case of the Godunov method:

$$\boldsymbol{F}_{x+\Delta x/2} = \boldsymbol{F}\left(\boldsymbol{U}_{x+\Delta x/2}(0)\right). \tag{5.2.4}$$

This flux assumes that $\boldsymbol{U}_{x+\Delta x/2}(0)$ is the exact similarity solution $\boldsymbol{U}_{x+\Delta x/2}(x/t)$ of the Riemann problem Eq. (5.2.3) evaluated at $x/t = 0$. Solving the Riemann problem at the cell interface (thus for a fixed x) yields $\boldsymbol{F}_{x+\Delta x/2}$. However, in contrast to the Godunov method which computes an exact solution of the Riemann problem, the HLLC method aims at solving the Riemann problem approximately. The idea behind this approximate solver is to assume a wave configuration that consists of three waves separating four constant states as depicted on Fig. 5.5. On this figure, S_L and S_R are respectively the upstream and downstream acoustic speeds and S^* is the speed associated to the eigenvalue of multiplicity D (i.e. $D = 1$ one entropy wave; $D = 2$ one entropy and one shear waves; $D = 3$ one entropy and two shear waves), in other words the speed of the contact discontinuity. The corresponding HLLC intercell flux reads [198]:

$$\boldsymbol{F}_{x+\Delta x/2} = \begin{cases} \boldsymbol{F}_L & \text{if } 0 \le S_L \\ \boldsymbol{F}_L^* & \text{if } S_L \le 0 \le S^* \\ \boldsymbol{F}_R^* & \text{if } S^* \le 0 \le S_R \\ \boldsymbol{F}_R & \text{if } 0 \ge S_R \end{cases}, \tag{5.2.5}$$

where $\boldsymbol{F}_{R,L}$ are known and can be computed from $\boldsymbol{U}_{R,L}$, and the flux on both sides of the contact discontinuity $\boldsymbol{F}_{R,L}^*$ remains to be determined. In this example, for the particular wave configuration displayed on Fig. 5.5, this approximated Godunov method imposes $\boldsymbol{F}_{x+\Delta x/2} = \boldsymbol{F}_L^*$.

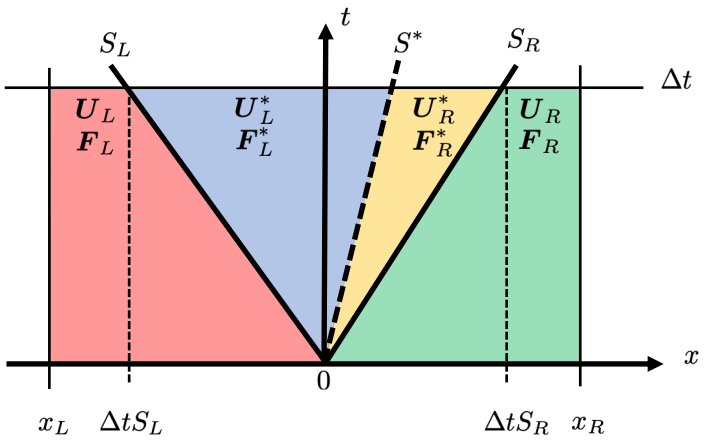

Figure 5.5 – A particular wave configuration illustrating the structure of the approximate HLLC Riemann solver in the x-t plane, adapted from [198]. Here the space origin is situated at the cell interface where the Riemann problem must be solved. The control volume is $[x_L, x_R] \times [0, \Delta t]$ where $x_L = -\Delta x/2$ and $x_R = \Delta x/2$ for Cartesian grid.

The key point of the HLLC is to solve the intermediate wave (contact discontinuity) by applying the Rankine-Hugoniot conditions across each of the waves which travels with speeds S_L, S^* and S_R. A set of equations is obtained, but with more unknowns than equations. Using the two following assumptions: (1) in the star region (both sides of the contact discontinuity) the pressure normal velocity are constant, and (2) the tangential velocities are constant in the regions formed by $[x_L, S^*t]$ and $[S^*t, x_R]$ (thus not constant across the contact discontinuity), makes it possible to solve this system and to find the expressions of S^*, p^* and the intermediate fluxes $\boldsymbol{F}_L^*$ and $\boldsymbol{F}_R^*$. The speed of the contact discontinuity is thus found as:

$$S^* = \frac{p_R - p_L + \rho_L u_L (S_L - u_L) - \rho_R u_R (S_R - u_R)}{\rho_L (S_L - u_L) - \rho_R (S_R - u_R)} \tag{5.2.6}$$

with the waves speeds S_L and S_R estimated as:

$$S_L = \min(\tilde{u} - \tilde{c}, u_L - c_L), \tag{5.2.7a}$$
$$S_R = \max(\tilde{u} + \tilde{c}, u_R + c_R). \tag{5.2.7b}$$
$$\tag{5.2.7c}$$

The latter are computed as:

$$\tilde{u} = \frac{\sqrt{\rho_L} u_L + \sqrt{\rho_R} u_R}{\sqrt{\rho_L} + \sqrt{\rho_R}} \tag{5.2.8a}$$
$$\tilde{H} = \frac{\sqrt{\rho_L} H_L + \sqrt{\rho_R} H_R}{\sqrt{\rho_L} + \sqrt{\rho_R}} \tag{5.2.8b}$$
$$\tilde{c} = \sqrt{(\gamma - 1)\left(\tilde{H} - \frac{1}{2}\tilde{u}^2\right)} \tag{5.2.8c}$$

with $\tilde{u}$, $\tilde{H}$ and $\tilde{c}$ corresponding respectively to the Roe–averaged velocity, specific enthalpy and speed of sound. Finally, the flux in the star region is given by:

$$\boldsymbol{F}^{*}_{L,R} = \boldsymbol{F}_{L,R} + S_{L,R}\left(\boldsymbol{U}^{*}_{L,R} - \boldsymbol{U}_{L,R}\right), \tag{5.2.9}$$

with the variables in the star regions being:

$$\mathbf{U}^{*}_{L,R} = \rho_{L,R}\left(\frac{S_{L,R}-u_{L,R}}{S_{L,R}-S^{*}}\right)\begin{bmatrix} 1 \\ S^{*} \\ v_{L,R} \\ w_{L,R} \\ \dfrac{E_{L,R}}{\rho_{L,R}} + (S^{*}-u_{L,R})\left[S^{*} + \dfrac{p_{L,R}}{\rho_{L,R}\,(S_{L,R}-u_{L,R})}\right]. \end{bmatrix} \tag{5.2.10}$$

Several variants exist for the HLLC solver, the one considered in this work is exactly the same as detailed above. This scheme is simple to implement on Cartesian grids since the normal vector with respect to the cell interface is always aligned with the velocity vector. Thus, no geometrical transformation are needed to compute u_L or u_R. For more details on the construction of this scheme, the reader may refer to the book of E. F. Toro [198].

Finally, since the momentum and the mass are computed with the LBM, we are only interested in solving the conservative total energy equation with such a scheme. This gives:

$$(\rho E)_{x}^{t+\Delta t} = (\rho E)_{x}^{t} - \frac{\Delta t}{\Delta x}\left[F^{E}_{x+\Delta x/2} - F^{E}_{x-\Delta x/2}\right], \tag{5.2.11}$$

with $F^{E}_{x\pm\Delta x/2}$ referring to the last component of the flux Eq. (5.2.2). The Fourier and viscous heat production terms are thereafter added to the r.h.s. of the scheme and are computed using standard second-order centered finite differences. Finally the temperature is obtained following:

$$T^{t+\Delta t} = \frac{1}{c_v}\frac{(\rho E)^{t+\Delta t}}{\rho^{t+\Delta t}} - \frac{1}{2c_v}\left(u_{\alpha}^{2}\right)^{t+\Delta t} \tag{5.2.12}$$

where $\rho^{t+\Delta t}$ and $u_{\alpha}^{t+\Delta t}$ are respectively the density and velocity computed by the LBM part of the HLBM scheme. In order to prevent any possible implementation errors, it is worth noting that the present HLLC scheme has been successfully tested before using its energy part for the creation of the HLBM.

5.2.2 One-dimensional stationary shock

As a first step, one proposes to test this new HLBM scheme on the test-case that most clearly highlights the conservativity issues: the computation of a one-dimensional stationary shock. Here, one considers the exact same case as the one seen in Sec. 5.1.3, which was performed with the HLBM based on the primitive variable formulation of the entropy equation. The numerical and physical parameters are thus chosen to be the same, and three different stationary shock waves with $\mathrm{Ma}_s = 1.2$, $\mathrm{Ma}_s = 1.5$ and $\mathrm{Ma}_s = 2$ are computed by the present HLBM-ρE model.

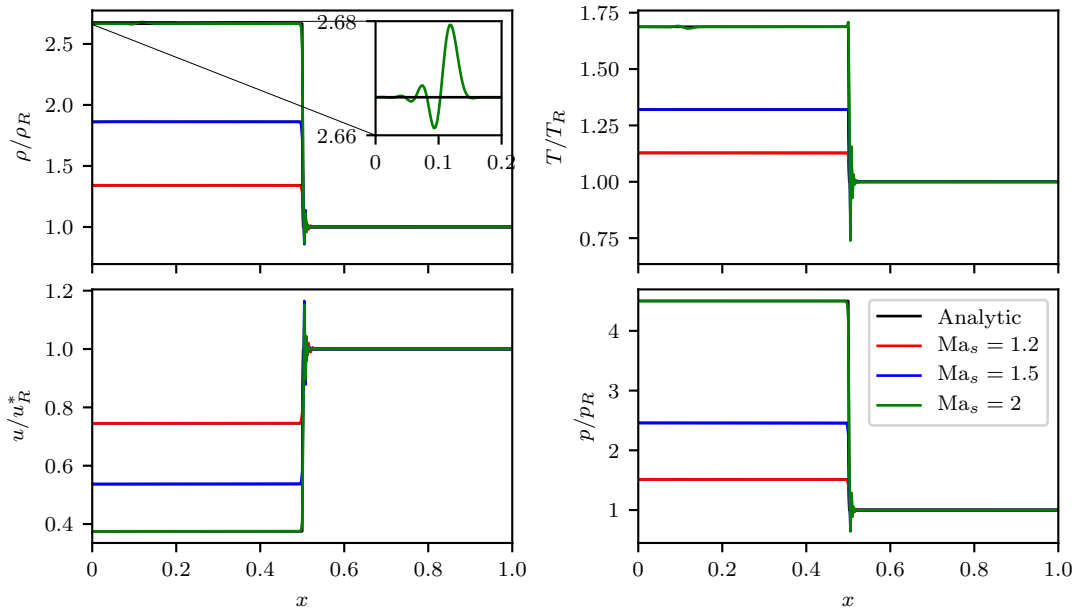

Figure 5.6 – Stationary shock problem at $t = t_c$ computed by the HLBM-ρE model. The present model is compared with the exact solution for three different shock Mach numbers.

Fig. 5.6 shows the density, temperature velocity and pressure profiles for time $t = t_c$. Apart from a slight sine wave visible on the density and temperature profile around $x \simeq 0.1$, one can see that the shocked state corresponds perfectly to the analytical solution in comparison to the primitive formulation of the entropy equation (see Fig.5.4a). Indeed, no spurious rarefaction or contact discontinuity waves appeared in the simulation, suggesting that the Rankine-Hugoniot jump conditions are satisfied on the shock wave. With these conditions respected, it can be seen that the discontinuity is still located at $x = 0.5$ and thus its speed still corresponds to $u_s = 0$ in the shock reference frame.

From these results, it can be concluded that the problem of conservativeness on the shock is solved by using the present HLBM-ρE model. Unfortunately, no solutions are available later in time since the computation diverged a few iterations after $t = t_c$. The oscillations generated by the shock interface are responsible for the instability of the scheme by triggering unstable waves which propagate at the flow velocity. These will be observed in more detail in the next section. The use of a higher viscosity, or a refined resolution of the domain does not stabilize the problem. This illustrates a lack of robustness of the present scheme compared to the primitive entropy based HLBM.

5.2.3 Shock tube with high pressure ratio

Here, the HLBM-ρE model is assessed on the same shock tube of Sec. 5.1.2. The numerical and physical parameters are chosen to be the same.

Fig. 5.7 compares profiles of the density, temperature, velocity and pressure obtained

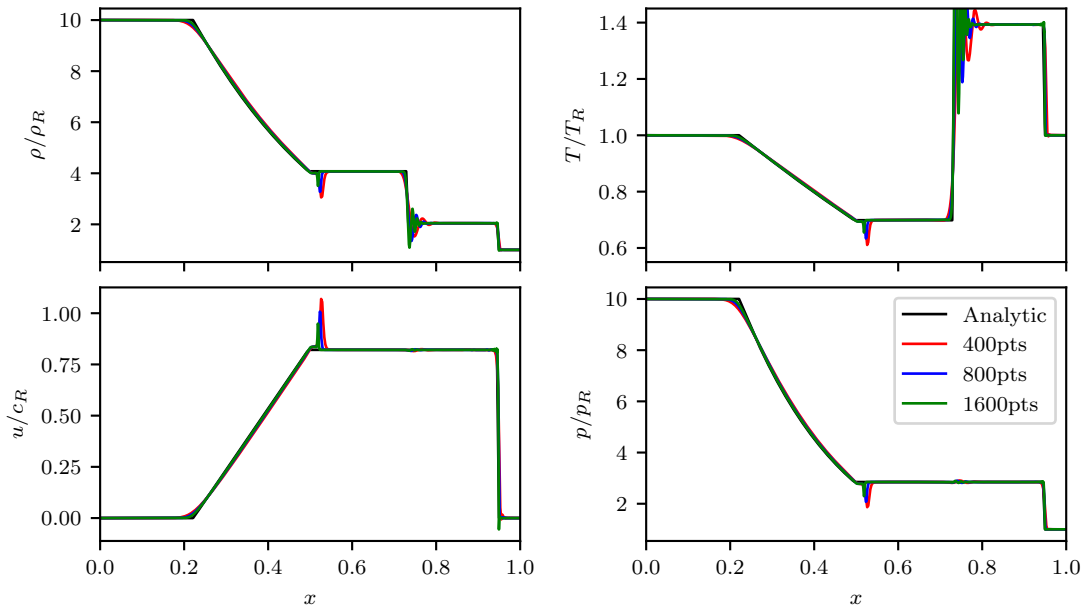

Figure 5.7 – Shock tube problem computed with the HLBM-ρE model. The present model is compared with the exact solution for different mesh resolutions.

by the hybrid scheme to the analytical solution. At first, one can notice the velocity overshoot and pressure, density, temperature undershoots appearing at $x \simeq 0.55$. These features are similar to the one observed on Fig. 5.3 for the original HLBM using the primitive variable formulation of the entropy equation. The change of energy equation and numerical scheme therefore did not solve this error. Nevertheless, as evoked in Sec. 5.1.2 this error disappears when using a tangent hyperbolic profile as initial condition or a higher value of viscosity. Next, one can observe that the correct values are retrieved by the scheme on the rarefaction wave and behind the contact discontinuity and the shock wave. More precisely, the temperature and density values behind the shock match perfectly with the analytical solution. One can therefore draw the same conclusions as for the 1D shock in Sec. 5.2.2 e.g., the conservativity issue of the HLBM scheme is fixed by using a conservative form of the energy equation.

Finally, large oscillations generated on the contact discontinuity interface can be observed on the temperature and density profiles. No blatant pressure or velocity variations can be seen in that area, which suggests that these waves carry entropic information. Actually, for long term calculations, these high frequency waves are responsible for the instability of the model as already mentioned in Sec. 5.2.2. Unfortunately, using a higher viscosity value does not change the result of the computation.

5.2.4 Two-dimensional Riemann problems

Although the model is less robust than the one based on the primitive variable formulation of the entropy equation, it still allows for two-dimensional computations. For

that purpose one considers the same two-dimentional Rimennan problem of Sec. 5.1.1 with identical numerical and physical parameters and post-processing.

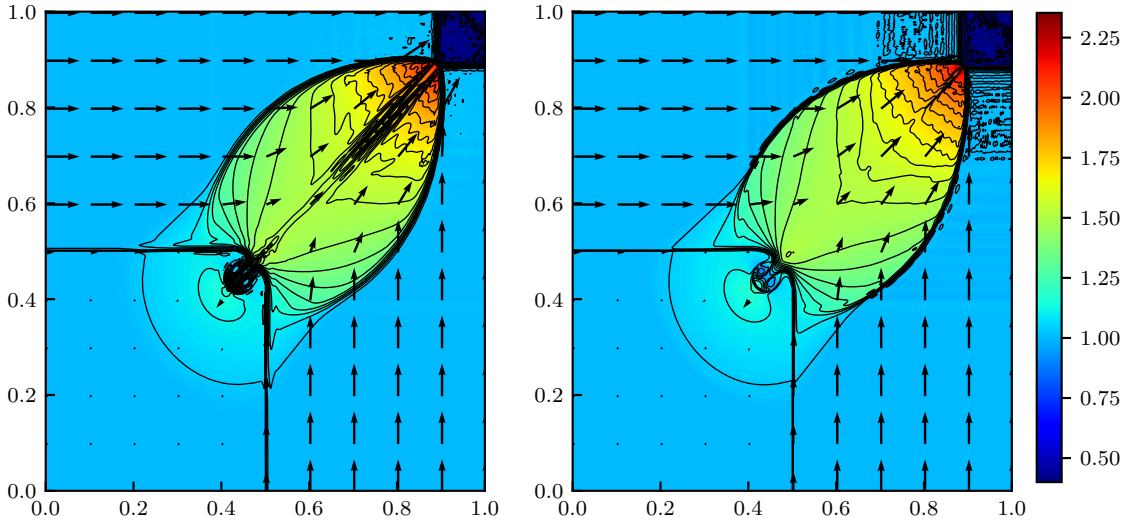

(a) Case 12 at $t = 0.25t_c$ with 30 density contours (0.54 to 1.7 step 0.04).

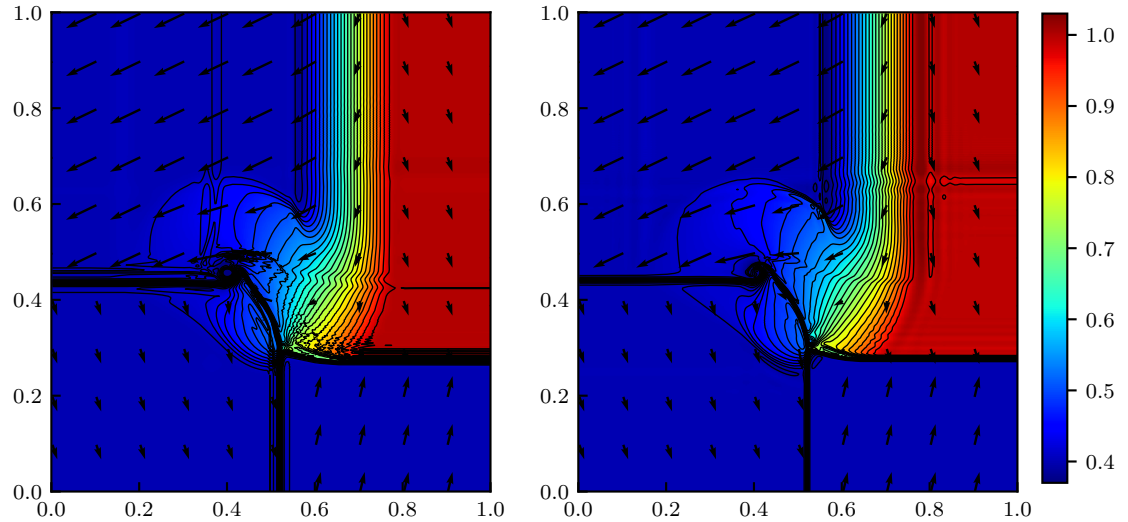

(b) Case 15 at $t = 0.2t_c$ with 29 density contours (0.43 to 0.99 step 0.02) .

Figure 5.8 – Two-dimensional Riemann problems computed with the HLBM-ρE model (left) and the HLBM-s model (right). Pressure is displayed by color, density by contours and velocity by arrows.

Fig. 5.8 compares the original HLBM-s with the present HLBM-ρE, in terms of pressure, density and velocity. On case 12, visible on Fig. 5.8a, one can see that the features of the flow are globally recovered by the HLBM-ρE model. The two shock waves propagating in the first quadrant are well captured by the scheme and generate less spurious density iso-contours compared to the HLBM-s model. This enhancement

is confirmed by considering the pressure field, where one can observe a diminution of the oscillations generated by the shock in comparison to the HLBM-s model. However, the density iso-contours between the two reflected shocks differ greatly from the ones recovered by the HLBM-s model (the latter being in agreement with the reference [204]). In addition, the two slip lines J_{32}^{+} and J_{34}^{+} are thicker compared to the HLBM-s as well as the spirals formed in the third quadrant. This feature is not surprising when one considers the unstable oscillations appearing on the contact discontinuity observed on the shock tube case of Sec.5.2.3. Indeed, the thickening on density contours corresponds actually to spurious oscillations appearing at the slip line interfaces.

For case 15 displayed on Fig. 5.8b, the HLBM-ρE model roughly reproduces the correct flow characteristics. The rarefaction wave is well captured and pressure oscillations behind the shock wave are less visible compared to the HLBM-s model. However, the two slip lines J_{34}^{+} and J_{32}^{-} of the present case look thicker in contrast to case 12. Indeed, unlike in case 12, the slip lines of case 15 propagate over the domain which scatter the oscillations generated at these interfaces. Their aspect therefore appears more spread out, but this is essentially due to spurious oscillations which bias the density iso-contours. Finally, the unique spiral appearing in the second quadrant becomes nearly invisible for the same reasons as mentioned above for case 12.

In the end, both vortical like two-dimensional structures generated by case 12 and case 15 are not accurately captured by the HLBM-ρE model. In addition to the oscillations generated on contact discontinuities, it will be shown in the next section that other phenomenon occurs when one consider smooth vortical test-case.

5.2.5 Convected and stationary isentropic vortex

Here one considers the transport of a vortical structure by computing a case of isentropic vortex convection. A $[L \times L]$ periodic domain is considered with $L = 1\,\mathrm{m}$, uniformly discretized with 200 points in each direction. The initialization is seen as a small perturbation of the mean flow and reads:

$$u_r(r) = 0 \quad \text{and} \quad u_\theta(r) = c_\infty \,\mathrm{Ma}_v \, r \exp\left(\frac{1-r^2}{2}\right), \tag{5.2.13}$$

where u_r and u_θ are respectively the radial and tangential velocity in polar coordinates and $c_\infty = \sqrt{\gamma_g r_g T_\infty}$ the mean flow speed of sound. Ma_v is the vortex Mach number and $r = \sqrt{(x-x_c)^2 + (y-y_c)^2}/R$ with R the vortex radius and (x_c, y_c) the initial position of the vortex center. For an isentropic vortex, the density and pressure fields are given by [212]:

$$\rho(r) = \rho_\infty \left[1 - \frac{\gamma_g - 1}{2}\mathrm{Ma}_v^2 r \exp\left(1 - r^2\right)\right]^{\frac{1}{\gamma_g - 1}}. \tag{5.2.14}$$

$$p(r) = p_\infty \left(\frac{\rho(r)}{\rho_\infty}\right)^{\gamma_g}. \tag{5.2.15}$$

In the present case, the vortex velocity is set in such a way that $\mathrm{Ma}_v = 0.05\,\mathrm{Ma}_\infty$, where one recalls that Ma_∞ denotes the free-stream Mach number. Finally, $R = 20\Delta x$, $T_\infty =$

300 K, p_∞ = 101325 Pa and $\rho_\infty = p_\infty/(r_g T_\infty)$. This test-case is performed with γ_g = 1.4, $\mu = 1.10^{-5}$ kg.m^{-1}.s^{-1}, σ = 0.0 and $T_r \simeq 1478$ K. The simulation is run for 6500 iterations, which corresponds to a single convective time $t_c = L/(c_\infty \mathrm{Ma}_\infty)$ with a mean advection velocity considered as $\mathrm{Ma}_\infty = 0.1$ along $\boldsymbol{e}_x$. For the purposes of the study, one additional stationary case ($\mathrm{Ma}_\infty = 0$) is also computed by the HLBM-ρE model for the same number of iterations of the convected one.

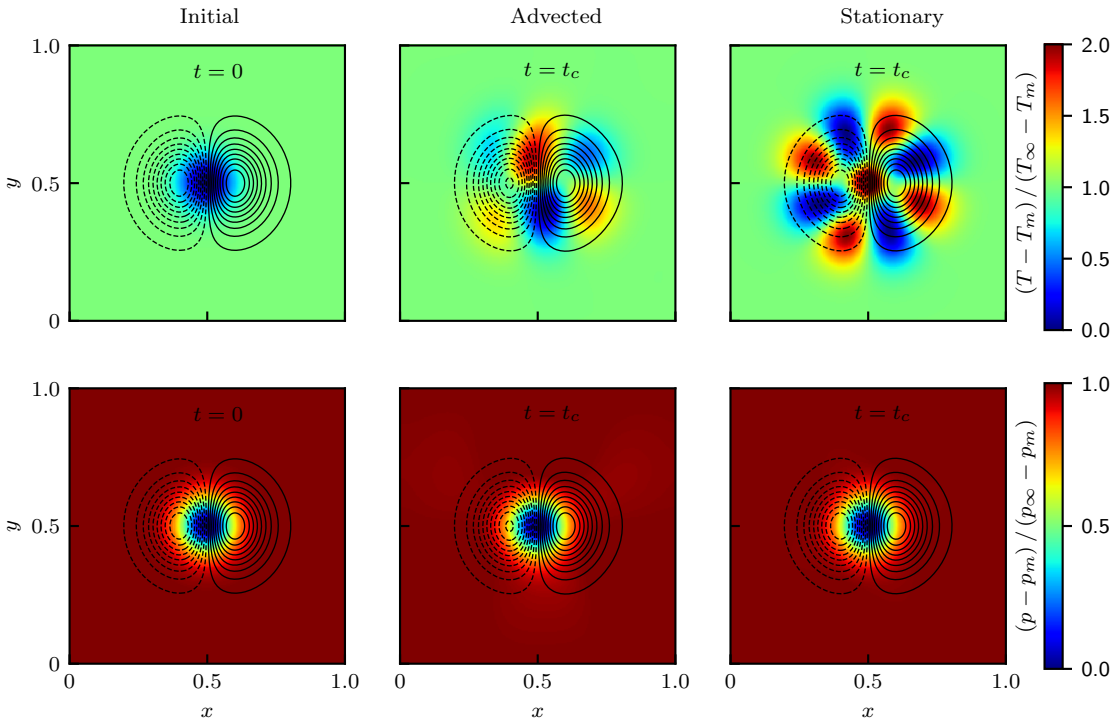

Figure 5.9 – Isentropic vortex convection computed with the HLBM-ρE model. Reduced temperature (top row) and pressure (bottom row) fields are displayed by color. T_m and p_m are respectively the minimum values of temperature and pressure of the initial state. Contours of u_y are superimposed on the two fields ($u_y < 0$ in dashed lines; $u_y > 0$ in solid lines).

Fig. 5.9 displays maps of reduced temperature (top row) and pressure (bottom row) for $t = 0$ and after one convective time $t = t_c$. Iso-contours of u_y are superimposed on the two fields. From left to right column: the solution at $t = 0$, the convected solution at $t = t_c$ and the stationary solution at $t = t_c$. Let's remembers that the reference solution corresponds to the solution at $t = 0$ for this test-case.

Considering first the u_y contours and the pressure fields of the convected and stationary cases, they are both found in good agreement with the reference solution. No noticeable distortion of the velocity field is observed which is also true for the pressure field. Indeed, no dispersion, dissipation or spurious acoustic waves are observed, and one can deduce that the model seems to accuratly reproduce the physics of both stationary and convected cases.

However, upon examining the temperature field, the previous deductions appear to be wrong for both stationary and advected cases. On this field one would expect a similar map as in the initial state (with perhaps, a small amount of dissipation), which is absolutely not the case. Instead, one can observe large deformations of the temperature field involving sinks and sources. A similar phenomenon, in inverse proportion, is also noticed on the density field as a consequence of the perfect gas coupling equation of state. Thus, based on the evolution of thermodynamic variables, one can conclude that unintended entropy waves are generated by the system, a totally unexpected feature for an isentropic test-case. Finally, the differences of temperature patterns between the stationary and advected cases can be attributed to the numerical dispersion and dissipation of the HLLC scheme.

5.2.6 Conclusion

In Sec. 5.1, the conservativity problems of the HLBM-s model at the shock wave interface have been attributed to the type of energy equation used. It was therefore chosen in this section to replace the entropy equation in primitive form with a total energy equation in conservative form. This energy equation was discretized using the approximate Riemann HLLC solver, as this proved to be the only stable scheme on this energy equation among the few other schemes tested by the author. The HLBM-ρE model thus obtained was then tested on different test cases.

On the one-dimensional stationary shock in Sec. 5.2.2, the new HLBM-ρE model proved to recover the correct physics in terms of shock speed and shocked values on the discontinuity. This test case confirmed that the problem of conservativeness comes from the energy part and not from the LBM part of the model. However, the scheme proved to be more unstable than its HLBM-s counterpart due to unstable waves generated on the shock which propagate at flow velocity in the numerical domain. These unstable waves were subsequently detected on the contact discontinuity of the shock tube case of Sec. 5.2.3. They were identified as entropic waves and were found to be amplified in time to eventually destabilize the computation for longer simulation times. Nevertheless, to simulate the shock wave of this test-case, this model has been found superior to its HLBM-s counterpart as it captured the correct temperature and density values behind this discontinuity. The HLBM-ρE was finally tested on two-dimensional Riemann problems in Sec. 5.2.4 and compared to the HLBM-s. The correct fluid behavior has been retrieved in a general way, although entropic oscillations similar to the ones observed in the shock tube case were observed on the slip-lines. This phenomenon biased the two-dimensional structures created by the slip line interaction making the results of the HLBM-ρE less satisfactory than those obtained by the HLBM-s model. Finally the model has been assessed on a smooth flow test-case in Sec. 5.2.5 involving the simulation of a stationary and a convected isentropic vortex. The aerodynamic variables computed with the HLBM-ρE model were in agreement with the reference, however spurious entropy waves were generated by the system. Finally, it is worth noting that the HLBM-ρE proved to correctly recover the acoustic propagation physics, but was not shown here for the sake of brevity.

There is therefore no doubt that the HLBM-ρE model built on the the conservative form of total energy equation is far superior for simulating shocks compared to the HLBM-s model. However, this model suffers from two flaws:

- A lack of robustness.

- A spurious entropy generation at contact discontinuity interfaces and for test cases involving shear.

The first point could be eventually addressed by using another type of numerical scheme to discretize the energy equation, while the second point is actually lot more challenging to solve. Indeed, it will be shown later in Chap. 6 (Sec. 6.6.1), that through an enhanced von Neumann analysis, the latter issue is in fact related to a mode transfer from the shear to entropy mode. Based on our observations, the cause of this transfer is independent of the numerical scheme discretizing the energy equation, or of the energy variable (s,e,E), but is essentially related to the use of the conservative formulation of the energy equation.

At this point, one might ask oneself why not take advantage of the HLBM-ρE model only in a localized manner e.g., solely on a few points to model shocks, and use the HLBM-s model everywhere else? This option unfortunately does not work because the mode coupling phenomenon is way too intense, even when applying the HLBM-ρE on a few points. Fig. 5.10 illustrates such case by showing four snapshots at different times of a simulation of a convected isentropic vortex in a smooth flow. The temperature in the domain is predominantly computed using the primitive entropy equation similarly to the HLBM-s, while the latter is obtained on only a few points using the conservative form of the total energy equation in the same vein as the HLBM-ρE. The LBM kernel is identical for both regions, the only difference is thus how T is obtained. One can observe that the simulation runs correctly up to $t = t_1$, but at $t = t_2$ as soon as the vortex enters the region that is computed by the HLBM-ρE model, strong mode transfer phenomena appear. The physical solution is therefore ultimately biased once the vortex passed through this region which makes the solution impractical.

In conclusion, although the use of a total energy equation in conservative form is the most natural option to remedy the conservativity problem on shocks, the issues engendered by the latter unfortunately makes it unworkable. In spite of many efforts, the use of the conservative form of the total energy equation is not a viable choice in the present HLBM framework.

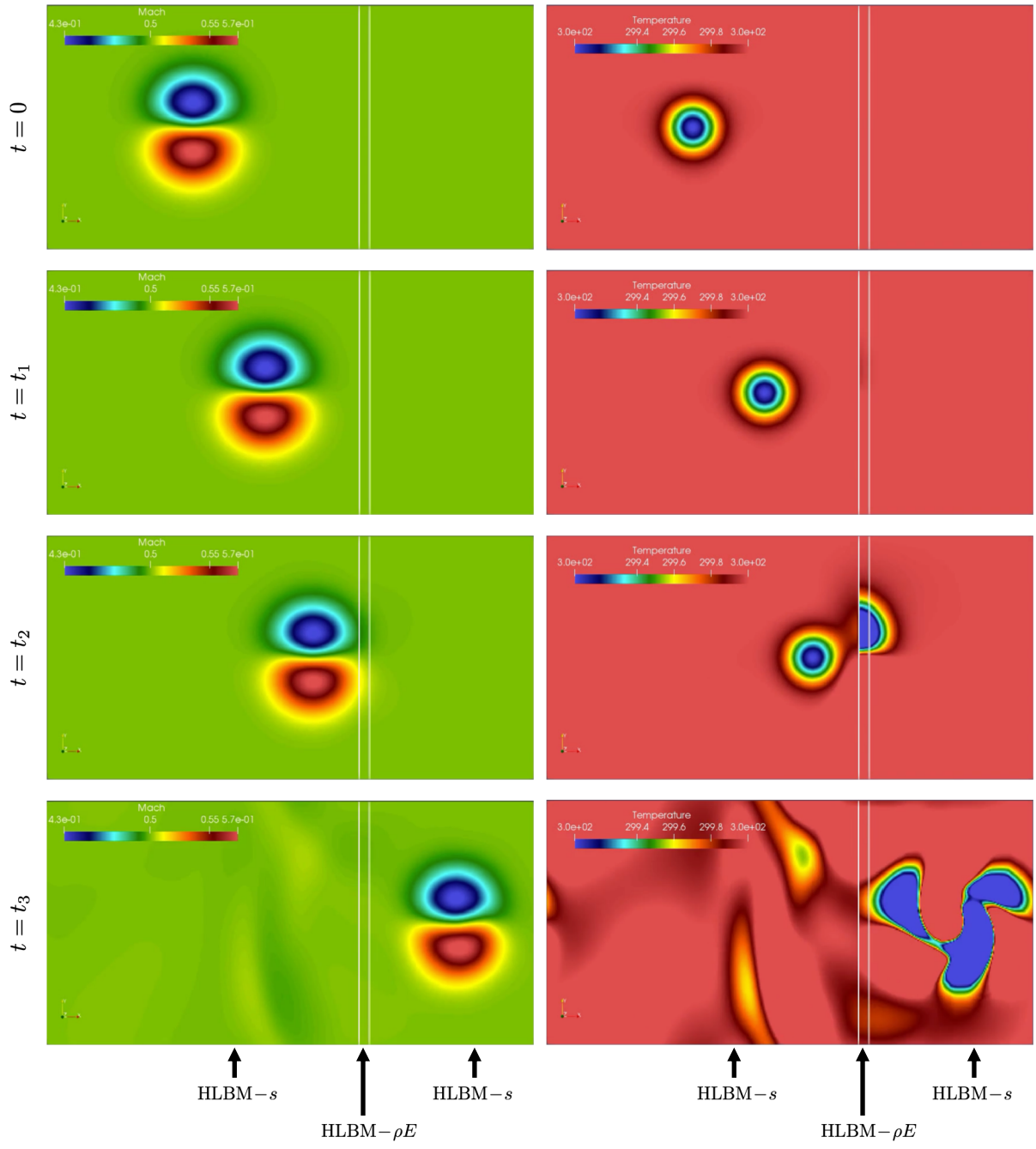

Figure 5.10 – Snapshots of Mach (left) and temperature (right) fields of an isentropic vortex convected at $\mathrm{Ma}_\infty = 0.5$ in a periodic domain of twice the width of the one described in Sec. 5.2.5. The solution is computed using the HLBM-s, and the HLBM-ρE is used locally between the two white lines which represents a distance of $10\Delta x$ positioned at $x = 1.275\,\mathrm{m}$. For $t = t_1$ one can see the correct transport of the temperature field by the HLBM-s model. As soon as the velocity field enters in the HLBM-ρE zone for $t = t_3$, the temperature field of the vortex is deformed in a similar way as seen on Fig. 5.9, while the velocity field (represented by the mach number) remains almost unchanged.

5.3 HLBM with artificial viscosity

We established in the previous section that the conservative form of the energy differential equation should be solved to get better solutions across shock waves. However, this strategy has proven to be less stable than the original HLBM-s, and provides non-physical solutions due to mode transfers, thus making it unusable in its current form. So far, in the absence of shocks, the best choice of energy equation remains the primitive form of the entropy equation in terms of stability and accuracy. In this section, an alternative approach is therefore proposed to solve the conservativity problems while keeping the entropy energy formulation.

For most of the numerical schemes for fluid dynamic, an artificial viscosity is needed to automatically capture the shock wave without explicitly solving the discontinuity [207]. For some of the methods, this viscosity is built in, and corresponds in fact to numerical dissipation induced by the leading order of the truncation error of the numerical scheme. For instance, it is well known that when considering a first-order upwind scheme, the truncation error induces a numerical viscosity of the order of $\mathcal{O}(\Delta x)$ [166] having the effect of dissipating a discontinuity. For instance, it is in that vein that TVD schemes have been developed, where using limiter functions, the accuracy of the numerical scheme is reduced to first-order at shocks to suppress the oscillations. It is also the case for more elaborated schemes, such as WENO schemes, where dissipation is added from their locally adaptative stencil [213] to avoid interpolation across discontinuities. However, for other numerical methods, the artificial viscosity can be explicitly added using dissipative source terms in the momentum and energy equation [135]. For both strategies, these implicit/explicit artificial diffusive terms aim to spread shockwaves to a thickness comparable to the local mesh spacing so that the numerical scheme is able to solve it, reducing at the same time the spurious (Gibbs) oscillations on the discontinuity. Finally, it is worth noting that the introduction of artificial viscosity is a common practice in the LBM field especially for compressible entropic LBM models. This method is called an entropic stabilizer and aims to obtain stable simulations in the low-viscosity limit and for the simulation of flows with discontinuities [66, 164].

Here, one proposes to study how the artificial viscosity impacts the simulation of shocks using the HLBM-s. It will be seen that, in addition to spreading the solution over more points, and thus suppressing the spurious oscillations on the shock, the injection of artificial viscosity will increase the heat production by means of the source terms included in the entropy equation. Using this approach it will be shown that it is possible to override the conservervativity issue of the HLBM-s.

5.3.1 Definition of the problem

At first, it is worth recalling the energy equation formula used by the model:

$$\frac{\partial s}{\partial t} + u_\alpha \frac{\partial s}{\partial x_\alpha} = \frac{\mu}{\rho T} \underbrace{\left[\underbrace{\frac{c_p}{\mathrm{Pr}} \frac{\partial^2 T}{\partial x_\alpha^2}}_{\text{Fourier}} + \underbrace{\frac{\partial u_\alpha}{\partial x_\beta} \left(\frac{\partial u_\alpha}{\partial x_\beta} + \frac{\partial u_\beta}{\partial x_\alpha} - \frac{2}{D} \frac{\partial u_\gamma}{\partial x_\gamma} \delta_{\alpha\beta} \right)}_{\text{viscous heat}} \right]}_{\text{entropic viscous sources}}. \tag{5.3.1}$$

From this equation, it clearly appears that in the limit of vanishing viscosity (r.h.s of the equation is equal to zero), the entropy variable is just a conserved quantity advected through the flow field. This statement is also valid for the conservative formulation of the equation which reads:

$$\frac{\partial \rho s}{\partial t} + \frac{\partial \rho u_\alpha s}{\partial x_\alpha} = \frac{\mu}{T} \left[\frac{c_p}{\mathrm{Pr}} \frac{\partial^2 T}{\partial x_\alpha^2} + \frac{\partial u_\alpha}{\partial x_\beta} \left(\frac{\partial u_\alpha}{\partial x_\beta} + \frac{\partial u_\beta}{\partial x_\alpha} - \frac{2}{D} \frac{\partial u_\gamma}{\partial x_\gamma} \delta_{\alpha\beta} \right) \right]. \tag{5.3.2}$$

However, in the presence of shock waves, mechanical energy is transformed into heat and this results in the production of entropy. Thus, the entropy conservation no longer holds even in the limit of vanishing viscosity ($\mu \to 0$) [207], and therefore one can see that Eq. 5.3.1 in this context, simply does not have adequate source terms to model any entropy production, and that even on a shock. This is part of the problem of working with a quantity s which is not conserved similarly to ρ, ρu_α and ρE. For a more theoretical understanding of the production of entropy on shock, we refer the reader to the following literature [214–216].

Thus as pointed-out by Salas et al. [214] although the entropy propagation equation can be expressed in the form of a conservation law, it cannot be used to obtain the correct entropy jump across a shock wave. Nevertheless, if one still wants to keep this equation, it must be somehow modified with a source term located on the shock discontinuity [215] to model the correct physics of a shock.

5.3.2 Correcting the physics using the viscous terms

The purpose of this section is to determine the feasibility of modeling entropy production on the shock, using the source terms that are naturally present in Eq. (5.3.1). It boils down to the addition of an artificial viscosity μ_{art} in the numerical scheme, and which is called second-order viscosity since it will act on second-order spatial derivatives. Here, one considers the same shock tube of Sec. 5.1.2 computed with the HLBM-s model for three different values of viscosity namely $\mu \in [1 \cdot 10^{-5}, 2 \cdot 10^{-1}, 8 \cdot 10^{-1}]$ kg.m^{-1}.s^{-1} . As this test case is essentially inviscid, one can interpret the viscosity μ directly as an artificial viscosity μ_{art}.

Fig. 5.11 shows different profiles obtained with the HLBM-s for different viscosity values. At first, one can clearly observe on the profiles of Fig. 5.11a, that the overshoot

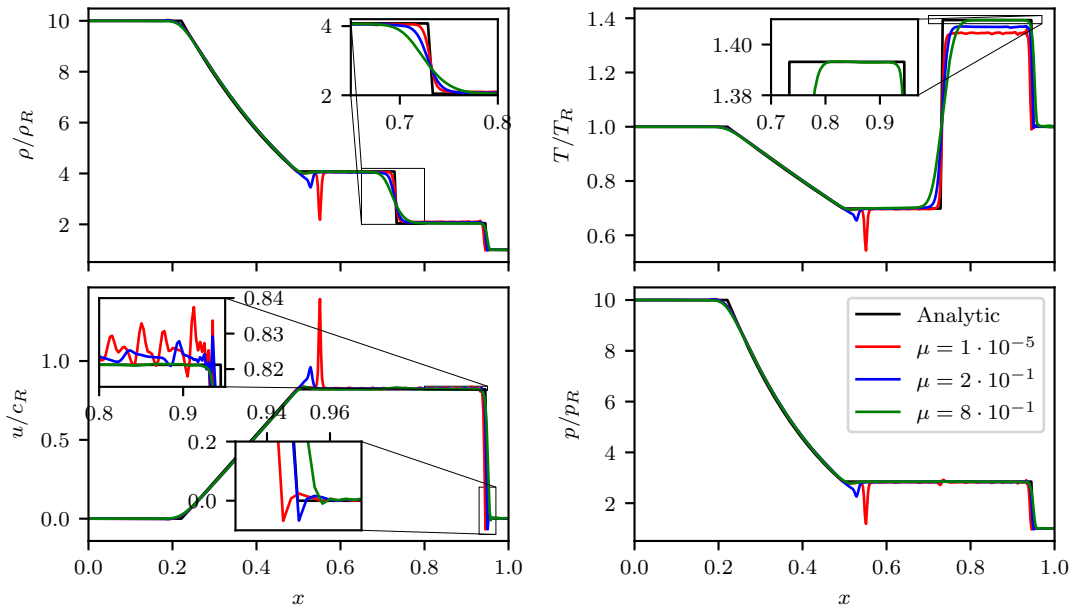

(a) Density, temperature, velocity and pressure profiles.

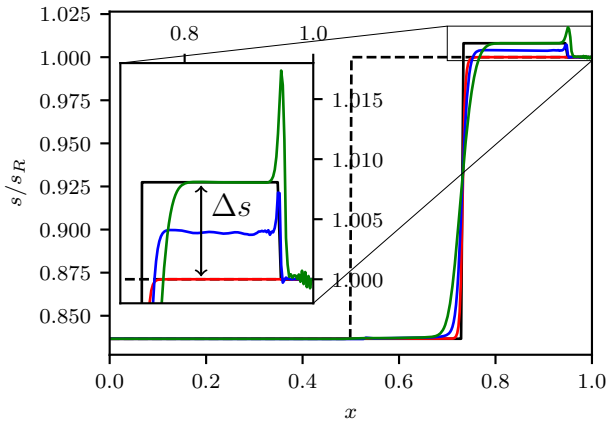

(b) Entropy profile with a zoom on the entropy production region. The dotted line corresponds to the initial profile of entropy (i.e., at $t = 0$), and Δs corresponds to the entropy generated on the shock.

Figure 5.11 – Shock tube problem computed with the HLBM-s model for different viscosity values and compared with the reference solution. Both sub-figures share the same legend, and the viscosity μ is in $\mathrm{kg.m^{-1}.s^{-1}}$.

appearing at $x \simeq 0.55$ reduces significantly as the viscosity increases, until it almost disappears for the highest viscosity value $\mu = 8 \cdot 10^{-1}\,\mathrm{kg.m^{-1}.s^{-1}}$. Next, it can be seen from the velocity profile on the bottom zoomed region that the undershoot on the shock wave is significantly reduced thanks to the artificial viscosity. This ultimately impacts the spurious oscillations generated on the shock, as one can seen on the top zoomed region,

which completely disappear at the highest viscosity value. However, looking at the density and temperature profiles, one can see a clear degradation of the contact discontinuity with respect to the reference which is much more spread out for high viscosity values. Finally, regarding the rarefaction wave, the artificial viscosity does not have a noticeable impact on the results.

By looking now at the temperature profile just behind the shock, one can see that the most viscous case ($\mu = 8 \cdot 10^{-1}\,\mathrm{kg.m^{-1}.s^{-1}}$) is found to be in good agreement with the reference, while a temperature loss is observed for $\mu = 2 \cdot 10^{-1}\,\mathrm{kg.m^{-1}.s^{-1}}$, which becomes even more striking for the $\mu = 1 \cdot 10^{-5}\,\mathrm{kg.m^{-1}.s^{-1}}$ case as already noticed in Sec. 5.1.2. So the greater is the viscosity, the closer the calculated solution is to the reference solution.

Let's consider now the entropy profile of Fig. 5.11b. In a first step, the analytical solution at final time (solid line) can be compared with the initial solution (dotted line). Two phenomena can be clearly identified: (1) an advection of the entropy profile at the same flow velocity (corresponding to the contact discontinuity), and (2) an entropy production on the shock wave (represented by Δs on the figure) reflecting the irreversible nature of the process. For the viscosity value $\mu = 1 \cdot 10^{-5}\,\mathrm{kg.m^{-1}.s^{-1}}$, one can see that the solution corresponds to the initial entropy profile which has been only advected by the flow generated by the shock wave. In the zoomed area, the post-shock value corresponds to the initial right state value, reflecting the fact that almost no entropy production occurred on the shock. Therefore, with this viscosity value, the problem reduces to a simple advection of the initial entropy profile without any source of irreversibility on the shock, which is in agreement with Eq. (5.3.1) when $\mu \to 0$, but which is far from being the expected solution. For the higher values of viscosity, one can observe a non-zero entropy production on the shock wave, which increases with the viscosity value. In the present test-case, for the particular value of $\mu = 8 \cdot 10^{-1}\,\mathrm{kg.m^{-1}.s^{-1}}$, one can observe that the entropy source term allows for the post-shock entropy to be perfectly matched with the reference solution, which results in the correct temperature profile as seen on Fig. 5.11a.

Finally from Eq. 5.3.1, the mechanism of the artificial entropy production on the shock can be interpreted as follow:

- The viscous heat term generates the entropy source on the shock due to the irregular solution of the velocity.

- The Fourier term subsequently smears the heat source generated on shock.

Thus, as expected, using an artificial second-order viscosity makes it possible to produce entropy locally on the shock through the viscous terms already present in the entropy equation. It allows to artificially recover the correct solution on shock and to cure the conservativeness issue of the HLBM-s. However, it has been shown that if the artificial viscosity is added uniformly in the calculation, it results in a bias of the physics elsewhere than on the shock e.g., the smearing of the contact discontinuity on Fig. 5.11a. It would then be interesting to introduce this numerical viscosity only on the shock wave in order to preserve the accuracy of the scheme in the smooth regions.

5.3.3 Guided artificial viscosity through Jameson-like shock sensor

In the previous section, it was observed that the artificial viscosity is a necessary ingredient to get a correct jump of entropy across a shock using the HLBM-s model. This second-order artificial viscosity also allows to smear the solution on the discontinuities suppressing the spurious oscillations generated at these interfaces. However, to preserve the smooth part of the solution, one has to introduce the smearing mechanism (i.e., the increase of the viscosity) only on the shock region.

For that purpose, and using the same approach proposed in the thesis of C. Coreixas [37], a Jameson-like sensor [217] will be used to locally add the second-order artificial viscosity. Following [37] and according to [218] this viscosity is related to the normalized pressure Laplacian and reads in one dimension:

$$\mu_{art} = A_J \frac{|p_{x+\Delta x} - 2p_x + p_{x-\Delta x}|}{|p_{x+\Delta x}| + 2|p_x| + |p_{x-\Delta x}|}. \tag{5.3.3}$$

The A_J coefficient is a free parameter which is usually set to the order of unity [217,218], and its influence will be studied in the following. This second-order artificial viscosity is subsequently included in the LBM part through the redefinition of the discrete relaxation time:

$$\check{\tau} = \frac{\mu}{p} + \frac{\Delta t}{2}, \quad \text{with} \quad \mu = \mu_\phi + \mu_{art}, \tag{5.3.4}$$

where the viscosity μ used in the HLBM-s model is redefined as the sum of the physical viscosity μ_ϕ and the artificial viscosity μ_{art}. It is worth noting that this approach differs on two points compared to the original Jameson scheme[2] [218]: (1) the former only introduces a second-order artificial viscosity where the original scheme also introduce a fourth order artificial viscosity[3], and (2) the artificial dissipation terms are only included in the momentum and energy equations where the original approach introduces one as well into the mass equation.

To assess the present approach, one considers exactly the same shock tube of the previous section 5.3.2 with zero physical viscosity $\mu_\phi = 0$ to study only the impact of the artificial viscosity on the results. In the following, the optimal viscosity found in Sec. 5.3.2 is considered as a reference viscosity $\mu_0 = 8 \cdot 10^{-1}$ for the purpose of comparison.

One can examine Fig. 5.12 to study the influence of the sensor for three different values of $A_J \in [1.0, 2.5, 5.0]$ for a numerical domain discretized on 400 cells. By looking at pressure and viscosity profiles, it can be clearly observed that the sensor applies artificial viscosity where it is required, i.e, near discontinuities and especially near the shock wave. For high values of A_j, the overshoots/undershoots located around $x \simeq 0.55$ are reduced. Moreover, if one compares the present results to Fig. 5.11a, one can observe that the sensor greatly reduces the smearing of the contact discontinuity, significantly

[2] Also called JST scheme after its authors A. Jameson, W. Schmidt and E. Turkel.

[3] In the same way as a second-order artificial viscosity acts on second-order spatial derivatives, a fourth-order artificial viscosity applies to fourth-order derivatives.

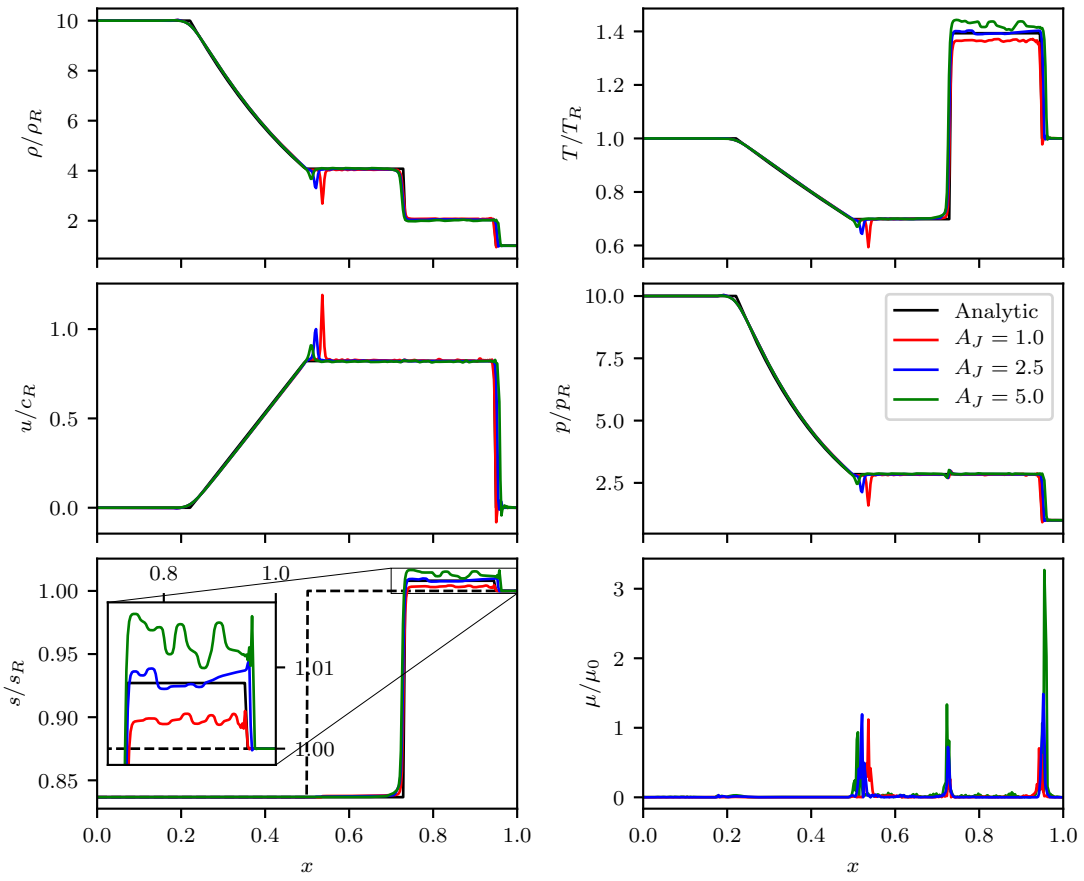

Figure 5.12 – Shock tube problem computed with the HLBM-s model on 400 cells. The present model is compared with the exact solution for different constant values A_J.

improving results. Considering now the temperature and entropy profiles, optimal results are obtained for $A_J = 2.5$ where $\mu/\mu_0 \simeq 1$ on the shock, and corresponds to the optimum viscosity value found in the previous section on Fig. 5.11a. For other choices of A_J, the entropy production at the shock is either too much or too little which deviates the temperature profiles from the original solution.

Fig. 5.13 shows the influence of the mesh resolution using the ad hoc value of $A_J = 2.5$. By looking at the temperature and entropy profiles situated just behind the shock, one can observe a slight deviation depending on the discretization of the domain. Although these deviations are smaller than those observed by varying the A_J constant as seen on Fig. 5.12, the fact remains that the production of entropy at the shock is affected by mesh size.

In conclusion, it has been shown that locally introducing an artificial viscosity via a shock sensor potentially allows to introduce the source of entropy required to compensate for the model's conservativeness defects. However, the subtlety of this method lies in the fact of introducing the correct source of entropy on the shock. Adding an overly large or overly small entropy source will lead to the wrong solution.

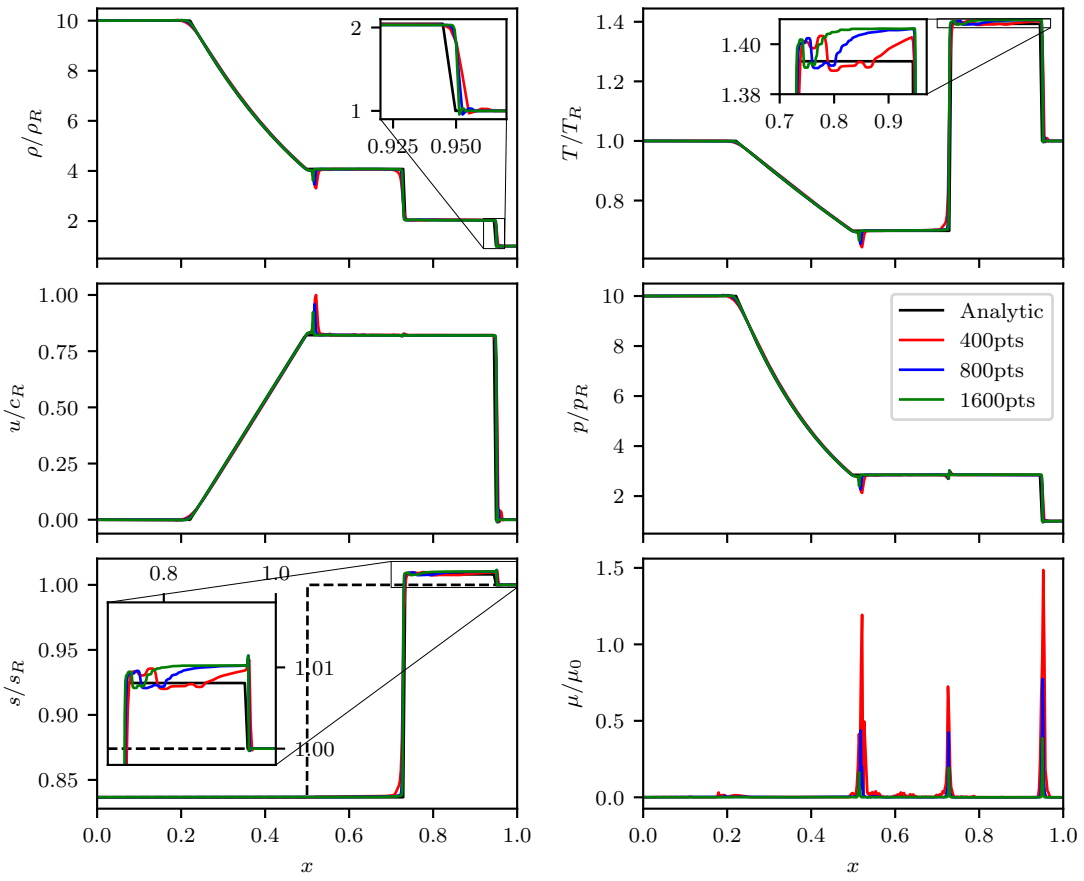

Figure 5.13 – Shock tube problem computed with the HLBM-s model using the ad hoc choice of $A_J = 2.5$. The present model is compared with the exact solution for different mesh resolutions.

5.3.4 Discussion

While the artificial viscosity is usually employed to suppress spurious oscillations on shocks [37, 217, 218], in the present work it has been shown that it can also be used to obtain the correct shock physics when considering the HLBM-s scheme. Using the viscous terms present in the entropy equation, the numerical viscosity coupled to a shock sensor allows to generate an adequate source of entropy localized on the shock. This entropy source counterbalances the damaging effects of the non-conservative nature of the scheme. Also, it can be hinted that the magnitude of the entropy source, controlled by μ_{art}, depends on the physical problem under consideration (e.g., the strength of the shock, the heat capacity ratio, the physical viscosity...) and potentially on numerical parameters such as mesh size. The development of a model based on this approach must therefore take into account a wide variety of cases to obtain the adequate entropy generation on the shock via the source terms. In fact, it can be found in the CFD literature that for non-conservative system, the correct shock relations can be recovered using viscous

terms [208]. For instance, while not eliminating conservation error entirely, Karni [209] successfully tested viscous correction terms on shock tube cases for schemes discretizing primitive form of the one-dimensional isothermal Euler equations. This viscous correction term is derived from the difference between the viscous leading error terms of the equivalent equations of the conservative system and those of the primitive system. Eventually, the same methodology could be applied in the present context and is left for a futur work. Finally, it should be kept in mind that what is being presented is only a proof of concept, no formal mathematical demonstration or proof has been shown regarding the convergence of this technique applied to the HLBM-s scheme.

In the present work, one used a pragmatic approach which consists of considering a second-order artificial viscosity acting on all the viscous terms of both momentum and entropy equation (5.3.1). However, an alternative approach exists where only a single bulk term is added into these two equations. This strategy can be found in the HLBM literature for compressible models based on the entropy equation. To the best of the author's knowledge, Nie and co-workers [150] were actually the first to introduce entropic source terms using artificial bulk viscosity to get a correct jump of entropy across a shock. They introduced the following bulk source terms:

$$\Phi = \mu_{art}\left(\frac{\partial u_\gamma}{\partial x_\gamma}\right)^2 \quad \text{and} \quad F_{diss,\alpha} = \frac{\partial}{\partial x_\alpha}\left(\mu_{art}\frac{\partial u_\gamma}{\partial x_\gamma}\right), \tag{5.3.5}$$

respectively in the entropy equation and in the α component of the momentum equation, where one can remark that the source term Φ is similar in nature to the viscous heat production term already present in the entropy equation (5.3.1). In their work, they choose an artificial viscosity μ_{art} that was proportional to the pressure gradient which reads in 1D:

$$\frac{\mu_{art}}{\rho} = a_1\left(r_g,\gamma\right)\rho\frac{|p_{i+1}-p_{i-1}|}{p_{i+1}+p_{i-1}}, \tag{5.3.6}$$

and where the value of the coefficient function $a_1(r_g,\gamma_g)$ has been determined by a series of numerical simulations of Sod test cases for different gas constants r_g and heat capacity ratios γ_g.

Infinite possibilities can be envisaged to improve this method such as: the use of other forms of entropy source terms, other types of shock sensors relying on other macroscopic quantities than the pressure[4] or exploiting the LBM part using kinetic sensors in a similar way of [66], replacing A_J with a polynomial function in the manner of [150] and using various arguments such as local viscosity[5], mesh size and so on. Concerning the last point, an interesting approach would be the use of uncertainty quantification, using for example canonical cases such as shock tube or stationary shock wave test case, in the aims of building a surrogate model to introduce the correct amount of entropic source.

[4]Except when using bulk terms in a similar way than [150], it is worth noting that sensors based on the first or second-order derivative of the pressure are not perfectly adapted for the simulation of compressible turbulent flows. Indeed, the latter will introduce artificial dissipation on vortical turbulent structures in a same manner as on shocks.

[5]For RANS or LES computations the viscosity may also vary locally which will influence the entropy production.

Here, the focus was put on the problem related to conservativeness with the help of artificial viscosity. Nevertheless, it goes without saying that a further study of this method could be carried out in order to more effectively suppress oscillations and overshoots on the results, which is one of the primary purposes of artificial viscosity.

As the purpose of this section was to show the existence of an alternative to the use of the conservative total energy equation studied in Sec. 5.2, the evaluation and use of these methods is left to further work.

5.4 Conclusion

In this chapter, the conservativity issue on shocks of the HLBM-s model has been presented. It was firstly attributed to the primitive formulation of the entropy equation, but it later turned out that this defect was in fact due to the use of the entropy variable itself, which is not a conserved quantity. Even put in the conservation form, this equation cannot be used to obtain the correct entropy jump across a shock wave [214], causing a conservativity issue on this type of discontinuity. The natural remedy of this conservativeness issue was the development of a HLBM-ρE scheme based on the conservative total energy equation. Although this new scheme solved the conservativity issue, it turned out to be less robust than the HLBM-s in terms of numerical stability. In addition, it has been observed that using a conservative formulation creates mode transfers between the shear and entropy waves, unfortunatly making the model unusable in its current form. The instability and mode transfert related to such conservative HLBM scheme will be further investigated in the next chapter 6.

It is known in the literature [219, 220] that the entropy equation allows to achieve an efficient implicit treatment of the acoustic terms, and also yield benefits in terms of increased robustness as compared to algorithms solving for the energy equation. To address the conservatity issue while keeping this equation, a methodology consisting in the introduction of additional entropic source terms has been presented. Through the introduction of an appropriate second-order artificial viscosity, it has been shown that the correct entropy production can be recovered on shock, and somehow correcting the conservativity issue. Thus, the use of the primitive entropy equation is not a roadblock for transonic or supersonic applications since, provided that a sufficient source of entropy is introduced at the shock, the correct shock behavior can be recovered. Even though it may seem like a do-it-yourself method, it has been employed in industry [150], and proved its viability for cases containing shocks through several communications [150, 153, 159].

Finally, from the observations made in the present chapter, it is worth noting that the conservativity error of the model can be difficult to notice when:

1. the strength of the shock is relatively weak,

2. the simulation time is small,

3. low Reynolds cases (with high values of viscosity) are computed.

This explains why it is possible to carry out test cases containing shocks without necessarily noticing these conservativeness problems, such as the shock-vortex interaction (gathering points 1,2 and 3) or the shock tube case (gathering points 1 and 2) seen in Chapter 4 Sec. 4.5.3 and Sec. 4.5.2 respectively.

Chapter 6

Linear Stability Analysis of the HLBM

Contents

6.1 Introduction . . . 188
6.2 Hybrid Lattice Boltzmann Method . . . 189
6.2.1 Corrected Discrete Velocity Boltzmann Equation . . . 190
6.2.2 Energy equation . . . 191
6.2.3 LBM with corrective terms . . . 192
6.2.4 Discrete energy equation . . . 193
6.3 The linear stability analysis . . . 194
6.3.1 Method and concept . . . 194
6.3.2 Comments on the corrected athermal DVBE LSA . . . 196
6.3.3 Von Neumann analysis of the athermal LBM schemes . . . 198
6.3.4 Two-dimensional LBM instabilities . . . 203
6.4 Extended linear analyses of the hybrid systems . . . 206
6.4.1 Method and concepts . . . 206
6.4.2 Linear analysis of the HDVBE . . . 209
6.4.3 Von Neumann analysis of the HLBM scheme . . . 211
6.5 Linear investigations of the HLBM scheme . . . 215
6.5.1 Stability results of various HLBM classes . . . 215
6.5.2 Stability range of HLBM entropic classes . . . 217
6.6 LBM coupled with an entropy equation . . . 219
6.6.1 Conservative form: shear-to-entropy production . . . 219
6.6.2 Primitive form: entropy-to-shear production . . . 224
6.7 Conclusion . . . 228

In this chapter, an original spectral study of the compressible HLBM on standard lattice is proposed. This work aims at answering some questions regarding the numerical stability of such models, which strongly depends on the choice of numerical parameters. To this extent, several one-and two-dimensional HLBM classes based on different energy variables, variable formulation (primitive or conservative), collision terms and numerical schemes are scrutinized. Once appropriate corrective terms introduced, it is shown that all continuous HLBM classes recover the Navier-Stokes Fourier behavior in the linear approximation. However, striking differences arise between HLBM classes when their discrete counterparts are analyzed. Multiple instability mechanisms arising at relatively high Mach number are pointed out and two exhaustive stabilization strategies are introduced: (1) decreasing the time step by changing the reference temperature T_{ref} and (2) introducing a controllable numerical dissipation σ via the collision operator. A complete parametric study reveals that only HLBM classes based on the primitive and conservative entropy equations are found usable for compressible applications. Finally, an innovative study of the macroscopic modal composition of the entropy classes is conducted. Through this study, two original phenomena, referred to shear-to-entropy and entropy-to-shear transfers, are highlighted and confirmed on standard two-dimensional test cases.

6.1 Introduction

In Chapter 4, a stable HLBM based on standard lattices and able to recover the full set of compressible Navier-Stokes equations, has been presented. However, building such a scheme to perform a stable simulation relies on a large number of parameters such as a reference temperature, a numerical criterion in the HRR model or the discretization scheme adopted in the computation of spatial gradients etc. Up to now, an optimal choice of parameters has only been possible by empirical conclusions drawn on several test cases, and no clear reason that makes a HLBM model more robust that another has been proposed yet. As an example, no convincing explanation has been provided so far regarding the variable adopted in the energy equation (temperature, entropy, internal or total energy,...), as well as its form (primitive or conservative). There is some evidence that the effect of any of these parameters is driven by the numerics, which makes the understanding of these phenomena very difficult.

Precisely, the linear stability analysis (LSA), initially proposed by von Neumann [174], can be systematically employed to exhibit the numerical properties of a given scheme. It relies on the resolution of an eigenvalue problem to obtain the dispersion and dissipation rates of plane monochromatic waves in the linear approximation. This methodology was first applied to the LBM by Sterling and Chen [221]. Their work paved the way to numerous other studies aiming to shed light on the impact of collision operators [23], to exhibit the low-dissipative properties of the LBM for the aeroacoustics [62], to optimize a choice of numerical parameters [23, 83, 84, 222, 223], to exhibit the spurious noise generated at grid refinement interfaces [193], or to investigate the effect of the reference temperature for isothermal flows [224]. All these publications illustrate the interests of performing a

spectral study of the LBM, which strips off the scheme and exposes it numerical properties. Nevertheless, up the the authors' knowledge, only Siebert *et. al* [24] applied this methodology to exhibit the stability of thermal LBM, and for SDF-MS models only.

The aim of the present Chapter is to perform such analyses of several HLBM schemes including the model described in Chapter 4. For this purpose, it is proposed to extend the standard methodology to a coupled system including an energy equation and an ideal gas equation of state. Furthermore, the improved von Neumann analysis of Wissocq et al. [63] will be employed in order to systematically identify the modes of a given scheme by the knowledge of the macroscopic information they carry. A similar analysis will be applied to several types of energy equations, depending on the considered variable or on its form itself (primitive or conservative). The objective of such studies is manifold: (1) objectively conclude on the ability of each model to handle compressible flows, (2) find optimal values for the parameters of the HRR collision model, and (3) exhibit the numerical dispersion and dissipation. Furthermore, unintended numerical phenomena induced by a mode coupling will be evidenced thanks to the extended analysis. Most of all, this work aims at retaining one or more model of interest beyond several HLBM classes, based on objective observations from the LSA.

In order to sort all the different models under consideration, the present chapter is articulated as follows. Sec. 6.2 recalls the governing discrete velocity Boltzmann equation (DVBE), the energy equations and their time and space discrete counterparts. Sec. 6.3 is dedicated to linear stability analyses of the DVBE and LBM in the athermal framework, including a corrective term in Mach number. Some notions on the LBM stability are recalled, and discussions regarding the corrective term and stabilization methods are provided. Sec. 6.4 extends the LSA to the hybrid DVBE (HDVBE) and the discrete HLBM. First elements of answer are brought on the choice of the energy variable, and the effects of the numerical parameters of the HRR collision model on the stability are discussed. A parametric study is then performed over the different HLBM classes in Sec. 6.5, which ultimately reduces the choice to only three possible HLBM classes. Sec. 6.6 investigates the spectral behavior of the usable classes in terms of modal macroscopic composition. This further put the light on spurious modes couplings and two newly identified phenomena, referred to as *shear-to-entropy* and *entropy-to-shear* production. Finally, conclusions are drawn in the last section.

6.2 Hybrid Lattice Boltzmann Method

First of all, the DVBE is introduced on standard lattices with corrective terms to get rid of lattice errors [55, 187] and the monatomic limitation [225]. Then, the spatio-temporal discretization of the DVBE is performed, giving rise to the LBM. Different regularized collision operators are introduced, including the hybrid recursive regularization [88] adopted in previous compressible HLBM models [187]. In a third step, the different variables and forms of energy equations considered in this work are detailed, followed by their temporal and spatial discretization schemes.

Given the previous chapters, this section may seem redundant. However, it is nonethe-

less essential because it introduces the notations necessary for the study that will follow and allows a clear delimitation of the subject.

6.2.1 Corrected Discrete Velocity Boltzmann Equation

In the present HLBM framework, the mass and momentum are computed by the moments of the corrected DVBE-BGK, presented in Sec 4.2.1, which reads:

$$\mathcal{B}_i : \frac{\partial f_i}{\partial t} = \underbrace{-c_{i,\alpha}\frac{\partial f_i}{\partial x_\alpha} - \frac{1}{\tau}\left(f_i - f_i^{eq,N}\right) + \psi_i}_{\mathcal{S}_i^{DVBE}}, \quad \forall i \in [\![0, m-1]\!]. \tag{6.2.1}$$

In this work, only the one-dimensional D1Q3 and two-dimensional D2Q9 standard lattices will be considered (they can be found in sec. 2.3.2).

$\mathcal{S}_i^{DVBE}$ corresponds to the spatial dependency of the DVBE and gathers a linear advection term, a non-linear collision and a body-force term ψ_i. The Hermite expansion is adopted for the equilibrium distribution function $f_i^{eq,N}$. The latter will be set such as $N = 2$ for the D1Q3 lattice and $N = 3$ for the D2Q9 lattice (for details see Sec. 2.3.1.a). Finally, for the D2Q9 lattice, even though $N = 3$ will be adopted, only the third-order off-diagonal moments $a_{xxy}^{eq,(3)}$ and $a_{yyx}^{eq,(3)}$ are considered in $f_i^{eq,3}$, the diagonal ones being not supported by the lattice [65].

Finally, one recalls the expression of the correction term ψ_i in Eq. (6.2.1), which reads:

$$\psi_i = w_i \frac{\mathcal{H}_{i,\alpha\beta}}{2c_s^4}\left(E_{1,\alpha\beta} + E_{2,\alpha\beta}\right), \tag{6.2.2}$$

and this term removes the lattice closure error induced by the standard lattice [55] ($E_{1,\alpha\beta}$ correction term) and the polyatomic inconsistency of the equilibrium distribution function in the hybrid framework ($E_{2,\alpha\beta}$ correction term as seen in Sec. 4.3.2). These terms read respectively:

$$E_{1,\alpha\beta} = -\frac{\partial}{\partial x_\alpha}\left(a_{\alpha\alpha\alpha}^{eq}\right)\delta_{\alpha\beta} \qquad \text{and} \qquad E_{2,\alpha\beta} = p\left(\frac{D+2}{D} - \gamma_g\right)\frac{\partial u_\gamma}{\partial x_\gamma}\delta_{\alpha\beta}, \tag{6.2.3}$$

and can both be used on a D1Q3 lattice with $f_i^{eq,2}$ or on a D2Q9 lattice with $f_i^{eq,3}$.

After performing a Chapman-Enskog expansion of this corrected DVBE (as seen in Sec. 4.2.4), its macroscopic hydrodynamic limit is found to be:

$$\frac{\partial \rho}{\partial t} + \frac{\partial(\rho u_\alpha)}{\partial x_\alpha} = 0, \tag{6.2.4a}$$

$$\frac{\partial(\rho u_\alpha)}{\partial t} + \frac{\partial}{\partial x_\beta}\left(\rho u_\alpha u_\beta + p\delta_{\alpha\beta}\right) = -\frac{\partial a_{\alpha\beta}^{(1)}}{\partial x_\beta}, \tag{6.2.4b}$$

with

$$p = \rho c_s^2 \theta \qquad \text{and} \qquad a_{\alpha\beta}^{(1)} = -\tau p\left(\frac{\partial u_\alpha}{\partial x_\beta} + \frac{\partial u_\beta}{\partial x_\alpha} - \frac{2}{D}\frac{\partial u_\gamma}{\partial x_\gamma}\delta_{\alpha\beta}\right), \tag{6.2.5}$$

being respectively the pressure and the error-free viscous stress tensor. This set of macroscopic equation is recovered for both the D1Q3 and D2Q9 lattices. In the present work and without loss of generality, $\mu = \tau p$ is considered as a constant fluid property, meaning that no temperature evolution of μ, *e.g.* with the Sutherland's law [226], will be considered.

Regarding the mass and momentum equations Eq. (6.2.4a) and Eq. (6.2.4b), the way in which θ is introduced leads to two distinct cases:

- Athermal case: θ is considered as a constant i.e. $\theta = \theta_0 = T_0/T_r$. The equation of state only depends on the density, and the athermal Newtonian speed of sound $c_s\sqrt{\theta_0}$ is recovered [63]. It can be freely adjusted with the arbitrary choice of θ_0 but remains constant over time and space. For $\theta_0 = 1$ and if the correction term ψ_i is neglected, the very standard athermal DVBE is recovered.

- Thermal case: $\theta = T/T_r$ is related to the fluid temperature, whose evolution in time and space is governed by an $(m+1)$ *energy* equation. The perfect gas equation of state is recovered as well as the isentropic speed of sound $c_s\sqrt{\gamma_g\theta}$.

In the HLBM framework, the athermal case can be adopted as far as the Boussinesq hypothesis applies [14]. Thus, an *ersatz* of the energy equation is sufficient, such as a single advection-diffusion of temperature, along with a buoyancy force term in the momentum equation as already seen in Sec. 3.7. Using this hypothesis, only incompressible flows with small temperature variations can be considered. To recover the compressible Navier-Stokes-Fourier equations, it is mandatory to consider the thermal case, where a fully detailed energy equation is solved and coupled to the DVBE through a perfect gas equation of state. It is the context of the present work, and the energy equation is further detailed in the next subsection.

6.2.2 Energy equation

Several energy equations will be considered in this work. They have already been presented in Sec.3.2. However, in order to ensure a certain fluidity of reading, they are briefly recalled here. The energy equation can be written in a general conservative form as:

$$\frac{\partial(\rho\phi)}{\partial t} + \frac{\partial(\rho u_\alpha \phi)}{\partial x_\alpha} = \mathcal{P}_\phi + \mathcal{F}_\phi + \mathcal{V}_\phi, \tag{6.2.6}$$

or, after expanding the left-hand side term of Eq. (6.2.6) and using the mass equation (6.2.4a), in a non-conservative form as:

$$\frac{\partial\phi}{\partial t} + u_\alpha\frac{\partial\phi}{\partial x_\alpha} = \frac{1}{\rho}\left(\mathcal{P}_\phi + \mathcal{F}_\phi + \mathcal{V}_\phi\right). \tag{6.2.7}$$

The quantity $\phi \in \{e, s, E\}$ corresponds to the energy variable, where $e = c_v T$ refers to the internal energy, $E = e + u_\alpha^2/2$ to the total energy and $s = c_v \ln\left(T/\rho^{\gamma_g - 1}\right)$ to the entropy, with $c_v = r_g/\left(\gamma_g - 1\right)$ the heat capacity at constant volume. $\mathcal{P}_\phi$ is the pressure work term modeling heat production induced by compressibility effects, $\mathcal{F}_\phi$ is the Fourier term

referring to the heat losses by diffusion and $\mathcal{V}_\phi$ is the viscous production term modeling the heat source by friction.

terms \ variables	E	e	s
T	$\frac{1}{c_v}\left(E-\frac{1}{2}u_\alpha^2\right)$	$\frac{e}{c_v}$	$\rho^{\gamma_g-1}\exp\left(\frac{s}{c_v}\right)$
$\mathcal{P}_\phi$	$-\frac{\partial(u_\alpha p)}{\partial x_\alpha}$	$-p\frac{\partial u_\alpha}{\partial x_\alpha}$	$\varnothing$
$\mathcal{F}_\phi$	$\frac{\partial}{\partial x_\alpha}\left(\lambda\frac{\partial T}{\partial x_\alpha}\right)$	$\frac{\partial}{\partial x_\alpha}\left(\lambda\frac{\partial T}{\partial x_\alpha}\right)$	$\frac{1}{T}\frac{\partial}{\partial x_\alpha}\left(\lambda\frac{\partial T}{\partial x_\alpha}\right)$
$\mathcal{V}_\phi$	$-\frac{\partial}{\partial x_\beta}\left(a_{\alpha\beta}^{(1)}u_\alpha\right)$	$-a_{\alpha\beta}^{(1)}\frac{\partial u_\alpha}{\partial x_\beta}$	$-\frac{a_{\alpha\beta}^{(1)}}{T}\frac{\partial u_\alpha}{\partial x_\beta}$

Table 6.1 – Energy variables and source terms associated to each form of the energy equation. $\lambda = \mu/\mathrm{Pr}$ is the heat conductivity of the fluid.

The expression of the temperature, as well as the source terms associated to each energy variable, are detailed in Table 6.1.

6.2.3 LBM with corrective terms

For the discrete counterparts of Eq. (6.2.1), both corrected LBM-BGK equation and corrected regularized LBM equation are considered. They read respectively:

$$g_i^+ = \underbrace{g_i - \frac{\Delta t}{\check{\tau}}\left(g_i - f_i^{eq}\right) + \frac{2\check{\tau}-\Delta t}{2\check{\tau}}\Delta t\,\psi_i}_{\mathcal{S}_i^{LBM}}, \tag{6.2.8}$$

and:

$$g_i^+ = \underbrace{f_i^{eq} + \left(1-\frac{\Delta t}{\check{\tau}}\right)g_i^{(1)} + \frac{\Delta t}{2}\psi_i}_{\mathcal{S}_i^{LBM}}. \tag{6.2.9}$$

Similarly to their continuous counterpart Eq. (6.2.1), $\mathcal{S}_i^{LBM}$ gathers all the spatial linear and nonlinear terms of these equations. If nothing else is specified, the space-derivatives of ψ_i are computed in the following using second-order centered (D1CO2) finite differences.

Thus, the study focuses on two classes of collision operators, namely (i) the BGK operator and (ii) regularized collision operators. For the latter, emphasis is placed on the HRR operator described in details in Sec 4.3.3 for the D2Q9 lattice. For D1Q3 lattice, the reconstruction order N_r of the off-equilibrium Hermite moment $\check{\boldsymbol{a}}^{1,(n)}$ is set to $N_r = 2$

instead of $N_r = 3$ for the D2Q9 lattice. Finally, it must be noted that when $\sigma = 1$ this operator is reduced to the BGK model for the D1Q3 lattice, and to the RR3 model [65,87] for the D2Q9 one.

6.2.4 Discrete energy equation

The spatio-temporal schemes discretizing the energy equation are presented in this section. For the sake of simplicity but without loss of generality, only its conservative form is considered. The energy equation can be split into two different parts, namely temporal and spatial ones, such that:

$$\frac{\partial(\rho\phi)}{\partial t} = \mathcal{S}^{En}\left(f_i, \rho\phi\right), \tag{6.2.10}$$

where $\mathcal{S}^{En}\left(f_i, \rho\phi\right)$ denotes the operator gathering all the spatial derivative terms (convection and source terms). Three types of derivatives have to be discretized in this equation: time derivatives, first-order spatial derivatives (convective and pressure work terms) and second-order spatial derivatives (diffusive terms).

Adopting a semi-discretization procedure in which the equations are firstly discretized in time and then in space, the most classic scheme for the temporal evolution is the first-order forward Euler scheme, which reads:

$$\begin{aligned} \mathrm{K}_1 &= \mathcal{S}^{En}\left(f_i^t, \phi^t\right), \\ (\rho\phi)^{t+\Delta t} &= (\rho\phi)^t + \Delta t \mathrm{K}_1. \end{aligned} \tag{6.2.11}$$

This Euler scheme can also be considered as a first-order Runge-Kutta (RK1) scheme. A fourth-order four-stage Runge-Kutta (RK4) [227] is also considered in this work:

$$\begin{aligned} &\mathrm{K}_1 = \mathcal{S}^{En}\left(f_i^t, \phi^t\right), \quad \mathrm{K}_2 = \mathcal{S}^{En}\left((\rho\phi)^t + \frac{\Delta t}{2}\mathrm{K}_1\right), \\ &\mathrm{K}_3 = \mathcal{S}^{En}\left((\rho\phi)^t + \frac{\Delta t}{2}\mathrm{K}_2\right), \quad \mathrm{K}_4 = \mathcal{S}^{En}\left((\rho\phi)^t + \Delta t \mathrm{K}_3\right), \\ &(\rho\phi)^{t+\Delta t} = (\rho\phi)^t + \frac{\Delta t}{6}\left(\mathrm{K}_1 + 2\mathrm{K}_2 + 2\mathrm{K}_3 + \mathrm{K}_4\right). \end{aligned} \tag{6.2.12}$$

Regarding first-order space derivatives for convective terms, two different schemes will be considered: a first-order upwind scheme, referred to as D1UPO1, and a second-order centered scheme, referred to as D1CO2. They respectively read:

$$\text{D1UPO1}: \quad \frac{\partial(\rho u_\alpha \phi)}{\partial x_\alpha} = \frac{(\rho u_\alpha \phi)_{\boldsymbol{x}+d^+\boldsymbol{e}_\alpha\Delta x} - (\rho u_\alpha \phi)_{\boldsymbol{x}-d^-\boldsymbol{e}_\alpha\Delta x}}{\Delta x} + \mathcal{O}\left(\Delta x\right), \tag{6.2.13}$$

$$\text{D1CO2}: \quad \frac{\partial(\rho u_\alpha \phi)}{\partial x_\alpha} = \frac{(\rho u_\alpha \phi)_{\boldsymbol{x}+\boldsymbol{e}_\alpha\Delta x} - (\rho u_\alpha \phi)_{\boldsymbol{x}-\boldsymbol{e}_\alpha\Delta x}}{2\Delta x} + \mathcal{O}\left(\Delta x^2\right), \tag{6.2.14}$$

with

$$d^+ = |sign(u_\alpha) - 1|/2 \quad \text{and} \quad d^- = |sign(u_\alpha) + 1|/2. \tag{6.2.15}$$

Regarding second-order space derivatives, a standard second-order scheme has been chosen for the discretization of $\mathcal{F}$ and $\mathcal{V}$. Applied on the variable T, it reads:

$$\text{D2CO2}: \quad \frac{\partial^2 T}{\partial x_\alpha^2} = \frac{T_{\boldsymbol{x}+\boldsymbol{e}_\alpha \Delta x} - T_{\boldsymbol{x}} + T_{\boldsymbol{x}-\boldsymbol{e}_\alpha \Delta x}}{\Delta x^2} + \mathcal{O}\left(\Delta x^2\right). \tag{6.2.16}$$

In summary, two combinations of these discrete schemes are retained for the present study: the so-called RK1UPO1 (fairly close to the scheme employed in the recent literature [187, 225]) and RK4CO2 schemes. Details of the particular discretizations used in each scheme are provided in Table 6.2. Also note that a completely similar approach is adopted for the non-conservative form of the energy equation.

	$\frac{\partial(\rho\phi)}{\partial t}$	$\frac{\partial(\rho u_\alpha \phi)}{\partial x_\alpha}$	$\mathcal{P}_\phi$	$\mathcal{F}_\phi$	$\mathcal{V}_\phi$
RK1UPO1	RK1	D1UPO1	D1CO2	D2CO2	D2CO2
RK4CO2	RK4	D1CO2	D1CO2	D2CO2	D2CO2

Table 6.2 – Discretization schemes used for the energy equation.

6.3 The linear stability analysis

In this section, the methodology of the linear stability analysis is recalled, based on the former work of von Neumann [174] and later adapted to the LBM formalism by Sterling and Chen [221]. Next, this analysis is applied to both standard athermal DVBE and LBM systems. When performed to the continuous system, this analysis allows highlighting the role of each corrective term. Applied to the discrete system, it can evidence the numerical effects of the discretization on both stability and accuracy.

6.3.1 Method and concept

For the sake of clarity, the DVBE system of Eq. (6.2.1) is considered here. As proposed in [221], the distribution functions f_i can be decomposed into two parts: (i) a mean flow $\overline{f_i} = \overline{f}_i^{eq}(\overline{\rho}, \overline{u}_\alpha)$ and (ii) a small perturbation f_i'. The mean flow is considered constant in time and space, and $\overline{\rho}$ and $\overline{u}_\alpha$ are respectively the mean density and velocity. The functions $f_i(x,t)$ then read:

$$f_i(x,t) = \overline{f_i} + f_i'(x,t), \tag{6.3.1a}$$

$$f_i'(x,t) = \widehat{f}_i e^{\mathrm{i}(k_\alpha x_\alpha - \omega t)}, \tag{6.3.1b}$$

where the fluctuating distribution functions have been expressed as complex monochromatic plane waves, as proposed by von Neumann [174]. Here, $\mathrm{i}^2 = -1$, $\omega \in \mathbb{C}$ is the complex temporal pulsation of the wave, k_α is the α component of the wavenumber vector and $\widehat{f}_i$ is the complex amplitude of the perturbation. Considering $f_i' \ll \overline{f_i}$, neglecting

the nonlinear terms and injecting Eq. (6.3.1a) into Eq. (6.2.1), the following linearized system is obtained:

$$\omega \widehat{f}_i = \widetilde{\mathrm{M}}_{ij}^{DVBE} \widehat{f}_j, \tag{6.3.2}$$

where $\widetilde{\mathrm{M}}_{ij}^{DVBE}$ is defined as the time-advance matrix in the spectral space. For the derivation of this matrix, the reader may relate to App. D.1.

Computing the eigenvalues $(\omega_l)_{l\in[\![0,m-1]\!]}$ and eigenvectors $(\mathrm{F}_i^l)_{l\in[\![0,m-1]\!]}$ of this matrix, m linear eigenmodes of $\mathcal{B}_i$ are obtained. The diagonalized system reads:

$$\omega_l \mathrm{F}_i^l = \widetilde{\mathrm{M}}_{ij}^{DVBE} \mathrm{F}_i^l. \tag{6.3.3}$$

The real and imaginary parts of ω_l, respectively $\mathrm{Re}(\omega_l)$ and $\mathrm{Im}(\omega_l)$, provide information on the propagation and the dissipation of the perturbation. If $\mathrm{Im}(\omega_l) > 0$, the perturbation associated to the lth mode is exponentially amplified in the time, and thus the system is unstable. On the other hand, if $\mathrm{Im}(\omega_l) < 0$ the mode is damped with time. The system is then linearly stable if and only if every mode behaves in this way. Finally, the phase velocity v_l^Φ and the group velocity v_l^g of each mode l are directly related to $\mathrm{Re}(\omega_l)$, and commonly defined as:

$$v_l^\Phi = \frac{\mathrm{Re}(\omega_l)}{\|k\|} \qquad \text{and} \qquad v_l^g = \frac{\mathrm{dRe}(\omega_l)}{\mathrm{d}\|k\|}. \tag{6.3.4}$$

To make sure that the system behaves properly in the linear approximation, the spectral properties can be compared with a reference. In this way, the same linear stability analysis can be applied to the Navier-Stokes equations [228,229] by solving the eigenvalue problem for $\widetilde{M}_{i,j}^{NS,ath}$, referred to as the time-advance matrix in the athermal case. It provides three linear modes in two dimension: one shear (or vortical) mode ω_{shear}, one upstream acoustic ω_{ac-} mode and one downstream acoustic ω_{ac+} mode. Their eigenvalues are:

$$\begin{aligned} \omega_{shear} &= k_\alpha \overline{u}_\alpha - \mathrm{i}\overline{\nu} \|k_\alpha\|^2 + O\left(k^3\right), \\ \omega_{ac\pm}^{ath} &= k_\alpha \overline{u}_\alpha \pm \|k_\alpha\| \sqrt{c_s^2 \theta_0} - \mathrm{i}\overline{\nu} \|k_\alpha\|^2 + O\left(k^3\right), \end{aligned} \tag{6.3.5}$$

where $\overline{\nu} = \mu/\overline{\rho}$ is the mean kinematic viscosity. In one dimension, only the two acoustic modes are present. For more details on the derivation of these expressions, the interested reader may refer to [228,229] or to App. D.3.

Moreover, following the methodology proposed by Wissocq et al. [63], the DVBE eigenvectors $(\mathrm{F}_i^l)_{i\in[\![0,m-1]\!]}$ can be used to provide an in-depth physical interpretation of the modes resulting from the linear analysis. This is made possible by computing their macroscopic counterpart $\mathcal{E}_l^{LB}$ as hydrodynamic moments of the DVBE eigenvectors:

$$\mathcal{E}_l^{DVBE} = \left[\widehat{\rho}^{DVBE} = \sum_i^{m-1} \mathrm{F}_i^l \quad , \quad \left(\widehat{u}_\alpha^{DVBE} = \frac{\sum_i^{m-1} c_{i,\alpha} \mathrm{F}_i^l - \overline{u}_\alpha \sum_i^{m-1} \mathrm{F}_i^l}{\overline{\rho}} \right) \right]^{\mathrm{T}}. \tag{6.3.6}$$

This macroscopic information is then compared with the (athermal) Navier-Stokes eigenvectors:

$$\boldsymbol{V}_{mode}^{NS,ath} = \left[\widehat{\rho}^{NS,ath} \quad , \quad \left(\widehat{u}_\alpha^{NS,ath} \right) \right]^{\mathrm{T}}, \quad \mathrm{mode} \in [shear, ac-, ac+]. \tag{6.3.7}$$

For details about the derivation of $\boldsymbol{V}_{mode}^{NS,ath}$, the reader can refer to App. D.3. The idea is then to access to the contribution of $\boldsymbol{\mathcal{E}}_l^{LB}$ in terms of physical macroscopic modes such as:

$$\boldsymbol{\mathcal{E}}_l^{LB} = a_l \boldsymbol{V}_{shear}^{NS,ath} + b_l \boldsymbol{V}_{ac-}^{NS,ath} + c_l \boldsymbol{V}_{ac+}^{NS,ath}, \tag{6.3.8}$$

where coefficients a_l, b_l and c_l then correspond to the complex contributions of $\boldsymbol{\mathcal{E}}_l^{LB}$ on each macroscopic modes.

Their value can be obtained thanks to the passage matrix $\boldsymbol{P}_{NS,ath} = \left[\boldsymbol{V}_{ac-}^{NS,ath}, \boldsymbol{V}_{ac+}^{NS,ath}, \boldsymbol{V}_{shear}^{NS,ath}\right]$ as:

$$(a_l, b_l, c_l)^T = \boldsymbol{P}_{NS,ath}^{-1} \boldsymbol{\mathcal{E}}_l^{LB}. \tag{6.3.9}$$

These coefficients are finally normalized, so that $|a_l| + |b_l| + |c_l| = 1$. Looking at the normalized modulus of each coefficient provides information on the physical content carried by a DVBE eigenmode, expressed as (athermal) NS waves. For instance, a mode l of the DVBE for which $(|a_l|, |b_l|, |c_l|)^T = (1, 0, 0)^T$ can be identified as a pure shear mode. However, in practice, no eigenmode is likely to carry a pure physical information and an arbitrary threshold η has to be specified in order to systematically identify the information carried by a mode. In this work, and unless otherwise specified, a mode is considered as a Navier-Stokes mode if the value of one of the normalized coefficients exceeds $\eta = 99\%$.

The analysis, recalled here for the DVBE, can be similarly applied to its discrete counterpart, namely the LBM system (6.2.8) [221], without any change in the methodology. Knowing that:

$$g_i'\left(x + c_{i,\alpha}\Delta t, t + \Delta t\right) = \widehat{g}_i e^{\mathrm{i}(k_\alpha(x_\alpha + c_{i,\alpha}\Delta t) - \omega(t+\Delta t))}, \tag{6.3.10}$$

an equivalent dispersion relation of the discrete equations is obtained and reads:

$$e^{-\mathrm{i}\omega\Delta t}\widehat{g}_i = \mathrm{M}_{ij}^{LBM}\widehat{g}_j. \tag{6.3.11}$$

Details about M_{ij}^{LBM} can be found in App. D.1. Once Eq. (6.3.11) is diagonalized, the very same linear analysis can be conducted considering the logarithm of the eigenvalue to compute ω, giving access to the spectral properties of the discrete system.

6.3.2 Comments on the corrected athermal DVBE LSA

This section focuses on the corrected athermal DVBE. Thus, the fluid temperature is considered constant as $T = T_0$ and only $E_{1,\alpha\beta}$ is present in the correction term ψ_i of Eq. (6.2.2). Note that μ is considered as a constant property of the fluid, so that the kinetic viscosity ν depends on the local fluid density and its mean value can be defined as $\overline{\nu} = \mu/\overline{\rho}$. Similarly, $\tau = \mu/(\rho r_g T_0)$ is a local variable, its mean counterpart can be defined as $\overline{\tau} = \mu/(\overline{\rho} r_g T_0)$.

In order to fully characterize the system, a dimensional analysis is first proposed. In one dimension, the system is described by seven independent variables ($\overline{\rho}$, $\overline{u}$, $\overline{\nu}$, $c = \sqrt{r_g T_0}$, $c_s = \sqrt{r_g T_r}$, k and ω) involving three fundamentals units (mass, length and time). Thus, the overall eigenvalue problem is bounded by considering four dimensionless parameters, *e.g.*:

$$\omega_\tau = \mathcal{L}\left(\overline{\mathrm{Ma}}, \overline{\mathrm{Kn}}, \theta_0\right), \tag{6.3.12}$$

where

$$\omega_\tau = \frac{\omega\overline{\nu}}{r_g T_0} = \omega\overline{\tau}, \quad \overline{\mathrm{Ma}} = \frac{\overline{u}}{\sqrt{r_g T_0}}, \quad \overline{\mathrm{Kn}} = \frac{\overline{\nu} k}{\sqrt{r_g T_0}} \quad \text{and} \quad \theta_0 = \frac{T_0}{T_r}. \tag{6.3.13}$$

$\overline{\mathrm{Ma}}$ and $\overline{\mathrm{Kn}}$ are respectively the Mach number of the mean flow and the Knudsen number of the considered perturbation. For larger dimensions, for instance a three-dimensional problem, one could consider an angle of Mach and Knudsen numbers per additional spatial degree of freedom ($\overline{\mathrm{Ma}_\theta}$, $\overline{\mathrm{Ma}_\phi}$, $\overline{\mathrm{Kn}_\theta}$, $\overline{\mathrm{Kn}_\phi}$).

Exploring this parameter space allows to investigate the linear system in all the possible configurations. Since the present work is applied to fluid mechanics, the Knudsen number will be restricted to $\overline{\mathrm{Kn}} \leq \mathrm{Kn}_c = 5{\cdot}10^{-3}$, so as to ensure the validity of the continuous medium assumption [38]. Furthermore, as underlined in previous investigations [185], the value of θ_0 has almost no influence on ω_τ for the considered Knudsen numbers. For this reason, the following analyses are performed with $\theta_0 = 1$, without any effect on the observations.

Propagation and dissipation curves of the D1Q3 lattice are displayed on Fig. 6.1c as function of Kn. Three modes of different nature are obtained and identified as two physical modes and one ghost mode thanks to the extended analysis. The ghost mode does not carry any macroscopic information and thus cannot be identified as a classical Navier-Stokes modes [63]. Note that the latter does not appear on the dissipation curve because its dissipation rate ($\mathrm{Im}(\omega_\tau) = 1$) is much larger than the physical one. Regarding the two physical modes, they can be identified as an upstream acoustic mode (◁) and a downstream one (▷) and their dispersion and dissipation properties match the Navier-Stokes theoretical values in solid lines.

From this brief modal analysis, the expected athermal Navier-Stokes behavior is recovered. However, close to the specific value $\mathrm{Ma} = 0.732$, the DVBE system starts diverging as a consequence of the well-known cubic Mach error present in the viscous stress tensor due to the lattice closure defect. It implies that the linear DVBE systems bearing this defect (*i.e.* D1Q3, D2Q9, D3Q27 lattices) [41, 55] are unstable above $\mathrm{Ma} = 0.732$. Such a critical Mach number has already been observed in previous work [40, 205, 223], its analytical value being found to $\sqrt{3}-1$ [185]. Thus, before moving to the space discretization, this lattice shortcoming has to be corrected in order to deal with compressible flows, thereby introducing the correction term $E_{1,\alpha\beta}$. Its influence around this critical Mach number can been see on Fig. 6.1. In the absence of $E_{1,\alpha\beta}$, the overall system remains stable for $\overline{\mathrm{Ma}} = 0.6$ (Fig. 6.1a), while for $\overline{\mathrm{Ma}} = 0.8$ (Fig. 6.1b), the downstream acoustic mode is amplified. For the same Mach number, taking $E_{1,\alpha\beta}$ into account, a correct dissipation behavior is recovered in perfect agreement with the theory as shown on Fig. 6.1c.

Despite its two-dimensional feature, same conclusions can be drawn for the D2Q9 lattice. On Fig. 6.2, propagation and dissipation curves of the corrected D2Q9 lattice are displayed for a mean flow at $\overline{\mathrm{Ma}} = 0.8$ along the x-direction. As expected and previously observed [63], nine modes are identified: six ghost modes, two acoustic ones and a shear

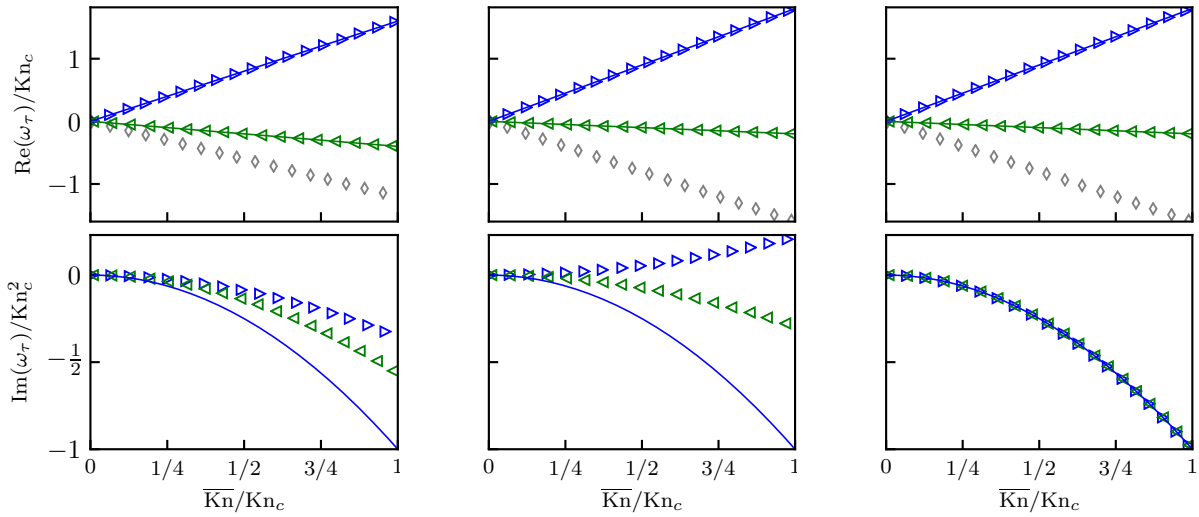

(a) $\overline{\mathrm{Ma}} = 0.6$, $E_{1,\alpha\beta} = \varnothing$ (b) $\overline{\mathrm{Ma}} = 0.8$, $E_{1,\alpha\beta} = \varnothing$ (c) $\overline{\mathrm{Ma}} = 0.8$, $E_{1,\alpha\beta} = \checkmark$

Figure 6.1 – Propagation and dissipation curves of the D1Q3 with $f_i^{eq,2}$ and $\theta_0 = 1$ around $\overline{\mathrm{Ma}} = 0.732$. Symbols correspond to ω_{ac+}: (▷) ; ω_{ac-}: (◁) ; ω_g:(◊) and solid lines correspond to the Navier-Stokes solution.

(or vortical) mode, represented by (□). The phase/group velocities and the dissipation rates of the physical modes are found in agreement with the analytical solution across the entire two-dimensional Knudsen space.

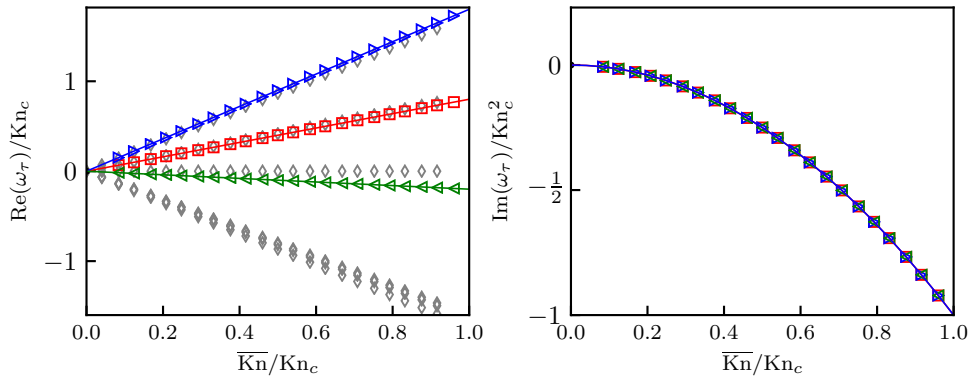

Figure 6.2 – Propagation and dissipation curves of the corrected D2Q9 along $\boldsymbol{e}_x$ at $\overline{\mathrm{Ma}} = 0.8$, $\mathrm{Ma}_\theta = 0$, $\theta_0 = 1$ and $f_i^{eq,3}$. Symbols correspond to ω_{ac+}: (▷) ; ω_{ac-}: (◁) ; ω_{shear}: (□) ; ω_g:(◊) and solid lines correspond to the Navier-Stokes solution.

6.3.3 Von Neumann analysis of the athermal LBM schemes

In this section, the athermal LBM is considered. In the same way as its continuous counterpart, the temperature is considered constant $T = T_0$ and only $E_{1,\alpha\beta}$ appears in the correction term ψ_i.

Here again, in order to fully characterize the system, a dimensional analysis is performed. For the one-dimensional discrete case, in addition to the seven independent variables of the continuous case, a numerical variable emerges as the time step Δt. It is worth noting that the space step Δx depends on c_s and Δt *via* the acoustic scaling [2], and cannot be considered as an independent variable. The three fundamental units remain unchanged, increasing the number of dimensionless parameters up to five. This linear analysis is then bounded considering:

$$\omega_\tau = \mathcal{L}\left(\overline{\mathrm{Ma}}, \mathrm{Kn}, \theta_0, \tau^*\right), \tag{6.3.14}$$

where ω_τ, $\overline{\mathrm{Ma}}$, Kn and θ_0 are still given by Eq. (6.3.13) and

$$\tau^* = \frac{\overline{\tau}}{\Delta t} = \frac{\mu}{\overline{\rho} c_s^2 \theta_0 \Delta t}. \tag{6.3.15}$$

Compared to the continuous case, two parameters are expected to have numerical effects only: τ^*, which appears as a direct consequence of the discrete nature of the system, and θ_0, which has no effect on the continuous DVBE in the low-Knudsen regime [185]. Regarding the unique number holding the spatial information k, *i.e.* Kn, a discussion should be held on its relevance in this discrete context, as well as for ω_τ. Indeeed, the Nyquist-Shannon sampling theorem [230] provides here the direct conditions: $k\Delta x \leq \pi$ and $\Re(\omega)\Delta t \leq \pi$. This condition is essential for a correct study of a numerical scheme, and for this reason Kn and ω^* are respectively replaced by $k^* = k\Delta x$ and $\omega^* = \omega\Delta t$ in the present discrete framework. This linear analysis now reads:

$$\omega^* = \mathcal{L}\left(\overline{\mathrm{Ma}}, k^*, \theta_0, \tau^*\right). \tag{6.3.16}$$

Exploring this parameter space allows assessing the system in all the possible configurations.

An additionnal dimensionless number can be considered as the Courant-Friedrich-Levy (CFL) number [170]. It is commonly employed in the stability study of explicit numerical schemes, as a criterion that must be met by the time and the space step. This number corresponds to the ratio of the maximum "physically expected" speed over the speed of the numerical information. For the present athermal system, acoustic waves have to be accounted for, which gives:

$$\mathrm{CFL}^{ath} = \left(\overline{\mathrm{Ma}} + 1\right)\sqrt{c_s^{*2}\theta_0}, \tag{6.3.17}$$

with $c_s^* = c_s\Delta t/\Delta x = 1/\sqrt{3}$ for both the D1Q3 and D2Q9 lattices. For an explicit scheme, it is recommended to set CFL < 1 and even lower, depending on the nature of the scheme and the spatial dimension [166]. In the standard athermal LBM (where $E_{1,\alpha\beta}$ is absent), the value $\theta_0 = 1$ is adopted to minimize the dissipation error in the macroscopic equations [55]. In such a case, the only flexibility over the CFL constraint is to act on the Ma number, which clearly reduces the physical scope of applications. However, one purpose of the $E_{1,\alpha\beta}$ correction term is precisely to remove this constraint [225], which

now makes it possible to modify the stability or accuracy by varying θ_0 without any impact on the macroscopic equations. Hence, the analyses below focus on the range of $\theta_0 \in [0, 1.2]$.

Finally, a last discussion has to be conducted regarding the range of interest of the dimensionless relaxation time τ^*. For typical CFD applications, it is fair to admit that the viscosity can vary in time and space, physically or numerically (through turbulence modeling for instance), all along a simulation. Thus, for the targeted applications, a decent range of viscosity $\nu \in [10^{-5}, 10^{-2}]\,\mathrm{m^2 s^{-1}}$ is adopted, as well as a minimal and maximal Δx encountered in standard applications *i.e.* $\Delta x \in [10^{-5}, 10^{1}]\,\mathrm{m}$. This parametric space spanned by ν and Δx is displayed on Fig. 6.3, which allows considering the lower bound of $\tau^* \simeq 10^{-8}$. Regarding the upper bound, $\tau^* = 1/2$ is considered. For this value, the collide and stream Eq. (6.2.8) is reduced to $g_i^+ = f_i^{eq}$, which will be considered for its interesting stability properties [72].

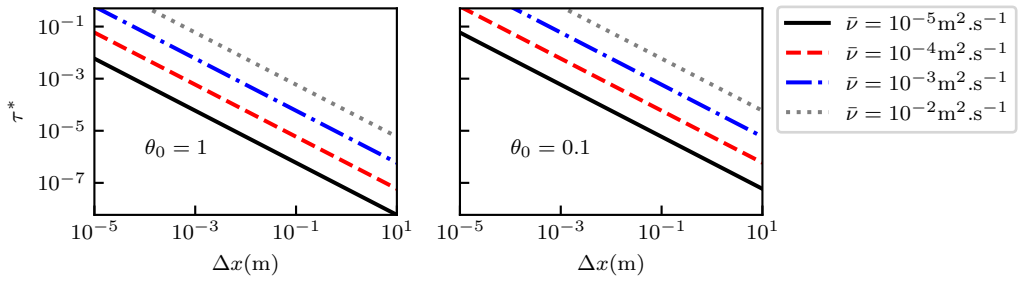

Figure 6.3 – Dimensionless relaxation time $\tau^* = \nu/(\Delta x \theta_0 c_s^* \sqrt{r_g T_0})$ as function of the mesh size Δx for $\theta_0 = 1$ (left) and $\theta_0 = 0.1$ (right). In both cases, different values of viscosity are displayed.

Fig. 6.4 displays dispersion and dissipation curves of the D1Q3 BGK-LBM model. Due to the space and time discretization, the D1Q3 lattice gives rise to a spurious macroscopic mode ω_{msp} (black dot), phase shifted by π at the origin. The latter carries some macroscopic contribution and can interact with other physical modes [63]. For the critical Mach number $\overline{\mathrm{Ma}} = \overline{\mathrm{Ma}^c} = 0.732$, with $\theta_0 = 1$, Fig. 6.4a shows an instability resulting from an eigenvalue collision between the downstream acoustic and the macroscopic spurious mode, which is therefore of a completely different nature than the instability shown in Sec. 6.3.2. The Mach error being corrected, this instability is uniquely related to numerical aspects as pointed out in [63].

In order to circumvent the issue, two strategies can be employed:

- The first one, showed on Fig. 6.4, consists in lowering the CFL number *via* θ_0, acting on the time step. It allows bypassing the eigenvalue collision by narrowing the sonic cone and lowering the group velocity of the spurious mode. For the D1Q3 lattice, the critical Mach number associated to the eigenvalue collision turns out to

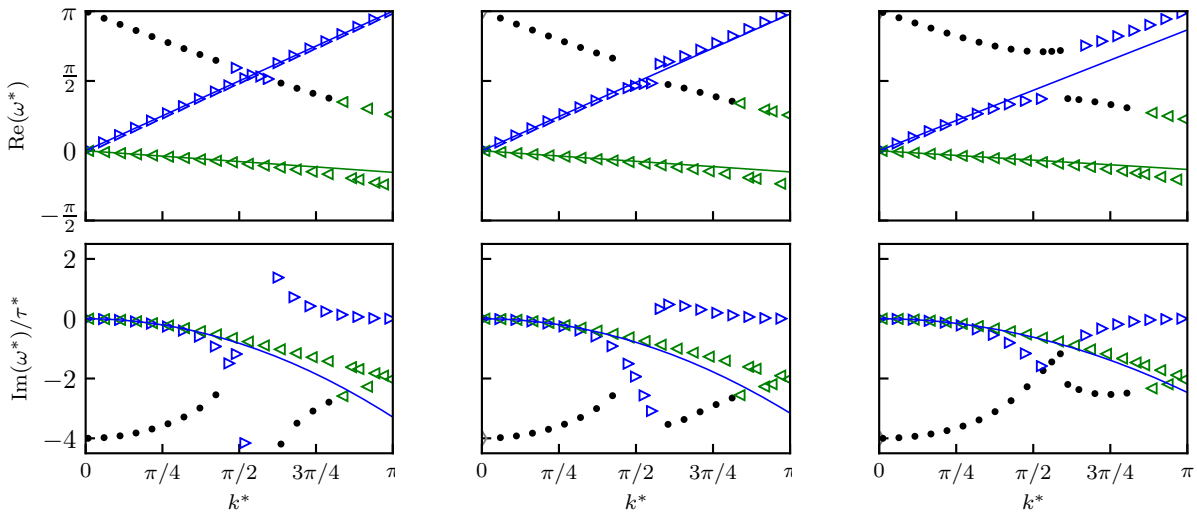

(a) $\theta_0 = 1$, unstable (b) $\theta_0 = 0.96$, unstable (c) $\theta_0 = 0.75$, stable

Figure 6.4 – Dispersion and dissipation curves of the D1Q3 LBM-HRR with $f_i^{eq,2}$. In the present case $\overline{\text{Ma}} = 0.732$ and $\tau^* = 10^{-5}$. Symbols correspond to ω_{ac+}: (▷) ; ω_{ac-}: (◁) ; ω_{msp}:(•) and solid lines correspond to the Navier-Stokes solution.

be obtained when $\text{CFL}^{ath} = 1$, *i.e.*:

$$\overline{\text{Ma}^c} = \frac{1}{c_s^* \sqrt{\theta_0}} - 1, \tag{6.3.18}$$

which, for some reason, exactly corresponds to the critical Mach number of the non-corrected athermal DVBE when $\theta_0 = 1$. Lowering θ_0 thus makes it possible to push back this constraint for the subsonic regime. Other types of instabilities are involved in supersonic configurations, as pointed out in App. C. This strategy allows stabilizing the scheme while preserving correct dissipation properties of well-resolved wavelengths, the drawback being the reduction of the time step increasing the CPU time.

- Instead of lowering the time step, the second strategy consists in adopting the HRR collision operator [88]. Its particularity is to avoid modal interactions [231] by partially reconstructing the second-order non-equilibrium moment with finite differences. This phenomenon is highlighted on Fig. 6.5, where the scheme is stabilized by increasing the FD part of $g_i^{(1)}$ in the regularization procedure. In this respect, the dispersion curve of Fig. 6.5b shows that the destructive eigenvalue collision can be avoided with $\sigma = 0.95$. Furthermore, note that the spurious mode completely disappears for a full FD reconstruction (*i.e.* $\sigma = 0$) as shown by Fig. 6.5c. However, despite accurate dispersion properties, the FD reconstruction bias the dissipation properties of the scheme acting as a low-pass filter.

Fig. 6.6 displays the spectral properties along $\boldsymbol{e}_x$ of the D2Q9-BGK model for $\overline{\text{Ma}} = 0.732$ and $\theta_0 = 0.75$. On these curves, no spurious amplification is obtained and the

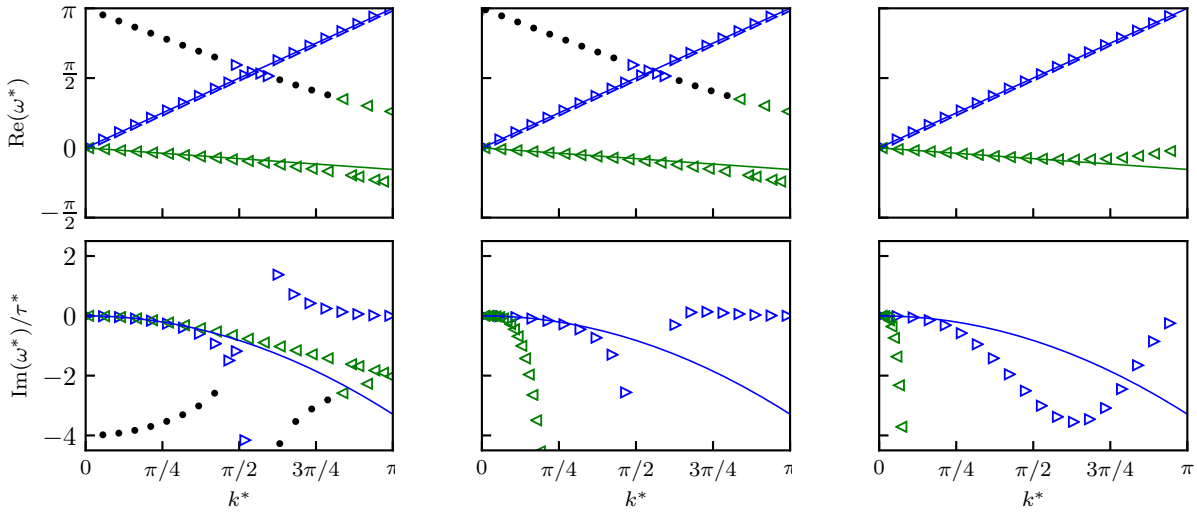

(a) $\sigma = 1$ unstable (b) $\sigma = 0.95$ unstable (c) $\sigma = 0$ stable

Figure 6.5 – Dispersion and dissipation curves of the D1Q3 LBM-HRR with $f_i^{eq,2}$. In the present case $\overline{\text{Ma}} = 0.732$ and $\tau^* = 10^{-5}$. When 100% of finite differences is employed in $g_i^{(1)}$ (ie $\sigma = 0$), the spurious macroscopic wave vanishes, suppressing the eigenvalue collision. Symbols correspond to ω_{ac+}: (▷) ; ω_{ac-}: (◁) ; ω_{msp}:(●) and solid lines correspond to the Navier-Stokes solutions.

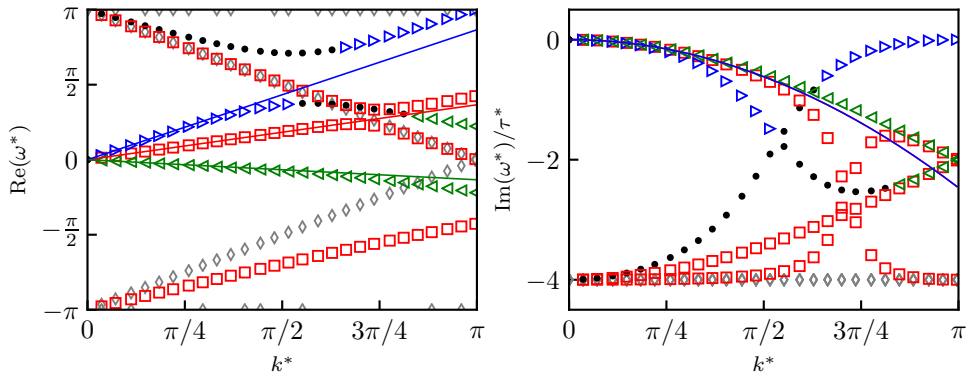

Figure 6.6 – Dispersion and dissipation curves of the corrected D2Q9 LBM-BGK along $\boldsymbol{e}_x$ for $\overline{\text{Ma}} = 0.732$, $\text{Ma}_\theta = 0$, $\theta_0 = 0.75$ and $f_i^{eq,3}$. Symbols correspond to ω_{ac+}: (▷) ; ω_{ac-}: (◁) ; ω_{shear}: (□) ; ω_{msp}:(●) ; ω_g:(◊) and solid lines correspond to the Navier-Stokes solution.

same stabilization phenomena of Fig. 6.4c is observed on the acoustics thank to the value of $\theta_0 \leq 1$. However, other kinds of modal interactions, related to the shear waves are underlined. On the dispersion curve, two shear modes emerge, interacting with each other as a curve veering phenomenon [63]. This indicates that other instabilities phenomena, directly related to the two-dimensional nature of the scheme, need to be taken into account. In reality, this scheme is found unstable in the spectral domain for wave numbers having a non-zero k_y component. This phenomenon will be further studied in the next subsection.

The two stabilization techniques introduced in this section (θ_0 and σ) will be extensively investigated throughout this Chapter as levers in the aim of stabilizing the HLBM.

6.3.4 Two-dimensional LBM instabilities

In the previous section, a similar behavior regarding the acoustic eigenvalues has been observed in the one and two-dimensional cases, *i.e.* the decrease of θ_0 helps avoiding the eigenvalue collision. However, for the D2Q9 lattice, this observation was made for horizontal plane waves only ($k_y = 0$), while nothing ensures that a generalization can be drawn over the whole spectrum. Moreover, the D2Q9 lattice being richer in terms of modes, Fig. 6.6 highlighted that other kinds of modal interactions can potentially emerge. Therefore, this section is devoted to the behavior of the D2Q9 lattice over its full spectrum, *i.e.* varying both k_x^* and k_y^*.

Fig. 6.7a displays the spectral properties of the D2Q9 BGK model with the same physical parameters as in the previous sub-section, namely $\overline{\text{Ma}} = 0.732$, $\tau^* = 10^{-5}$ and $\theta_0 = 0.75$, this time plotted for 45°-inclided waves with the e_x axis. It can be observed that this model is unstable in this direction of the spectrum. Two eigenvalue collisions are highlighted, one of acoustic nature for $k^* < \pi/2$, and one of shear nature for $k^* > \pi/2$. On the stability map of the model (Fig. 6.7a-right), several instability bubbles (characterized by a very large value of $\text{Im}(\omega^*)/\tau^*$) are observed, consequent to these eigenvalue collisions. It is important to note that this kind of instability has also been detected at lower Mach numbers [40]. Unfortunately, and contrary to the one-dimensional D1Q3 case, these instabilities cannot be addressed by changing the θ_0 parameter, suggesting the use of another collision operator.

For this purpose, Fig. 6.7b displays the spectral properties of the D2Q9 HRR model with $\sigma = 1$ for similar conditions as Fig. 6.7a. Note that for the particular value $\sigma = 1$, this operator is reduced to the recursive regularized operator with $N_r = 3$ (RR3). On the dispersion curve, it can be observed that the eigenvalue collision disappears. This is made possible thanks to the mode filtering properties of the regularized operators [72]. Unfortunately, this scheme remains unstable due to large areas of instability as shown on the $\max(\text{Im}(\omega^*)/\tau^*)$ map, also exhibited in previous work [72]. Even though these instabilities are much less brutal than the ones caused by the eigenvalue collision phenomenon, it is noticed that their amplitude is increased by a decrease of θ_0. This observation suggests that decreasing the value of θ_0 should not be advised with this model. However, for $\overline{\text{Ma}} \geq 0.732$ the decrease of θ_0 is a necessary ingredient to avoid acoustic eigenvalue collision, as illsutrated in the one-dimensional cases of Sec. 6.3.3. The spurious wave

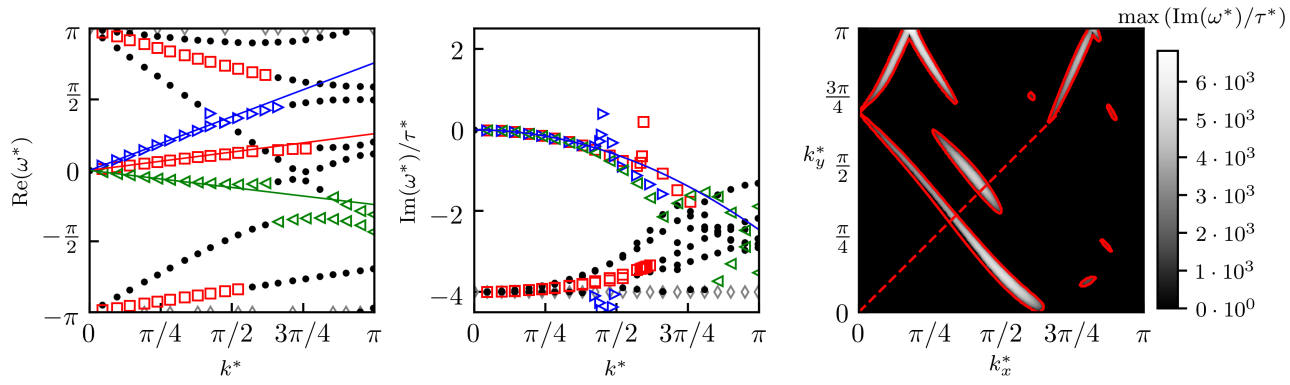

(a) BGK, unstable

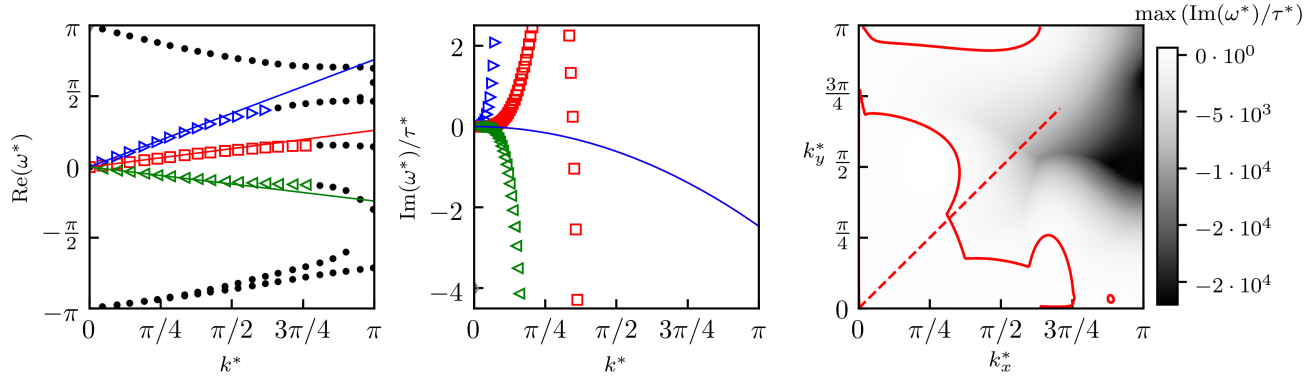

(b) HRR $\sigma = 1$, unstable

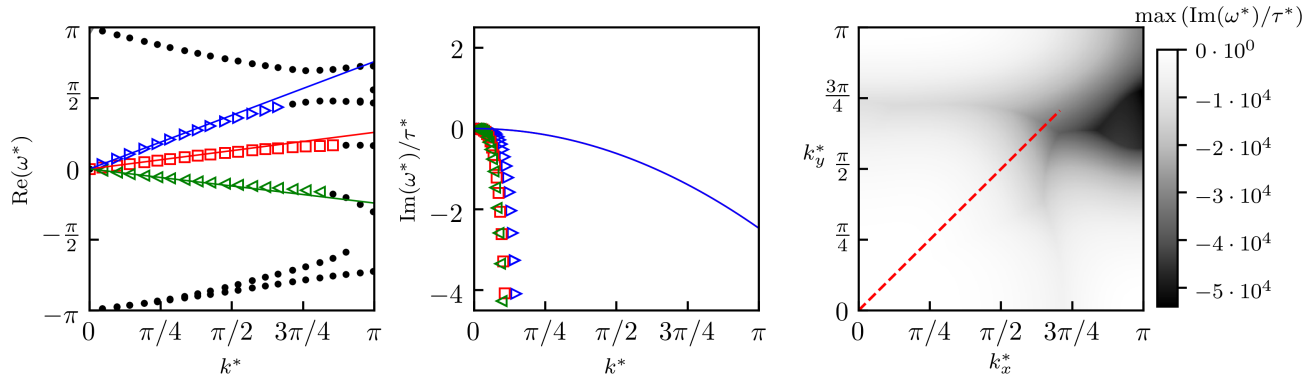

(c) HRR $\sigma = 0.7$, stable

Figure 6.7 – Spectral properties of the corrected LBM D2Q9 for three collision models : BGK (a), HRR $\sigma = 1$ (b) and HRR $\sigma = 0.7$. Here, $\overline{\mathrm{Ma}} = 0.732$, $\mathrm{Ma}_\theta = 0$, $\theta_0 = 0.75$, $\tau^* = 1.10^{-5}$ and $f_i^{eq,3}$. From left to right : Dispersion graph, dissipation graph and absolute stability map. On this map, the dashed line represents the line along the dispersion and dissipation graphs are plotted ; the solid line represents the unstable regions and therefore corresponds and iso-contour of $\max(\mathrm{Im}(\omega^*)/\tau^* = 0)$. Symbols correspond to ω_{ac+}: (▷) ; ω_{ac-}: (◁) ; ω_{shear}: (□) ; ω_{msp}:(●) ; ω_g:(◊) and solid lines correspond to theory.

responsible for this phenomenon remains present despite the use of the RR3 collision model. To summarize the observations drawn on the D2Q9-RR3 model:

- a standard value $\theta_0 \approx 1$ leads to an acoustic eigenvalue collision for $\overline{\text{Ma}} \approx 0.7$,
- decreasing θ_0 yields an amplification of isolated modes, responsible for an unstable scheme,

Thus, unlike in one-dimensional cases, the θ_0 parameter is not sufficient to increase the robustness of 2D compressible LB schemes. It leads to the use of the second stabilization lever, *i.e.* the finite-differences reconstruction parameter σ. This stabilization phenomenon is illustrated on Fig. 6.7c, where the HRR model is used with $\sigma = 0.7$. As observed previously, this parameter leads to a dissipation of the physical waves, restoring the numerical stability of the model whatever the wavenumber of the perturbation.

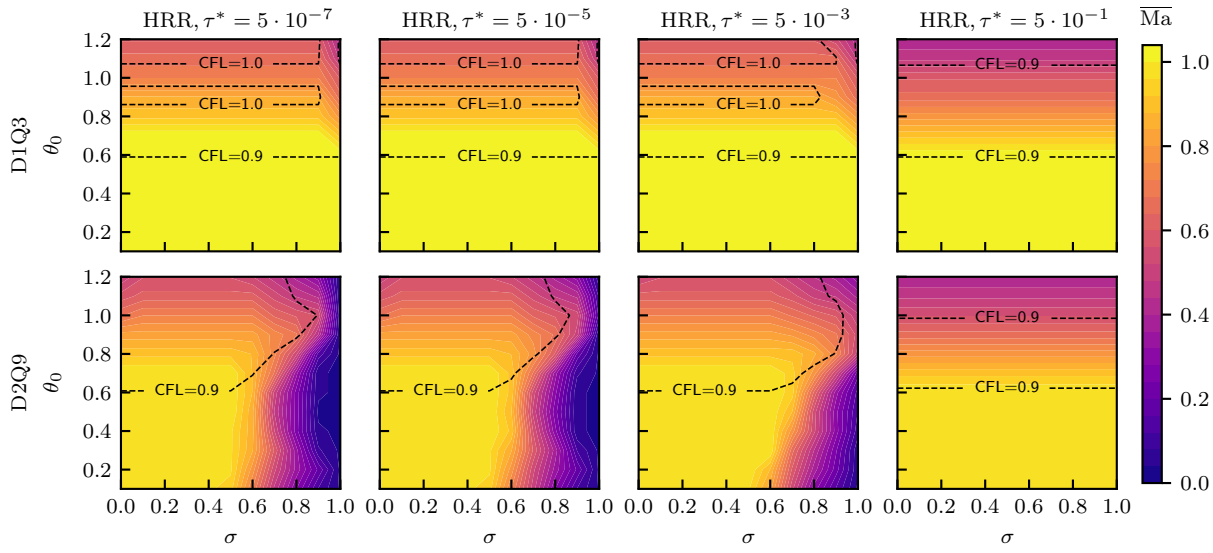

Figure 6.8 – Maximum achievable Mach number acting on both θ_0 and σ stabilization levers. D1Q3 lattice (top) D2Q9 lattice (bottom). Iso level of CFL number are displayed in dashed lines for the single value of CFL = 0.9 and for ten values evenly distributed for CFL $\in [1.0, 1.1]$.

Thus, in order to ensure numerical stability for relatively large Mach numbers, there is a competition between the destabilizing effects of the θ_0 parameter and the dissipative effects induced by the σ parameter. To shed light on this phenomenon, a stability study on the parametric space is carried out for the D1Q3 and the D2Q9 lattices. For four values of the dimensionless relaxation time $\tau^* \in [5.10^{-7}, 5.10^{-5}, 5.10^{-3}, 5.10^{-1}]$, the space formed by $[\theta_0, \sigma]$ is scanned to find the maximum Mach number allowed by the model. In this case, twelve values are considered for $\theta_0 \in [0.1, 1.2]$ and ten values for $\sigma \in [0, 1]$. The maximum Mach number is found using a bisection method with a convergence criterion taken as $\Delta\overline{\text{Ma}} < 0.05$, where the delta represents the difference of the values found between two

iterations. For the D2Q9 case, the angle of the average velocity field Ma_θ is scanned for 13 values evenly distributed between 0 and 45 degrees. The wavenumber space is defined such as $k_x^* \in [-\pi, \pi]$ and $k_y^* \in [0, \pi]$, and discretized by 160 and 80 points respectively. For the D1Q3 lattice, $k^* \in [0, \pi]$ and is discretized by 80 points. The results of this study are shown on Fig. 6.8 for both lattices. As previously mentioned, decreasing θ_0 has stabilizing effects on the D1Q3 lattice. The latter directly drives the CFL constraint which, according to the iso-countour, never exceeds CFL = 1. On the contrary, σ has very little influence on the stability.

Regarding the D2Q9 case, and as for the 1D case, CFL > 1 cannot be reached. Moreover it is clearly visible that for values $\theta_0 \neq 1$, the maximum Mach number is much more strongly correlated to the value of σ, which confirms the previous observations. It is worth noting that both schemes have a limit close to $\overline{\mathrm{Ma}}$ =1. This limit can be addressed by upwinding the correction term ψ_i, as illustrated in App. C, and explains why the model is limited to subsonic regime when a centered discretization is used for ψ_i as observed in Chap. 4. Finally one can see that the two schemes have a nearly similar behavior for the particular value of $\tau^* = 0.5$, where the collide and stream algorithm simply reduces to $g_i^+ = f_i^{eq}$, a singular configuration as referred in [40] . In any event, the closer τ^* is to one-half, the less dissipation needs to be added *via* σ to keep the model stable.

6.4 Extended linear analyses of the hybrid systems

The main numerical properties of the LB models of interest in the present work (especially the role of θ and σ) have been investigated, up to now, in the athermal framework. The aim of the present section is now to perform an original extended analysis of the hybrid method, so as to better understand the numerical behavior of the HLBM for compressible flows. The influence of the choice of the thermodynamic variable for the energy equation is also investigated, since this point has been proved to have a strong influence on the properties of the global numerical methods for discretized Euler and Navier-Stokes equations, e.g. [220, 232].

6.4.1 Method and concepts

Without loss of generality, the methodology will be detailed here for a set of continuous equations only, knowing that it can be directly transposed to discrete numerical schemes. In this case, the hybrid system is composed of the DVBE coupled with the energy equation. It can be written as:

$$\begin{cases} \dfrac{\partial f_i}{\partial t} = \mathcal{S}_i^{DVBE}(f_j, \rho\phi), \\ \dfrac{\partial (\rho\phi)}{\partial t} = \mathcal{S}^{En}(f_j, \rho\phi), \end{cases} \tag{6.4.1}$$

where in the present case, only the conservative form of the energy equation is considered, without loss of generality for its primitive form. Note that, like μ, the heat conductivity

λ will be considered as a constant property of the fluid in what follows, as well as c_p and c_v. Once the system is linearized (with $f_i = \overline{f_i} + f_i'$ and $\rho\phi = \overline{\rho\phi} + (\rho\phi)'$), a time-advance matrix M_{ij}^{HDVBE} is obtained. It can be decomposed into four distinct blocks: two diagonal and two off-diagonal ones. Fig. 6.9 details the composition of each block according to the choice of the energy variable. The diagonal parts model the influence of an equation (resp. DVBE or energy equation) on its involved variable (resp. f_i and $\rho\phi$). The off-diagonal parts are responsible for the coupling between the DVBE and the energy equation. The upper-right block of the matrix is the interaction of the aerodynamic variables ρ and u (computed by the DVBE) onto the energy, while the lower-left block is the thermal feedback of the energy equation onto the DBVE system.

$$\mathrm{M}_{ij}^{HDVBE} = \begin{pmatrix} \overset{\boldsymbol{m\times m}}{\dfrac{\partial \mathcal{S}_i^{DVBE}}{\partial f_j}\Big|_{\overline{f}_j,\overline{\phi}}} & \overset{\boldsymbol{m\times 1}}{\dfrac{\partial \mathcal{S}_i^{DVBE}}{\partial \phi}\Big|_{\overline{f}_j,\overline{\phi}}} \\ \underset{\boldsymbol{1\times m}}{\dfrac{\partial \mathcal{S}^{En}}{\partial f_j}\Big|_{\overline{f}_j,\overline{\phi}}} & \underset{\boldsymbol{1\times 1}}{\dfrac{\partial \mathcal{S}^{En}}{\partial \phi}\Big|_{\overline{f}_k,\overline{\phi}}} \end{pmatrix} = \begin{pmatrix} \mathbf{I} & \mathbf{II} \\ \mathbf{III} & \mathbf{IV} \end{pmatrix}$$

Block **III**: LBM on Hybrid

	conservative			primitive		
	E	e	s	E	e	s
convection	✓	✓	✓	✗	✗	✗
$\mathcal{P}$	✓	✓	∅	✓	✓	∅
$\mathcal{F}$	✗	✗	✓	✗	✗	✓
$\mathcal{V}$	✓	∅	∅	✓	∅	∅

Block **IV**: Hybrid on Hybrid

	conservative			primitive		
	E	e	s	E	e	s
convection	✓	✓	✓	✓	✓	✓
$\mathcal{P}$	✗	✗	∅	✗	✗	∅
$\mathcal{F}$	✓	✓	✓	✓	✓	✓
$\mathcal{V}$	✗	∅	∅	✗	∅	∅

Figure 6.9 – Multiblock arrangement of the linearized HDVBE Matrix and their contributions. Block I models the DVBE system acting on itself similarly to block IV for the energy. Block II is responsible for the perfect gas coupling through f_i^{eq} and ψ_i the thermal correction. The contribution of the different energy terms in blocks III and IV are given in the tables in function of the various configurations; the term is present: ✓, missing: ✗ or does not exist in the linearized equation: ∅.

Following Eq. (6.3.1b), the fluctuations f_i' and $(\rho\phi)'$ are expressed under the form of plane monochromatic waves leading to the following eigenvalue problem:

$$\omega \widehat{\mathcal{X}}_i = \widetilde{\mathrm{M}}_{ij}^{HDVBE} \widehat{\mathcal{X}}_i. \tag{6.4.2}$$

Here, $\widehat{\boldsymbol{\mathcal{X}}} = \left(\widehat{f_0}, ..., \widehat{f_{m-1}}, \widehat{\rho\phi}\right)^T$ is the vector gathering the amplitude fluctuations of both distribution functions and energy variable, and $\widetilde{\mathrm{M}}_{ij}^{HDVBE}$ is the time advance matrix in the Fourier space. For more details on the derivation of this matrix, one can relate to App. D.2. Diagonalizing the matrix $\widetilde{\mathrm{M}}_{ij}^{HDVBE}$ provides $(m+1)$ eigenvalues $(\omega_l)_{l\in[\![0,m]\!]}$ and eigenvectors $(\mathrm{Y}_i^l)_{l\in[\![0,m]\!]}$. Thus, $m+1$ linear eigen-modes of the system (6.4.1) are obtained.

Once diagonalized it reads:

$$\omega_l \mathrm{Y}_i^l = \widetilde{\mathrm{M}}_{ij}^{HDVBE} \mathrm{Y}_i^l. \tag{6.4.3}$$

Like in the athermal case of Sec. 6.3, the spectral behavior of the system has to be compared with a reference. Linearizing the Navier-Stokes-Fourier equations, an entropy mode ω_{entr} is obtained in addition to those present in the athermal case. The eigenvalues of these modes are:

$$\begin{aligned}
\omega_{shear} &= k_\alpha \overline{u}_\alpha - \mathrm{i}\overline{\nu} \left\| k_\alpha \right\|^2 + O\left(k^3\right), \\
\omega_{entr} &= k_\alpha \overline{u}_\alpha - \mathrm{i}\overline{\kappa} \left\| k_\alpha \right\|^2 + O\left(k^3\right), \\
\omega_{ac\pm} &= k_\alpha \overline{u}_\alpha \pm \left\| k_\alpha \right\| \sqrt{\gamma c_s^2 \overline{\theta}} - \mathrm{i}\left(\frac{D-1}{D} \overline{\nu} + \frac{\gamma_g - 1}{2} \overline{\kappa} \right) \left\| k_\alpha \right\|^2 + O\left(k^3\right),
\end{aligned} \tag{6.4.4}$$

with $\overline{\theta} = \overline{T}/T_r$ the dimensionless temperature and $\overline{\kappa} = \lambda/(\overline{\rho} c_p)$ the mean heat diffusivity. Compared to the athermal case, the shear mode ω_{shear} (only present in 2D) remains unchanged while the two acoustic modes are altered in terms of dispersion and dissipation, which is a direct consequence of taking into account the energy fluctuations. The speed of sound is now isentropic and the thermal diffusivity is now involved in the acoustic dissipation.

Similarly to the athermal study of Sec. 6.3, a physical interpretation of the modes obtained by the linear analysis can be done. In that respect, an extension of the methodology of Wissocq et al. [63] applied to the hybrid LB models is proposed. First, a macroscopic counterpart $\boldsymbol{\mathcal{E}}_l^{HLB}$ of the hybrid LB eigenvectors is defined such as:

$$\boldsymbol{\mathcal{E}}_l^{HLB} = \left[\widehat{\rho}^{HLB} = \sum_{i=0}^{m-1} \mathrm{Y}_i^l, \quad \left(\widehat{u}_\alpha^{HLB} = \frac{1}{\overline{\rho}} \left(\sum_{i=0}^{m-1} c_{i,\alpha} \mathrm{Y}_i^l - \overline{u}_\alpha \sum_{i=0}^{m-1} \mathrm{Y}_i^l \right) \right), \quad \widehat{T}_{\rho\phi}^{HLB} \right]^{\mathrm{T}}, \tag{6.4.5}$$

where the expression of $\widehat{T}_{\rho\phi}^{HLB}$ can be found in Table 6.3 for the conservative and primitive forms.

	Convervative	Primitive
$\widehat{T}_{\rho E,E}^{HLB}$	$\dfrac{1}{\overline{\rho} c_v} \left(\widehat{\rho E}^{HLB} - \left(c_v \overline{T} + \overline{u}_\alpha^2/2 \right) \widehat{\rho}^{HLB} - \overline{\rho u}_\alpha \widehat{u}_\alpha^{HLB} \right)$	$\dfrac{1}{c_v} \left(\widehat{E}^{HLB} - \overline{u}_\alpha \widehat{u}_\alpha^{HLB} \right)$
$\widehat{T}_{\rho e,e}^{HLB}$	$\dfrac{1}{\overline{\rho} c_v} \left(\widehat{\rho e}^{HLB} - c_v \overline{T} \widehat{\rho}^{HLB} \right)$	$\dfrac{\widehat{e}^{HLB}}{c_v}$
$\widehat{T}_{\rho s,s}^{HLB}$	$\dfrac{\overline{T}}{\overline{\rho} c_v} \left\{ \widehat{\rho s}^{HLB} - c_v \left[\ln\left(\overline{T}\right) - (\gamma - 1) \left(\ln\left(\overline{\rho}\right) + 1 \right) \right] \widehat{\rho}^{HLB} \right\}$	$\overline{T} \left(\dfrac{\widehat{s}^{HLB}}{c_v} + \dfrac{\gamma - 1}{\overline{\rho}} \widehat{\rho}^{HLB} \right)$

Table 6.3 – Expression of the temperature fluctuations depending on the HLB energy variables and formulation.

A similar linear stability analysis of the continuous Navier-Stokes-Fourier equations yields the following eigenvectors, written here according to the primitive variables:

$$\boldsymbol{V}_{mode}^{NS} = \left[\widehat{\rho}^{NS}, \quad \left(\widehat{u}_\alpha^{NS} \right), \quad \widehat{T}^{NS} \right]^{\mathrm{T}}, \quad \mathrm{mode} \in \left[shear, ac-, ac+, entr \right]. \tag{6.4.6}$$

Similarly to the athermal analysis of Sec. 6.3.1, the contribution of each HLB mode $\boldsymbol{\mathcal{E}}_l^{LB}$ in terms of physical macroscopic modes can then be expressed as:

$$\boldsymbol{\mathcal{E}}_l^{HLB} = a_l \boldsymbol{V}_{shear}^{NS} + b_l \boldsymbol{V}_{ac-}^{NS} + c_l \boldsymbol{V}_{ac+}^{NS} + d_l \boldsymbol{V}_{entr}^{NS}, \tag{6.4.7}$$

where the new coefficient d_l corresponds to the complex contributions of $\boldsymbol{\mathcal{E}}_l^{HLB}$ on the entropy mode. The passage matrix is now built such as $\boldsymbol{P}_{NS} = \left[\boldsymbol{V}_{ac-}^{NS}, \boldsymbol{V}_{ac+}^{NS}, \boldsymbol{V}_{shear}^{NS}, \boldsymbol{V}_{entr}^{NS}\right]$ and allows computing each of these coefficients:

$$(a_l, b_l, c_l, d_l)^T = \boldsymbol{P}_{NS}^{-1} \boldsymbol{\mathcal{E}}_l^{HLB}. \tag{6.4.8}$$

These coefficients are finally normalized so that $|a_l| + |b_l| + |c_l| + |d_l| = 1$. In this way, the macroscopic nature of the modes resulting of the hybrid LB linear analysis is directly accessible by looking to the module of each coefficient. For details about the derivation of $\boldsymbol{V}_{mode}^{NS,ath}$, the interested reader can refer to App. D.3.

The methodology introduced here with a set of continuous equations can directly be applied to a discrete system such as the HLBM. In this case, the matrix system reads:

$$e^{-\mathrm{i}\omega_l \Delta t} \mathrm{Y}_i^l = \widetilde{\mathrm{M}}_{ij}^{HLBM} \mathrm{Y}_i^l. \tag{6.4.9}$$

where details on $\widetilde{\mathrm{M}}_{ij}^{HLBM}$ can be found in App. D.2. Like in the athermal case, the logarithm of the eigenvalues has to be computed in order to obtain the complex temporal pulsations ω_l.

6.4.2 Linear analysis of the HDVBE

Here again, a dimensional analysis is first conducted to clearly underline the number of independent parameters of the HDVBE. Compared to the athermal DVBE system, adding an energy equation implies the consideration of the temperature as a new fundamental unit. Furthermore, four additional independent variables naturally emerge from the energy equation, namely the heat capacity ratio at constant pressure c_p and volume c_v, the mean fluid temperature $\overline{T}$ and the mean heat diffusivity $\overline{\kappa} = \lambda/(\overline{\rho} c_p)$. It gives rise to two additional dimensionless numbers to fully characterize the system, which now reads in one dimension:

$$\omega_\tau = \mathcal{L}\left(\overline{\mathrm{Ma}}, \overline{\mathrm{Kn}}, \overline{\theta}, \gamma_g, \mathrm{Pr}\right), \tag{6.4.10}$$

with

$$\begin{gathered} \omega_\tau = \frac{\omega \overline{\nu}}{r_g \overline{T}}, \quad \overline{\mathrm{Ma}} = \frac{\overline{u}}{\sqrt{\gamma_g r_g \overline{T}}}, \quad \overline{\mathrm{Kn}} = \frac{\overline{\nu} k}{\sqrt{\gamma_g r_g \overline{T}}}, \quad \overline{\theta} = \frac{\overline{T}}{T_r}, \\ \gamma_g = \frac{c_p}{c_v} \quad \text{and} \quad \mathrm{Pr} = \frac{\mu c_p}{\lambda}. \end{gathered} \tag{6.4.11}$$

Here, Pr is the Prandtl number of the considered fluid and γ_g its heat capacity ratio. In this work, the value of these parameters, which are related to the fluid characteristics,

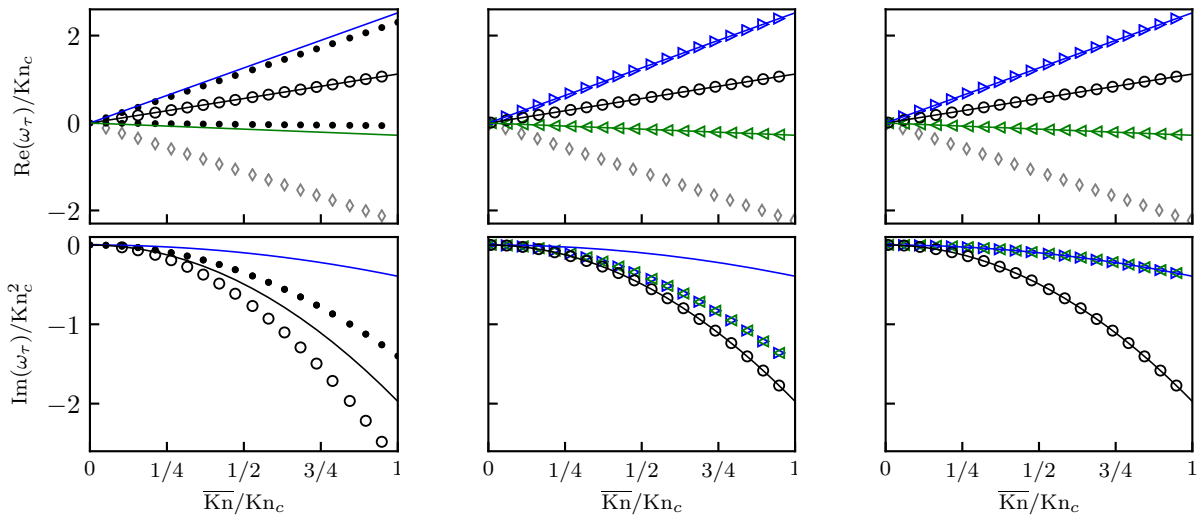

(a) $\mathscr{P} = \varnothing$, $E_{2,\alpha\beta} = \varnothing$. (b) $\mathscr{P} = \checkmark$, $E_{2,\alpha\beta} = \varnothing$. (c) $\mathscr{P} = \checkmark$, $E_{2,\alpha\beta} = \checkmark$.

Figure 6.10 – Propagation (top) and dissipation (bottom) curves of the Hybrid $D1Q3$ on ρe with $f_i^{eq,2}$ and for $\overline{\text{Ma}} = 0.8$. Fig. (a-b) shows the influence of the pressure work term on the acoustic propagation and Fig. (b-c) the influence of the $E_{2,\alpha\beta}$ correction acting on the acoustic dissipation. Symbols correspond to ω_{ac+}: (▷) ; ω_{ac-}: (◁) ; ω_{entr}: (○) ; ω_{msp}:(●) ; ω_g:(◊) and solid lines correspond to theory.

are set constant as Pr = 0.71 and $\gamma_g = 1.4$. Similarly to the DVBE system in Sec (6.3.2), the same argument stands regarding $\overline{\text{Kn}} \ll 1$. Exploring this parameter space allows studying the system in all the possible configurations.

The spectral analysis of the fully corrected D1Q3 HDVBE is displayed on Fig. 6.10c, where the conservative form of the internal energy equation is considered. First, one can notice that this system is linearly stable for $\overline{\text{Ma}} = 0.8$, a mean Mach number larger than the critical value without Mach correction. Thus, one can conclude that: (1) the correction term $E_{1,\alpha\beta}$ still owns stabilizing properties in this hybrid context, and (2) coupling the mesoscopic system (DVBE) and the macroscopic energy equation does not lead to singularities. Secondly, the propagation curves of Fig. 6.10a and Fig. 6.10b indicate that the pressure work $\mathscr{P}$ is directly involved in the isentropic speed of sound $\sqrt{\gamma c_s^2 \theta}$. On Fig. 6.10a, where $\mathscr{P}$ is missing, two modes of macroscopic nature (black dot) are identified instead of the expected acoustics. They do not propagate the exact acoustic information at the expected isentropic speed of sound. Nevertheless, the propagation of the entropic mode is well recovered, whereas its dissipation rate is overestimated compared to the theoretical value. From the two dissipation curves Fig. 6.10b and Fig. 6.10c, it is possible to see the influence of $E_{2,\alpha\beta}$: correcting the polyatomic deficiency of the DVBE affects the trace of the viscous stress tensor [225]. In addition to grant the correct dissipation, modifying this term in a straightforward way also allows adding a potential volume viscosity which is a desirable feature in CFD context [67, 233].

Finally, the very same behavior is observed for the two-dimensional case on Fig. 6.11, where propagation and dissipation curves of the D2Q9 HDVBE are conducted for $k_y = 0$

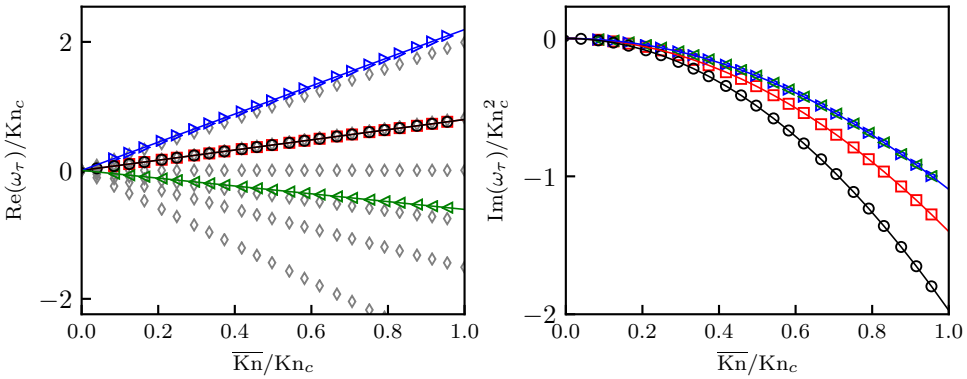

Figure 6.11 – Propagation and dissipation curves of the corrected hybrid D2Q9 along $\boldsymbol{ex}$ at $\overline{\mathrm{Ma}} = 0.8$, $\mathrm{Pr} = 0.71$, $\gamma_g = 1.4$ $\mathrm{Ma}_\theta = 0$, $\overline{\theta} = 1$ and $f_i^{eq,3}$. Symbols correspond to ω_{ac+}: (▷) ; ω_{ac-}: (◁) ; ω_{entr}: (○) ; ω_{shear}: (□) ; ω_g:(◇) and solid lines correspond to theory.

and a horizontal mean flow at $\overline{\mathrm{Ma}} = 0.8$. Here, both $E_{1,\alpha\beta}$ and $E_{2,\alpha\beta}$ are included. The spectral properties of this hybrid system perfectly match the Navier-Stokes theoretical values in terms of dispersion and dissipation, suggesting that the system faithfully recovers the targeted equations. Thus, a numerical method based on this set of equations should converge to the resolution of the compressible Navier-Stokes system. The analysis of such scheme is precisely the subject of the next section.

6.4.3 Von Neumann analysis of the HLBM scheme

Compared to the continuous HDVBE and similarly to the athermal LBM, the time step Δt has to be considered as an additional independent variable. The number of fundamental units remains unchanged (mass, length, temperature and time), which gives rise to one additional dimensionless number τ^* to fully characterize the system. The discrete system now reads:

$$\omega^* = \mathcal{L}\left(\overline{\mathrm{Ma}}, k^*, \overline{\theta}, \gamma_g, \mathrm{Pr}, \tau^*\right), \tag{6.4.12}$$

with

$$\omega^* = \omega\Delta t, \quad \overline{\mathrm{Ma}} = \frac{\overline{u}}{\sqrt{\gamma_g r_g \overline{T}}}, \quad k^* = k\Delta x, \quad \overline{\theta} = \frac{\overline{T}}{T_r}, \quad \gamma_g = \frac{c_p}{c_v}, \quad \mathrm{Pr} = \frac{\mu c_p}{\lambda} \quad \text{and} \quad \tau^* = \frac{\overline{\tau}}{\Delta t}. \tag{6.4.13}$$

Based on the sampling rate arguments detailed in Sec. 6.3.3, k^* has been preferred to $\overline{\mathrm{Kn}}$ for this discrete study, along with ω^* instead of ω_τ. Moreover, since the isentropic speed of sound is expected to be recovered, $\sqrt{\gamma_g c_s^{*2}\overline{\theta}}$ is the maximal speed allowed by the system for $\overline{\mathrm{Ma}} = 0$. Thus, dividing it by the speed of the numerical information $(\Delta x/\Delta t)$, the CFL number related to the HLBM reads:

$$\mathrm{CFL} = \left(\overline{\mathrm{Ma}} + 1\right)\sqrt{\gamma c_s^{*2}\overline{\theta}}. \tag{6.4.14}$$

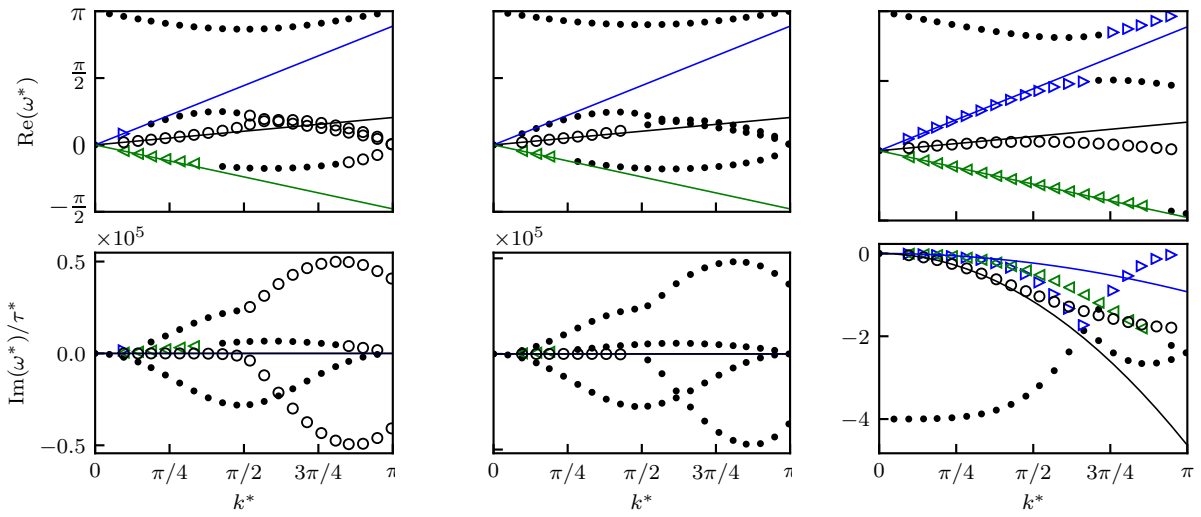

(a) ρe. (b) ρE. (c) ρs.

Figure 6.12 – Dispersion (top) and dissipation (bottom) curves of the D1Q3-BGK-RK4C02 scheme for $\overline{\theta} = 1$, $\overline{\mathrm{Ma}} = 0.3$, $\tau^* = 10^{-5}$. Symbols correspond to ω_{ac+}: (▷) ; ω_{ac-}: (◁) ; ω_{entr}: (○) ; ω_{msp}:(●) ; ω_g:(◊) and solid lines correspond to the NS theory.

This number is, by construction, always larger than its athermal counterpart since $\gamma_g > 1$. As previously adopted, $\overline{\theta}$ is set as $\overline{\theta} \in [0, 1.2]$, so that the CFL number remains below, or close to, unity. Finally, the study holds on $\tau^* \in [10^{-8}, 0.5]$ for the same reason as mentioned in Sec. 6.3.3. Exploring this parameter space allows evaluating the system in all the possible configurations of interest.

Fig. 6.12 displays the spectral behavior of the D1Q3-BGK-RK4CO2 scheme for three conservative forms of the energy equation, based on: ρe, ρE and ρs. In the present case $\overline{\theta} = 1$, $\overline{\mathrm{Ma}} = 0.3$ and $\tau^* = 10^{-5}$. First, note that the internal and total energy-based HLBM schemes are found unstable, unlike the entropy-based scheme. The dispersion and dissipation behaviors of the two unstable schemes are rather similar. The dispersion curve highlights a destructive interaction close to $k^* = \pi/2$ between two modes of the HLBM. The nature of this instability appears similar to that observed in Sec. 6.3.3, hinting towards the use of the same levers to circumvent this kind of instability.

The use of the HRR collision operator can be considered, as well as lowering the time step *via* a change of $\overline{\theta}$. However, as observed in Sec. 6.3.3, a reduction of θ is expected to decrease the group velocity of each numerical mode, which might enhance the mode coupling observed in the present case, resulting in lower numerical stability. Yet, the use of σ as stabilizing lever will be *a priori* preferred in such a case. Nevertheless, before changing the collision operator, Fig. 6.12c shows that the entropy-based model is stable and has correct spectral properties. This suggests that the form of the considered equation is at least as important as the type of collision operator, the adopted FD scheme or the value of the $\overline{\theta}$. At last, despite the relatively low Mach number of Fig. 6.12c, note that a curve veering is observed regarding the downstream acoustic information, contrary to the athermal case, where this only occurs when $\overline{\mathrm{Ma}} \approx 0.6$. This is probably due to

the fact that, in the hybrid case, the sound speed is increased by a factor $\sqrt{\gamma_g}$. As a consequence, the eigenvalue collision phenomenon mentioned in Sec. 6.3.3 for $\theta_0 = 1$ turns out to appear, in the hybrid framework, below $\overline{\mathrm{Ma}^c} = 0.732$. Further observations indicate that this critical value can be, like its athermal counterpart, correlated to the CFL number at unity, so that:

$$\overline{\mathrm{Ma}^c} = \frac{1}{c_s^* \sqrt{\gamma \overline{\theta}}} - 1, \tag{6.4.15}$$

which suggests that the $\overline{\theta}$ stabilization lever can play an even more important role in the hybrid context.

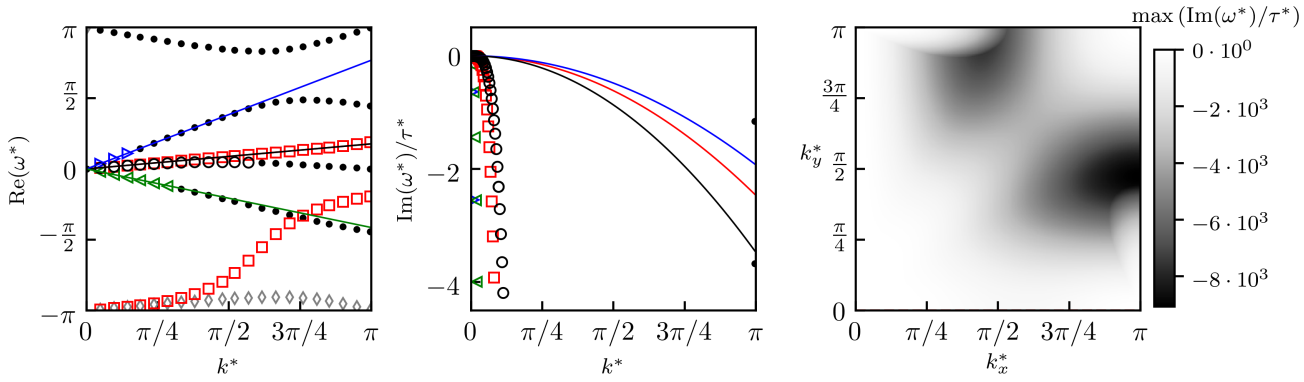

(a) Conservative form, stable

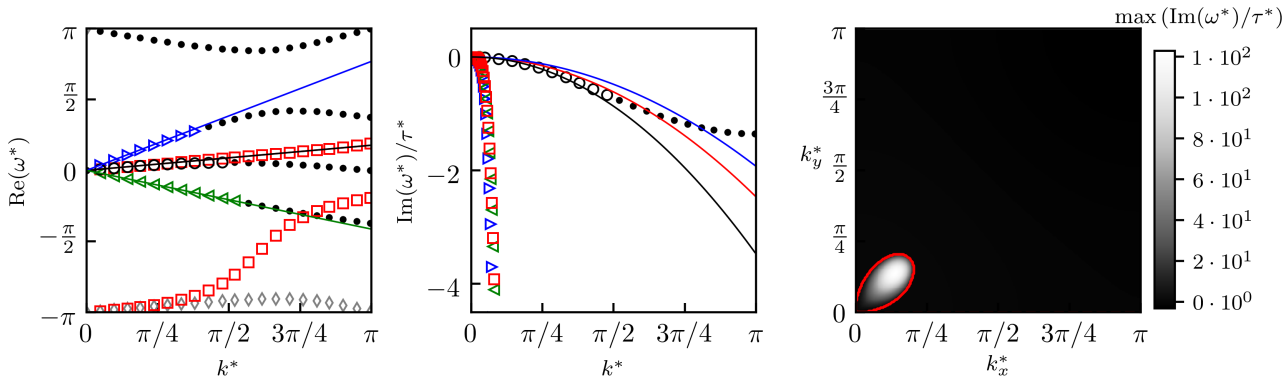

(b) Primitive form, unstable

Figure 6.13 – Spectral properties of the D2Q9 RK2CO2 HRR on entropy for : conservative form (a) and primitive form (b). In the present case, $\overline{\mathrm{Ma}} = 0.3$, $\mathrm{Ma}_\theta = 0$, $\theta = 0.75$, $\tau^* = 1.10^{-5}$, $f_i^{eq,3}$ and $\sigma = 0.5$. From left to right : Dispersion graph, dissipation graph (both plotted along $\boldsymbol{e}_x$) and absolute stability map. On this map the solid line represents the unstable regions which corresponds to iso-contour of $\max(\mathrm{Im}(\omega^*)/\tau^* = 0)$. Symbols correspond to ω_{ac+}: (▷) ; ω_{ac-}: (◁) ; ω_{entr}: (○) ; ω_{shear}: (□); ω_{msp}:(●) ; ω_g:(◊) and solid lines correspond to theory.

Let us now focus on the coupled D2Q9 lattice. In Sec. 6.3.4, the two-dimensional athermal models based on the BGK and RR3 collision operators were found to be unstable for Mach numbers of interest in the compressible regime. Among the collision models under consideration, only the use of the HRR one allowed stabilizing the scheme. Consequently, the σ parameter turns out to be an essential ingredient in the hybrid context, where compressible applications are targeted. Fig. 6.13 displays the spectral properties of the hybrid D2Q9 HRR scheme based on the conservative and primitive forms of the entropy equation for an horizontal mean flow at $\overline{\mathrm{Ma}} = 0.3$. With similar numerical parameters, striking differences can be observed depending on the formulation used. First, the $\max(\mathrm{Im}(\omega^*)/\tau^*)$ maps on Fig. 6.13 exhibit the stability of the conservative formulation, while the primitive formulation is found unstable. Thus, in addition to the energy variable used, the formulation of the energy equation is a crucial parameter to take into account regarding the stability of the models. However, based on these observations, there is no proof that the primitive form is unconditionally unstable. As in Sec. 6.3.4, a wiser choice of the $\overline{\theta}$ or σ parameters could lead to a stable scheme. Such an investigation is the purpose of Sec. 6.5. Looking at the dissipation curves, both conservative and primitive models over-dissipate acoustic and shear waves compared to the expected Navier-Stokes behavior. The rate of acoustic dissipation seems to be more impacted in the conservative case than in the primitive one, while the shear dissipation seems to be equivalent. This over-dissipation, also noticed in the athermal cases of Sec. 6.3.4, can be attributed to time and space errors of the regularized scheme [72] as well as the over-dissipation brought by the σ parameter. However, it is noteworthy that the entropic wave of the primitive case does not seem to suffer from the same over-dissipation and correctly recovers the NS expectations. Indeed its dissipation curve is very similar to that of the RK4CO2 scheme applied solely to an advection diffusion equation. This suggests that the numerical errors of the LB scheme only impact the entropic wave in the conservative case, while usual low-dissipation properties of the RK4CO2 scheme are recovered in the primitive case.

Last, the acoustic waves are carried at more than $\eta = 99\%$ for very low wavenumbers only in the conservative case (less than 16 points per wavelength for $\omega^*_{r,ac+}$), while in the primitive case, they are identified up to 6 points per wavelength. Thus, if a wave is under-resolved, any combination of macroscopic modes (shear, acoustic and entropic) can be carried at an acoustic group velocity close to the speed of sound, which could be damaging for a simulation. Despite all these observations, this brief preliminary study does not make it possible to choose between the two formulations, but only to note their main differences. It therefore reinforces the relevance of a parameter study on both primitive and conservative formulations, as proposed in Sec. 6.5.

Finally, although the hybrid system has been shown stable for continuous equations regardless the energy variables and the primitive/conservative formulation used, this is far from being the case once the equations are written in a discrete form. Throughout this section, extremely different behaviours have been observed only changing these two parameters, reflecting the non-triviality of the problem. In addition, it can be expected that the FD scheme applied to the energy equation along with the parameters $\overline{\theta}$ and σ can also alter the dispersion, dissipation and the macroscopic content of the waves propagated, further increasing the scope of the study. Before going deeper into the analysis of these

schemes, a first sorting must be done to rule out unusable combinations. The following section will therefore be dedicated to a simple stability study of these schemes to establish a certain trend for the possible stable configurations and the possible causes of instability.

6.5 Linear investigations of the HLBM scheme

In this section, the potential of different classes of hybrid schemes is discussed. All of the HLBM schemes under consideration are based on the HRR collision operator, and differ by the choice of: (1) the energy variable (e, E or s), (2) the formulation of the energy equation (primitive or conservative form), (3) the FD scheme applied to the energy equation (RK1UPO1 or RK4CO2) and (4) whether pressure work is considered. This leads to the study of twenty different models in one and two dimensions over the parametric space described in Sec. 6.4.3. The different models are first sorted from a stability viewpoint, then the parameter space of the most linearly stable classes is discussed.

6.5.1 Stability results of various HLBM classes

The stability of the one- and two-dimensional hybrid classes is investigated over the parameter space described in Sec. 6.4.3. Linear studies are conducted for: $\tau^* \in [5.10^{-8}, 5.10^{-1}]$ discretized with sixteen logarithmically-spaced values, twelve evenly-spaced values of $\overline{\theta} \in [0.1, 1.2]$ and ten evenly-spaced values of $\sigma \in [0, 1]$. The procedure described in Sec. 6.3.4 is employed, where the space formed by $[\overline{\theta}, \sigma]$ is scanned to find the maximum Mach number ensuring linear stability. For the two-dimensional models, the orientation of the mean velocity field Ma_θ is scanned for thirteen evenly distributed values between 0° and 45°. The wavenumber space is defined such as $k_x^* \in [-\pi, \pi]$ and $k_y^* \in [0, \pi]$, respectively discretized using 160 and 80 points. For one-dimensional cases, the wavenumber space is composed of 80 evenly-spaced points for $k^* \in [0, \pi]$. To put it in a nutshell, this parametric study is about 640 different calculations on the $[\overline{\theta}, \sigma]$ space.

Plotting the 640 graphs like the ones shown in Fig. 6.8 would be a tedious way to interpret all these results. Fortunately, a first sort, based on the viability of a class in the compressible context, can be done. In this spirit, Fig. 6.14 displays the maximum reachable Mach number on $[\overline{\theta}, \sigma]$ as function of τ^* for the twenty different hybrid classes assessed in one and two dimension. Each class is labelled "Usable" if its maximum Mach number exceeds $\overline{\mathrm{Ma}} = 0.3$ for all the values of τ^*, meaning that it potentially meets the required standards for compressible simulations, and "Unusable" otherwise.

One-dimensional results are displayed on Fig. 6.14a and Fig. 6.14b for the RK1UPO1 and RK4CO2 FD schemes respectively. It is worth recalling that the HRR model used with the D1Q3 lattice encompasses the BGK collision model, which is then naturally considered in this study. First, note that all the classes are restricted to a Mach number close to one. As mentioned in Sec. 6.3.4, this limit can be also addressed in the hybrid framework by modifying the FD scheme of the corrective term ([225]), more details can

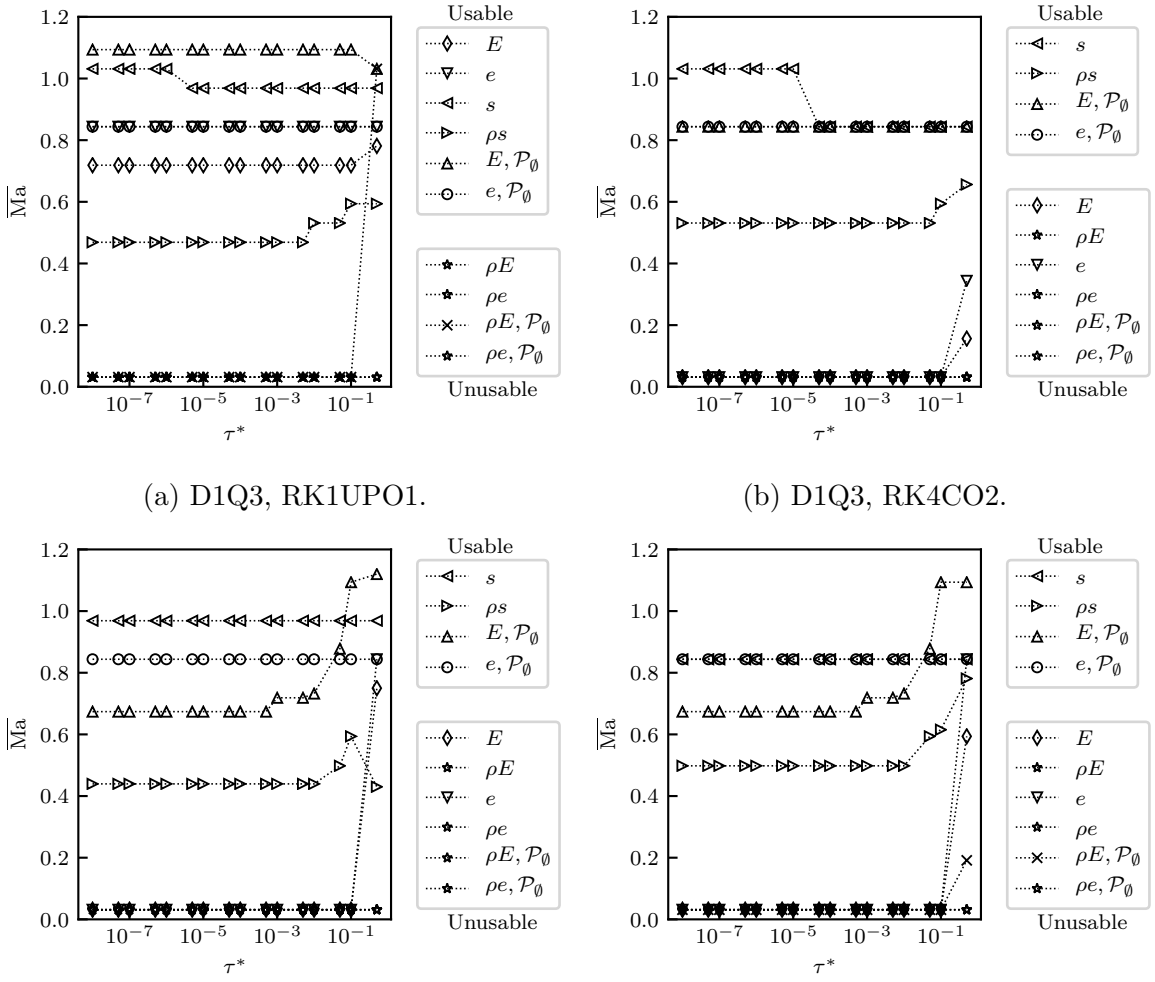

(a) D1Q3, RK1UPO1.

(b) D1Q3, RK4CO2.

(c) D2Q9, RK1UPO1.

(d) D2Q9, RK4CO2.

Figure 6.14 – Maximum stable mean flow Mach number of the hybrid D1Q3 (a)-(b) and D2Q9 (c)-(d) models, investigated over the parametric space $[\overline{\theta}, \sigma]$ for different relaxation times and energy equations. Here $\mathcal{P}_\varnothing$ denotes the absence of pressure work in the equation. Labels "Usable" and "Unusable" indicate whether or not the class can be considered for a compressible simulation.

be found in App. C. First, except for the entropy-based classes, all conservative forms are "Unusable" whatever the numerical scheme used. It is also noticeable that, working on the conservative form of the entropy equation, the maximum Mach number is found to be lower than its primitive counterpart for the two FD schemes used. This suggests that the conservative formulation may induce stronger instabilities, hinting towards the use of a primitive form in terms of robustness. Secondly, classes based on internal and total energy are clearly impacted by the change in the numerical scheme of the energy equation. These forms are found stable for the RK1UPO1 scheme only, which is a first-order scheme, therefore more dissipative. However, once the pressure work is removed

from these equations, larger Mach numbers can be reached with both FD schemes. This gain in terms of stability explains the choice made in some previous work to neglect the pressure work in the energy equation [180, 192], leading to stable systems with a perfect gas equation of state. In addition, no noticeable effect of the discrete scheme used in the pressure work computation has been observed. This indicates that the pressure work is an intrinsic cause of instability. This observation is reinforced by better stability properties of the ρs-based energy equation, which does not require an explicit computation of the pressure work (see Eq. (3.2.5)).

Two-dimensional results are displayed on Fig. 6.14c and Fig. 6.14d, for the RK1UPO1 and RK4CO2 schemes. In the athermal case of Sec. 6.3.4, the two-dimensional model was found much more restrictive than the one-dimensional one, which is due to a larger number of degrees of freedom and the existence of an additional physical shear wave. The same conclusions are drawn from this parametric study on the hybrid classes. Only four of them are found "Usable" using the D2Q9 lattice: the models based on the variables (s), (ρs), $(E, \mathscr{P}_\varnothing)$ and $(e, \mathscr{P}_\varnothing)$. Henceforth, no primitive nor conservative classes including the pressure work are found stable. Only the entropy-based classes are found "Usable" in a full compressible context, which remains true for two FD schemes with the primitive formulation. From these results, the same conclusions as the one-dimensional study can be drawn, namely that:

- classes owning an explicitly pressure work are unstable,
- classes based on the conservative formulation are less robust than the primitive one.

A conclusion of practical interest can then be drawn: the only "Usable" classes for real compressible applications (including pressure work) turn out to be based on the entropy equation.

6.5.2 Stability range of HLBM entropic classes

This first sorting being made, the linear analyses of the entropy-based models can be further studied. From now on, only the classes based on (s) and (ρs) are considered. Fig. 6.15 displays the maximum Mach number allowed by each class on the parameter space $[\overline{\theta}, \sigma]$ with the RK1UPO1 and RK4CO2 schemes, for four typical values of τ^*.

First, the primitive form has rougthly the same behavior whatever the FD scheme used. It is found stable for $\overline{\theta} \in [0.1, 0.8]$ yet for the single value $\sigma = 0$ only. This point is extremely restrictive since, for low values of σ, under-resolved shear and acoustic modes are highly attenuated, as shown in Sec. 6.4.3. Nevertheless, these schemes are found stable and "Usable" for compressible applications, with a limit of $\overline{\mathrm{Ma}} = 0.85$ for the RK4CO2 scheme and $\overline{\mathrm{Ma}} = 0.95$ for the RK1UPO1 one. As the RK1UPO1 scheme is more dissipative than the RK4CO2 one, this gain in robustness in the upwind case is however to be paid in terms of accuracy.

Regarding the conservative form, the RK1UPO1 scheme is found to be "Usable" on only a single point $\left[\sigma = 0; \overline{\theta} = 1\right]$ except for high values of τ^* which evinces the non-viability of this class. Indeed, for a truly compressible application, the temperature may

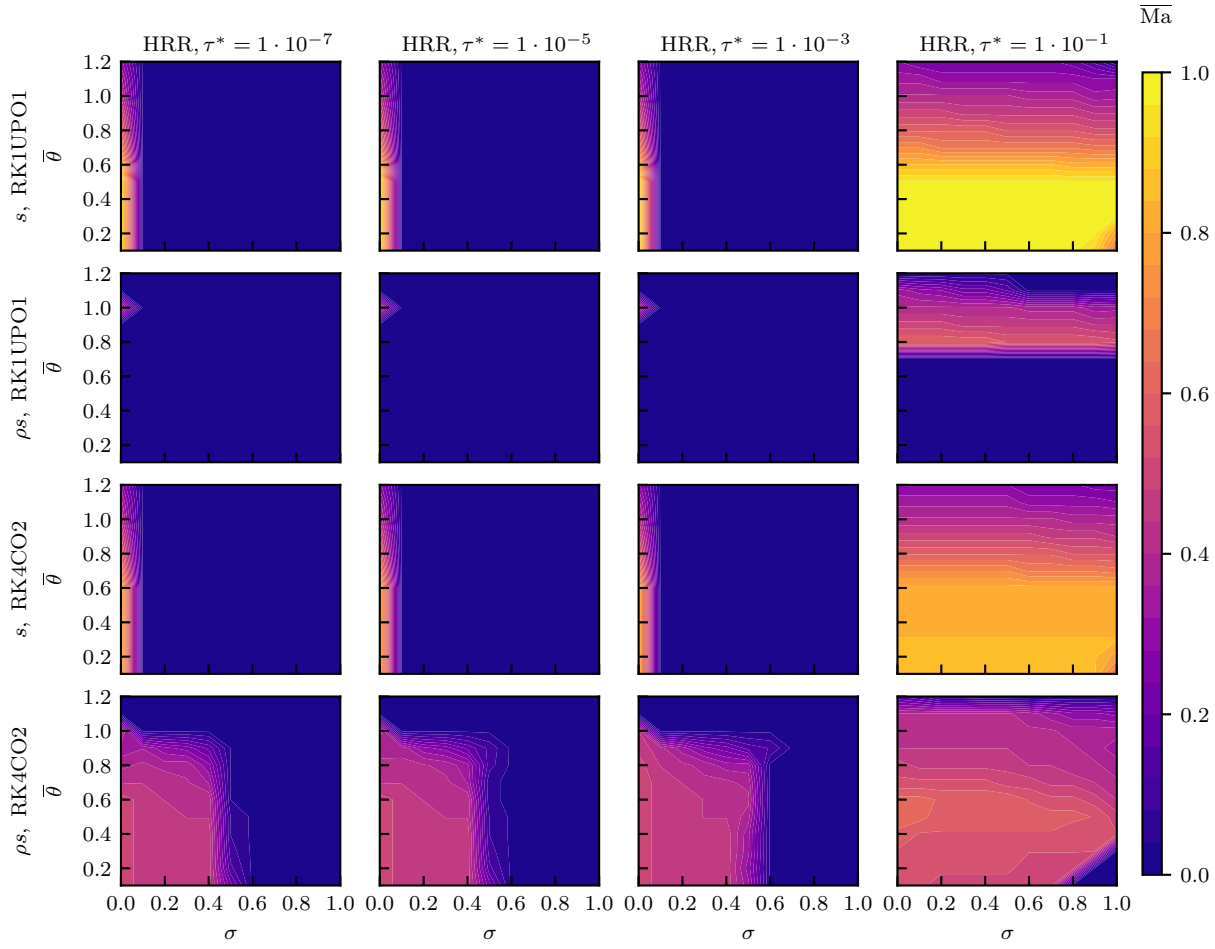

Figure 6.15 – Maximum achievable Mach number of the D2Q9 HRR models based on primitive and conservative entropy equations, acting on both $\overline{\theta}$ and σ stabilization levers, and for the RK1UPO1 and RK4CO2 schemes.

strongly varies in the numerical domain and thus $\overline{\theta}$ will never be fixed near unity, which will make the calculation unstable. Regarding the RK4CO2 scheme, one can see that it is much more tolerant with regard to the allowed values of σ compared to the primitive form. This parameter can be set up to $\sigma = 0.4$ even for low values of τ^*. However, for a low value of τ^*, the maximum Mach number is restricted to $\overline{\mathrm{Ma}} = 0.5$ which is very constraining for compressible applications.

Finally, for $\tau^* = 10^{-1}$ the stability range of the classes is greatly improved, this trend being already observed for the athermal model of Sec. 6.3.4. Thus, for large values of τ^*, both models allow values of σ close to unity, which helps recover acceptable dissipation properties. In addition, according to Fig. 6.3, it is recalled that for a fixed viscosity, τ^* is inversely proportional to Δx. It might then seem wise to adapt the value of σ according to the local mesh size: in coarse regions, a value $\sigma \approx 0$ can be advised to enhance numerical stability (yet at the cost of an over-dissipation), while $\sigma \approx 1$ can be adopted in more

refined zones.

To summarize this section, only three "Usable" classes, all based on the entropy variable, can be retained for compressible applications, out of the twenty models initially proposed. The first one deals with the conservative equation discretized with the RK4CO2 scheme while the two other ones lie on the primitive form discretized with the RK1UPO1 and RK4CO2 schemes respectively which roughly corresponds to the model presented in Chap. 4. Even though some advantages of one model over the other have been discussed above, a more in-depth study is now mandatory to clearly direct a choice. This task is proposed in Sec. 6.6.

6.6 LBM coupled with an entropy equation

In the previous section, an absolute parametric stability study of twenty HLBM classes showed that the RK4CO2 scheme on ρs and s and the RK1UPO1 scheme on s, were the only three stable models for compressible applications. In this section, the major flaws of both of these conservative and primitive classes will be investigated thanks to the extended von Neumann Analysis described in Sec. 6.4.2. The observations evidenced by the LSA will be assessed using numerical simulations of canonical test-cases. Note that all the results presented in this section with the primitive form of the entropy equation can be recovered with both the RK1UPO1 and the RK4CO2 schemes. For this reason, and for the sake of clarity, only the RK4CO2 scheme will be detailed hereafter.

6.6.1 Conservative form: shear-to-entropy production

A HLBM involving the conservative form of the entropy equation, discretized with the RK4CO2 scheme, is considered in this section. The advanced von Neumann analysis, introduced in [63] and adapted to thermal cases in Sec. 6.4.1, makes it possible to investigate the macroscopic behaviour of the HLBM in terms of modal composition. Without loss of generality, the analyses of this section are performed for $\overline{\mathrm{Ma}} = 0.1$, $\tau^* = 1.10^{-5}$ and $\sigma = 0.5$. Furthermore, note that the properties highlighted below seem to concern this model whatever the considered Mach number and relaxation time.

Fig. 6.16a displays maps of absolute dispersion error for the four physical modes, $\mathrm{Re}(\omega_l^{th})$, $l \in [entr, ac+, ac-, shear]$ being the Navier-Stokes theoretical values. These maps are proposed for $\overline{\theta} = 1$ (top) and $\overline{\theta} = 0.5$ (bottom). The tolerance parameter is set to $\eta = 0.9$, meaning that only modes containing more than 90% of one of the Navier-Stokes waves are identified, a dashed region is represented otherwise. Note that, if several modes of the HLBM system carry the same macroscopic information, only the one with the larger dissipation rate ω_i is considered. This criterion explains the discontinuities observed on the maps, which are caused by a curve veering phenomenon [63] involving the physical and the spurious macroscopic wave located close to $\mathrm{Re}(\omega^*) = \pi$, as illustrated on Fig. 6.12c for the downstream acoustic mode.

At first, for $\overline{\theta} = 1$, both acoustic and shear modes are identified over a large part of the spectral space. Regarding the entropy mode, it is detected all over the wavenum-

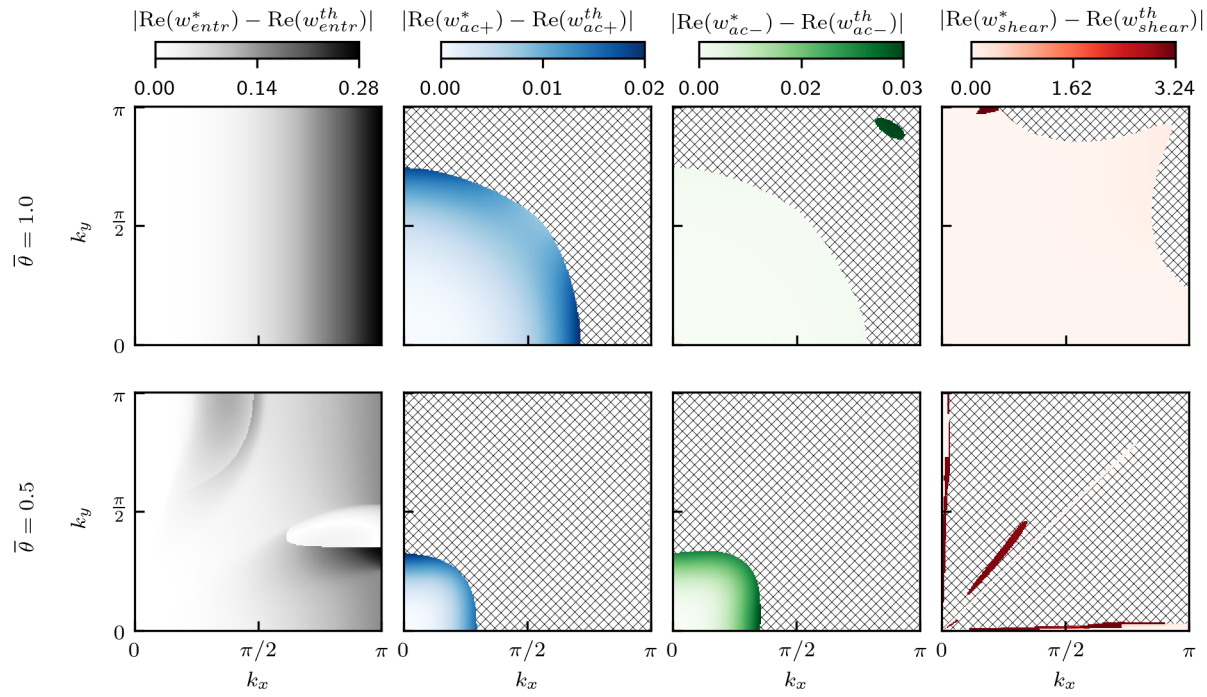

(a) Maps of absolute dispersion absolute error, $\eta = 0.9$.

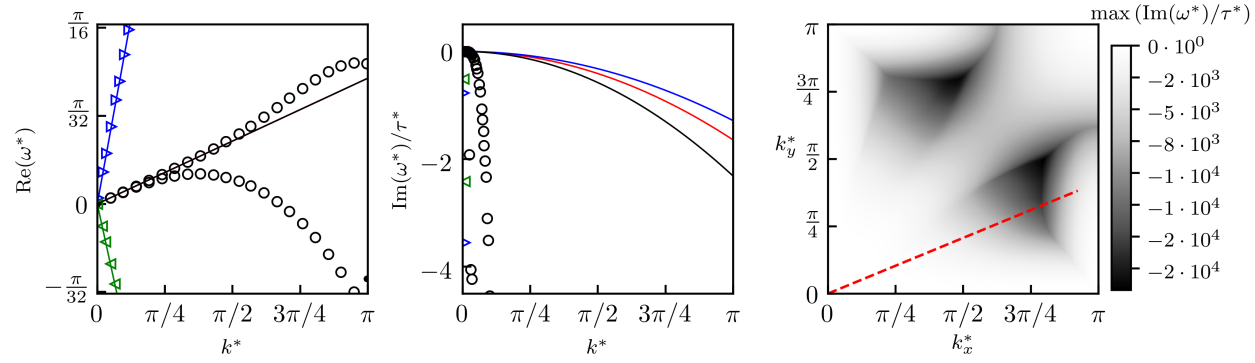

(b) Spectral Properties for $\overline{\theta} = 0.5$, $\eta = 0.9$

Figure 6.16 – D2Q9 HRR RK4CO2 scheme based on the conservative entropy equation for $\sigma = 0.5$, $\overline{\mathrm{Ma}} = 0.1$ and $\tau^* = 10^{-5}$. Fig. (a) displays the absolute dispersion error for $\overline{\theta} = 1$ (top) and $\overline{\theta} = 1/2$ (bottom). From left to right: entropic, upstream acoustic, downstream acoustic, shear mode ; Dashed regions corresponds to zones where the physical wave is not identified with $\eta = 0.9$. Fig. (b) displays the spectral properties for $\overline{\theta} = 1/2$ from left to right : dispersion curve, dissipation curve and absolute stability map. On the latter, the dashed line represents the line along which dispersion and dissipation curves are plotted. Symbols correspond to ω_{ac+}: (▷) ; ω_{ac-}: (◁) ; ω_{entr}: (○) ; ω_{shear}: (□); ω_{msp}:(●) and solid lines correspond to the NS theory.

ber space. For this value of $\overline{\theta}$, all Navier-Stokes Fourier modes being recovered from low to moderately large wavenumbers, the ability of this model to recover the intended macroscopic behavior cannot be questioned.

A radical change can be observed in the case $\overline{\theta} = 0.5$. The acoustics modes are identified for much lower wavenumbers than with $\overline{\theta} = 1$, *i.e.* for $\|\boldsymbol{k}\| < \pi/4$ only. This is, however, not too restrictive since acoustic waves with more than four points per wavelength are still correctly considered. Regarding the entropy wave, some discontinuous areas can be observed, suggesting that an abrupt change of mode with a lower dissipation rate is detected. Finally, and more importantly, no shear wave can be identified with $\eta = 0.9$ on the majority of the spectral space, even for well-resolved wavelengths. Only entropy waves travelling in some particular directions, aligned with the lattice velocities, seem not to suffer from this apparent strong issue.

To further investigate this deficiency, Fig. 6.16b displays dispersion and dissipation curves for waves for which $\widehat{(k_x, k_y)} = 22.5°$. Instead of one entropy and one shear mode, two entropy modes are identified along this direction. It indicates an inablity of this HLBM system to simulate a pure shear wave in this direction. Indeed, if one would like to initialize such a model with a shear wave, it would unavoidably be converted into two entropy waves, thus generating spurious temperature fluctuations. It is important to note that this phenomenon does not appear in the one-dimensional case and is specific to the multi-dimensional one. Finally, this surprising observation explains the appearance of discontinuous zones on the entropy map: the unintended coexistence of two entropy modes gives birth to abrupt changes of the less attenuated one, represented on Fig. 6.16b.

To illustrate the consequences of this spectral defect on the shear wave, a vortical convection test-case is considered with the same parameters as the LSA study; *i.e.* $\overline{\mathrm{Ma}} = 0.1$ along $\boldsymbol{e}_x$ and $\tau^* = 10^{-5}$. Even though the convected isentropic vortex is based on the Euler equations, it has been extensively used to assess LBM schemes solving the Navier-Stokes equation [187,194,196,225]. The initialization can be seen as a small perturbation compared to a mean flow $\overline{\rho}, \overline{T}, \overline{u}$ which reads:

$$u_r(r) = 0 \quad \text{and} \quad u_\theta(r) = \overline{c}\,\mathrm{Ma}_v\, r \exp\left(\frac{1-r^2}{2}\right), \tag{6.6.1}$$

where u_r and u_θ are respectively the radial and tangential velocity in polar coordinates and $\overline{c} = \sqrt{\gamma_g r_g \overline{T}}$ the mean flow speed of sound. Ma_v is the vortex Mach number and $r = \sqrt{(x-x_c)^2 + (y-y_c)^2}/R$ with R the vortex radius and (x_c, y_c) the initial position of the vortex center. For an isentropic vortex, the density and pressure fields are given by [212]:

$$\rho(r) = \overline{\rho}\left[1 - \frac{\gamma_g - 1}{2}\mathrm{Ma}_v^2 r \exp\left(1 - r^2\right)\right]^{\frac{1}{\gamma_g - 1}}. \tag{6.6.2}$$

$$p(r) = \overline{p}\left(\frac{\rho(r)}{\overline{\rho}}\right)^{\gamma_g}. \tag{6.6.3}$$

In the present case, the vortex velocity is set so that $\mathrm{Ma}_v = 0.05\,\overline{\mathrm{Ma}}$, where one recalls that $\overline{\mathrm{Ma}}$ denotes the free-stream Mach number. A $[L \times L]$ periodic domain is considered

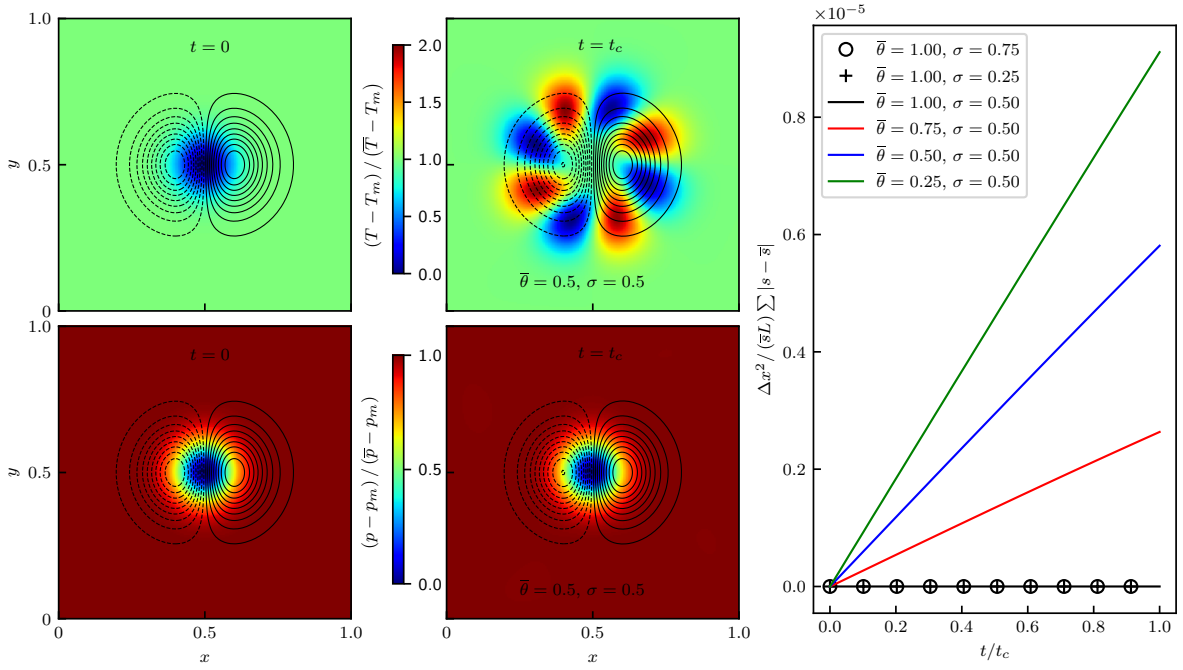

Figure 6.17 – Isentropic vortex for $t = 0$ (left) and $t = t_c$ (middle) colored by the reduced temperature (top) and pressure (bottom) with T_m and p_m referring to the minimum temperature and pressure at $t = 0$, respectively. Twenty iso-contours ranging from minimum to maximum of u_y are displayed ; solid and dashed contours correspond respectively to positive and negative values. Right: dimensionless entropy variation integrated over the numerical domain over the time, for different simulations parameters $\overline{\theta}$ and σ. $\overline{s}(\overline{\rho}, \overline{T})$ corresponds to the mean flow entropy.

with $L = 1\,\mathrm{m}$, uniformly discretized with 200 points in each direction. Finally, $R = 20\Delta x$, $\overline{p} = 101325\,\mathrm{Pa}$, $\overline{T} = 300\,\mathrm{K}$, $\overline{\rho} = \overline{p}/(r_g \overline{T})$. The simulation is run for 4140 iterations, which corresponds to a single convective time $t_c = L/(\overline{c}\,\overline{\mathrm{Ma}})$ in the case $\overline{\theta} = 0.5$.

Fig. 6.17 displays maps of reduced temperature and pressure, of a simulation run with $\overline{\theta} = 0.5$ and $\sigma = 0.5$, for $t = 0$ and and after one convective time $t = t_c$. One recalls that the reference solution corresponds to the initialization state for this test-case. Iso-contours of u_y are superimposed on the two fields. At first, they are found in good agreement with the analytical solution, and no noticeable distortion of the velocity field is observed. Same conclusion stands for the pressure field where nor dispersion, dissipation or spurious acoustic waves are observed. If one confines oneself to these observations, the model seems to well reproduce the physics of the test-case. Regarding the temperature field, one would expect a similar map as in the initial state, only eventually dissipated, which is, however, not recovered by the model. Indeed, large deformations of the temperature field, involving sinks and sources, can be observed. A similar phenomenon, in inverse proportion, is also noticed on the density field as a consequence of the perfect gas coupling equation of state. Thus, based on the evolution of thermodynamic variables, one concludes that unintended entropy waves are generated by the system, a totally unexpected feature for an isentropic

test case.

This behavior is a direct consequence of the spectral discrepancy of the shear wave mentioned above. Since this HLBM model is not able to properly simulate a shear wave in every direction, an unavoidable conversion to an entropy wave occurs, at the origin of the highlighted non-physical temperature fluctuations. Moreover, one can notice that in the directions of the lattice, no sinks nor entropic sources are observed, which supports the previous analysis. Finally, the right-hand-side curve of Fig. 6.17, displaying the integrated entropy variation over the time, confirms that the value of $\overline{\theta}$ is directly involved in this phenomenon. On the contrary, changing the values of σ does not seem to cause such an issue: as far as $\overline{\theta} = 1$, no entropy production is observed. Therefore, the lower $\overline{\theta}$ is, the higher the entropy production occurs. As a consequence, the simulated physics is biased, especially if it includes shear flows. Unfortunately, and as already discussed in Sec. 6.5.2 for the RK1UPO1 scheme, keeping $\overline{\theta} = 1$ is impossible in a compressible simulation, which will inevitably significantly bias the physics.

Note that all the phenomena described in this section have been observed for many different values of the mean flow Mach number, its orientation and the value of τ^*. In any case, observations done with the extended von Neumann analysis, and corroborated by numerical simulations, showed that this HLBM class, based on the conservative entropy equation, is not recommended for compressible applications, due to:

- the restriction to $\overline{\mathrm{Ma}} < 0.5$ because of its linear stability,
- a shear-to-entropy production for values $\overline{\theta} \neq 1$.

Note that a similar phenomenon as pointed out on Fig. 6.17 has already been observed in Sec. 5.2.5 for the HLBM-ρE and for this vortical convection case. In addition, the very same phenomenon was also observed by Guo et al. [234] for a comparable vortical case. Using a D3Q19 HLBM based on a conservative equation on ρs, the authors noticed a large deformation of the density field, whereas the same model using a primitive formulation of the entropy equation did not suffer from this discrepancy. The deformation observed with these conservative formulations might be thus explained by the shear-to-entropy transfer exhibited in this section.

Moreover, spurious mode couplings were also mentioned by Lallemand et Luo [31, 71] with a multi-speed D2Q13 model. They noticed an unstable coupling between the shear and entropic modes and proposed a hybrid model to overcome the issue. In the light of the present modal study, it would appear that the form of the supplemental equation is at least as important as the choice of dealing with a hybrid method to address this problem. Indeed, such a mode coupling is equally observed on the present hybrid model based on a conservative form of the entropy equation, while Lallemand & Luo adopted a primitive form of the temperature equation to get rid of this issue. Note that, in the context of the present work, similar analyses have been performed with the primitive form of the entropy equation discretized with the RK4CO2 scheme, and no such problems have been identified. This point out that such a mode transfer is linked to the primitive form. Nevertheless, the latter is affected by a phenomenon of another nature, which will be presented in the following section.

6.6.2 Primitive form: entropy-to-shear production

The primitive form of the entropy equation, discretized with the RK4CO2 scheme, is now considered in this section. The same study as in Sec. 6.6.1 is conducted, where the scheme is analyzed in terms of modal composition. Using the advanced von Neumann analysis on several points of the parametric space, a rather similar issue as the one observed with the conservative form occurs, here referred to as an entropy-to-shear production. To illustrate this phenomenon, and without loss of generality, the analysis is proposed for the same flow parameters as in Sec.6.6.1, *i.e.* $\overline{\mathrm{Ma}} = 0.1$, $\tau^* = 10^{-5}$ and $\overline{\theta} = 0.5$.

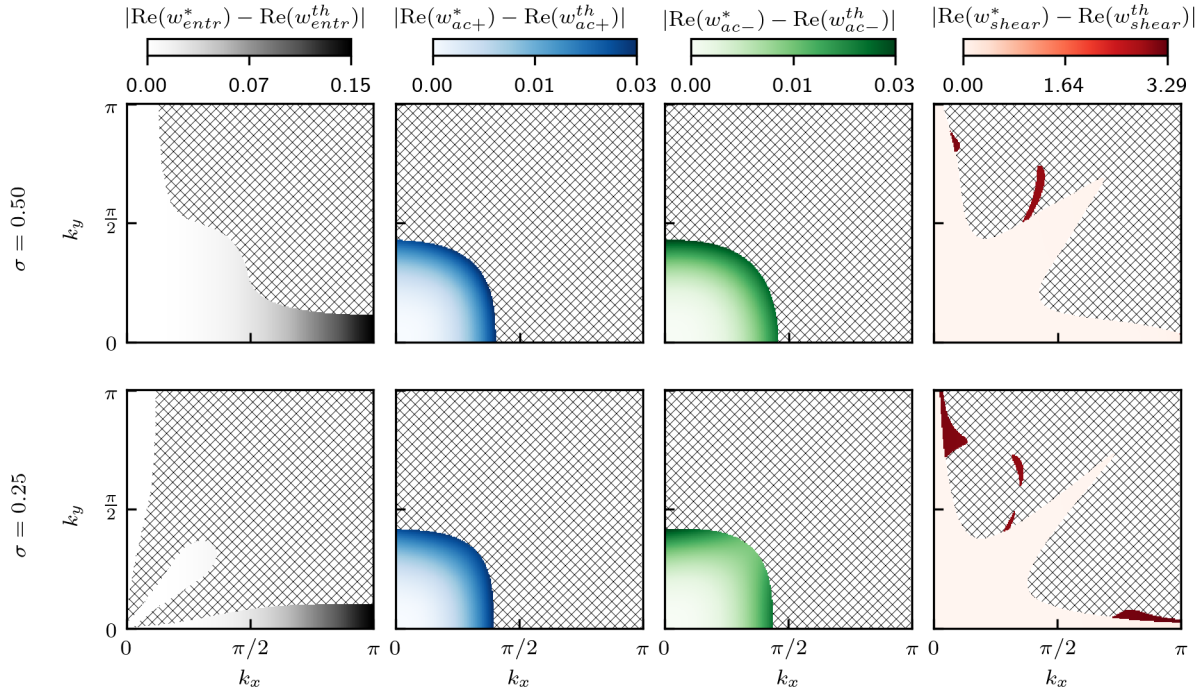

Figure 6.18 – D2Q9 HRR RK4CO2 on primitive entropy equation for $\overline{\theta} = 0.5$, $\overline{\mathrm{Ma}} = 0.1$ and $\tau^* = 10^{-5}$. Maps of absolute dispersion error for $\sigma = 0.5$ (top) and $\sigma = 0.25$ (bottom). From left to right: entropy, downstream acoustic, upstream acoustic and shear mode ; Dashed regions indicate zones where the physical wave is not identified with $\eta = 0.99$.

Fig. 6.18 displays maps of the absolute dispersion error for $\sigma = 0.5$ (top) and $\sigma = 0.25$ (bottom). In the present case, the tolerance parameter has been set to $\eta = 0.99$ in order to evidence the phenomenon of interest. With $\sigma = 0.5$, entropic, acoustic and shear modes are identified over the majority of the spectral space. Large error areas (as observed in Sec. 6.6.1) are present for the shear modes, but for high wavenumbers only. Essentially, the ability of the present configuration to correctly simulate a Navier-Stokes Fourier behaviour cannot be questioned.

Different conclusions can be drawn from the case $\sigma = 0.25$. Even though the acoustic and shear modes show little change, no entropy mode is identified on the majority of the

spectral space, even for low wavelengths, *i.e.* well resolved fluctuations. In fact, only entropy waves travelling along the directions of the lattice can be correctly considered by this model. This phenomenon is very reminiscent of the shear mode behavior in the primitive case of Sec. 6.6.1.

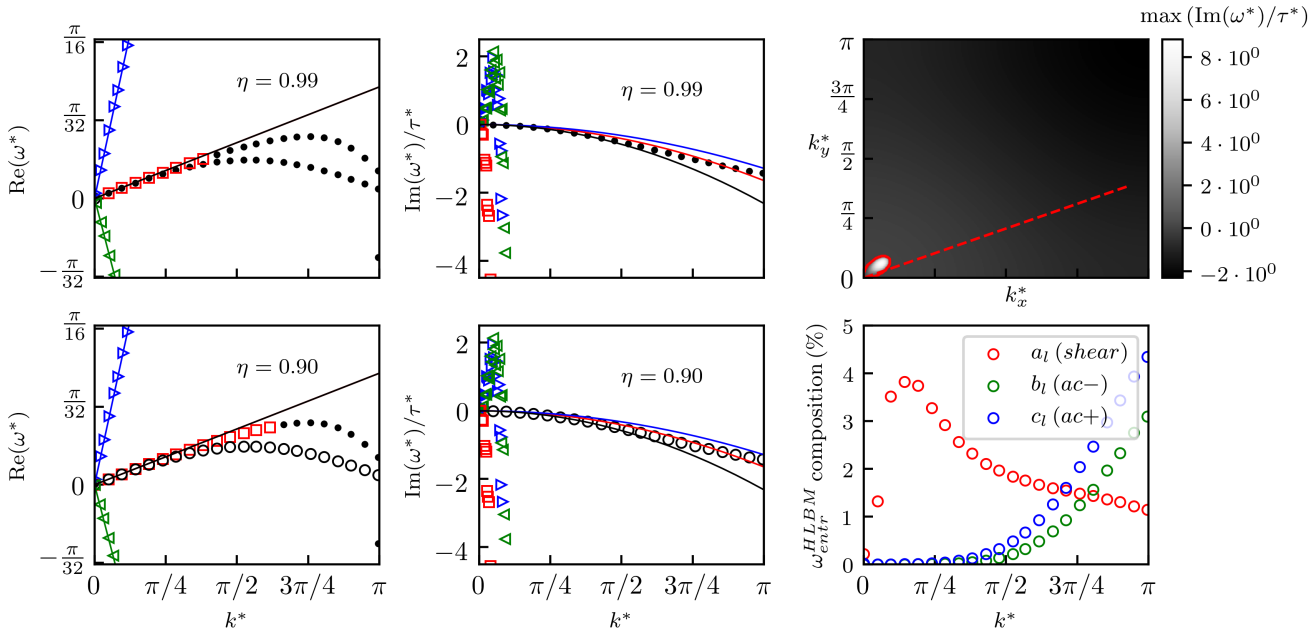

Figure 6.19 – D2Q9 HRR RK4CO2 on primitive entropy equation for $\overline{\theta} = 0.5$, $\overline{\mathrm{Ma}} = 0.1$, $\tau^* = 10^{-5}$ and $\sigma = 0.25$. Left: dispersion and dissipation curves for two values of η. Symbols correspond to ω_{ac+}: (▷) ; ω_{ac-}: (◁) ; ω_{entr}: (○) ; ω_{shear}: (□); ω_{msp}:(•) and solid lines correspond to the NS theory. Top right: absolute stability map, the dashed line represents the line along which dispersion and dissipation curves are plotted. Bottom right: Entropy HLBM mode decomposition in terms of NS macroscopic contribution Eq. (6.4.8).

To investigate the deficiency in the hashed area of Fig. 6.18, dispersion and dissipation curves for an angle $(\widehat{k_x, k_y}) = 22.5°$ are drawn on Fig. 6.19. These curves are displayed for two values of the tolerance parameter $\eta = 0.99$ and $\eta = 0.90$. As expected, acoustic and shear waves are well identified, although unstable in the low k^* limit, and over-dissipated above. On the contrary, an entropy wave can only be identified by lowering η to 90%. Hence, despite the fact that this mode carries more than 90% percent of an expected entropy wave, a significant percentage of parasitic macroscopic information is also transported.

By construction of the analysis, the macroscopic composition of this mode, in the sense of the compressible NS equations, is directly accessible thanks to Eq. (6.4.8). Normalized coefficients a_l, b_l and c_l, corresponding to the percentage of shear, upstream and downstream acoustics carried by the entropic HLBM mode respectively, are displayed on the bottom-right curve of Fig. 6.19. It can be observed that this mode can carry up to 4%

of acoustic and shear information. Its larger values of acoustic contributions are located for $k^* = \pi$, and tend rapidly to zero for well-resolved waves, ensuring the convergence of the mode in terms of entropic composition. However, a more singular behavior is observed regarding the content of shear information (a_l). Although it also tends to zero for well-resolved waves, the non-monotony of the curve yields a surprising larger error for some well-resolved waves than under-resolved ones. Its maximum value is found for $k^* = \pi/16$ *i.e.* 16 points per wavelength. Similarly to the issue shown in Sec. 6.6.1, it is important to note that this phenomenon does not appear in the one-dimensional case, and is specific to the multi-dimensional one. This type of mode transfer is therefore likely to lead to similar adverse effects as those observed with the conservative form.

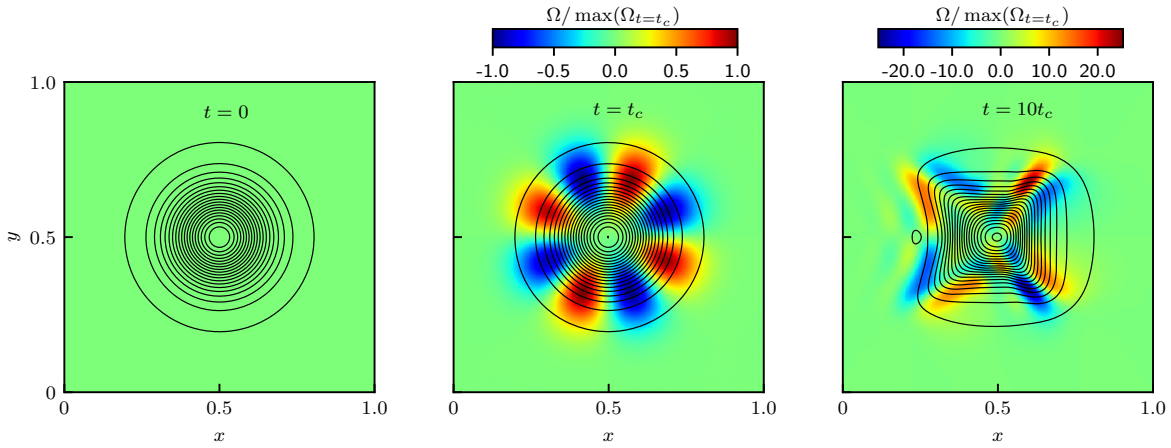

Figure 6.20 – Entropic spot convection for $\overline{\theta} = 0.5$ and $\sigma = 0.25$, for $t = 0$ (left), after one period of the computational domain $t = t_c$ (middle) and after ten periods $t = 10t_c$ (right). Colormaps of vorticity with twenty iso-contours of temperature ranging from the minimum to the maximum amplitude for $t = 0$ are displayed.

To illustrate the consequences of this spectral defect on the HLBM entropy mode, the convection of a Gaussian entropic spot is considered. Its exact solution consists in the simple advection-diffusion of the initial condition over the time. Same parameters as those of the LSA are employed *i.e.* $\overline{\mathrm{Ma}} = 0.1$ along $\boldsymbol{e}_x$ and $\tau^* = 10^{-5}$. The fluid is initialized with a small perturbation over the mean flow, convected along $\boldsymbol{e}_x$, which reads:

$$T(r) = \overline{T} + \Delta T \exp\left(-r^2/2\right) \quad \text{and} \quad \rho(r) = \frac{\overline{p}}{r_g T}. \tag{6.6.4}$$

Here, $\Delta T = 0.05\overline{T}$ corresponds to the amplitude of the fluctuation. The radius of entropic spot is set to $R = 20\Delta x$ and the same mean flow conditions, numerical domain, convective time t_c, number of iterations and grid specifications as described in Sec. 6.6.1 are adopted. Given the mesh size and the value of τ^*, the dissipation induced by the heat diffusivity is considered negligible, so that only a hot spot convection is expected.

Vorticity colormaps and temperature iso-contours can be found on Fig. 6.20 for the initial state, after one and after ten convective times. One recalls that the vorticity is

positive for anti-clockwise rotation and negative for clockwise rotation. For $t = t_c$, one can see the emergence of several pairs of azimuthally-distributed counter rotating vortices all around the spot. This phenomenon is similar in all respects to that observed in Sec. 6.6.1, except that the mode transfer occurs now from entropy to shear production. For such a test case, the entropic spot is supposed to be solely advected, which confirms that the production of vorticity is due to a spurious numerical mode transfer. In addition, along the lattice direction, where the entropic macroscopic information is spectrally recovered, no vorticity is produced, which comforts the results of the LSA. This behavior is a direct experimental observation of the spectral discrepancy of the entropy wave in non lattice-aligned directions. Since this last holds few percents of shear information even for moderate wavenumbers, a spurious shear behavior resulting in the appearance of vortices is observed.

As a consequence of these spurious vortices, the hot spot is stretched along the diagonal directions and compressed along the $\boldsymbol{e}_x$ and $\boldsymbol{e}_y$ axes. This phenomenon therefore adds errors to both the hydrodynamics and the thermodynamic quantities, where the temperature iso-contours after $t = 10t_c$ adopt a square shape. Moreover, one can observe that the solution is no longer symmetric with respects to $\boldsymbol{e}_y$. This is directly linked to the dispersion error of the scheme induced by a non zero advection velocity. This dispersion is a common defect for a numerical scheme, and is not related to the observed mode transfer. Nevertheless, it can be mitigated by using a higher-order centered scheme on the convective part of the entropy equation. For a stationary entropic spot, a symmetric solution, but still affected by spurious vortices, would have been observed.

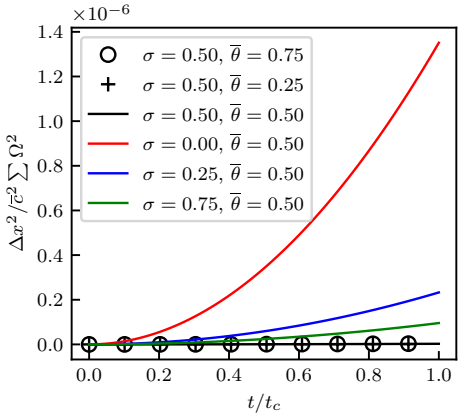

Figure 6.21 – Dimensionless enstrophy variation over the time for different $\overline{\theta}$ and σ parameters.

Finally, Fig. 6.21 displays the dimensionless enstrophy variation over the time, up to $t = t_c$. Multiple simulations for several values of σ and $\overline{\theta}$ are proposed. The curves confirm that the value of the σ parameter is responsible for the entropy-to-shear production, whereas $\overline{\theta}$ has no influence. The independent character of $\overline{\theta}$ on this phenomenon has also been observed through other maps similar to Fig. 6.18.

Among the values investigated, the spurious vorticity production is maximum for

$\sigma = 0$, minimum for $\sigma = 0.5$ and non zero for $\sigma = 0.75$. This suggests an optimal value $\sigma \neq 1$ ensuring a minimum enstrophy creation together with a stable numerical scheme, which could possibly be found through this analysis for each point of $[\overline{\mathrm{Ma}}, \tau^*]$ space in the spirit of [23, 83, 84].

Finally, this entropy-to-shear mode transfert explains what has already been observed on Fig. 4.16 and Fig. 4.17 in Sec. 4.6. Moreover, exactly the same phenomenon has already been observed but for a different energy equation, for a different collision operator and for a different lattice. Indeed one refers the reader to Fig. 3.14 and Fig. 3.15 in Sec. 3.8, where this entropy-to-shear mode transfert has been observed for a BGK operator, on a D2V17 lattice and for an internal energy equation (just before the computation diverges). Therefore, although the σ parameter has an obvious effect on this mode transfer, within the limit of the tests that have been carried out, this mode transfer is not necessarily related to the use of the HRR operator. It is also not related to the use of standard lattice nor to the use of an entropy equation.

At last, a discussion should be held regarding the stability of the model, which is only guaranteed when $\sigma = 0$ for low values of τ^* as evidenced in Sec. 6.5.2. For $\sigma = 0.25$, the dissipation curve and the absolute stability map of Fig. 6.19, show that instabilities of the two acoustic modes are responsible for the divergence of the model. An instability bubble can be seen for very low wavenumbers, with however a relatively low positive amplification rate of $\omega^* \approx 8$. For numerical simulations with outlet boundary conditions, these slightly unstable waves can be easily evacuated during the simulation, not affecting the stability of the simulation. For non-acoustic cases, such unstable low-frequency waves may not be triggered, which makes it possible to perform cases such as vortex or hot-spot convection without any problem. However, this model cannot be used in a straightforward way for $\sigma \neq 0$ as it is intrinsically unstable. Some improvements will have to be proposed in order to enforce its robustness for $\sigma \neq 0$, especially for the simulation of acoustic cases.

6.7 Conclusion

In this Chapter, an original von Neumann analysis of the hybrid lattice Boltzmann method under ideal gas thermodynamic closure has been conducted. Inspired by the current state of the art [150, 180, 187, 225] and what has been seen in Chap. 4, numerous compressible hybrid classes have been derived and investigated.

A preliminary spectral study on the athermal equations revealed that the Mach error of standard lattices is effectively removed using appropriate corrective terms. Moreover, the latter allows acting on the acoustic CFL constraint by modifying the θ parameter, without biasing the resolved physics. In the present work, this parameter was one of the two levers that have been introduced to address the eigenvalue collision [63] present in the standard LBM. Lowering this parameter reduces the sonic cone and permits to bypass this destabilizing phenomenon, further extending the stability of the LBM to $\mathrm{Ma} > 0.732$. The second lever is the use of the HRR collision operator [88] which makes it possible to alleviate the modal interactions [193] through the FD parameter σ. In the end, eigenvalue collisions can be avoided if a sufficiently low value of σ is considered.

Finally, the combination of both levers have been proved to be all the more crucial for bi-dimensional case, ensuring the stability of the LBM system for compressible Mach number ranges.

Once these observations have been made, a von Neumann analysis of the hybrid system corrected in terms of Mach number error and monatomic deficiency [225], has been conducted. The methodology of Wissocq et al. [63] adapted in this work to the hybrid system, shown that the compressible Navier-Stokes behavior was spectrally recovered in terms of dispersion, dissipation and modal composition, and further confirms that the correct macroscopic equations derived in Sec. 4.2.4 are correctly recovered. Moreover, in this hybrid context it has been pointed out that the sonic cone is increased by a factor of $\sqrt{\gamma_g}$, making the eigenvalue collision arising for lower Mach values compared to the athermal case. Thus, it is all the more necessary, at first sight, to use both stabilization levers $\overline{\theta}$ and σ. A basic study of few HLBM classes revealed a completely different spectral behavior compared to the athermal system, which strongly supports the pertinence of this new analysis. Furthermore, variable stability outcomes were obtained depending on the energy variable, type of equation or numerical scheme applied to the energy equation. In that respect, a parametric study of twenty HLBM classes has been conducted to determine "Usable" models for compressible applications, over a space that has been rigorously derived using the Vaschy-Buckingham theorem. It has been observed that classes owning an explicit pressure work are unstable as well as classes based on the conservative formulation, apart from the entropy. Thus, the entropy classes proved to be the only ones "Usable" for compressible applications, and stable up to Ma = 0.5 and Ma = 0.95 for the conservative and primitive formulations respectively. This study is therefore in line with the choice of the primitive form of the entropy equation made in the literature [150, 187] and the model presented in Chap. 4 for the sake of robustness. It is also worth noting that, in absence of pressure work in the energy equation, other classes turn out to be stable, but they cannot be categorized as "Usable" even though encountered in the literature to model low Mach thermal flow [180] or reactive flows [192]. In the latter, the fluid is only expanded under the effects of strong temperature gradients, modeled by the perfect gas equation of state, and not under compressible effects.

The methodology [63] extended to the hybrid method in the present work, makes it possible to access to the macroscopic composition of the modes. In that respect, the two "Usable" entropy classes have been investigated. This Chapter highlighted original modal transfers from the entropy mode to the shear mode for the primitive formulation, and from the entropy mode to the shear mode for the conservative formulation. These spectral analyses have been qualitatively corroborated by canonical testcases where, because of this mode transfer, large biases relative to the analytical solutions were observed. This mode transfer was found to be correlated to σ in the primitive case and to $\overline{\theta}$ in the conservative case. As $\overline{\theta} = \overline{T}/T_{ref}$ is directly related to the local temperature (through $\overline{T}$) and to the time step (through T_{ref}), improving the conservative form proves more complicated than the primitive form, where σ can be freely adjusted in space and time.

This work can be used as a basis for further research, to establish a quantitative link between the prediction of spectral analyses in terms of modal composition, and the experimentally observed phenomena. In future studies, other energy-conservative LBM

schemes under a perfect gas equation of state, such as double distribution functions methods [44, 141] or multispeed methods [49, 50, 66, 87], will have to be investigated to establish whether the mode transfer observed in Sec. 6.6.1 is related to the use of a conservative formulation, or only to the use of the hybrid method. Moreover, it is important to note that only a fraction of the HLBM classes have been studied in this work. Further research will have to be carried out on classes built using other collision operators such as TRT [222], MRT [23, 27, 235] or the entropic collision operator [28, 73, 90–92] to complete this study.

Chapter 7

Hybrid Lattice Boltzmann Method on D3Q19 lattice

Contents

7.1 The ProLB solver 232

7.2 Three-dimensional HLBM 232

7.2.1 Developed D3Q19 lattice closure correction terms 232

7.3 Boundary condition 234

7.4 Mesh refinement algorithm 236

7.5 Numerical validation 238

7.5.1 Shock vortex interaction 238

7.5.2 Blasius boundary layer 240

7.5.3 Supersonic viscous flow past a NACA0012 aerofoil 244

7.5.4 Supersonic flow around a sphere 247

7.5.5 Performance 250

7.6 Conclusion 252

In this chapter, the three-dimensional extension of the HLBM seen in Chap. 4 is presented. The model is implemented in the ProLB software with boundary conditions and mesh transition algorithm. Compressible test cases are performed and show the overall correct behavior of the model from subsonic to supersonic regime and with shock waves. Finally, the performance of the method is discussed.

7.1 The ProLB solver

The ProLB software is a parallel C++ LBM solver. It relies on the standard D3Q19 lattice and is implemented in a cell-vertex formulation. The solver's architecture is conceived in such a way that the MPI (Message Passing Interface) parallelism is hidden when developing physical routines, which greatly simplifies their implementation. This solver was based on the DRT [236] (Dual Relaxation Time) collision operator until 2019. Later, the HRR collision operator [88] was adopted. Using a moderate value of the FD parameter ($\sigma = 0.98$), it improved the robustness and precision of the solver and greatly enhanced the results at mesh refinement interface [231], a significant improvement for aeroacoustic problems.

Various thermal versions of this solver exist and are either based on the DDF method or on the hybrid method. However, at the beginning of this thesis, these were only valid for incompressible flows under the Boussinesq approximation and did not benefit from the recent advances in terms of collision operator. As a matter of fact, the commercial version of the solver is the athermal one. It is therefore the most robust version and contains most of the recent advances in terms of physical modeling and CPU performance. Thus, the implementation of the present HLBM model is based on the most advanced version of the athermal solver which already contains the HRR collision operator.

7.2 Three-dimensional HLBM

The present compressible HLBM is the direct extension in three-dimension of the method described in Chap. 4. It is based on the same HRR collision operator and primitive formulation of the entropy equation. However, as a first try and for reasons of ease of implementation, only a RK1UPO1 scheme has been implemented on the energy equation instead of the MUSCL scheme. Moreover, the diffusive terms are discretized using second-order centered schemes. A third-order expansion $f_i^{eq,3}$ in terms of Hermite polynomial is considered and the regularization procedure is conducted up to the third-order off-equilibrium moment.

However, the peculiarity of the D3Q19 lattice leads to a change in the expression of the correction term. The latter is detailed in the following.

7.2.1 Developed D3Q19 lattice closure correction terms

As already discussed in Sec. 2.3.3, the tensorized basis built from the D1Q3 lattice (i.e., D2Q9 and D3Q27) recover all the third-order moments except the diagonal components

due to $\mathcal{H}_{\alpha\alpha\alpha} = 0$. However, the D3Q19 lattice does not respect this property since none of its third-order order moments are correct. Indeed, due to its reduced number of discrete velocities, the lattice closure error applies on all the third-order moments. Thus, in order to recover the correct viscous stress tensor, one must use a corrective term $E_{1,\alpha\beta}$ which account for all the erroneous third-order equilibrium moments computed by the D3Q19 lattice. This corrective terms can be computed as:

$$E_{1,\alpha\beta} = -\frac{\partial}{\partial x_\gamma}\left(a^{eq}_{\alpha\beta\gamma} - a^{eq,\mathrm{Q19}}_{\alpha\beta\gamma}\right), \tag{7.2.1}$$

with $a^{eq,\mathrm{Q19}}_{\alpha\beta\gamma}$ corresponding to the erroneous third-order equilibrium moments computed by the D3Q19 lattice. The correction $E_{1,\alpha\beta}$, in Eq. (7.2.1) corresponds thus to the subtraction of the "false moments" calculated by the D3Q19 i.e., $a^{eq,\mathrm{Q19}}_{\alpha\beta\gamma}$ and to its replacement by the true moment $a^{eq}_{\alpha\beta\gamma}$. For a more detailed understanding, we refer the reader back to Sec. 4.2.4. Once Eq. (7.2.1) is developed in three-dimension, the lattice closure correction term at the Boltzmann level reads:

$$\psi_i = \frac{w_i}{2c_s^4}\left[\frac{\partial}{\partial x}D_X + \frac{\partial}{\partial y}D_Y + \frac{\partial}{\partial z}D_Z\right], \tag{7.2.2}$$

with,

$$\begin{aligned} D_X =& \mathcal{H}_{i,xx}\rho u_x\left(1-\theta-u_x^2\right) + \mathcal{H}_{i,yy}\frac{1}{6}\rho u_x\left(1-\theta-3u_z^2\right) + \mathcal{H}_{i,zz}\frac{1}{6}\rho u_x\left(1-\theta-3u_y^2\right) \\ &+2\mathcal{H}_{i,xy}\frac{1}{6}\rho u_y\left(1-\theta-3u_z^2\right) + 2\mathcal{H}_{i,xz}\frac{1}{6}\rho u_z\left(1-\theta-3u_y^2\right) + 2\mathcal{H}_{i,yz}(-1)\rho u_x u_y u_z \end{aligned} \tag{7.2.3a}$$

$$\begin{aligned} D_Y =& \mathcal{H}_{i,xx}\frac{1}{6}\rho u_y\left(1-\theta-3u_z^2\right) + \mathcal{H}_{i,yy}\rho u_y\left(1-\theta-u_y^2\right) + \mathcal{H}_{i,zz}\frac{1}{6}\rho u_y\left(1-\theta-3u_x^2\right) \\ &+2\mathcal{H}_{i,xy}\frac{1}{6}\rho u_x\left(1-\theta-3u_z^2\right) + 2\mathcal{H}_{i,xz}(-1)\rho u_x u_y u_z + 2\mathcal{H}_{i,yz}\frac{1}{6}\rho u_z\left(1-\theta-3u_x^2\right) \end{aligned} \tag{7.2.3b}$$

$$\begin{aligned} D_Z =& \mathcal{H}_{i,xx}\frac{1}{6}\rho u_z\left(1-\theta-3u_y^2\right) + \mathcal{H}_{i,yy}\frac{1}{6}\rho u_z\left(1-\theta-u_x^2\right) + \mathcal{H}_{i,zz}\rho u_z\left(1-\theta-u_z^2\right) \\ &+2\mathcal{H}_{i,xy}(-1)\rho u_x u_y u_z + 2\mathcal{H}_{i,xz}\frac{1}{6}\rho u_x\left(1-\theta-3u_y^2\right) + 2\mathcal{H}_{i,yz}\frac{1}{6}\rho u_y\left(1-\theta-3u_x^2\right). \end{aligned} \tag{7.2.3c}$$

It is worth noting that for a different choice of polynomial basis in the equilibrium function, the expression of ψ_i can be simplified. For instance, Jacob et al. [88] used a judicious combinations of third-order Hermite polynomials to built the third-order contributions of f_i^{eq}, reducing the erroneous moments to the number of four (xxx, yyy, zzz and xyz components). This equilibrium formulation can be found in compressible HLBM models [234]. However, no studies have yet been conducted to demonstrate the superiority of this choice over the conventional Hermite basis used in this work. There is no doubt that this kind of study will have to be conducted at a later stage.

With regard to the work presented in Chap .4 and in App. C, to ensure the stability in the supersonic regime, the gradients of Eq. (7.2.3) are discretized using first-order upwind finite difference scheme. Classical backward or forward formulas are employed on $\partial D_\alpha/\partial x_\alpha$ depending on the sign of u_α. Finally, due to lack of time, the $E_{2,\alpha\beta}$ correction term Eq. (4.3.10) was not implemented.

7.3 Boundary condition

The Boundary conditions are equally important than the governing equations. They are applied on the edges of the computational domain as well as inside the latter, for example to compute flows over solid bodies. In the Lattice Boltzmann method like with any other CFD method, boundary conditions ultimately decide the quality of simulation's results.

As already mentioned in Sec. 2.6.2, knowing the fact that $g_i = f_i^{eq} + g_i^{(1)}$ permits to adapt the Navier-Stokes BCs to the LBM formalism in a straightforward manner. The boundary macroscopic variables (and their gradients) are used to compute the equilibrium f_i^{eq} and off-equilibrium part $g_i^{(1)}$ of g_i. In the present case, the off-equilibrium part of all the g_i is fully reconstructed with finite differences by imposing the HRR collision parameter as $\sigma = 0$. Thus, on the boundary points all the g_i are reconstructed using the macroscopic variables ρ, T, u_α defining inlet, outlet and wall types of Navier-Stokes BCs. In fact, this subject has been very recently addressed in the HLBM framework by Feng et al. [237] in the end of 2019. The conditions that have been implemented are based on the same method, which is why only the main principles of the method will be presented. However, they used characteristic boundary conditions to find the macroscopic variables on the boundary points. In the present case, no characteristic boundary conditions are employed. The missing variables are directly computed using first- or second-order interpolation or FD schemes from the interior of the domain.

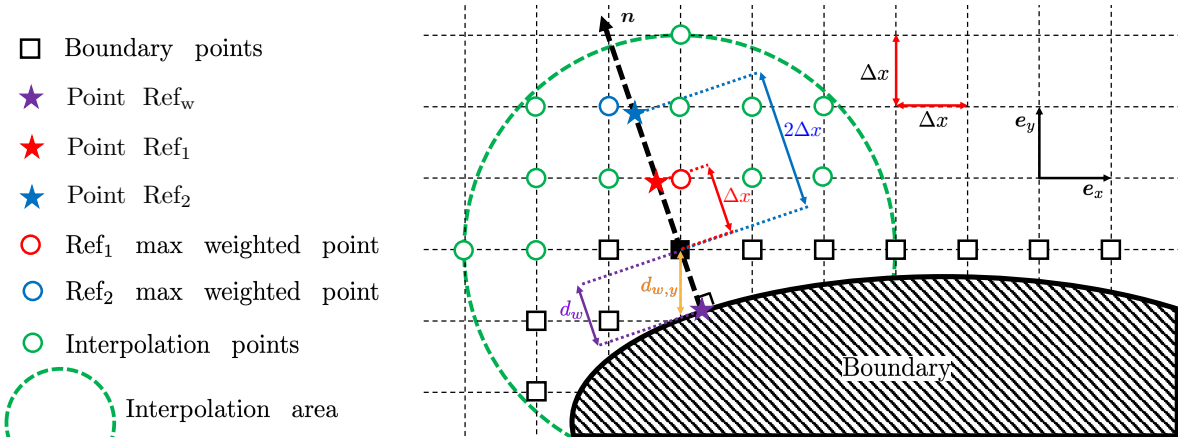

Figure 7.1 – Cut cell approach for boundary conditions treatment. Here, $\boldsymbol{n}$ is the outward pointing local surface unit normal, and d_w and $d_{w,y}$ are respectively the normal distance and the distance along $\boldsymbol{e}_y$ between the boundary point ■ and the boundary surface.

In the CFD world, the mesh generation is most of the time extremely complex and requires specialized softwares to build body-fitted meshes. The latter allow to capture accurately the physical phenomenon near the boundary. Since the LBM is defined on Cartesian meshes, it is not possible to obtain such meshes on curved BCs. In this context, several options can be considered such as the ad hoc stair case approximation, the immersed boundary method or the cut-cell approach [166]. The approach used in this work is still different and is based only on interpolations between the boundary surface and the first fluid node.

Without loss of generality, a two-dimensional case is considered. Fig. 7.1 shows a typical configuration of a curved boundary immersed in a Cartesian mesh modeled by a dotted grid. The boundary macroscopic values are known at the boundary surface. However, it can be observed that the boundary points (□) do not lie on the surface of the boundary. If the boundary macroscopic values are directly imposed on the boundary points, a stair-case approximation would be done leading to a wrong approximation of the curvature. To face this issue, the macroscopic values must be interpolated from the surface of the boundary to the boundary nodes. Taking the example of the particular boundary point (■) on Fig. 7.1, three reference points aligned on the vector $\boldsymbol{n}$ (normal to the boundary surface and passing through the boundary point), can be defined:

- Ref_w (★) located on the boundary surface at d_w from the boundary point,
- Ref_1 (★) located at Δx from the boundary point,
- Ref_2 (★) located at $2\Delta x$ from the boundary point.

On Ref_w, the macroscopic variables and their gradients are known[1] from the Navier-Stokes BCs. On points Ref_1 and Ref_2, they are obtained using the inverse distance weighting (IDW) method [238] using a known scattered set of points defined by the green doted region on Fig. 7.1. In practice, the interpolation area used in the solver can includes points up to the third neighbor.

Once the macroscopic values on points Ref_w, Ref_1 and Ref_2 are known, second-order interpolations schemes are used to find their values on the boundary point (■). Then the gradients are computed using second- or first-order biased finite difference schemes depending on the availability of nodes. Finally, all the distribution function can be reconstructed at the point (■). The very same process is applied on all the boundary points (□). Regarding the energy part, once the temperature and density values are known on (□), the entropy variable can be reconstructed classically following Eq. (4.2.6).

For the detail of the interpolation and non-standard FD formulas to compute the gradients on (■), one can refer to Feng et al. [237].

[1] The gradients are not always know on the BC. However, they can be computed numerically using FD schemes.

7.4 Mesh refinement algorithm

To achieve an accurate modeling of fluid flows, a numerical method must be able to capture the spatial and temporal flow field scales. The latter can be solved entirely or partially depending if the fluid is laminar or turbulent, and/or if a turbulent model is used. In any cases, the spatial grid required to capture efficiently the flow dynamic is related to the size of the targeted smallest scale structures. However, using a uniform mesh based on the size of the smallest scales would be counterproductive and could lead to unaffordable computational costs for realistic applications.

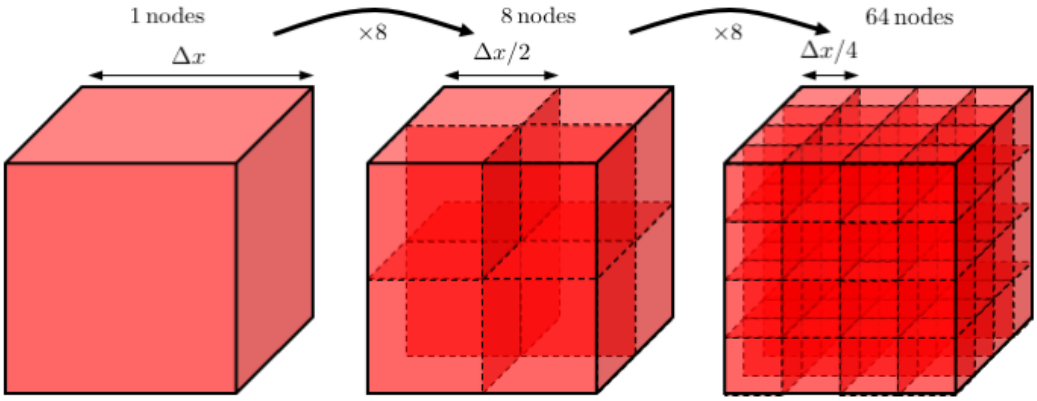

Figure 7.2 – Illustration of an octree type mesh refinement on a single cube. One step refinement gives eight nodes (hence the name octree), two steps refinement give sixty four nodes. The nodes are located at the center of each cubic element (cell-centered).

A refinement technique particularly compliant with the collide and stream algorithm is the octree type mesh refinement (quadtree in two-dimension). It consists to subdivide an initial Cartesian grid in sub-cells of same the size, and results in the generation of distinct coarse and refined regions. For each regions, this technique allows to keep a constant node spacing and therefore to stream the LBM populations. The principle of the octree type refinement is illustrated on Fig. 7.2 using a cubic cell in cell-centered formulation. It can be seen that the number of nodes in the refined area is increased by a factor of eight in three-dimension, hence its name "octree". Increasing the resolution of a simulation will therefore generate at least a factor of eight on the number of points in the region concerned.

Fig. 7.3 illustrates in two-dimension a numerical domain with a coarse and a refined region in cell-vertex formulation. These regions have different space steps linked together through $\Delta x^f = \Delta x^c/2$. The c superscript stands for coarse grid units, while f for fine grid units. This refinement technique generates non-conformal grids (in red circles on the figure) i.e., some nodes of the fine region do no match with the nodes of the coarse region. In two dimension (quadtree refinement), these nodes are located in the middle of the coarse edges interfaces. In three dimension (octree refinement) non-conformal nodes are also located on the face of the coarse cubes. Therefore, special treatment such as space interpolations are necessary to link the coarse and fine regions together.

Furthermore, because of the LBM's acoustic scaling, the difference between the mesh size of the coarse and fine regions results in two different time steps, and yields $\Delta t^f = \Delta t^c/2$. Thus for one iteration in the coarse region, two iterations are performed in the fine region. LBMs using such refinement technique become temporal adaptative methods, and has the advantage of keeping the CFL number constant between the fine and coarse region. Finally, due to the difference in time steps, the temporal evolution between the two regions is carried out asynchronously (Fig. 7.3). Thus, special treatment such as time interpolation are be necessary to link the coarse and fine regions together for asynchronous iterations.

In the light of what was presented here, a last remark must be made regarding the cost of a refined zone compared to a coarse zone of equivalent volume. Using an octree refinement, the fine zone will have eight times more points and twice as many time steps to perform as the coarse zone. Its numerical cost will therefore be sixteen times more expensive than the coarse zone. Then, the total cost of an LBM simulation depends much more on the refined areas than on the coarse areas.

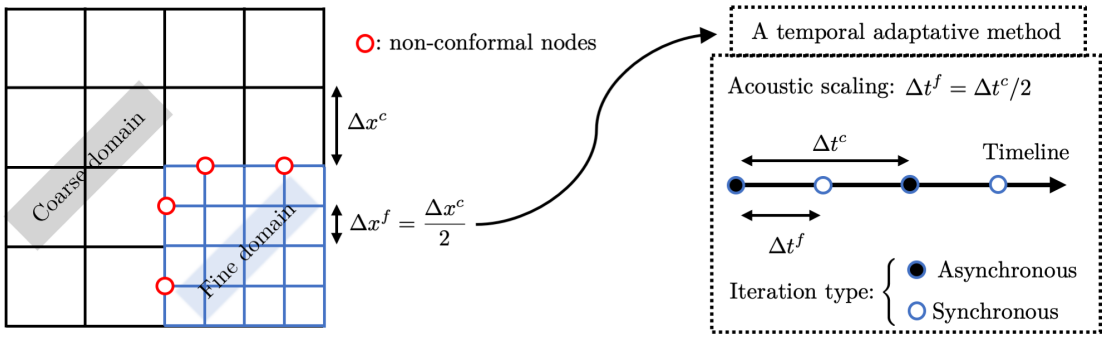

Figure 7.3 – Two-dimensional numerical domain with quadtree refinement. The nodes are located at the intersection of each line (cell-vertex). The c superscript stands for coarse grid units, while f for fine grid units.

In this section, only general statement and principle about the transition algorithm have been given. It is because the transition algorithm implemented in the present work is similar to the one recently published in 2020 by Feng et al. [239]. The latter is based on the already existing cell-vertex mesh refinement algorithm developed by Lagrava et al. in 2012 [240] for athermal LBM, and further extended in three-dimension by Touil et al. [241]. It has been recently adapted to the HRR collision operator by Astoul et al. [231], and finally extended to the HLBM framework [239] using standard space and time interpolations for the energy part. Thus for more details about this algorithm, one refers the reader to the publication of Feng et al. [239].

7.5 Numerical validation

7.5.1 Shock vortex interaction

One proposes to validate the model on the same test case seen previously in Sec. 4.5.3 i.e., case C of the shock vortex interaction of Inoue et al. [200]. The FD parameter is set to $\sigma = 0$ and the same initialization, physical and numerical parameters are employed. The size of the numerical domain remains also unchanged. However, to investigate the capability of the method to handle correctly grid refinement, two mesh refinements parallel to the shock have been added. The interfaces are located at $x = \pm R$ and $x = \pm 2R$ and for $y \in [-12; 12]$. Thus, three different resolution domains (RD) appear:

$$\begin{aligned} &\underline{RD_3:} && x \in [-1;+1] && \Delta x = 1/60\,\text{m}, \\ &\underline{RD_2:} && x \in [-2;+2] \text{ exclude } RD_3 && \Delta x = 1/30\,\text{m}, \\ &\underline{RD_1:} && x \in [-20;+8] \text{ exclude } RD_2, RD_3 && \Delta x = 1/15\,\text{m}. \end{aligned} \tag{7.5.1}$$

The mesh size of the finest resolution (RD_3) corresponds to the one used in Sec. 4.5.3. Finally, as the present model is three-dimensional, one Δx of RD_1 is considered along the z-axis with periodic boundary conditions.

For this test case, the method is severely challenged because the vortex is initialized on two resolution transitions. Fig. 7.4 displays Mach number and reduced pressure fields for different characteristic times. The mesh refinement interfaces are indicated by the black dotted lines. One can see that no obvious discontinuities appear on both of these hydrodynamic and acoustic fields, which proves the correct functioning of the refinement algorithm. More quantitatively, Fig. 7.5 and Fig. 7.6, compare the circumferential and radial distributions of the sound pressure Δp computed by the present model (symbols) to the DNS results (solid lines). The precursor wave and the second sound are well captured on both circumferential and radial profiles, and the results are found to be in agreement with the DNS data. More specifically, although the two graphs on Fig. 7.5 cross the RD_3/RD_2 and RD_2/RD_1 interfaces, no discontinuity appear which proves the effectiveness of the refinement algorithm.

The small overshoot visible in Fig. 7.6 at $r = 12$ and for $t = 6t_c$ is due to the initialization of the vortex on the shock wave. Moreover, the present solution is comparable to the one of Sec. 4.5.3 for $\sigma = 0$. Indeed, the solutions share the same small defects such as the slight shift below the DNS results visible on Fig. 7.6, or the overshoot visible on Fig. 7.5 for $r = 3.7$ and the angle $\theta = -7\pi/8$. In Sec. 4.5.3 it was seen that the use of a higher σ value, such as $\sigma = 0.9$, significantly reduces these defects. However, as shown in Sec. 6.5.2, for cases with a low value of the dimensionless relaxation time τ^*, a small value of σ is mandatory to obtain stable results. Unfortunately, a computation with $\sigma = 0.9$ could not be carried out because the value of τ^* in the coarse region RD_3 was too low making the computation unstable. Again, this motivates the development of a model based on a dynamic σ value ensuring a good compromise between precision and stability.

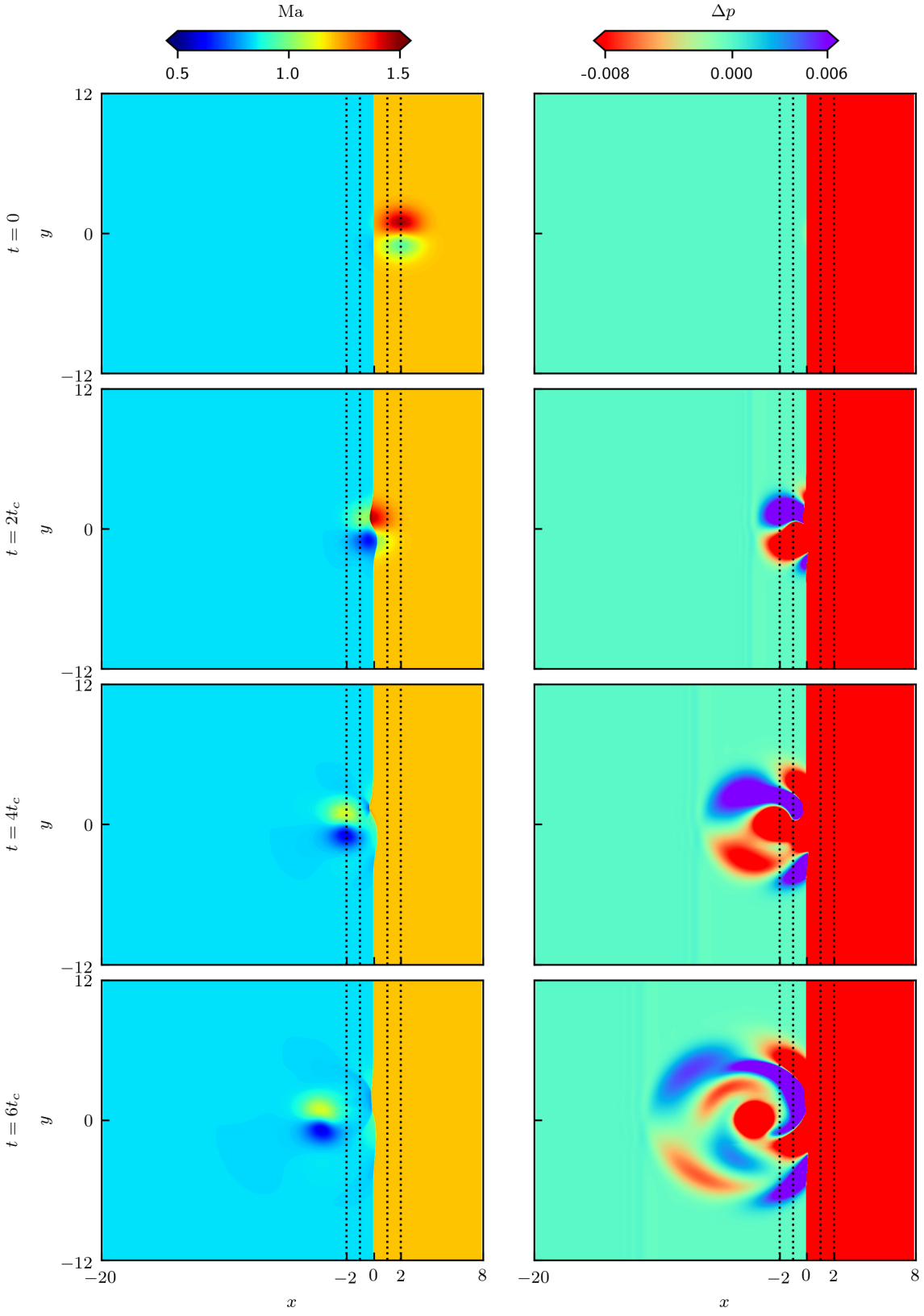

Figure 7.4 – Mach number (left) and reduced pressure (right) fields at different characteristic times. The black dotted lines represent the mesh refinement interfaces. The Δp scale has been chosen to coincide with the one of Fig. 7.5 and Fig. 7.6.

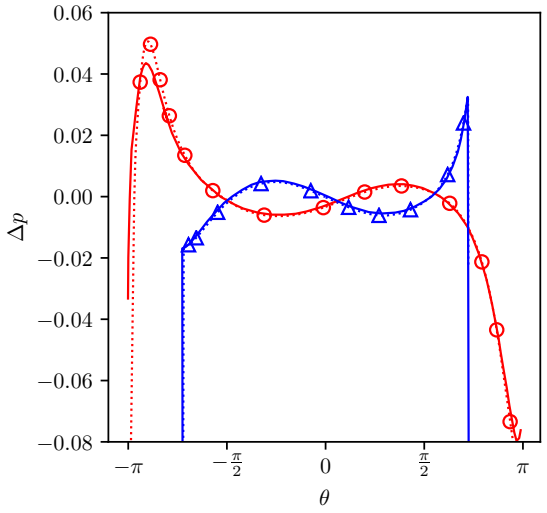

Figure 7.5 – Case C with $\sigma = 0$. Circumferential cut of the pressure variation Δp at $t = 6t_c$. Here symbols correspond to the present HLBM model while solid line to the DNS [200]. The symbols ··△· correspond to the precursor at $r = 6$ while ··⊙· refer to the second sound at $r = 3.7$.

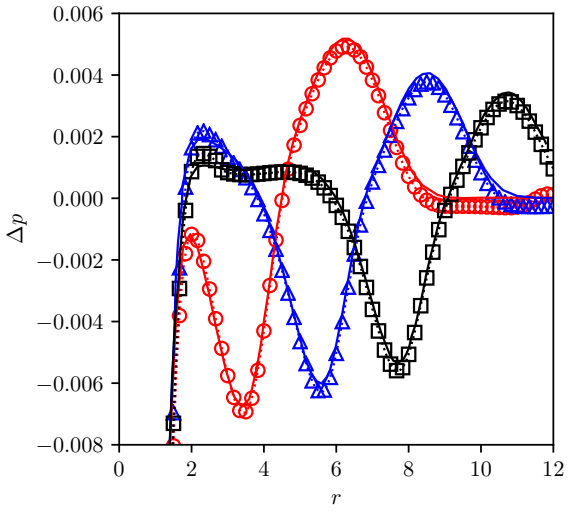

Figure 7.6 – Case C with $\sigma = 0$. Radial cut at $\theta = -\pi/4$ of the pressure variation Δp. Solid lines correspond to the DNS [200] and symbols refers to the present HLBM for $t = 6t_c$ ··⊙·, $t = 8t_c$ ··△· and $t = 10t_c$ ··⊡·

7.5.2 Blasius boundary layer

To investigate the capability of the method to handle correctly inlet, outlet and slip/no-slip wall boundary conditions, a compressible laminar flow over a flat plate of length $L = 0.1\,\mathrm{m}$ is considered. Three free-stream Mach number ranging from subsonic to supersonic regime $\mathrm{Ma}_\infty = 0.5, 1.0, 1.5$ are examined. A uniform square numerical domain of $x \in [-L/4, L] \times y \in [0, 5L/4] \times z \in [0, \Delta x]$ is employed with 10^3 points taken along the x- and y-axis. An outflow condition is applied on the top and on the right of the domain[2] while an isothermal inflow condition is considered on the left with $T_{in} = 300\,\mathrm{K}$. On the bottom, a slip wall condition is considered on $-L/4 \leq x < 0$ and an adiabatic no-slip condition is applied on $0 \leq x \leq L$. Here, $\gamma_g = 1.4$, $\mathrm{Pr} = 1$, $\rho_\infty = 1\,\mathrm{kg.m^{-3}}$ and $T_\infty = 300\,\mathrm{K}$ with $\theta_\infty = 0.3$ and $\sigma = 0.95$. The Reynolds number based on the flat plate length is taken at $\mathrm{Re} = 10^4$ to obtain a steady laminar solution. Finally, the flow is initialized using the free stream values ρ_∞, Ma_∞ and T_∞.

Analyzing the laminar boundary layer developing over the flat plate allows to assess the capability of the method to handle viscous effects. Moreover, this benchmark is particularly relevant since it owns an analytical solution. The latter is derived from the compressible boundary layer equations and can be found in the literature [242]. Under the assumption that the edge values of the boundary layer are invariant along the flat

[2]For the subsonic case at $\mathrm{Ma}_\infty = 0.5$ the outlet pressure is set to $p_{out} = \rho_\infty r_g T_\infty$.

plate axis, the Illingworth transformation gives the following self-similar variable:

$$\eta = y\sqrt{\frac{u_e}{2\rho_\infty \mu_\infty x}} \int_0^y \rho \mathrm{d}y, \tag{7.5.2}$$

where the subscript e denotes the value at the edge of the boundary layer. This transformation allows to remodel compressible boundary layers equations to their equivalent incompressible counterpart. Imposing $\mu\rho = \mu_\infty \rho_\infty$ [187, 234], it reduces to the original Blasius solution which reads for the velocity:

$$\frac{u(\eta)}{u_e} = \frac{\partial F(\eta)}{\partial \eta}, \tag{7.5.3}$$

and the temperature:

$$\frac{T(\eta)}{T_e} = 1 + \frac{\gamma_g - 1}{2} \mathrm{Ma}_e^2 \left(1 - \frac{u^2}{u_e}\right). \tag{7.5.4}$$

Assuming that even in a compressible boundary layer, the normal pressure gradient is usually negligible [242] ($p = p_e$), the density can be computed from the temperature via the perfect gas equation:

$$\rho(\eta) = \frac{p_e}{r_g T(\eta)}. \tag{7.5.5}$$

The function $F(\eta)$ in Eq. (7.5.3) refers to as the normalized stream function. The values of $\partial F/\partial \eta$ with their corresponding η are found by solving the third order ordinary differential equation originally derived by Blasius:

$$\frac{\partial^3 F}{\partial \eta^3} + F\frac{\partial^2 F}{\partial \eta^2} = 0, \quad \text{with} \frac{\partial F(0)}{\partial \eta} = F(0) = 0 \quad \text{and} \quad \frac{\partial F(\infty)}{\partial \eta} = 1. \tag{7.5.6}$$

The Blasius equation has never yielded to exact analytic solution [242]. Nevertheless it can be solved numerically and can be found in Table 7.1 from $\eta = 0$ to $\eta = 7.4$. Finally, to compare the numerical solution to the Blasius profile, the integral in Eq. (7.5.2) is evaluated using a second order trapezoidal rule.

Fig. 7.7 shows the Mach, pressure, temperature and density fields obtained with the present model for $\mathrm{Ma}_\infty = 1.5$. From these figures, one can see a boundary layer developing from $x = 0$ and whose thickness increases along the x-axis. In addition, a Mach line can be observe in the middle of the domain which is characteristic of supersonic flows over flat plate. On Fig. 7.7b one can observe that the temperature is much higher in the vicinity of the wall. The boundary surface being adiabatic, this heating is only attributed to viscous effects. Still near the wall, it clearly appears on Fig. 7.7c that the pressure is constant in the boundary layer which implies that the normal pressure gradient is zero which is in accordance with the theory [242]. The density therefore varies de facto inversely proportional to the temperature due to the perfect gas coupling.

For quantitative validation, Fig. 7.8 shows the profiles of horizontal velocity, temperature, density and skin friction coefficient obtained by the present model for Ma = $0.5, 1.0, 1.5$. From the figure, it can be found that the simulated velocity profiles are in good agreement with the reference solution. For the density and temperature, the results

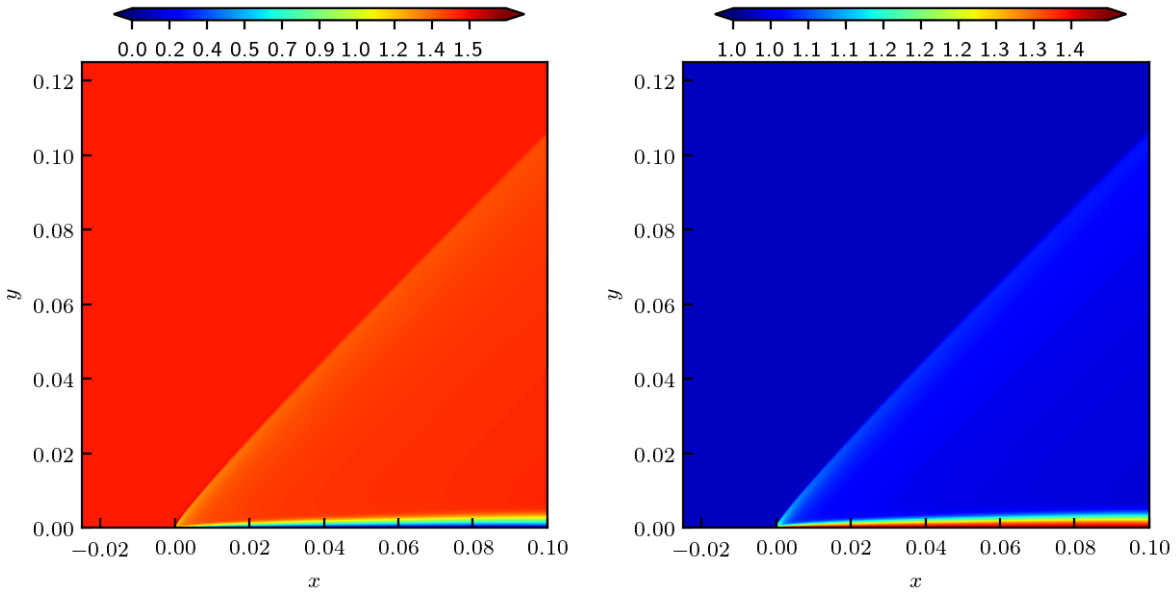

(a) Mach number

(b) Dimensionless temperature T/T_∞

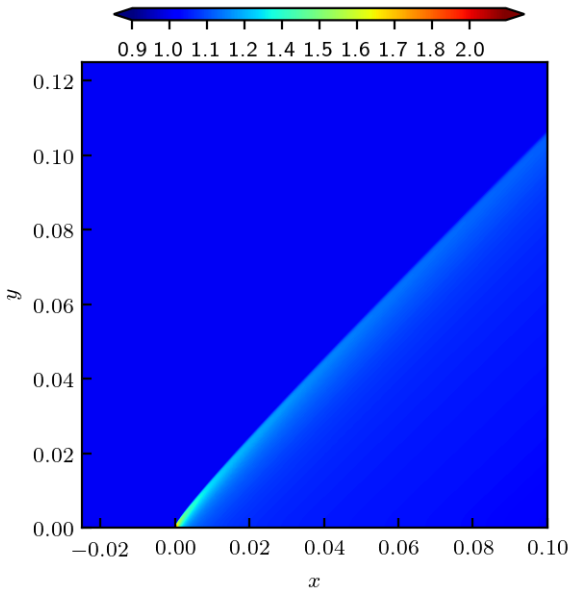

(c) Dimensionless pressure p/p_∞

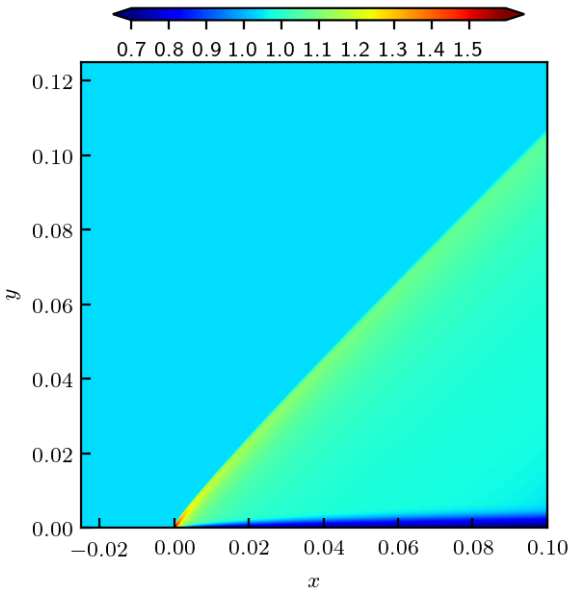

(d) Dimensionless density ρ/ρ_∞

Figure 7.7 – Hydrodynamic fields of a Re = 10^4 supersonic Ma = 1.5 laminar boundary layer.

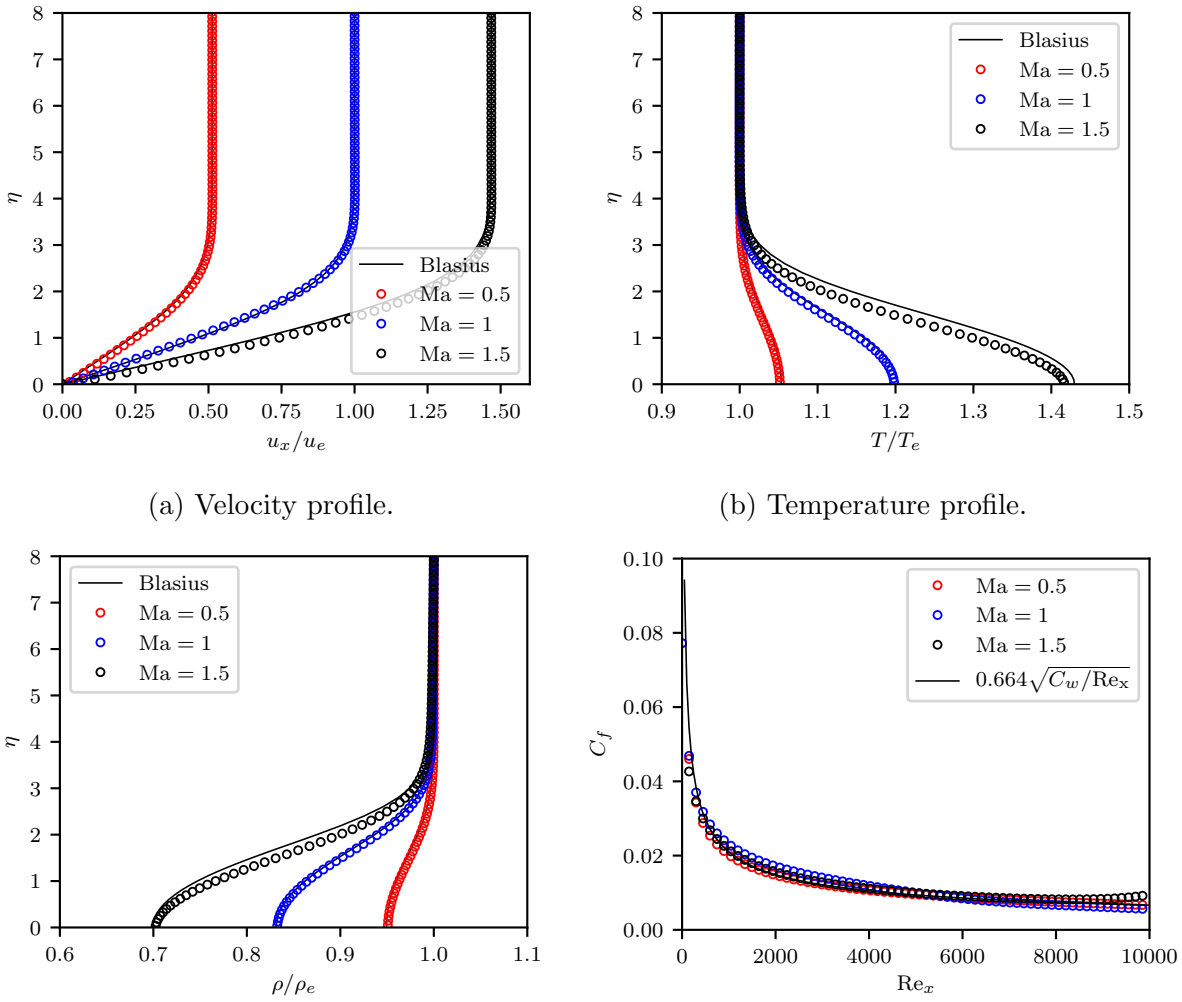

(a) Velocity profile.

(b) Temperature profile.

(c) Density profile.

(d) Skin friction.

Figure 7.8 – Horizontal profiles and skin friction coefficient of the $\mathrm{Re} = 10^4$ laminar boundary layer for $\mathrm{Ma} = 0.5, 1.0, 1.5$. Re_x is the Reynolds number along the flat plate and C_w is the Chapman-Rubesin parameter which is equal to 1 under the condition of $\rho\mu = \rho_\infty\mu_\infty$ [242].

η	0.0	0.1	0.2	0.3	0.4	0.5	0.6	0.7
$F'(\eta)$	0.0	0.04696	0.09391	0.14081	0.18761	0.23423	0.28058	0.32653
η	0.8	0.9	1.0	1.1	1.2	1.3	1.4	1.5
$F'(\eta)$	0.37196	0.41672	0.46063	0.50354	0.54525	0.58559	0.62439	0.66147
η	1.6	1.7	1.8	1.9	2.0	2.2	2.4	2.6
$F'(\eta)$	0.69670	0.72993	0.76106	0.79000	0.81669	0.86330	0.90107	0.93060
η	2.8	3.0	3.2	3.4	3.6	3.8	4.0	4.2
$F'(\eta)$	0.95288	0.96905	0.98037	0.98797	0.99289	0.99594	0.99777	0.99882
η	4.4	4.6	4.8	5.0	5.2	5.4	5.6	5.8
$F'(\eta)$	0.99940	0.99970	0.99986	0.99994	0.999971	0.999988	0.999995	0.999998
η	6.0	6.2	6.4	6.6	6.8	7.0	7.2	7.4
$F'(\eta)$	0.999999	~ 1	~ 1	~ 1	~ 1	~ 1	~ 1	~ 1

Table 7.1 – Numerical solution of the Blasius flat-plate equation (7.5.6) taken from [242].The primes denote differentiation with respect to η.

obtained by the present HLBM method and the reference solution matched reasonably for the three Mach number. The skin friction predicted by the method can also be found in good agreement with the one of the Blasius solution. The results show that the current hybrid model has the capability to simulate heat transfer problems. This test case validate in the same time the good behavior of the boundary conditions implemented in the solver.

At last, a remark on the value of the FD parameter $\sigma = 0.95$. It was possible to use this value while maintaining the numerical stability because the viscosity value and mesh size allowed to get a very high value of relaxation time ($\tau^* = 0.44$). For a lower value of σ, the results are degraded near the plate due to over-dissipation of the model.

7.5.3 Supersonic viscous flow past a NACA0012 aerofoil

This validation test consists in the simulation of the flow past a NACA0012 aerofoil in the supersonic regime. The Mach number of the case is Ma = 1.5 and the Reynolds number is Re = 10^4 (the same as for the Blasius boundary layer of Sec. 7.5.2). In the present case, $\gamma_g = 1.4$, Pr = 0.71 and the upstream temperature and pressure conditions are $T_\infty = 300\,\mathrm{K}$ and $p_\infty = 101325\,\mathrm{Pa}$ respectively. Here, the FD parameter is set to $\sigma = 0$ and $\theta_\infty = 0.15$ which corresponds to an upstream Courant number of CFL ~ 0.66. The simulation domain is defined on Fig.7.9 along with the mesh arrangement. A numerical domain composed of $[n_x, n_y, n_z] = [800, 600, 1]$ points with five different resolutions have been employed. The finest resolution RD_5 is situated on a layer thickness of 20 points along the aerofoil. The chord of the aerofoil is discretized by 800 points. While the supersonic inlet conditions is imposed on the left, an outlet pressure boundary condition is imposed at the top, bottom and right (outlet) of the domain. The Dirichlet no-slip boundary condition is imposed on the aerofoil. The simulation last $50 \cdot 10^3$ iterations fine.

The results will be compared to three references: (1) the D3Q343Q343 entropic LBM model of Frapolli [243], (2) the D3Q39Q39 entropy based moment marching equilibrium

LBM model of Latt et al. [66] and finally the upwind finite volume method of Hafez et al. [244].

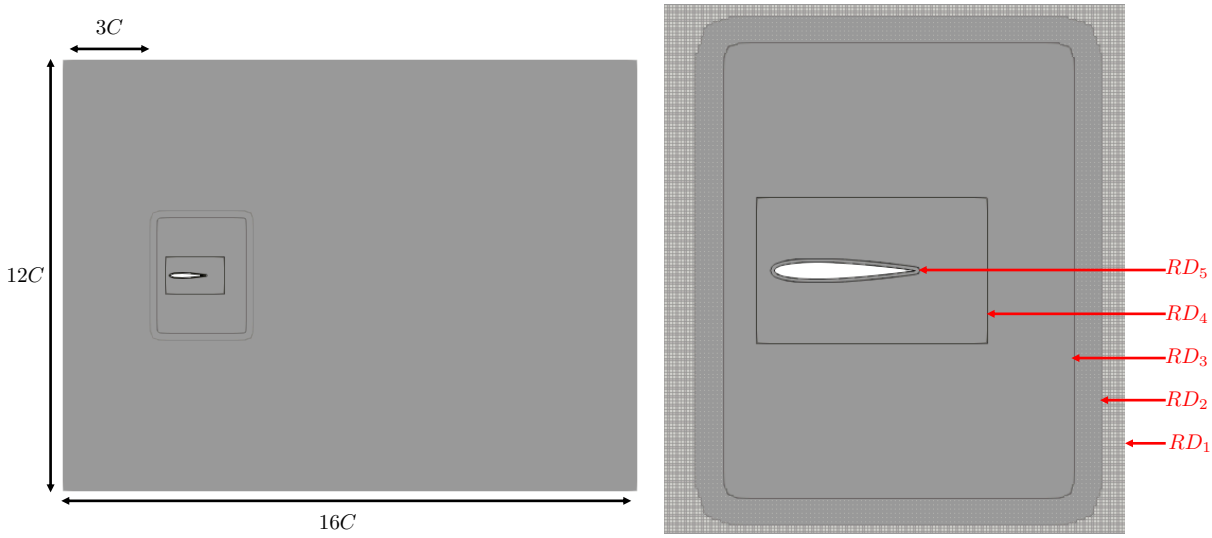

Figure 7.9 – Simulation domain and mesh of the supersonic Naca0012 aerofoil.

As a first insight on the physical phenomena related to this numerical validation, the local Mach number, temperature and pressure fields are plotted in Fig. 7.10. The main features of the flow are: (1) a primary strong bow shock upward the leading edge, (2) a secondary weak shock close to the trailing edge, and (3) a vortex shedding downward the aerofoil. The same behavior can be observed compared to results published in [66, 243]. This qualitatively confirms the good behavior of the present hybrid D3Q19 model for a supersonic configuration. Finally, the wiggles appearing near the bow shock at $y/C = \pm 0.5$ can be attributed to the change of mesh resolution from RD_4 to RD_3. The shock front in the RD_3 regions does not contains enough points which produces oscillations. This problem can be fixed by the use of a shock sensor, whereby a local artificial viscosity can be applied on the shock spreading the latter over more points.

For more quantitative comparisons, the pressure coefficient defined as:

$$C_p = \frac{p - p_\infty}{\frac{1}{2}\rho_\infty u_\infty}, \tag{7.5.7}$$

is plotted on Fig. 7.11. The parietal C_p profile ($0 \leq x/C \leq 1$) is in good agreement with reference studies as well as the C_p in the wake region ($1 \leq x/C \leq 1.5$). Regarding the shock regions ($-1.5 \leq x/C \leq 0$), the amplitude of the the bow shock is well captured by the present model. Regarding the shock localization, it is found to be slightly offset in the direction of the profile with respect to the finite volume reference [244] and can be attributed to the non-conservativity issue of the energy part of the scheme. Nevertheless, a slightly larger shift, but in the opposite direction, can be seen for the others LBM methods [66, 243]. Although the results are not exactly on the FV reference, they are still within the range of error of other compressible LBMs.

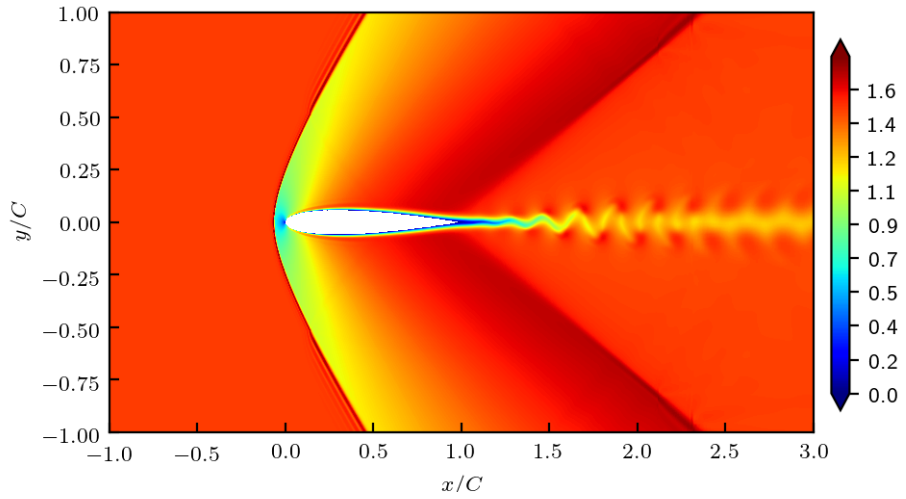

(a) Mach number

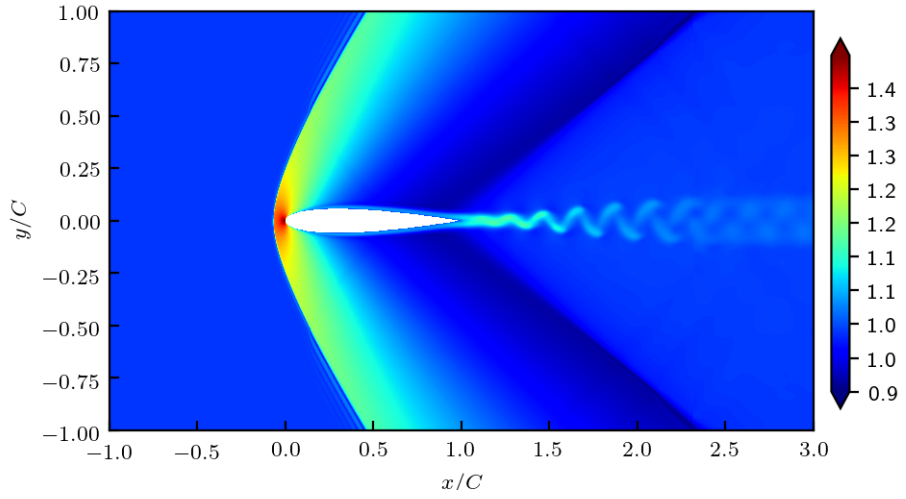

(b) Dimensionless temperature T/T_∞

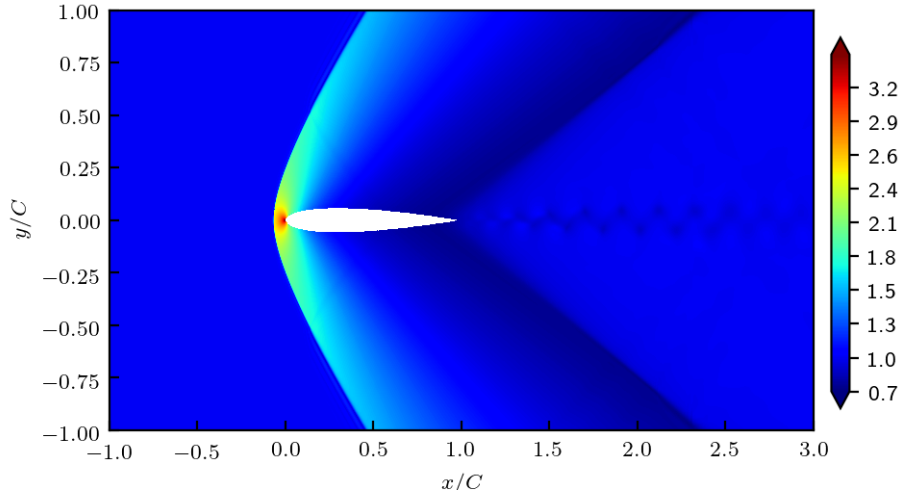

(c) Dimensionless pressure p/p_∞

Figure 7.10 – Instantaneous hydrodynamic fields of a supersonic flow over a NACA0012 aerofoil (Re = 10^4, Ma = 1.5).

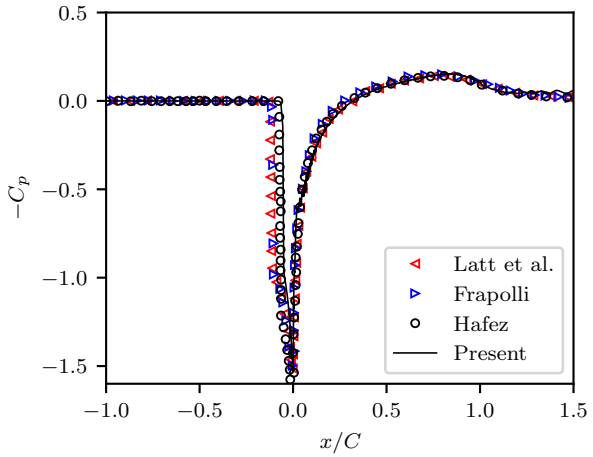

Figure 7.11 – Pressure coefficient. References are Latt et al [66], Hafez et al [244] and Frapolli [243].

7.5.4 Supersonic flow around a sphere

Finally the three-dimensional behaviour of the present HLBM is investigated in the low-Reynolds, supersonic regime, by the simulation of flow around a sphere. The purpose is to track the position of the stationary detached shock wave for different Mach number values. The results will be compared to the following references: the experimental results of Heberle et al. [245] and Sugimoto et al. compiled in the publication of Hida [246], the prediction model of Ambrosio and Wortman [247] built from experimental data of flow around sphere in air, the DNS of Nagata et al. [248], and finally the D3Q39 DDF-MS LBM model of Latt et al. [66]. In the present case, the Reynolds number, based on the sphere diameter D, reads:

$$\mathrm{Re} = \frac{\mathrm{Mac}_\infty D}{\mu/\rho_\infty} \tag{7.5.8}$$

and is set to Re = 300. Multiple simulations are performed for a Mach number ranging from $1.05 \leq \mathrm{Ma} \leq 1.9$. The same cubic domain $[n_x, n_y, n_z] = [100D, 100D, 100D]$ than [248] is used for the simulation to avoid any interaction with the boundary conditions. This domain is centered around the sphere, and 15 points are considered in its radius, corresponding to a relatively coarse mesh. According to [66] this discretization is sufficient to study the impact of the Mach number on the main characteristics of the flow. Fig. 7.12 displays the mesh where the finest resolution can be found in a radius of $5D$ around the sphere, and is gradually coarsened five time using a ProLB built-in layer refinement technique, leaving 10 points between each resolution zones. In the simulation, $\gamma_g = 1.4$, $\mathrm{Pr} = 0.71$, the upstream temperature and pressure conditions are $T_\infty = 300\,\mathrm{K}$ and $p_\infty = 101325\,\mathrm{Pa}$ respectively and finally $\theta_\infty = 0.15$. A supersonic inlet conditions is imposed on the face $n_x = 0$ and an outlet pressure boundary condition is imposed on all other faces of the cubic domain. The adiabatic no-slip boundary condition is imposed on the sphere. The simulation lasts $4 \cdot 10^3$ iterations which showed to ensure the convergence of the results for all cases. This corresponds to 37 convective times based on the sphere

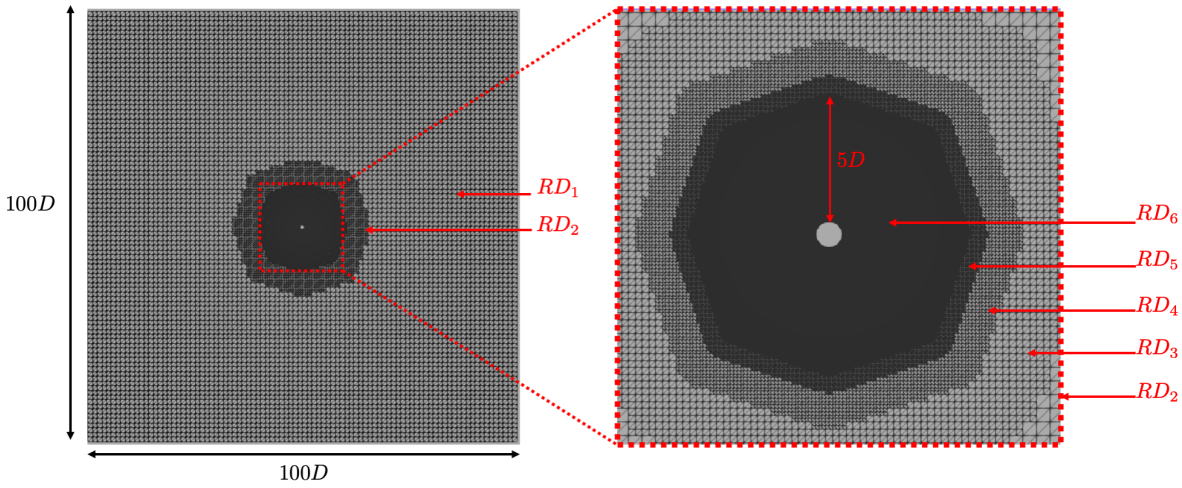

Figure 7.12 – Computational domain of the flow past a sphere.

diameter for Ma = 1.05 and 67 convective times for the Ma = 1.9 case.

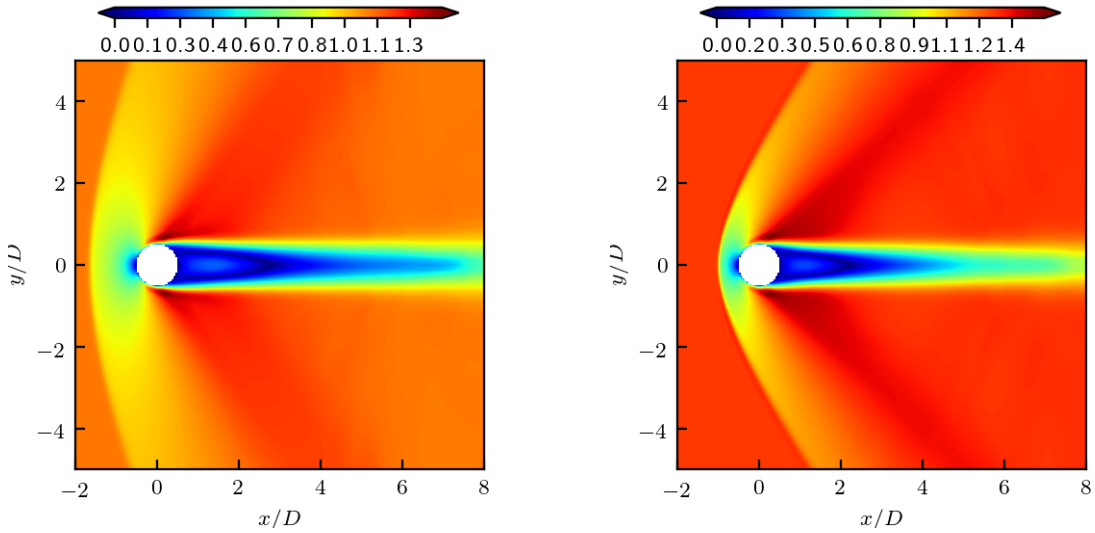

(a) Ma = 1.1 (b) Ma = 1.3

Figure 7.13 – Mach number field of the flow past a sphere at Re = 300.

Fig. 7.13 exhibits instantaneous snapshots of the Mach number around the sphere for Ma = 1.1 and Ma = 1.3. These supersonic flows are found to be steady and axi-symmetric accordingly to the DNS study of Nagata et al. [248]. For the present values of Mach and Reynolds numbers, a bow shock is formed at a distance L_s from the surface of the sphere, and its curvature increases with the Mach number. Moreover, one can observe that L_s decreases when the Mach number increases which is in agreement with the expected flow behavior. To observe in more detail this effect, Fig. 7.14a compares L_s to the multiple theoretical, experimental and numerical references. The shock-detachment distance is

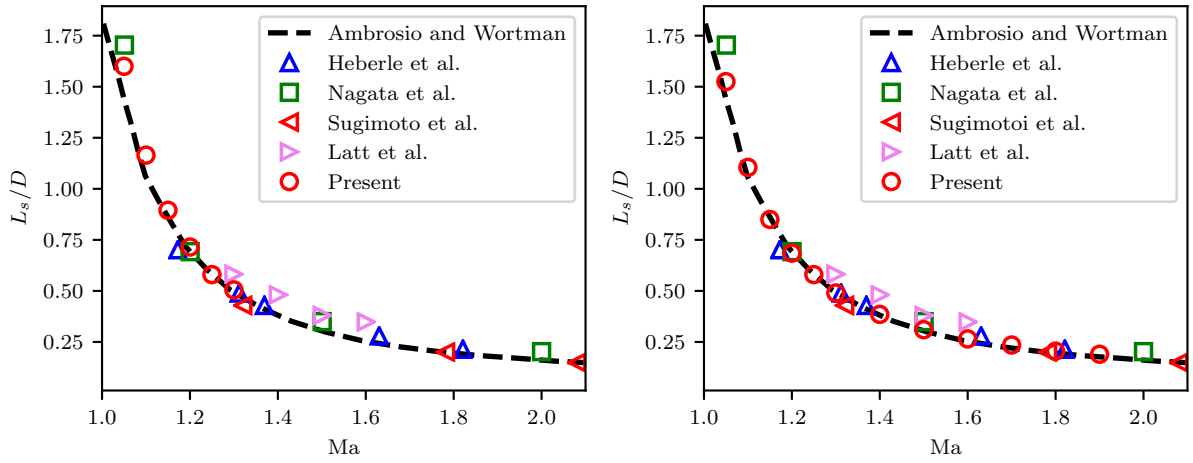

(a) Re = 300 (b) Re = 750

Figure 7.14 – Shock-detachment distance for different Mach numbers against experimental data (Sugimoto et al. and Herbele et al. compiled by Hida [246]), prediction model (Ambrosio and Wortman [247]) and numerical simulations (Nagata et al. [248] and Latt et al [66]).

computed considering Ma = 1 criterion and six simulations have been conducted for $1.05 \leq \text{Ma} \leq 1.3$ where the latter values has been identified as the upper limit in terms of numerical stability for Re = 300. A good agreement can be observed with the references data suggesting that the present method recover the correct tendency of the flow.

Actually, the stability limit have been found to be dependent to the value of τ^* which is particularly high in these simulations because of the low Reynolds number regime. Indeed, for the present test case it reads:

$$\tau^* = \frac{\tau}{\Delta t} = \frac{\text{Ma}\sqrt{\gamma_g}}{\text{Re}\, c_s^*} \frac{D}{\Delta x} \frac{1}{\sqrt{\theta_\infty}} \tag{7.5.9}$$

and is found to be equal to ~ 0.56 for Ma = 1.05 and ~ 0.69 for Ma = 1.3. One observed that for values higher than 0.5, the scheme operates in the under-relaxation regime and unfortunately presents stability issues. To lower the value of τ^* while keeping the physics, it can be seen from Eq. (7.5.9) that one can either increase Δx or θ_∞. Unfortunately, increasing the former would leads to a way too coarse mesh while increasing the latter would also increase the CFL number[3] leading to instabilities. Then, to perform computations for Mach number higher than 1.3 it has been chosen to increase the Reynolds number to Re = 750 to maintain the scheme in the over-relaxation regime. Using this new value, the latter is found to be equal to ~ 0.22 for Ma = 1.05 and ~ 0.41 for Ma = 1.9. Fig. 7.14b compares the shock-detachment distance computed by the scheme for Re = 750 with the same references as Fig. 7.14a. The results are found to be in agreement with the references up to Ma = 1.9 which has been found to be the upper stability limit of

[3] One reminds that $\text{CFL} = (\text{Ma} + 1)\sqrt{\gamma_g c_s^{*2} \theta_\infty}$.

the scheme. For Ma = 1.05, the result is more similar to the one obtained by Ambrosio and Wortman [247] than the DNS of Nagata [248] contrarily to Fig. 7.14a. As a matter of fact, the results of Nagata [248] and Latt et al. [66] are the only ones obtained for Re = 300. The other references (also used for comparison in [66, 248]) are either obtained for air value, such that Ambrosio and Wortman [247] suggesting that the Reynolds number must be much more higher, or are used for comparison in an inviscid framework such as the data of Sugimoto and Herbele et al. [245] in the work of Hida [246].

Finally, if one returns to Fig. 7.13 obtained for Re = 300, one can qualitatively observe that the separation length decreases as the Mach number increases, which is also an expected behavior of the flow [248]. Unfortunately the present model does not allows to properly study such phenomenon into more details, because considering a finer mesh equivalent to the DNS of Nagata [248] would automatically increase the value of relaxation time and produce instabilities.

To conclude, The physics of the flow is qualitatively well recovered by the numerical scheme when stable solutions are found. Unfortunately further investigation cannot be conducted due to the too viscous nature of the flow inducing instabilities. Thus, the present scheme seems to have a limit in terms of diffusive CFL number like the FD schemes seen in Sec. 3.6.2.b (see particularly Fig. 3.6). Eventually, this limit can be studied in future work thanks to the linear stability analysis of the HLBM developed in Chap. 6.

7.5.5 Performance

Here, the performance of the method is discussed. The aim is not to carry out an in-depth study of the solver's performance (scaling, parallelism, etc.), but rather to give an order of magnitude of the HLBM's performance compared to the standard athermal LBM. Moreover, no optimisations of hybrid routines have been carried out, and thus it would be unfair at this stage to make a quantitative comparison. Nevertheless it remains interesting to give an order of magnitude of the extra cost of the hybrid compared to the athermal version.

The LBM kernels of the hybrid and athermal versions are rather similar. Both of them have the HRR collision operator and Mach error corrective terms developed in terms of $\theta = T/T_r$ (resp. $\theta_0 = T_0/T_r$ for athermal). However, for the hybrid version no optimisation has been carried out on the expression of ψ_i. Thus, in addition to the extra cost related to the routines associated to the energy equation, one expects also an increase of the cost of the routines which include ψ_i. The same compilation options are used for the two versions, and they are compared on four uniform cubic domains of dimension 32^3, 64^3, 128^3 and 256^3 points. As the focus is on the performance of the code, the initialization and the physical and numerical parameters are irrelevant. The computations are carried out on a single node of the Kraken cluster[4] owned by CERFACS, and one hundred iterations are considered for all the cases.

Fig. 7.15 shows the strong scaling of the two versions in terms of MLUPS [5] (Million

[4] Bi-socket node Intel 18 cores Xeon Gold 6140 (Skylake) 2.3 Ghz with 96 GO of memory

[5] 1 MLUPS = 1/(microsecond/iterations/points).

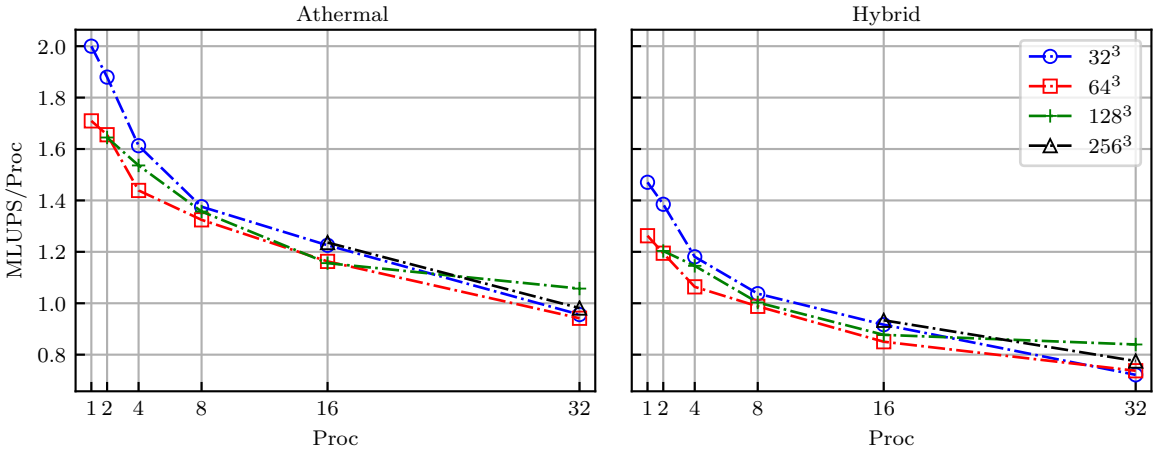

Figure 7.15 – Weak scaling of the athermal (left) and hybrid (right) versions for different numerical domains. Both graphs share the same legend.

Lattice Update Per Second) per processor (Proc). It can be seen that some points are missing for the 128^3 and 256^3 cases. This is due to memory overflows when an insufficient number of processors is used compared to the number of points of the simulation. On the figure, one can note the similar behavior of the two versions in terms of speedup. However, and as expected, the figure also evidences a loss of efficiency of the hybrid version compared to the athermal version. Averaging over all the cases, the hybrid version is found to be 33% more expensive than the athermal version (minimun 26%, maximum 38%). Nevertheless, it still remains in the order of magnitude of the athermal version.

In the recent publication of Hou et al. in 2019 [249], the same athermal version of ProLB has been compared to the finite volume solver OpenFOAM. The two solvers are used to simulate the noise emitted by a landing gear. Their accuracy and efficiency are tested on grids refined in an identical octree manner, with identical refinement regions and resolutions. The LBM solver obtained more accurate results and has been shown to be nine time faster than the NS solver OpenFOAM (see Sec.IV.C in [249]). The extra cost of the hybrid, which is estimated around 33%, is far from the factor 9 found in [249]. Moreover, the previous test cases proved that the hybrid method can operate with roughly the same CFL number as standard explicit compressible solver (CFL $\simeq$ 0.7). Thus, the present HLBM could be a future CPU efficient alternative - in the same way that the standard isothermal LBM is - to classical Navier-Stokes solvers for the computation of compressible flows. Of course, these conjectures are based only on the efficiency of the solver and not on its accuracy. Nevertheless, this shows the potential and viability of the method for future industrial applications.

7.6 Conclusion

In this chapter, the three-dimensional extension of the model presented in Chap. 4 was carried out on a D3Q19 lattice. This hybrid method based on the primitive form of the entropy equation was implemented in the industrial solver ProLB. The boundary conditions and transition algorithm were adapted from the athermal to the compressible framework.

Compressible test cases involving shock waves were carried out. Although no shock sensors were implemented, and a low order scheme was used for the energy equation, satisfactory results were obtained. The various computations also showed that the boundary conditions and the mesh refinement algorithm worked well. Moreover, the extra cost of the hybrid method was evaluated at 33% compared to the athermal version. Even thought further studies concerning its accuracy will have to be conducted, this HLBM model therefore remains competitive in terms of computational performance compared to other compressible Navier-Stokes solvers. Moreover, the model has a good potential for further improvements (e.g., on the form of the equilibrium function, the numerical scheme on the entropy equation, etc.), which encourages further research to improve the method.

Similarly to the two-dimensional model of Chap. 4, the quality of the results was found to be extremely dependent on the σ parameter. Although a low value of this parameter ensures numerical stability, it also introduces an over-dissipation of the scheme, and automatically leads to the degradation of the results. The development of a dynamic model of σ seems to be mandatory to ensure the stability of the model on all points of the computation while keeping optimal accuracy. This dynamic model could eventually be developed through spectral analysis, in the same way that some MRT operator find their values of relaxation times to guarantee accuracy and numerical stability [23,83,84].

Finally, the hybrid method was only tested for low Reynolds cases. To compute turbulent configurations with higher Reynolds numbers, the sub-grid model and the solver's wall-law will have to be adapted to account for the energy aspect of the HLBM.

Chapter 8

Conclusion and perspectives

Compressible flows are an important part of the problems encountered in the aeronautical industry. To better understand them, the development of numerical methods in line with the time constraints imposed by the industrial design cycle have become crucial. For this reason, the lattice Boltzmann method is becoming increasingly popular since it efficiently produces LES level resolution with an affordable restitution time. However, despite a wide range of validity of standard LBMs, the simulation of compressible flows remains a tedious task as the standard method is restricted to the simulation of athermal weakly compressible flows.

This thesis was devoted to the development and understanding of compressible LBM with the final aim of extending the ProLB software to compressible flows. Through the literature review of Chap. 2, the hybrid LBM stands out from the others method since it has been found to be compliant with all the requirements of this PhD. The work carried out during this thesis was therefore essentially focused on compressible HLBMs.

After a general presentation of the hybrid method, Chap. 3 highlighted two types of instabilities that needed to be solved in order to develop a compressible model: (1) the instabilities introduced by the perfect gas coupling and, (2) the instabilities restricting the LBM to relatively low Mach number computations. Based on the literature, these instabilities were removed using the HRR collision operator along with a non-conservative formulation of the entropy equation. With a tailored discretization of the corrective terms, a compressible HLBM based on the standard D2Q9 lattice and stable from subsonic to supersonic regime, was obtained and validated in Chap. 4. Up to the author's knowledge, this original model is the first supersonic HLBM based on a standard lattice. Nevertheless, the resulting model suffers from two distinct flaws: (1) a problem of conservativity occurring on shock interfaces and, (2) a non-physical phenomenon occurring for simulations involving the entropy mode.

Regarding the conservativity issue, Chap. 5 questioned the use of the entropy equation, the quantity of which is not preserved on shock waves. Although this defect can be corrected by using artificial sources of entropy, the most direct method remains the use of the total energy equation in conservative formulation. Unfortunately, the HLBM based on this energy equation was found less stable than the entropy-based HLBM and generates a non-physical phenomenon when simulating vorticity waves.

In Chap. 6, an original linear stability analysis of numerous compressible hybrid models was conducted. By studying the composition of the eigenvectors, the non-physical phenomena observed in Chap. 4 and Chap. 5 on entropy and vorticity waves respectively, were attributed to mode transfers which depend on the collision operator and the formulation of the energy equation. More generally, this spectral analysis answered many other questions about the stability of compressible HLBMs depending on the choice of numerical schemes, collision operators, energy equation or various numerical parameters so far unexplained. In the future, this analysis can avoid the standard and iterative trial and error process in the development of HLBM models.

Finally in Chap. 7, the extension in three-dimension of the compressible HLBM presented in Chap. 4 was performed. Once implemented in the industrial solver ProLB, the model was successfully assessed on compressible test cases containing boundary conditions and mesh refinement interfaces. Compared to the athermal weakly compressible version of ProLB, the extra cost of the hybrid model has been estimated to be around 33%. At first sight, it makes the present HLBM a possible CPU efficient alternative to classical compressible Navier-Stokes solvers. .

The hybrid method therefore has a great potential, nevertheless additional work need to be carried out. Indeed, to obtain a fully functional, robust and accurate compressible HLBM for industrial applications, this three points must be addressed:

1. The numerical dissipation induced by the HRR operator must be controlled.

2. Mode transferts must be suppressed.

3. For the simulation of shocked flows, the model must relies on the conservative total energy equation.

Eventually, points (1) and (2) can be solved by the recent HLBM of Farag et al. [250]. Using a pressure-based equilibrium, the authors developed a stable hybrid method even for high values of σ, thus reducing the numerical dissipation introduced by the HRR operator. However, unlike the canonical density-based model, this model uses a predictor/corrector step that can possibly introduce numerical dissipation. Moreover, the CFL number of this model seems to be much lower compared to the density-based model. These two points therefore motivates a future comparative study of density-based and pressure-based models. Nevertheless, the great interest of this model (and what makes it really superior to the density-based model) lies in the fact that it does not produce entropy-shear mode transfer. This is therefore a significant advantage when simulating compressible thermal or reactive flows [251]. Finally, regarding the point (3), Zhao and co-workers [251] further improved the pressure-based HLBM of Farag et al. [250] by means of a conservative total energy equation. Using an energy flux derived consistently from the mass and momentum flux, they developed a stable HLBM which captures accurately shock discontinuities without any conservativity issues.

Note finally that the present PhD work, and parallel activities, have yielded to the following publications, conference papers and face-to-face/online teaching sessions.

Scientific publications

- **Renard, F.**, Feng, Y., Boussuge, J. F., Sagaut, P. (2021). Improved compressible hybrid lattice Boltzmann method on standard lattice for subsonic and supersonic flows. Computers & Fluids, 219, 104867 [225].
- **Renard, F.**, Wissocq, G., Boussuge, J. F., Sagaut, P. (2020). A Linear Stability Analysis of Compressible Hybrid Lattice Boltzmann Methods. Journal of Computational Physics. Submitted on June 15th, 2020. [252].
- Guo, S., Feng, Y., Jacob, J., **Renard, F.**, Sagaut, P. (2020). An efficient lattice Boltzmann method for compressible aerodynamics on D3Q19 lattice. Journal of Computational Physics, 109570. [234].

International conference

- **Renard, F.**, Feng, Y., Boussuge, J. F., Sagaut, P.,Improved compressible hybrid lattice Boltzmann method on standard lattice for subsonic and supersonic flows, 28th International Conference on Discrete Simulation of Fluid Dynamics, 2019, Bangalore India.

Online course – Trainings

- Small private online course (SPOC): Fundamentals of Lattice Boltzmann Method
- Instructor-led training session at CERFACS: https://cerfacs.fr/en/event/basic-lattice-boltzmann-methods/
- Practicals about the lattice Boltzmann method, at ISAE-Supaero (graduate school of aeronautical engineering).

Appendix A

Moment matching equilibrium

Here is an overview of how a discrete equilibrium distribution function can be built directly from a given lattice and equilibrium macroscopic moments. This construction is an alternative to the Gauss-Hermite construction seen in Sec. 2.3.1. The discrete equilibrium function is obtained simply in inverting a linear system defined by the lattice and the moments, and using the lattice closure relation [55].

A.1 D1Q3 Equilibrium construction

The discrete equilibrium construction technique will be presented using the simple symmetric one-dimensional D1Q3 lattice [6]. This lattice is defined as:

$$\begin{aligned} \xi_0 &= 0, \\ \xi_{1,2} &= \pm r, \end{aligned} \tag{A.1.1}$$

with $r = \|\xi_{1,2}\|$ the norm of the discrete velocities. With this discretization, the purpose is now to find the appropriate equilibrium distribution functions allowing to recover the Navier-Stokes equations. As seen in Sec. 2.2.5, only the moments of this function are needed to obtain the correct macroscopic equations. The D1Q3 lattice offers then a system of three equations for the three unknowns $(f_0^{eq}, f_1^{eq}, f_2^{eq})$ which reads:

$$\sum_i f_i^{eq} = \int_{\mathbb{R}} f^{eq} \mathrm{d}\xi = m_{eq}^{(0)} = \rho, \tag{A.1.2}$$

$$\sum_i \xi_i f_i^{eq} = \int_{\mathbb{R}} \xi f^{eq} \mathrm{d}\xi = m_{eq}^{(1)} = \rho u, \tag{A.1.3}$$

$$\sum_i \xi_i^2 f_i^{eq} = \int_{\mathbb{R}} \xi^2 f^{eq} \mathrm{d}\xi = m_{eq}^{(2)} = \rho u^2 + \rho r_g T. \tag{A.1.4}$$

Once this system is re-written on a matrix form, it comes down to solve:

$$\underbrace{\begin{bmatrix} 1 & 1 & 1 \\ 0 & r & -r \\ 0 & r^2 & r^2 \end{bmatrix}}_{\boldsymbol{M}} \begin{pmatrix} f_0^{eq} \\ f_1^{eq} \\ f_2^{eq} \end{pmatrix} = \begin{pmatrix} \rho \\ \rho u \\ \rho u^2 + \rho r_g T \end{pmatrix}$$

The matrix $\boldsymbol{M}$ appearing on the l.h.s allows the transformation from the distribution space to the moment space. The latter is widely used in the MRT-LBM community and is usually called the moment matrix. Considering r as reference velocity, one can obtain the following dimensionless variables:

$$u^* = \frac{u}{r} \quad \text{and} \quad c_s^* = \frac{\sqrt{r_g T}}{r}, \tag{A.1.5}$$

from which the system can be re-written as:

$$\begin{bmatrix} 1 & 1 & 1 \\ 0 & 1 & -1 \\ 0 & 1 & 1 \end{bmatrix} \begin{pmatrix} f_0^{eq} \\ f_1^{eq} \\ f_2^{eq} \end{pmatrix} = \begin{pmatrix} \rho \\ \rho u^* \\ \rho u^{*2} + \rho c_s^{*2} \end{pmatrix} \tag{A.1.6}$$

The matrix $\boldsymbol{M}$ has a non-zero determinant ($\det(\boldsymbol{M}) = 2$) which allows the resolution of the system. The inverse of $\boldsymbol{M}$ can be computed manually or using a symbolic computation tool such as wxMaxima, and the solution reads:

$$f_0^{eq} = \rho \left(1 - u^{*2} - c_s^{*2}\right), \tag{A.1.7}$$

$$f_1^{eq} = \frac{\rho}{2} \left(u^{*2} + u^* + c_s^{*2}\right), \tag{A.1.8}$$

$$f_2^{eq} = \frac{\rho}{2} \left(u^{*2} - u^* + c_s^{*2}\right). \tag{A.1.9}$$

At this stage, the discrete equilibrium distribution function is almost built. The only unknown remains the norm of the discrete velocity $r = ||\xi_{1,2}||$ which is used to obtain the dimensionless expressions of Eq. (A.1.5). The latter will be found using the concept of lattice closure relation [55]. As a consequence of the discretization of the velocity space, the following relation for the D1Q3 lattice exists:

$$\frac{\xi_i}{||\xi_{1,2}||} = \frac{\xi_i^3}{||\xi_{1,2}||^3}, \tag{A.1.10}$$

and links the first- and third-order equilibrium moments together. Indeed, multiplying by f_i^{eq} on both side of the relation and summing over the discrete velocities leads to the following relation:

$$\sum_i \frac{\xi_i}{||\xi_{1,2}||} f_i^{eq} = \sum_i \frac{\xi_i^3}{||\xi_{1,2}||^3} f_i^{eq} = \rho u^*. \tag{A.1.11}$$

Thus an aliasing phenomenon can be clearly observed between the first and the third order moments. The present third-order moment clearly differs from the expected Maxwellian

moment $m_{eq}^{(3)} = \rho\left(u^{*3} + 3u^* c_s^{*2}\right)$, and is responsible for the so-called cubic Mach error in the viscous stress tensor. Nonetheless, the error induced by this aliasing can be reduced by trying to match the discrete moment to the exact moment issued from the Maxwellian equilibrium. This is the so-called moment matching condition and reads:

$$\sum_i \frac{\xi_i^3}{\|\xi_{1,2}\|^3} f_i^{eq} \simeq m_{eq}^{(3)} \iff \rho u^* \simeq \rho\left(u^{*3} + 3u^* c_s^{*2}\right). \tag{A.1.12}$$

It clearly appears that the equality cannot be strictly respected due to the asymmetric presence of a cubic term on the r.h.s. of the equation. Nevertheless, this error can be restricted to the third-order by matching the first-order term such as:

$$u^* = 3u^* c_s^{*2} \tag{A.1.13}$$

leading to:

$$c_s^{*2} = \frac{1}{3}. \tag{A.1.14}$$

Thus, in the light of Eq. (A.1.5), the following relation is obtained on the norm of the discrete velocity:

$$r = \frac{\sqrt{r_g T}}{c_s^*} \Rightarrow r = \sqrt{3 r_g T} \tag{A.1.15}$$

Imposing a constant temperature T_r in the velocity norm, so that the streaming step of the LBM algorithm can be respected, one get:

$$\|\xi_{1,2}\| = \sqrt{3 r_g T_r}. \tag{A.1.16}$$

Here the argument used to find the value of the lattice constant c_s^* is essentially based on the matching of the first- and the third-order moments to reduced the error created by the velocity space discretization.

Finally, for higher order lattices such as the D1Q5 or D1Q7, the very same procedure can be applied to find the discrete equilibrium and lattice constant expression. Also, formulas found in one-dimension can be used to obtain expressions in two- and three-dimension by means of tensor product. For more details, the interested reader can refer to the work of Karlin et al. [55].

Appendix B

The entropy equation

The aim of this appendix is to provide a good overview and understanding on how to derive the entropy governing equation, where does it comes from and which terms it involves. Most of the following formulas can be found in [253, 254] and applied in the CFD framework in [150, 254–258].

B.1 The entropy expression from the Gibbs relation

Lets us start from the following fundamental relation of thermodynamic, also called Gibbs equation, which reads:

$$T\mathrm{d}s = \mathrm{d}e + p\mathrm{d}v, \tag{B.1.1}$$

where s, e, p and $v = 1/\rho$ refer respectively to the entropy, the internal energy, the pressure and the volume per mass unit. Finally, d corresponds to the total derivative. Using this relation, the objective is to find the expression of entropy s as a function of the thermodynamic quantities ρ, T and p. Knowing the fact that that $\rho = 1/v$ so that the derivative of v gives:

$$\mathrm{d}v = -\frac{1}{\rho^2}\mathrm{d}\rho, \tag{B.1.2}$$

one can plug this expression into Eq. (B.1.1) one obtain:

$$T\mathrm{d}s = \mathrm{d}e - \frac{p}{\rho^2}\mathrm{d}\rho, \tag{B.1.3}$$

Using the perfect gas relation $p = \rho r_g T$, one can rewrite this equation as:

$$\mathrm{d}s = \frac{1}{T}\mathrm{d}e - \frac{r_g}{\rho}\mathrm{d}\rho, \tag{B.1.4}$$

Assuming that $e = c_v T$ (with a constant c_v) and considering the ideal gas constant on the form $r_g = c_v\left(\gamma_g - 1\right)$, one gets:

$$\mathrm{d}s = c_v\left(\frac{1}{T}\mathrm{d}T - \frac{\gamma_g - 1}{\rho}\mathrm{d}\rho\right), \tag{B.1.5}$$

The primitive form of the equation naturally comes as:

$$s = c_v \left(\ln (T) - (\gamma_g - 1) \ln (\rho) \right), \tag{B.1.6}$$

and finally one get $s(\rho, T)$:

$$\boxed{s = c_v \ln \left(\frac{T}{\rho^{(\gamma_g - 1)}} \right)}. \tag{B.1.7}$$

The above formula of the entropy is the one which will be used in the following parts.

B.2 The speed of sound

It is to be noted that the isentropic speed of sound can be computed from Eq. (B.1.7). Using the ideal gas relation, one can rewrite Eq. (B.1.7) as:

$$s = c_v \ln \left(\frac{p}{\rho^{\gamma_g}} \right) - c_v \ln (r_g), \tag{B.2.1}$$

with $c_v \ln (r_g) = cst$. Inverting this equation so as to get p in function of ρ and s, it follows:

$$p = \rho_g^{\gamma} r_g \exp \left(\frac{s}{c_v} \right). \tag{B.2.2}$$

It is well known that the square of the sound velocity can be obtained from the partial derivative of p with respect to ρ keeping the entropy constant (isentropic). Computing such derivative from Eq. (B.2.2) one get:

$$\left. \frac{\partial p}{\partial \rho} \right|_s = \frac{\gamma_g}{\rho} \rho^{\gamma_g} r_g \exp \left(\frac{s}{c_v} \right) = \frac{\gamma_g}{\rho} p = \gamma_g r_g T \tag{B.2.3}$$

and thus the isentropic speed of sound is obtained and reads:

$$\boxed{c = \sqrt{\gamma_g r_g T}} \tag{B.2.4}$$

B.3 The entropy equation

The purpose here is to obtain the space and time evolution of the entropy variable $s(x, t)$. First, Eq. (B.1.1) is considered on the convective form of the Gibbs equation [253]:

$$\rho T \frac{Ds}{Dt} = \rho \frac{De}{Dt} - \frac{P}{\rho} \frac{D\rho}{Dt}, \tag{B.3.1}$$

with D/Dt being the material derivative. Let us recall the expression of the internal energy equation:

$$\rho \frac{De}{Dt} + p \frac{\partial u_\alpha}{\partial x_\alpha} = - \frac{\partial}{\partial x_\alpha} \left(-\lambda \frac{\partial T}{\partial x_\alpha} \right) + \Pi^{(1)}_{\alpha\beta} \frac{\partial u_\alpha}{\partial x_\beta}, \tag{B.3.2}$$

and the expression of the mass equation on the following form:

$$p\frac{\partial u_\alpha}{\partial x_\alpha} = -\frac{p}{\rho}\frac{D\rho}{Dt}. \tag{B.3.3}$$

Replacing now Eq. (B.3.3) into Eq. (B.3.2) it follows:

$$\rho\frac{De}{Dt} - \frac{p}{\rho}\frac{D\rho}{Dt} = -\frac{\partial}{\partial x_\alpha}\left(-\lambda\frac{\partial T}{\partial x_\alpha}\right) + \Pi^{(1)}_{\alpha\beta}\frac{\partial u_\alpha}{\partial x_\beta}. \tag{B.3.4}$$

Finally, substituting Eq. (B.3.1) in the equation above, one gets:

$$\rho T\frac{Ds}{Dt} = -\frac{\partial}{\partial x_\alpha}\left(-\lambda\frac{\partial T}{\partial x_\alpha}\right) + \Pi^{(1)}_{\alpha\beta}\frac{\partial u_\alpha}{\partial x_\beta}, \tag{B.3.5}$$

which corresponds to the evolution equation of the entropy. One can develop the later expression as:

$$\boxed{\frac{\partial s}{\partial t} + u_\alpha\frac{\partial s}{\partial x_\alpha} = -\frac{1}{\rho T}\frac{\partial}{\partial x_\alpha}\left(-\lambda\frac{\partial T}{\partial x_\alpha}\right) + \frac{1}{\rho T}\Pi^{(1)}_{\alpha\beta}\frac{\partial u_\alpha}{\partial x_\beta}}, \tag{B.3.6}$$

and remarks that thanks to Eq. (B.3.1), the pressure work term is intrinsic to the definition of the entropy Eq. (B.1.7) which can be advantageous in a CFD context. Indeed, this term do not need to be discretized, possibly leading to less expensive computation. Finally, the entropy equation can be also found in the litterature expressed in the following form [219, 220, 259]:

$$\frac{\partial s}{\partial t} + u_\alpha\frac{\partial s}{\partial x_\alpha} + \frac{1}{\rho}\frac{\partial}{\partial x_\alpha}\left(-\frac{\lambda}{T}\frac{\partial T}{\partial x_\alpha}\right) = \frac{\lambda}{\rho T^2}\left(\frac{\partial T}{\partial x_\alpha}\right)^2 + \frac{1}{\rho T}\Pi^{(1)}_{\alpha\beta}\frac{\partial u_\alpha}{\partial x_\beta} \geq 0, \tag{B.3.7}$$

which is in compliance with the second law of thermodynamic stating that the entropy always increases.

B.4 Intrinsic pressure work in the entropy equation

The pressure work term is implicitly contained in the advection part of the entropy equation and can be highlighted by chain rule. Thus, the objective is to rewrite the l.h.s of Eq. (B.3.7) to obtain, with no loss of generality, the equivalent equation in terms of internal energy. From Eq. (B.1.7), one can compute:

$$\left.\frac{\partial s}{\partial e}\right|_\rho = \frac{c_v}{e} \qquad \text{and} \qquad \left.\frac{\partial s}{\partial \rho}\right|_e = -\left(\gamma_g - 1\right)\frac{c_v}{\rho}. \tag{B.4.1}$$

Developing now the l.h.s of Eq. (B.3.7), one obtain the following equality:

$$\begin{aligned}\frac{\partial s}{\partial t}+u_\alpha\frac{\partial s}{\partial x_\alpha} &= \frac{\partial s}{\partial e}\bigg|_\rho\frac{\partial e}{\partial t}+\frac{\partial s}{\partial \rho}\bigg|_e\frac{\partial \rho}{\partial t}+u_\alpha\left(\frac{\partial s}{\partial e}\bigg|_\rho\frac{\partial e}{\partial x_\alpha}+\frac{\partial s}{\partial \rho}\bigg|_e\frac{\partial \rho}{\partial x_\alpha}\right)\\ &= \frac{c_v}{e}\frac{\partial e}{\partial t}+(\gamma_g-1)\frac{c_v}{\rho}\frac{\partial \rho u_\alpha}{\partial x_\alpha}+u_\alpha\left(\frac{c_v}{e}\frac{\partial e}{\partial x_\alpha}-(\gamma_g-1)\frac{c_v}{\rho}\frac{\partial \rho}{\partial x_\alpha}\right)\\ &= \frac{1}{T}\left[\frac{\partial e}{\partial t}+u_\alpha\frac{\partial e}{\partial x_\alpha}+\underbrace{r_gT\frac{\partial u_\alpha}{\partial x_\alpha}}_{\text{pressure work}}\right].\end{aligned} \tag{B.4.2}$$

Thus, the pressure work term is intrinsically contained in the definition of the entropy Eq. (B.1.7). So by using the entropy equation, it makes it possible to get rid of the discretization of the pressure work term while keeping the associated physical phenomena.

Appendix C

Linear investigation of the supersonic limit of LBM schemes

In this appendix, the phenomena limiting athermal and hybrid models to the subsonic regime are shown by means of the linear stability analysis presented in Chap. 6. Only the D1Q3 lattice will be considered, which is sufficient to exhibit the phenomena involved. Chapter 4 shown that one of the ways to obtain a stable calculation for supersonic flows is based on two ingredients, identified as follows:

- The HRR collision operator (see Sec. 4.3.3),
- An upwind FD scheme applied on $E_{1,\alpha\beta}$ in the correction term ψ_i (see Sec. 4.3.2).

Thus, only the HRR collision operator will be considered, gathering for the D1Q3 lattice both BGK ($\sigma = 1$) and fully reconstructed operators ($\sigma = 0$). Two types of discretization of $E_{1,\alpha\beta}$ are investigated, the standard CO2 scheme Eq. (6.2.14) and the first-order upwind scheme Eq. (6.2.13).

C.1 Supersonic limit of the athermal LBM

In this section, the supersonic limit of the athermal LBM is investigated. Fig. C.1 shows the dispersion and dissipation graphs of the model for $\overline{\text{Ma}} = 1.1$, $\theta = 0.5$ and $\tau^* = 1.10^{-5}$. On Fig. C.1a, the results for the BGK collision operator using a centered discretization of $E_{1,\alpha\beta}$ can be found. According to the dissipation graph, the scheme is unstable. This instability is a direct consequence the eigenvalues collision located around $k^* = 3\pi/4$. It is worth noting that this collision is of different kind than the one mentioned in Sec. 6.3.3 for $\overline{\text{Ma}} = 0.732$ since, in the present case, it involves the downstream and upstream acoustic modes. Indeed, for $\theta = 0.5$, the critical Mach number Eq. (6.3.18) is $\overline{\text{Ma}^c} \simeq 1.45$ ensuring that the spurious macroscopic mode located at $\text{Re}(\omega^*) = \pi$ (for $k^* = 0$ and $k^* = \pi$) do not collide with the downstream acoustic. Thus, reducing θ in the expectation of stabilizing the schemes would be pointless since, on the contrary, the sonic cone will be reduced and the two acoustic modes will interact all the more. This feature hints that these modes must be decoupled, and this brings to the second stabilization

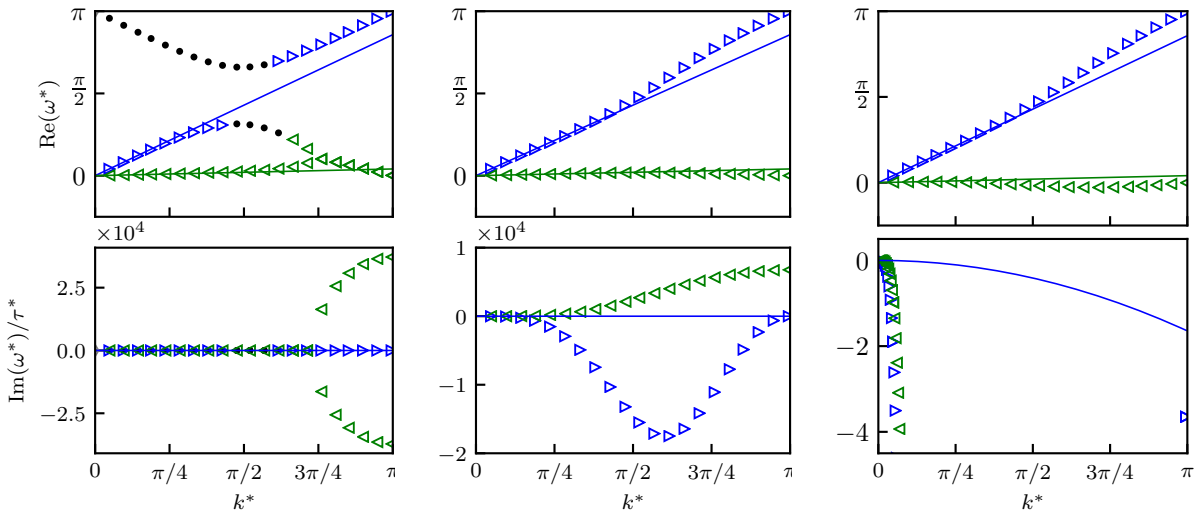

(a) $\sigma = 1$, D1CO2($E_{1,\alpha\beta}$) (b) $\sigma = 0$, D1CO2($E_{1,\alpha\beta}$) (c) $\sigma = 0$, D1UPO1($E_{1,\alpha\beta}$)

Figure C.1 – Dispersion (top) and dissipation (bottom) graph of the LBM D1Q3 HRR model. In the present case $\overline{\text{Ma}} = 1.1$, $\theta = 0.5$ and $\tau^* = 1.10^{-5}$. Symbols correspond to ω_{ac+}: (▷) ; ω_{ac-}: (◁) ; ω_{msp}:(●) and solid lines correspond to theory.

lever i.e. the σ parameter of the HRR. Fig. C.1b shows the results for the HRR at $\sigma = 0$. It can be seen that the use of HRR has the desired effect, the acoustic eigenvalue collision is now suppressed. Nevertheless the scheme remains unstable, which is due to the centered discretization of $E_{1,\alpha\beta}$. Once this term is discretized using the first-order upwind scheme, the model is found to be stable as shown on Fig. C.1c. Tests have been done using higher order scheme such as: second and third order upwind and fourth order centered scheme, and the conclusion remains the same: only the upwind class is stable for $\overline{\text{Ma}} > 1$. This behavior could be certainly explained by an heuristic analysis of the equivalent equation of the hybrid LBM system. It can be assumed that the sign of the coefficients in factor of the even derivatives of error terms changes sign for $\overline{\text{Ma}} = 1$ in the centered case. This analysis may be the subject of future work.

C.2 Supersonic limit of the hybrid LBM

In this section, the supersonic limit of the hybrid LBM is investigated. On Fig. C.2, the study is now conducted on the hybrid scheme based on primitive entropy equation and discretized by RK4CO2 scheme. Results are obtained for the same parameters as the athermal case. If the BGK operator is employed, (see Fig. C.2a) the same collision between the acoustic eigenvalues is observed. Moreover, one can see an other collision occurring for $k^* = \pi/2$ between the spurious macroscopic and the downstream acoustic mode. As a matter of fact, for $\overline{\theta} = 0.5$ and $\gamma = 1.4$ the critical Mach number of the hybrid model Eq. (6.4.15) is $\overline{\text{Ma}^c} \simeq 1.07$ and therefore below the current value. Lowering $\overline{\theta}$ would fix this collision, but the other one involving the two acoustic will still be there.

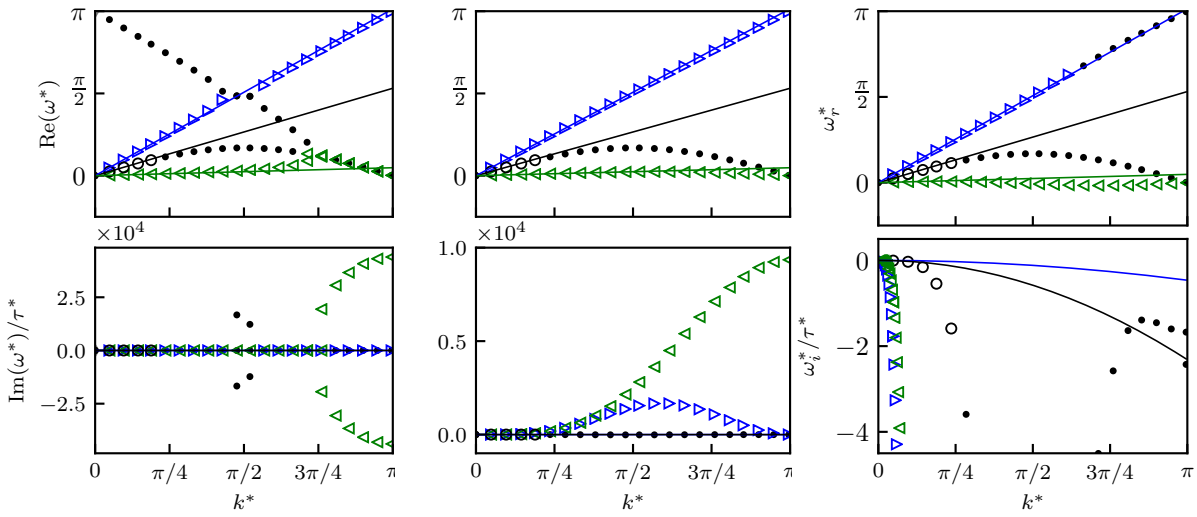

(a) $\sigma = 1$, D1CO2($E_{1,\alpha\beta}$) (b) $\sigma = 0$, D1CO2($E_{1,\alpha\beta}$) (c) $\sigma = 0$, D1UPO1($E_{1,\alpha\beta}$)

Figure C.2 – Dispersion (top) and dissipation (bottom) graph of the hybrid D1Q3 RK4C02 HRR based on the primitive entropy equation. In this case, $\overline{\theta} = 0.5$, $\overline{\mathrm{Ma}} = 1.1$ and $\tau^* = 1.10^{-5}$. Symbols correspond to ω_{ac+}: (▷) ; ω_{ac-}: (◁) ; ω_{entr}: (○) ; ω_{msp}:(●) ; ω_g:(◊) and solid lines correspond to theory.

Similarly to the athermal case, Fig. C.2b shows the results for $\sigma = 0$ where the two collision disappeared but the scheme remains unstable due the the centered discretization of $E_{1,\alpha\beta}$. And finally for an upwind discretization Fig. C.2c, one obtains stable results for supersonic configuration.

In the end, same conclusions than the athermal case are drawn for the hybrid scheme. To obtain a stable model for $\overline{\mathrm{Ma}} > 1$:

- The physical modes somehow must be decoupled.
- An upwind discretization scheme has to be adopted for $E_{1,\alpha\beta}$.

This analysis explains how the supersonic limitation of the original model of Feng et al. [187] (shown in Chap.4) has been removed simply discretizing $E_{1,\alpha\beta}$ using an upwind scheme. At a later stage, it would be interesting to see whether the use of higher-order upwind schemes would improve the results.

Appendix D

Calculation details of the linear stability analysis

The purpose of this appendix is to give the calculation details of the linear stability analysis presented in Chap. 6.

D.1 Athermal Matrix

In this section, the expression of the time advance matrix of the corrected DVBE and LBM systems are derived in the spectral space. Emphasis will be placed on the spacial derivatives contributions in Fourier space. In the following, Jacobian matrix can be either obtained analytically [72], or using a formal calculation library such as *SymPy* or *Theano* as done in [63, 193]. The second option using the *Theano* library was used in this work.

D.1.1 Corrected DVBE

Starting from Eq. (6.2.1) and following the linearization procedure around an equilibrium state Eq. (6.3.1a), one get:

$$\frac{\partial f_i'}{\partial t} = \underbrace{\left.\frac{\partial \mathcal{S}_i^{DVBE}}{\partial f_j}\right|_{\overline{f_j^{eq}}}}_{\mathrm{M}_{ij}^{DVBE}} f_j' + O\left(f_j'^2\right), \tag{D.1.1}$$

where M_{ij}^{DVBE} refers to as the Jacobian matrix of r.h.s. of Eq. (6.2.1). This matrix is the so-called time advance matrix of the DVBE system. At the moment, it is to be noted that M_{ij}^{DVBE} is essentially composed of constant terms and space derivative operators applied to f_i'. Once Eq. (6.3.1b) substituted, the derivative operators can be analytically computed in the spectral space changing M_{ij}^{DVBE} into $\widetilde{\mathrm{M}}_{ij}^{DVBE}$. Keeping only the first-order distribution functions fluctuations, this system reads:

$$\omega \widehat{f_i} = \widetilde{\mathrm{M}}_{ij}^{DVBE} \widehat{f_j}, \tag{D.1.2}$$

with

$$\widetilde{\mathrm{M}}_{ij}^{DVBE} = c_{i,\alpha}k_\alpha\delta_{ij} - \mathrm{i}\frac{1}{\overline{\tau}}\left(\delta_{ij} + \frac{\partial f_i^{eq}}{\partial f_j}\Big|_{\overline{f_j^{eq}}}\right) - \Psi_{ij}, \tag{D.1.3}$$

and

$$\Psi_{ij} = w_i\frac{\mathcal{H}_{i,\alpha\alpha}}{2c_s^4}k_\alpha\frac{\partial\left(-a_{\alpha\alpha\alpha}^{eq,(3)}\right)}{\partial f_j}\Big|_{\overline{f_j^{eq}}}. \tag{D.1.4}$$

Here, Ψ_{ij} corresponds to the Jacobian of the corrective body-force term expressed in the Fourier space, where the space derivative present in $E_{1,\alpha\beta}$ Eq. (6.2.3) is now simply k_α.

D.1.2 Corrected LBM

In this subsection, the time advance matrix of the LBM-BGK and LBM-HRR respectively Eq. (4.3.6) and Eq. (6.2.9) will be derived. Following the linearization procedure around a mean equilibrium state Eq. (6.3.1a), one gets for both cases:

$$g_i'^{+} = \underbrace{\frac{\partial \mathcal{S}_i^{LBM}}{\partial g_j}\Big|_{\overline{f_j^{eq}}}}_{\mathrm{M}_{ij}^{LBM}} g_j' + O\left(g_j'^2\right), \tag{D.1.5}$$

where M_{ij}^{LBM} refers to as the Jacobian matrix of the LBM r.h.s discrete system. Once Eq. (6.3.10) substituted, the discrete derivative operators can be analytically computed in the spectral space changing M_{ij}^{LBM} into $\widetilde{\mathrm{M}}_{ij}^{LBM}$. Keeping only the first-order distribution function fluctuations, this system reads:

$$e^{-\mathrm{i}\omega\Delta t}\widehat{g}_i = \widetilde{\mathrm{M}}_{ij}^{LBM}\widehat{g}_j. \tag{D.1.6}$$

From here, the two collision operator will be treated independently.

Time-advance matrix of the corrected LBM-BGK

Starting from the most classical case, the time advance matrix of the LBM-BGK system Eq. (4.3.6) reads:

$$\text{BGK}: \quad \widetilde{\mathrm{M}}_{ij}^{LBM} = e^{-\mathrm{i}k_\alpha\Delta x}\left[\delta_{ij} - \frac{\Delta t}{\check{\tau}}\left(\delta_{ij} - \frac{\partial f_i^{eq}}{\partial g_j}\Big|_{\overline{f_j^{eq}}}\right) + \frac{2\check{\tau}-\Delta t}{2\check{\tau}}\Delta t\,\Psi_{ij}\right], \tag{D.1.7}$$

where Ψ_{ij} refers to as the Jacobian of the corrective term including space derivatives expressed in the Fourier space and reads:

$$\Psi_{ij} = w_i\frac{\mathcal{H}_{i,\alpha\alpha}}{2c_s^4}\mathcal{K}_\alpha^{\mathrm{D1CO2}}\frac{\partial\left(-a_{\alpha\alpha\alpha}^{eq,(3)}\right)}{\partial g_j}\Big|_{\overline{f_j^{eq}}}. \tag{D.1.8}$$

Here $\mathcal{K}_\alpha^{\mathrm{D1CO2}}$ corresponds to the modified wave number of the second order centered finite difference, applied in the present case to $E_{1,\alpha\beta}$ Eq. (6.2.3). One can relate to D.4 for its

expression.

Time-advance matrix of the corrected LBM-HRR
Regarding LBM-HRR system Eq. (6.2.9), the matrix can be expressed as:

$$\text{HRR}: \quad \widetilde{\mathrm{M}}_{ij}^{LBM} = e^{-\mathrm{i}k_\alpha \Delta x}\left[\frac{\partial f_i^{eq}}{\partial g_j}\Big|_{\overline{f_j^{eq}}} + \left(1-\frac{\Delta t}{\check{\tau}}\right)G_{ij}^{(1)} + \frac{\Delta t}{2}\Psi_{ij}\right], \tag{D.1.9}$$

where Ψ_{ij} can be found in Eq. (D.1.8), and $G_{ij}^{(1)}$ refers to as the Jacobian of the off-equilibrium moments. To take into account the finite difference contributions induced by the HRR collision and the corrective term, $G_{ij}^{(1)}$ is expressed such as:

$$G_{ij}^{(1)} = \frac{\partial}{\partial f_j}\left(w_i \frac{\mathcal{H}_{i,\alpha\beta}}{2c_s^4}\left[\sigma A_{\alpha\beta}^{PR,(2)} + (1-\sigma)\,A_{\alpha\beta}^{FD,(2)}\right] + w_i \frac{1}{6c_s^6}\left[\mathcal{H}_{i,xxy}A_{xxy}^{(3)} + \mathcal{H}_{i,yyx}A_{yyx}^{(3)}\right]\right)\Big|_{\overline{f_j^{eq}}} \tag{D.1.10}$$

with

$$A_{\alpha\beta}^{PR,(2)} = \sum_i \left[\mathcal{H}_{i,\alpha\beta}\left(f_i - f_i^{eq}\right)\right] + \frac{\Delta t}{2}\mathcal{K}_\alpha^{\mathrm{D1CO2}}\left(-a_{\alpha\alpha\alpha}^{eq,(3)}\right), \tag{D.1.11a}$$

$$A_{\alpha\beta}^{FD,(2)} = -\check{\tau}\overline{p}\left(\mathcal{K}_\beta^{\mathrm{D1CO2}}u_\alpha + \mathcal{K}_\alpha^{\mathrm{D1CO2}}u_\beta\right), \tag{D.1.11b}$$

respectively the second order off-equilibrium moment partially computed using projection procedure and finite difference scheme modeling the viscous stress tensor. The third order off-equilibrium moments read:

$$A_{xxy}^{(3)} = 2\overline{u}_x\left(\sigma A_{xy}^{PR,(2)} + (1-\sigma)\right)A_{xy}^{FD,(2)} + \overline{u}_y\left(\sigma A_{xx}^{PR,(2)} + (1-\sigma)\right)A_{xx}^{FD,(2)}, \tag{D.1.12a}$$

$$A_{yyx}^{(3)} = 2\overline{u}_y\left(\sigma A_{xy}^{PR,(2)} + (1-\sigma)\right)A_{xy}^{FD,(2)} + \overline{u}_x\left(\sigma A_{yy}^{PR,(2)} + (1-\sigma)\right)A_{yy}^{FD,(2)}. \tag{D.1.12b}$$

where Eq. (6.3.6) imposes the mean value for the velocities, since the later contains only first order fluctuation [193].

D.2 Thermal Matrix

In this section, the expression of the time advance matrix of the HDVBE and HLBM systems are given in the spectral space. These matrix are detailed on the form of blocks, presented by Fig. 6.9. One recalls that, for $\widetilde{\mathrm{M}}_{ij}^{HDVBE}$ (and reciprocally for $\widetilde{\mathrm{M}}_{ij}^{HLBM}$), the blocks are defined such that:

- Block I: $i, j \in [0, m-1]$
- Block II: $i \in [0, m-1]$, $j = m$
- Block III: $i = m$, $j \in [0, m-1]$
- Block IV: $i = m$, $j = m$

Emphasis will be placed on the shape of these block in Fourier space, specially in the discrete case where the finite difference contributions are detailed. For the sake of brevity, and without loss of generality, only the total energy equation on conservative form is considered. Similarly to D.1, the Jacobian are computed numerically using the *Theano* library.

D.2.1 HDVBE

Starting from the system. (6.4.1) and following the linearization procedure around the mean equilibrium state Eq. (6.3.1a) and around the mean total energy, one gets:

$$\begin{cases} \dfrac{\partial f_i'}{\partial t} = \overbrace{\left.\dfrac{\partial \mathcal{S}_i^{DVBE}}{\partial f_j}\right|_{\left(\overline{f_j^{eq}},\overline{\rho E}\right)}}^{\text{Block I}} f_j' + \overbrace{\left.\dfrac{\partial \mathcal{S}_i^{DVBE}}{\partial(\rho E)}\right|_{\left(\overline{f_j^{eq}},\overline{\rho E}\right)}}^{\text{Block II}} (\rho E)' + O\left(f_j'^2, (\rho E)'^2\right), \\ \dfrac{\partial (\rho E)'}{\partial t} = \underbrace{\left.\dfrac{\partial \mathcal{S}^{En}}{\partial f_j}\right|_{\left(\overline{f_j^{eq}},\overline{\rho E}\right)}}_{\text{Block III}} f_j' + \underbrace{\left.\dfrac{\partial \mathcal{S}^{En}}{\partial(\rho E)}\right|_{\left(\overline{f_j^{eq}},\overline{\rho E}\right)}}_{\text{Block IV}} (\rho E)' + O\left(f_j'^2, (\rho E)'^2\right), \end{cases} . \tag{D.2.1}$$

where the four blocks appear naturally depending on the nature of the fluctuation in factor of the partial derivatives. Once these blocks are gathered, the time advance matrix M_{ij}^{HDVBE} of Fig. 6.9 is obtained. It is worthy to note that M_{ij}^{HDVBE} is essentially composed of constant terms and space derivative operators applied to f_i' and $(\rho E)'$. Once Eq. (6.3.1b) substituted, the derivative operators can be analytically computed in the spectral space changing M_{ij}^{HDVBE} into $\widetilde{\mathrm{M}}_{ij}^{HDVBE}$. This system reads:

$$\omega \widehat{\mathcal{X}}_i = \widetilde{\mathrm{M}}_{ij}^{HDVBE} \widehat{\mathcal{X}}_i, \tag{D.2.2}$$

where $\widehat{\mathcal{X}} = \left(\widehat{f}_0, ..., \widehat{f}_{m-1}, \widehat{\rho E}\right)^T$. Along this section, each blocks of the time advance matrice in the Fourier space $\widetilde{\mathrm{M}}_{ij}^{HDVBE}$ will be detailed.

Block I: $i, j \in [0, m-1]$
The upper left block is similar to the athermal matrix Eq. (D.1.3). The only difference lies in the fact that the Jacobian of the equilibrium distribution function is computed holding ρE constant and is evaluated in $(f_j, \rho E) = \left(\overline{f_j^{eq}}, \overline{\rho E}\right)$. Moreover, for the thermal case the force term also needs to be modified since it includes $E_{2,\alpha\beta}$ Eq. (6.2.3). Now it reads:

$$\Psi_{ij} = w_i \frac{\mathcal{H}_{i,\alpha\alpha}}{2c_s^4} \left(k_\alpha \left.\frac{\partial\left(-a_{\alpha\alpha\alpha}^{eq,(3)}\right)}{\partial f_j}\right|_{\left(\overline{f_j^{eq}},\overline{\rho E}\right)} + \overline{p}\left(\frac{D+2}{D} - \gamma_g\right) k_\gamma \left.\frac{\partial u_\gamma}{\partial f_j}\right|_{\left(\overline{f_j^{eq}},\overline{\rho E}\right)} \right). \tag{D.2.3}$$

Block II: $i \in [0, m-1]$, $j = m$
The upper right block corresponds to a column vector and gather all the energy contri-

bution contained in the LB system. It reads:

$$\widetilde{\mathrm{M}}_{ij}^{HDVBE} = \mathrm{i}\frac{1}{\overline{\tau}}\left(\left.\frac{\partial f_i^{eq}}{\partial \rho E}\right|_{\left(\overline{f_j^{eq}},\overline{\rho E}\right)}\right) - \Psi_{ij}. \tag{D.2.4}$$

with:

$$\Psi_{ij} = w_i \frac{\mathscr{H}_{i,\alpha\alpha}}{2c_s^4}\left(k_\alpha \left.\frac{\partial\left(-a_{\alpha\alpha\alpha}^{eq,(3)}\right)}{\partial \rho E}\right|_{\left(\overline{f_j^{eq}},\overline{\rho E}\right)}\right), \tag{D.2.5}$$

the thermal contribution of the corrective term carried through $E_{1,\alpha\beta}$. It is to be noted that this block is responsible for the perfect gas coupling carried out through the equilibrium distribution function.

Block III: $i = m,\ j \in [0, m-1]$
The lower left block corresponds to a line vector and gathers all the aero contribution contained in the energy system. It reads:

$$\widetilde{\mathrm{M}}_{ij}^{HDVBE} = k_\alpha \overline{\rho E}\left.\frac{\partial u_\alpha}{\partial f_j}\right|_{\left(\overline{f_j^{eq}},\overline{\rho E}\right)} + k_\alpha \left.\frac{\partial u_\alpha p}{\partial f_j}\right|_{\left(\overline{f_j^{eq}},\overline{\rho E}\right)} - \mathrm{i}k_\alpha^2 \lambda \left.\frac{\partial T}{\partial f_j}\right|_{\left(\overline{f_j^{eq}},\overline{\rho E}\right)} - \mathrm{i}\tau \overline{p} k_\alpha^2 \overline{u}_\beta \left.\frac{\partial u_\beta}{\partial f_j}\right|_{\left(\overline{f_j^{eq}},\overline{\rho E}\right)}. \tag{D.2.6}$$

From left to right, one has the convective, the pressure work, the heat diffusion and the viscous heat productions terms. The presence of these terms depends directly on the variable and the formulation of the energy equation used as shown on Fig. 6.9. Finally, the total energy is the only one that linearly contains the viscous heat production term. For other energy variables this term vanish since it contains only second order contributions.

Block IV: $i = m,\ j = m$
Finally, the lower right block corresponds to a scalar involving only the energy system. It reads:

$$\widetilde{\mathrm{M}}_{ij}^{HDVBE} = k_\alpha \overline{u}_\alpha + k_\alpha \left.\frac{\partial u_\alpha p}{\partial \rho E}\right|_{\left(\overline{f_j^{eq}},\overline{\rho E}\right)} - \mathrm{i}k_\alpha^2 \lambda \left.\frac{\partial T}{\partial \rho E}\right|_{\left(\overline{f_j^{eq}},\overline{\rho E}\right)} \tag{D.2.7}$$

and its composition depending on the formulation and energy variables can be found on Fig. 6.9.

D.2.2 HLBM

Following the same procedure as D.2.1, one obtains a linear discrete system. Using Eq. (6.3.10) to express the finite difference operators in the Fourier space, one obtains the HLBM eigenvalue problem which reads:

$$e^{-\mathrm{i}\omega\Delta t}\widehat{\mathcal{X}}_i = \widetilde{\mathrm{M}}_{ij}^{HLBM}\widehat{\mathcal{X}}_i. \tag{D.2.8}$$

Here, $\widehat{\mathcal{X}} = \left(\widehat{g}_0, ..., \widehat{g}_{m-1}, \widehat{\rho E}\right)^T$ and $\widetilde{\mathrm{M}}_{ij}^{HLBM}$ refers to the time advance matrix of the system in the Fourier space. Similarly to it continuous counterpart, this matrix is composed of blocks sketched on Fig. 6.9, which will be detailed along this section.

Block I: $i, j \in [0, m-1]$
The upper left block is very similar to the athermal matrix for both BGK Eq. (D.1.7) and HRR Eq. (D.1.9) collision operators. Nevertheless, some modifications are needed for the thermal matrix. First, the Jacobians must be evaluated in $(f_j, \rho E) = \left(\overline{f_j^{eq}}, \overline{\rho E}\right)$ holding ρE constant. Second, the force term Eq. (D.1.8) must be modified to includes the corrective term $E_{2,\alpha\beta}$ Eq. (6.2.3), and reads:

$$\Psi_{ij} = w_i \frac{\mathcal{H}_{i,\alpha\alpha}}{2c_s^4} \left(\mathcal{K}_\alpha^{\mathrm{D1CO2}} \frac{\partial \left(-a_{\alpha\alpha\alpha}^{eq,(3)}\right)}{\partial g_j}\bigg|_{\left(\overline{f_j^{eq}}, \overline{\rho E}\right)} + \overline{p} \left(\frac{D+2}{D} - \gamma_g \right) \mathcal{K}_\gamma^{\mathrm{D1CO2}} \frac{\partial u_\gamma}{\partial g_j}\bigg|_{\left(\overline{f_j^{eq}}, \overline{\rho E}\right)} \right). \tag{D.2.9}$$

For the expression of the modified wavenumber $\mathcal{K}^{\mathrm{D1CO2}}$ one can relate to D.4. And finally, for the HRR collision operator, the off-equilibrium moments must be corrected accordingly to the traceless viscous stress tensor. They now read:

$$A_{\alpha\beta}^{PR,(2)} = \sum_i \left[\mathcal{H}_{i,\alpha\beta} \left(f_i - f_i^{eq} \right) \right] + \frac{\Delta t}{2} \mathcal{K}_\alpha^{\mathrm{D1CO2}} \left(-a_{\alpha\alpha\alpha}^{eq,(3)} \right) + \overline{p} \left(\frac{D+2}{D} - \gamma_g \right) \mathcal{K}_\gamma^{\mathrm{D1CO2}} u_\gamma, \tag{D.2.10a}$$

$$A_{\alpha\beta}^{FD,(2)} = -\check{\tau}\overline{p} \left(\mathcal{K}_\beta^{\mathrm{D1CO2}} u_\alpha + \mathcal{K}_\alpha^{\mathrm{D1CO2}} u_\beta - \frac{2}{D} \mathcal{K}_\gamma^{\mathrm{D1CO2}} u_\gamma \right), \tag{D.2.10b}$$

where the higher order moment are computed using Eq. (D.1.12).

Block II: $i \in [0, m-1]$, $j = m$
Similarly to its continuous counterpart, the upper right block is responsible for the perfect gas equation of state *via* the equilibrium distribution function. It reads for the BGK collision:

$$\mathrm{BGK}: \quad \widetilde{\mathrm{M}}_{ij}^{LBM} = e^{-\mathrm{i}k_\alpha \Delta x} \left[\frac{\Delta t}{\check{\tau}} \frac{\partial f_i^{eq}}{\partial \rho E}\bigg|_{\left(\overline{f_j^{eq}}, \overline{\rho E}\right)} + \frac{2\check{\tau} - \Delta t}{2\check{\tau}} \Delta t \, \Psi_{ij} \right], \tag{D.2.11}$$

where

$$\Psi_{ij} = w_i \frac{\mathcal{H}_{i,\alpha\alpha}}{2c_s^4} \mathcal{K}_\alpha^{\mathrm{D1CO2}} \frac{\partial \left(-a_{\alpha\alpha\alpha}^{eq,(3)}\right)}{\partial \rho E}\bigg|_{\left(\overline{f_j^{eq}}, \overline{\rho E}\right)}, \tag{D.2.12}$$

refers to as the energy dependence of the corrective term. Finally for the HRR collision operator, this block reads:

$$\mathrm{HRR}: \quad \widetilde{\mathrm{M}}_{ij}^{LBM} = e^{-\mathrm{i}k_\alpha \Delta x} \left[\frac{\partial f_i^{eq}}{\partial \rho E}\bigg|_{\left(\overline{f_j^{eq}}, \overline{\rho E}\right)} + \left(1 - \frac{\Delta t}{\check{\tau}}\right) G_{ij}^{(1)} + \frac{\Delta t}{2} \Psi_{ij} \right], \tag{D.2.13}$$

with

$$G_{ij}^{(1)} = \frac{\partial}{\partial \rho E}\left(w_i \frac{\mathcal{H}_{i,\alpha\beta}}{2c_s^4}\left[\sigma A_{\alpha\beta}^{PR,(2)} + (1-\sigma)\, A_{\alpha\beta}^{FD,(2)}\right] + w_i \frac{1}{6c_s^6}\left[\mathcal{H}_{i,xxy}A_{xxy}^{(3)} + \mathcal{H}_{i,yyx}A_{yyx}^{(3)}\right]\right)\Big|_{\left(\overline{f_j^{eq}},\overline{\rho E}\right)}, \tag{D.2.14}$$

and Ψ_{ij} corresponding to Eq. (D.2.12). A particular attention must be paid on the second order off-equilibrium moments:

$$A_{\alpha\beta}^{PR,(2)} = \sum_i \left[\mathcal{H}_{i,\alpha\beta}\left(f_i - f_i^{eq}\right)\right] + \frac{\Delta t}{2}\mathcal{K}_\alpha^{\mathrm{D1CO2}}\left(-a_{\alpha\alpha\alpha}^{eq,(3)}\right), \tag{D.2.15a}$$

$$A_{\alpha\beta}^{FD,(2)} = 0, \tag{D.2.15b}$$

where the thermal dependence is only present in the projection part. Here again, the higher order moment are computed using Eq. (D.1.12).

Block III: $i = m,\ j \in [0, m-1]$
The lower left block of the discrete matrix is given by:

$$\begin{aligned}\widetilde{\mathrm{M}}_{ij}^{HDVBE} = &-\mathcal{K}_\alpha^{\mathrm{D1CO2}}\overline{\rho E}\frac{\partial u_\alpha}{\partial g_j}\bigg|_{\left(\overline{f_j^{eq}},\overline{\rho E}\right)} - \mathcal{K}_\alpha^{\mathrm{D1CO2}}\frac{\partial u_\alpha p}{\partial g_j}\bigg|_{\left(\overline{f_j^{eq}},\overline{\rho E}\right)} \\ &+ \mathcal{K}_\alpha^{\mathrm{D2CO2}}\lambda\frac{\partial T}{\partial g_j}\bigg|_{\left(\overline{f_j^{eq}},\overline{\rho E}\right)} - \tau\overline{p}\mathcal{K}_\alpha^{\mathrm{D2CO2}}\overline{u}_\beta\frac{\partial u_\beta}{\partial g_j}\bigg|_{\left(\overline{f_j^{eq}},\overline{\rho E}\right)},\end{aligned} \tag{D.2.16}$$

and its composition can be found on Fig. 6.9 according to the energy equation considered. In accordance with the RK1UPO1 and RK4CO2 schemes, the modified wave number in factor of the convective term corresponds either to $\mathcal{K}_\alpha^{D1UPO1}$ or $\mathcal{K}_\alpha^{D1CO2}$. Finally, as only the fluctuations related to the LBM system are considered in this block, the temporal integration of ρE does not affect this block.

Block IV: $i = m,\ j = m$
Finally, the lower right block corresponds to a scalar involving only the energy system. Depending on the temporal integration, two different expressions are obtained:

$$\text{RK1UPO1}: \quad \widetilde{\mathrm{M}}_{ij}^{HLBM} = 1 + z, \tag{D.2.17a}$$

$$\text{RK4CO2}: \quad \widetilde{\mathrm{M}}_{ij}^{HLBM} = 1 + z + \frac{z^2}{2} + \frac{z^3}{3!} + \frac{z^4}{4!}, \tag{D.2.17b}$$

where

$$z = \Delta t\left(-\mathcal{K}_\alpha^{\mathrm{D1CO2}}\overline{u}_\alpha - \mathcal{K}_\alpha^{\mathrm{D1CO2}}\frac{\partial u_\alpha p}{\partial \rho E}\bigg|_{\left(\overline{f_j^{eq}},\overline{\rho E}\right)} + \mathcal{K}_\alpha^{\mathrm{D2CO2}}\lambda\frac{\partial T}{\partial \rho E}\bigg|_{\left(\overline{f_j^{eq}},\overline{\rho E}\right)}\right). \tag{D.2.18}$$

For more details on how to obtain Eq. (D.2.17), one can refers to Sec. 3.5.2. Here again, the modified wave number in factor of the convective term must be chosen accordingly to the RK1UPO1 or RK4CO2 schemes.

D.3 Dispersion relation of the Navier Stokes systems

Here the dispersion relation of the Navier-Stokes system for athermal and thermal cases are derived. In this way, the macroscopic quantities are systematically developed in small perturbations of a base flow:

$$\rho = \overline{\rho} + \rho', \quad u_\alpha = \overline{u}_\alpha + u'_\alpha \quad \text{and} \quad T = \overline{T} + T' \tag{D.3.1}$$

to obtain the linearized equations. Once this linearization is achieved, the perturbations are considered as solution of monochromatic wave:

$$\rho' = \widehat{\rho}\exp\left(\mathrm{i}\left(k_\alpha x_\alpha - \omega t\right)\right), \quad u'_\alpha = \widehat{u_\alpha}\exp\left(\mathrm{i}\left(k_\alpha x_\alpha - \omega t\right)\right) \quad \text{and} \quad T' = \widehat{T}\exp\left(\mathrm{i}\left(k_\alpha x_\alpha - \omega t\right)\right), \tag{D.3.2}$$

where $\widehat{\rho}$, $\widehat{u_\alpha}$ and $\widehat{T}$ are the complexe amplitude of the perturbations. Computing the eigenvalue of the problem gives the dispersion relation of the system.

D.3.1 Athermal equations

Lets consider the athermal Navier-Stokes equations in the following form:

$$\frac{\partial \rho}{\partial t} = -u_\alpha \frac{\partial \rho}{\partial x_\alpha} - \rho \frac{\partial u_\alpha}{\partial x_\alpha} \tag{D.3.3a}$$

$$\frac{\partial u_\alpha}{\partial t} = -u_\beta \frac{\partial u_\alpha}{\partial x_\beta} - c_s^2\theta \frac{\partial \rho}{\partial x_\beta}\delta_{\alpha\beta} + \nu \frac{\partial}{\partial x_\beta}\left(\frac{\partial u_\alpha}{\partial x_\beta} + \frac{\partial u_\beta}{\partial x_\alpha}\right), \tag{D.3.3b}$$

where $\sqrt{c_s^2\theta} = \sqrt{r_g T}$ the newtonian sound speed (with T considered as a constant of the fluid) and $\nu = \mu/\rho$ being the kinematic viscosity. Using Eq. (D.3.1), the linearized system is obtained:

$$\frac{\partial \rho'}{\partial t} = -\overline{u}_\alpha \frac{\partial \rho'}{\partial x_\alpha} - \overline{\rho} \frac{\partial u'_\alpha}{\partial x_\alpha} \tag{D.3.4a}$$

$$\frac{\partial u'_\alpha}{\partial t} = -\overline{u}_\beta \frac{\partial u'_\alpha}{\partial x_\beta} - c_s^2\theta \frac{\partial \rho'}{\partial x_\beta}\delta_{\alpha\beta} + \overline{\nu} \frac{\partial}{\partial x_\beta}\left(\frac{\partial u'_\alpha}{\partial x_\beta} + \frac{\partial u'_\beta}{\partial x_\alpha}\right), \tag{D.3.4b}$$

with $\overline{\nu} = \mu/\overline{\rho}$. Using Eq. (D.3.2), the dispersion relation of the system is obtained and reads:

$$\begin{aligned} \omega\widehat{\rho} &= k_\alpha \overline{u}_\alpha \widehat{\rho} + k_\alpha \overline{\rho}\widehat{u}_\alpha, \\ \omega\widehat{u}_\alpha &= k_\beta \overline{u}_\beta \widehat{u}_\alpha + k_\beta \frac{c_s^2\theta}{\overline{\rho}}\delta_{\alpha\beta}\widehat{\rho} - \mathrm{i}\overline{\nu}k_\beta\left(k_\beta \widehat{u}_\alpha + k_\alpha \widehat{u}_\beta\right). \end{aligned} \tag{D.3.5}$$

Considering a two-dimensional problem, one can define a vector $V_i^{NS} = \left[\widehat{\rho}, \widehat{u}_x, \widehat{u}_y\right]^T$ gathering the complex amplitude of the perturbations and allows to write Eq. (D.3.5) on the form of an eigenvalue problem:

$$\omega V_i^{NS} = \widetilde{M}_{ij}^{NS,ath} V_i^{NS}, \tag{D.3.6}$$

with the matrix:

$$\widetilde{M}_{ij}^{NS,ath} = \begin{pmatrix} k_\alpha \overline{u}_\alpha & k_x \overline{\rho} & k_y \overline{\rho} \\ k_x \dfrac{c_s^2 \theta}{\overline{\rho}} & k_\alpha \overline{u}_\alpha - \mathrm{i}\overline{\nu}\left(k_\alpha^2 + k_x^2\right) & -\mathrm{i}\overline{\nu} k_x k_y \\ k_y \dfrac{c_s^2 \theta}{\overline{\rho}} & -\mathrm{i}\overline{\nu} k_y k_x & k_\alpha \overline{u}_\alpha - \mathrm{i}\overline{\nu}\left(k_\alpha^2 + k_y^2\right) \end{pmatrix} \tag{D.3.7}$$

being the space and time evolution matrix of the athermal Navier-Stokes equations in the Fourier space. Once diagonalized, the system gives three eigenmodes: two acoustic (ω_{ac-}^{ath} upstream and ω_{ac+}^{ath} downstream) and one transverse or shear mode ω_{shear}^{ath}. These modes can be either computed numerically using a linear algebra library such as *numpy* or analytically by expanding the solution in terms of wavenumber k, which gives:

$$\begin{aligned} \omega_{shear} &= k_\alpha \overline{u}_\alpha - \mathrm{i}\nu \left\| k_\alpha \right\|^2 + O\left(k^3\right), \\ \omega_{ac\pm}^{ath} &= k_\alpha \overline{u}_\alpha \pm \left\| k_\alpha \right\| \sqrt{c_s^2 \theta} - \mathrm{i}\nu \left\| k_\alpha \right\|^2 + O\left(k^3\right), \end{aligned} \tag{D.3.8}$$

In this work, the eigen-vectors used for the extended analysis of [63] are computed numerically.

D.3.2 Compressible equations

Lets now consider the compressible Navier-Stokes Fourier equations in the following form:

$$\frac{\partial \rho}{\partial t} = -u_\alpha \frac{\partial \rho}{\partial x_\alpha} - \rho \frac{\partial u_\alpha}{\partial x_\alpha} \tag{D.3.9a}$$

$$\frac{\partial u_\alpha}{\partial t} = -u_\beta \frac{\partial u_\alpha}{\partial x_\beta} - c_s^2 \frac{\partial \rho\theta}{\partial x_\beta}\delta_{\alpha\beta} - \nu \frac{\partial}{\partial x_\beta}\left(\frac{\partial u_\alpha}{\partial x_\beta} + \frac{\partial u_\beta}{\partial x_\alpha} - \frac{2}{D}\frac{\partial u_\gamma}{\partial x_\gamma}\delta_{\alpha\beta}\right) \tag{D.3.9b}$$

$$\frac{\partial T}{\partial t} = -u_\alpha \frac{\partial T}{\partial x_\alpha} - \left(\gamma_g - 1\right) T \frac{\partial u_\alpha}{\partial x_\alpha} + \gamma_g \kappa \frac{\partial^2 T}{\partial x_\alpha^2} + \frac{\nu}{c_v}\frac{\partial u_\alpha}{\partial x_\beta}\left(\frac{\partial u_\alpha}{\partial x_\beta} + \frac{\partial u_\beta}{\partial x_\alpha} - \frac{2}{D}\frac{\partial u_\gamma}{\partial x_\gamma}\delta_{\alpha\beta}\right) \tag{D.3.9c}$$

where $c_s^2 = r_g T_r$, $\theta = T/T_r$, $\nu = \mu/\rho$, $\gamma_g = c_p/c_v$ and $\kappa = \lambda/(\rho c_p)$. It is worth noting that the choice of the energy equation do not have any impact on the solution. Here the work is conducted using the internal energy equation in primitive form and assuming that c_v and r_g are constant. Once Eq. (D.3.1) is replaced, the linearized system is obtained:

$$\frac{\partial \rho'}{\partial t} = -\overline{u}_\alpha \frac{\partial \rho'}{\partial x_\alpha} - \overline{\rho}\frac{\partial u'_\alpha}{\partial x_\alpha} \tag{D.3.10a}$$

$$\frac{\partial u'_\alpha}{\partial t} = -\overline{u}_\beta \frac{\partial u'_\alpha}{\partial x_\beta} - r_g \frac{\partial T'}{\partial x_\beta}\delta_{\alpha\beta} - \frac{r_g \overline{T}}{\overline{\rho}}\frac{\partial T'}{\partial x_\beta}\delta_{\alpha\beta} + \overline{\nu}\frac{\partial}{\partial x_\beta}\left(\frac{\partial u'_\alpha}{\partial x_\beta} + \frac{\partial u'_\beta}{\partial x_\alpha} - \frac{2}{D}\frac{\partial u'_\gamma}{\partial x_\gamma}\delta_{\alpha\beta}\right) \tag{D.3.10b}$$

$$\frac{\partial T'}{\partial t} = -\overline{u}_\alpha \frac{\partial T'}{\partial x_\alpha} - \left(\gamma_g - 1\right)\overline{T}\frac{\partial u'_\alpha}{\partial x_\alpha} + \gamma_g \overline{\kappa}\frac{\partial^2 T'}{\partial x_\alpha^2}, \tag{D.3.10c}$$

with $\overline{\kappa} = \lambda/\overline{\rho}$ the mean heat conductivity. For the sake of clarity, c_s and θ have been replaced by their expressions. It is important to notice that the equation above do not

contain the viscous heat production term in the energy equation. This non-linear term being essentially composed of velocity derivative products vanish once the linearization is conducted. Classically, using Eq. (D.3.2), the dispersion relation of the compressible system is obtained and reads:

$$\begin{aligned}
&\omega\widehat{\rho} = \overline{u}_\alpha k_\alpha \widehat{\rho} + \overline{\rho} k_\alpha \widehat{u}_\alpha, \\
&\omega\widehat{u}_\alpha = \overline{u}_\beta k_\beta \widehat{u}_\alpha + r_g k_\beta \delta_{\alpha\beta} \widehat{T} + \frac{r_g \overline{T}}{\overline{\rho}} k_\beta \delta_{\alpha\beta} \widehat{\rho} - \mathrm{i}\overline{\nu} k_\beta \left(k_\beta \widehat{u}_\alpha + k_\alpha \widehat{u}_\beta - \frac{2}{D} k_\gamma \delta_{\alpha\beta} \widehat{u}_\gamma \right), \\
&\omega\widehat{T} = \overline{u}_\alpha k_\alpha \widehat{T} + (\gamma_g - 1)\,\overline{T} k_\alpha \widehat{u}_\alpha - \mathrm{i}\gamma_g \overline{\kappa} k_\alpha^2 \widehat{T}.
\end{aligned} \tag{D.3.11}$$

Considering a two-dimensional problem, one can define a vector $V_i^{NS} = \left[\widehat{\rho}, \widehat{u}_x, \widehat{u}_y, \widehat{T}\right]^T$ gathering the complex amplitude of the perturbations and allows to write Eq. (D.3.11) on the form of an eigenvalue problem:

$$\omega V_i^{NS} = \widetilde{M}_{ij}^{NS} V_i^{NS}, \tag{D.3.12}$$

with the matrix:

$$\widetilde{M}_{ij}^{NS} = \begin{pmatrix}
\overline{u}_\alpha k_\alpha & \overline{\rho} k_x & \overline{\rho} k_y & 0 \\
\dfrac{r_g \overline{T}}{\overline{\rho}} k_x & \overline{u}_\alpha k_\alpha - \mathrm{i}\overline{\nu}\left(k_\alpha^2 + k_x^2 - \dfrac{2}{D} k_x^2 \right) & -\mathrm{i}\overline{\nu}\left(k_x k_y - \dfrac{2}{D} k_x k_y \right) & r_g k_x \\
\dfrac{r_g \overline{T}}{\overline{\rho}} k_y & -\mathrm{i}\overline{\nu}\left(k_y k_x - \dfrac{2}{D} k_y k_x \right) & \overline{u}_\alpha k_\alpha - \mathrm{i}\overline{\nu}\left(k_\alpha^2 + k_y^2 - \dfrac{2}{D} k_y^2 \right) & r_g k_y \\
0 & (\gamma_g - 1)\,\overline{T} k_x & (\gamma_g - 1)\,\overline{T} k_y & \overline{u}_\alpha k_\alpha - \mathrm{i}\gamma_g \overline{\kappa} k_\alpha^2
\end{pmatrix} \tag{D.3.13}$$

From the zeros present in the matrix above, in the absence of a perfect gaz coupling ($\widetilde{M}_{13}^{NS} = \varnothing$ and $\widetilde{M}_{23}^{NS} = \varnothing$), the thermal feedback of the energy equation would be impossible. Similarly to the athermal case, these modes can be either computed numerically using a linear algebra library such as *numpy* or analytically by expanding the solution in terms of wavenumber k, which gives:

$$\begin{aligned}
\omega_{shear} &= k_\alpha \overline{u}_\alpha - \mathrm{i}\nu \left\| k_\alpha \right\|^2 + O\left(k^3\right), \\
\omega_{entr} &= k_\alpha \overline{u}_\alpha - \mathrm{i}\overline{\kappa} \left\| k_\alpha \right\|^2 + O\left(k^3\right), \\
\omega_{ac\pm} &= k_\alpha \overline{u}_\alpha \pm \left\| k_\alpha \right\| \sqrt{\gamma r_g \overline{T}} - \mathrm{i}\left(\frac{D-1}{D}\nu + \frac{\gamma_g - 1}{2}\kappa \right) \left\| k_\alpha \right\|^2 + O\left(k^3\right),
\end{aligned} \tag{D.3.14}$$

Finally in the specific case of the entropic energy variable, the modulus of eigenvectors are found to be very low and the library *mpmath* [260] allowing an arbitrary-precision floating-point operations is preferred as *numpy*.

D.4 Modified wave number of finite difference schemes

In this section, the spatial finite difference operators in the Fourier space denoted $\mathcal{K}_\alpha^{scheme}$ are presented. Lets consider a second-order centered finite difference scheme of

a quantity ϕ:

$$\text{D1CO2}: \quad \frac{\partial \phi}{\partial x_\alpha} = \frac{\phi_{\boldsymbol{x}+\boldsymbol{e}_\alpha \Delta x} - \phi_{\boldsymbol{x}-\boldsymbol{e}_\alpha \Delta x}}{2\Delta x} + \mathcal{O}\left(\Delta x^2\right). \tag{D.4.1}$$

Once this expression is linearized in the manner of Eq (6.3.1a), and once the small perturbation is expressed using Eq (6.3.1b), one gets:

$$\mathrm{i}k_\alpha \widehat{\phi} e^{\mathrm{i}(k_\alpha x_\alpha - \omega t)} = \frac{e^{\mathrm{i}k_\alpha \Delta x} - e^{-\mathrm{i}k_\alpha \Delta x}}{2\Delta x} \widehat{\phi} e^{\mathrm{i}(k_\alpha x_\alpha - \omega t)} + \mathcal{O}\left(\Delta x^2\right). \tag{D.4.2}$$

On the l.h.s, the exact wave number modeling the space derivative in the Fourier space is $\mathrm{i}k_\alpha$. By identification, the r.h.s of the equation gives the so-called modified wave number of the scheme:

$$\mathcal{K}_\alpha^{D1CO2} = \frac{e^{\mathrm{i}k_\alpha \Delta x} - e^{-\mathrm{i}k_\alpha \Delta x}}{2\Delta x} = \mathrm{i}\frac{\sin\left(k_\alpha \Delta x\right)}{\Delta x}. \tag{D.4.3}$$

This modified wave number characterizes the dispersion and dissipation properties of the scheme. The same manipulation can be done on the other space schemes considered in the LSA study, resulting in:

$$\mathcal{K}_\alpha^{\text{D1UPO1}} = \frac{2\sin^2\left(k_\alpha \Delta x/2\right) + \mathrm{i}\sin\left(k_\alpha \Delta x\right)}{\Delta x}, \tag{D.4.4a}$$

$$\mathcal{K}_\alpha^{\text{D2CO2}} = 2\frac{\cos\left(k_\alpha \Delta x\right) - 1}{\Delta x^2}. \tag{D.4.4b}$$

Bibliography

[1] J. Tyacke, N. Vadlamani, W. Trojak, et al. Turbomachinery simulation challenges and the future. *Progress in Aerospace Sciences*, 110:100554, 2019. 3

[2] T. Kruger, H. Kusumaatmaja, A. Kuzmin, et al. *The Lattice Boltzmann Method: Principles and Practice*. Springer International Publishing, 2017. 11, 16, 18, 22, 25, 26, 41, 42, 48, 99, 100, 115, 131, 199

[3] J. Hardy, Y. Pomeau, and O. De Pazzis. Time evolution of a two-dimensional classical lattice system. *Physical Review Letters*, 31(5):276, 1973. 11, 12

[4] S. Succi and S. Succi. *The lattice Boltzmann equation: for complex states of flowing matter*. Oxford University Press, 2018. 11, 14, 15, 16, 22, 115

[5] U. Frisch, B. Hasslacher, and Y. Pomeau. Lattice-gas automata for the navier-stokes equation. *Physical review letters*, 56(14):1505, 1986. 11

[6] Y.-H. Qian, D. d'Humières, and P. Lallemand. Lattice bgk models for navier-stokes equation. *EPL (Europhysics Letters)*, 17(6):479, 1992. 11, 31, 54, 257

[7] G. R. McNamara and G. Zanetti. Use of the boltzmann equation to simulate lattice-gas automata. *Physical review letters*, 61(20):2332, 1988. 11

[8] F. Higuera, S. Succi, and R. Benzi. Lattice gas dynamics with enhanced collisions. *EPL (Europhysics Letters)*, 9(4):345, 1989. 11

[9] P. L. Bhatnagar, E. P. Gross, and M. Krook. A model for collision processes in gases. i. small amplitude processes in charged and neutral one-component systems. *Physical review*, 94(3):511, 1954. 11, 17, 44

[10] X. He and L.-S. Luo. A priori derivation of the lattice boltzmann equation. *Physical Review E*, 55(6):R6333, 1997. 12

[11] S. Chapman and T. Cowling. The mathematical theory of non-uniform gases, cambridge univ. *Press, Cambridge, England*, 1970. 12, 22, 119

[12] P. J. Dellar. Lattice kinetic schemes for magnetohydrodynamics. *Journal of Computational Physics*, 179(1):95–126, 2002. 12

[13] A. J. Ahrar and M. H. Djavareshkian. Novel hybrid lattice boltzmann technique with tvd characteristics for simulation of heat transfer and entropy generations of mhd and natural convection in a cavity. *Numerical Heat Transfer, Part B: Fundamentals*, 72(6):431–449, 2017. 12, 60, 106

[14] Y. Feng, P. Boivin, J. Jacob, and P. Sagaut. Hybrid recursive regularized lattice boltzmann simulation of humid air with application to meteorological flows. *Physical Review E*, 100(2):023304, 2019. 12, 106, 191

[15] X. Shan and H. Chen. Lattice boltzmann model for simulating flows with multiple phases and components. *Physical review E*, 47(3):1815, 1993. 12

[16] S. Chen and G. D. Doolen. Lattice boltzmann method for fluid flows. *Annual review of fluid mechanics*, 30(1):329–364, 1998. 12

[17] H. Yu, S. S. Girimaji, and L.-S. Luo. Lattice boltzmann simulations of decaying homogeneous isotropic turbulence. *Physical Review E*, 71(1):016708, 2005. 12

[18] P. Sagaut. Toward advanced subgrid models for lattice-boltzmann-based large-eddy simulation: theoretical formulations. *Computers & Mathematics with Applications*, 59(7):2194–2199, 2010. 12

[19] M. Mendoza, B. Boghosian, H. J. Herrmann, and S. Succi. Fast lattice boltzmann solver for relativistic hydrodynamics. *Physical review letters*, 105(1):014502, 2010. 12

[20] S. Succi, E. Foti, and F. Higuera. Three-dimensional flows in complex geometries with the lattice boltzmann method. *EPL (Europhysics Letters)*, 10(5):433, 1989. 12

[21] T. Ye, N. Phan-Thien, and C. T. Lim. Particle-based simulations of red blood cells—a review. *Journal of biomechanics*, 49(11):2255–2266, 2016. 12

[22] S. Li, J. Latt, and B. Chopard. The application of the screen-model based approach for stents in cerebral aneurysms. *Computers & Fluids*, 172:651–660, 2018. 12

[23] P. Lallemand and L.-S. Luo. Theory of the lattice boltzmann method: Dispersion, dissipation, isotropy, galilean invariance, and stability. *Physical Review E*, 61(6):6546, 2000. 12, 26, 44, 45, 54, 188, 228, 230, 252

[24] D. Siebert, L. Hegele Jr, and P. Philippi. Lattice boltzmann equation linear stability analysis: Thermal and athermal models. *Physical Review E*, 77(2):026707, 2008. 12, 28, 44, 54, 189

[25] D. Ricot, S. Marié, P. Sagaut, and C. Bailly. Lattice boltzmann method with selective viscosity filter. *Journal of Computational Physics*, 228(12):4478–4490, 2009. 12

[26] X. Shan and X. He. Discretization of the velocity space in the solution of the boltzmann equation. *Physical Review Letters*, 80(1):65, 1998. 12, 28, 29, 30, 46

[27] D. D'Humières. Generalized Lattice-Boltzmann Equations. *Rarefied Gas Dynamics: Theory and Simulations*, pages 450–458, 1992. 12, 26, 44, 230

[28] I. V. Karlin and S. Succi. Equilibria for discrete kinetic equations. *Physical Review E*, 58(4):R4053, 1998. 12, 46, 230

[29] J. Latt and B. Chopard. Lattice boltzmann method with regularized pre-collision distribution functions. *Mathematics and Computers in Simulation*, 72(2-6):165–168, 2006. 13, 44, 45, 106, 126

[30] F. J. Alexander, S. Chen, and J. Sterling. Lattice boltzmann thermohydrodynamics. *Physical Review E*, 47(4):R2249, 1993. 13, 50, 52, 54, 115

[31] P. Lallemand and L.-S. Luo. Hybrid finite-difference thermal lattice boltzmann equation. *International Journal of Modern Physics B*, 17(01n02):41–47, 2003. 13, 14, 50, 59, 106, 115, 223

[32] X. He, S. Chen, and G. D. Doolen. A novel thermal model for the lattice boltzmann method in incompressible limit. *Journal of Computational Physics*, 146(1):282–300, 1998. 13, 41, 56, 57

[33] Z. Guo and C. Shu. *Lattice Boltzmann method and its applications in engineering*, volume 3. World Scientific, 2013. 14, 15, 27, 33, 48, 49, 52, 115, 131

[34] J. C. Maxwell. Iv. on the dynamical theory of gases. *Philosophical transactions of the Royal Society of London*, (157):49–88, 1867. 15

[35] L. Boltzmann. Weitere studien über das wärmegleichgewicht unter gasmolekülen. In *Kinetische Theorie II*, pages 115–225. Springer, 1970. 15

[36] L. H. Holway Jr. New statistical models for kinetic theory: methods of construction. *The physics of fluids*, 9(9):1658–1673, 1966. 18, 26

[37] C. G. Coreixas. *High-order extension of the recursive regularized lattice Boltzmann method*. PhD thesis, 2018. 19, 25, 110, 118, 126, 128, 143, 181, 183

[38] G. A. Bird and J. Brady. *Molecular gas dynamics and the direct simulation of gas flows*, volume 42. Clarendon press Oxford, 1994. 22, 197

[39] H. Chen, P. Gopalakrishnan, and R. Zhang. Recovery of galilean invariance in thermal lattice boltzmann models for arbitrary prandtl number. *International Journal of Modern Physics C*, 25(10):1450046, 2014. 24

[40] G. Wissocq. *Investigation on the use of lattice Boltzmann methods for turbomachinery secondary air system simulations,* under preparation. PhD thesis, 2019. 25, 109, 118, 137, 197, 203, 206

[41] Q. Li, K. H. Luo, Y. L. He, Y. J. Gao, and W. Q. Tao. Coupling lattice Boltzmann model for simulation of thermal flows on standard lattices. *Physical Review E - Statistical, Nonlinear, and Soft Matter Physics*, 85(1):1–16, 2012. 25, 115, 118, 197

[42] Q. Li, Y. He, Y. Wang, and W. Tao. Coupled double-distribution-function lattice boltzmann method for the compressible navier-stokes equations. *Physical Review E*, 76(5):056705, 2007. 25, 52

[43] Z. Guo, C. Zheng, B. Shi, and T. Zhao. Thermal lattice boltzmann equation for low mach number flows: decoupling model. *Physical Review E*, 75(3):036704, 2007. 25, 56, 57, 89, 90, 94, 95, 96, 97, 106

[44] Q. Li, K. Luo, Y. He, Y. Gao, and W. Tao. Coupling lattice boltzmann model for simulation of thermal flows on standard lattices. *Physical Review E*, 85(1):016710, 2012. 25, 57, 106, 230

[45] E. Shakhov. Generalization of the krook kinetic relaxation equation. *Fluid dynamics*, 3(5):95–96, 1968. 26

[46] E. Shakhov. Approximate kinetic equations in rarefied gas theory. *Fluid Dynamics*, 3(1):112–115, 1968. 26

[47] J. Meng, Y. Zhang, N. G. Hadjiconstantinou, G. A. Radtke, and X. Shan. Lattice ellipsoidal statistical bgk model for thermal non-equilibrium flows. *arXiv preprint arXiv:1209.6548*, 2012. 26

[48] G. R. McNamara, A. L. Garcia, and B. J. Alder. Stabilization of thermal lattice boltzmann models. *Journal of Statistical Physics*, 81(1-2):395–408, 1995. 28, 52

[49] P. C. Philippi, L. A. Hegele Jr, L. O. Dos Santos, and R. Surmas. From the continuous to the lattice boltzmann equation: The discretization problem and thermal models. *Physical Review E*, 73(5):056702, 2006. 28, 34, 36, 39, 230

[50] X. Shan, X.-F. Yuan, and H. Chen. Kinetic theory representation of hydrodynamics: a way beyond the navier–stokes equation. *Journal of Fluid Mechanics*, 550:413–441, 2006. 28, 29, 30, 31, 32, 33, 34, 35, 36, 39, 46, 60, 119, 230

[51] H. Grad. On the kinetic theory of rarefied gases. *Communications on pure and applied mathematics*, 2(4):331–407, 1949. 28, 29, 46

[52] P. Viot. Méthode d'analyse numérique. 2006. 31

[53] X. Shan. The mathematical structure of the lattices of the lattice boltzmann method. *Journal of Computational Science*, 17:475–481, 2016. 31, 32, 33, 34, 35, 36

[54] S. S. Chikatamarla and I. V. Karlin. Lattices for the lattice boltzmann method. *Physical Review E*, 79(4):046701, 2009. 32

[55] I. Karlin and P. Asinari. Factorization symmetry in the lattice Boltzmann method. *Physica A*, 389(8):1530–1548, 2010. 32, 118, 189, 190, 197, 199, 257, 258, 259

[56] C. Sun. Lattice-boltzmann models wfor high speed flows. *Physical review E*, 58(6):7283, 1998. 32, 52

[57] C. Sun. Adaptive lattice boltzmann model for compressible flows: viscous and conductive properties. *Physical review E*, 61(3):2645, 2000. 32, 52

[58] C. Sun. Simulations of compressible flows with strong shocks by an adaptive lattice boltzmann model. *Journal of Computational Physics*, 161(1):70–84, 2000. 32, 52

[59] P. J. Dellar. Nonhydrodynamic modes and a priori construction of shallow water lattice boltzmann equations. *Physical Review E*, 65(3):036309, 2002. 38, 44, 109

[60] Y. Qian and S. Orszag. Lattice bgk models for the navier-stokes equation: Nonlinear deviation in compressible regimes. *EPL (Europhysics Letters)*, 21(3):255, 1993. 38

[61] Y. Chen, H. Ohashi, and M. Akiyama. Thermal lattice bhatnagar-gross-krook model without nonlinear deviations in macrodynamic equations. *Physical Review E*, 50(4):2776, 1994. 38

[62] S. Marié, D. Ricot, and P. Sagaut. Comparison between lattice boltzmann method and navier–stokes high order schemes for computational aeroacoustics. *Journal of Computational Physics*, 228(4):1056–1070, 2009. 38, 188

[63] G. Wissocq, P. Sagaut, and J.-F. Boussuge. An extended spectral analysis of the lattice boltzmann method: modal interactions and stability issues. *Journal of Computational Physics*, 380:311–333, 2019. 38, 44, 107, 109, 110, 118, 189, 191, 195, 197, 200, 203, 208, 219, 228, 229, 269, 277

[64] N. I. Prasianakis and I. V. Karlin. Lattice boltzmann method for thermal flow simulation on standard lattices. *Physical Review E*, 76(1):016702, 2007. 39, 57

[65] O. Malaspinas. Increasing stability and accuracy of the lattice boltzmann scheme: recursivity and regularization. *arXiv preprint arXiv:1505.06900*, 2015. 39, 46, 115, 118, 190, 193

[66] J. Latt, C. Coreixas, J. Beny, and A. Parmigiani. Efficient supersonic flows through high-order guided equilibrium with lattice boltzmann. *arXiv preprint arXiv:1910.13515*, 2019. 39, 58, 164, 177, 184, 230, 245, 247, 249, 250

[67] P. J. Dellar. Bulk and shear viscosities in lattice boltzmann equations. *Physical Review E*, 64(3):031203, 2001. 40, 43, 210

[68] X. He, X. Shan, and G. D. Doolen. Discrete boltzmann equation model for nonideal gases. *Physical Review E*, 57(1):R13, 1998. 40, 41

[69] P. J. Dellar. An interpretation and derivation of the lattice boltzmann method using strang splitting. *Computers & Mathematics with Applications*, 65(2):129–141, 2013. 41

[70] S. Ubertini, P. Asinari, and S. Succi. Three ways to lattice boltzmann: a unified time-marching picture. *Physical Review E*, 81(1):016311, 2010. 42, 43

[71] P. Lallemand and L.-S. Luo. Theory of the lattice boltzmann method: Acoustic and thermal properties in two and three dimensions. *Physical review E*, 68(3):036706, 2003. 44, 60, 88, 106, 109, 223

[72] G. Wissocq, C. Coreixas, and J.-F. Boussuge. Linear stability and isotropy properties of athermal regularized lattice boltzmann methods. *Physical Review E*, 102(5):053305, 2020. 44, 45, 109, 118, 200, 203, 214, 269

[73] I. V. Karlin, F. Bösch, and S. Chikatamarla. Gibbs' principle for the lattice-kinetic theory of fluid dynamics. *Physical Review E*, 90(3):031302, 2014. 44, 47, 230

[74] B. Dorschner, S. S. Chikatamarla, and I. V. Karlin. Transitional flows with the entropic lattice boltzmann method. *Journal of Fluid Mechanics*, 824:388–412, 2017. 44, 47

[75] N. Frapolli, S. S. Chikatamarla, and I. V. Karlin. Entropic lattice boltzmann simulation of thermal convective turbulence. *Computers & Fluids*, 175:2–19, 2018. 44, 47

[76] D. d'Humieres. Multiple–relaxation–time lattice boltzmann models in three dimensions. *Philosophical Transactions of the Royal Society of London. Series A: Mathematical, Physical and Engineering Sciences*, 360(1792):437–451, 2002. 44, 45

[77] X. Shan and H. Chen. A general multiple-relaxation-time boltzmann collision model. *International Journal of Modern Physics C*, 18(04):635–643, 2007. 45, 132

[78] M. Geier, A. Greiner, and J. G. Korvink. Cascaded digital lattice boltzmann automata for high reynolds number flow. *Physical Review E*, 73(6):066705, 2006. 45

[79] M. Geier, M. Schönherr, A. Pasquali, and M. Krafczyk. The cumulant lattice boltzmann equation in three dimensions: Theory and validation. *Computers & Mathematics with Applications*, 70(4):507–547, 2015. 45

[80] I. Ginzburg, F. Verhaeghe, and D. d'Humieres. Two-relaxation-time lattice boltzmann scheme: About parametrization, velocity, pressure and mixed boundary conditions. *Communications in computational physics*, 3(2):427–478, 2008. 45

[81] I. Ginzburg, F. Verhaeghe, and D. d'Humieres. Study of simple hydrodynamic solutions with the two-relaxation-times lattice boltzmann scheme. *Communications in computational physics*, 3(3):519–581, 2008. 45

[82] C. Coreixas, B. Chopard, and J. Latt. Comprehensive comparison of collision models in the lattice boltzmann framework: Theoretical investigations. *Physical Review E*, 100(3):033305, 2019. 45, 46

[83] H. Xu and P. Sagaut. Optimal low-dispersion low-dissipation lbm schemes for computational aeroacoustics. *Journal of Computational Physics*, 230(13):5353–5382, 2011. 45, 188, 228, 252

[84] M. Chávez-Modena, E. Ferrer, and G. Rubio. Improving the stability of multiple-relaxation lattice boltzmann methods with central moments. *Computers & Fluids*, 172:397–409, 2018. 45, 188, 228, 252

[85] P. Skordos. Initial and boundary conditions for the lattice boltzmann method. *Physical Review E*, 48(6):4823, 1993. 45, 48, 50

[86] J. Latt and B. Chopard. Lattice Boltzmann method with regularized pre-collision distribution functions. 72:165–168, 2006. 46, 127

[87] C. Coreixas, G. Wissocq, G. Puigt, J. F. Boussuge, and P. Sagaut. Recursive regularization step for high-order lattice Boltzmann methods. *Physical Review E*, 96(3), 2017. 46, 55, 61, 106, 115, 118, 128, 164, 193, 230

[88] J. Jacob, O. Malaspinas, and P. Sagaut. A new hybrid recursive regularised bhatnagar–gross–krook collision model for lattice boltzmann method-based large eddy simulation. *Journal of Turbulence*, 19(11):1051–1076, 2018. 46, 111, 115, 123, 125, 152, 189, 201, 228, 232, 233

[89] I. V. Karlin, A. Ferrante, and H. C. Öttinger. Perfect entropy functions of the lattice boltzmann method. *EPL (Europhysics Letters)*, 47(2):182, 1999. 46

[90] B. M. Boghosian, J. Yepez, P. V. Coveney, and A. Wager. Entropic lattice boltzmann methods. *Proceedings of the Royal Society of London. Series A: Mathematical, Physical and Engineering Sciences*, 457(2007):717–766, 2001. 46, 47, 230

[91] S. Ansumali, I. V. Karlin, and H. C. Öttinger. Minimal entropic kinetic models for hydrodynamics. *EPL (Europhysics Letters)*, 63(6):798, 2003. 46, 230

[92] N. Frapolli, S. S. Chikatamarla, and I. V. Karlin. Entropic lattice boltzmann model for compressible flows. *Physical Review E*, 92(6):061301, 2015. 46, 57, 58, 230

[93] S. Ansumali and I. V. Karlin. Single relaxation time model for entropic lattice boltzmann methods. *Physical Review E*, 65(5):056312, 2002. 46

[94] B. M. Boghosian, P. J. Love, P. V. Coveney, et al. Galilean-invariant lattice-boltzmann models with h theorem. *Physical Review E*, 68(2):025103, 2003. 46

[95] S. Chikatamarla, S. Ansumali, and I. V. Karlin. Entropic lattice boltzmann models for hydrodynamics in three dimensions. *Physical review letters*, 97(1):010201, 2006. 46, 47

[96] N. Frapolli, S. Chikatamarla, and I. Karlin. Multispeed entropic lattice boltzmann model for thermal flows. *Physical Review E*, 90(4):043306, 2014. 46, 55, 57, 58, 61

[97] S. Ansumali, S. S. Chikatamarla, C. E. Frouzakis, and K. Boulouchos. Entropic lattice boltzmann simulation of the flow past square cylinder. *International Journal of Modern Physics C*, 15(03):435–445, 2004. 47

[98] X. He, Q. Zou, L.-S. Luo, and M. Dembo. Analytic solutions of simple flows and analysis of nonslip boundary conditions for the lattice boltzmann bgk model. *Journal of Statistical Physics*, 87(1-2):115–136, 1997. 49

[99] M. Bouzidi, M. Firdaouss, and P. Lallemand. Momentum transfer of a boltzmann-lattice fluid with boundaries. *Physics of fluids*, 13(11):3452–3459, 2001. 49

[100] D. Yu, R. Mei, and W. Shyy. A unified boundary treatment in lattice boltzmann method. In *41st aerospace sciences meeting and exhibit*, page 953, 2003. 49

[101] Q. Zou and X. He. On pressure and velocity boundary conditions for the lattice boltzmann bgk model. *Physics of fluids*, 9(6):1591–1598, 1997. 49

[102] J. Latt, B. Chopard, O. Malaspinas, M. Deville, and A. Michler. Straight velocity boundaries in the lattice boltzmann method. *Physical Review E*, 77(5):056703, 2008. 49, 50

[103] Z. Guo, B. Shi, and C. Zheng. A coupled lattice bgk model for the boussinesq equations. *International Journal for Numerical Methods in Fluids*, 39(4):325–342, 2002. 50, 56, 94, 95, 97, 106

[104] G. Wissocq, N. Gourdain, O. Malaspinas, and A. Eyssartier. Regularized characteristic boundary conditions for the lattice-boltzmann methods at high reynolds number flows. *Journal of Computational Physics*, 331:1–18, 2017. 50

[105] T. J. Poinsot and S. Lelef. Boundary conditions for direct simulations of compressible viscous flows. *Journal of computational physics*, 101(1):104–129, 1992. 50

[106] O. Filippova and D. Hänel. Grid refinement for lattice-bgk models. *Journal of Computational physics*, 147(1):219–228, 1998. 50

[107] X. Shan. Simulation of rayleigh-bénard convection using a lattice boltzmann method. *Physical review E*, 55(3):2780, 1997. 50, 56

[108] K. Xu. A gas-kinetic bgk scheme for the navier–stokes equations and its connection with artificial dissipation and godunov method. *Journal of Computational Physics*, 171(1):289–335, 2001. 51

[109] L. Pan and K. Xu. A compact third-order gas-kinetic scheme for compressible euler and navier-stokes equations. *arXiv preprint arXiv:1412.4489*, 2014. 51

[110] K. Xu. *Direct modeling for computational fluid dynamics: construction and application of unified gas-kinetic schemes*. World Scientific, 2015. 51

[111] S. Lenz, M. Krafczyk, M. Geier, S. Chen, and Z. Guo. Validation of a two-dimensional gas-kinetic scheme for compressible natural convection on structured and unstructured meshes. *International Journal of Thermal Sciences*, 136:299–315, 2019. 51

[112] K. Xu and J.-C. Huang. A unified gas-kinetic scheme for continuum and rarefied flows. *Journal of Computational Physics*, 229(20):7747–7764, 2010. 51

[113] J.-C. Huang, K. Xu, and P. Yu. A unified gas-kinetic scheme for continuum and rarefied flows ii: multi-dimensional cases. *Communications in Computational Physics*, 12(3):662–690, 2012. 51

[114] Z. Guo, K. Xu, and R. Wang. Discrete unified gas kinetic scheme for all knudsen number flows: Low-speed isothermal case. *Physical Review E*, 88(3):033305, 2013. 52

[115] Z. Guo, R. Wang, and K. Xu. Discrete unified gas kinetic scheme for all knudsen number flows. ii. thermal compressible case. *Physical Review E*, 91(3):033313, 2015. 52

[116] L. M. Yang, C. Shu, and J. Wu. A moment conservation-based non-free parameter compressible lattice Boltzmann model and its application for flux evaluation at cell interface. *Computers and Fluids*, 79:190–199, 2013. 52

[117] Y. Wang, L. Yang, and C. Shu. From lattice boltzmann method to lattice boltzmann flux solver. *Entropy*, 17(11):7713–7735, 2015. 52

[118] P. Pavlo, G. Vahala, and L. Vahala. Higher order isotropic velocity grids in lattice methods. *Physical Review Letters*, 80(18):3960, 1998. 52

[119] G. R. McNamara, A. L. Garcia, and B. J. Alder. A hydrodynamically correct thermal lattice boltzmann model. *Journal of Statistical Physics*, 87(5-6):1111–1121, 1997. 52

[120] R. Mei and W. Shyy. On the finite difference-based lattice boltzmann method in curvilinear coordinates. *Journal of Computational Physics*, 143(2):426–448, 1998. 52

[121] H. Xi, G. Peng, and S.-H. Chou. Finite-volume lattice boltzmann method. *Physical Review E*, 59(5):6202, 1999. 52

[122] M. Watari and M. Tsutahara. Two-dimensional thermal model of the finite-difference lattice boltzmann method with high spatial isotropy. *Physical Review E*, 67(3):036306, 2003. 52

[123] T. Kataoka and M. Tsutahara. Lattice boltzmann model for the compressible navier-stokes equations with flexible specific-heat ratio. *Physical review E*, 69(3):035701, 2004. 52

[124] P. J. Dellar. Two routes from the boltzmann equation to compressible flow of polyatomic gases. *Progress in Computational Fluid Dynamics, an International Journal*, 8(1-4):84–96, 2008. 52

[125] G. Strang. On the construction and comparison of difference schemes. *SIAM journal on numerical analysis*, 5(3):506–517, 1968. 53

[126] F. Chen, A. Xu, G. Zhang, Y. Li, and S. Succi. Multiple-relaxation-time lattice boltzmann approach to compressible flows with flexible specific-heat ratio and prandtl number. *EPL (Europhysics Letters)*, 90(5):54003, 2010. 53

[127] F. Chen, A. Xu, G. Zhang, and Y. Li. Multiple-relaxation-time lattice boltzmann model for compressible fluids. *Physics Letters A*, 375(21):2129–2139, 2011. 53

[128] Y.-L. He, Q. Liu, and Q. Li. Three-dimensional finite-difference lattice boltzmann model and its application to inviscid compressible flows with shock waves. *Physica A: Statistical Mechanics and its Applications*, 392(20):4884–4896, 2013. 53

[129] K. Li and C. Zhong. A lattice boltzmann model for simulation of compressible flows. *International Journal for Numerical Methods in Fluids*, 77(6):334–357, 2015. 53

[130] L. Kai and Z. Cheng-Wen. A multiple-relaxation-time lattice boltzmann method for high-speed compressible flows. *Chinese Physics B*, 24(5):050501, 2015. 53

[131] F. J. Alexander, H. Chen, S. Chen, and G. D. Doolen. Lattice Boltzmann model for compressible fluids. *Physical Review A*, 46(4):1967–1970, 1992. 53, 54

[132] Y. Chen, H. Ohashi, and M. Akiyama. Two-parameter thermal lattice bgk model with a controllable prandtl number. *Journal of scientific computing*, 12(2):169–185, 1997. 54

[133] Y. Guangwu, C. Yaosong, and H. Shouxin. Simple lattice boltzmann model for simulating flows with shock wave. *Physical review E*, 59(1):454, 1999. 54

[134] Y. Chen, H. Ohashi, and M. Akiyama. Heat transfer in lattice bgk modeled fluid. *Journal of Statistical Physics*, 81(1-2):71–85, 1995. 54

[135] G. A. Sod. A survey of several finite difference methods for systems of nonlinear hyperbolic conservation laws. *Journal of computational physics*, 27(1):1–31, 1978. 54, 177

[136] P. D. Lax. Weak solutions of nonlinear hyperbolic equations and their numerical computation. *Communications on pure and applied mathematics*, 7(1):159–193, 1954. 54

[137] H. Yu and K. Zhao. Lattice boltzmann method for compressible flows with high mach numbers. *Physical Review E*, 61(4):3867, 2000. 54, 60

[138] K. K. Mattila, P. C. Philippi, and L. A. Hegele. High-order regularization in lattice-Boltzmann equations. *Physics of Fluids*, 29(4), 2017. 55, 61

[139] Z. Guo, B. Shi, and N. Wang. Lattice bgk model for incompressible navier–stokes equation. *Journal of Computational Physics*, 165(1):288–306, 2000. 56

[140] V. Rykov. A model kinetic equation for a gas with rotational degrees of freedom. *Fluid Dynamics*, 10(6):959–966, 1975. 57

[141] M. H. Saadat, F. Bösch, and I. V. Karlin. Lattice boltzmann model for compressible flows on standard lattices: Variable prandtl number and adiabatic exponent. *Physical Review E*, 99(1):013306, 2019. 58, 230

[142] N. Frapolli, S. S. Chikatamarla, and I. V. Karlin. Lattice kinetic theory in a comoving galilean reference frame. *Physical review letters*, 117(1):010604, 2016. 58

[143] O. Filippova and D. Hänel. Lattice-bgk model for low mach number combustion. *International Journal of Modern Physics C*, 9(08):1439–1445, 1998. 59

[144] O. Filippova and D. Hänel. A novel lattice bgk approach for low mach number combustion. *Journal of Computational Physics*, 158(2):139–160, 2000. 59

[145] A. Mezrhab, M. Bouzidi, and P. Lallemand. Hybrid lattice-boltzmann finite-difference simulation of convective flows. *Computers & Fluids*, 33(4):623–641, 2004. 60

[146] A. Mezrhab, M. Jami, M. Bouzidi, and P. Lallemand. Analysis of radiation–natural convection in a divided enclosure using the lattice boltzmann method. *Computers & Fluids*, 36(2):423–434, 2007. 60

[147] C. Van Treeck, E. Rank, M. Krafczyk, J. Tölke, and B. Nachtwey. Extension of a hybrid thermal lbe scheme for large-eddy simulations of turbulent convective flows. *Computers & Fluids*, 35(8-9):863–871, 2006. 60, 106

[148] F. Verhaeghe, B. Blanpain, and P. Wollants. Lattice boltzmann method for double-diffusive natural convection. *Physical Review E*, 75(4):046705, 2007. 60

[149] S. Bettaibi, F. Kuznik, and E. Sediki. Hybrid lattice boltzmann finite difference simulation of mixed convection flows in a lid-driven square cavity. *Physics Letters A*, 378(32-33):2429–2435, 2014. 60, 106

[150] X. Nie, X. Shan, and H. Chen. Lattice-Boltzmann/ Finite-Difference Hybrid Simulation of Transonic Flow. *47 th AIAA Aerospace Sciences Meeting*, (January):2009, 2009. 60, 61, 62, 106, 107, 143, 144, 148, 184, 185, 228, 229, 261

[151] H. Fan, R. Zhang, and H. Chen. Extended volumetric scheme for lattice boltzmann models. *Physical Review E*, 73(6):066708, 2006. 60, 106

[152] Y. Li, H. Fan, X. Nie, et al. Application of a higher order lattice boltzmann/hybrid method for simulation of compressible viscous flows with curved boundary. In *47th AIAA Aerospace Sciences Meeting including The New Horizons Forum and Aerospace Exposition*, page 1336, 2009. 60, 106

[153] E. Fares, M. Wessels, R. Zhang, et al. Validation of a lattice-boltzmann approach for transonic and supersonic flow simulations. In *52nd Aerospace Sciences Meeting*, page 0952, 2014. 60, 61, 62, 106, 185

[154] P.-T. Lew, P. Gopalakrishnan, D. Casalino, et al. An extended lattice boltzmann methodology for high subsonic jet noise prediction. In *20th AIAA/CEAS Aeroacoustics Conference*, page 2755, 2014. 60, 61, 62

[155] H. Chen, R. Zhang, and P. Gopalakrishnan. Lattice Boltzmann Collision Operators Enforcing Isotropy and Galilean Invariance. *Patent*, US20150356217A1, 2013. 60

[156] P. Gopalakrishnan, R. Zhang, and H. Chen. Temperature coupling algorithm for hybrid thermal lattice boltzmann method, 2016. US Patent App. 14/909,055. 60, 100

[157] P. Gopalakrishnan, R. Zhang, and H. Chen. Lattice Boltzmann Based Solver for High Speed Flows. *Patent*, 19158256.8, 2019. 60

[158] D. Casalino, A. Hazir, and A. Mann. Turbofan broadband noise prediction using the lattice boltzmann method. *AIAA Journal*, pages 609–628, 2018. 61

[159] S. Mancini, A. Kolb, I. Gonzalez-Martino, and D. Casalino. Very-large eddy simulations of the m219 cavity at high-subsonic and supersonic conditions. In *AIAA Scitech 2019 Forum*, page 1833, 2019. 61, 185

[160] D. Singh, A. F. Ribeiro, B. Konig, and E. Fares. Lattice boltzmann simulations of a supersonic cavity. In *35th AIAA Applied Aerodynamics Conference*, page 4461, 2017. 61

[161] M. L. Nickerson, R. Ferris, and W. C. P. van der Velden. Simulations of chevrons on single flow hot jets. In *AIAA Scitech 2019 Forum*, page 1837, 2019. 61

[162] Dassault Systèmes. PowerFLOW – CFD Software Solution for Aerodynamic Design. https://www.3ds.com/products-services/simulia/products/powerflow/. [Online; accessed 10-December-2020]. 61, 62

[163] N. Frapolli, S. S. Chikatamarla, and I. V. Karlin. Entropic lattice Boltzmann model for compressible flows. *Physical Review E - Statistical, Nonlinear, and Soft Matter Physics*, 92(6):1–5, 2015. 61, 62

[164] N. Frapolli, S. S. Chikatamarla, and I. V. Karlin. Entropic lattice boltzmann model for gas dynamics: Theory, boundary conditions, and implementation. *Physical Review E*, 93(6):063302, 2016. 61, 62, 177

[165] S. Noelting and E. Fares. The lattice-boltzmann method: an alternative to les for complex aerodynamic and aeroacoustic simulations in the aerospace industry. Technical report, SAE Technical Paper, 2015. 62

[166] C. Hirsch. *Numerical computation of internal and external flows: The fundamentals of computational fluid dynamics*. Elsevier, 2007. 67, 70, 73, 75, 79, 80, 82, 84, 85, 164, 177, 199, 235

[167] J. C. Butcher and N. Goodwin. *Numerical methods for ordinary differential equations*, volume 2. Wiley Online Library, 2008. 68, 79, 80, 81

[168] E. Toro. Primitive, conservative and adaptive schemes for hyperbolic conservation laws. In *Numerical methods for wave propagation*, pages 323–385. Springer, 1998. 73, 164

[169] E. Toro and A. Siviglia. Price: primitive centred schemes for hyperbolic systems. *International Journal for Numerical Methods in Fluids*, 42(12):1263–1291, 2003. 73

[170] R. Courant, K. Friedrichs, and H. Lewy. Über die partiellen differenzengleichungen der mathematischen physik. *Mathematische annalen*, 100(1):32–74, 1928. 84, 199

[171] P. Lax. Systems of conservation laws. Technical report, LOS ALAMOS NATIONAL LAB NM, 1959. 84

[172] C. W. Hirt. Heuristic stability theory for finite-difference equations. *Journal of Computational Physics*, 2(4):339–355, 1968. 85

[173] R. Warming and B. Hyett. The modified equation approach to the stability and accuracy analysis of finite-difference methods. *Journal of computational physics*, 14(2):159–179, 1974. 85

[174] J. VonNeumann and R. D. Richtmyer. A method for the numerical calculation of hydrodynamic shocks. *Journal of applied physics*, 21(3):232–237, 1950. 85, 188, 194

[175] A. Mohamad and A. Kuzmin. A critical evaluation of force term in lattice boltzmann method, natural convection problem. *International Journal of Heat and Mass Transfer*, 53(5-6):990–996, 2010. 90

[176] Z. Guo, C. Zheng, and B. Shi. Discrete lattice effects on the forcing term in the lattice boltzmann method. *Physical review E*, 65(4):046308, 2002. 90, 100

[177] M. Hortmann, M. Perić, and G. Scheuerer. Finite volume multigrid prediction of laminar natural convection: bench-mark solutions. *International journal for numerical methods in fluids*, 11(2):189–207, 1990. 94, 95, 96, 97

[178] T. Lee and C.-L. Lin. A stable discretization of the lattice boltzmann equation for simulation of incompressible two-phase flows at high density ratio. *Journal of Computational Physics*, 206(1):16–47, 2005. 100

[179] A. Wagner and Q. Li. Investigation of galilean invariance of multi-phase lattice boltzmann methods. *Physica A: Statistical Mechanics and its Applications*, 362(1):105–110, 2006. 100

[180] Y.-L. Feng, S.-L. Guo, W.-Q. Tao, and P. Sagaut. Regularized thermal lattice boltzmann method for natural convection with large temperature differences. *International Journal of Heat and Mass Transfer*, 125:1379–1391, 2018. 101, 126, 127, 217, 228, 229

[181] Y.-H. Qian. Fractional propagation and the elimination of staggered invariants in lattice-bgk models. *International journal of modern physics C*, 8(04):753–761, 1997. 106

[182] H. Chen. Volumetric formulation of the lattice boltzmann method for fluid dynamics: Basic concept. *Physical Review E*, 58(3):3955, 1998. 106

[183] R. Zhang, H. Chen, Y. H. Qian, and S. Chen. Effective volumetric lattice boltzmann scheme. *Physical review E*, 63(5):056705, 2001. 106

[184] I. Karlin, D. Sichau, and S. Chikatamarla. Consistent two-population lattice boltzmann model for thermal flows. *Physical Review E*, 88(6):063310, 2013. 106

[185] P.-A. Masset and G. Wissocq. Linear hydrodynamics and stability of the discrete velocity boltzmann equations. *Journal of Fluid Mechanics*, 897, 2020. 107, 197, 199

[186] C. Coreixas, G. Wissocq, B. Chopard, and J. Latt. Impact of collision models on the physical properties and the stability of lattice boltzmann methods. *arXiv preprint arXiv:2002.05265*, 2020. 108

[187] Y. Feng, P. Boivin, J. Jacob, and P. Sagaut. Hybrid recursive regularized thermal lattice Boltzmann model for high subsonic compressible flows. *Journal of Computational Physics*, 394:82 – 99, 2019. 111, 115, 116, 119, 123, 125, 127, 128, 131, 132, 133, 135, 137, 138, 139, 141, 145, 152, 189, 194, 221, 228, 229, 241, 267

[188] A. Sengissen, J.-C. Giret, C. Coreixas, and J.-F. Boussuge. Simulations of lagoon landing-gear noise using lattice boltzmann solver. In *21st AIAA/CEAS Aeroacoustics Conference*, page 2993, 2015. 115

[189] M. R. Khorrami and E. Fares. Toward noise certification during design: airframe noise simulations for full-scale, complete aircraft. *CEAS Aeronautical Journal*, 10(1):31–67, 2019. 115

[190] P. J. Dellar. Lattice boltzmann algorithms without cubic defects in galilean invariance on standard lattices. *Journal of Computational Physics*, 259:270–283, 2014. 115

[191] X. Shan et al. Central-moment-based galilean-invariant multiple-relaxation-time collision model. *Physical Review E*, 100(4):043308, 2019. 115

[192] Y. Feng, M. Tayyab, and P. Boivin. A Lattice-Boltzmann model for low-Mach reactive flows. *Combustion and Flame*, 196:249–254, 2018. 124, 217, 229

[193] T. Astoul, G. Wissocq, J.-f. Boussuge, A. Sengissen, and P. Sagaut. Analysis and reduction of spurious noise generated at grid refinement interfaces with the lattice Boltzmann method. *Submitted*, 2019. 126, 188, 228, 269, 271

[194] M. H. Saadat, F. Bösch, and I. V. Karlin. Lattice Boltzmann model for compressible flows on standard lattices : Variable Prandtl number and adiabatic exponent Lattice Boltzmann model for compressible flows on standard lattices : Variable Prandtl number and adiabatic exponent. *Physical Review E*, 99(1):13306, 2019. 132, 133, 221

[195] B. B.-t. Chu and L. S. G. Kovasznay. Non-linear interactions in a viscous heat-conducting compressible gas. 1957. 132

[196] N. Frapolli, S. S. Chikatamarla, and I. V. Karlin. Lattice Kinetic Theory in a Comoving Galilean Reference Frame. *Physical Review Letters*, 117(1):1–4, 2016. 133, 221

[197] C. K. Tam and J. C. Webb. Dispersion-relation-preserving finite difference schemes for computational acoustics. *Journal of computational physics*, 107(2):262–281, 1993. 141

[198] E. F. Toro. *Riemann solvers and numerical methods for fluid dynamics: a practical introduction*. Springer Science & Business Media, 2013. 143, 144, 166, 167, 168

[199] E. F. Toro and C. Street. PRIMITIVE , CONSERVATIVE AND ADAPTIVE SCHEMES FOR HYPERBOLIC CONSERVATION LAWS. pages 323–385, 1965. 143, 165

[200] O. Inoue and Y. Hattori. Sound generation by shock–vortex interactions. *Journal of Fluid Mechanics*, 380:81–116, 1999. 144, 145, 146, 147, 238, 240

[201] P. D. Lax and X.-D. Liu. Solution of two-dimensional riemann problems of gas dynamics by positive schemes. *SIAM Journal on Scientific Computing*, 19(2):319–340, 1998. 156, 157

[202] C. W. Schulz-Rinne, J. P. Collins, and H. M. Glaz. Numerical solution of the riemann problem for two-dimensional gas dynamics. *SIAM Journal on Scientific Computing*, 14(6):1394–1414, 1993. 156, 157

[203] A. Kurganov and E. Tadmor. Solution of two-dimensional riemann problems for gas dynamics without riemann problem solvers. *Numerical Methods for Partial Differential Equations: An International Journal*, 18(5):584–608, 2002. 156

[204] R. Liska and B. Wendroff. Comparison of several difference schemes on 1d and 2d test problems for the euler equations. *SIAM Journal on Scientific Computing*, 25(3):995–1017, 2003. 156, 157, 158, 172

[205] D. Wilde, A. Krämer, K. Küllmer, H. Foysi, and D. Reith. Multistep lattice boltzmann methods: Theory and applications. *International Journal for Numerical Methods in Fluids*, 90(3):156–169, 2019. 157, 197

[206] P. Clavin and G. Searby. *Combustion waves and fronts in flows: flames, shocks, detonations, ablation fronts and explosion of stars*. Cambridge University Press, 2016. 161

[207] S. Pirozzoli. Numerical methods for high-speed flows. *Annual review of fluid mechanics*, 43:163–194, 2011. 164, 177, 178

[208] T. Y. Hou and P. G. LeFloch. Why nonconservative schemes converge to wrong solutions: error analysis. *Mathematics of computation*, 62(206):497–530, 1994. 164, 184

[209] S. Karni. Viscous shock profiles and primitive formulations. *SIAM Journal on Numerical Analysis*, 29(6):1592–1609, 1992. 164, 184

[210] E. F. Toro, M. Spruce, and W. Speares. Restoration of the contact surface in the hll-riemann solver. *Shock waves*, 4(1):25–34, 1994. 165

[211] A. Harten, P. D. Lax, and B. v. Leer. On upstream differencing and godunov-type schemes for hyperbolic conservation laws. *SIAM review*, 25(1):35–61, 1983. 165

[212] Z. J. Wang, K. Fidkowski, R. Abgrall, et al. High-order cfd methods: current status and perspective. *International Journal for Numerical Methods in Fluids*, 72(8):811–845, 2013. 172, 221

[213] V. Weirs, G. Candler, V. Weirs, and G. Candler. Optimization of weighted eno schemes for dns of compressible turbulence. In *13th Computational Fluid Dynamics Conference*, page 1940, 1997. 177

[214] M. D. Salas and A. Iollo. Entropy jump across an inviscid shock wave. *Theoretical and computational fluid dynamics*, 8(5):365–375, 1996. 178, 185

[215] M. Hafez and W. Guo. Some anomalies of numerical simulation of shock waves. part ii: effect of artificial and real viscosity. *Computers & fluids*, 28(4-5):721–739, 1999. 178

[216] R. S. Baty, F. Farassat, and J. A. Hargreaves. Nonstandard analysis and shock wave jump conditions in a one-dimensional compressible gas. Technical report, Los Alamos National Laboratory (LANL), Los Alamos, NM, 2007. 178

[217] E. Garnier, M. Mossi, P. Sagaut, P. Comte, and M. Deville. On the use of shock-capturing schemes for large-eddy simulation. *Journal of computational Physics*, 153(2):273–311, 1999. 181, 183

[218] A. Jameson, W. Schmidt, and E. Turkel. Numerical solution of the euler equations by finite volume methods using runge kutta time stepping schemes. In *14th fluid and plasma dynamics conference*, page 1259, 1981. 181, 183

[219] D. Modesti and S. Pirozzoli. An efficient semi-implicit solver for direct numerical simulation of compressible flows at all speeds. *Journal of Scientific Computing*, 75(1):308–331, 2018. 185, 263

[220] A. E. Honein and P. Moin. Higher entropy conservation and numerical stability of compressible turbulence simulations. *Journal of Computational Physics*, 201(2):531–545, 2004. 185, 206, 263

[221] J. D. Sterling and S. Chen. Stability analysis of lattice boltzmann methods. *Journal of Computational Physics*, 123(1):196–206, 1996. 188, 194, 196

[222] I. Ginzburg, D. d'Humières, and A. Kuzmin. Optimal stability of advection-diffusion lattice boltzmann models with two relaxation times for positive/negative equilibrium. *Journal of Statistical Physics*, 139(6):1090–1143, 2010. 188, 230

[223] S. A. Hosseini, C. Coreixas, N. Darabiha, and D. Thévenin. Stability of the lattice kinetic scheme and choice of the free relaxation parameter. *Physical Review E*, 99(6):063305, 2019. 188, 197

[224] S. Hosseini, N. Darabiha, and D. Thévenin. Compressibility in lattice boltzmann on standard stencils: effects of deviation from reference temperature. 2019. 188

[225] F. Renard, Y. Feng, J.-F. Boussuge, and P. Sagaut. Improved compressible hybrid lattice boltzmann method on standard lattice for subsonic and supersonic flows. *Computers & Fluids*, 219:104867, 2021. 189, 194, 199, 210, 215, 221, 228, 229, 255

[226] W. Sutherland. Lii. the viscosity of gases and molecular force. *The London, Edinburgh, and Dublin Philosophical Magazine and Journal of Science*, 36(223):507–531, 1893. 191

[227] W. Bao and S. Jin. High-order i-stable centered difference schemes for viscous compressible flows. *Journal of Computational Mathematics*, pages 101–112, 2003. 193

[228] B.-T. Chu and L. S. Kovásznay. Non-linear interactions in a viscous heat-conducting compressible gas. *Journal of Fluid Mechanics*, 3(5):494–514, 1958. 195

[229] L. S. Kovasznay. Turbulence in supersonic flow. *Journal of the Aeronautical Sciences*, 20(10):657–674, 1953. 195

[230] C. E. Shannon. Communication in the presence of noise. *Proceedings of the IRE*, 37(1):10–21, 1949. 199

[231] T. Astoul, G. Wissocq, J.-F. Boussuge, A. Sengissen, and P. Sagaut. Analysis and reduction of spurious noise generated at grid refinement interfaces with the lattice boltzmann method. *arXiv preprint arXiv:2004.11863*, 2020. 201, 232, 237

[232] G. Coppola, F. Capuano, S. Pirozzoli, and L. de Luca. Numerically stable formulations of convective terms for turbulent compressible flows. *Journal of Computational Physics*, 382:86–104, 2019. 206

[233] A. W. Cook. Artificial fluid properties for large-eddy simulation of compressible turbulent mixing. *Physics of fluids*, 19(5):055103, 2007. 210

[234] S. Guo, Y. Feng, J. Jacob, F. Renard, and P. Sagaut. An efficient lattice boltzmann method for compressible aerodynamics on d3q19 lattice. *Journal of Computational Physics*, page 109570, 2020. 223, 233, 241, 255

[235] D. DHumieres, D. D'Humieres, I. Ginzburg, et al. Multiple–relaxation–time lattice Boltzmann models in three dimensions. *Philosophical Transactions of the Royal Society of London A: Mathematical, Physical and Engineering Sciences*, 360(1792):437–451, 2002. 230

[236] E. Leveque, H. Touil, S. Malik, D. Ricot, and A. Sengissen. Wall-modeled large-eddy simulation of the flow past a rod-airfoil tandem by the lattice boltzmann method. *International Journal of Numerical Methods for Heat & Fluid Flow*, 2018. 232

[237] Y. Feng, S. Guo, J. Jacob, and P. Sagaut. Solid wall and open boundary conditions in hybrid recursive regularized lattice boltzmann method for compressible flows. *Physics of Fluids*, 31(12):126103, 2019. 234, 235

[238] T. Gao, Y.-H. Tseng, and X.-Y. Lu. An improved hybrid cartesian/immersed boundary method for fluid–solid flows. *International Journal for Numerical Methods in Fluids*, 55(12):1189–1211, 2007. 235

[239] Y. Feng, S. Guo, J. Jacob, and P. Sagaut. Grid refinement in the three-dimensional hybrid recursive regularized lattice boltzmann method for compressible aerodynamics. *Physical Review E*, 101(6):063302, 2020. 237

[240] D. Lagrava, O. Malaspinas, J. Latt, and B. Chopard. Advances in multi-domain lattice boltzmann grid refinement. *Journal of Computational Physics*, 231(14):4808–4822, 2012. 237

[241] H. Touil, D. Ricot, and E. Lévêque. Direct and large-eddy simulation of turbulent flows on composite multi-resolution grids by the lattice boltzmann method. *Journal of Computational Physics*, 256:220–233, 2014. 237

[242] F. M. White and I. Corfield. *Viscous fluid flow*, volume 3. McGraw-Hill New York, 2006. 240, 241, 243, 244

[243] N. Frapolli. *Entropic lattice Boltzmann models for thermal and compressible flows*. PhD thesis, ETH Zurich, 2017. 244, 245, 247

[244] M. Hafez and E. Wahba. Simulations of viscous transonic flows over lifting airfoils and wings. *Computers & fluids*, 36(1):39–52, 2007. 245, 247

[245] J. Heberle, G. Wood, and P. Gooderum. Data on sphere and location of detached shock waves on cones and spheres naca tech. Technical report, Note 2173, 1950. 247, 250

[246] K. Hida. An approximate study on the detached shock wave in front of a circular cylinder and a sphere. *Journal of the Physical Society of Japan*, 8(6):740–745, 1953. 247, 249, 250

[247] A. Ambrosio and A. Wortman. Stagnation-point shock-detachment distance for flow around spheres and cylinders in air. *Journal of the Aerospace Sciences*, 29(7):875–875, 1962. 247, 249, 250

[248] T. Nagata, T. Nonomura, S. Takahashi, Y. Mizuno, and K. Fukuda. Investigation on subsonic to supersonic flow around a sphere at low reynolds number of between 50 and 300 by direct numerical simulation. *Physics of Fluids*, 28(5):056101, 2016. 247, 248, 249, 250

[249] Y. Hou, D. Angland, A. Sengissen, and A. Scotto. Lattice-boltzmann and navier-stokes simulations of the partially dressed, cavity-closed nose landing gear benchmark case. In *25th AIAA/CEAS Aeroacoustics Conference*, page 2555, 2019. 251

[250] G. Farag, S. Zhao, T. Coratger, et al. A pressure-based regularized lattice-boltzmann method for the simulation of compressible flows. *Physics of Fluids*, 32(6):066106, 2020. 254

[251] S. Zhao, G. Farag, P. Boivin, and P. Sagaut. Toward fully conservative hybrid lattice boltzmann methods for compressible flows. *Physics of Fluids*, 32(12):126118, 2020. 254

[252] F. Renard, G. Wissocq, J.-F. Boussuge, and P. Sagaut. A linear stability analysis of compressible hybrid lattice boltzmann methods. *arXiv preprint arXiv:2006.08477*, 2020. 255

[253] B. J. Cantwell. Lecture notes: Aa210a fundamentals of compressible flow, 2009. 261, 262

[254] B. Weigand and A. Birkefeld. Similarity solutions of the entropy transport equation. *International Journal of Thermal Sciences*, 48(10):1863–1869, 2009. 261

[255] G. Naterer and J. Camberos. Entropy and the second law fluid flow and heat transfer simulation. *Journal of Thermophysics and Heat Transfer*, 17(3):360–371, 2003. 261

[256] F. Kock and H. Herwig. Entropy production calculation for turbulent shear flows and their implementation in cfd codes. *International Journal of Heat and Fluid Flow*, 26(4):672–680, 2005. 261

[257] H. Herwig and F. Kock. Direct and indirect methods of calculating entropy generation rates in turbulent convective heat transfer problems. *Heat and mass transfer*, 43(3):207–215, 2007. 261

[258] J. Herpe, D. Bougeard, S. Russeil, and M. Stanciu. Numerical investigation of local entropy production rate of a finned oval tube with vortex generators. *International Journal of Thermal Sciences*, 48(5):922–935, 2009. 261

[259] K. Masatsuka. I do like cfd. vol. 1: Governing equations and exact solutions. *Katate Masatsuka, Lulu. com*, 2009. 263

[260] F. Johansson et al. *mpmath: a Python library for arbitrary-precision floating-point arithmetic (version 0.18)*, 2013. `http://mpmath.org/`. 278